TARGETING THE NOVEL CD248-MMRN2-CLEC14A PATHWAY IN AGE-RELATED BONE LOSS

By
Georgiana Neag



UNIVERSITY OF BIRMINGHAM

A thesis submitted to the University of Birmingham for the degree

of

DOCTOR OF PHILOSOPHY

Institute of Inflammation and Ageing

College of Medical and Dental Sciences

The University of Birmingham

April 2022

UNIVERSITY OF
BIRMINGHAM

University of Birmingham Research Archive

e-theses repository

This unpublished thesis/dissertation is copyright of the author and/or third parties. The intellectual property rights of the author or third parties in respect of this work are as defined by The Copyright Designs and Patents Act 1988 or as modified by any successor legislation.

Any use made of information contained in this thesis/dissertation must be in accordance with that legislation and must be properly acknowledged. Further distribution or reproduction in any format is prohibited without the permission of the copyright holder.

ABSTRACT

Resolving the mechanisms underlying bone formation would represent an important advancement to our fundamental understanding of bone homeostasis. We have recently identified a novel interaction between three proteins all with established angiomodulatory proprieties. Namely, we showed that the extracellular matrix protein MMRN2 is a shared ligand by the C-type lectin domain 14 family members CLEC14A and CD248 (1). Here, we explore the role of this interaction in regulation of trabecular bone formation during bone growth. H-type capillaries are a newly identified bone vessel subtype localised in the metaphysis, an anatomically distinct region of the long bone metaphysis where trabecular bone is formed (2). These vessels regulate osteoprogenitor migration to the metaphysis and their subsequent maturation by acting as an architectural and nourishing vascular meshwork. Unfortunately, in spite of the importance of H-type EC-osteoblast cross talk for the migration and maturation of osteoblasts, our understanding of the molecular constituents driving this bidirectional interaction are not yet fully understood.

Using high-resolution confocal microscopy, we imaged murine tibia sections labelled with immunofluorescent antibodies against endothelial cells and immature osteoblasts. Image analysis showed that that genetic deletion CLEC14A results in no alteration of H-type capillaries density or morphology, however, it does lead to shortening of the H-type vascular front in juvenile mice, indicating skeletal maturation-dependent plateauing of H-type vasculature development. In addition, imaging of CLEC14A$^{-/-}$ tibia sections uncovered changes in osteoblast angiotropism, marked by variation in the anatomical distribution of osteoblasts and type I collagen in the murine tibia. Micro–computed tomography and bone length analysis of CLEC14A$^{-/-}$ tibiae revealed increased tibia lengths and elevated trabecular bone parameters

and an elongation of the trabecular bone front in CLEC14A$^{-/-}$ mice in a skeleton maturity stage-dependent fashion. Bulk RNA sequencing of the CLEC14A$^{-/-}$ neonatal pup calvaria revealed enrichment of genes in gene sets related to endochondral ossification and osteoblast maturation in addition to downregulation of mRNA expression of tight junction, extracellular matrix receptor interaction and cell adhesion molecules. *In vitro* culturing of CLEC14A$^{-/-}$ isolated osteoblasts confirmed a change in the status of osteoblast activity in response to induction of mineralisation stimulation. CLEC14A$^{-/-}$ osteoblasts produced more alkaline phosphatase and a higher density of bone mineral nodules in response to osteoinductive treatment. Blockade of the CLEC14A-MMRN2 interactions during bone development or in a disease model of ovariectomy-induced osteoporosis, did not phenocopy the genetic deletion of CLEC14A, indicating that perhaps the role of CLEC14A in bone formation is mediated by interactions with binding partners other than MMRN2. Data presented here provides evidence that CLEC14A plays an important role in regulating signalling in the bone during early postnatal bone development by supporting osteoblast maturation and mineralisation activity. Further research into the molecular mechanisms regulated by CLEC14A and its potential therapeutic translation is therefore warranted.

ACKNOWLEDGEMENTS

Firstly, I would like to express my sincere thanks to the Medical Research Council, Versus Arthritis and the Centre for Musculoskeletal Ageing Research for funding this PhD project. A particular mention must go to Professor Janet Lord for her continuous support and guidance.

I would like to take this opportunity to thank my primary supervisor, Dr. Amy Naylor, for the opportunity to work as part of her group. I am ever so grateful for her advice, patience, knowledge, and guidance throughout this project. Without her constructive feedback and continuous support, the work presented here would not have come to fruition. I would like to express my endless gratitude for her positive way of thinking and for the support offered during harsh times.

I would also like to thank Professor Roy Bicknell, my secondary supervisor, for his time and dedication, specifically for our engaging scientific discussions and general sharing of ideas. His insightful recommendations helped shape the methodology used in many experiments.

I would like to also thank Dr. Vicky Heath, Dr. Jason Turner, Dr. Jennifer Marshal, Dr. David Gardner, Dr. Saba Nayar, Dr. John O'Neil, Dr. Sally Clayton, Charlotte Smith and Isaac Dean for sharing their expertise and enthusiasm for science with me.

Next, I wish to extend my gratitude to all members of the Naylor research group as well as to all members of the Rheumatology Research Group (RRG) past and present for being so welcoming and helpful. I am especially thankful to Dr. Jonathan Lewis and Laurence Hill, for all the constructive early morning experiment discussions in the laboratory and for all their support with method development for this project. Their support helped me grow as a researcher and helped keeping me both motivated and focussed. I am thankful to Melissa Finlay for all the engaging science talks.

Finally, I must acknowledge the support and love of family and boyfriend throughout the past few years. Their constant encouragement has helped me prevail the challenges encountered during my PhD.

TABLE OF CONTENTS

1. **CHAPTER I INTRODUCTION** 1

1.1. The role and anatomy of the skeletal system 2

1.2. Cellular regulators of bone homeostasis 4

1.2.1. Osteoclasts 5

1.2.2. Osteoblasts 6

1.2.3. Osteocytes 8

1.3. Bone embryogenesis – the art of converting cartilage into bone 9

1.4. Bone growth and bone repair in adulthood 12

1.5. The role of the vascular system in osteogenesis and osteoblast angiotropism 13

1.5.1. Key steps and regulators of angiogenesis 14

1.5.2. Characteristics and anatomical description of newly identified bone blood vessel capillaries 15

1.5.3. H-type capillaries – the main drivers of osteoblast migration 19

1.5.3.1. The role of H-type vessels in bone formation 21

1.6. Molecular signatures regulating the EC-Osteoblast crosstalk 24

1.7. Ageing-related changes in bone homeostasis 26

1.7.1. Osteoporosis 29

1.7.1.1. Osteoporosis classification and prevalence 29

1.7.1.2. Osteoporosis aetiology and treatment 30

1.7.1.3. EC-osteblast interaction as a novel target for development of bone anabolic agents? 31

1.8. The role of the extracellular matrix in bone health and disease 33

1.8.1. CD248 35

1.8.1.1. CD248 and pathological conditions 41

1.8.2. CLEC14A 43
1.8.2.1. CLEC14A regulates EC tip cell formation and guides vessel formation directionality 44
1.8.2.1. The role of CLEC14A in endothelial cell migration 45
1.8.2.2. CLEC14A and cell-cell interactions 47
1.8.2.3. The angiostatic role of soluble CLEC14A 47
1.8.2.4. The role of CLEC14A in disease 48
1.8.3. MMRN2 50
1.8.3.1. MMRN2 as a mediator of EC-ECM interactions 51
1.8.3.2. The role of MMRN2 in regulation of angiogenesis via sequestration of VEGFA 52
1.8.3.3. The role of MMRN2 in angiogenesis via interaction with CLEC14A 53
1.8.3.4. The role of MMRN2 in vessel maturation 54
1.8.3.5. Summary 54
1.9. Hypothesis 55
2. **CHAPTER II MATERIALS AND METHODS** 60
2.1. Reagents 61
2.2. Animal models 66
2.3. Analysis of gene expression by bulk RNA sequencing 68
2.3.1. Analysis of RNA sequencing of the H-type and L-EC transcriptome (dataset E-MTAB-4066) 68
2.3.2. RNA sequencing analysis of the CLEC14A-/- and WT neonatal calvarial lysates 72
2.3.2.1. Calvaria lysates and NGS library preparation 72
2.3.2.2. Library sequencing 73
2.3.2.3. Analysis of single cell sequencing publicly available datasets 75
2.4. Flow cytometry 76
2.5. 3D immunofluorescent staining 77

2.6. Mouse calvaria cleaning and immunofluorescent imaging 79

2.1. Bone length measurements 80

2.2. Measurement of metatarsal bone length 84

2.3. Micro-computed tomography 85

2.4. Measuring bone turnover in mice using In vivo calcein labelling 86

2.5. Bone Mechanical testing by Three-Point Bending 90

2.6. Extraction and isolation of calvarial osteoblasts 93

2.7. Osteoblast maturation in vitro assays 95

2.7.1.1. Alkaline Phosphatase activity ELISA 95

2.7.1.2. Alizarin Red staining for bone nodule formation assay 96

2.8. RNA extraction and isolation for RNA sequencing and quantitative real-time PCR (qPCR) 96

2.8.1.1. RT qPCR 97

2.9. Serum analysis of circulating P1NP 97

2.10. Ovariectomy-induced osteoporosis in C57Bl/6J WT and CLEC14A$^{-/-}$ female mice 99

2.11. *In vivo* blocking of CLEC14A MMRN2 interaction during postnatal bone growth and in an ovariectomy-induced osteoporosis model of bone loss 99

3. **CHAPTER III ENDOTHELIAL and OSTEOBLAST CELLULAR MECHANISMS REGULATED BY CLEC14A IN THE GROWING POSTNATAL BONE** 101

3.1. Introduction 102

3.2. Single cell (sc) – RNA sequencing of the bone and bone marrow cells 103

3.3. Bulk RNAseq analysis of H-type ECs transcriptomic signature 106

3.4. Expression of CLEC14A and MMRN2 in the mouse tibia 119

3.5. Exploration of the distribution pattern of H type capillaries in CLEC14A$^{-/-}$ murine tibiae 122

3.6. H-type endothelial cell fractions are reduced in CLEC14A$^{-/-}$ mice 124

3.7. Density of osteoblasts and geographical distribution of immature and mature osteoblasts in CLEC14A$^{-/-}$ tibiae 135

3.8. Discussion 149

3.8.1. Patterns of expression of CLEC14A, MMRN2 and CD248 in the murine tibia 149

3.8.2. Characterisation of the effect of genetic deletion of CLEC14A on the vascular network morphology in the tibia 151

3.8.3. Potential redundancy for CLEC14A in mediation of the angiogenesis process in the bone 154

3.8.4. Acceleration of bone vessel maturation in the CLEC14A-/- tibia 154

3.8.5. Osteoblast and COL1A1 imaging 155

3.8.1. Limitations 157

3.8.2. Conclusion 158

4. **CHAPTER IV THE ROLE OF CLEC14A AND CD248 IN BONE FORMATION DURING BONE GROWTH** 159

4.1. Introduction 160

4.2. Bone length measurements 161

4.3. Trabecular bone in the metaphysis is increased in CLEC14A and CD248 deficient C57BL/6J male mice 166

4.4. Minor cortical differences were detected in male CLEC14A$^{-/-}$ and CD248$^{-/-}$ tibiae 178

4.5. Mechanical testing of cortical bone strength of mouse tibiae and femora 179

4.6. CLEC14A$^{-/-}$ pups are born with more mineralised calvariae 179

4.7. Minimal differences were identified in the trabecular and cortical bone of CLEC14A and CD248 deficient C57BL/6J female mice 184

4.8. Targeting the CLEC14A MMRN2 interaction *In vivo* 192

4.9. Discussion 195

4.9.1. Increased bone elongation in CLEC14A-/- mice 196

4.9.2. Morphometric and biomechanical changes in the CLEC14A$^{-/-}$ and CD248$^{-/-}$ tibia 199

4.9.3. Morphometric changes in the CLEC14A$^{-/-}$ and CD248$^{-/-}$ female tibia 201

4.9.4. Blockade of CLEC14A MMRN2 interaction in 4-week old C57Bl/6J male mice 202

4.9.5. Conclusion 204

5. **Chapter V MOLECULAR MECHANISMS REGULATED BY CLEC14A MMRN2 CD248 INTERACTION IN THE BONE** 205

5.1. Introduction 206

5.2. Bulk RNA sequencing identification of molecular changes in the CLEC14A$^{-/-}$ murine calvaria lysates 207

5.3. Gene set enrichment analysis 208

5.3.1. Differential gene expression analysis 216

5.4. Mining of bone and bone marrow sc-RNA seq dataset to deconvolute cellular sources for the differentially expressed cellular markers in bulk RNA sequencing of CLEC14A calvaria lysates 217

5.5. Assembly of an osteoblast maturation gene signature from single cell RNA sequencing data 226

5.6. Validation of RNA sequencing differentially expressed genes by RT qPCR 227

5.7. Increased mineralisation activity of CLEC14A$^{-/-}$ osteoblasts in vitro 233

5.7.1. Expression pattern of osteoblast maturation genes - RT qPRC 233

5.7.1. Alizarin Red nodule staining 235

5.7.2. P1NP 243

5.8. Discussion 246

5.8.1. Summary and interpretation of molecular and functional changes pertaining to osteoblast maturation in response to CLEC14A deficiency 246

5.8.2. Variation in patterns of expression of genes upregulated in response to osteoblast maturation 247

5.8.3. Changes in ALPL activity in CLEC14A$^{-/-}$ osteoblasts 250

5.8.4. Type I collagen expression in CLEC14A$^{-/-}$ isolated osteoblasts 250

5.8.5. Additional potential biological and functional implications for the enriched or differentially expressed genes identified by bulk RNA sequencing of the CLEC14A$^{-/-}$ pup calvaria 251

5.8.5.1. Predicted changes in vessel permeability in CLEC14A$^{-/-}$ pups 251

5.8.5.2. Alteration of tissue remodelling and bone resorption in the skeletal system of CLEC14A$^{-/-}$ mice 253

5.8.5.3. Changes in the expression of CLEC14A regulators and interacting partners 254

5.8.6. Limitations 255

5.8.7. Conclusion 255

6. THE ROLE OF CLEC14A AND ITS INTERACTION WITH MMRN2 IN BONE LOSS IN OVARIECTOMY INDUCED OSTEOPOROSIS 257

6.1. Introduction 258

6.2. Induction of osteoporosis by bilateral ovariectomy 259

6.3. Trabecular bone analysis of CLEC14A deficient and WT control adult (12-week-old) C57BL/6J ovariectomised mice 263

6.4. Trabecular bone in 12-week-old C57BL/6J ovariectomised mice following treatment with a CLEC14A-MMRN2 blocking antibody 265

6.5. Discussion 268

6.6. Conclusion 270

7. **DISCUSSION** 271

7.1. Bone formation EC-osteoblast communication - gaps in research 272

7.2. Summary of findings 273

7.3. Phenotype comparison to other EC molecules 275

7.4. Mechanism of action 278

7.5. Similarity in mechanism to CD248 281

7.6. Wider impact of this project and further research 283

7.7. Conclusion 287

8. **REFERENCE LIST** 288

9. **APPENDIX** I

9.1. Script for RNA seq QC VI

9.1.1. Quality Control VI

9.1.2. Quantitation of differential gene expression with DEseq2 XV

9.1.3. Heatmap generation code XVIII

9.2. Code for single-cell sequencing analysis of GSE 128423 XXIV

9.3. Published review XXXII

TABLE OF FIGURES

Figure 1.1. Macroscopic bone structure A) Micro-computed tomography reconstructed image of the murine long bone illustrating bone compartmentalisation. 3

Figure 1.2 Bone cell types regulating bone growth..... 10

Figure 1.3 Compartmentalization of the murine long bone and its capillary network. 18

Figure 1.4 Cellular and molecular factors regulating EC- osteoblast crosstalk during bone growth and repair. 28

Figure 1.5 Schematic diagram illustrating the C-type lectin domain group 14 family members' domain architecture and binding partners. 46

Figure 1.6. Illustration of the CLEC14A - MMRN2 - CD248 protein interactions that may facilitate endothelial-osteoblast crosstalk in tibias at bone formation sites.. 56

Figure 2.1 Generation of homozygous CLEC14A and CD248 knock-out mice. Ev mice. 67

Figure 2.2. Diagram of enrichment plot output by GSEA. 71

Figure 2.3 3D high-resolution imaging of mouse tibia sections method workflow. 82

Figure 2.4. High resolution of thick mouse tibia sections 83

Figure 2.5. microCT data acquisition and analysis workflow..... 88

Figure 2.6 Graphic illustration of three-point bending mechanical testing key analysis terms. 91

Figure 3.1. Single Cell RNA sequencing of cells in the bone and bone marrow of 8-10 weeks C57BL/6J male mice (GSE128423).. 104

Figure 3.2 Expression of CLEC14A and MMRN2 in the bone stroma of adult mice (GSE128423). 105

Figure 3.3 RNAseq transcriptomic quality control analysis of bone capillaries (E-MTAB-4066 dataset). A) Schematic demonstrating the experimental process performed and reported by Langen et al. (2017). 109

Figure 3.4 Clustering and gene ontology analysis of H-type and L-type EC RNA sequencing samples (E-MTAB-4066 dataset)..... 110

Figure 3.5 Gene set enrichment (GSE) analysis, enrichment plots show gene sets enriched in H-type ECs compared to L-type ECs..... 111

Figure 3.6 H-type ECs are responsible for the management of the extracellular matrix in the neonatal long bone as identified by gene set enrichment (GSE) analysis..... 112

Figure 3.7 L-type ECs are show enrichment of genes involved in the maintenance of hemopoiesis and inflammation responses in the neonatal long bone as identified by gene set enrichment (GSE) analysis (E-MTAB-4066 dataset). 113

Figure 3.8 Identification of differentially expressed genes between H-type and L-type capillary endothelial cells (ECs) (E-MTAB-4066 dataset). 114

Figure 3.9 Clustering of differentially expressed genes in H- and L-type E*C*s, clusters 1 and 3 (E-MTAB-4066 dataset).. 115

Figure 3.10 Clustering of differentially expressed genes in H- and L-type ECs, cluster 2 (E-MTAB-4066 dataset). 116

Figure 3.11 RNA-seq expression of mRNA transcript values for genes of interest (E-MTAB-4066 dataset).. 117

Figure 3.12 STITCH database mining showing the known interactome of MMRN2 and C-type lectin domain family 14 members. 118

Figure 3.13 Immunofluorescent staining of C57Bl/6J mouse tibia at sites of bone formation. 120

Figure 3.14 Immunofluorescent staining of MMRN2 and CLEC14A in the metaphyseal region of the mouse tibia..... 121

Figure 3.15 High-resolution 3D confocal microscopy of the C57Bl/6J mouse tibia capillary network.. 125

Figure 3.16 High-resolution 3D confocal microscopy of the neonatal WT and CLEC14A$^{-/-}$ mouse tibia vascular network. 126

Figure 3.17 High-resolution 3D confocal microscopy of the juvenile (4-weeks old) WT and CLEC14A$^{-/-}$ mouse tibia capillary network.. 127

Figure 3.18 Characterisation of H-type vessel tube angularity in neonatal and juvenile CLEC14A$^{-/-}$ and WT mice..... 128

Figure 3.19 Characterisation of H-type vessel density in neonatal and juvenile WT and CLEC14A$^{-/-}$ mice. 129

Figure 3.20 Characterisation of H-type vessel coverage in neonatal (P4) WT and CLEC14A$^{-/-}$ mice ... 130

Figure 3.21 Characterisation of H-type vessel coverage in juvenile (4-week old) WT and CLEC14A$^{-/-}$ mice. 131

Figure 3.22 Gating strategy for the flow cytometric analysis of CD31^{high} EMCN^{high} EC. 132

Figure 3.23 CD31^{high} EMCN^{high} EC gating strategy optimised against staining for CD31^{high} EMCN^{high} EC in the spleen, liver and kidney..... 133

Figure 3.24 CLEC14A$^{-/-}$ mice have lower levels of CD31^{high} EMCN^{high} endothelium..... 134

Figure 3.25. Geographical distribution of osteoblasts in neonatal (P4) WT and CLEC14A$^{-/-}$ murine tibia. ding front of the expanding vasculature which are void of osteoblast coverage..... 138

Figure 3.26. Geographical distribution of osteoblasts in juvenile (4-weeks) WT and CLEC14A$^{-/-}$ murine tibia..... 139

Figure 3.27 High-resolution confocal images showing the distribution of osteoblasts in the murine tibia A) metaphysis B) diaphysis. 140

Figure 3.28 Distance of OSX^{+} cells from vessels in the murine tibia metaphysis and diaphysis in juvenile (4-week-old) WT and CLEC14A$^{-/}$ male mice. 141

Figure 3.29 Osteoblast density in neonatal (P4) WT and CLEC14A$^{-/-}$ mouse tibiae 142

Figure 3.30 Osteoblast density in juvenile (4-week-old) WT and CLEC14A$^{-/-}$ mouse tibiae.. 143

Figure 3.31 Characterisation of the osteoblast-covered front in murine tibia sections..... 144

Figure 3.32 Nuclear circularity in neonatal and juvenile WT and CLEC14A$^{-/-}$ mouse tibiae..... 145

Figure 3.33. CLEC14A$^{-/-}$ (4-week-old) mice COL1A1^{+} cell chords extend further down in the inferior metaphysis and diaphysis compared to WT controls. 146

Figure 3.34 Quantification of COL1A1 deposition in the tibia of WT and CLEC14A$^{-/-}$ 4-week-old mice. 147

Figure 3.35 Quantification of the length of type I collagen chords in the juvenile (4-week-old) murine tibia..... 148

Figure 4.1 Body mass and body length measurement methodology outline. 163

Figure 4.2 Bone mass and long bone measurements in CLEC14A$^{-/-}$ vs WT male mice. 164

Figure 4.3 Analysis of bone length in embryonic metatarsal explant cultures of CLEC14A$^{-/-}$ vs WT male mice. 165

Figure 4.4 Diagram illustrating the timepoints utilised for morphometry analyses for C57Bl/6J males and females. 171

Figure 4.5. Quantitative morphometry of trabecular microarchitectural parameters of CLEC14A$^{-/-}$ and CD248$^{-/-}$ vs WT male mice 173

Figure 4.6. Representative µCT analysis transverse plane images starting at the end of the proximal growth plate of 4- and 30- weeks old WT, CD248$^{-/-}$ and CLEC14A$^{-/-}$ male mouse tibias..... 174

Figure 4.7 Trabecular parameter changes in CLEC14A$^{-/-}$ and CD248$^{-/-}$ vs WT male mice. 175

Figure 4.8. Extension of trabecular bone measured from the inferior part of the proximal growth plate to the most distal point in space occupied by trabecular bone towards the diaphysis in CLEC14A$^{-/-}$, CD248$^{-/-}$ and WT male mice..... 176

Figure 4.9. Representative µCT sagittal plane images of trabecular bone of 4- and 30- weeks old WT, CD248$^{-/-}$ and CLEC14A$^{-/-}$ male mouse tibias..... 177

Figure 4.10. Cortical parameter changes in CLEC14A$^{-/-}$ and CD248$^{-/-}$ vs WT male mice tibial midshaft. ative µCT analysis transverse plane images starting at the end of the proximal growth plate of 4- and 30- weeks old WT, CD248$^{-/-}$ and CLEC14A$^{-/-}$ male mouse tibias. 180

Figure 4.11. Increased mineralisation in the postnatal calvaria of P4 CLEC14A-/- male pups. 181

Figure 4.12. Material proprieties of long bones in CLEC14A$^{-/-}$ and CD248$^{-/-}$ vs WT male mice.. 183

Figure 4.13 Quantitative morphometry of CLEC14A$^{-/-}$, CD248$^{-/-}$ and WT female mouse tibia.. 186

Figure 4.14 Representative µCT analysis transverse plane images starting at the end of the proximal growth plate of 4- and 8- week-old WT, CD248$^{-/-}$ and CLEC14A$^{-/-}$ female mouse tibiae. 187

Figure 4.15 Trabecular parameter changes in CLEC14A$^{-/-}$ and CD248$^{-/-}$ compared to WT female mice. 188

Figure 4.16 Extension of trabecular bone measured from the inferior part of the proximal growth plate to the most distal point in space occupied by trabecular bone towards the diaphysis CLEC14A$^{-/-}$ and CD248$^{-/-}$ vs WT female mice. 189

Figure 4.17. Representative µCT sagittal plane images of trabecular bone extent of 4- and 30- weeks old WT, CD248$^{-/-}$ and CLEC14A$^{-/-}$ female mouse tibias. 190

Figure 4.18 . Cortical parameter changes in CLEC14A$^{-/-}$ and CD248$^{-/-}$ compared to WT female mice tibial midshaft. 191

Figure 4.19 Blockade of CLEC14A-MMRN2 interaction in C57Bl/6J 4-week old male mice. 193

Figure 4.20 *In vivo* blockade of CLEC14A-MMRN2 interaction does not affect trabecular bone mass. 4-week-old C57Bl/6J male mice were injected with PBS, an antibody binding to CLEC14A without blocking MMRN2 interactions (C2) or an antibody binding to CLEC14A and blocking its interaction with MMRN2 (C4). 194

Figure 5.1. RNAseq transcriptomic analysis of neonatal WT and CLEC14A-/- calvarial bone lysates . 209

Figure 5.2. Clustering and gene ontology analysis of WT and CLEC14A$^{-/-}$ pup calvaria lysates. 210

Figure 5.3 List of tested gene sets with top enrichment scores identified by GSEA analysis..... 211

Figure 5.4. GSEA heatmap showing the list of leading edge genes enriched at the top of the Hallmark Hypoxia gene set. 212

Figure 5.5. GSEA heatmap showing the list of leading edge genes enriched at the top of the KEGG Tight Junction gene set..... 213

Figure 5.6. GSEA heatmap showing the list of leading edge genes enriched at the top of the KEGG ECM Receptor Interaction gene set. 214

Figure 5.7. GSEA heatmap showing the list of leading edge genes enriched at the top of the Wikipathways Endochondral Ossification gene set. Heatmap presents upregulation of transcripts relevant to endochondral ossification in CLEC14A$^{-/-}$ samples. 215

Figure 5.8. Regulation of the CLEC14A interactome in response to CLEC14A loss of function..... 220

Figure 5.9. Expression levels of genes related to bone resorption. 221

Figure 5.10. Expression of genes regulating bone formation and growth..... 222

Figure 5.11 Patterns of expression of *Col1a1* in the murine long bone (GSE). 223

Figure 5.12 Identification of bone cellular sources for proteins of interest for this project using single-cell sequencing (dataset GSE128423). 224

Figure 5.13. Expression of genes regulating expansion of the vascular bed during bone growth..... 225

Figure 5.14. Expression of master regulators of commitment to osteoblast differentiation in stromal cells isolated from the murine bone and bone marrow..... 229

Figure 5.15 Identification of top markers defining osteoblast subsets. 230

Figure 5.16. Osteoblast maturation gene signature. Dotplot showing gene expression levels across the three different stages of osteoblast maturation 231

Figure 5.17. Analysis of expression of genes linked to osteoblast maturation and osteogenic activity. P4 pup calvarial lysates were subjected to RT qPCR analysis to dissect expression patterns of genes known to regulate commitment to osteoblast lineage and osteoblast maturation, gene expression was normalised to *Gapdh*, shown as arbitrary units (2^-ΔCT). 232

Figure 5.18. Analysis of in vitro osteoblast maturation..... 236

Figure 5.19. No baseline changes in skeletogenic markers gene expression identified between WT and CLEC14A$^{-/-}$ isolated osteoblasts.. 237

Figure 5.20. No significant changes in expression of markers of osteoblast immaturity and lineage commitment over 21 days in culture. 238

Figure 5.21 Tissue non-specific alkaline phosphatase gene expression peaks earlier in CLEC14A$^{-/-}$ isolated osteoblasts. 239

Figure 5.22. Changes in mRNA levels in mature osteoblast markers *Col1a1* and *Bglap* in WT and CLEC14A$^{-/-}$ calvarial osteoblasts over 21 days in culture. 240

Figure 5.23. Proliferation of calvarial osteoblast lineage cells in culture. 241

Figure 5.24. CLEC14A$^{-/-}$ mouse calvarial osteoblasts have increased ALPL activity (ELISA) in response to differentiation stimulation. 242

Figure 5.25. CLEC14A$^{-/-}$ calvarial osteoblasts have an increased bone mineral coverage over 18 days in culture. 244

Figure 5.26. CLEC14A$^{-/-}$ does not affect serum circulating pro-collagen levels (P1NP). 245

Figure 6.1. Induction of osteoporosis by bilateral ovariectomy (OVX). 12-week-old C57Bl/6J female mice were anesthetised, ovaries were removed through a midline laparotomy incision. 260

Figure 6.2. Timeline of trabecular bone loss in 12-week-old ovariectomised C57Bl/6J female mice. 261

Figure 6.3. Timeline of cortical changes in 12-week-old ovariectomised C57Bl/6J female mice tibial midshaft.. 262

Figure 6.4. CLEC14A$^{-/-}$ mice are not protected from ovariectomy-induced bone loss. 264

Figure 6.5. Blockade of CLEC14A-MMRN2 interaction in ovariectomy induced osteoporosis bone loss.. 266

Figure 6.6. Blockade of CLEC14A-MMRN2 interaction does not protect against ovariectomy induced osteoporosis bone loss.. 267

Figure 7.1 Overview of mechanisms of action important for CLEC14A-driven mediation of bone formation..... 282

Figure 9.1 Top markers in single cell RNA sequencing clusters (GSE128423). I

Figure 9.2 Expression of Nes in single cell RNA sequencing clusters (dataset GSE128423). II

Figure 9.3 GSEA heatmap showing the list of leading edge genes enriched at the top of the Regulation of expression of SLITs and ROBOs gene set..... III

Figure 9.4 GSEA heatmap showing the list of leading edge genes enriched at the top of the Osteogenesis Imperfecta gene set. IV

Figure 9.5 GSEA heatmap showing the list of leading edge genes enriched at the top of the Endochondral Ossification in Skeletal Dysplasia gene set. V

TABLE OF TABLES

Table 1. The role of the ECM in bone homeostasis 37

Table 2. Expression patterns and pathological disease associated with CLEC14A, MMRN2 and CD248 57

Table 3 Commonly used solutions, reagents, and biological products 61

Table 4 PCR primers..... 62

Table 5 Antibodies, IF = immunofluorescence, FC = flow cytometry 63

Table 6 Commercial solutions and kits 64

Table 7 Cell culture solutions 65

Table 8 Sample RNA Quality Control (QC) – RNA concentration and integrity were checked before the cDNA library preparation 73

Table 9 DNA library QC – DNA concentration and fragment size 73

Table 10 Definition and description of micro-computed tomography trabecular and cortical morphology analysis..... 89

Table 11. Summary of biomechanical parameters generated from three-point bending analysis 92

Table 12 Micro-computed tomography 3D trabecular bone parameters – males. Not Applicable (N/A) indicates less than 3 measurements, no statistical analysis was conducted. 172

Table 13 CLEC14A$^{-/-}$, CD248 $^{-/-}$ and WT long bones biomechanical parameters of 8-week-old C57BL/6J males. Data is presented as Mean ± SEM..... 182

ABBREVIATIONS

ALPL	Alkaline phosphatase
ADAMTS1	A disintegrin and metalloproteinase with thromobospondin motifs 1
ADAMTS5	A disintegrin and metalloproteinase with thromobospondin motifs 5
ADAMTS15	A disintegrin and metalloproteinase with thromobospondin motifs 15
ADAMTS19	A disintegrin and metalloproteinase with thromobospondin motifs 19
AUC	Area under the curve
BGLAP	Osteocalcin
BMP	Bone morphogenetic protein
BMP2	Bone morphogenetic protein 2
BMP4	Bone morphogenetic protein 4
BERSC	Birmingham Ethical Review Subcommittee
BS	Bone surface
BFR	Bone formation unit
BV	Bone Volume
B.Ar	Bone Area
COL1A1	Collagen type I alpha I
COL1A2	Collagen type I alpha 2
CD	Cluster of differentiation
CLEC14A	C-type lectin domain family 14 member A
CTLD	C-type lectin domain
C.th	Cortical thickness
Cxcl12	C-X-C motif chemokine ligand 12
DNA	Deoxyribonucleic acid
DKK1	Dickkopf WNT signalling pathway inhibitor 1
DLL1	Delta like canonical Notch ligand 1
DLL4	Delta like canonical Notch ligand 4
DMP-1	Dentin matrix protein-1
DMSO	Dimethyl sulfoxide
DCM	Dichloromethane
EC	Endothelial cell
EMCN	Endomucin
ECM	Extracellular matrix
EDTA	Ethylenediaminetetraacetic acid
FACS	Flow activated cell sorting
FGF1	Acidic fibroblast growth factor
FDR	False discovery rate
FBS	Foetal bovine serum
FZD4	Frizzled-4
Gbp	Giga base pair
GSE	Gene set enrichment
GSEA	Gene set enrichment analysis
HUVEC	Human umbilical vein endothelial cells
HA	Hydroxyapatite
Hsp70	70 kilodalton Heat shock proteins

HSPA1A	Heat shock 70 kilodalton protein 1A
HSPA1B	Heat shock 70 kilodalton protein 1B
IBSP	Integrin binding sialoprotein
IDA	Intensity difference analysis
iDISCO	Immunolabeling-enabled imaging of solvent-cleared organs
i.p.	Intraperitoneal
ITGB1	Integrin β1
IGF-1	Insulin-like growth factor 1
KEGG	Kyoto Encyclopaedia of Genes and Genomes
KLF2	kruppel-like factor 2
KLF4	kruppel-like factor 4
LEPR	Leptin receptor
LAMA5	Laminin Subunit Alpha 5
M-CSF	Macrophage colony-stimulating factor
MSC	Mesenchymal stem cell
MMP2	Matrix metalloproeinase-2
MMP9	Matrix metaloproeinase-9
MMP11	Matrix metaloproeinase-11
MMP14	Matrix metaloproeinase-14
MMRN2	Multimerin 2
MAR	Mineral apposition rate
MS	Mineralising surface
NK-kB	Nuclear factor kappa β
NOG	Noggin
NaAz	Sodium Azide
NOTCH4	Neurogenic locus notch homolog 4
N/A	Not applicable
NES	Nestin
ns	Not significant
OPG	Osteoprotegerin
OSX	Osterix
OVX	Ovariectomy
O-glyc	O-linked glycosation site
O.D.	Optical Density
PECAM-1	Platelet endothelial cell adhesion molecule
PDGFA	Platelet derived growth factor subunit A
PDGFB	Platelet derived growth factor subunit B
PDGFR-B	Platelet derived growth factor receptor β
PBS	Phosphate buffered saline
PVP	Polyvinylpyrrolidone
PFA	Paraformaldehyde
PCR	Polymerase chain reaction
NPP	p-nitrophenol
PCA	Principle component analysis
PGP	Proximal growth plate
P1NP	Procollagen type 1 N-terminal propeptide
PC	Principle component
padj	Adjusted p value
RT qPCR	Quantitative real-time PCR
QC	Quality control
RANK	Receptor activator of nuclear factor kappa B

RANKL	Receptor activator of nuclear factor kappa B ligand
RUNX2	Runt-related transcription factor 2
RNA	Ribonucleic acid
RIN	RNA integrity number
RT-qPCR	Quantitative reverse transcription PCR
ROBOS	Roundabout guidance receptors
ROI	Region of interest
rDNA	Ribosomal DNA
RPM	Reads per million
SP7	Transcription factor Sp7
SLRPs	Small leucine-rich proteoglycans
SIBLINGS	Small Integrin Binding Ligand N-Linked Glycoproteins
SPARC	Secreted protein acidic and rich in cysteine
sCLEC14A	Soluble CLEC14A
sMMRN2	Soluble MMRN2
STITCH	Search tool for interactions of chemicals
s.c.	Subcutaneous
SC	Single cell
SLITS	Slit guidance ligands
Spock3	SPARC/Osteonectin, CWCV, And Kazal Like Domains Proteoglycan 3
SOST	Sclerostin
STAR	Spliced Transcripts Alignment to a Reference
SD	Standard Deviation
SEM	Standard error of the mean
TIMP1-4	Tissue inhibitor of metalloproteinase inhibitors 1-4
TGFB1	Transforming growth factor Beta-1
TNF-α	Tumour necrosis factor alpha
tSNE	t-distributed stochastic neighbor embedding
TMB	3,3',5,5'-Tetramethylbenzidine
TV	Tissue Volume
Tb.N	Trabeculae number
Tb.Th	Trabeculae thickness
Tb.Sp	Trabeculae separation
T.Ar	Total bone area
TM	Transmembrane domain
UMAP	Uniform manifold approximation and projection
VEGFA	Vascular endothelial growth factor alpha
VEGFR2	Vascular endothelial growth factor receptor 2
VLA4	Very Late Antigen 4
VE-cadherin	Vascular endothelial cadherin
WT	Wildtype

1. CHAPTER I INTRODUCTION

1.1. The role and anatomy of the skeletal system

Parts of this introduction have also been published in a review paper [(3) Appendix 9.3].

The mammalian skeletal system is highly dynamic and crucial to ensuring architectural and mechanical support to the whole body. In addition, it also confers protection to vital organs, it ensures modulation of metabolic and endocrine responses, and in the case of long bones, it acts as a site for haematopoiesis (4, 5)**.**

Bones are sub compartmentalised into two contrasting structural bone types, a porous cancellous type (trabecular/spongy bone) and a compact solid type (cortical bone) (Figure 1.1). Anatomically long bones are split in four main sections: the epiphysis, growth plate, metaphysis and diaphysis. The epiphysis represents the uppermost and lowermost region of long bones, homing the secondary ossification centre, it is formed of trabecular bone on the interior and cortical bone on the exterior. The growth plate is an avascular region formed of cartilage laid down by chondrocytes and it is located in continuation of the epiphysis at both ends of the bone. Growth plates serve as an interface between the epiphysis and the metaphysis, providing a space which can be expanded and mineralised during postnatal bone growth to allow longitudinal expansion of the bone. The cortical bone envelope forms the exterior part of long bones, allowing the central space of the metaphysis to be populated by trabecular bone and the medial part of the diaphysis to be occupied by the bone marrow (6)(Figure 1.1 A). The structure of cortical bones varies in different animal species, for example, in large mammals and humans cortical bone is composed of osteons which are parallel concentric lamellar units built around a vessel canal (Figure 1.1 C). On the other hand, in rodents, osteons are missing, and cortical bone is composed or mineralised collagen fibres (Figure 1. B and D) (7).

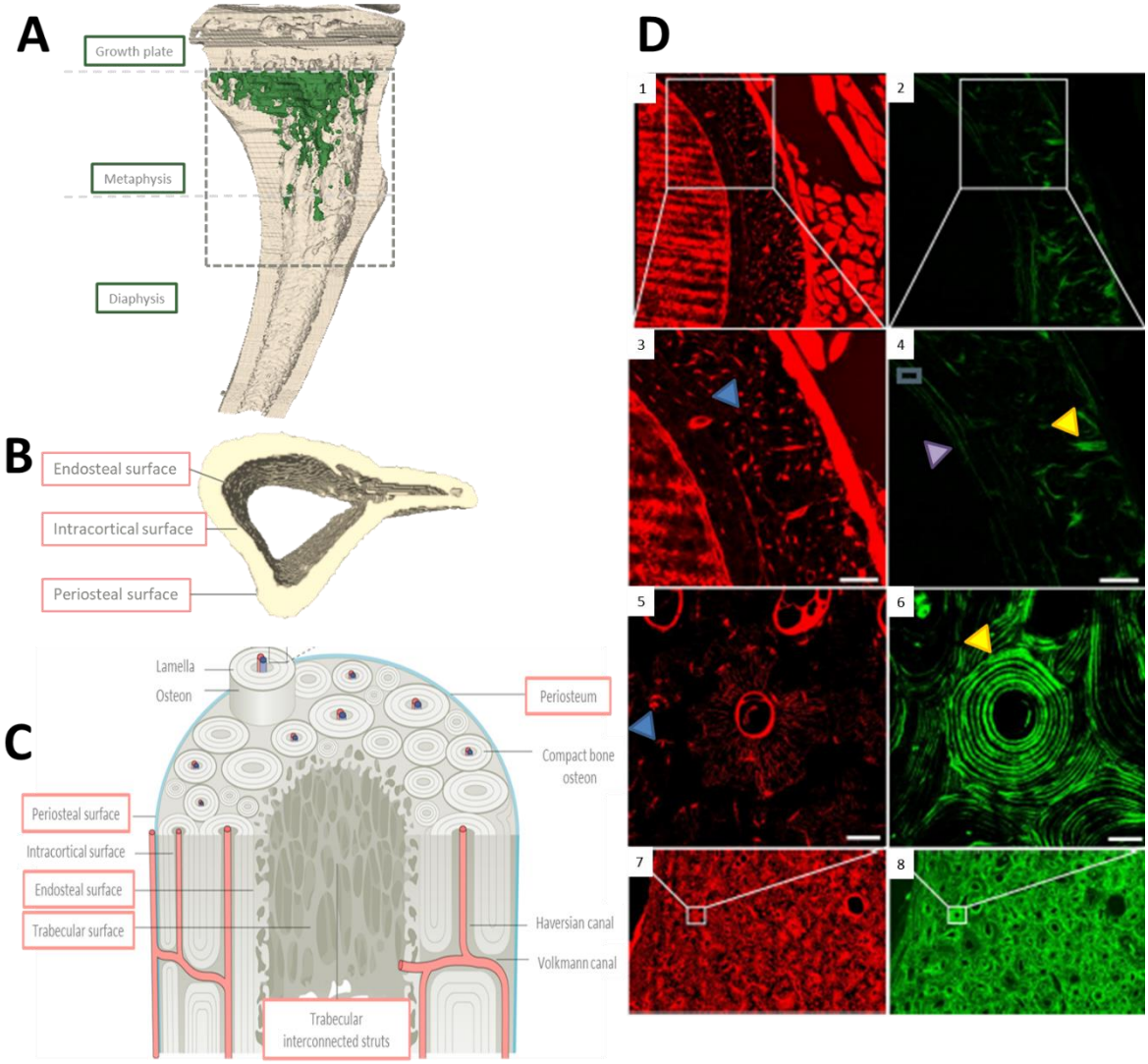


Figure 1.1. Macroscopic bone structure A) Micro-computed tomography reconstructed image of the murine long bone illustrating bone compartmentalisation. **B)** Micro-computed tomography reconstructed axial plan image illustrating the structure of the murine cortical bone. Note the absence the absence of osteons. **C**) Illustration of cortical and trabecular bone anatomy in the human long bone (from Seeman and Martin 2019). Lateral to medial: periosteum, cortical bone, endosteum, trabecular bone. Human cortical bone is organised in osteons whilst trabecular bone is organised in bone plates and struts. **D)** Panels 1, 3, 5, 7 show organisation of the lacuna-canalicular network in the murine and human bone as counterstained with rhodamine, panels 2, 4, 6 and 8 show the organisation of collagen network as imaged with second generation harmonic microscopy in the murine and human bone as labelled. Blue arrow heads indicate osteocytes in the bone cortex, yellow arrow heads indicate collagen fibres in the bone cortex, purple arrow heads indicate collagen fibres in the endosteum (from Moreno-Jimenez et al 2020).

Cortical bone represents the main and most exterior phase of every bone in the skeletal system including: long and short bones, vertebral bodies, the iliac crest and the skull. Trabecular bone is represented by the total sum of a myriad of highly interconnected bone plates and struts which are more sporadically organised than the lamellar units in cortical bone. This multidirectional orientation of trabecular bone plates increases the load carrying capacity of bones exposed to high mechanical stress (8). Whilst cortical bone is stiffer and bears most of the mechanical load in the body, it is also more brittle than trabecular bone (9). Hence, during periods of high mechanical intensity such as the ones induced by locomotion, trabecular bone acts as an additional stress support (10). It comes then as no surprise that trabecular bone is found only in bones that are most exposed to compression and tension loads including: long bones of the arms and legs, vertebral bodies, ribs, and the iliac crest (11). In long bones, trabecular bone extends longitudinally from the distal border of the avascular growth plate into the metaphysis and up to the area where bone marrow resides, the bone diaphysis. Trabecular bone density is highest in the proximal area of the metaphysis, decreasing progressively as trabecular bone extends centrally towards the diaphysis (4, 12) (Figure 1.1 A).

1.2. Cellular regulators of bone homeostasis

Although the predominant appearance of bone matrix is that of a compact mineralised tissue, this unique biomaterial is highly cellular and contains a wide variety of specialised cell types that contribute to its formation, maintenance, and continual remodelling. At a cellular level, all bones are comprised of three main classes of bone cells: bone forming osteoblasts, bone resorbing osteoclasts, and bone-maintenance regulating osteocytes (13). In addition, various cell types with supportive or regulatory roles have been shown to be of tremendous

importance for maintenance of bone homeostasis including but not limited to: endothelial cells (EC), neurons, and stromal cells (14-17). Highly regulated processes establish intercellular communication between bone cells (osteoblasts, osteoclasts and osteocytes) and all the other cell types residing in the bone, to ensure a finely tuned balance between bone resorption and bone formation (14, 18).

1.2.1. Osteoclasts

The major bone-resorbing cell type is the osteoclast (19) (Figure 1.2). Osteoclasts are multinucleated cells formed by the fusion of mononuclear, monocyte or tissue resident macrophage-derived precursors. The main function of osteoclasts is resorption of cartilage and bone matrices. Both processes are independently regulated by two distinct osteoclast subtypes: vessel-associated osteoclasts which drive cartilage resorption during bone growth (20), whereas bona fide osteoclasts (bone-associated osteoclast) regulate resorption of mineralised bone matrix during bone maintenance and repair (20-22). At a molecular level, osteoclast maturation is regulated by secretion of macrophage colony-stimulating factor (M-CSF) and receptor for activation of nuclear factor kappa B (NF-kB) (RANK) ligand (RANKL) (23-28). Mature osteoclasts ensure degradation of the inorganic phase of bone and resorption of extracellular matrix (28, 29). Inorganic matter degradation is accomplished by HCl-mediated acidification of the bone surfaces come in in close contact with osteoclasts (30, 31), whilst breakdown of organic matter is mediated by cathepsin K, a lysosome-derived protease (32, 33). Absorption of degradation by-products are transported into osteoclasts by endocytosis. Once the resorption process is completed, osteoclasts mobilise away from the resorption site and are replaced by bone forming osteoblasts (34).

1.2.2. Osteoblasts

Osteoblasts play the opposite role to osteoclasts, constituting the major bone-forming cell type (19) (Figure 1.2). Osteoblasts are derived from mesenchymal stem cells (MSC) which are situated at the apex of the osteoblast lineage cell hierarchy, differentiating stepwise into osteoprogenitors, bone lining cells, immature and mature osteoblasts, and, ultimately, osteocytes (35, 36). Throughout this document the term pre-osteoblast is used interchangeably with the term osteoprogenitor; both terms define osteolineage committed cells which express transcription factors zinc finger transcription factor SP7/osterix (SP7/OSX) and RUNX family transcription factor 2 (RUNX2).

Osteoblast lineage cells accomplish numerous roles depending on their differentiation state. Osteoprogenitors for instance, constitute a pool of cells from which immature osteoblasts originate and are maintained in a quiescent state until they are required to support bone formation processes during postnatal bone growth, and for bone remodelling or repair (37-39). It is important to note that a clear anatomical and molecular timeline has not yet been established to differentiate osteoprogenitors from immature osteoblasts. This is an important gap in the field because osteoprogenitors constitute a pool of self-renewing bone forming cells which play a significant role in maintenance of bone homeostasis and unfortunately this cell population can be easily depleted following bone anabolic pharmacological intervention. Being able to target bone forming therapies towards stimulation of activity of immature osteoblasts would thus require an in depth understanding of the molecular and spatial characterisation of these two population subtypes. Mature osteoblasts ensure production and secretion of new protein-rich bone matrix and its subsequent mineralisation.

Osteoblast-driven mineralisation is a process split into three chronologically sequential events, each characterised by different molecular signatures. The first phase, osteoblast initial maturation, is marked by type I collagen synthesis, the second phase, maturation of the newly deposited extracellular matrix, is marked by alkaline phosphatase activity, and lastly, extracellular matrix mineralisation is marked by expression of osteocalcin. The role and expression of the osteoblast extracellular matrix is presented in detail in section 1.8. Here, the main markers controlling or marking osteoblast differentiation and maturation are presented. Osteolineage commitment of MSC to osteoblasts is regulated by transcription factors: RUNX2 (40-46) and SP7 (47-51). MSC to osteoprogenitor differentiation occurs during embryogenesis on the outside of the bone cartilage template collar (52). Postnatally, the long bone metaphysis is populated mainly by osteoprogenitors and mature osteoblasts; RUNX2 and SP7 mark osteoprogenitors bound to endothelial cell (EC) capillaries as well as mature collagen expressing osteoblasts (52-54). Once maturation of osteoblasts is initiated by the microenvironmental niche in the metaphysis, osteoprogenitors lose their close connection and proximity to blood vessels and change their activity from a migratory and proliferation orientated one to a collagenous and non-collagenous secretory one (52). The cellular and molecular regulation of this switch has not yet been identified. The organic protein secreted at the highest levels by mature osteoblasts is type I collagen (COL1A1 and COL1A2), this protein forms the architectural matrix template of osteoid (5, 55-58). The second phase of the bone formation process is directed by the effects of alkaline phosphatase (ALPL), which is also secreted by mature osteoblasts and is one of the most abundant glycoprotein in the bone ECM. ALPL is expressed on the surface of mineralising osteoblasts and regulates the early stages of bone mineralisation by controlling propagation of hydroxyapatite in the extracellular matrix on collagenous fibrils (59, 60). ALPL expression in osteoblasts is positively correlated with the

levels of crystallised calcium phases in the bone (61). Osteocalcin (BGLAP) is one of the most abundant non-collagenous proteins in the bone and plays an important role in the mineralisation of the ECM (62-64). Studies with BGLAP deficient mice have demonstrated the critical involvement of BGLAP in alignment of hydroxyapatite crystals to collagen fibrils which is important for bone strength (65). This change is undoubtedly contributing to the reduction in bone strength during mechanic stress reported in these mice, reiterating the importance of BGLAP for efficient formation of bone tissue (66). Following completion of the bone mineralisation phase osteoblasts can either become apoptotic, they can change their phenotype to bone lining cells, or they can encase themselves in mineral matrix and differentiate further to become osteocytes (67). The exact mechanisms regulating osteoblast cell fate at this stage, however, remain largely unexplored.

1.2.3. Osteocytes

Osteocytes are terminally differentiated osteoblasts, entombed within mineralised bone, acting as the main regulatory unit of skeletal homeostasis (Figure 1.2). When some of the mature osteoblasts become completely surrounded by the mineral matrix they produced, they shape a lacuna by remodelling the mineral matrix in their immediate vicinity. The mature osteoblast to osteocyte transition is also accompanied by formation of cellular extensions which develop further and become dendrites. These cellular extensions elongate through canaliculi in the bone and establish a mean of communication with the surrounding environment (68-72). Interconnection of osteocyte lacunae and bone canaliculi leads to formation of the osteocyte lacunocanalicular network which plays a vital role in maintenance of bone homeostasis (73, 74). The lacunocanalicular network ensures maintenance of communication between osteocytes and other bone cells and exchange of nutrients, whilst

also acting as a structure through which osteocytes can respond to mechano-stimulation (75). Mechanosensing is important in this context, because osteocytes are the main regulatory bone cell mediating both bone formation and bone resorption in response to mechanosensing stimuli detected in the bone local environment (76, 77). Osteocytes secrete factors to modulate osteoclast and osteoblast activity, a few key proteins include: sclerostin and dickkopf WNT signalling pathway inhibitor 1 (DKK1) which downregulate osteoblast formation (78-81), or: RANKL and osteoprotegerin (OPG) which regulate osteoclast behaviour, RANKL upregulates osteoclast maturation and activity while OPG prevents osteoclast maturation (75, 82). Additionally, osteocytes also secrete paracrine factors which induce osteoblast-driven bone formation: prostaglandin E2, insulin growth factor 1, free radicals such as nitric oxide and nucleotides such as adenosine triphosphate (83-86).

1.3. Bone embryogenesis – the art of converting cartilage into bone

Embryonic and postnatal long bones are formed and elongated via endochondral ossification, a process by which the pre-existing matrix of avascular cartilaginous tissue is converted into highly vascularised new bone and bone marrow via degradation of the existing matrix and invasion of vessels, osteoprogenitors and hematopoietic stem cell precursors (87-94)**.** By contrast, flat bones form directly (without a cartilaginous template) via intramembranous ossification, a local process during which mesenchymal stem cells undergo differentiation into osteoprogenitors and then osteoblasts (95).

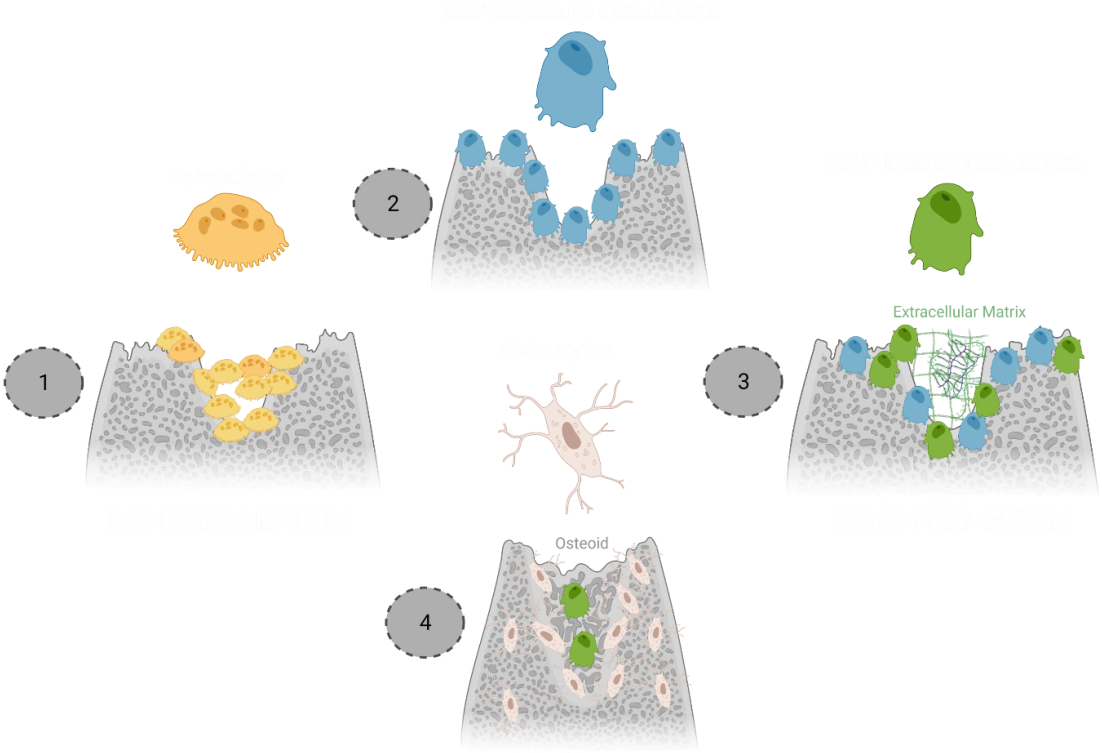


Figure 1.2 Bone cell types regulating bone growth. Bone development is initiated by cartilage template resorption which is moderated by endothelial cells and vessel-associated osteoclasts **(1)** (yellow), endothelial cells not shown; osteoclasts are monocyte-originated phagocytic cells which are stepwise specialised from preosteoclasts into osteoclasts and degrade and engulf the pre-existing cartilage matrix. This first step is then succeeded by migration of osteoprogenitors and immature osteoblasts **(2)** (blue) to areas of new bone formation; osteoblasts are formed by the specialisation of mesenchymal stem cells into osteoprogenitors and then into immature and mature osteoblasts. Immature osteoblasts and osteoprogenitors migrate to sites of bone formation alongside invading blood vessels (not shown). The last phase of bone formation is regulated by matrix-producing mature osteoblasts **(3)** (green), and finally maintenance of bone homeostasis is ensured by the bone master regulator cells – **(4)** the osteocytes (ivory).

In essence, embryonic endochondral ossification originates in the centre of long bones, where the primary ossification centre is formed, extending longitudinally (52, 53). This process starts when MSC successively differentiate into chondroblasts and chondrocytes and generate a cartilage template that will later be used as a matrix for bone deposition (96). The canonical ossification process, subsequent to the laying down of the cartilaginous template, is driven by a plethora of ossification promoting biological signals expressed by the local bone niche and relies on invasion of endothelial cells (EC) into the primary ossification centre (52, 53). Vascular expansion of blood capillaries is concurrent with osteoclast- and septoclast-mediated template degradation, which is facilitated by proteases that gradually dissolve and absorb the extracellular matrix, creating space for expansion of the vascular bed (20, 22, 97, 98). Blood vessel invasion is also coupled with nesting of hematopoietic stem cells in the diaphyseal bone marrow space (94) and with the invasion of Osx^{+} osteoprogenitors which accumulate and localise to the metaphysis (52). A distinct cellular spatial organisation in the bone has been reported for osteoblasts according to their maturation stage (53, 99). Osteoprogenitors and immature osteoblasts act as pericytes, extending their cellular processes and wrapping themselves around vessels in the initial stages of endochondral ossification, whilst mature osteoblasts relinquish their close connection to vessels to migrate a few micrometres away from vessels and to commence their ECM secretory activity (52). Specifically, studies have shown that during migration to sites of bone formation, osteoprogenitors navigate bound to a newly identified and specific capillary vessel subtype - termed H type (2). This exclusive interaction between H-type EC and immature osteoblasts, whose molecular basis is yet to be fully characterised, explains the spatial localisation of osteoblasts in close proximity to endothelial cells in the metaphysis and their absence in the bone marrow space (2). Mature osteoblasts lose their attachment to endothelial cells and have

been reported to localise further away from blood vessels compared to immature osteoblasts which are intimately connected to vessels (52, 53)**.** Mature osteoblasts lay down new osteoid (premineralised bone matrix) in the form of proteins and inorganic material including but not limited to: collagen, the bone sialo protein, osteocalcin, osteopontin, and osteonectin, all which regulate different aspects of the bone mineralisation process (100). The concerted and cumulated actions of all these proteins with hydroxyapatite leads to formation of new bone. The proteomic signature of mature osteoblasts is presented in more detail in a section below (1.8) and in Table 1.

1.4. Bone growth and bone repair in adulthood

After birth, long bones continue to grow longitudinally and radially, until skeletal maturity is achieved, in humans this is marked by the complete ossification of long bone growth plates which is reached at approximately 27-30 years of age (101-103). Murine skeleton maturation is reached at approximately 12-weeks of age, and it constitutes the time point at which peak bone mass is achieved (53). It is worth taking note that growth plates never fully mineralise in mice allowing for continuous bone growth (104-106). In addition to longitudinal and radial growth, bone also requires constant remodelling to support repair of microdamage, damage induced by fractures or to release of Ca^{2+} in the circulation, making it a highly dynamic organ (95).

Postnatal bone growth and remodelling processes also occur through endochondral ossification. Bone growth occurs in a similar manner to the mechanisms that regulate embryonic bone formation, as presented in the section above (1.3) (39). Bone remodelling is controlled by the same three tightly coordinated mechanisms as bone growth: bone resorption, angiogenesis and bone formation, however, bone remodelling happens in the

absence of chondrogenic matrix. If any three of these mechanisms are out of proportion, excessive or abnormal bone maintenance occurs. The first step in the trabecular bone remodelling process is removal of a proportion of the existing bone by mature osteoclasts via breakdown of the mineralised ECM (28, 84, 107, 108). The second step is governed by vessel and osteoprogenitor invasion, which is coupled, this is followed by deposition of new ECM from mature osteoblasts and follows the same mineralisation molecular and cellular pathways as the ones employed during embryogenic bone formation (107, 108). Bone remodelling is more active in trabecular bone areas, as opposed to the cortex, however, with age, remodelling increases at both sites (109). Cortical remodelling occurs both at the endocortical and periosteal surfaces as well as deep within the cortex. At the endocortical and periosteal surfaces, remodelling occurs in a similar manner to the one described for trabecular bone. Within the cortical envelope bone remodelling is mediated by osteoclasts which erode an absorption lacuna shaped tunnel termed the “cutting-cone”, this process is closely followed by the activity of osteoblasts which lay dawn new bone in the “closing cone” (110-113). The main difference between murine and human cortical bone remodelling consists in the absence of Haversian canals. This effectively means that human cortical bone remodelling also implicates the blood vessels localised inside the canals, with vessels acting as conduits of osteoclast and osteoblast delivery. Whilst murine cortical bones are also traversed by vessels, these do not seem to cross the bone longitudinally inside osteons but rather transversely {Jilka, 2013 #156}. In conclusion, bone homeostasis relies on the collaborative actions of osteoclasts and osteoblasts and the coupling of their activities by EC, to adapt to the multiple and asynchronous sites of constant bone remodelling of the skeletal system.

1.5. The role of the vascular system in osteogenesis and osteoblast angiotropism

1.5.1. Key steps and regulators of angiogenesis

The cardiovascular system ensures delivery of nutrients and metabolites, oxygen availability, removal of waste (i.e., CO2) and trafficking of a wide variety of cells using a series of vessels of different sizes and structures (114, 115). The bone vascular network is composed of arterioles, arteries, a large central draining vein, and a myriad of capillaries. The lining of all blood vessels is composed of ECs (116) which accomplish a series of pivotal roles in the vascular system including: vasculogenesis, angiogenesis, vascular maturation and remodelling, vascular tone and blood flow (117). In addition to these traditional roles, the bone vascular endothelium mediates osteogenesis and haematopoiesis by creating niche local environments favourable of these two processes (2, 52, 53, 94, 118-121).

Embryonic and post-natal osteogenesis are preceded by expansion of the existing vascular bed which is accomplished by sprouting angiogenesis. This process is sequential and involves: 1) selection of the tip cells that initiate and lead the vessel sprouting, 2) EC-migration for extension of the sprout and vessel tube formation, connection of sprouts via anastomosis and sprout pruning and finally 3) vessel stabilisation with the aid of osteoprogenitor wrapping around the newly formed vessels (122-126). These processes are regulated by various pathways including vascular endothelial growth factor (VEGFA)- VEGF receptors (VEGFR2) (119, 120, 127-129), NOTCH-NOTCH ligands (DLL1, DLL4, JAG1), B ephrin ligand – Ephrin β receptor (121, 130-132).

1.5.2. Characteristics and anatomical description of newly identified bone blood vessel capillaries

The importance of angiogenesis to osteogenesis coupling has been previously demonstrated, especially in embryogenesis (52, 53, 133-135). However, the precise cellular, spatio-temporal and molecular aspects coupling angiogenesis to bone formation during postnatal bone growth have remained elusive until recently. Kusumbe and colleagues identified three distinct types of blood capillaries in the murine bone with roles in osteogenesis and bone marrow haematopoiesis: type H, L and E capillaries (2, 136). Fluorescent immunolabelling and high-resolution imaging of the bone vasculature have indicated that, in the murine tibia, blood enters the bone periosteum through transcortical vessels which exhibit arterial phenotypes, these vessels exit the cortex at the endosteum and are connected to $CD31^{hi}Emncn^{neg}$ arteries which are in turn connected to $CD31^{hi}Emncn^{neg}$ arterioles (137, 138). Arterioles selectively interconnect with 15-20 µm wide type H or type E vessels (138). Blood from H- and E-capillaries flows into 10-15 µm wide L-type sinusoids which drain into veins, the later converge to collect blood into the central bone sinus (138).

Type H vessels are the most studied of the three capillary subtypes, their presence has been confirmed at various sites in the mouse and human skeleton including: long bones [mouse (2) and human (139)], dental alveolar bones, the spine, sternum, and calvarium [murine (2, 22, 140, 141)]. L- and E-type type capillaries have only been studied in the mouse long bone (94, 136).

These newly identified capillaries can be distinguished according to their quantitative expression of endomucin (Emcn), a marker for non-arterial vessels, and CD31 (PECAM-1), a pan marker expressed amongst other cells on EC (142, 143). Specifically, H- and E-type capillaries can be identified and distinguished from L-type capillaries based on their NOTCH

signalling driven higher expression of CD31 ($CD31^{hi}$) and endomucin ($Emcn^{hi}$) (130, 138, 144). L-type capillaries also express these markers but at a lower-level (2).

Using antibodies to target these two markers and flow activated cell sorting (FACS) analysis, a picture of the dynamic changes in the proportion of these capillaries in the bone was contoured in mice during embryogenesis and postnatal growth (136). Type L vessels are present during both embryogenesis [(from embryonic day (E)16.5)] and in the postnatal long bone in juvenile and adult mice (assessed from birth until 70 weeks of age) (2, 136, 145). The proportion of ECs with the type L phenotype increases steadily from embryogenesis to maturity (32% to 88.9%, at E16.5 and postnatal day (P)28, respectively) (136). On the other hand, type E and H vessels present a contrasting trend, type E capillaries decrease from E16.5 until nearly undetectable at P28 (58% and 2%, respectively), while type H capillaries increase from E16.5 to P6, then decrease at a steady pace until P28 (9%, 26%, and 9%, respectively) (136). During embryogenesis, the majority of vessels in the murine long bone are type H or E capillaries, whereas postnatally, type L vessels comprise the majority of capillary ECs (136). Lineage-tracing experiments have identified type E EC as the most developmentally upstream capillary EC in the bone, constituting the origin of types L and H ECs (136).

During embryonic development bone vasculogenesis is initiated by invasion of the type E vascular plexus into the long bone template which occurs between E15.5 and E16.5. This invasion succeeds initiation of mesenchymal stem cell (MSC) to osteoblast differentiation at E14.5 and precedes initiation of bone formation at the primary ossification centre (52, 146). At birth, type E and H vessels are present in the long-bone vascular bed, occupying the metaphysis and part of the diaphysis, endosteum and periosteum. Postnatally, E-type vessels completely disappear whilst H-type vessels are anatomically restrained almost exclusively to the metaphysis region. A few H-type vessels remain present in the endosteum and periosteum

(2, 136) (Figure 1.3).In the postnatal long bone, type H and L vessels can be distinguished according to their localisation, morphological organisation and increased expression of CD31 and Emcn (136). For instance, type H vessels are organised in columnar and relatively parallel vessel tubes which end in lumenised anastomosis bulges at the caudal point of the avascular growth plate. They also form a highly branched and interconnected vascular web which is interlinked by endothelial cell tubular arches at their proximal end (2, 130, 138)(Figure 1.3).

In the murine long bone, peak type-H vessel density is reached at P6, however, this progressively declines during adulthood and aging in both humans and mice (136, 139, 145, 147).

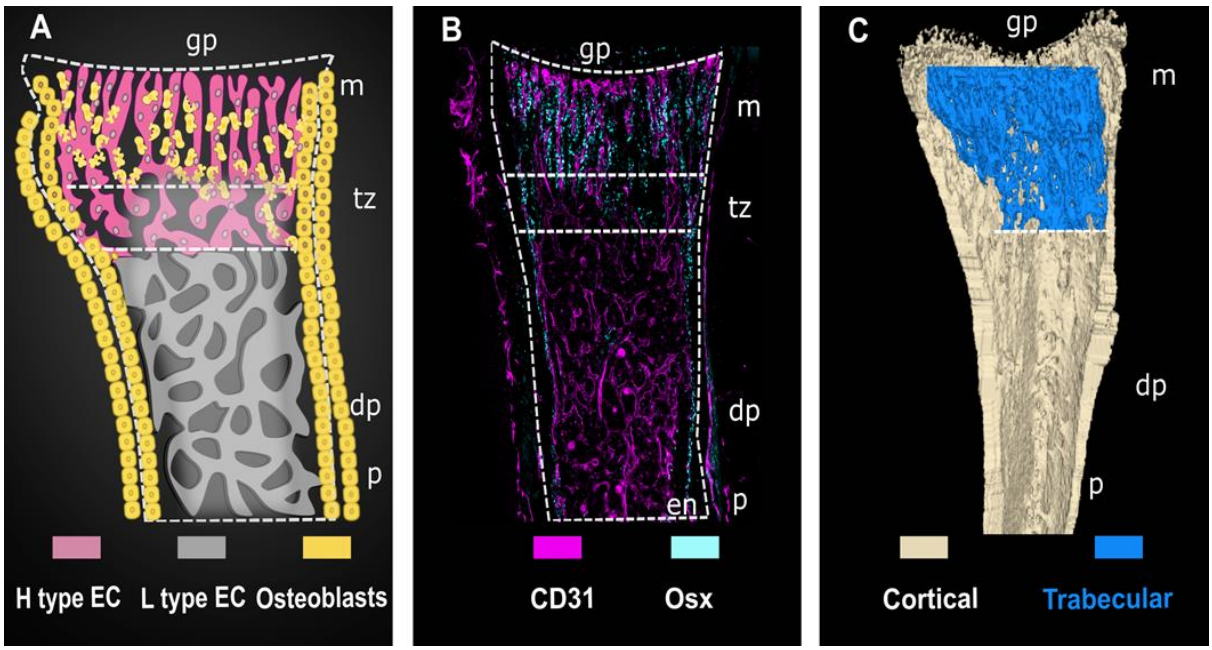


Figure 1.3 Compartmentalization of the murine long bone and its capillary network. H-type vessels are presented with their main interacting partners, Osx+ cells, in the postnatal murine long bone. Left to right: **A)** Schematic diagram illustrates H- (magenta) and L-type (grey) vessels with their distinct morphology and emphasizes the restricted geographical distribution of Osx+ cells to the metaphysis. Osteoprogenitors in the metaphysis (indicated by yellow, irregular-shaped cells) are presented closely associated to H-type capillaries during their migration to sites of trabecular bone formation. Located in the endosteum and periosteum is a pool of skeletal and stem cell osteoprogenitors (indicated by yellow, cuboid-shaped cells). H-type vessels are columnar formations perpendicularly oriented against the lowermost point of the avascular growth plate in long bones. L-type vessels are localised to the diaphysis where they form a sinusoidal hypoxic vessel bed surrounded by bone marrow cells (not represented). H- and L-type vessels form a continuous vascular network; the area where these H-type capillaries begin to converge into L-type capillaries has been branded the transition zone, an area with a vascular web of an intermediate phenotype between these two capillaries. **B)** High-resolution confocal imaging of CD31 and Osx, labelling endothelial cells (magenta) and osteoprogenitors (cyan), respectively. Postnatal day 4 (P4) tibia sectioned on the sagittal plane illustrates the specific localization of bone-forming cells around H vessels in the metaphysis, endosteum, and periosteum. Note the formation of arches and bulges at the caudal point of the growth plate, as previously described. **C)** Illustration of the compartmentalization of the long bone. Pseudocolored, micro-computed tomography, 2D plane snapshot from a 3D bone mesh model. Trabecular bone (blue) is superimposed on cortical bone (ivory). The uppermost and lowermost regions of the long bone start and end at the epiphysis at each end of the bone (not shown). The growth plate is localised at the interface between the epiphysis, and the metaphysis the region where trabecular bone is localised in the long bone (blue). The middle part of the bone, the diaphysis, is void of trabecular bone and houses the bone marrow. Abbreviations: diaphysis-dp, endosteum-en, growth plate-gp, metaphysis-m, periosteum-p, H-type vessel to L-type vessel transition zone-tz.

Whilst the presence of type-H vessels has been confirmed in the endosteum and periosteum, it remains unclear if they fulfil the same functions in cortical bone or if indeed, they are different from the newly identified bone cortex-permeating trans-cortical capillaries (137, 148-150). Similar to H-type vessels, these transitional capillaries connect arterial capillaries to the sinusoid network in the diaphysis (137).

Type L vessels are confined to the diaphysis, where they form a sinusoidal, highly branched, and relatively hypoxic vessel bed which is exposed to low blood shear rates (40 s^{-1}) (138). It is these qualities that provide a suitable environment for immune cell evasion from the bone marrow and into systemic circulation (94) and which also constitute a supportive and regulatory niche to hematopoietic stem cells in the bone marrow (99).

1.5.3. H-type capillaries – the main drivers of osteoblast migration

Longitudinal bone growth is coordinated by blood vessels and bone cells (osteoblasts, vessel associated osteoclasts and septoclasts) (2, 20, 22). In summary, postnatal bone growth is initiated by the expansion of H-type EC capillary bulges into the immediately superior growth plate followed by co-migration of osteoprogenitors alongside vessels (138), this is closely followed by a sustained osteogenic process leading to mineralisation of the newly invaded area (52, 53, 118, 136). Recent studies have shown that the capability of osteolineage cells to traffic to site of bone formation coupled to H-type capillaries is restricted to osteoprogenitors (151). H-type capillaries are the main capillary present in the postnatal long bone which mediates osteoprogenitor trafficking, this is supported by bone imaging data showing that H-type vessels have an exclusive interconnection with osteoblasts, an observation lacking in type-L capillaries (2).

Bone growth is initiated by elongation of type H vessel bulges into the growth plate matrix, a process that requires the extension of EC filopodia into inter-chondrocyte canals (130, 138). The H-type capillary bud-shaped protrusions are built as a polycellular unit composed of EC and perform the equivalent function to EC tip cells whilst vessel bulges represent vessel sprouts (138). The H-type expanding vasculature and the newly identified mesenchymal stem cell-derived septoclasts drive resorption of the chondrocyte-deposited matrix and coordinate removal of dead chondrocytes. This is achieved with the aid of the catalytic activity of a plethora of proteases, for instance, type H EC at the leading edge secrete metallopeptidase proteases such as: matrix metalloproteinases (MMP2, MMP9, MMP11, MMP14), inhibitors of matrix metalloproteinases (TIMP1-4) and disintegrin and metalloproteinase with thrombospondin motif protein family members (ADAMTS1, ADAMTS5 and ADAMTS15) (20). The $FABP5^{+}$ septoclasts located immediately behind the bud-like protrusions also secrete: matrix metalloproteinases (MMP9, MMP11, MMP13, MMP14) and disintegrin and metalloprotease domain family member ADAMTS19 (16). When vessel bed expansion concludes, vessel associated osteoclasts support the union of two neighbouring bulges into a vessel arch (20).

The expansion of the vascular network is subsequently followed by migration of osteoblasts to the newly invaded area. Essentially**,** type-H capillaries act as transporting ships for osteoprogenitors (2), a process also known as angiotropism. This is better defined as the propensity of cells to have an affinity for and move towards and along blood vessels, and was first described in the 1980s in lymphoma migration (152). Osteoprogenitor angiotropism has only been recently characterised in detail (52), however, it has since been further studied to show that osteoprogenitors require a close and direct interaction with EC to be able to migrate (153). To accomplish this, osteoprogenitors extend their cellular processes around invading

blood vessels and migrate towards the direction of expansion of vessels (52, 130). Studies have demonstrated that blood vessels are the *sine qua non* of bone ossification and growth by showing that inhibition of angiogenesis via physical barriers or by blocking VEGFA signalling results in a decreased invasion of blood vessels which is matched by defective recruitment of osteoblasts and osteoclasts (154-157).

Rheology experiments have helped investigate the blood flow in type H and E capillaries which are characterised by high blood velocity and high shear rates (800 s^{-1}, 40 times higher than the one measured in L-type capillaries) (138). The high blood velocity and the high shear rates are probably another contributing factor to osteoblast angiotropism. Migratory osteoblasts exhibit a preference for higher shear stress, which positively correlates with regulation of flow directionality (158). Modelling of low blood pressure through pharmaceutical interventions or artery ligation reduces shear rates and shear stress at the vessel wall, resulting in a decreased density of OSX^+ cells in the metaphysis which is matched by a loss of bone formation capacity (138).

1.5.3.1. The role of H-type vessels in bone formation

Whilst type L vessels constitute the main population of EC in the postnatal bone, it is the H-type vessels that play a major role in bone formation during embryonic development and in postnatal bone growth and repair (141, 144). The osteomodulatory function of type-H vessels is fulfilled by their highly oxygenated status, in addition to a good supply of nutrients conferred by their direct coupling to the arteries in the diaphysis (130). From an anatomical perspective, the reported higher shear rates linked to high blood velocity in types H and E vessels (compared to sinusoidal type L capillaries in the diaphysis) can be explained by their direct connection to arteries and arterioles, which also grants them a highly oxygenated status (138).

Elevated oxygen concentrations (compared to type L capillaries) allow them to meet the greater energy demands of bone formation in the metaphyseal region, which is the site of trabecular bone formation. This is in accordance with the high turnover rate of trabecular bone, making this area more metabolically active than the bone cortex (2, 138).

The functional importance of type-H and -E EC in supporting osteoprogenitor differentiation into immature osteoblasts and subsequently mature osteoblasts has been demonstrated with the aid of EC-MSC co-culture experiments (2, 136). *In vitro* co-culture of H or E type ECs with MSCs has demonstrated that either of the two EC type induced morphological changes in 3D spheroids after 7 days in culture. Specifically, MSCs underwent osteo-lineage commitment in the presence of H- or E- ECs, as confirmed by increased expression of runt-related transcription factor 2 (RUNX2), osteocalcin (BGLAP), and alkaline phosphatase (ALP). Over time, MSC co-cultured with H-type or E-type EC also migrated to the edges of the spheroid, whereas EC condensations formed in the centre (136). This would resemble the incipient stages of vessel formation with an EC central localisation and an exterior coating of the vessel template with blood vessel-adhering pericytes (159-161).

Another seminal study by Langen and colleagues identified that changes in the expression of EC adhesion molecules, such as the ones described by the EC-specific genetic deletion of Integrin β-1 (ITGB1), can also affect osteoblast differentiation and, potentially, angiotropism (136). ITGB1 is a multifaceted integrin that is the component of various integrin complexes including Very Late Antigen 4 (VLA4), a protein with an ascribed role in cell adhesion (162). EC-specific genetic deletion of ITGB1 in mice leads to transformation of type H vasculature morphology, function, and metabolism. Namely, type H vessel columns are shorter, more branched, and lose their specific parallel organization. This is accompanied by a sustained reduction in osteoblast proliferation and a decrease in the highly oxygenated area

characteristic of the metaphysis where type H vessels reside. Changes in the metabolic function of these ITGB1-deficient ECs are also driven by a decrease in the activity of the phosphorylated mitogen activated protein kinase ERK (phospho-ERK1/2) (136). These type H vessel changes coincide with defective bone formation, as exemplified by shorter bones with reduced trabecular bone parameters. Additionally, considering the reported bone shortening alongside contraction of the type H capillary columnar front in ITGB1 knockout mice, abnormal osteoblast angiotropism is also strongly suspected (162).

H-type bone capillaries do not only regulate osteoblast maturation, but they also guide the architectural arrangement of the bone collagenous template in the metaphysis and consequently that of trabecular bone. This is substantiated by previous research demonstrating the link between vascular patterning in the mouse bone and the deposition pattern of bone mineral (163).

Current research into the role played by murine cortical capillaries in bone homeostasis is currently mostly limited to their anatomical and functional characterisation in health (137, 145), warranting further research into their role in modulation of bone pathologies. No major studies have been carried out to investigate the human cortical bone vasculature.

The *in vivo* osteogenic potential of H-type capillaries was functionally confirmed by their ability to induce bone formation when they were boosted in murine models of ageing. Stimulation of angiogenesis and formation of new H-type vessels in response to deferoxamine mesylate treatment, a Hif-1α stabiliser, led to the reintroduction of OSX^{+} cells in the metaphysis and increased trabecular formation (145). Similarly, activation of NOTCH-DLL4 EC autocrine signalling, also resulted in the reappearance of type H vessels, and an enhancement of

trabecular bone parameters (130, 138). The role of H vessels in regulation of osteogenesis has also been tested and confirmed in various murine models. Data published over the past 5 years indicates that H vessels expansion is important for the formation and remodelling of trabecular bone in various parts of the skeleton including: alveolar bone following extraction in young mice and long bone in fracture healing models. Finally, an increase in H-type vessel density is succeeded by increased trabecular bone parameters reversing thus osteoporosis-related bone loss (141, 145, 164). The osteogenic molecular pathways governed by type-H EC with an important role for osteogenesis have been reviewed in the section below (1.6).

Understanding EC heterogeneity in the bone is of uttermost importance given the specialised roles they undertake in maintaining bone formation and resorption as well as haematopoiesis. Furthermore, it is vitally important that changes in the different EC subtypes is studied further in the context of disease, as this currently constitutes the steppingstone to developing new therapies aimed at re-establishing homeostasis in the bone in ageing.

In conclusion, capillaries, including H type vessels are important mediators of trabecular osteogenesis. They support the bone forming process by acting as navigation aids, coupling angiogenesis with osteogenesis.

1.6. Molecular signatures regulating the EC-Osteoblast crosstalk

Unfortunately, in spite of the importance of EC-osteoblast cross talk for the angiotropism and maturation of osteoblasts, our understanding of the molecular constituents driving this bidirectional interaction are not yet fully understood. However, recent studies have begun to underscore gaps in research on this topic.

Whilst the importance of cell-to-cell contact has been proven unequivocally important for osteoblast angiotropism, previous work has indicated that it is not required for osteoblast differentiation by EC, thus beautifully showcasing the importance of EC-secreted factors in driving osteoblast differentiation (165). In these experiments, non-contact co-culture of human umbilical vein endothelial cells (HUVEC) and human osteoblasts also resulted in increased osteoblast differentiation and a sustained rise in secretion of ALP from osteoblasts (165). Work published in the past decade has demonstrated that H-type EC act as positive regulators of osteoprogenitor angiotropism and depending on context as regulators of maturation by secreting soluble factors in their nearby environment (2). PCR analysis of the transcriptomic signature of H-type EC shows that they are indeed extremely metabolically active cells, producing a plethora of well-known mediators of bone growth factors including survival (TGFB1), proliferation (PDGFA and PDGFB) and growth mediators (FGF1) (2). Notably, TGFB1 and PDGFB have proven roles in suppression of osteoblast differentiation (53, 166-170). In order to enable their maturation, osteoprogenitors need to detach and separate from H-type vessels EC interrupting thus the exposure to negative regulators of osteoblast maturation to the like of PDGF-BB and TGFB1 (53, 166, 167).

H-type EC also manage osteoprogenitor differentiation and bone formation depending on NOTCH-DLL4 signalling. In this context NOTCH plays an autocrine role by binding DLL4 on EC, downstream signalling triggers release of noggin (NOG), a secreted antagonist of bone morphogenetic proteins (BMP) to negatively regulate MSC differentiation into osteoprogenitors (130). It is important to highlight that inhibition of this molecular pathway leads to suppression of normal bone formation and growth and causes depletion of $RUNX2^{+}$ preosteoblasts, accumulation of OSX^{+} immature osteoblasts and a decrease in generation of mature osteoblasts secreting osteocalcin (BGLAP) and bone sialoprotein (IBSP) (130).

EC integrins also play an important role in regulation of bone formation. Namely, perturbed osteoblast differentiation was reported in ITGB1-null murine bones, whereby improper osteoblast differentiation and maturation was reported (136). Mutant mice displayed increased density of RUNX2-positive cells and decreased OSX^{+} cell abundance as well as a diminished deposition of proteins secreted by mature osteoblasts or osteocytes (collagen type I and osteocalcin). The same study reported similar but milder observations following genetic deletion of genes coding for the extracellular matrix (ECM) proteins, LAMA5 and osteopontin, suggesting that ECM proteins are key drivers of osteoblast maturation and vascular angiogenesis, an area that warrants further investigation.

Osteoblasts have also been shown to secrete factors that help expanding the H-type vascular bed (145, 171, 172). For instance, recent work indicates that H-type EC, promote VEGF secretion by chondrocytes and osteoprogenitors to support their active expansion into the growth plate during bone growth (145, 171). More recent studies have also identified osteoblast secrete ligands that act in a paracrine manner to influence EC activity. Such a recently unveiled pathway is SLIT3-ROBO1 signalling, which upregulates H-type endothelium levels and as a subsequent effect it also helps increase trabecular bone mass (172).

Figure 1.4 provides a visual summary of the main molecular interaction regulating osteoblast angiotropism and differentiation.

1.7. Ageing-related changes in bone homeostasis

The bone is highly responsive to changes in metabolism, endocrine or cellular signalling. These occur as a function of ageing-related deficiencies and other imbalances impacting mineral availability (173). Ageing cells in the bone become senescent and lose their capability to replace themselves and to function correctly (174, 175). Moreover, in ageing, bone cells are

replaced by adipocytes as mesenchymal stem cells lose their ability to differentiate into osteoblasts (176, 177)**.** This results in a decreased maintenance of the organic and inorganic bone matrixes, affecting the mechanical proprieties of the bone and resulting in a pathologically low bone mass and reduced bone density (178-182).

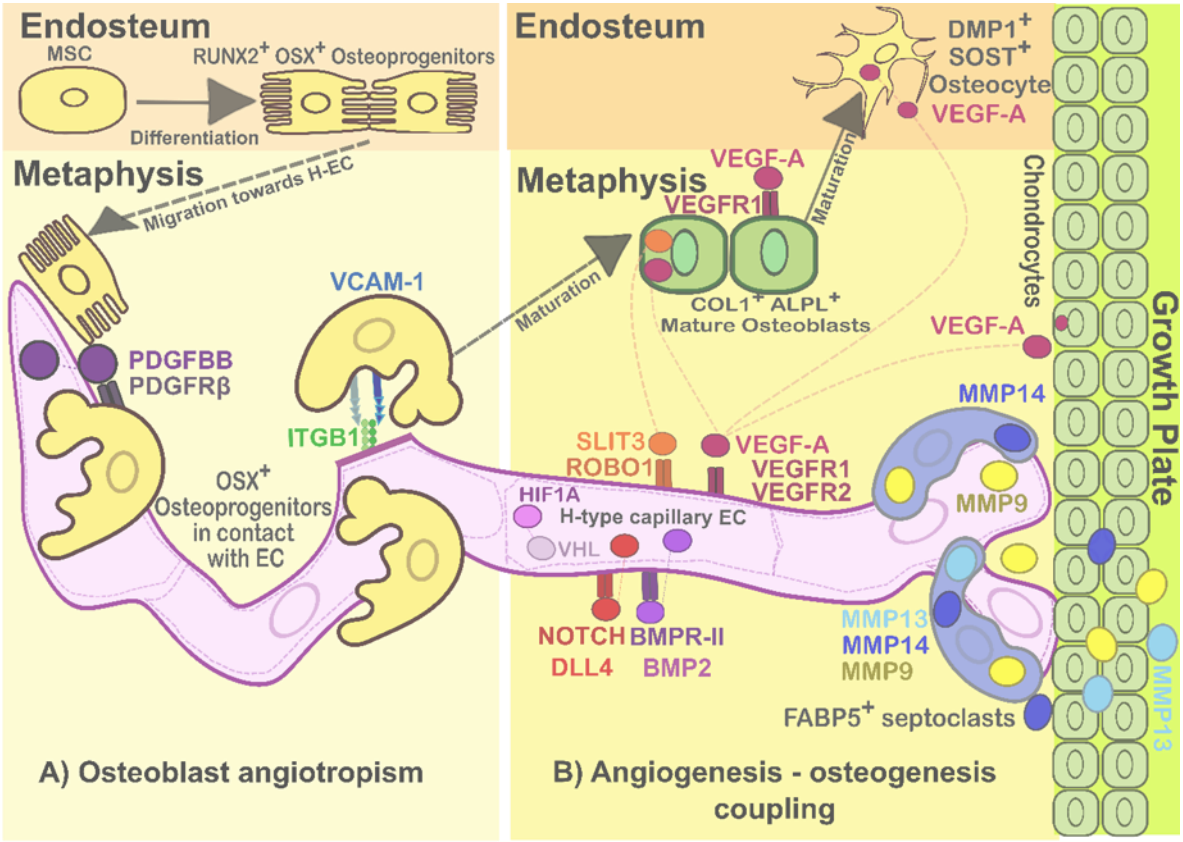


Figure 1.4 Cellular and molecular factors regulating EC- osteoblast crosstalk during bone growth and repair. Schematic diagram illustrates **A)** Osteoblast angiotropism – osteoprogenitors in the bone postnatal bone metaphysis originate from mesenchymal stem cells (MSC) in the endosteum during embryogenesis, H-type capillaries act as guides and support to osteoprogenitors during bone growth. Proliferation-dependent expansion of the Osx^{+} osteoprogenitor pool is moderated by PDGF-PDGFRβ signaling, which acts as a chemoattractant and favours maintenance of a pro-migratory immature osteoblast phenotype. Osteoblast migration to sites of bone formation and repair alongside expanding H-type capillaries is mediated by VLA4-VCAM-1 interactions which facilitate osteoblast angiotropism by enabling anchorage of the osteoblast cell membrane to type-H endothelial cells (EC). **B)** Angiogenesis and osteogenesis coupling is mediated by the independent and concerted signaling of a plethora of pathways including: bone morphogenetic proteins (BMP2-BMPR-II), pro-angiogenic factors: NOTCH1-DLL4 and VEGFA-VEGFR1 / VEGFR2, SLIT3-ROBO1. The angiogenic activity of H-type vessels is important for regulation of osteoblast survival and maturation, all factors presented here upregulate expansion of the vascular bed in the metaphysis and contribute to upregulation of mineralisation of the bone matrix via modulation of osteoblast activity. H-type EC also confer guidance to MSC-derived septoclasts which coordinate matrix and chondrocyte resorption at the metaphysis – growth plate interface during postnatal bone growth, this is accomplished via secretion of various metalloproteinases including: MMP9, MMP13 and MMP14.

1.7.1. Osteoporosis

1.7.1.1. Osteoporosis classification and prevalence

Low trabecular and cortical bone mass and deterioration of the quality of bone are prime characteristics of osteoporosis, one of the most common age-related bone degeneration diseases (183). Osteoporosis is classified into either primary (type I and II) or secondary, depending on its aetiology. Primary type I osteoporosis affects post-menopausal women and mainly results in reduced trabecular bone mass and increased trabecular separation (178, 184-188), whilst primary type II osteoporosis is caused by ageing and results in a decrease of both trabecular and cortical bone mass (189-192). Secondary osteoporosis has been reported in patients on glucocorticoid therapy (glucocorticoid-induced osteoporosis) (193-199) or in patients with limited mobility (disuse osteoporosis) (200-202), whose trabecular and cortical bone microarchitecture deteriorates. Patients with glucocorticoid-induced osteoporosis present with reduced osteoblast maturation and activity which is regulated by an increased SOST production by osteocytes, simultaneously, this is also accompanied by an imbalanced RANKL/OPG ratio which triggers increased osteoclast maturation and thus intense bone resorption activity in the bone (197). This is of uttermost importance for patient quality of life as low bone mass is highly associated with increased fracture risks (203). Osteoporosis is more prevalent in women than men, a 2017 estimation using the novel criteria published by National Bone Health Alliance indicates that approximately 16% of men and 30% of women aged ≥50 years old suffer from osteoporosis. The prevalence increases massively to 46% in men and 77% in women by the age of ≥80 years old (204). Moreover, osteoporosis-related fractures are also predicted to increase by association with the increase in the total number of elderly citizens aged 65 years old and over by 2050 (205, 206). Osteoporosis constitutes a major health crisis

for the near future and is rapidly climbing to the top as one of the ten most costly diseases to treat, mainly due to the difficult diagnosis and reduced treatment uptake.

1.7.1.2. Osteoporosis aetiology and treatment

As previously explained, bone remodelling, a fine-tuned collaborative effort between bone resorption and bone formation processes is constantly required for maintenance of bone integrity. Unfortunately, whilst bone turnover increases in ageing, overall bone remodelling becomes imbalanced, favouring resorption. Whilst activity on the formation front is also increased, this does not keep pace with the resorption rate, resulting in net bone loss (207). Changes like the plummeting of oestrogen (208, 209) and testosterone (188, 210, 211) in the elderly, render the bone porous and fragile making it susceptible to fractures following sustained mechanical stress such as the one induced by a fall (183). This is of great importance, considering that following a fracture, the risk for subsequent fractures in the elderly increases by 86%, making them the major factor contributing to reduced mobility and loss of independence (212, 213). The most common type of osteoporotic fractures are those at the hip, forearm, upper arm and the spine (183).

Effective osteoporosis treatment in the elderly is important to prevent further fractures. Blocking osteoclast activity has been at the forefront of therapeutic strategies, but while this approach prevents removal of existing bone it does not support formation of new one. For this reason, long-term use of osteoclast inhibitors like bisphosphonates can still result in fractures due to the lack of remodelling of the existing bone (214-216). In addition, biphosphonates are associated with side effects that include jawbone osteonecrosis, atypical femur fractures and cancer or atrial fibrillation, respectively, leading to poor medication uptake (217, 218). Whilst this is a small risk and the benefits far outweigh it, a temporary discontinuation after 5 years

of treatment is also recommended, this also results in an increased risk of fracture depending on patients' age and bone mineral density (219, 220).

Currently there is scarcity in bone formation supporting treatment excepting synthetic parathyroid hormone and sclerostin targeting antibodies (221-227). This has occurred due to lack of reliable targets that induce bone formation. Personalised medicine approaches in the bone research field are currently focusing on patient stratification targeting especially subsets of patients which are unresponsive to currently available therapies. Of particular importance would be the development of therapeutical approaches that are gender targeted given the highly discrepant osteoporosis pathobiology mechanisms between different sexes.

1.7.1.3. EC-osteblast interaction as a novel target for development of bone anabolic agents?

Novel findings in the field of bone formation have provided evidence for an important cellular interaction moderating bone formation – the interaction between EC and osteoprogenitors. Kusumbe et al. have shown that trabecular bone formation is reliant on H-type blood vessel expansion during postnatal bone formation (2). To further clarify this paradigm, the same author showed that in ageing, type H vessel numbers are reduced, however, restoration of type H vessels in aged mice was accompanied by increased bone formation, protecting against osteoporosis-induced bone loss (145). Follow-up studies have also demonstrated the existence of a constant cross talk between osteoprogenitors and endothelial cells. For instance, osteoblast secrete SLIT3 which interacts with VEGF signalling mediator, ROBO1, expressed on ECs, to positively regulate both endothelium expansion and bone formation. The potent role of SLIT3 was evidenced during bone growth and in murine models of ovariectomy-induced osteoporosis and fracture. Administration of exogenous SLIT3 to mice with an open femoral

midshaft fracture results in an increase in bone vascularisation matched by an augmentation of callus bone volume, resulting in stiffer bones which are able to withstand higher mechanical forces. Likewise, bi-weekly intravenous SLIT3 injections in 7-week-old C57Bl/6J females is protective against osteoporosis-related bone loss, treated mice exhibited higher trabecular bone mass and thicker cortical bones (172).

1.8. The role of the extracellular matrix in bone health and disease

The bone EC extracellular matrix (ECM) has recently started to gain attention as a key regulator of bone homeostasis, however, the precise mechanisms mediating these processes have remained unidentified thus far (228). The bone ECM is composed of inorganic material such as calcium and phosphate (calcium carbonate, calcium phosphate, apatite) and trace elements, as well as organic material such as collagen (type I, III and V, all these three types constitute up to 90% of all collagenous organic material in the bone) and non-collagenous proteins (proteoglycans, glycoproteins, γ-carboxyglutamate-containing proteins and small integrin-binding ligands N-linked glycoproteins) (229-231). The highest proportion of ECM in the bone is deposited by osteoblasts during their maturation process and is made up of both inorganic and organic compounds (232). The organic component of the ECM has been ascribed roles in all stages of bone homeostasis including bone mineralisation and bone degradation, influencing most cellular processes from cell proliferation to cell maturation(233-235). Additionally, the bone ECM is able to interact with cell surface receptors and can bind and store tissue growth factors (PDGFB, TGF-β, IGF-I), bone morphogenetic proteins (BMP4, BMP2) and cytokines (TNF-α) near bone formation or resorption sites as and when required (236, 237). Moreover, much of the osteolineage cell-derived ECM has been identified by immunolabelling and biochemical studies in close association with collagen fibrils, acting sometimes in opposing manners by promoting or limiting bone formation and other times also conferring redundancy for one another (Table 1).

Type I collagen (COL1A1) is an ECM molecule which plays a vital role in shaping the bone environment. COL1A1 is the most important collagenous protein in the bone as it constitutes the architectural foundation to bone development; as demonstrated by COL1A1 genetical

deletion in cell populations most involved in its production (osteoblasts and fibroblasts) (238). COL1A1 has a triple helical structure composed of two α1 and one α2 COL1A1 chains. The COL1A1 trimer is produced intracellularly as a propeptide - type I procollagen, which is then secreted extracellularly and then cleaved to produce mature COL1A1. Once in the extracellular space, COL1A1 forms protein aggregates giving rise to collagen fibrils and through further crosslinking fibrils form large bundles of fibres (238). Organic bone ECM mineralisation is a stepwise mechanism which is initiated by the secretion of calcium ions (Ca^{2+})-enriched osteoblast-derived vesicles localising to the pre-laid organic matrix, mineralisation of these vesicles requires formation of hydroxyapatite (HA) crystal nuclei inside vesicles, a process relying on Ca^{2+} binding to phosphate ions (PO_4^{3-}) (59). Phosphate is released from nearby phosphate containing compounds under the action of ALP(239, 240). Excessive formation of crystals leads to disruption of the vesicle membrane which results in spreading of HA crystals in the surrounding ECM (241). A summary of the cellular source of the osteolineage ECM and the respective cellular mechanisms affected by bone cell-originated ECM proteins is presented in Table 1.

Whilst the ECM deposited by osteoblasts has been extensively studied, resulting in an improved understanding of their biology and role in pathogenesis, the EC ECM remains largely understudied in the context of bone homeostasis. The ECM surrounding blood vessels is a recognised modulator of local niche environments ensuring vascular homeostasis and endochondral bone formation (136). Deposition of ECM proteins around vessels creates an adhesive stratum which acts as a scaffold used by cells to actively migrate, a process also known as angiotropism (242-245).

A recently identified pathway brings forward evidence for an extracellular matrix protein, multimerin 2 (MMRN2), which could explain osteoblast angiotropism on ECs. A novel protein-

protein interaction and signalling pathway, initially described by Khan and colleagues, provides a potential molecular explanation for the close proximity of osteoprogenitors and immature osteoblasts to H-type endothelial cells (1). Specifically, we hypothesise that EC and osteoprogenitors could be engaging in cell to cell contact with the aid of a three protein complex: CLEC14-MMRN2-CD248. Spatially this protein complex is organised as follows: EC-expressed CLEC14A binds the ECM protein MMRN2 which concomitantly binds immature osteoblast-expressed CD248, warranting thus further investigation (1) (Figure 1.5). Co-localisation of CLEC14A, MMRN2 and CD248 was initially confirmed in pancreatic tumour sections immunolabelled with fluorescent antibodies which co-localised in areas where ECs and pericytes were present (1).

Both CD248 and CLEC14A are C-type lectin domain (CTLD) group 14 members, alongside CD93 and thrombomodulin (Figure 1.5). CTLD group 14 proteins are part of a superfamily comprising 17 families of CTLD containing superfamily. CLEC14A and CD248 in particular have been postulated as regulators of embryonic and pathologic angiogenesis, cellular adhesion and migration, immune responses and tumour metastasis (246-249). MMRN2 is an ECM glycoprotein secreted by ECs whose role has been ascribed to angiogenesis modulation (both angiostatic and pro-angiogenic) (250), partly due to its interaction with CLEC14A but also due to its ability to sequester VEGFA (250). All these three proteins have been nominated as part of the tumour angiogenesis signature and their expression is upregulated in progressing mouse tumours, making them important targets for the mediation of angiogenesis (251, 252). Each member of this interaction is described in more detail below (sections: 1.8.1, 1.8.2, 1.8.3).

1.8.1. CD248

CD248 (TEM-1, endosialin) is a type 1 transmembrane glycoprotein which is highly expressed on cells of mesenchymal lineage in the embryo with the earliest expression confirmed at embryonic day 9.5 in the: cephalic mesenchyme, genital tubercle, mesonephros, whisker follicles, mesenchymal tissues around the eye, lung as well as the spinal cord (253, 254). The expression of CD248 has been reported on capillary pericytes, embryonic fibroblasts, tumour stromal fibroblasts, sub-lining synovium fibroblasts, and immature osteoblasts (246, 248, 255-257). A detailed summary of patterns of expression of CD248 is presented in Table 2. CD248 has not been detected in leukocytes and osteoclasts (255).

It is important to note that CD248 expression in mesenchymal cells is transient and dependent on cell differentiation or activation state. For instance, single cell RNA sequencing of the bone mesenchyme confirmed Tem1 (the gene encoding for CD248) RNA expression in perivascular immature osteoblasts but not on extracellular matrix producing mature osteoblasts (258). Furthermore, CD248 expression is generally diminished postnatally, but can be induced by hypoxia inducible factor-2α (259), or in the stromal compartment of organs affected by inflammatory diseases or cancer (Table 2). CD248 can interact with a vast array of ECM proteins including collagen I and IV, fibronectin, Mac-2 BP/9 Mac-2 BP/90K.0K, and MMRN2 (1, 249, 260, 261). Manipulation of CD248 expression (256, 262, 263) helped portray CD248 as a protein mediating a plethora of cellular processes including: adhesion (262), sprouting angiogenesis (247), pericyte and fibroblast migration (248, 260) and proliferation (87, 246, 248, 260, 262, 264-268).

Table 1. The role of the ECM in bone homeostasis

Extracellular component	Expression	Cellular mechanisms affected	References
Collagen (I, III, V)	Expressed by most stromal cells, type I collagen is mostly expressed by fibroblasts and mature osteoblasts	Formation of collagen fibrils and fibres, important for bone mechanical proprieties.	(163, 269-271)
Proteoglycans Small leucine-rich proteoglycans (SLRPs)	**SLRPs** Mostly expressed by mesenchymal lineage cells including osteoblasts	Cell proliferation, growth, and apoptosis Angiogenesis Osteogenesis Potentiation of WNT/β-catenin and BMP/SMAD signalling. Osteoclast maturation. Organic matrix and mineral deposition. Collagen formation and mineralisation. Collagen fibril diameter. Collagen fibril shape.	(236, 272-281)
γ-Carboxyglutamic Acid-Containing Proteins	**Osteocalcin (Bone Gla protein),** binds strongly to hydroxyapatite crystals in the mineralized matrix (282) . Secreted by mature osteoblasts and osteocytes (283)	Insulin secretion. Ca metabolism and Ca incorporation in hydroxyapatite. Negative regulator of collagen crosslink maturity.	(63, 284-286)
	Matrix Gla Protein secreted by osteoblasts, osteocytes, chondrocytes	Regulator of osteoblast proliferation, differentiation, and maturation. Upregulation WNT/β-catenin signalling. Inhibition of osteoclast differentiation, positive regulator of early endothelial differentiation	(287-290)

	Periostin secreted by fibroblasts, osteoblasts and pre-osteoblasts, periosteal stem cells	Pre-osteoblast adhesion to ECM and reduced migration, proliferation, and differentiation, collagen fibril formation and folding, bone growth, upregulation WNT/β-catenin signalling	(291-298)
Small Integrin-Binding Ligand N-Linked Glycoproteins (SIBLINGS)	**Osteopontin,** potent inhibitor of bone matrix mineralisation (299) Secreted by osteoblasts and osteoclasts (283)	Negative regulator of bone formation and mineralisation. Down regulation of osteoblast proliferation and differentiation. Upregulation of osteoblast adhesion. Upregulation of collagen fibril formation Inhibitor of apatite mineral crystal formation co-dependent to osteocalcin. Bone marrow mesenchymal and hematopoietic stem cell recruitment and adhesion. Downregulation of proliferation of bone marrow progenitors and upregulated commitment to myeloid/granulocytic lineage during embryonic development. EC migration	(63, 300-314)

	Dentin matrix protein-1 (DMP-1) Secreted by osteocytes, odontoblasts	Stem cell and immature osteoblast cell attachment, proliferation and differentiation, matrix mineralisation, osteocyte maturation, regulation of phosphate metabolism, hydroxyapatite formation, docking of integrin receptors.	(315-323)
	Osteonectin (SPARC) Secreted by osteoblasts, odontoblasts, fibroblasts, hypertrophic chondrocytes, endothelial cells, macrophages (283)	Enhancer of collagen fibril formation and its mineralisation depending on p38 signalling, fibroblast proliferation, down regulator of cell attachment and spreading linked to inhibition of focal adhesion formation, down regulates cell proliferation	(324-331)
	Bone sialoprotein, positive regulator of bone, nucleator of bone hydroxyapatite crystals (332). Secreted by osteoblasts, hypertrophic chondrocytes, and osteoclasts	Enhances osteoblast differentiation, stem cell commitment to osteogenic lineage, ECM mineralisation, hydroxyapatite formation, osteoclast differentiation and activity, haematopoiesis, bone vascularisation, binds metalloproteinases and regulates their activity	(333-337)

At a mechanistic level these outcomes were linked to the CD248-mediated regulation of platelet derived growth factor receptor β (PDGFR- β) downstream signalling in mesenchymal lineage cells (247, 260, 264). This was demonstrated with the aid of CD248 gene silencing, or antibody-mediated blocking of the CD248 C-type lectin domain (CTLD) experiments, which resulted in obstruction of PDGF-BB – PDGFRβ - mediated responses (261). The regulation of PDGFRβ signalling by CD248 was confirmed in fibroblasts and osteoblasts by data published by our group and others (255, 264). Functionally, CD248 deficiency in fibroblasts is accompanied by a change in cellular and molecular responses to PDGF-BB and TGF-β stimulation and is characterised by diminished cell migration and decreased cell-to-cell adhesion (256).

Of particular interest for this project is the ability of CD248 to regulate bone formation (255). CD248 is expressed by osteoblasts, and its genetic deficiency results in decreased osteoblast migration (scratch wound healing assays, data generated in the Naylor group, not published), and an increased osteoblast maturation resulting in higher bone mass in mice that are CD248-null (255). The stimulation of osteoblast maturation in CD248 deficiency osteoblasts was partially explained by a perturbation in PDGF-BB-PDGFR-β signalling (255). Interestingly, the exact same changes in osteoblast maturation and bone mineralisation were also reported following the genetic deletion of PDGFR-β in osteoblasts, whereby impaired PDGFR-β signalling results in differentiation of osteoblasts alongside an increased bone mineral deposition (53).

In spite of the demonstrated ability of CD248 to bind to ECM proteins (338), the precise effect of CD248 on the interaction of osteoblasts with the EC ECM or whether this directly regulates osteoblast migration has not yet been investigated in detail.

Data published to date thus characterises CD248 as an instrumental governor of mesenchymal lineage cells mitogenic and migratory capacity and a key regulator of osteoprogenitor maturation. Of particular importance for bone formation, CD248 acts as an important controller of PDGFR-β signalling to help maintain osteoblasts in an immature state. Establishing whether CD248 is of vital importance for osteoblast migration alongside blood vessels during postnatal bone growth and warrants further research.

1.8.1.1. CD248 and pathological conditions

CD248 also plays a role in the regulation of angiogenesis and vascular homeostasis. Genetic deletion of CD248 *In vivo* results in sustained neovascularisation and increased vascular density in the retina (339) and in renal fibrosis (265) in mice. The vessel density changes were not permanent, and this observation was explained by a self-resolving delay in vessel regression (339)**.** To extend upon this knowledge, additional work was conducted using explanted aortic mouse ring experiments. These studies reported that increased vascularisation corresponded to aberrant sprouting angiogenesis (339). Genetic deletion of CD248 was associated with sprouting of longer but more disorganised vessels with increased branching points compared to wild-type controls; this was linked to reduced vessel pruning rather than increased vessel sprouting (339). Furthermore, another tumour angiogenesis study reported ablation of endothelial cell/pericyte-driven vessel tube formation and downregulation of cellular migration in the absence of CD248 (246). This was accompanied by a sustained reduction in tumour invasion and growth (256, 263, 340). *In vivo* experiments by Nanda and colleagues provide evidence of a site-dependent tumour angiogenesis response in $CD248^{-/-}$ mice, with unaltered growth of subcutaneous tumours but diminished growth in

orthotopic colon tumours (263). The observations reported for CD248 deletion in relation to tumour growth could be a downstream effect of ineffective angiogenesis.

Expression of CD248 on pericytes during tumour angiogenesis also favours tumour metastasis by favouring tumour cell – pericytes cell-to-cell contact and leading to tumour cell intravasation (340). Due to the correlation between high expression of CD248 and increased incidence of metastasis and decreased survival rates in cancer patients, CD248 is now considered a strong candidate biomarker for metastasis (341, 342).

Our group has also demonstrated that CD248 deficiency in the muscle results in a total failure to induce sprouting angiogenesis in response to an acute muscle overload model (247). In contrast, no angiogenesis changes were reported in response to CCl4 – induced liver injury in CD248 knock out mice (264).

CD248 also mediates inflammation in a site specific manner. For example, CD248 blockade the joint in murine models of rheumatoid arthritis is marked by lower levels of proinflammatory cytokines, fewer leukocyte aggregates in the joint and a decrease in bone and cartilage damage (256, 343). No effect on inflammatory responses was reported in liver injury, with no changes in the numbers of leukocyte infiltrates in CD248 knock-out mice (264), reinforcing the idea of organ dependent mediation of responses.

In summary, CD248 is a protein that plays a multitude of roles both in health and disease. It mediates angiogenesis, cell adhesion, proliferation, and migration. Of particular interest for our group CD248 negatively regulates bone formation, CD248-null mice presented with higher trabecular bone mass and stronger bones, making it an interesting therapeutic target for bone anabolic therapies.

1.8.2. CLEC14A

CLECL14A is a single pass, cell surface, sialoglycoprotein with a profile of expression limited to ECs (344). The structural domains contributing to the structure of CLEC14A are presented in Figure 1.5 A. A detailed summary of patterns of expression of CLEC14A is presented in Table 2. In brief, during embryonic formation CLEC14A is expressed by endothelial progenitor cells and EC (345); the earliest detectable expression of CLEC14A has been reported in whole mount sections of murine embryo at E10.5 (346, 347). Postnatally, CLEC14A is highly expressed on human and murine endothelial cells of different tumours but its expression is low or absent on the vasculature of healthy tissues. Absence of CLEC14A staining was reported in human: breast, prostate, kidney, thyroid, bladder, liver, and ovary tissue sections, whilst CLEC14A staining was observed in adjacent tumour tissue (252, 345, 346, 348). Very low levels of CLEC14A have also been reported in the healthy adult mouse brain, retina, liver, lungs, lymph nodes and ears (346, 347).

CLEC14A expression at mRNA and protein level were confirmed *in vitro* in different human endothelial cell types (mRNA: human umbilical vein endothelial, human dermal microvascular endothelial cells (345), protein expression: human outgrowth endothelial cells, human umbilical vein endothelial cells and human umbilical artery endothelial cells) (346). No CLEC14A transcripts were identified in peripheral blood mononuclear cells or hepatocytes, reiterating the fact that expression of CLEC14A is exclusive to endothelial cells (123, 349).

CLEC14A is a relatively promiscuous protein with multiple interacting partners. Previous work has shown that CLEC14A can interact with a variety of ECM molecules including: LAMA4, LYRIC, (350) heparin and heparan sulphate glycans to the like of HSPG2 (351), and MMRN2 (1, 348).

1.8.2.1. CLEC14A regulates EC tip cell formation and guides vessel formation directionality

Increased cellular production of CLEC14A and that of its cognate ligand MMRN2 occurs in EC which actively undergo neoangiogenesis or angiogenesis (345, 347, 348, 350, 352). Specifically, CLEC14A is highly expressed during cell spreading and endothelial tube formation, suggesting an important role in tip cell polarisation and filopodia formation to guide directionality of the newly forming vessel tube (345, 346, 348, 353). This was confirmed by further studies which have indicated that CLEC14A expression is polarised on the plasma membrane at cell junctional regions on the leading edge of migrating cells during wound scratch-induced angiogenesis (346, 354). CLEC14A genetic deletion has also been reported to result in defective sprouting angiogenesis. This has been confirmed by *in vitro* endothelial aortic ring experiments and *in vivo* implantation of subcutaneous sponges (348). In both instances, CLEC14A deletion resulted in impaired sprouting angiogenesis. In aortic ring experiments, CLEC14A deficient aorta slices were characterised by an endothelial sprout outgrowth with fewer and shorter EC tubes formed in response to VEGFA stimulation over 7 days (348). Likewise, a severe limitation in vascular invasion was reported in subcutaneous sponges implanted in CLEC14A-null mice in response to stimulation with basic fibroblast growth factor (348).

Conflicting reports have been published regarding the effect of CLEC14A knock out or loss of function on filopodia formation in EC. Knock down or antibody-driven targeting of CLEC14A *in vitro* in HUVECs resulted in a reduction in filopodia formation (345, 346, 348, 353). In contrast, a follow up study has reported increased filopodia formation in the postnatal day 5 mouse retina and in aortic ring experiments in response to genetic deletion of CLEC14A (347). The reasoning behind these opposing results have not yet been encoded, however, incongruency in the outcomes of these studies might stem from use of mice with different genetic

backgrounds. In contrast to this observation, upregulation of finger-like extensions in in HUVEC were reported when overexpressing CLEC14A (353).

1.8.2.1.The role of CLEC14A in endothelial cell migration

CLEC14A also regulates endothelial cell migration, for instance, CLEC14A knock out has been shown to downregulate HUVEC migration (*in vitro*) (345, 348). Ki et al. have shown that antibody-mediated blockade of the CLEC14A CTLD mimic the results reported in genetic deletion of CLEC14A and results in a 44% - 54 % reduction in the migratory capacity of HUVEC cells (353). Providing further strength to the theory that CLEC14A is a of vital importance for EC migration, subsequent studies have shown that overexpression of CLEC14A on COS-7 fibroblast-like cells, results in increased migration of cells and a more rapid wound healing in scratch assays (353). Mechanistically, CLEC14A has been shown to regulate migration by mediation of cell-to-cell adhesion interactions via its cell-surface expressed C-type lectin domain (CTLD) (346, 353). Altogether these experiments indicate that migration of EC is regulated by CLEC14A depending on interactions with its CTLD which is expressed on EC surface (1, 348).

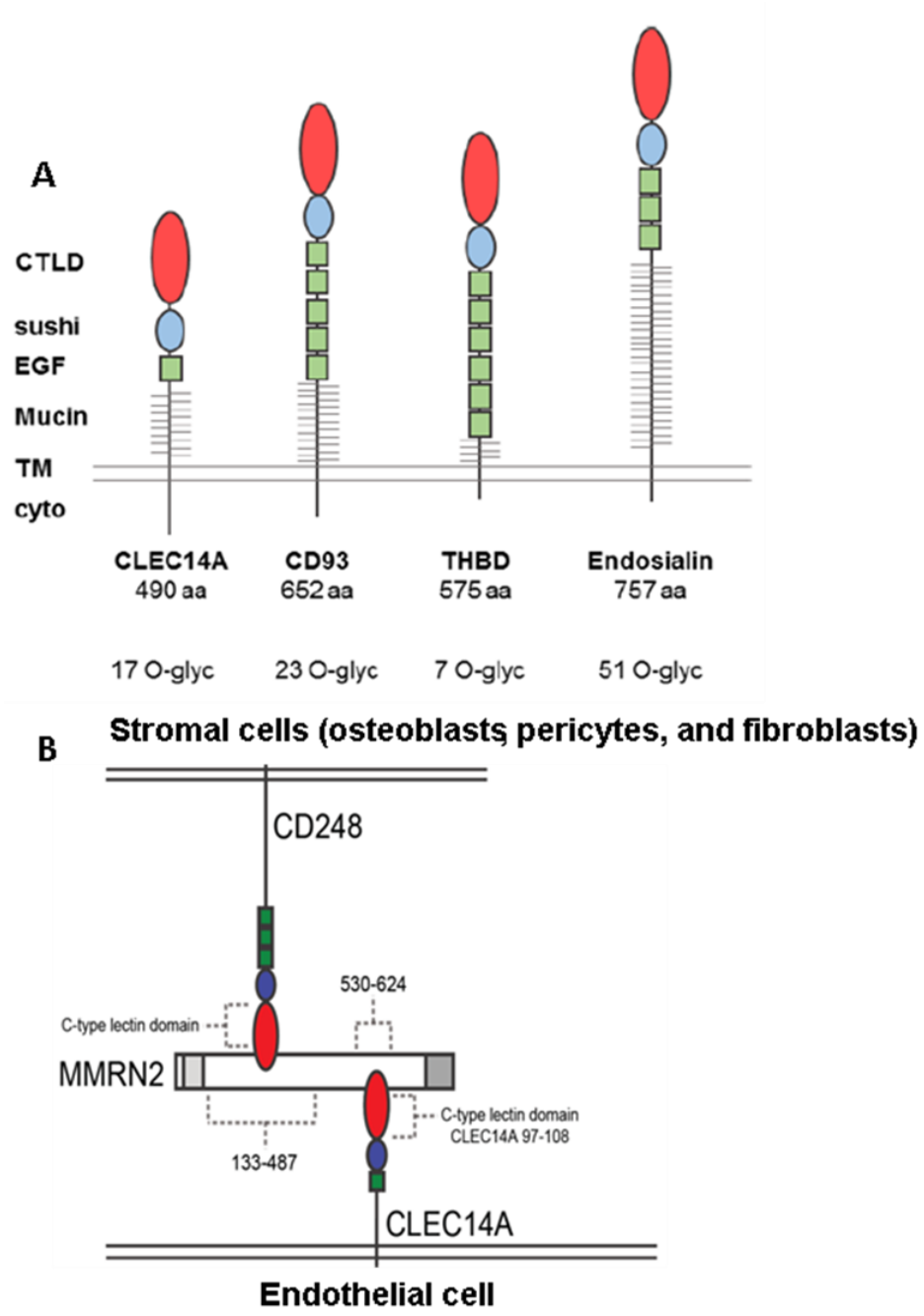


Figure 1.5 Schematic diagram illustrating the C-type lectin domain group 14 family members' domain architecture and binding partners. A) Diagram of regional organisation of C-type lectin domain family 14members, all CLEC14A family members are composed of (from N- to C-terminals): a C-type lectin domain (CTLD) (red), one sushi sequence (blue), a variable number off epithelial growth factor (EGF)-like domain repeats (green), a variable length mucin-like region [(predicted O-linked glycosylation sites (O-glyc) are presented underneath each mucin-like region)], a transmembrane domain (TM), and short cytoplasmic tail (cyto). **B)** Diagram illustrating simultaneous binding of CLEC14A and CD248 to shared ligand MMRN2. CLEC14A binds MMRN2 in its non-glycosylated coiled-coil domain region, between amino acids 530 and 624, CLEC14A binds MMRN2 at its CTLD domain. CD248 also binds MMRN2, via the CTLD, between amino acids 133 and 487 (1). It is important to note that mouse CLEC14A binds mouse MMRN2 in the same region (between amino acids 495 and 674, not shown here).
Diagrams were adapted after a previously published thesis (355).

1.8.2.2. CLEC14A and cell-cell interactions

Overexpression of CLEC14A, triggers the formation of cell-to-cell aggregates, partly owing to the interaction of the CLEC14A CTLD domain with the heat shock protein HSP70-1A (356). siRNA-mediated silencing or polyclonal antiserum-dependent blocking of CLEC14A have both been shown to downregulate angiogenesis processes in HUVECs, resulting in reduction in the ability of EC to form tubes, a decline in cell migration and a decrease of vascular branching (345, 346, 348, 353).

CLEC14A expression is also critical in vessel stabilisation due to mediation of cell-to-cell interaction between EC and pericytes. Namely imaging data has shown CLEC14A to be expressed at the interface of ECs with pericytes (252) and genetic deletion of CLEC14A has been accompanied by decreased adhesion of pericytes to ECs which rendered the blood vasculature highly permeable (347).

1.8.2.3. The angiostatic role of soluble CLEC14A

The extracellular domain (including the CTLD) of CLEC14A can be cleaved. Rhomboid-like 2 protein cleaves CLEC14A making it soluble (sCLEC14A) (354). sCLEC14A binds to endothelial tip cells resulting in downregulation of sprouting angiogenesis in HUVEC spheroids as well as in a reduction in EC migration. *In vivo* experiments have documented the spatial localisation of sCLEC14A establishing its local retention via binding to the ECM protein MMRN2 in direct competition to cell-bound CLEC14A. Further ex vivo (aortic ring explants), *in vitro* (HUVEC spheroids) and i*n vivo* (subcutaneous sponge barrel studies) confirmed the angiostatic role of sCLEC14A, which essentially phenocopied the CLEC14A knock-down and knock-out data (348, 354), resulting in a decline in sprout formation in HUVEC spheroids, a diminishment in tube

formation in aortic explants, and a reduction in cellular invasion and a decrease in vessel density in subcutaneous sponge barrel experiments following treatment with sCLEC14A (354).

1.8.2.4. The role of CLEC14A in disease

CLEC14A has been most studied in the context of cancer, and it is now a recognised player in mediation of tumour development. Clinical studies have reported the association between increased CLEC14A levels in some cancers including: non-small human lung carcinoma or bladder cancer and improved clinical outcomes (357, 358). No significant correlation between CLEC14A expression and clinical outcomes was reported in ovarian and breast cancer patients (359, 360). These diverging observations might reflect a tumour type specific effect of CLEC14A on tumour growth, or it might stem from differences in methodologies and samples size across different studies.

Increased CLEC14A expression in bladder cancer and renal clear cell carcinoma was also correlated with higher levels of vascular density and increased infiltration of immune and stroma cells into tumours, offering a potential expression for the improved clinical outcomes observed in patients with high expression of CLEC14A (358, 361). Data reported from *in vivo* moused models of tumour growth have demonstrated that CLEC14A loss of function by genetic deletion hinders Lewis lung carcinoma tumour growth by preventing vessel formation (345). Whilst the lack of CLEC14A expression has been shown to downregulate angiogenesis processes leading to a restriction on tumour growth, it currently remains unclear how CLEC14A expression favours cancer survival. It is plausible to theorise that the expression of CLEC14A on EC tip cells drives sprouting angiogenesis resulting in better vascularisation and improvement of the tumour vasculature function, allowing for efficient immunoclearing and drug targeted clearing of tumour cells.

CLEC14A is also an attractive target for treatment of solid tumours due to its specific expression on EC of the tumour vasculature and due to its lack of expression on EC of vascular beds in healthy tissues (345, 346). Targeting CLEC14A in tumour vasculature with the aid of CAR T cells can be achieved safely and effectively (362). CAR T cell targeting of CLEC14A inhibited tumour growth in Lewis lung carcinoma, Rip-Tag2 and mPDAC mouse models of cancer by reducing tumour vascularisation (362).

In a different disease context, CLEC14A upregulation was identified in aortic plaques in areas of disturbed flow (363) (not published, data was produced in the Bicknell group). This could be explained when taking in consideration regulation of CLEC14A expression mechanisms. Specifically, CLEC14A is upregulated in response to low shear stress (345), or during hypoxia (364). It is therefore expected for CLEC14A to be expressed in the aorta considering the well-recognised disturbed flow patterns of blood downstream atherosclerotic plaques or at bifurcation sites (364). Upregulation of CLEC14A has also been identified in inflammatory conditions such as rheumatoid arthritis (unpublished data from the Naylor group), however, the functional role played by CLEC14A in these conditions, currently remains understudied, warranting further research. Of interest for our project, disease-gene association database mining indicated a strong association between CLEC14A and diffuse idiopathic skeletal hyperostosis, a systemic condition characterised by ossification of the joint as well as urolithiasis (365, 366).

All these data helped build a profile for CLEC14A as one of the main players in the so-called tumour angiogenesis signature (251, 367, 368). In addition, the role of CLEC14A in pathogenic angiogenesis outside the realm of cancer research is slowly gaining more attention, proposing an overarching influence of CLEC14A in the regulation of sprouting angiogenesis and blood

vessel homeostasis in different contexts, making it worthy of vasculature targeting for anti-angiogenesis therapeutic interventions.

1.8.3. MMRN2

MMRN2 is an extracellular matrix protein secreted by EC, upon secretion MMRN2 forms MMRN2-rich protein complexes to build an intricate fibre network in juxtaposition with blood vessels (250, 355). A detailed summary of patterns of expression of MMRN2 is presented in Table 2.

During mouse embryogenesis, MMRN2 is expressed in the developing spinal cord starting with E 10.5 (253). Additionally, MMRN2 is expressed at high levels in the central nervous system and brain tumours (369). MMRN2 has multiple interacting partners including: LAMA4, fibronectin, CD248 and MMRN2 (355).

The most studied protein interactor for MMRN2 is CLEC14A, previous work by our group uncovered the role played by MMRN2 in docking molecules to moderate cell-to-cell proximity by non-mutually exclusive binding CLEC14A and CD248 (1). This was confirmed in an ELISA revealing that CD248 can bind MMRN2 which in turn can still interact with CLEC14A. This novel interaction provides a new molecular explanation for the proximity of mesenchymal lineage cells to the like of pericytes and osteoprogenitors, to ECs. Co-localisation of CLEC14A, MMRN2 and CD248 was confirmed using human pancreatic cancer tumour sections probed with antibodies against CD248, CLEC14A and MMRN2, showing that antibody labelling of the three proteins decorated areas covered by ECs and pericytes (1). The functional characterisation of the interaction between CLEC14A and MMRN2 is presented in more detail below in section 1.8.3.2.

1.8.3.1. MMRN2 as a mediator of EC-ECM interactions

Functionally, MMRN2 acts as a moderator of EC interactions with the ECM. For instance, MMRN2 has been shown to increases HUVEC adherence (355, 370). Follow up studies have provided evidence that HUVEC adherence is mediated via interaction between MMRN2 and CLEC14A (1). However, it remains unclear if interactions between MMRN2 and CD93 mediate the same function and if so, whether redundancy exists between CLEC14A and CD93 in binding MMRN2. Previous work published by our group has indeed confirmed binding of CLEC14A and CD93 to MMRN2 in the same region of MMRN2 which was determined to be located between amino acid sequence 530 and 624 (1) (Figure 1.5). Additional work has also confirmed that CD93 genetic deletion and blockade of the CD93-MMRN2 interaction mirrors the same observations published for CLEC14A genetic deletion in EC and blockade of CLEC14A-MMRN2 interaction, resulting in reduced sprouting angiogenesis-dependent vascularisation of the retina i*n vitro and in vivo (371).* The theory that redundant mechanisms for the activity of CLEC14A exist has been postulated before. Namely, whilst CLEC14A knock down in zebra fish embryos results in defective formation of vessels and a severe phenotype, characterised by defects in intersomitic and dorsal longitudinal anastomotic vessels (345) and delays in sprouting angiogenesis-dependent development of intersegmental vessels (352), its genetic deletion in mice presents with no obvious vascular defects, making even the homozygous deletion of this gene compatible with life (346, 348). Recent work has confirmed the ability of CD93 to interact with MMRN2 providing a molecular explanation for the redundancy observed in CLEC14A deficient mice (371-373). Further studies are warranted to inspect whether or not CLEC14A and CD93 bind to exact same region on MMRN2 and if binding to CLEC14A or CD93 confers redundancy for angiogenesis processes.

1.8.3.2. The role of MMRN2 in regulation of angiogenesis via sequestration of VEGFA

Contrasting roles have been ascribed to MMRN2 in angiogenesis. On one hand, in high similarity to the observations reported for sCLEC14A (354), soluble MMRN2 (sMMRN2) has been shown to downregulate angiogenesis and tumour development by hindering EC migration and by preventing EC tube formation (1, 370, 374). This was partly explained by the ability of MMRN2 to bind VEGF-A hence sequestering it away from EC (370, 374), but also due to its binding of CLEC14A (1). sMMRN2 has a demonstrated ability to impair migration of EC towards a VEGF chemotactic stimulus. Functional assays have reported disturbed EC migration in wound healing assays in addition to decreased EC tube formation in matrigel assays in response to treatment with sMMRN2 (370, 374). In addition, the same study also reported similar angiostatic observations for sMMRN2 with EC-fibroblast cocultures and 3D organoids, aortic ring assays and *in vivo* in vessel development models using chorioallantoic membrane chicken embryo assays (370, 374). sMMRN2 treatment in all three assays resulted in a decrease in vessel density (370, 374). To further understand this interaction, the same study confirmed that sMMRN2 inhibits angiogenesis by preventing binding of VEFGA to its receptor, VEGFR2 (370, 374). This was confirmed by the capability of MMRN2 to displace radiolabelled VEGFA bound to VEGFR2 in a dose dependent manner and without the need of any other proteins expressed on ECs. Ectopic overexpression of sMMRN2 in i*n vivo* tumours resulted in distancing of MMRN2-bound VEGFA from vessels (370). The effect of sMMRN2 on VEFGA-VEGFR2 interaction is also reflected by the ablation of VEGFR2 phosphorylation following incubation with VEGF-A and MMRN2. In contrasting effect, MMRN2 deficient mice are characterised by increased phosphorylation of VEGFR2 at Tyr949 (370).

In vivo experiments have reported that treatment with sMMRN2 resulted in intra tumoral vessels that were less dense, less mature, and presumably less functional (374).

Reinforcing the angiostatic role of MMRN2, opposite functional observations were reported following downregulation of MMRN2 expression with the aid of siRNA resulting in increased cellular migration. siRNA-mediated silencing or genetic deletion of MMRN2 also resulted in downregulation of tight junction and adherens junction molecules in EC (VE-cadherin, actin, ZO-1, JAM-A), interfering both with their numbers and extracellular localisation (370, 375). Functionally, this change in expression of cell adhesion molecules also resulted in increased EC monolayer permeability and increased EC interspacing (375).

The role of MMRN2 has also been investigated *in* vivo, B16F10 melanoma tumour cells injected subcutaneously in the flank of MMRN2-null mice formed tumours with an increased number of collapsed vessels (375). The blood vessels in these tumours were also smaller, improperly covered by pericytes, poorly vascularised and leaky, leading to intra-tumoral haemorrhage and increased intra-tumoral hypoxia (375). Moreover, a poor response to cisplatin anti-cancer treatment was reported in tumours in MMRN2-null mice compared to WT controls. This is likely to be linked to poor intra-tumoral vascular function leading to reduced distribution of treatment across the tumour.

1.8.3.3. The role of MMRN2 in angiogenesis via interaction with CLEC14A

Noy and colleagues proposed a contrasting pro-angiogenic role for MMRN2 in connection to its interaction with CLEC14A; their study and a follow up report have shown that blocking of CLEC14A-MMRN2 interaction downregulates angiogenesis responses in tumours (1, 348). To confirm this, the binding of MMRN2 to CLEC14A was blocked and results replicated the

observations reported for CLEC14A deficiency. Namely, blocking of the CLEC14A-MMRN2 interaction downregulated angiogenesis and reduced tumour growth (348). Using *in vitro* assays downregulation of HUVEC tube formation, and of sprouting angiogenesis and upregulation of vessel branching were reported in response to blockade of CLEC14A-MMRN2 interaction. Antibody-mediated blockade of CLEC14A and MMRN2 interaction was also investigated *in vivo in vivo* and resulted in reduced cellular infiltration and decreased vessel density in subcutaneous sponge barrel experiments as well as decreased tumour growth and diminished vascular density in a Lewis Lung Carcinoma tumour model (1, 348). The opposite effects of MMRN2 on angiogenesis reported by this report might be explained by the independent regulation of angiogenesis by CLEC14A-MMRN2-CD248 and VEGFA-MMRN2 interactions, as two separate mechanisms.

1.8.3.4. The role of MMRN2 in vessel maturation

In addition to the VEGFA decoy role ascribed to MMRN2 by research presented above, MMRN2 has also been attributed a role in vessel maturation. Imaging of the P5 neonatal mouse retina in MMRN2 deficient mice has provided evidence of a decrease in blood vessel pericyte coverage accompanied by an increase in vascular leakage in FITC-dextran and Evans Blue experiments (375). Pericyte adhesion to EC could be intermediated through interactions between and its ligand CD248 which is expressed by pericytes and has already been shown to regulate pericyte recruitment (246). It is thus possible to posit that MMRN2-CD248 interactions are important for vessel stabilisation at the end of the angiogenetic process.

1.8.3.5. Summary

In summary, CLEC14A, MMRN2 and CD248 regulate different aspects of angiogenesis in health and disease. MMRN2 acts as a molecular glue binding to both pericyte and osteoblast-expressed CD248 and EC-expressed CLEC14A, bringing the two cell types close together. Pairing this with the well-known role of CD248 in pericyte recruitment, the CLEC14A-MMRN2-CD248 interaction is likely important in vessel stabilisation following angiogenesis. In addition, as we have previously shown that CD248 regulates osteogenesis, we argue for an additional role for the CLEC14A-MMRN2-CD248 pathway in bone homeostasis. Recent data provides additional credence to this hypothesis showing that immature osteoblast angiotropism on H-type vessels is invaluable for effective angiogenesis-dependent bone repair (53, 118). However, data pertaining to the molecular interaction linking ECs and osteoblasts is scarce and it is still unclear which are the main players regulating skeletal endothelium-osteoblast crosstalk. We hypothesize that the CLEC14A-MMRN2-CD248 interaction is a key component of bone formation and here we provide data showing it to be an interesting therapeutic target for bone homeostasis

1.9. Hypothesis

Given the above we posit that the CD248-MMRN2-CLEC14A protein interaction complex negatively regulates maturation of osteoprogenitors during bone growth and it constitutes a novel therapeutic target for stimulation of bone formation (Figure 1.6).

To further test this hypothesis the project aims to:

I. Characterise the effect of CLEC14A on bone formation during postnatal bone growth.
II. Identify and dissect any signalling pathways induced by CLEC14A-MMRN2-CD248 interaction.

III. Assess the therapeutic potential of in-house blocking antibodies to protect against age-induced bone loss using murine models of osteoporosis.

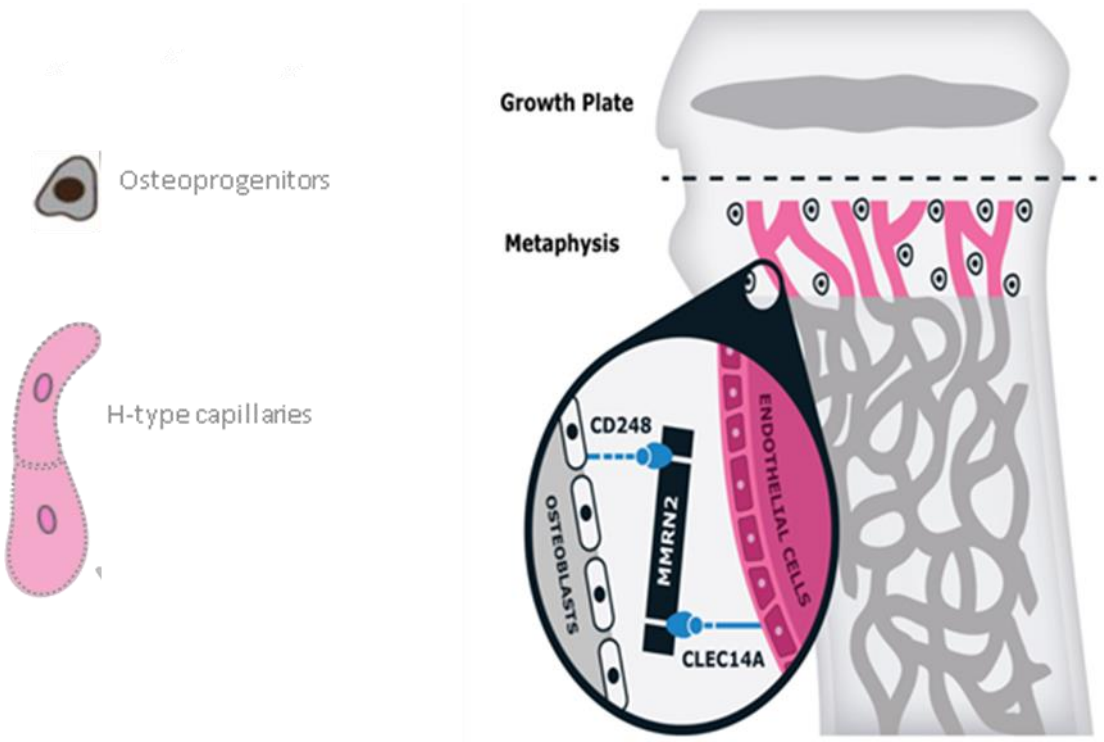


Figure 1.6. Illustration of the CLEC14A - MMRN2 - CD248 protein interactions that may facilitate endothelial-osteoblast crosstalk in tibias at bone formation sites. Schematic diagram illustrates the working hypothesis for this project. Pictogram depicts the molecular interaction between metaphyseal osteoprogenitors and H-type capillaries. We hypothesise that EC-osteoprogenitor crosstalk and proximity of osteoprogenitors to H-type EC is moderated by interactions between CLEC14A, MMRN2 and CD248. Work previously published by our group identified a novel protein-protein interaction that links osteoprogenitors to endothelial cells. Namely, CLEC14A and CD248 non-competitively bind MMRN2 at different locations as previously published (1). Being able to simultaneously bind CD248 and CLEC14A on separate binding regions, MMRN2 functions as an adhesive and interactive interface between endothelial cells expressing CLEC14A and osteoprogenitors expressing CD248 on their surface membranes.

Table 2. Expression patterns and pathological disease associated with CLEC14A, MMRN2 and CD248

Protein	Cellular expression	Pathology
CD248	Embryo	High expression, development Huang, Hong (254) Decidual stromal cells, placenta (376)
	Kidney (interstitial cells) Uterus, Colon, Prostate, Pancreas, skin fibroblasts and liver hepatic stellate cells	Low expression, postnatally non-pathologic conditions (255, 262, 264, 265, 377-380)
	Fat pads, adipose stem, and progenitor cells	Moderate expression, steady state expression in the mouse adipose tissue (381)
	Brain, perivascular cells	High expression at mRNA level in Pdgfrb Ng2 positive perivascular cells in steady state of mouse brain (382)
	Bone, osteoprogenitors	High expression, postnatal bone growth, (255)
	Synovium, pericytes and fibroblasts	High expression, rheumatoid and psoriasis-induced arthritis (266, 343, 383)
	Liver, endothelial cells	High expression, hepatic fibrosis (264)
	Tumours, pericytes	High expression, sarcoma, carcinoma (384-386), glioma (338), glioblastoma, astrocytoma (386), ovarian and colon neoplasms (246)

CLEC14A	Embryo, endothelial progenitor cells	High expression, development (346)
	Brain, retina, liver, lungs, lymph nodes, kidneys, bladder and ears, endothelial cells	Low expression, postnatally non-pathologic conditions (346, 347) High expression at mRNA level in 10-15 week old mouse lung and brain (387) Moderate expression at mRNA level in 10-15 week old mouse kidney and
	Subcutaneous and gonadal fat pad, brown adipose tissue	Moderate expression at mRNA level in 10-15 week old mouse fat pads (387) Mesenteric adipose tissue, gonadal fat pat(387)
	Tumours, endothelial cells	High expression, liver, pancreatic, prostate, breast, ovarian, bladder, kidney, thyroid, stomach, cervix (252, 345) High expression at mRNA level, tumour and lymph node endothelial cells
	Blood vessels and lymphatic vessels, endothelial cell lines,	High expression during angiogenesis, on outgrowth endothelial cells, human umbilical vein endothelial cells and human umbilical artery endothelial cells (123, 346, 347, 349)
	Embryo (human and mouse), maternal placenta and uterine endothelial cells Foetal fibroblasts	High expression in endothelial cells of the murine yolk sac (387) High expression at mRNA level in maternal placenta and uterine endothelial cells and very low expression in fetal fibroblasts (376)
	Monocytes	Low expression, steady state, CD45+F4/F80+CD11c-Ly6Chi Cd64- (390)
MMRN2	Cell lines, EC	Moderate expression, steady state, high expression during angiogenesis (1)
	EC in liver, heart, aorta, skeletal muscle,	Low expression, steady state (387)
	EC and mural cells in the brain,	High expression at mRNA level in 10–19-week-old mouse endothelial cells and moderate expression in mural cells (382)
	Subcutaneous and gonadal fat pad, brown adipose tissue	High expression at mRNA level in 10-15 week old mouse fat pads (387)

	Lung, blood vessel and lymphatic endothelial cells	High expression at mRNA level in 10–19-week-old mice (382, 391)
	Tumours, endothelial cells	High expression, cancer (369)
	Fibrosis lung, endothelial cells	High expression in endothelial cells of fibrosis lungs (392)

2. CHAPTER II

MATERIALS AND METHODS

2.1. Reagents

Table 3 Commonly used solutions, reagents, and biological products

Name	Concentrations and Company
Phosphate buffered saline (PBS)	(Oxoid, UK, cat no: BR0014, prepared in ddH2O as per the manufacturer's instructions) 137 mM NaCl, 8 mM Na_2HPO_4, 3 mM KCl and 1.5 mM KH_2PO_4, pH 7.4
Flow Cytometry MACS buffer	0.5-10% FBS (w/v) (Biosera, UK, cat no: FB1001), 1.538 mM Sodium Azide, (Sigma-Aldrich, UK, cat no: S8032-100G)
Decalcification Solution (bone embedding)	0.5 M ethylenediaminetetraacetic acid (EDTA) (Sigma-Aldrich, UK, cat no: EDS-1KG), adjusted to a pH of 7.4-7.6 in ddH2O with NaOH pellets (Sigma-Aldrich, UK, cat no: 567530-500GM)
Cryoprotection Solution	0.58 M sucrose, 0.17 M polyvinylpyrrolidone (PVP; Sigma-Aldrich, UK, cat no: P5288-500G), in sterile PBS.
Embedding Solution	0.58 M sucrose (Sigma-Aldrich, UK, cat no: S0387-1KG), 8% gelatine (Sigma, UK, cat no: G9382-500G), 0.17 M PVP in sterile PBS, made fresh before use
PTx.2 (iDISCO)	2 mL TritonX-100 (Sigma-Aldrich, UK, cat no: X100-5ML) in 98 mL 10x sterile PBS
PTwH (iDISCO)	2mL Twewen-20 (Sigma-Aldrich, UK, cat no: P1379-25ML), 1 mL of 10 mg/mL heparin stock solution (Leo, UK, cat no: 009878-06, 500 U/mL), 97 mL sterile PBS
Permeabilisation solution (iDISCO)	100 mL DMSO (Sigma-Aldrich, UK, cat no: D8418-100ML),0.15 M glycine (Sigma-Aldrich, UK, cat no: G7126-100G), 400 mL PTx.2
Blocking solution (iDISCO)	3 ml donkey serum (Abcam, UK, cat no: ab7475), 5 mL DMSO, 42 mL PTx.2

Table 4 PCR primers

Gene name	Code	Company
Gapdh	Mm99999915	Taqman, UK
Col1a1	Mm08801666	Taqman, UK
Runx2	Mm00501584	Taqman, UK
Sp7	Mm04209856	Taqman, UK
B2m	Mm00437762	Taqman, UK
Bglap	Mm03413826	Taqman, UK
Ibsp	Mm00492555	Taqman, UK
Nes	Mm00450205	Taqman, UK
Mmp9	Mm00442991	Taqman, UK
Vegfa	Mm00437306	Taqman, UK
Alpl	Mm01187117	Taqman, UK
Spock3	Mm00470030	Taqman, UK
Klf2	Mm00500486	Taqman, UK
Cd93	Mm00440239	Taqman, UK
Mmrn2	Mm00467640	Taqman, UK
Pdgfrb	Mm00435546	Taqman, UK
Tem1	Mm00547485	Taqman, UK
Cxcl12	Mm00445553	Taqman, UK

Table 5 Antibodies, IF = immunofluorescence, FC = flow cytometry

Target	Manufacturer and catalogue number	Final working dilution
Emcn	Purified, IF, Santa Cruz Biotechnology Inc, United States, cat no: sc-65495	1:100
Emcn	FITC, FC, Santa Cruz Biotechnology Inc, United States, cat no: sc-65495-FITC	1:100
CD31	Purified, IF, BD Pharmigen, UK, cat no: 553370	1:100
CD31	PE, FC, Biolegend, cat no: 102408	1:200
COL1A1 (Type I Collagen 1α)	Purified, IF, EMD Millipore Corporation, United States, cat no: AB765P	1:100
Osx (Osterix)	Purified, IF, Abcam, UK, cat no: ab227820	1:500
Donkey anti-rabbit IgG	AF647, IF, Jackson Immuno Research, cat no: 711-605-152	1:200
Goat anti-rat IgG	AF546, IF, Invitrogen, UK, cat no: A11081	1:200
CD45	APC, FC, Invitrogen, UK, cat no: 17-0451-83	1:100
TER-119	PE-Cy7, FC, eBioscience, UK, cat no: 25-5921-82	1:100
Rat IgG_{2b} kappa Isotype control	PE-Cy7, FC, eBioscience, UK, cat no: 25-4031-82	As required
Rat IgG_{2a} kappa Isotype control	FITC, Biolegend, UK, cat no: 400505	1:100
Rat IgG_{2a} kappa Isotype control	PE, Biolegend, UK, cat no: 400507	1:100
Rat IgG_{2a} kappa Isotype control	APC, Biolegend, UK, cat no: 400511	1:100
CLEC14A (CRT4)	In house, IF, monoclonal antibody	100 µg injected i.p.
MMRN2	Purified, IF, Abnova, UK, cat no: H00079812-B01P	1:100

Table 6 Commercial solutions and kits

Name	Manufacturer and catalogue number
Paraformaldehyde (PFA)	Sigma,UK, cat no: HT5011-1CS
P1NP ELISA Immunoassay kit (Rat/Mouse P1NP EIA)	Ids (Immunodiagnostic system), UK, cat no: AC-33F1, assay range 0.7-75 ng/ml.
RNeasy Micro Kit (50)	Qiagen, UK, cat no: 74104
High-Capacity cDNA Reverse Transcription Kit	Applied Biosystems, UK, cat no: 4368814
Clear adhesive film (PCR plate)	Applied Biosystems, UK, cat no: PN 4306311
MicroAmp™ Optical 96-Well Reaction Plates and Optical Caps	Applied Biosystems, UK, cat no: PN 403012
384 PCR plates	Roche, UK, cat no: 04729749001
MicroAmp™ Optical Adhesive Film	Applied Biosystems, UK, cat no: 4311971
RNase inhibitor	Applied Biosystems, UK, cat no: N80801119
Red Blood cell lysis buffer	Roche, UK, cat no: 45464300
Alkaline Phosphatase yellow	Sigma, UK, cat no: P7998-100
TaqMan Gene Expression Mastermix	Applied Biosystems, UK, cat no: 4369016
Reb Blood Cell Lysis buffer	Roche, UK, cat no: 454643000
Hoechst 3342, Trihydrochloride, Trihydrate	Hoechst 1:400 in PBS, freshly made, Thermo Fisher Scientific, H3570
Calcein for i*n vivo* injections	Sigma-Aldrich, UK, cat no: C0875
Collagenase D	Sigma Aldrich Roche, UK, cat no: COLLD-RO
Collagenase A	Roche Diagnostics, Germany, cat no: 10103586001
B-mercaptoethanol	Sigma, UK, cat no: M-6250
Gelatine from bovine skin	Sigma, UK, cat no: G9382-500G
Ethanol absolute	VWR Chemicals, UK, cat no: 2081.330
RIPA Buffer	Sigma, UK, cat no: R0278-50ML
Calcein for *In vivo* injections	Sigma-Aldrich, UK, cat no: C0875
Sucrose	Sigma-Aldrich, UK, cat no: S9378-1KG
Polyvinylpyrrolidone (PVP)	Sigma-Aldrich, UK, cat no: PVP40-500G
Ethylenediaminetetraacetic acid	Sigma-Aldrich, UK, cat no: T4174
TritonX-100	Sigma-Aldrich, UK, cat no: X100-5ML
Tween-20	Sigma-Aldrich, UK, cat no: P1379-25ML
Heparin stock solution	Leo, UK, cat no: 009878-06, 500 U/mL
Glycine	Sigma-Aldrich, UK, cat no: G7126-100G
Alkaline phosphatase (ELF™ 97 Endogenous Phosphatase Detection Kit)	Invitrogen, UK, cat no: E6601

Dimethyl sulfoxide (DMSO)	Sigma-Aldrich, UK, cat no: D8418-100ML
DiBenzyl Ether	Sigma-Aldrich, UK, cat no:108014-1KG
Dichloromethane (DCM)	Sigma-Aldrich, UK, cat no:270997-12X100ML
Ethyl Cinnamate	Sigma-Aldrich, UK, cat no: 8.00238.0250
H_2O_2	Sigma-Aldrich, UK, cat no: H1009-5ML
Methanol	VWR Chemicals, UK, cat no: 20847.307
Hoechst	Thermo Scientific, UK, cat no: 62249
Biotin antibody labelling kit	Sigma-Aldrich, UK, cat no: MXBIOS50-1KT

Table 7 Cell culture solutions

Name	Manufacturer and catalogue number
Foetal bovine serum	Labtech.com, UK, cat no: FCS-SA, concentration: 10%
L-Glutamine–Penicillin–Streptomycin solution	Sigma, UK, cat no: G1146, total concentration of each component in the final solution: 1%, concentration of each individual component: 100 µl/ml Streptomycin, 100 U/ml Penicillin and 2 mM L-Glutamine
α-MEM: Minimum Essential Medium Eagle	Biosera, UK, cat no: FB1001, concentration: 89%
β- Glycerol phosphate	Sigma-Aldrich, UK, cat no: G9422, concentration: 10mM
L- Ascorbic acid	Sigma-Aldrich,UK, cat no: A5960, concentration: 50 µg/ml

2.2. Animal models

CD248$^{-/-}$ and CLEC14A$^{-/-}$ mice were generated and genotyped as previously described (263, 348)(Figure 2.1) and maintained at the Biomedical Services Unit, University of Birmingham. C57BL6/J control mice were obtained from Charles River. Mice had ad libitum access to food and water and were maintained in an environment with alternative 12-hour long light dark cycles. All animal experiments were performed under Dr Naylor's Home Office Project licence (PFBB3DA4C) by a Personal Licence holder abiding by the UK Animal (Scientific Procedures) Act 1986 and approved by the local ethics committee (BERSC: Birmingham Ethical Review Subcommittee). For all experiments (except the CLEC14A-MMRN2 interaction blocking *In vivo* experiments), CD248$^{-/-}$ and CLEC14A$^{-/-}$ and control C57Bl/6J wildtype (WT) mice were bred locally in the Biomedical Services Unit at the University of Birmingham. WT mice for breeding and for the antibody experiments were obtained from Charles River, UK and then subsequently bred locally at the University of Birmingham or used for experiments following a 7-day period of rest for acclimatisation.

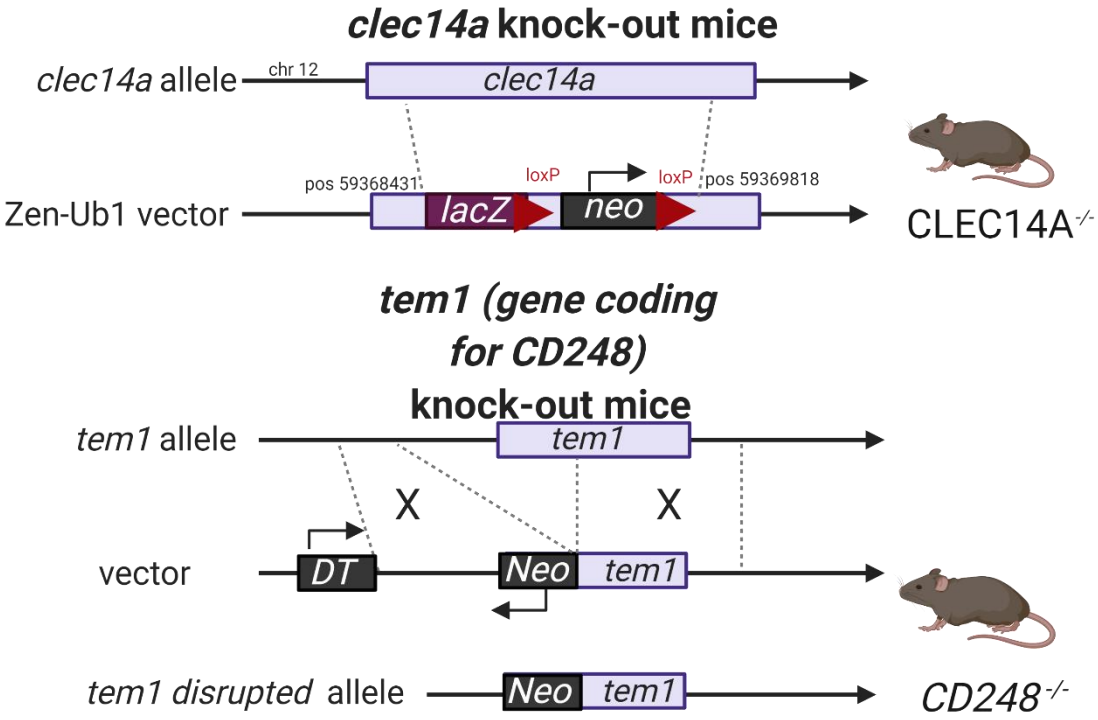


Figure 2.1 Generation of homozygous CLEC14A and CD248 knock-out mice. A) CLEC14A$^{-/-}$ chimeric mice were generated by injecting albino C57BL/6J mice with C57BL/6N VGB6 stem cells that contained a CLEC14A deletion cassette Clec14A$^{atm1(KOMP)Vlcg}$. **B)** Targeted disruption of the Cd248 single exon gene was achieved by homologous recombination in 129SvEv mice. Resulting offspring from each genotype were crossed to C57BL/6 females for ten generations to generate progeny that were CLEC14A$^{+/-}$ (348), or CD248$^{+/-}$ (263) and on the C57Bl/6J background, breeding of CLEC14A$^{+/-}$ and CD248$^{+/-}$ was then used to generate homozygous mice (CLEC14A$^{-/-}$ and CD248$^{-/-}$) .

2.3. Analysis of gene expression by bulk RNA sequencing

2.3.1. Analysis of RNA sequencing of the H-type and L-EC transcriptome (dataset E-MTAB-4066)

All methods were optimised by the student within the PhD study period unless stated otherwise. Micro-computed tomography methods have been previously optimised and set up locally by Dr Amy Naylor. Development of ovariectomy induced osteoporosis models and embryonic metatarsal bone elongation methods were developed in collaboration with Jonathan Lewis a fellow PhD student in the Naylor laboratory.

Analysed data was generated in another laboratory and published recently **(136)** the dataset is publicly available via the ArrayExpress database (http://www.ebi.ac.uk/arrayexpress/), accession number E-MTAB-4066, and was accessed on January 28th 2020. In summary, the dataset was generated by Langen and colleagues as follows: RNA sequencing (RNASeq) was performed on samples pooled from 20 C57Bl/6J mice at postnatal day 6. Endothelial cells (EC) were sorted by flow cytometry into type H and L vessels, based on the level of Endomucin (EMCN) and CD31 expression. Sequencing libraries were prepared using 100 ng of RNA. For our independent analysis of these data, publicly available files were downloaded from the array database, raw sequences were checked for quality control using FastQ. Raw reads were then trimmed to remove low quality reads and adapters using Cutadapt (Bioconductor: https://bioconductor.org), then finally reads were mapped to the mouse genome assembly GRCm38 (mm 10). Quantitation of mRNA transcripts was achieved using the SeqMonk software (Babraham Institute, Cambridge, UK). All empty transcripts (value = 0) were excluded from any subsequent analysis. Transcripts corresponding to pseudogenes or non-coding RNA were excluded, transcript isoforms were merged as a single measurement for

each gene. Data was corrected for potential DNA contamination by evaluating the reading density in intergenic regions as a basis for an estimated DNA contamination, using this estimate individual corrections were applied to each transcript to increase the accuracy of counts for each transcript. For quality control purposes all samples were verified for the percentages of genes falling into exons and the percentage of ribosomal RNA or mitochondrial RNA, based on raw counts. A Pearson correlation was employed to calculate a distance matrix between all the 6 data stores (3 samples for H-type ECs and 3 samples for L-type EC), this analysis was then used to construct a neighbour joining tree from the data matrix (SeqMonk, Babraham Institute, UK). Quantitation of differential gene expression was performed in SeqMonk by either using a negative binomial generalized linear model (DESeq2) or by testing for variance of gene expression intensity difference (SeqMonk), herein called intensity difference testing. Intensity difference testing is a more stringent analysis which accounts for a low number of samples included in differential gene expression analysis and was employed to identify changes in gene expression considering the distribution of expression differences to identify those whose change is not explained by the general level of disruption in the system. Similar results were obtained for quantitation of reads per gene with both methods. All reported values for DESeq2 analysis were adjusted for multiple testing with the Benjamini-Hochberg method to control for false discovery rate (FDR). Heatmaps of differentially expressed genes were produced using R (The R Foundation for Statistical Computing, Vienna, Austria). Gene set enrichment analysis was performed to identify pathways, rather than individual transcripts that are changed in response to loss of CLEC14A function. This was accomplished using the GSEA software (MSigDBv6, Broad Institute) (393), using gene lists with log2 normalised gene sets, gene lists were probed against the Hallmark, Kyoto Encyclopedia

of Genes and Genomes (KEGG), and Reactome gene sets from the GSEA signatures database collection; an example plot with a legend can be found in Figure 2.2.

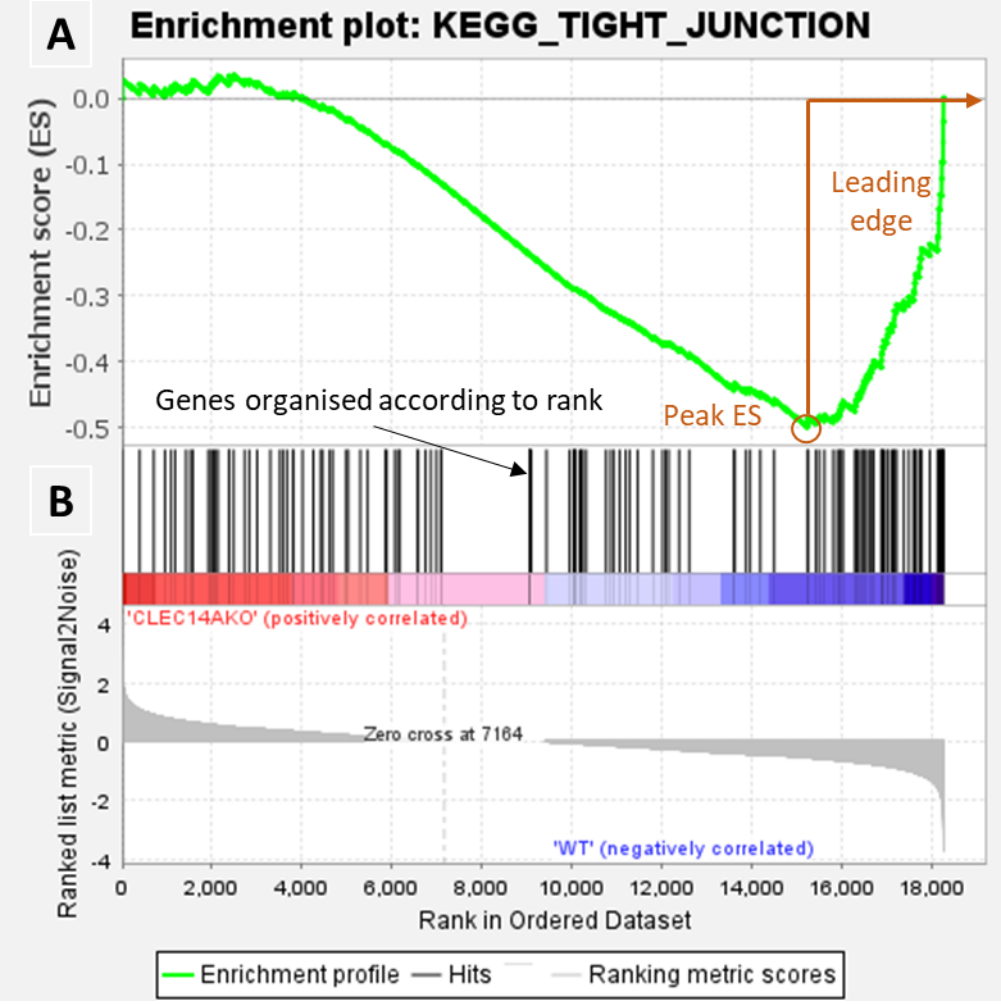


Figure 2.2. Diagram of enrichment plot output by GSEA. A) GSEA plot showing enrichment scores for all genes in the dataset studied identified in the KEGG Tight Junction gene set. The Y axis displays the enrichment score (ES) for genes in the KEGG Tight Junction gene set. A positive ES is representative of genes enriched in CLEC14A$^{-/-}$ samples, whilst a negative ES represents genes enriched in WT samples. This example plot shows enrichment of tight junction molecule genes in WT murine calvarial lysate cells. The X axis shows genes (marked by black parallel lines) in the dataset ordered according to their ranking score. The leading-edge subset of a gene set is composed of genes that are the main contributors to the enrichment in that gene set. For positive ES the leading edge is located before the peak ES (to the left), for negative ES the leading-edge genes are located before the peak ES (to the right). **B)** GSEA plot displaying gene ranking metric against the ranking order for genes present in our dataset and in KEGG Tight Junction gene set. Y axis represents the gene ranking metric calculated via the Signal to Noise method and represents the gene's correlation with the phenotype. X axis discloses gene rank in the Tight Junction gene set. Genes positively correlated with CLEC14A$^{-/-}$ samples are located to the left side of the plot, genes negatively correlated with CLEC14A$^{-/-}$ samples are located to the right side of the graph.

2.3.2. RNA sequencing analysis of the CLEC14A$^{-/-}$ and WT neonatal calvarial lysates

2.3.2.1. Calvaria lysates and NGS library preparation

RNA sequencing of calvaria lysates was performed locally, at the University of Birmingham. Osteoblast-enriched cell suspensions were prepared from C57BL/6J WT and CLEC14A$^{-/-}$ pups at postnatal day 4 (P4) as described in section 2.10 (Isolation of calvaria osteoblasts). RNA was extracted using the Qiagen Micro RNA extraction kit as described in section 2.12 (RNA extraction and isolation for RNA sequencing and quantitative real-time PCR (qPCR). RNA purity and quantity were analysed on the High Sensitivity RNA ScreenTape® (Agilent, California) and on the Qubit High Sensitivity RNA (ThermoFisher Scientific, UK), RNA quantity per sample varied between 102 and 234 ng/µl, all RNA integrity number (RIN) scores were higher than 9 ensuring the preparation of a high-quality library (Libraries were equalised to the lowest DNA concentration in the sample group (Table 8). 150ng of RNA were used for the NGS library prep which was generated with the aid of the Lexogen QuantSeq 3' mRNA-Seq Library Prep Kit FWD for Illumina (Lexogen, US), this kit allows for the preparation of an NGS library of mRNA sequences close to the 3' end of polyadenylated RNAs ensuring selection of mature mRNA which has not been marked for degradation. The resulting dsDNA library was checked for quality by the Birmingham Genomics personnel using the Agilent TapeStation DNA 1000 tape (Aligent) and DNA HS Qubit™ (ThermoFisher). Libraries were equalised to the lowest DNA concentration in the group of samples (7nM) (Table 9).

Table 8 Sample RNA Quality Control (QC) – RNA concentration and integrity were checked before the cDNA library preparation

Sample Name	Stock Concentration (ng/µl)	RIN score
WT-1	139	9.2
WT-2	102	9.2
WT-3	126	9
WT-4	111	9.4
CLEC14AKO-1	234	9.4
CLEC14AKO-2	168	9.0
CLEC14AKO-3	132	9.2
CLEC14AKO-4	155	9.0

2.3.2.2. Library sequencing

Equal concentrations of 4nM per sample were pooled for sequencing which was completed on a v2.5 150 cycles Mid output (75 single read) flowcell, ran in a NextSeq 500 (Illumina, California) on the run had a yield of 14.10 (Gbp) and an average %Q30 of 91.13, indicating a successful run and indicating that analysis could be performed in house.

Table 9 DNA library QC – DNA concentration and fragment size

Sample Name	Concentration (ng/µl)	Concentration (nM)	Size (bp)
WT-1	1.56	10	248
WT-2	1.41	9	251
WT-3	3.06	22	231
WT-4	1.92	17	271
CLEC14AKO-1	3.3	22	250
CLEC14AKO-2	3.36	22	250
CLEC14AKO-3	0.97	7	215
CLEC14AKO-4	2.54	17	243

Analysis codes for quality control analysis of files obtained from the NextSeq 500 sequencer are attached in the Appendix (section 9.1), the pipeline for this step in the analysis followed the steps described in section 2.3. Briefly, raw sequences were checked for quality control

using FastQC (394) and multiQC (395). Raw reads were then trimmed to remove low quality reads and adapters using Cutadapt (396), and finally reads were mapped to the mouse genome assembly GRCm38 (mm 10) with the aid of STAR aligner (397). Final transcript counts were obtained utilising Subread (398). Differential gene expression was performed against a negative binomial generalized linear model (DESeq2) (399) followed by a Benjamini-Hochberg correction to correct for multiple comparisons. Transcript reads over exons were obtained then log2 transformed for follow up analyses (GSEA, heatmaps) excepting differential gene expression analysis (DESeq2) which required a raw read value input. Gene Set Enrichment Analysis (GSEA) was performed using the GSEA 4.2.2 software (Broad Instititue, UC San Diego, US) (393, 400). The log normalised expression profile of samples was generated in R Studio (R Studio, US) and data was prepared for analysis following the GSEA online guidelines (Using RNA-seq Datasets with GSEA- link) (401). GSEA identifies enrichment of most differentially expressed genes between the WT and CLEC14A$^{-/-}$ samples in predefined gene set lists curated by Molecular Signatures Database v7.5.1 (Broad Instititue, UC San Diego, US). Briefly, GSEA calculates the average variation across all gene counts in between the 2 genotypes compared producing a list of ranked genes. Genes are ranked from the most upregulated to the most downregulated gene. This dataset is then compared to nominated gene sets to produce enrichment scores for each gene set investigated.

For heatmaps, differences in gene expression was presented as a Z score which was calculated as follows: raw data reads were log 2 normalised, to show transcript expression differences between WT and CLEC14A$^{-/-}$ samples for each gene the mean count value for each gene was subtracted from the individual gene counts for each sample (4x WT samples and 4x CLEC14A$^{-/-}$ samples) and the resulting number was divided by the standard deviation in each gene set (code in Appendix section9.1.3).

Interacting partners for CD93, CLEC14A, CD248 and MMRN2 were searched for using an online database – search tool for interactions of chemicals (STITCH) (402). STITCH allows exploration of the network of protein-protein interactions by relying on information from metabolic pathway, crystal structure, and binding experiments.

2.3.2.3. Analysis of single cell sequencing publicly available datasets

Genes, barcodes and matrix files were downloaded from the Gene Expression Omnibus website for publicly available datasets GSE128423 (403) and GSE154076 (22) and analysed using Seurat (R Studio package) (404, 405). The code used for the analysis is available in the Appendix (9.2). Individual objects were loaded and merged into a single data matrix. All cells that had more than 200 and fewer than 6000 transcripts and a lower than 5% mitochondrial gene transcripts were sub-set and analysed further. All reads were log normalised at a scale factor of 10^3 and variable features were identified to produce a set of genes that was most variable across the single-cell data set. Unsupervised dimensional reduction (tSNE and UMAP) was conducted on the single cell object using the variable features identified in the previous step to ensure identification of the primary structures in the dataset. Neighbouring cells and cell clusters were identified with the aid of the FindNeighbors and FindClusters commands. FindNeighbors analyses transcripts for each cell to construct a nearest-neighbour graph whilst FindClusters is a feature used to arrange nearest-neighbour cells into cell clusters utilising a shared nearest neighbour modularity optimisation-based clustering algorithm. Cell markers for each cell cluster were identified, using the FindAllMarkers command, to aid in cluster naming. Top markers utilised for each single cell RNA sequencing cluster naming can be visualised in Figure 9.1. Clusters of interest were than analysed independently to probe gene expression patterns of interest for our project – stromal cells – chondrocytes, osteoblasts,

fibroblasts, mesenchymal stem cells and endothelial cells (EC). The osteoblast and EC clusters were subclustered to identify different cell subtypes. For osteoblasts, subs-clustering of the main osteoblast cluster allowed for identification of osteoblast transition states, allowing for clustering of cells according to their osteolineage maturation stage: pre-osteoblasts/osteoprogenitors, immature osteoblasts and mature osteoblasts. Gene expression in different clusters was mapped using the violin feature and dot plots.

2.4. Flow cytometry

Mouse tibiae and femurs were collected from 28-day old mice and all adjacent muscle and connective tissue was removed. The epiphysis was removed with a scalpel and the remaining metaphysis and diaphysis regions were crushed in 3 mL of ice-cold PBS (Oxoid, UK, cat no: BR0014) in a mortar with a pestle then transferred into a polystyrene tube. Single cell suspensions were obtained by digesting the crushed bone in 1 mg/ml type A collagenase (Roche Diagnostics, Germany, cat no: 10103586001) diluted in sterile PBS. To ensure constant agitation cells were incubated with a magnetic stirrer at 37.5°C for 20 minutes on a magnetic hot plate. The resulting cell suspension was filtered through a 100 µm cell filter to remove any undigested parts of the bone and to enrich for single cells in the suspension. The cell filter was washed with MACS buffer (10% FBS, Biosera FB1001; 0.002M EDTA, Merck 324506-100ML; 0.1% Sodium Azide (NaAz), Sigma-Aldrich, cat no: S2002) to ensure maximisation of the yield. The collagenase was inactivated by washing cell suspensions with MACS buffer twice. Red blood cells were removed using an RBC lysis buffer (Roche,UK, cat no: 454643000), cells were incubated with 1mL lysis buffer for 5 minutes followed by neutralisation with 1mL PBS, cells were centrifuged and washed 1 x in MACS. Cells were then blocked with 1:100 anti CD16/32 antibody (eBioscience, 14-0161-82) diluted in MACS buffer, for 20 minutes on ice to prevent

Fc receptor binding. Cells were washed in MACS buffer in between different incubations unless stated otherwise. Equal number of cells (1 x 10^7) were subjected to immunostaining with 1:200 antibodies (Emcn conjugated to FITC, Santa Cruz, sc-65495 FITC; CD31 conjugated to PE, Biolegend, 102408; CD45 conjugated to PerCP-Cy5.5, Biolegend, 103130; 1:100 Ter119 conjugated to PerCP-Cy5.5, Biolegend 116226) diluted in MACS buffer, for 45 min on ice. All antibodies were tested against isotype controls and incorporated in fluorescence minus 1 panel to ensure antibody specificity. Antibody titration was also performed (not shown) for protocol optimisation. For the next stage, cells were washed in PBS, then incubated with a cell viability dye 1:500 Zombie NIR (Biolegend, 423105) diluted in PBS, on ice and in the dark. Cells were washed and filtered through a 70 µm strainer and immediately acquired on a Fortessa flow cytometer (BD Biosciences, US). Data was analysed using Flow Jo (FlowJo LLC, US).

2.5. 3D immunofluorescent staining

Tissue was prepared as previously described (406) (Figure 2.3). Briefly, mouse tibiae and femurs were collected and lightly fixed in 10% formalin for 4 hours on ice and under gentle but constant agitation. To remove formalin excess, bones were washed thrice in 7 ml ice-cold PBS for a minimum of 5 minutes/wash cycle. New-born (P1-P5 postnatal day), juvenile (2-4 weeks old) and young (8-12 weeks old) mouse bones underwent a mild decalcification process by incubation of a maximum of 4 long bones (2 tibiae, 2 femurs) in decalcification solution (0.5 M ethylenediaminetetraacetic acid EDTA (Sigma-Aldrich, UK, cat no: T4174), adjusted to a pH of 7.4-7.6 in ddH_2O with NaOH pellets (Sigma-Aldrich, UK, cat no: 567530-500GM) for 24 hours. The tissue was washed in PBS and incubated for 24 hours in a cryoprotective solution (20% sucrose, 2 % polyvinylpyrrolidone -PVP in PBS). Finally, bones were incubated for 45 minutes at 60°C in 5 mL of embedding solution (20% sucrose, 8% gelatine, 2% PVP) before

they were embedded in 2 mL of the same solution in cryomolds (standard size, Tissue-Tek Cryomold, Agar Scientific, UK). The specimens were allowed to set for at least 30 minutes before long term storage at -80°C. In preparation for staining, longitudinal 100 µm thick sections were cut (on a Leica CM1950 cryostat – chamber temperature set at -23°C, specimen head temperature set at -21°C), air-dried overnight and then stored at -20°C in dry storage conditions. Prior to immunostaining, sections were allowed to thaw for 5 minutes at room temperature, then they were carefully contoured with a wax pen allowing the wax to dry. The tissue was rehydrated in PBS for 10 minutes and blocked for 30 minutes in 10% horse serum (Sigma-Aldrich, UK, H0146) diluted in PBS. Sections were incubated with primary antibodies (1:100 Emcn, Santa Cruz, US, cat no: sc-65495 or 1:100 CD31, BD Biosciences, cat no: 553370, 1:500 Osx, Abcam, UK, cat no: ab227820, 1:100 COL1A1, EMD Millipore Corporation, US, cat no: AB749P) for 1 hour at RT, then they were carefully washed with PBS and incubated with Alexa Fluor conjugated secondary antibodies (AF546, Invitrogen, A11081; and 1:100 anti-rabbit AF647, Jackson Immuno Research, US, 711-606-152, 1:400 Hoechst diluted in MACS). Before imaging, excess and unbound antibodies were removed by washing in PBS and sections were mounted with Prolong Diamond Antifade Mountant (Thermo Fisher Scientific, UK, P36961) with coverslips. Coverslips were sealed with nail polish and the specimens were allowed to cure dry overnight. Details of image acquisition can be found in Figure 2.3.

Following acquisition, images were Airyscan processed with ZenBlack and analysed with Image J. Total number of osteoblasts was quantified in ImageJ using the “Analyse Particles” function following image thresholding and cell segmentation of the image mask. The following settings were utilised for the “Analyze particles” plugin: Size 0.02-Infinity, m2, Circularity 0.1-1.0. Briefly, images were transformed with a Gaussian blur filter of a sigma radius of 0.5, this was applied to the image to dampen background noise, then, automated thresholding was

applied utilising the “Li“ method. An example of an image thresholding mask is presented in Figure 2.4 C. Cells were segmented using the “Watershed” function to separate cells that are in contact or overlapping, otherwise, cells that are in contact would have been counted as one singular object. When optimising this method, the total cell numbers obtain from this analysis strategy were compared with manual counting, resulting in similar values.

Osteoblast nuclear circularity was calculated in Image J with the “Analyse Particles” function as: 4pπ(Area)/(Perimeter^2).

For the *in vivo* labelling of CLEC14A in the mouse bone, the C4 clone of our in house monoclonal anti CLEC14A antibody was labelled with biotin (Sigma-Aldrich, UK, cat no: MXBIOS50-1KT), as per the manufacturer’s instructions. 100 µg antibody diluted in sterile PBS was injected i.p., hind legs were collected 24 hours post injection and tissue was prepared for imaging of thick bone sections as described in this section. Sections were probed with streptavidin APC to track the C4 antibodies (ThermoFisher Scientific, UK, cat no: SA1005).

2.6. Mouse calvaria cleaning and immunofluorescent imaging

Postnatal day 4 calvariae were collected from C57Bl/6J pups in sterile PBS on ice and fixed in 5 ml 10% formalin for 24 hours at 4°C under gentle but constant agitation followed by 30 minutes long three consecutive washes in PBS. Calvaria were prepared following a previously published protocol (407). Briefly, calvariae were dehydrated in methanol (VWR Chemicals, UK, cat no: 20847.307)/ ddH_2O series for 1 hour each: 20%, 40%, 60%, 80%, 100% (twice) at room temperature; to remove lipids in the tissue, calvaria were then incubated overnight in 66% dichloromethane (DCM) (Sigma-Aldrich, UK, cat no:270997-12X100ML) / 33% methanol

under gentle but constant agitation. The following day, all samples were washed twice in 100% methanol at room temperature. Calvaria were bleached in freshly made 5% H_2O_2 (Sigma-Aldrich, UK, cat no: H1009-5ML) overnight on ice. Samples were rehydrated in methanol / ddH_2O series for 1 hour each: 80%, 60%, 40%, 20%, PBS at room temperature.

Calvaria were then prepared for immunolabelling, samples were incubated at 37°C under constant but gentle agitation for all steps below: firstly, tissues were permeabilised for 24 hours in permeabilization solution (Table 3), tissues were blocked over 48 hours in blocking solution (Table 3), then they were incubated with primary antibodies (rat anti-mouse CD31 antibody, BD Pharmigen, UK, cat no: 553370; anti-Osx rabbit anti-mouse, Abcam, UK, cat no: ab227820) for 2 days, followed by five washes in PTwH solution over 24 hours (Table 3). Lastly, samples were incubated with secondary antibodies (1:200 AF647 goat anti rabbit, Jackson Immuno Research, UK, cat no: 711-605-152; 1: 200 AF546 Invitrogen, UK, cat no: A11081) for another 48 hours then they were washed in PTwH solution as described for the step above. For the final clearing steps, samples were dehydrated in methanol as described above, then specimens were incubated in 66% DCM /33% methanol under gentle but constant agitation for three hours and in 100% DCM for two 15 minutes sessions. Lastly, samples were incubated in dibenzyl ether where they were kept until imaging. Samples were immersed in ethyl cinnamate for imaging and images were acquired on an Olympus MVX 10 Fluorescence Microscope fitted with a Andor Zyla 5.5. sCMOS camera. Images were analysed using the Arivis Vision 4D software.

2.1. Bone length measurements

To assess the effect of CLEC14A deletion on body mass and skeletal development during growth and in middle age, data on body mass and long bone length was collected. In brief,

mice were weighed then sacrificed by cervical dislocation before tissue collection, left hind legs were collected in PBS, bones were cleaned to remove all surrounding tissue, the femur was dislocated from the hip at its proximal joint, the tibia and femur were detached from each other by sectioning the cruciate and collateral ligaments followed by gentle destabilisation of the joint with torsion movements, the tibia was separated from the ankle at the subtalar joint just above the calcaneus, care was taken not to damage articular cartilages. Callipers (Digi-Key, UK, cat no: 3C301-NB) were used to measure the length of each bone by measuring the distance between the proximal and distal epiphysis (tibia) and the distance between the proximal and distal femur heads (femur), to ensure high reproducibility, callipers were placed between the medial and lateral condyle in the intercondylar fossa at the distal end of the femur and in the trochanteric fossa for the proximal end.

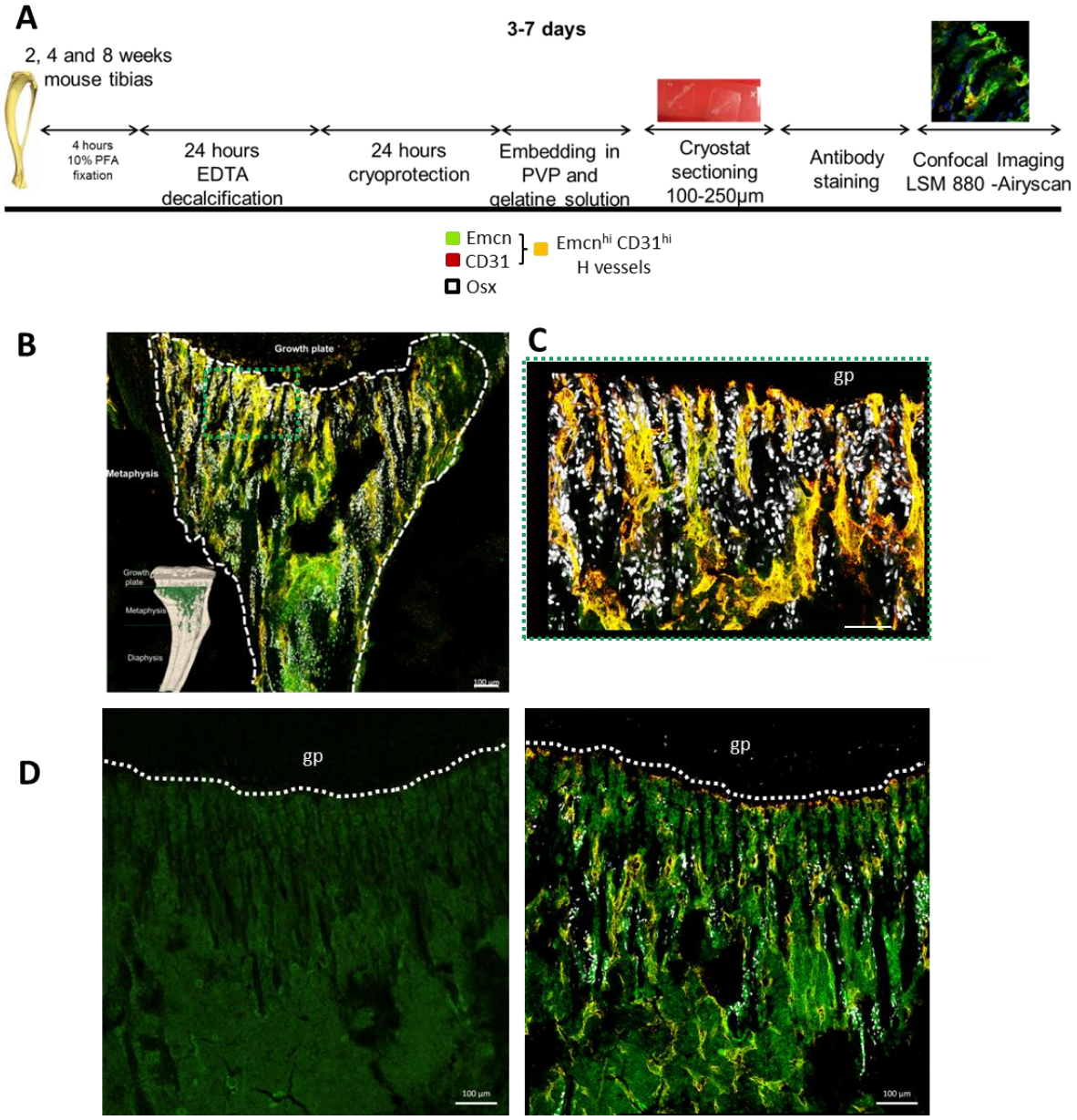


Figure 2.3 3D high-resolution imaging of mouse tibia sections method workflow. A) Overview of tissue collection and preparation of frozen bone sections for immunofluorescence staining. Mouse tibias were collected from 2- and 4-weeks old males and prepared as previously described in section 2.5**.** PVP – polyvinylpyrrolidone. **B)** Representative image of tile scans. Images were taken at an acquisition time of 1.5 hours per section followed by processing and stitching using Zen Black software. **C)** Representative maximum intensity projection image of Z stack imaging in the metaphysis region. Scale bar 100µm **D)** Secondary antibodies staining only (left) and primary and secondary staining demonstrating antibody specificity. Note autofluorescent background on FITC channel an artefact specific to the bone. Emcn – Endomucin and CD31 (endothelial markers used to identify H-type capillaries in the metaphysis region of long bones) Osx – Osterix (immature osteoblast marker), gp – growth plate.

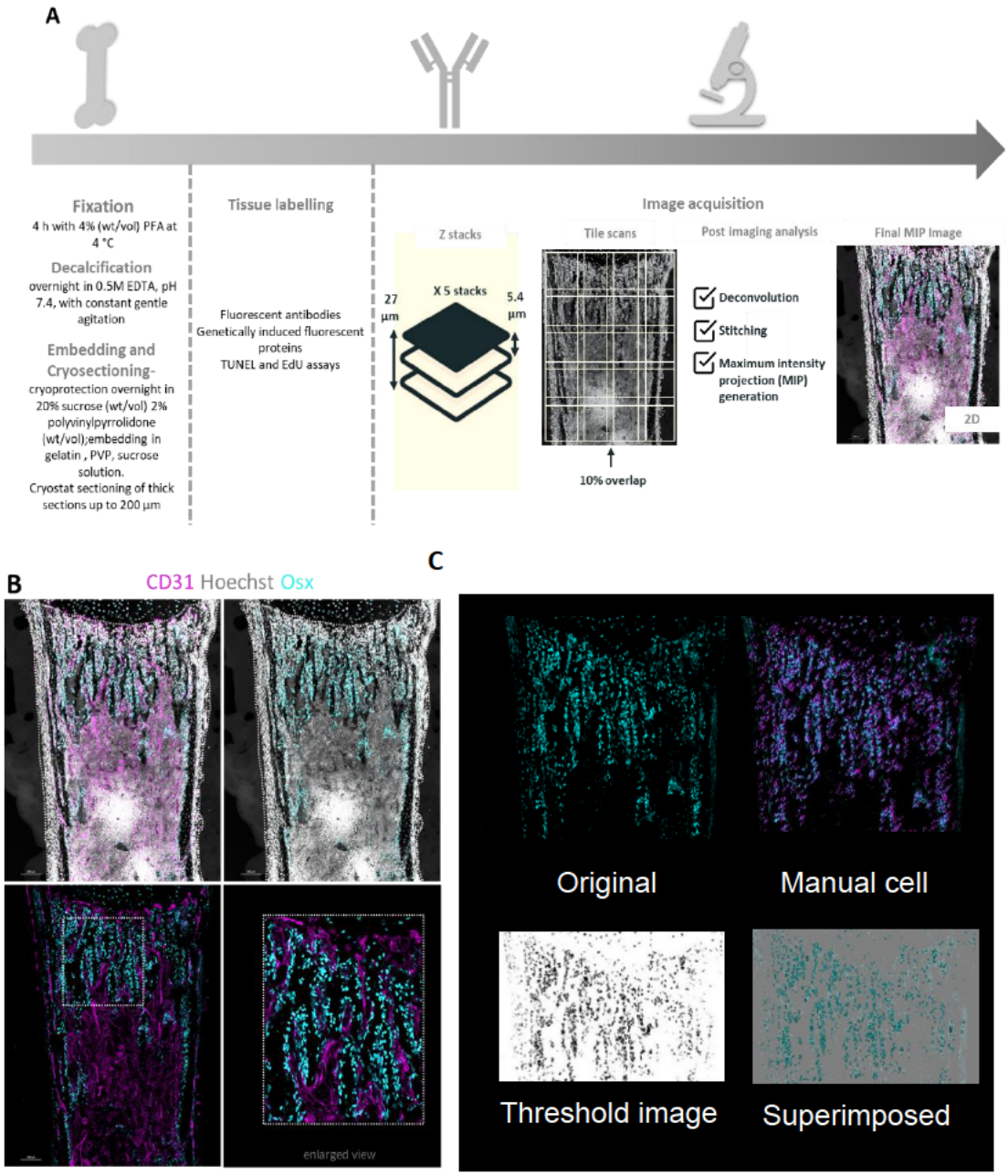


Figure 2.4. High resolution of thick mouse tibia sections. A) Diagram showing the imaging strategy employed for 3D high-resolution confocal microscopy imaging of tibia sections. Tibia sections obtained from C57Bl/6J mice were imaged with a 10X objective (C-Apochromat 10X/NA 0.45), 3.8 X optical zoom, 9 vertical images X 11 horizontal were taken for each bone section using a tile scan and Z-stack configuration. Images were taken with a frame size of 1024X1024. **B)** Example immunofluorescent maximum projection images showing H-type vessels surrounded by Osx+ cells. Vessels are labelled with CD31 (magenta), whilst osteoblasts are identified by their expression of OSX (cyan), the entire tissue section is counterstained with Hoechst to identify nuclei (grey). **C)** Example image processing example for automated cell counting strategy (ImageJ). Top left image shows the original image, top right image shows manual cell counting using the cell counter plugin, bottom left image shows a thresholded image, and bottom right image shows the threshold image superimposed on the original file. The number of osteoblast cells was analysed using the following settings in Image J: the analyse particles plugin was employed following image thresholding and cell fragmentation, Analyse Particles function settings: Size 0.02-Infinity, m2, Circularity 0.1-1.0.

2.2. Measurement of metatarsal bone length

Embryonic metatarsal elongation was used to measure the effect of CLEC14A on bone growth. Metatarsals were isolated from E14.5 C57Bl/6J WT and CLEC14A$^{-/-}$ embryos using a previously published method (408). This highly physiological *in vitro* explant culturing method allows for measurement of linear bone growth as serial and subsequent measurements can be acquired for each metatarsal over time. Embryos were collected and euthanised via decapitation. Tissue was collected in ice cold dissection medium: α-Minimum Essential Media (with no ribonuclosides and no deoxyribonuclosides) (ThermoFisher Scientific, UK, cat no: 32561037) diluted 1:3 in sterile PBS. Following removal of skin, and of the first (I) and fifth (V) metatarsals, the connective tissue between metatarsals: II, III and IV was disrupted and phalanges were carefully detached with tweezers. After tarsals were removed and all three metatarsals were separated, each explant was placed in a drop of fresh dissection medium. Metatarsals were then cultured in 24 well plates in 300 µl osteoinductive media: αMEM media (Sigma) supplemented with 10% FBS, 2mM L-Glutamine, 100U/ml Penicillin, 100 µg/ml Streptomycin, 50 µg/ml L-ascorbic acid (Sigma, UK, cat no: A5960) and 10 mM β-glycerophosphate (Sigma, UK, cat no: G9422). Metatarsals were cultured at 37 °C and 5 % CO2 for 7 days. Media was not changed for the first 5 days in culture. Metatarsal length was measured at days 1, 3, 5 and 7 through imaging on a Zeiss Primostar 3 widefield microscope. Metatarsal length was analysed in Image J using the straight line tool.

2.3. Micro-computed tomography

Structural analysis of the bone was performed using micro-computed tomography (µCT) and three-point bending tests. For the measurement of trabecular and cortical bone parameters tibiae were collected from age-matched 4-, 8-, 12- and 30-week old C57Bl6/J WT, CLEC14A$^{-/-}$ and CD248$^{-/-}$ mice, were scanned using a Skyscan 1172 Micro-CT scanner (Bruker, Belgium) as previously described (63), the protocol employed was previously optimised by our previously published work (255). Briefly, bones were collected and cleaned to remove all surrounding tissue followed by a 24-hour 10% formalin-fixation (Sigma, UK, cat no: HT5011-1CS) at room temperature, to remove all formalin remnants, bones underwent a 3 cycle was consisting of incubation in 7 ml PBS under constant agitation for 5 minutes per cycle. Bones were preserved for long-term storage at 4°C in 0.02% NaAz PBS (Sigma, UK, S8032-1004). In preparation for the scan, bones were incubated in a 70% ethanol solution (Ethanol absolute VWR Chemicals, UK, cat no: 2081.330, diluted with ddH2O to 70%) to prevent ring artefact formation and dehydration in universal tubes (DJB Labcare, UK, 309202).

All bones were stabilised inside the tube using bespoke polystyrene moulds to prevent movement artefacts during rotation of the sample. The tube was fixed with Blu tack (Bostik, UK) on a metal base specimen holder inside the scanner, care was used to align the tube with the analog video camera. During the scan, X-ray transmission images of the bone were obtained from multiple angles, image acquisition was performed at 60 kV, 167 µA. The exposure time was set at 580 ms, this was increased over time to reflect the ageing of the X-ray tubes to 1 s, however each experiment set was always scanned with the same setup. X-Ray images were acquired 360° around the bone with a rotation step of 0.45°, a frame average of 4 and random movement of 0. These images were utilised to generate a 3D reconstruction

of the internal structure and density of the calcified tissue using NRecon (version 1.4.4, SkyScan, Belgium). Beam hardening was set at 20% whilst ring artefacts correction was set at 4.

The resulting reconstructed bone structures were analysed using CTAn (version 1.7.0.2, SkyScan, Bruker) to obtain morphometry data using a method optimised by our group (unpublished data). When calculating trabecular bone parameters, a set area in the proximal metaphysis of the tibia was chosen, starting at the end of the proximal growth plate and extending 1370 µm caudally towards the diaphysis. To disseminate between trabecular and cortical bone regions of interest were manually drawn by a blinded researcher. The extent of trabecular bone from the metaphysis to the diaphysis was measured in a cranial-caudal direction. Details on the analysis standard operating procedure and parameters obtained are detailed in Figure 2.5**.**

Cortical morphology was evaluated from 100 slices morphed from a ~1.37 mm region at the midshaft. The inferior point of the midshaft analysis region was identified at 350 slices from the lowest slice in the proximal growth plate.

2.4. Measuring bone turnover in mice using In vivo calcein labelling

Resting 5-weeks old C57Bl/6J WT and CLEC14A$^{-/-}$ male mice were injected intraperitoneally with 20mg/kg of calcein (Sigma-Aldrich, UK, cat no: C0875) (255), six and two days prior to sacrifice by cervical dislocation. Hind limbs were dissected, cleaned, fixed, and washed as described in the section above. Tibiae were maintained in 70% ethanol (VWR, UK, cat no:20821) at 2-8°C until analysis. Undecalcified bones were embedded in methylmethacrylate, sectioned then analysed by members of the Skelet.AL core facility at the University of Sheffield. The rate of new bone formation was measure by analysing calcein

labels in 8 µm thick bone sections obtained from 3 tissue levels. Specifically, the bone cortex was shaved until a complete section containing trabecular bone could be obtained, then 3 tissue sections were taken at 30 µm distance from each other. Images of calcein labelling were analysed using the Osteomeasure software (Osteometrics, United States) which was installed on a computer connected to an inverted microscope fitted with a 20X objective. Measurements were obtained from 6 fields of view in an attempt to cover all areas of the trabecular bone metaphysis to investigate trabecular bone formation; separate measurements were obtained at the endocortical surface to measure endocortical bone formation. The most caudal point of measurement for both measurement areas was 100µm distally from the proximal growth plate. Parameters obtained included: mineral apposition rate (MAR) (calculated as the distance between the midpoints of the two calcein labels divided by the time between the 2 calcein injections, in this case 4 days), mineralising surface (MS) per bone surface (BS) (MS/BS – which is a representation of the volume of mineralised bone deposited per unit time and per unit bone surface), and bone formation rate (BFR) normalised to bone surface area (BS). BFR is calculated using the following equation: BFR = MAR x (MS/BS).

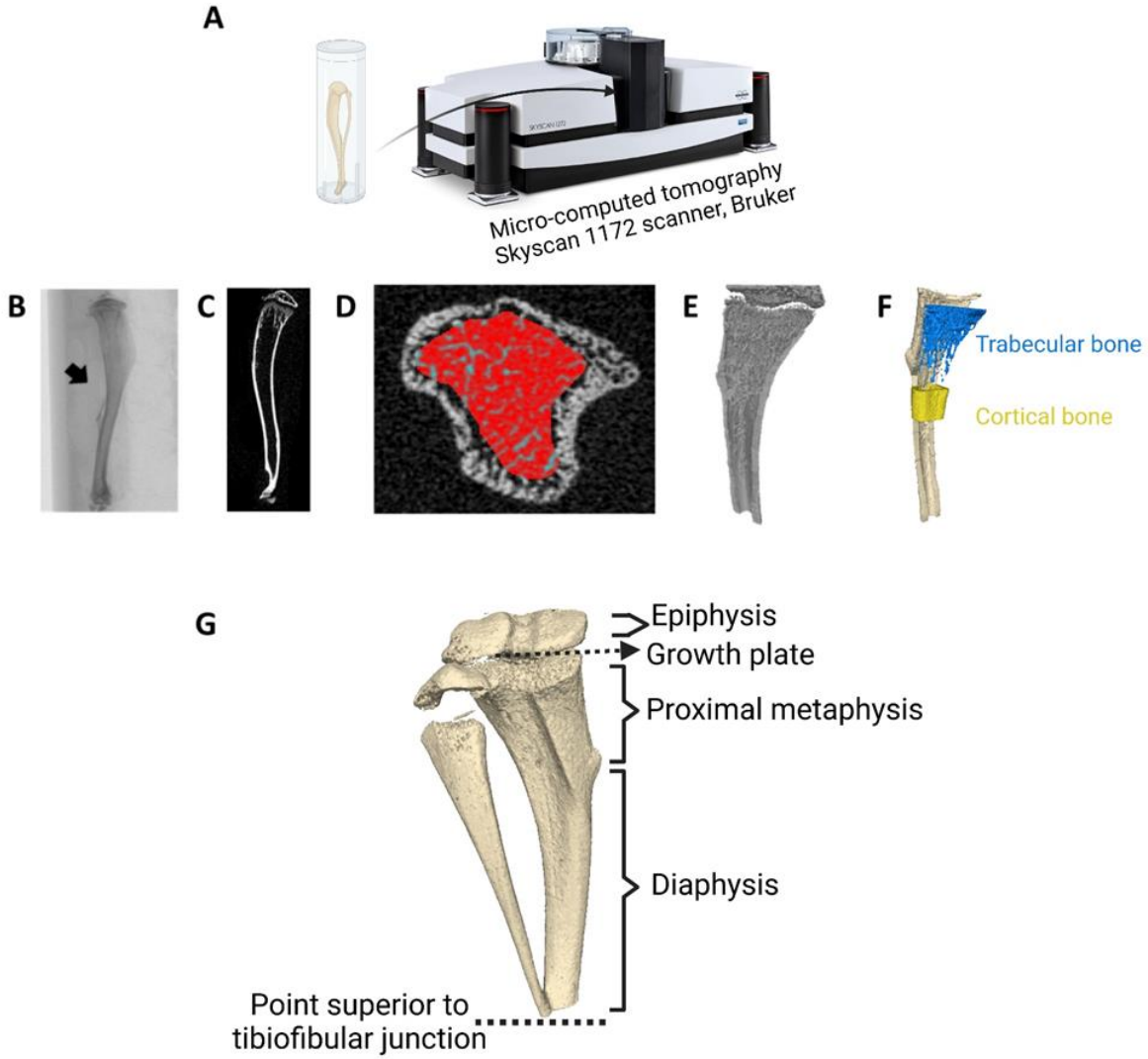


Figure 2.5. microCT data acquisition and analysis workflow. A) Mouse tibias were scanned using a Skyscan 1172 specimen scanner which produces shadow transmission images of the bone from multiple angles by rotating the specimen on a high precision stage. Images B-F are a workflow of the data analysis standard operating procedure followed to obtain histomorphometric measurements of bone tissue. **B)** Example of shadow projection image obtained following initial CT scan. Arrow indicates the tibiofibular junction. **C)** Reconstructed X-ray image of mouse tibia in the sagittal plane. Upper arrow indicates the lowermost point of the growth plate and the uppermost place in the bone where trabecular bone is identified which is used as a start point for region of interest (ROI) selection of trabecular bone. Lower arrow indicates the lowermost point where trabecular bone is identified during ROI selection (this point is variable). **D)** Image demonstrating the selection of the ROI (red) in the mouse tibia (axial plane of view). This is drawn to include trabecular and exclude cortical bone data. **E)** Image of mouse tibia 3D mesh model in sagittal plane. **F)** Image of pseudocoloured bone mesh model, trabecular bone (blue) is superimposed on cortical bone (ivory), the analysed area of cortical bone is also emphasised in yellow. Trabecular extent was calculated by measuring the extent of trabecular bone (blue) (mm) from the lowermost point in the growth plate to the most caudal point in the tibia where trabecular bone was identified. Data was normalised to the to distance between the most inferior point of the growth plate and the tibiofibular junction. **G)** Schematic diagram illustrating main long bone anatomical regions.

Table 10 Definition and description of micro-computed tomography trabecular and cortical morphology analysis

Trabecular Parameter	Description
Percentage Bone Volume	A measure of the volume of trabecular bone contained within the entire volume defined by the region of interest. Abbreviation: BV/TV (%)
Bone Surface	The surface area covered by trabecular bone contained within the manually drawn regions of interest. Abbreviation: B.S (mm^2)
Trabecular Thickness	The average width of trabecular bone within the region of interest calculated as a mean of the widest point of each trabecula. Abbreviation: Tb.Th (mm)
Trabecular Number	The average number of trabeculae contained per millimetre within the defined region of interest. Abbreviation: Tb.N (mm^{-1})
Trabecular Separation	The average distance between each trabecular bone plate or strut contained within the region of interest. Abbreviation: Tb.Sp (mm)
Cortical Parameter	**Description**
Cortical Cross-Sectional Bone Area	The area of cortical bone contained within the region of interest throughout the selection of region. This area is calculated from the 2D analysis of the region of interest drawn only around cortical bone. This area is calculated as: Cortical bone area = cortical volume ÷ (number of slices × slice thickness). Abbreviation: B.Ar (mm^2), also defined as Ct.Ar in other studies (409).
Total cross-sectional bone area	This area represents the entire area of bone contained within a region of interest drawn over the entire periosteal envelope. This includes the area covered by cortical bone as well as the interior core of the bone, starting at the endocortex and extending internally towards the bone marrow area. Abbreviation: T.Ar (mm^2)
Percentage cortical bone	Normalisation of B.Ar to T.Ar, data is presented as a percentage.
Average cortical bone thickness	The average cortical thickness, calculated as the average of the widest cortical measurement in each slice throughout the bone section investigated. The average cortical thickness is calculated from the 2D analysis of the regions of interest drawn around cortical bone only, the same regions of interest utilised for the calculation of B.Ar. Abbrevation: C.Th (mm)

2.5. Bone Mechanical testing by Three-Point Bending

Tibiae and femora were collected from 8-week-old WT, CLEC14A$^{-/-}$ and CD248$^{-/-}$ male mice, euthanised by cervical dislocation. Skin, muscle, and connective tissue were removed from the hind limbs, which were disconnected from the main body at the pelvic hip joint. Bones were fresh frozen wrapped in gauze swabs soaked in PBS to prevent dehydration, then stored at -80°C before use. Samples were allowed to thaw for approximately 30 minutes before being loaded and tested to fracture on the ElectroForce® BioDynamic® 5500 biomechanical testing instrument (TA Instruments, USA) fitted with a 22 N load cell. A three-point bending test provides information on the mechanical proprieties of the mid-diaphysis. To test the structural mechanical proprieties of cortical bone, long bones were centred on a two-end support set at a constant span length of 8mm, a load of <1 N was vertically applied to the midshaft of the bone to ensure its initial stabilisation. To ensure consistency, tibiae were placed horizontally with the fibula facing down, while femora were placed horizontally with the anterior side of the intercondyloid fossa facing down. An increasing amount of force was then applied perpendicular to the mid-diaphysis using a flat-tipped wedge connected to a motorized force transducer, controlled via a software interface (WinTest); the constant displacement rate was set at 0.5 mm/s. Force and displacement were measured every 0.005 seconds until complete fracture of the bone. The biomechanical proprieties of each bone were calculated by generating several parameters as presented in Table 11. A summary and explanation of the key analysis terms can be found in Figure 2.6.

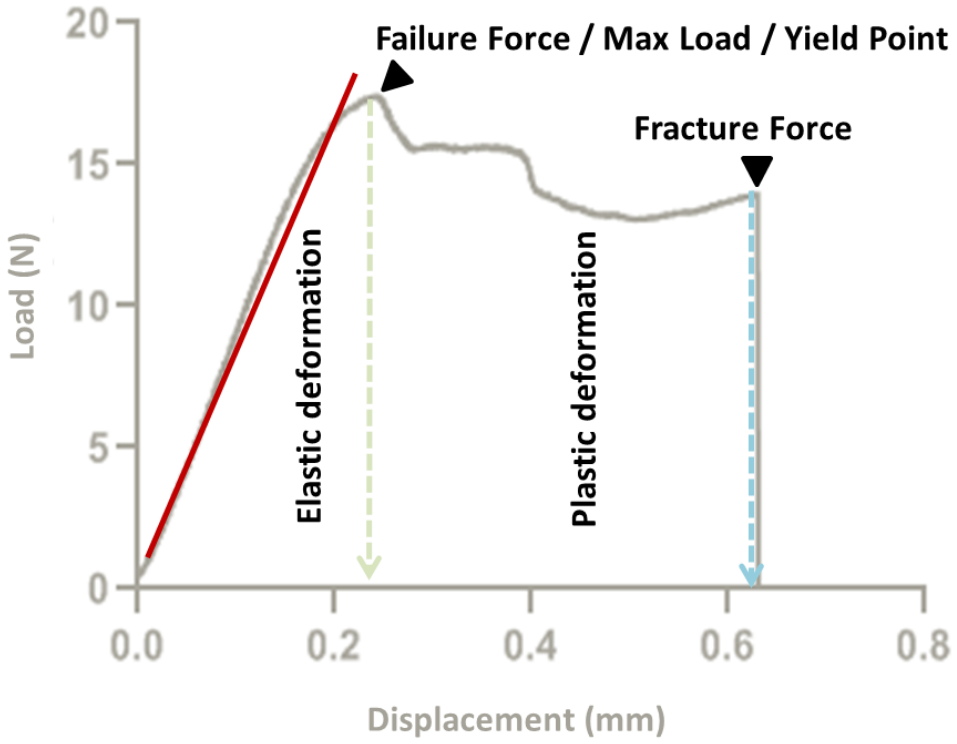


Figure 2.6 Graphic illustration of three-point bending mechanical testing key analysis terms. A three-point bending load vs displacement graph (load deformation curve) of an 8-week-old WT murine tibia is shown as an example. Arrow heads indicate the maximum force achieved during testing (this point is used to calculate the failure force) as well as the maximum force recorded after the yield point and just before bone fracture (fracture force). The failure force point, also known as the yield point, is used as a reference point to determine the end of the elastic deformation (delineated by the black dashed green arrow) phase of the bone during testing, before reaching the yield point. The elastic deformation denomination is explained by the fact that, should the force imposed onto the bone cease, the bone would be expected to return to its original position. The area under the curve (AUC) pertaining to the elastic deformation phase is calculated to obtain work to failure values. On the other hand, work to fracture is calculated as the AUC composed of the combined elastic and plastic deformation phases. Plastic deformation starts at the end of the elastic deformation phase after the yield point and extends to the end of the trace graph when the tested bone is fully fractured; the border of this area is delineated by the dashed blue arrow. The red line indicates the simple linear regression line of best fit drawn over the elastic region. Work to failure, work to fracture and stiffness were calculated from the load deformation curve. The yield point was determined from the load deformation curve at the point at which the curve deviated from linearity, stiffness was calculated by plotting the force-displacement curve for each bone and calculating the slope of the linear fit over the elastic region ending at the yield point.

Table 11. Summary of biomechanical parameters generated from three-point bending analysis

Three-point bending generated parameters	Unit name and symbol	Description
Failure Force (alternative literature names for the same parameter include maximum load or ultimate force)	Newton (N)	The maximum force sustained by the tested bone at the yield point during elastic deformation, this is calculated from the load displacement curve
Fracture Force (Breaking Force)	Newton (N)	The force sustained by the tested bone just at the point of fracture at the end of the plastic deformation phase
(Elastic) Stiffness	Newton / mm (N/mm)	Elastic stiffness is calculated from the slope in the linear region of the load displacement curve
Work to Failure (Elastic Work to Failure)	AUC	The amount of energy a bone absorbs before yielding and losing its elastic proprieties. The Work to Failure is calculated as the area under the curve (AUC) of the load displacement curve from the start of the experiment until the yield point (which coincides with the point at which the failure force is calculated).
Work to Fracture (Total Work to Failure)	AUC	The total work to failure is the amount of energy a bone absorbs before fracturing; this is calculated as the area under the curve (AUC) of the load displacement curve from the start of the experiment until the point of bone fracture.

2.6. Extraction and isolation of calvarial osteoblasts

Osteoblast lineage enriched cells were isolated from C57Bl/6J, CD248$^{-/-}$ and CLEC14A$^{-/-}$ postnatal day 4 pup calvaria in sterile conditions using the Bakker and Klein-Nulend protocol (410). This method was optimised for the use of Collagenase D (Sigma Aldrich Roche, UK, cat no: COLLD-RO) and EDTA (Sigma-Aldrich, UK, cat no: T4174) as digestion components (410). Briefly, calvaria were dissected from postnatal day 4 mouse pups euthanised by decapitation. Mouse heads were collected in foetal bovine serum (FBS)-free Minimum Essential Medium Eagles media (αMEM) enriched with 2mM L-Glutamine, 100U/ml Penicillin and 100µg/ml Streptomycin (Table 7) on ice. Heads were initially disinfected in 70% ethanol (Sigma, UK, cat no: 51976) for 30 seconds, to remove all traces of alcohol, heads were washed three times in sterile PBS. From this point forward all work was carried out in sterile conditions in a cell culture hood. Calvaria were cleaned and dissected to remove the surrounding cartilage or brain tissue matter, and washed in αMEM to reduce contamination with neurons, chondrocytes and adipose cells, before being added to capped polystyrene 5 mL tubes (Appleton Woods, UK, cat no: BF221) with 3 mL of FBS free αMEM media and 1 mg/ml Collagenase D. Tubes were incubated with a 2 cm magnetic stirrer for 30 minutes at 37°C in water on a hot plate stirrer. The first cell fraction was discarded and the calvaria were carefully washed in FBS free αMEM media to remove all potential contaminating non-osteoblastic cells. Calvaria were then re-incubated with the same digestion solution for another 30 minutes, cells resulting from this incubation were collected and washed in αMEM enriched with 2mM L-Glutamine, 100U/ml Penicillin and 100µg/ml Streptomycin and 10% FBS. To obtain the third cell fraction, which was collected as well, cells were incubated for 10 minutes with sterile 5µM

EDTA solution in FBS-free Minimum Essential Medium Eagles media (αMEM) enriched with 2mM L-Glutamine, 100U/ml Penicillin and 100µg/ml Streptomycin. The final incubation was a repeat of the same steps as the one performed to obtain the second cell fraction – calvaria were incubated in αMEM media with collagenase D for another 30 minutes. Cells from the last 3 cell fractions were cumulated, washed and filtered through a 100 µm cell strainer and incubated overnight in cap-vented Corning T25 cm^2 cell culture flasks (Sigma-Aldrich, UK, cat no: CLS430641) in expansion media: αMEM media enriched with 2mM L-Glutamine, 100U/ml Penicillin and 100 µg/ml Streptomycin and 10% FBS. After 24-hours the media was changed to remove all floating dead cells or non-adherent cells. Osteoprogenitors were then allowed to expand for up to 7 days until they reached 85-95% confluency, when they were transferred into a Corning T75 cm^2 cell culture flask (Sigma-Aldrich, UK, cat no: CLS430641) before use for *in vitro* experiments. Unless stated otherwise cell were cultured at 37°C, 5% CO_2. When transferring, cells were washed with sterile PBS, then they were detached by incubation with a freshly prepared 2X Trypsin-EDTA solution (1g/L porcine trypsin and 400mg/L EDTA, Sigma-Aldrich, UK, cat no: T4717, diluted in sterile PBS) for 5-10 minutes at 37°C, if cells were not completely detached, gentle tapping was employed to aid complete cell detachment. The trypsin-EDTA solution was neutralised using expansion media. Cells were centrifuged at 300-350g for 4 minutes, then they were resuspended in αMEM media and diluted to the working concentration if used for a protocol or split 1:3 if passaging.

2.7. Osteoblast maturation in vitro assays

To induce maturation, osteolineage enriched cells, herein called osteoblasts, were seeded into a 48 well plate at a density of 8 $\times 10^3$ per well (as previously optimised in our lab) and grown to confluence. Subsequently, cells were incubated with either expansion media or osteoinduction media: αMEM media (Sigma) supplemented with 10% FBS, 2mM L-Glutamine, 100U/ml Penicillin, 100 µg/ml Streptomycin, 50 µg/ml L-ascorbic acid (Sigma, UK, cat no: A5960) and 10 mM β-glycerophosphate (Sigma, UK, cat no: G9422) for 21 days as previously published (411). To ensure a reliable control for these assays, osteoblasts were also separately cultured in expansion media lacking β-glycerophosphate and L-ascorbic acid. Half of the relevant culture media was changed every second day taking caution not to disturb the cell monolayer.

2.7.1.1. Alkaline Phosphatase activity ELISA

Pre-osteoblasts were washed in Ca^{2+} and Mg^{2+} free (unless otherwise stated) 1x phosphate buffered saline (PBS) two times with a 2-minute incubation period, cells were detached from wells using trypsin, washed with twice the volume of trypsin α MEM media, then lysed in RIPA Buffer for 15 minutes on ice. Cell lysates were collected following centrifugation at 13,000 g, the collected cell lysate was mixed with alkaline phosphatase yellow stain at a ratio of 1:5 in a final volume of 100 µl of solution then incubated with constant gentle agitation for 30 minutes at 37°C in an incubator shaker (Sciquip). ALPL activity was measured in osteoblast cell lysates with the use of a buffered alkaline phosphate substrate containing p-nitrophenyl phosphate (pNPP), which reduces alkaline phosphatase to produce p-Nitrophenol (PNP) and inorganic phosphate, when this occurs the substrate turns yellow and alkaline phosphatase

fluorescence can be read at a 405 nm wavelength. Technical replicates were run in triplicate, plates were read on the BioTek® synergy HT plate reader and analysed using BioTek® Gen5 plate reading software.

2.7.1.2. Alizarin Red staining for bone nodule formation assay

Pre-osteoblasts were cultured for up to 18 days. When stained for alizarin red coverage and bone nodule formation cells were washed in 1x PBS twice and fixed in 200 µl 10% formaldehyde (for 15 minutes at RT. Cells were washed with distilled water henceforth to prevent cell dislodgement from the bottom of the plate. Cells were stained with 40 mM alizarin red stain (ScienCellTM, UK, cat no: 8678) and then incubated under constant gentle agitation (~ 90 rpm) on an orbital shaker (Heathrow Scientific, UK), for 30 minutes, at RT, in the dark. Cells were washed to remove excess dye, stored in distilled sterile water at 2-8 ° C until images were acquired at 4X magnification using the Cytation 5 microscope (Biotek/Agilent, United States). To measure bone nodule formation, images were analysed in ImageJ (NIH, United States) by mapping a colour threshold over the acquired images, obtaining thus the percent of area covered by alizarin red staining.

The same protocol was also utilised when staining mineralisation in the P4 C57Bl/6J pups calvaria.

2.8. RNA extraction and isolation for RNA sequencing and quantitative real-time PCR (qPCR)

Total RNA was extracted from calvarial osteoblasts with the RNeasy Micro Kit (50) (Qiagen, UK, cat no: 74104) immediately after cell isolation or at the passage indicated as per the manufacturer's instructions. Residual genomic RNA was removed using DNase I. The quantity and purity of total RNA was assessed using a Nanodrop 2000 analyser (ThermoFisher, UK),

RNA quantity was assessed from absorbance at 260 optical density reading and quality was assessed from the 260/280 and 260/230 optical density readings ratios.

2.8.1.1. RT qPCR

500 ng RNA per sample (equalised in RNAse free water) was added to a MicroAmp™ Optical 96-Well Reaction Plate (ThermoFisher, UK, cat no: N8010560) at 1:1 ratio of RNA to cDNA master mix (High-Capacity cDNA Reverse Transcription Kit, ThermoFisher, UK, cat no: 4368814), the master mix was prepared with kit components as per manufacturer's instructions. RNA was denatured for 5 mins at 65°C and reverse transcribed for 1 hour at 50°C. Gene expression and reference gene *Gapdh* levels were detected using Applied Biosystems® TaqMan® Gene Expression Master Mix and FAM-conjugated Taqman probes (listed in Table 4). Amplification conditions were 95°C for a 2-minute cycle followed by 40 cycles at 95°C for 15 seconds and 60°C for 1 min. Quantitative reverse transcription PCR (RT-qPCR) was performed in a Roche LC480 real-time thermal cycler (F. Hoffmann- La Roche, UK) in a reaction volume of 5 µL consisting of a mix of: 2.52 µl Applied Biosystems® TaqMan® Gene Expression Master Mix, 0.28 µl relevant Taqman primer, and 2.3 µl cDNA per sample.

2.9. Serum analysis of circulating P1NP

Serum samples were collected by cardiac puncture from WT and CLEC14A$^{-/-}$ male mice. Following a 30-60 mins resting period at room temperature, samples were prepared by centrifugation of the blood (1.600 g for 10 min RT), then stored in aliquots at −80°C for biochemical assays. Serum P1NP was assayed using the RatLapsTM total procollagen type-1 N terminal propeptide ELISA kit (Immunodiagnosticsystems, UK, cat no: AC-33F1); all reagents required were provided in the kits. Serum samples, calibrators, positive and negative controls

were prepared as per the manufacturer's instructions. All incubations were carried out at room temperature unless stated otherwise. Briefly, for the P1NP analysis, serum samples were thawed on ice, then they were diluted 1:9 (30-weeks old mouse samples) or 1:80 (4-weeks old mouse samples), (following identification of the suitable dilution in previous experiments-not shown). Note calibrators and controls were allowed to reach room temperature for an hour before the start of the experiment (as advised by the manufacturer). All samples, calibrators and controls were ran in duplicate in a 96-well plate provided with the kit. Immediately thereafter, 50 µl of biotinylated P1NP was added to all wells and the plate was covered and incubated for 60 minutes. Wells were washed x 5 times, following removal of the wash buffer, the plate was vigorously tapped on tissue paper to remove all excess liquid in between washes to ensure efficient removal of excess product. All wells were then incubated with an enzyme conjugate for 30 minutes at, followed by another 30 minutes incubation with a 3,3',5,5'-Tetramethylbenzidine (TMB) substrate, the reaction was stopped with 50 µl HCl. The plate was read on a Synergy HT (BioTek, UK) plate reader at 450nm. Data analysis was performed in GraphPad Prism (GraphPad Software Inc, California, USA), by fitting the calibrator optical density reads against a 4-parameter logistic (4PL) regression curve. Four parameters were obtained from the linear regression calculation: a = Minimum value, b = Hills slope of curve c = Point of inflection and d = Maximum value. These values were utilised in the following equation model $x = c(a - d)/(y - d) - 1)^{1/b}$. Note, x = the independent variable (P1NP concentration in the serum samples) and y = the dependent variable (optical density reading for each sample studied). Using the above equation, the value for P1NP was calculated and then this was corrected against the relevant dilution factor to obtain a final total concentration for P1NP in ng/µl.

2.10. Ovariectomy-induced osteoporosis in C57Bl/6J WT and CLEC14A$^{-/-}$ female mice

In preparation for surgery all mice were allowed ad libitum access to Medigel (ClearH2O, US, cat no: 74-02-5022), 24 hours prior to surgery. Half an hour before surgery all mice were administered buprenorphine subcutaneously (s.c.) to help with post-surgery pain management. 12-week-old C57Bl/6J female mice were initially anesthetised with 5% isoflurane, anaesthesia was further maintained with 3.5-4.5% isoflurane. Ovaries were removed through a midline laparotomy incision as previously described (412). Briefly, the ovarian fat pad was retracted outside of the peritoneal cavity through a small incision (< 1 cm), ovaries were separated from the oviduct taking care not to rupture the uterus in order to limit the amount of inflammation induced by surgery and other surgical complications. All mice were injected s.c. with a bolus of 500 ml sterile PBS before being allowed to recover. Tissue was collected at 1-, 2- and 4 weeks following surgery. Two mice from the WT OVX, one mouse in the CLEC14A$^{-/-}$ OVX, one mouse in the WT OVX C2 and one mouse in the WT OVX C4 group had to be euthanised due to post-surgery complications prior to the end of the study when bones were collected for analysis. For this reason, those samples were not included in our analyses. Monitoring of the remaining mice revealed no other complications related to surgery, mice were weighed daily for 7 days post-surgery and biweekly thereafter, in addition mice were observed to ensure the lack of mobility issues in all mice as this could potentially affect bone formation.

2.11. *In vivo* blocking of CLEC14A MMRN2 interaction during postnatal bone growth and in an ovariectomy-induced osteoporosis model of bone loss

In-house monoclonal antibodies, hereafter referred to as C2 and C4 previously generated by Noy et al., were used to either bind CLEC14A without blocking its interaction with MMRN2

(C2) or to bind CLEC14A and block its interaction with MMRN2 (C4) (348). C2 was used as control and C4 was used as treatment. When testing the effect blockade of CLEC14A MMRN2 interaction in young mice, 100 µl of 1 mg/ml C2 or C4 antibody or sterile PBS (vehicle control) were intraperitoneally administered to 4-week-old C57BL6/J male mice twice a week for 4 weeks.

When testing the effect blockade of CLEC14A MMRN2 interaction in ovariectomy-induced osteoporosis models, 12-13 weeks old C57BL6/J ovariectomised female mice were treated with 100 µg C2 or C4 antibody or sterile PBS (vehicle control) administered biweekly i.p for 4 weeks.

For both experiment sets mice were sacrificed at day 28 and tissue was collected and processed for micro-computed tomography as described in section 2.2.

2.12. Statistical analyses

Parametric tests were employed if data was continuous, normally distributed and presented equal variance. If one of these requirements was not satisfied, non-parametric testing was employed. A Student's t-test or a parametric one-way ANOVA were used to compare two groups, or to compare three groups or more, respectively. A Mann Whitney U test or a Kruskal Wallis test were employed to compare two groups, or to compare three groups or more, respectively. When two dependent variables were compared a two-way ANOVA was employed for parametric data, or alternatively, multiple Mann Whitney U tests were employed to compare two groups at a time if data was non-parametric.

For all *in vivo* experiments power calculations were used to estimate sample size. This was accomplished with the aid of G Power v3.1 (Allgemeine Psychologie und Arbeitspsychologie, Dusseldorf, Germany).

3. CHAPTER III ENDOTHELIAL AND OSTEOBLAST CELLULAR MECHANISMS REGULATED BY CLEC14A IN THE GROWING POSTNATAL BONE

3.1. Introduction

Blood vessels are well-known regulators of bone homeostasis, and a growing body of work has been dedicated to the biological processes regulated by the vascular endothelium in the bone. Technological advances in confocal and light sheet microscopy coupled with the development of novel bone processing techniques (2, 137), have provided the bone imaging field the ability to investigate the entire vascular network of the bone in 2D and 3D, leading to the discovery of new capillary subtypes. One of these capillaries, the H-type vascular capillary, has been described as an active modulator of osteogenesis. H-type capillaries actively expand during bone formation and bone growth (2, 145), both processes shown to be heavily reliant on angiogenesis.

CD248 and CLEC14A have previously been shown to regulate angiogenesis (246, 338, 339, 345, 352-354, 356, 413, 414) as described in detail in sections 1.8.1 and 1.8.2. Moreover, CD248 has previously been ascribed a role in regulation of osteogenesis during postnatal bone growth (255). We therefore hypothesised that the CLEC14-MMRN2-CD248 protein complex regulates osteogenesis by modulating endothelial-cell osteoblast crosstalk. Work presented in this chapter has focused on addressing aim I (Characterise the effect of CLEC14A on bone formation during postnatal bone growth). To accomplish this and to obtain a better understanding of the role of CLEC14A in angiogenesis and its potential implication in coupling angiogenesis to bone accrual, we established the patterns of expression of CLEC14A and MMRN2 in single-cell sequencing and bulk RNA-sequencing publicly available datasets (sections 3.2 and 3.3), the expression of all three proteins was also probed in the murine long bone (section 3.4). Furthermore, tibiae collected from CLEC14A knock out mice ($CLEC14A^{-/-}$) were investigated to measure the effect of CLEC14A deficiency on morphology and density of

H-type endothelium in the murine tibia (sections 3.5 and 3.6). To probe our theory that CLEC14A is important for coupling of EC to osteoblast crosstalk we also set to study the effect of CLEC14A genetic deletion on the patterning of osteoblast localisation in different bone compartments (section 3.7). This was achieved via immunolabelling of immature and mature osteoblasts as differentiated by Osterix (OSX) and Type-I Collagen (COL1A1) fluorescent staining, respectively, in tibia sections.

3.2. Single cell (sc) – RNA sequencing of the bone and bone marrow cells

To better understand the pattern of expression of CLEC14A and MMRN2 in the long bone at cellular level, expression of CLEC14A and MMRN2 were probed in a previously published dataset (GSE128423), where single cell (sc) RNA sequencing was performed on bone and bone marrow cells of 8-week-old C57Bl/6J mice (403). Following quality control analysis which involved exclusion of genes with a high mitochondrial or ribosomal RNA content, cells were distributed into clusters according to similarities and differences in their transcriptomic repertoire. Cluster naming was completed taking in consideration the top 10 most differentially expressed genes in each cluster (Figure 3.1). A figure illustrating all the cell-specific genes used to name each cluster is available in the Appendix (Figure 9.1). Both mesenchymal and haematopoietic lineage cells were captured in this data set, no osteoclast or osteocytes could be identified (Figure 9.1). The stroma component was investigated further and expression of CLEC14A and MMRN2 transcripts was probed. CLEC14A and MMRNA transcriptomic expression was exclusive to the endothelial cell (EC) cluster demonstrating that both proteins are highly and specifically expressed in EC (Figure 3.2).

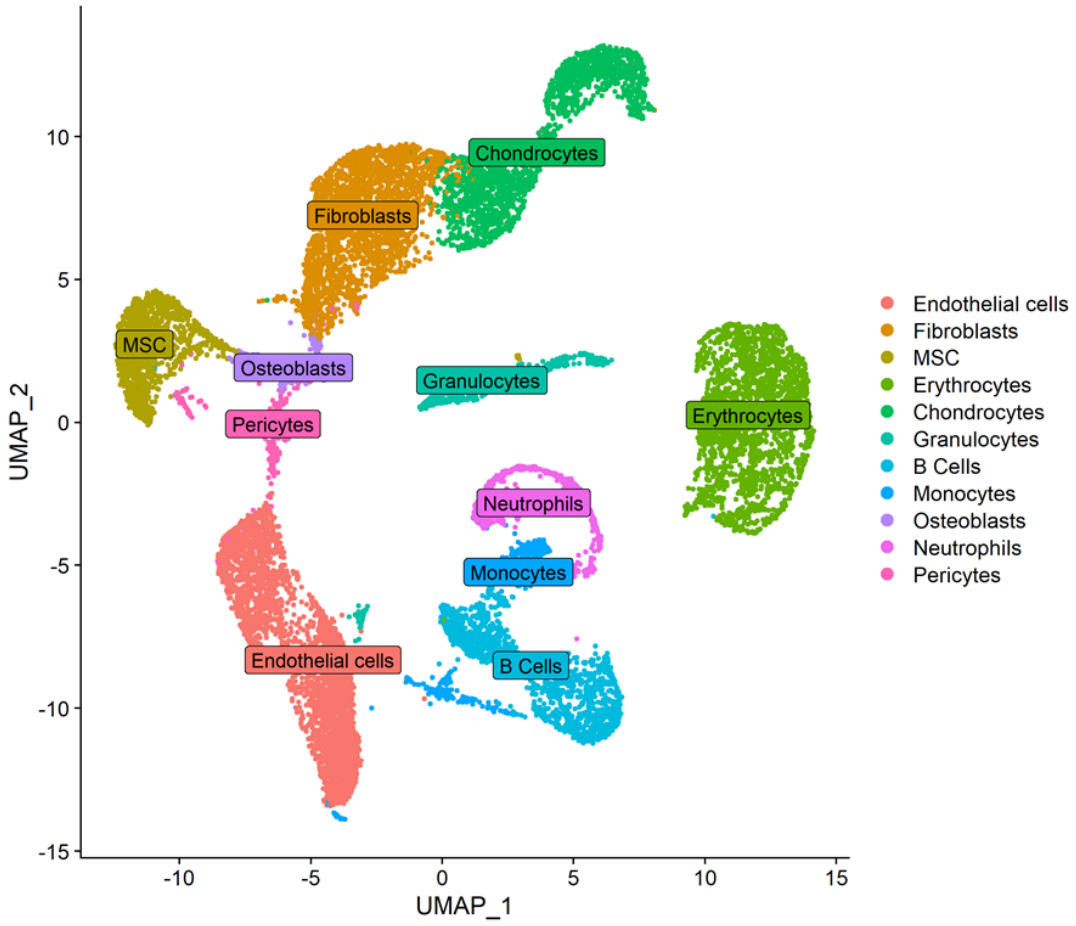


Figure 3.1. Single Cell RNA sequencing of cells in the bone and bone marrow of 8-10 weeks C57BL/6J male mice (GSE128423). T-SNE map of bone and bone marrow cells coloured-coded according to the clusters they belong to. Clusters were annotated post-hoc, a figure showing the top markers for each cluster is available in the Appendix Figure 9.1 .

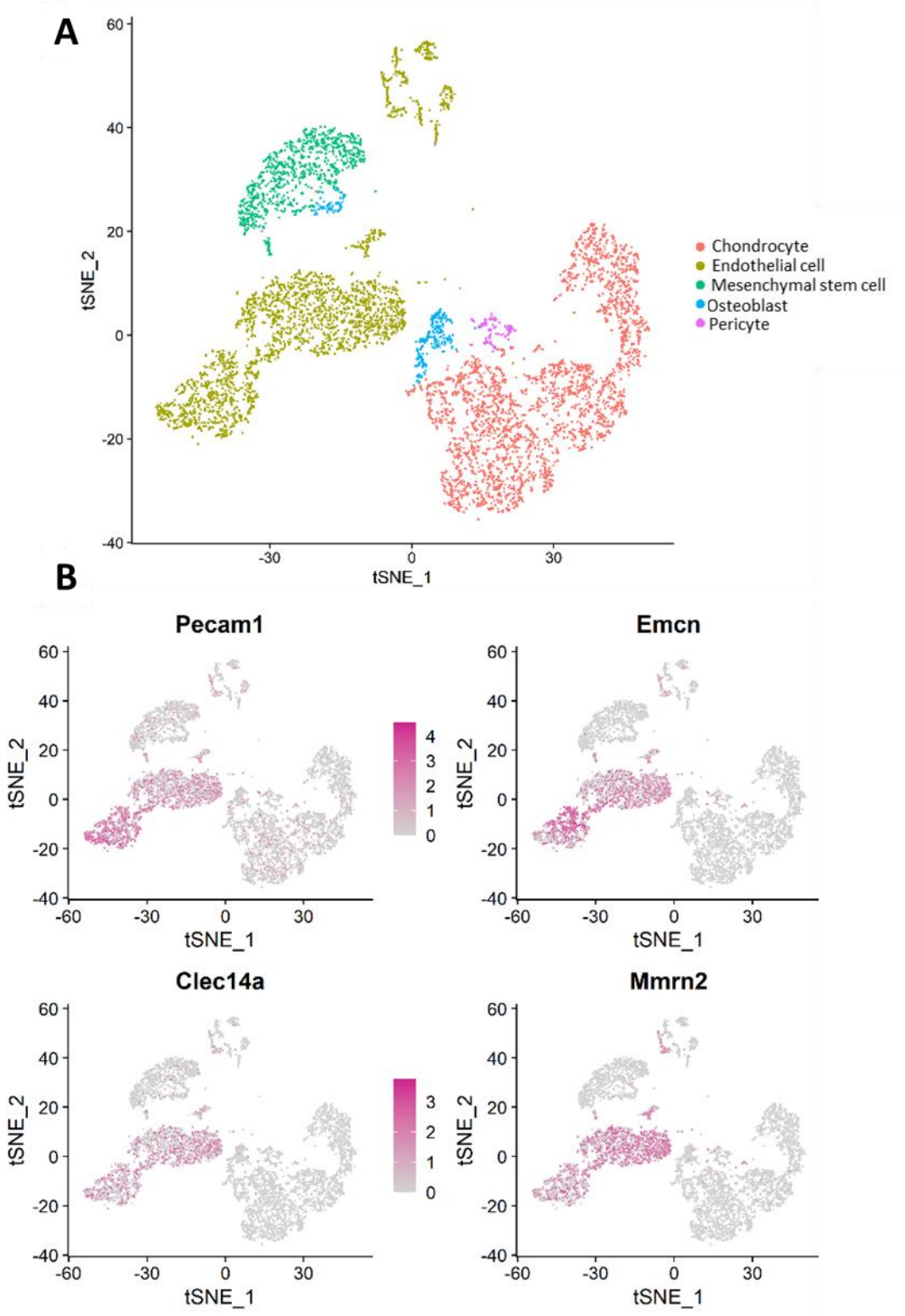


Figure 3.2 Expression of CLEC14A and MMRN2 in the bone stroma of adult mice (GSE128423). **A)** t-SNE map of the stromal clusters in the bone coloured-coded according to their cluster name. **B)** t-SNE maps reveal expression of H-type pe EC markers Pecam1 and Emcn as well as Clec14a and Mmrn2. Emcn, Clec14a and Mmrn2 expression is shown to be specific to EC clusters, whilst Pecam1 is shown to also be expressed by a low minority of MSC and chondrocytes.

3.3. Bulk RNAseq analysis of H-type ECs transcriptomic signature

Distinct genomic regulation of H- and L-type capillaries was previously confirmed using RNA sequencing of H type and L-type EC sorted from postnatal day 6 C57BL/6J male mice tibiae and femora (136). Moreover, ECM molecules and cell–matrix receptors genes were shown to be enriched in H-type EC, however, the exact genes contributing to this enrichment were not listed. (Figure 3.3 A). Hence, we set to investigate the publicly available RNA sequencing dataset (E-MTAB-4066) (136), to probe for the expression of CLEC14A and MMRN2 at transcriptomic level in H- and L-type EC during bone growth.

Initial quality control analysis steps were as follows: transcripts corresponding to pseudogenes or non-coding RNA were excluded, resulting in the identification of a total number of 35579 transcripts in all EC types. No major differences were observed in the percentages of genes falling into exons or the percentage of ribosomal RNA or mitochondrial RNA (Figure 3.3 B). Neighbour joining clustering analysis (SeqMonk) separated samples in a data store tree according to the capillary type they were originating from (Figure 3.4 A). Unsupervised hierarchical clustering (tree store) and unbiased principle component analysis (PCA) confirmed high reproducibility between each sample set and, in line with the widely accepted distinct roles of these two EC types samples separated from each other and clustered together according to their cell or of origin (Figure 3.4 B).

Next, the RNA-seq dataset was probed to identify the main molecular pathways behind the different functional proprieties of these two EC subtypes. Gene set enrichment (GSE) analysis was performed to identify gene sets enriched in H-type and L-type ECs. Genes with higher expression levels in H-type ECs were markedly enriched in pathways involved in: the modulation of angiogenesis (gene set enrichment terms: VEGF signalling, hypoxia responses),

regulation of cell motility (gene set enrichment terms: focal adhesion, apical junction), regulation of cell-cell interactions (gene set enrichment terms: integrin cell surface interactions) (Figure 3.5), and finally, moderation of the surrounding extracellular matrix (ECM) in the bone as well as bone formation via control of collagen metabolism (gene set enrichment terms: RUNX2 regulated bone development, collagen formation and degradation, extracellular matrix organisation and degradation, extracellular matrix receptor integration) (Figure 3.6). GSE analysis also revealed striking gene set enrichment for regulation of the immune system and maintenance of haematopoiesis in the bone marrow (gene set enrichment terms: hematopoietic cell lineage, cytokine-cytokine receptors interaction, inflammatory response, and others) (Figure 3.7) for the L-type EC group.

Filtering of transcripts was performed to identify significantly different expression gene patterns between H- and L-type vessels (DESeq2, $p<0.01$ or intensity difference analysis (IDA), $p < 0.01$). These analyses lead to the identification of 3989 (Figure 3.8 A) or 148 differentially expressed transcripts (Figure 3.8 B), for DESeq2 or IDA respectively. Confirming the arteriole-like structure and function of H-type vessels, H-type EC showed significantly higher expression of markers pertaining to an arterial signature including: CD34, LY6C1, CAV1, SPARCL1, TM4SF1, GNAS, and ICAM2. Surprisingly, H-type EC also expressed higher mRNA levels of markers more usually associated with sinusoidal endothelial cells whose morphology more closely resembles L type endothelial cells: FLT4, SELE, STAB2, SEPP1, FABP4, IL6ST, VCAM1, ADAMTS5, ICAM1. GSEA and differential gene expression analyses indicated that L-type EC were also enriched for markers expressed by haematopoietic-lineage cells, and included RNA transcripts which modulate immune regulation responses, inflammation, cell adhesion and chemotaxis: CCL3, CCL4, CCL9; CXC3CR1, ITGAB. In addition, transcripts specific to expression by immune cells including macrophage markers: CD163, CD86, CLEC10A, and T-cell markers: CD4, CD8

were also identified, perhaps indicating contamination of the sorted L type endothelial cells with non-endothelial cell types.

The 148 transcripts, identified by intensity difference analysis, were further clustered in 3 main subsets (analysed by hierarchical clustering (R = 0.96) (Figure 3.9 and Figure 3.10). Hierarchical clustering allowed for the identification of 3 clusters of genes separated by their direction of regulation (up or down) in the 2 groups compared (Figure 3.9 and Figure 3.10). CLEC14A, CD93 and MMRN2 transcript levels were increased in the H-type EC group and were distributed to a cluster of genes with angiogenesis and cell-to-cell interaction properties. CD31 (Pecam1) and EMCN, the transcripts defining the H-type EC population, were also enriched in the H-type EC group and were also distributed to the same cluster as CLEC14A and MMRN2 (Figure 3.8 and Figure 3.10). Of relevance to our hypothesis, other members of the CLEC14A/CD93-MMRN2 interactome were also identified as upregulated in H-type ECs: ROBO4, CDH5, CLDN5, HSPG2 (345, 351, 414)(Figure 3.8, Figure 3.10, Figure 3.11, and Figure 3.12). An upregulation of transcripts with confirmed osteogenic (FZD4, SOX18) and angiogenic (NOTCH4, SEMA6A, SEMA3F, ROBO1, EPHB4, TIE1, FLT4) roles were also upregulated in H-type EC (Figure 3.10 and Figure 3.11) (138, 415, 416).

In summary, analysis of this dataset identified upregulation of transcripts which provide a molecular support to the proangiogenic and osteogenic role performed by the H-type ECs. In addition, increased mRNA levels of CLEC14A and MMRN2 as well as other members of their interactome were identified at higher levels in H type endothelium compared to L type EC.

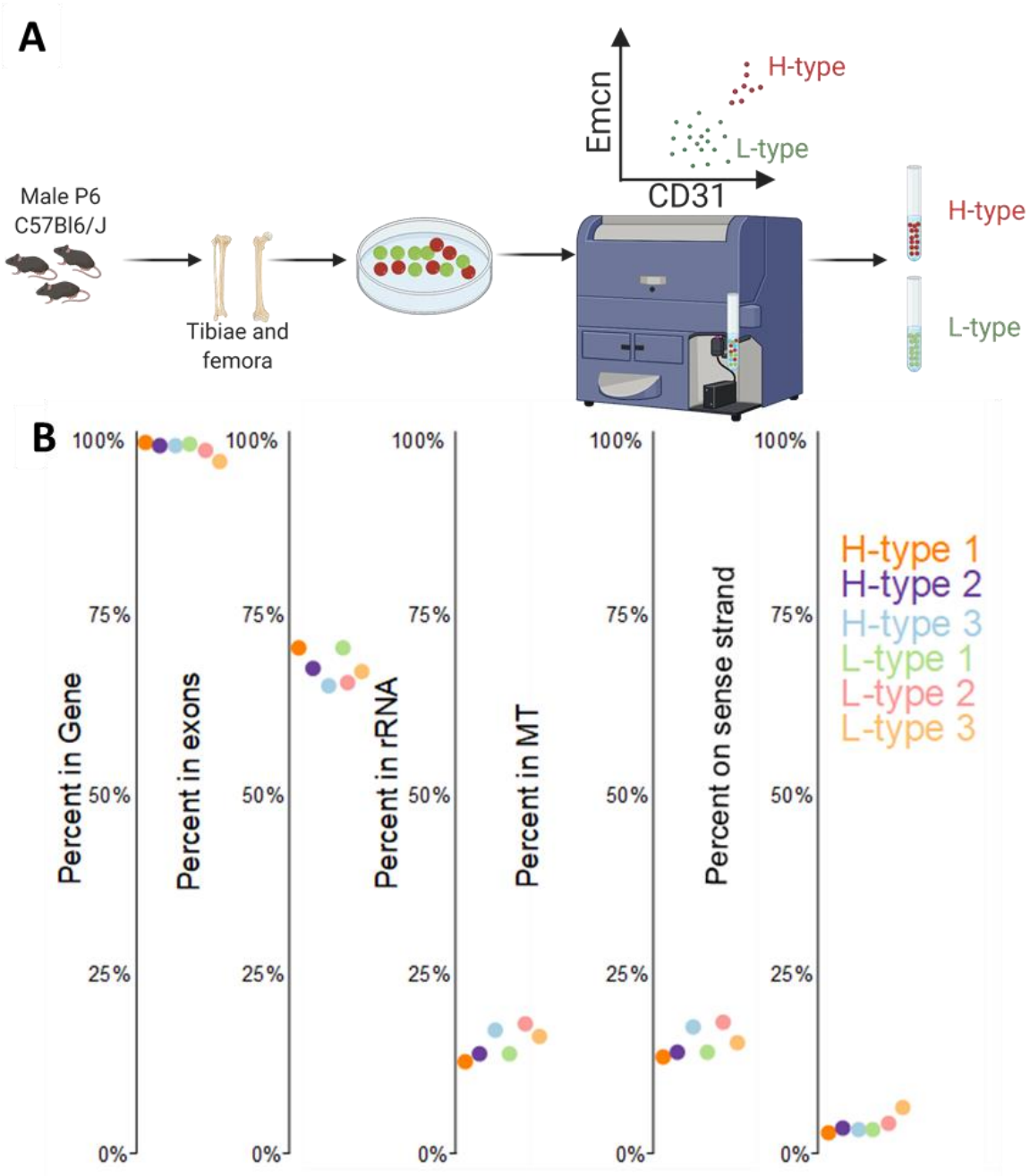


Figure 3.3 RNAseq transcriptomic quality control analysis of bone capillaries (E-MTAB-4066 dataset). A) Schematic demonstrating the experimental process performed and reported by Langen et al. (2017): Endothelial cell extraction from the bone (tibiae and femora together) and flow activated cell sorting isolation protocol. Database accession number E-MTAB-4066. **B)** Quality control graphs of our analysis of the E-MTAB-4066 dataset, plot shows the percentage of reads reported in genes, exons and the percentage of reads originating from ribosomal sRNA) and mitochondrial RNA (MT), and the sense strand, illustrating no overt differences between all samples analysed and a relatively high sample quality on the overall.

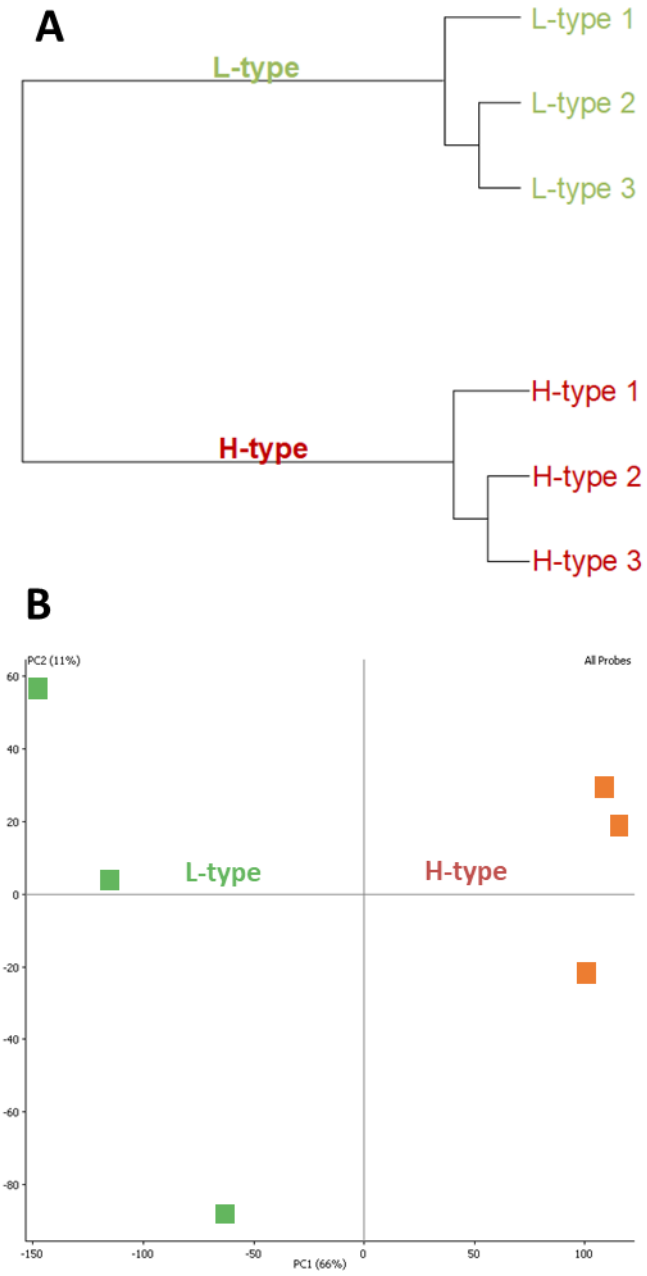


Figure 3.4 Clustering and gene ontology analysis of H-type and L-type EC RNA sequencing samples (E-MTAB-4066 dataset). A-B) Unsupervised hierarchical clustering, (dendrogram – A and principal component analysis – **B)** of log2 normalised counting reads over exons (RPM) for all detected genes. Samples are separated according to cell type, providing an overview of the differential transcriptomic regulation of H- and L-type EC.

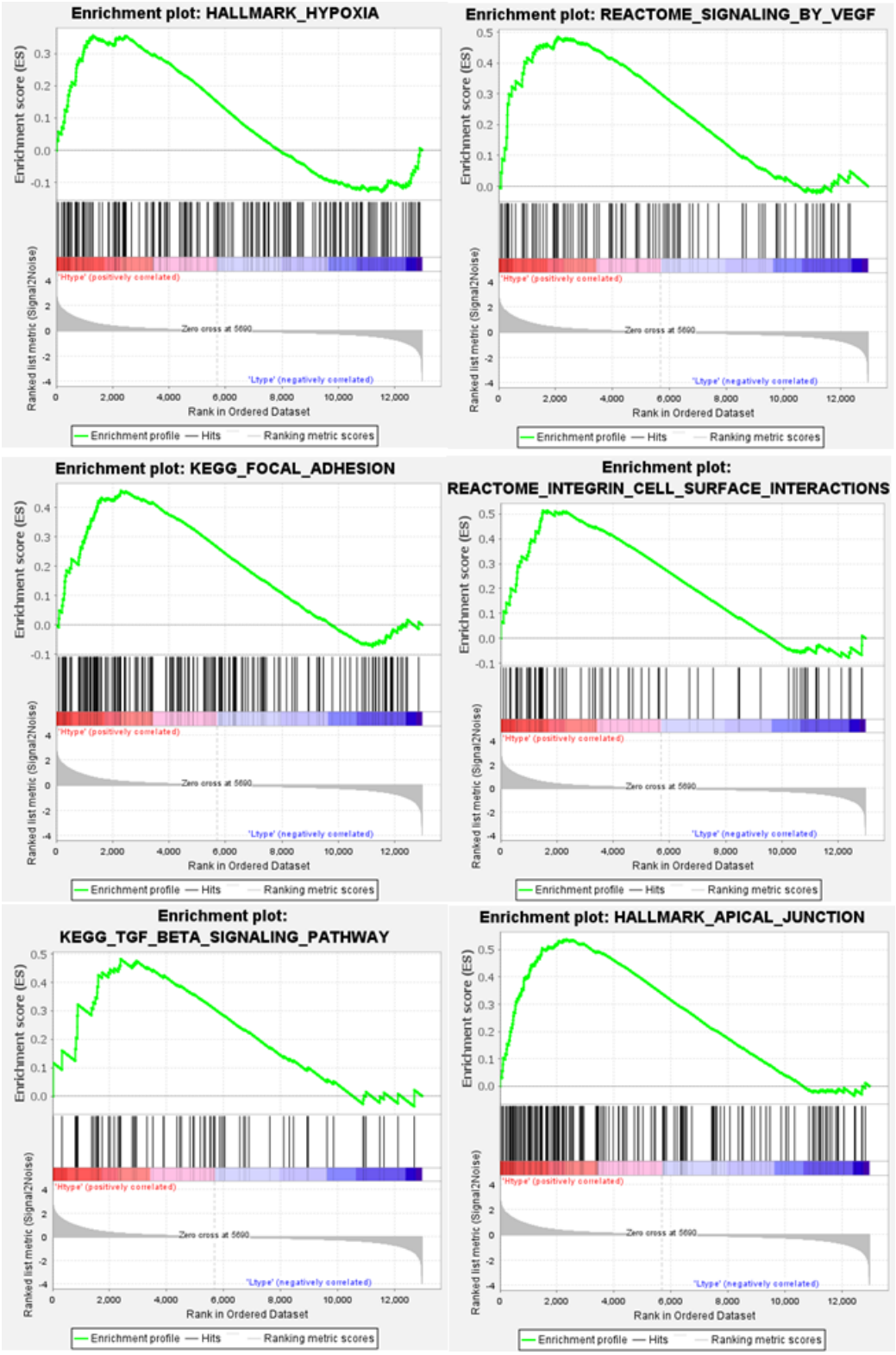


Figure 3.5 Gene set enrichment (GSE) analysis, enrichment plots show gene sets enriched in H-type ECs compared to L-type ECs. All gene sets presented had a nominal p value<0.05 and an FDR <0.25.

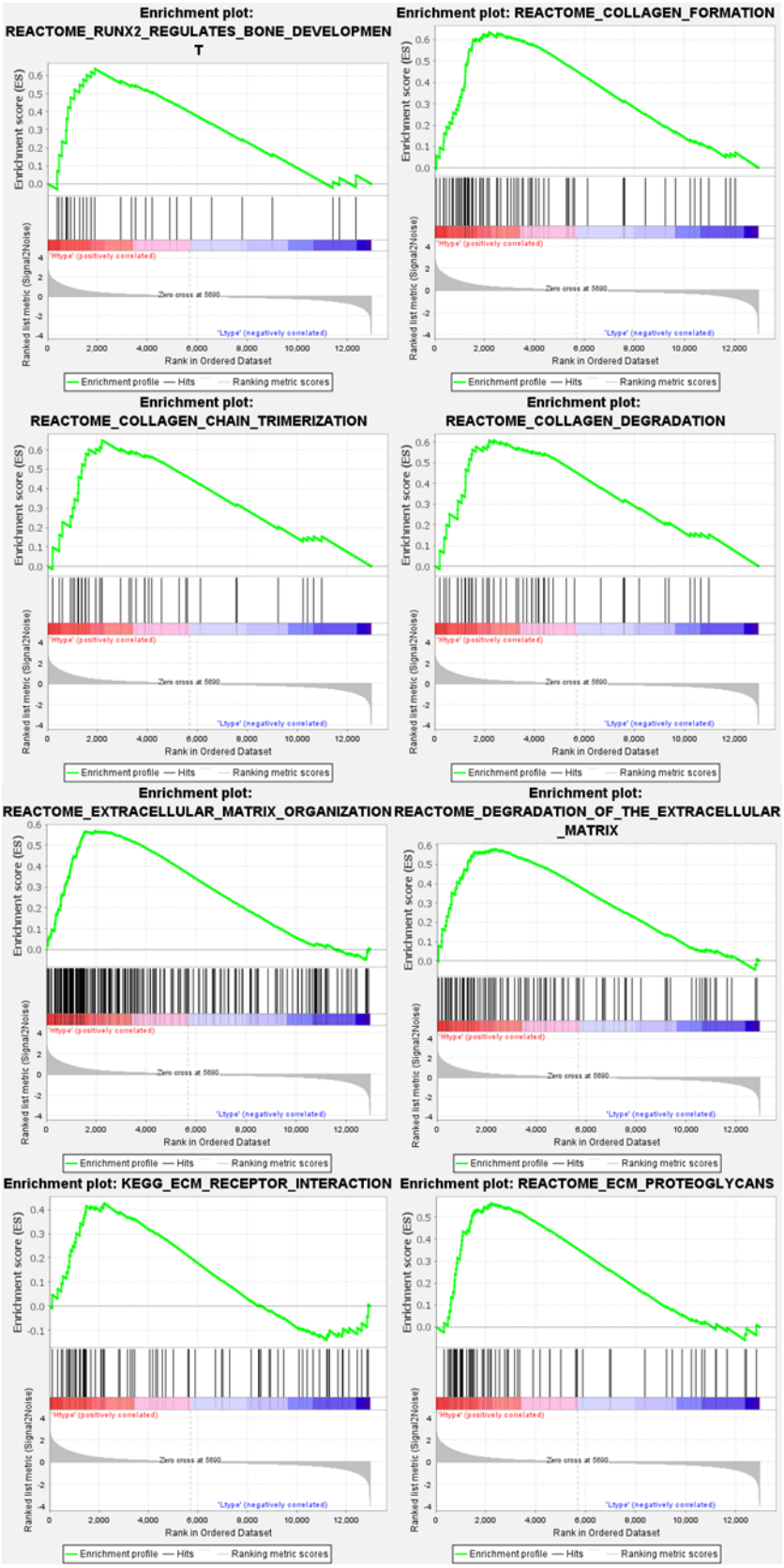


Figure 3.6 H-type ECs are responsible for the management of the extracellular matrix in the neonatal long bone as identified by gene set enrichment (GSE) analysis. Enrichment plots show gene sets enriched in H-type ECs compared to L-type ECs. All gene sets presented had a nominal p value<0.05 and an FDR <0.25.

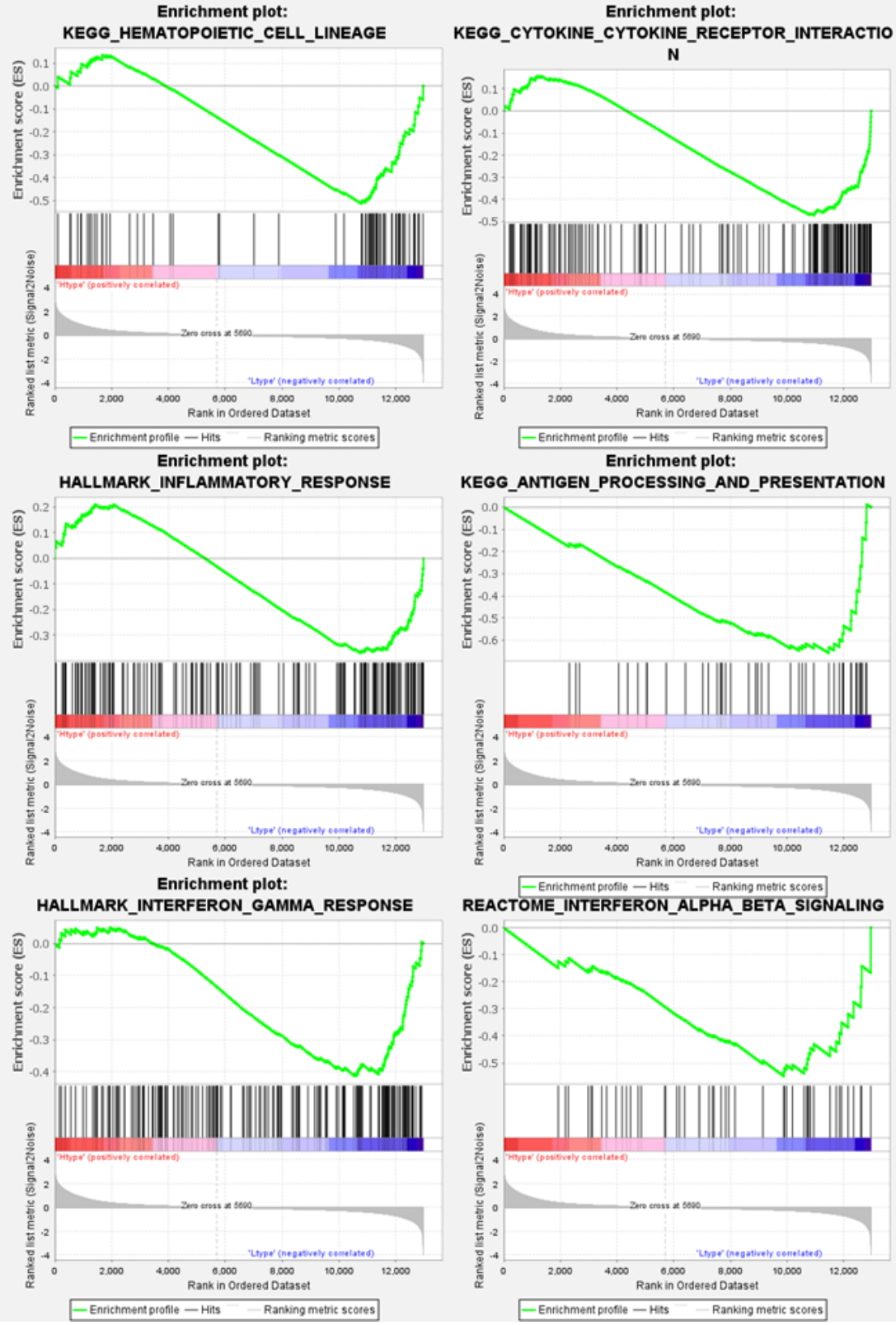


Figure 3.7 L-type ECs are show enrichment of genes involved in the maintenance of hemopoiesis and inflammation responses in the neonatal long bone as identified by gene set enrichment (GSE) analysis (E-MTAB-4066 dataset). Enrichment plots show gene sets enriched in L-type ECs compared to H-type ECs. All gene sets presented had a nominal p value < 0.05 and an FDR < 0.25.

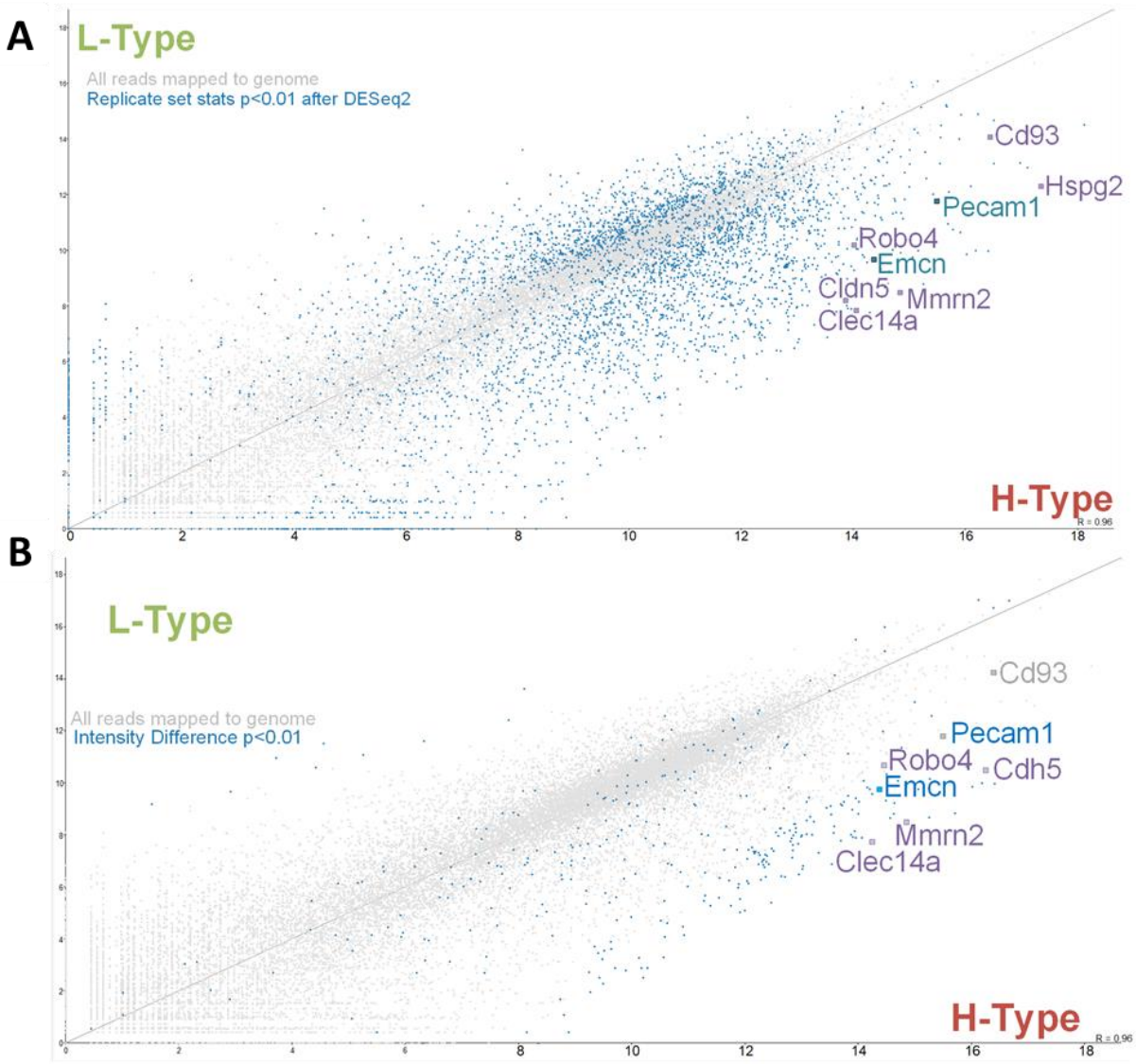


Figure 3.8 Identification of differentially expressed genes between H-type and L-type capillary endothelial cells (ECs) (**E-MTAB-4066 dataset).** Scatter plots of log2 normalised counts for gene transcripts identified as differentially expressed between H- and L-type EC. Grey points represent all the transcript counts mapped back to the genome, blue points represent differentially expressed transcripts ($p < 0.01$), purple points represent C-type lectin 14 domain family members identified as upregulated in H-type ECs or transcripts encoding proteins known to interact with these family members. Blue points correspond to transcripts used to characterise H-type EC upon their initial discovery (2). **A)** Differentially expressed genes identified by DESeq2 analysis, $p < 0.01$ **B)** Differentially expressed genes identified by IDA, $p < 0.01$.

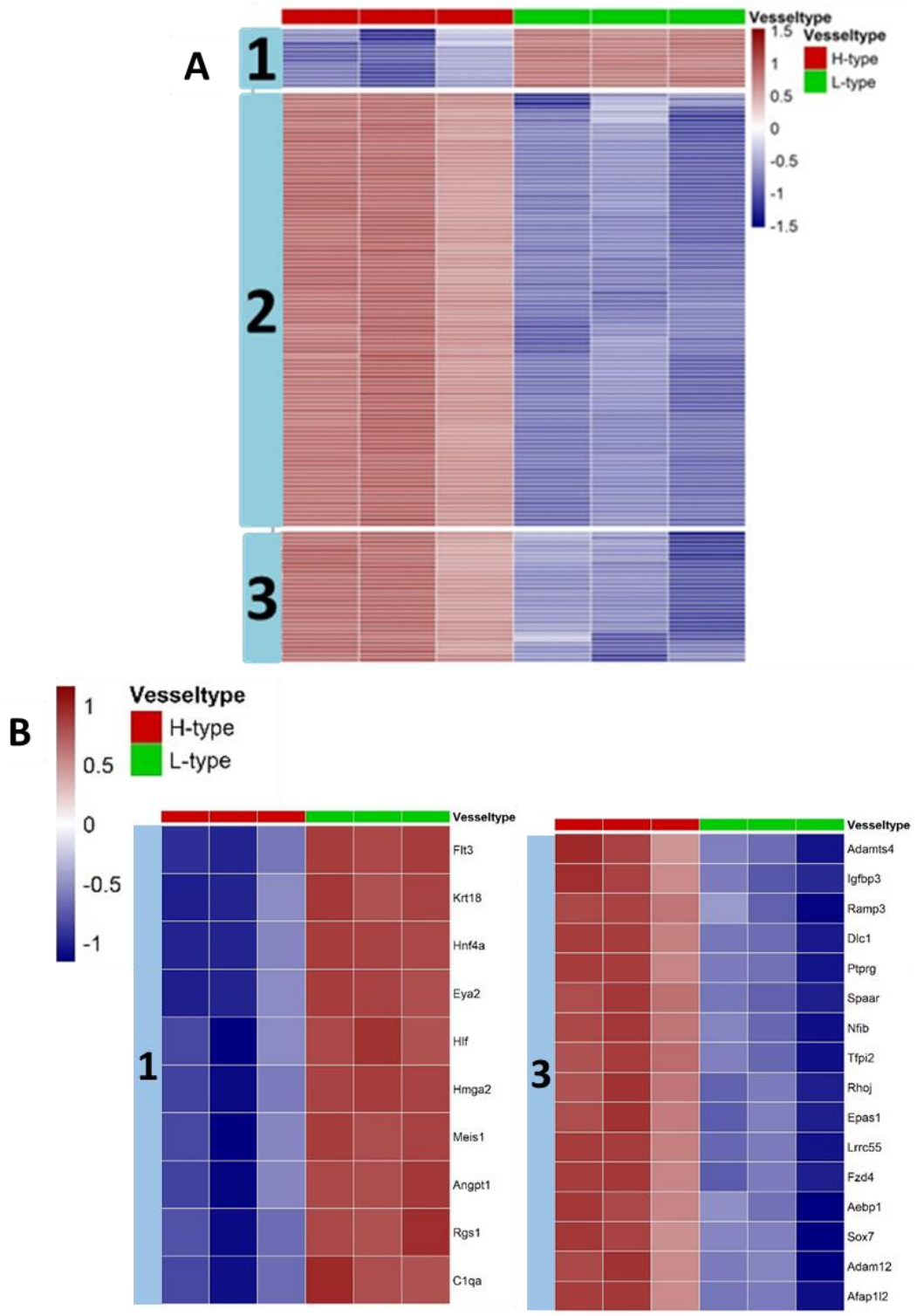


Figure 3.9 Clustering of differentially expressed genes in H- and L-type ECs, clusters 1 and 3 (E-MTAB-4066 dataset). A) Heatmap presents normalised (Z score) transcript levels of transcripts for differentially expressed genes (148/35579 total gene reads, differentially expressed genes were identified by intensity difference analysis (IDA) in tibia derived H- and L-type endothelial cells isolated from postnatal day 6 pups. **B)** Heatmaps display Z-score normalised data for different sets of upregulated (red) and downregulated (blue) genes, each heatmap corresponds to an independent cluster (1 and 3 shown here) generated via non-supervised clustering analysis to identify sets of genes that are upregulated in L-type vessels (heatmap 1) or H-type vessels (heatmap 3). Differentially expressed genes identified by variance of intensity difference analysis $p<0.05$.

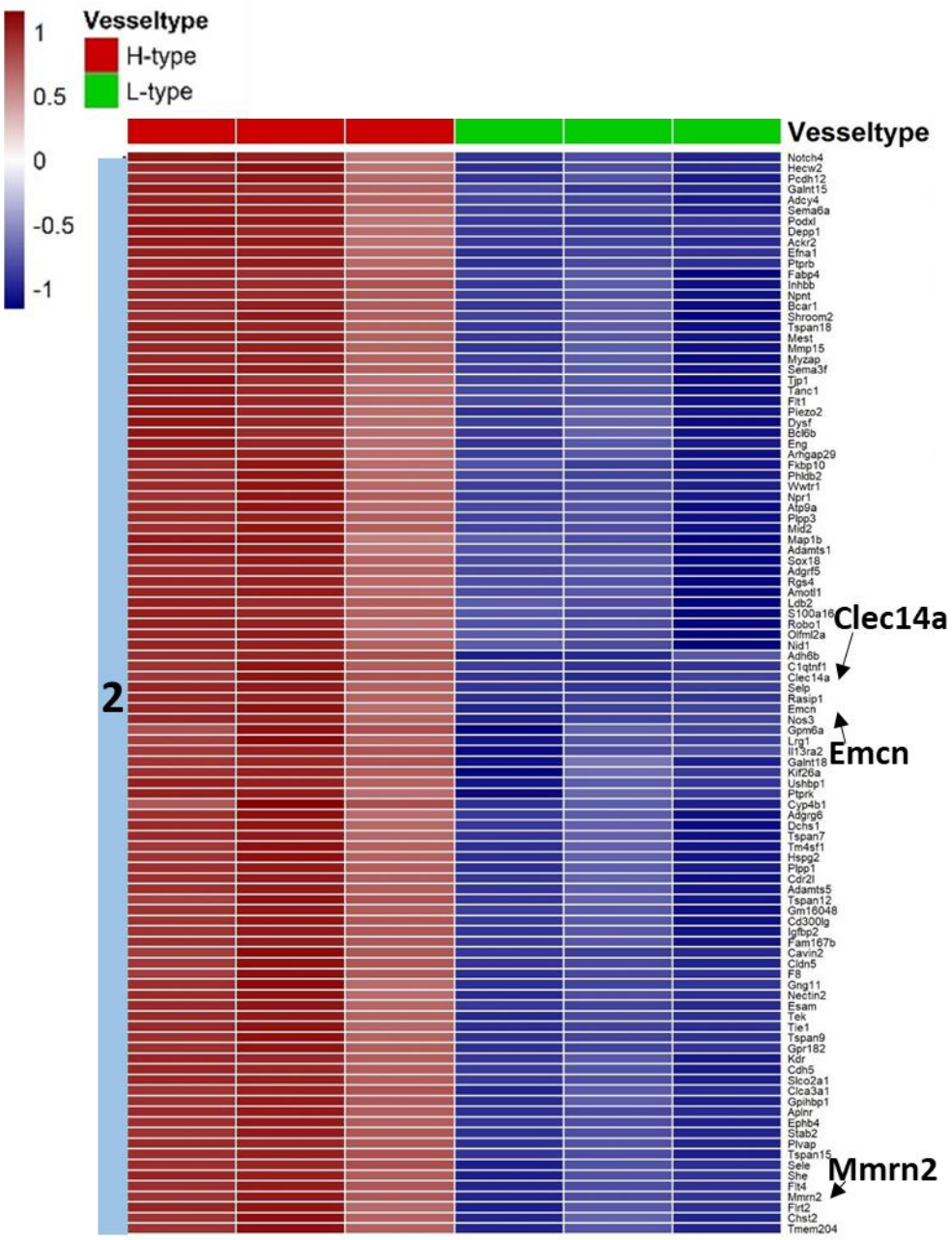


Figure 3.10 Clustering of differentially expressed genes in H- and L-type ECs, cluster 2 (E-MTAB-4066 dataset). Heatmap illustrations of Z-scorenormalised gene expression values for differentially expressed genes (148/35579 differentially expressed genes/total gene reads, differentially expressed genes were identified by IDA, $p < 0.01$) in tibia derived H- and L-type endothelial cells isolated from postnatal day 6 pups. Heatmap displays data for genes upregulated (red) in H-type EC. Black arrows indicate genes of interest for this project.

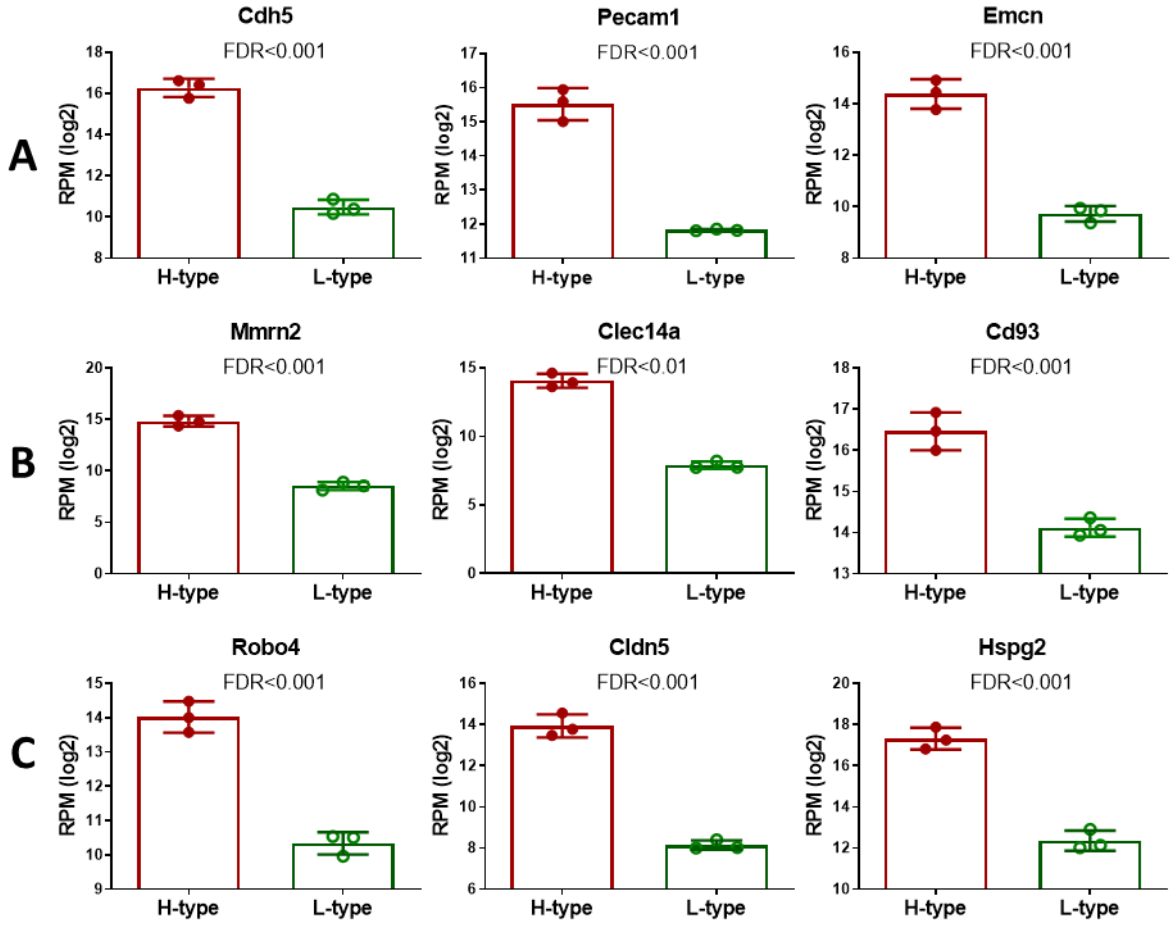


Figure 3.11 RNA-seq expression of mRNA transcript values for genes of interest (E-MTAB-4066 dataset). A) Increased transcription of known H-type endothelial cell markers in H-type EC samples, demonstrating efficient separation of H-type and L-type EC through FACS sorting; **B-C)** Increased transcription of members of the CLEC14A/CD93-MMRN2-CD248 interactome was also identified in H-type EC samples. Log2 normalised counts are shown, N=3 for all groups. Values are presented as Mean ± SD.

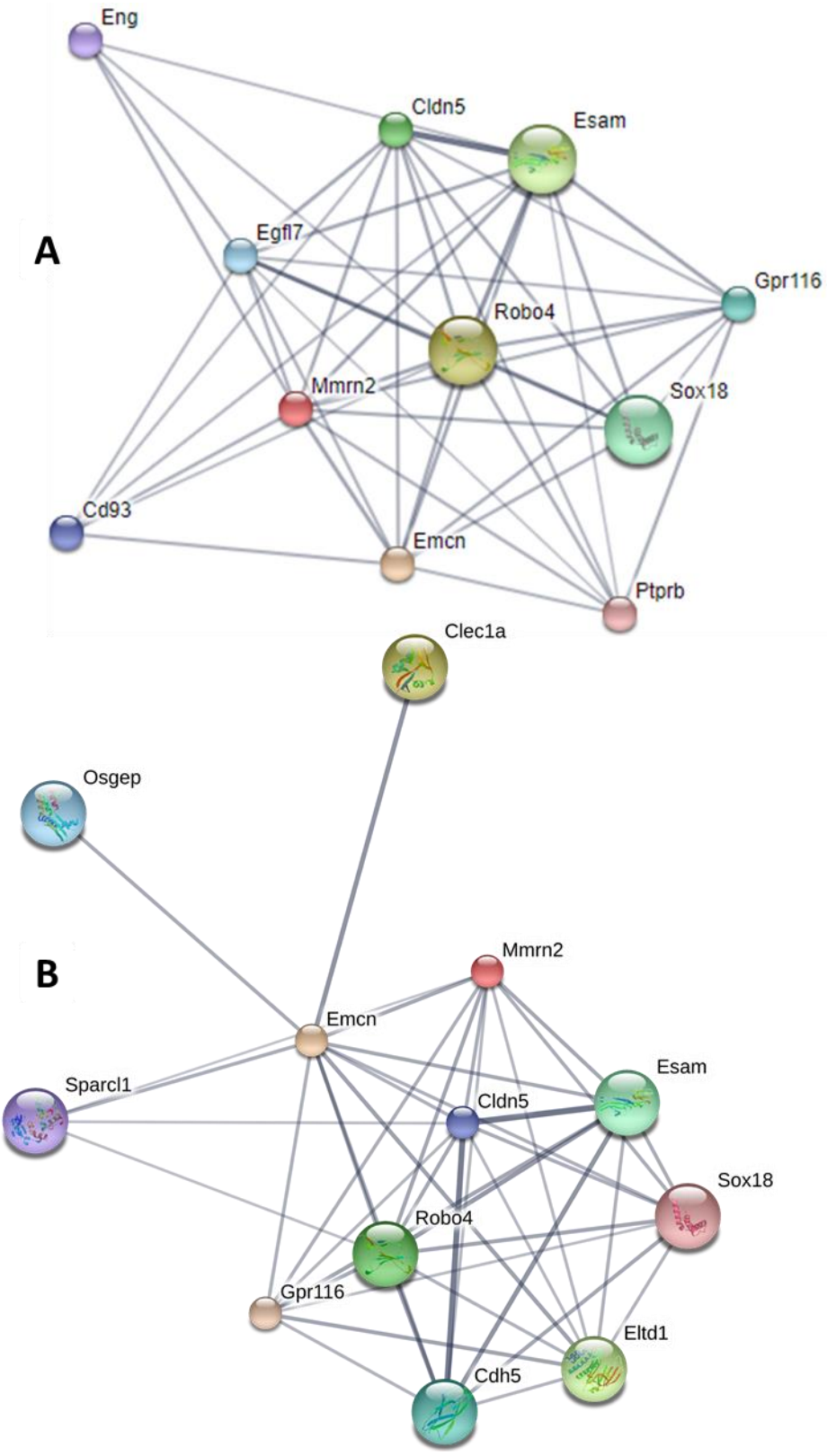


Figure 3.12 STITCH database mining showing the known interactome of MMRN2 and C-type lectin domain family 14 members. A) Map illustration of known protein-protein interactions with CD93 and MMRN2 (Mus musculus). **B)** Illustration of the MMRN2 known interactome (Homo sapiens). No curated data was available for CLEC14A in this database.

3.4. Expression of CLEC14A and MMRN2 in the mouse tibia

Following the confirmed expression of CLEC14A and MMRN2 at the mRNA level in the murine long bone, it was vital to corroborate this expression at protein level. This was accomplished via immunolabelling of the murine tibia with antibodies against CLEC14A, MMRN2 and CD248. Analysis of tibial sections confirmed the expression of all three proteins investigated in the bone metaphysis (Figure 3.13). CD248 positive ($CD248^+$) cells were located in the bone metaphysis and in the endosteum. A clear geographical distinction between the two groups of $CD248^+$ cells was observed, in the top part of the metaphysis, $CD248^+$ cells highly expressed type-1 collagen (COL1A1) and alkaline phosphatase (ALP), whilst the $CD248^+$ cells in the lower part of the metaphysis expressed COL1A1 and had lower levels of ALP expression. CLEC14A and MMRN2 expression were confirmed in the bone metaphysis and in the endosteum on cells surrounding $COL1A1^+$ cells. In some instances, colocalization of CLEC14A and MMRN2 was observed. Enriched expression of CLEC14A and MMRN2 was also observed at the top part of the metaphysis just underneath the growth plate compared to regions more distant from this site. Further imaging has confirmed expression of both CLEC14A and MMRN2 in areas where H-type vessels are localised in the metaphysis. Due to its high sensitivity to shear stress changes, CLEC14A was also labelled *in vivo*, by injecting biotin labelled antibodies. Labelling of the biotin positive primary antibody (anti-CLEC14A, clone C4) with streptavidin evidenced CLEC14A expression in the top part of the bone metaphysis. MMRN2 expression was highest at the top part of the metaphysis, however, more dispersed staining could also be observed in the area where L-type vessels are normally localised (Figure 3.14).

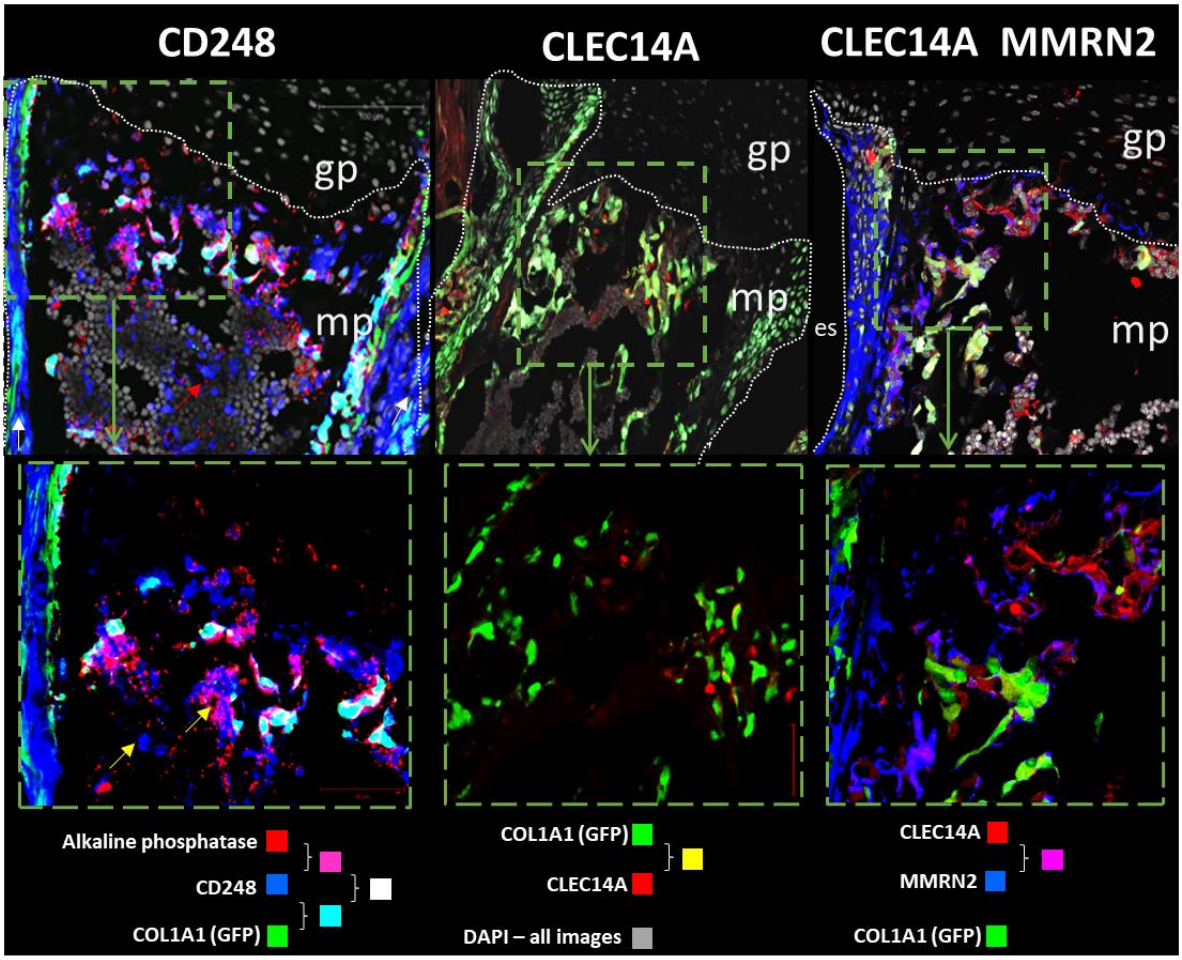


Figure 3.13 Immunofluorescent staining of C57Bl/6J mouse tibia at sites of bone formation. Images depict expression of CD248, CLEC14A and MMRN2 in the bone metaphysis. White arrows in the top left image indicate CD248 expression in the bone endosteum, red arrow in the top left image indicates $CD248^{+}$ expression on cells which do not express osteoblast maturation markers alkaline phosphatase (ALP) and collagen type 1 (COL1A1), yellow arrows in the bottom left image indicate CD248 expression in the metaphysis where it colocalises with ALP and COL1A1. A pool of CD248+ cells was also observed in the endosteum, CD248+ cells were bordered on each side by COL1A1. Image panels on the top and bottom right show colocalization of CLEC14A and MMRN2. White dashed line helps demarcate the metaphysis and growth plate regions. Scale bar is 100 µm for the top images and 50µm for the zoomed in images at the bottom of this panel. Abbreviations: gp-growth plate, mp-metaphysis.

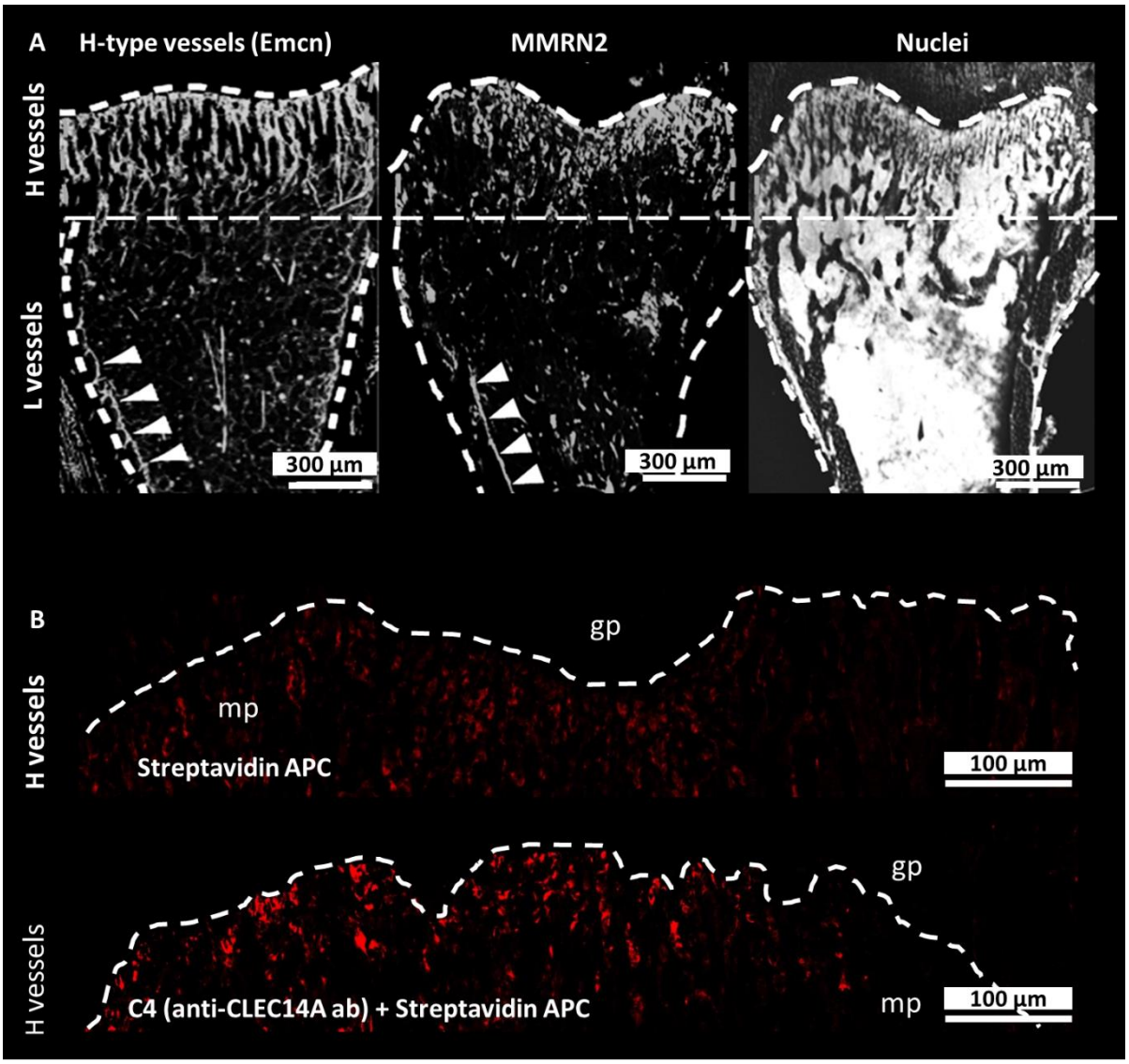


Figure 3.14 Immunofluorescent staining of MMRN2 and CLEC14A in the metaphyseal region of the mouse tibia. A) Maximum intensity projection images show comparative staining of CD31 (left image), MMRN2 (centre image) and nuclei (right image). Of note is the secretion of MMRN2 in the anatomical area covered by H-type vessels, moderate expression of MMRN2 is also observed in the region where L-type vessels reside. However, the pattern of staining is more punctate by comparison to the top part of the metaphysis. White arrowhead indicates staining for both CD31 and MMRN2 on an arterial vessel. **B)** Maximum intensity projection images of CLEC14A immunofluorescent staining. CLEC14A expression was tracked *in* vivo, a biotin-labelled monoclonal antibody (C4) raised against CLEC14A was injected i.p. and tissue was collected 24 hours post injection. Top image represents a control slide stained only with streptavidin APC, the fluorescent signal in the background stems from binding of streptavidin to endogenous biotin. Bottom image shows labelling of C4 bound to CLEC14A in the top part of the metaphysis in the region where H-type buds actively elongating are localised. In all images dashed line demarcates the growth plate metaphysis border, in figure A this also outlines the bone muscle interface. Abbreviations: gp-growth plate, mp-metaphysis.

3.5. Exploration of the distribution pattern of H type capillaries in CLEC14A$^{-/-}$ murine tibiae

Previous *in vitro* work has shown that genetic deletion of CLEC14A alters sprouting angiogenesis by diminishing sprout formation capacity of EC resulting in downregulation of EC tube formation, this is accompanied by a reduction of EC migration (1, 345, 348). Changes in angiogenesis in response to genetic deletion of CLEC14A were also reported *in vivo,* where CLEC14A$^{-/-}$ mice were subcutaneously implanted with sponges, upon assessment of vascular invasion into the sponge downregulation in vessel penetration and a diminished vascular density were observed (348). To assess the impact of germline deletion of CLEC14A on the vascularisation of the bone under physiological conditions, we employed immunofluorescent imaging of bone sections collected from CLEC14A$^{-/-}$ and WT mice. Recently developed 3D high-resolution microscopy techniques in the bone allow for a detailed morphological characterisation of bone resident cells (406). The Kusumbe method of tissue preparation and labelling was employed on tibiae collected from postnatal day 4 (P4) neonatal pups or postnatal day 28 (4-week-old) juvenile male mice. 100 µm thick tibia sections were probed with antibodies against EC (CD31 or EMCN - as stated) and image analysis was performed to provide information on vessel density, pattern of distribution of H-type vessels in different bone compartments, orientation and morphology of H-type vessels in the long bone metaphysis (Figure 3.15 B).

Imaging of sagittal plane bone sections revealed and confirmed the previously described heterogeneity of the bone vascular bed (2), showing the distinct geographical separation and morphology of H- and L-type vessels. CD31 or EMCN antibodies labelled H-type capillaries in the metaphysis, endosteum and periosteum, and L-type capillaries in the bone diaphysis

(Figure 3.15 A). At the leading edge of H-type vessels, bud-like vessel protrusions were visible and anastomosis of those protrusions by arches were observed.

At P4, both WT and CLEC14A$^{-/-}$ images presented a heavily interconnected vascular bed with an approximately equal coverage of H- and L-type capillaries. In the juvenile mouse (4 week old) sections, the H-type bed was diminished by comparison to the neonatal images and became distinctly localised to the superior part of the metaphysis (Figure 3.16, Figure 3.17). By comparison to WT controls, CLEC14A$^{-/-}$ H-type bulges formed an invading vessel front line which appeared more disorganised, with advancing H-type bulges unevenly protruding into the growth plate. In addition, blunting of H-vessel buds was also detected in CLEC14A$^{-/-}$ images at 4-weeks but not immediately after birth (Figure 3.17).

Quantification of the directional orientation of H-type capillaries in the metaphysis relative to the direction of bone growth also identified no substantial change in vessel orientation in any of the groups (Figure 3.18). Overall, no changes were identified in the morphology of H-type vessels in any of the control or knock-out groups in either new-born, or in juvenile mice (Figure 3.16, Figure 3.17). Given the well-known association of H-type capillary density to bone mass (145, 172), the number of H capillaries (Figure 3.19), the area they cover and their length (Figure 3.20, Figure 3.21) were also analysed. The number of capillaries in both WT control and CLEC14A$^{-/-}$ samples increased over time from P4 to 4-weeks, in positive correlation with the increase in bone diameter (Figure 3.19 B). No alteration in the number of type H capillaries or in their density was observed at any of the timepoints investigated (Figure 3.19 C and D). The relative CD31^{+} (P4) or EMCN^{+} (4-weeks) covered vessel area was measured in the metaphysis in a predefined area, and no difference was identified between WT and CLEC14A^{-}

$^{/-}$ images (Figure 3.20 B, Figure 3.21 A). However, a decrease in the length of H-type columns and a corresponding decrease in the area covered by the H-type column vascular front in the metaphysis was detected in CLEC14A$^{-/-}$ samples at 4-weeks, but not in P4 samples (Figure 3.20 C-E, Figure 3.21 B-D).

3.6. H-type endothelial cell fractions are reduced in CLEC14A$^{-/-}$ mice

As an alternative means of investigating the changes in H-type vascular front coverage discovered by the imaging analysis, the fraction of CD31^{high} EMCN^{high} type-H EC was quantified using flow cytometry. Tibiae were collected from 2-week-old mice and prepared for flow cytometry analysis as previously described (2, 172). The percentage of H-type EC was quantified as live cells/CD45^{-}/TER119^{-}/CD31^{high}/EMCN^{high}, whilst the fraction of cells corresponding to L-type EC was quantified as live cells/CD45^{-}/TER119^{-}/CD31^{low}/EMCN^{low} . This strategy was employed to distinguish H-type EC from EMCN^{-} arterial and EMCN^{low} L-type EC sinusoidal and venous cells. An overview of method optimisation, including the gating strategy, is presented in Figure 3.22 and Figure 3.23. A significant decrease in H-type endothelium percentage and a corresponding increase in L-type endothelium were identified in 2-week-old CLEC14A$^{-/-}$ male mice, however, the latter did not attain a statistically significant difference (Figure 3.24).

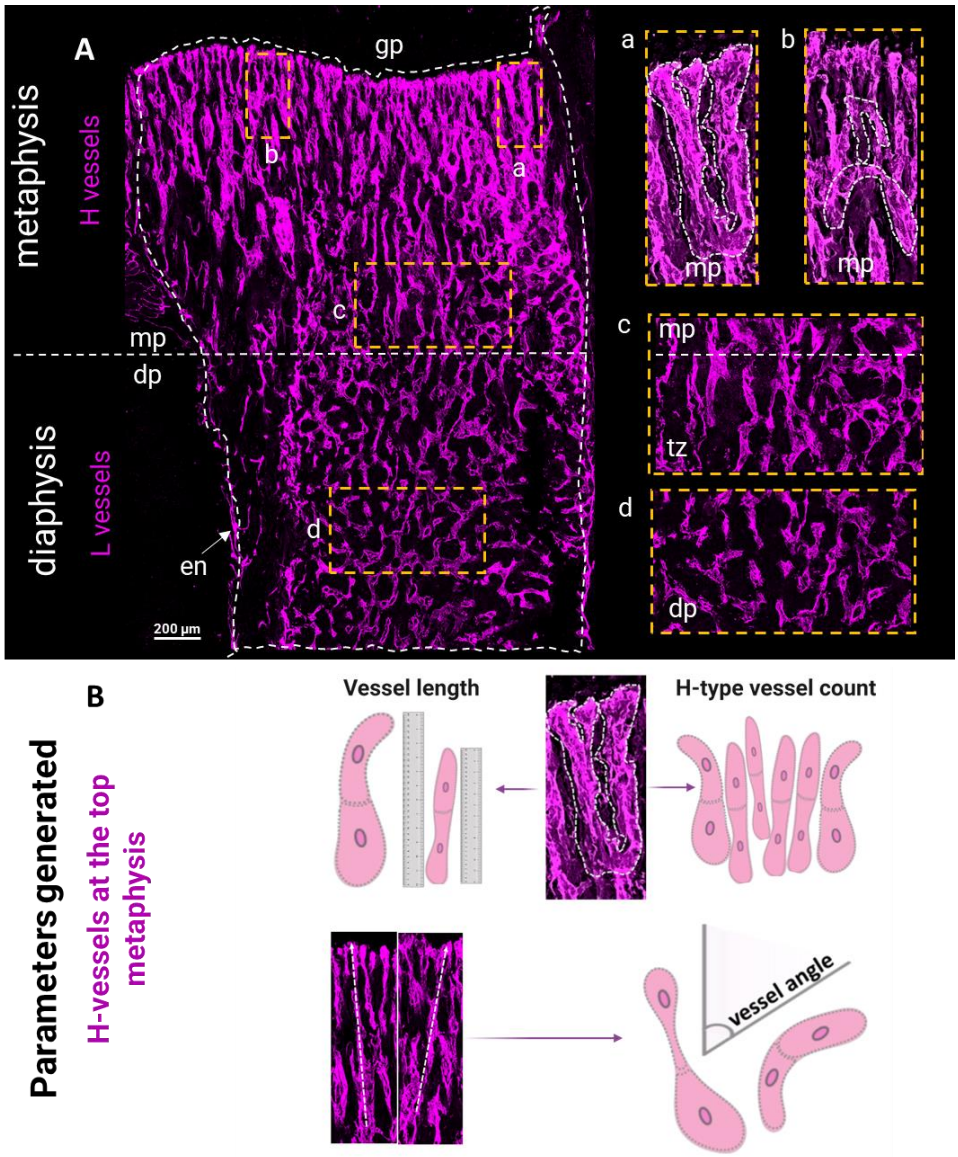


Figure 3.15 High-resolution 3D confocal microscopy of the C57Bl/6J mouse tibia capillary network. **A)** Example of a maximum intensity projection tile scan image of a sagittal 100 µm-thick tibia section. Image shows immunolabeling of $Emcn^{+}$ (magenta) EC counterstaining the bone capillary network. White dashed line indicates the vascular area encased in the cortical bone envelope interior to the bone endosteum and demarcates the growth plate – top metaphysis boundary. Note the distinct geographical orientation and morphology of vessels in the metaphysis (bone site housing H-type vessels) compared to the diaphysis (site housing L-type vessels). Yellow quadrants highlight regions enlarged in the right side images representing: a- H-type vessel anastomosis bulges (demarked by the white dashed outlining) which lead the extending vascular network during embryonic bone formation or postnatal bone growth; b- arches mediating interconnection of H-type endothelial blood vessel tubes (demarked by the white dashed outlining); c- the transition zone, a mixed H- and L-type vessel area where active remodelling of the of H-type capillary into L-type capillary occurs; d- an enlarged view of the L-type sinusoidal network in the bone diaphysis, a site with a vital role in haematopoiesis. **B)** Infographic outlying the parameters obtained from the analysis of the H-type vascular system in C57Bl/6J WT and $CLEC14A^{-/-}$ murine tibiae. Abbreviations: Dp-diaphysis, gp-growth plate, mp-metaphysis, tz-transition zone.

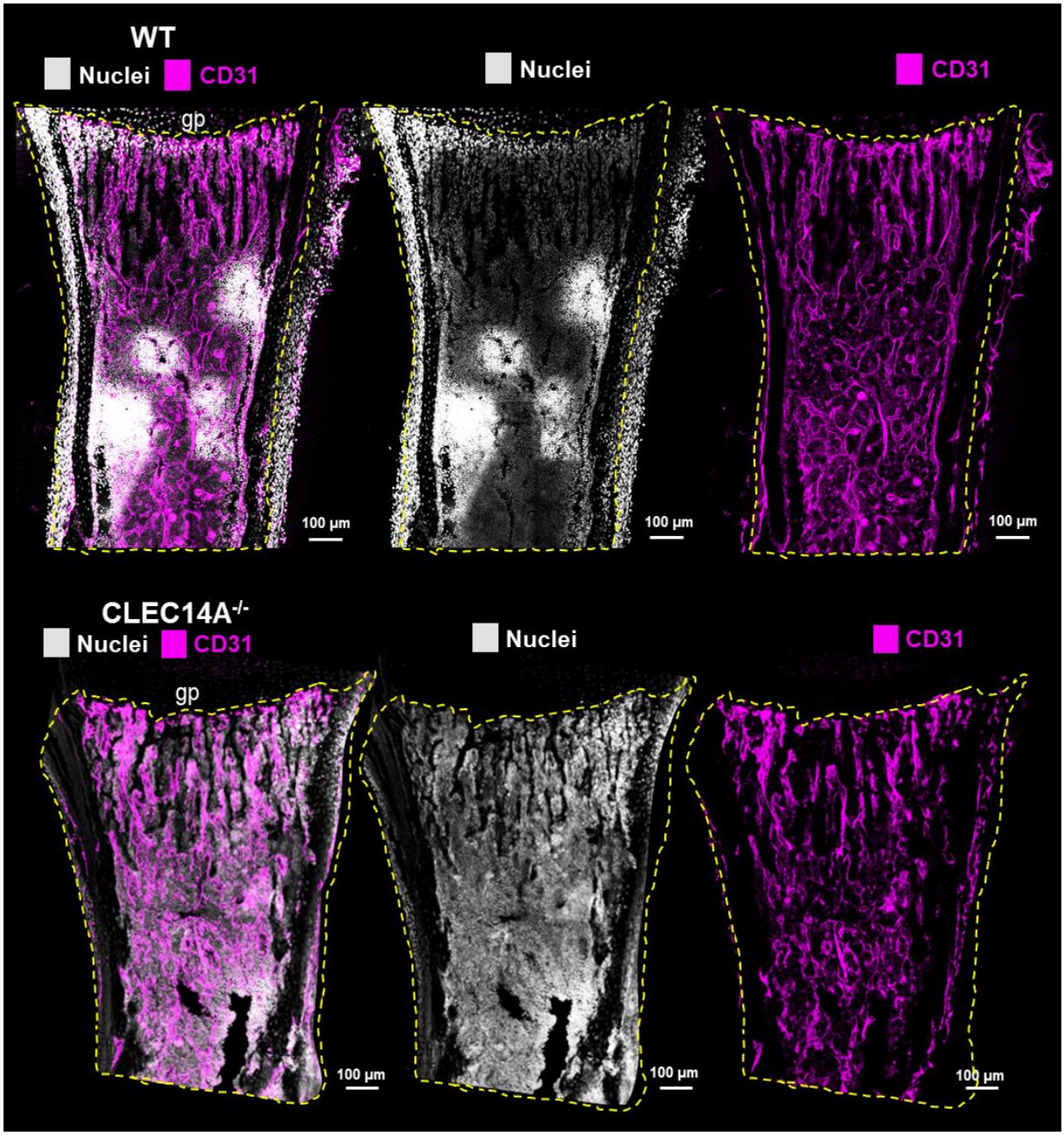


Figure 3.16 High-resolution 3D confocal microscopy of the neonatal WT and CLEC14A$^{-/-}$ mouse tibia vascular network. Representative maximum intensity projection renderings of sagittal plane bone sections immunolabelled against CD31 (magenta) and counterstained with Hoechst to identify nuclei (grey). Left: merged image; Middle: nuclei alone; Right: CD31 alone. Images show no striking differences between the WT and CLEC14A$^{-/-}$ H-type vascular network of postnatal day 4 (P4) mouse pups. Yellow dashed line demarcates the vascular area encased in the cortical bone envelope interior to the bone endosteum and demarcates the growth plate (avascular) – top metaphysis boundary. Abbreviations: gp-growth plate. Scale bar = 100 µm.

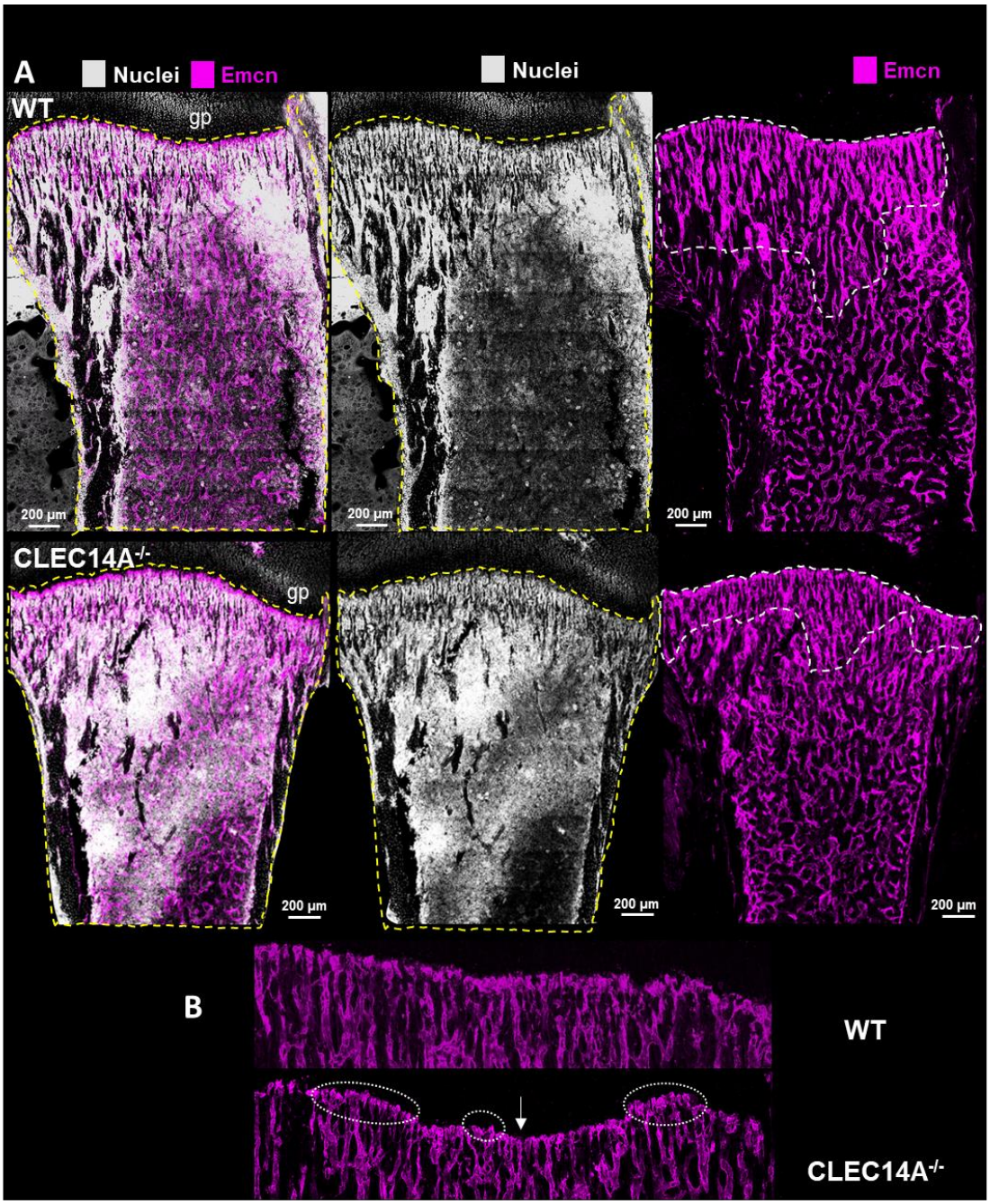


Figure 3.17 High-resolution 3D confocal microscopy of the juvenile (4-weeks old) WT and CLEC14A$^{-/-}$ mouse tibia capillary network. A) Representative maximum intensity projection images show organisation of H-type vessels in WT and CLEC14A$^{-/-}$ tibia. Vessels in the tibia section have been immunolabelled with CD31 (magenta), nuclei were stained with Hoechst (grey). Yellow dashed line demarcates the vascular area encased in the cortical bone envelope interior to the bone endosteum and demarcates the growth plate (avascular) – top metaphysis boundary. White line marks the limits of the H-type vessel front, note the shorter H-capillary front in the CLEC14A$^{-/-}$ images. Left: merged image; Middle: nuclei alone; Right: CD31 alone. **B)** Representative enlarged images of the leading H-type vascular front (CD31, magenta) in WT and CLEC14A$^{-/-}$ mice, note dysregulation of the advancing H-type bulges protruding into the growth plate (highlighted by the white dashed ovals in the CLEC14A$^{-/-}$ image. Blunting of the H-type vessel bulges can also be observed in CLEC14A$^{-/-}$ sections (identified by a white arrow).

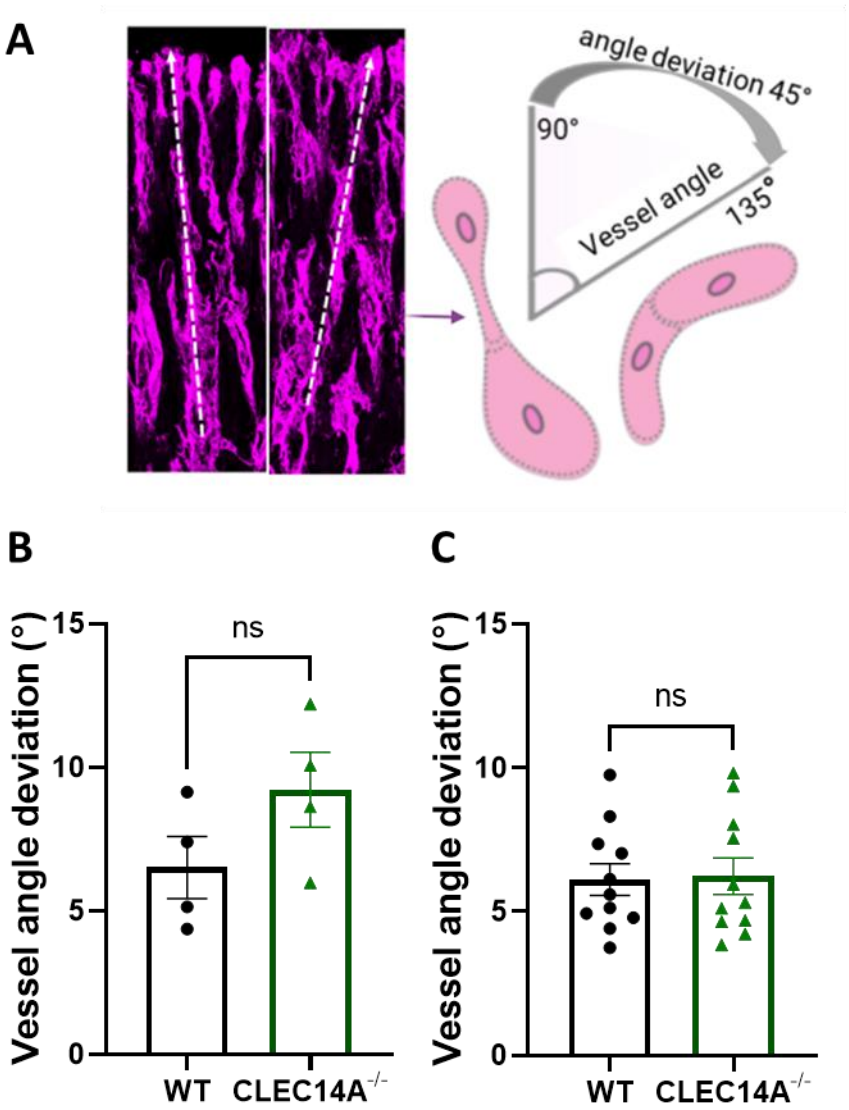


Figure 3.18 Characterisation of H-type vessel tube angularity in neonatal and juvenile CLEC14A$^{-/-}$ and WT mice. A) Schematic illustrating the measurement technique utilised to assess the directional distribution of H-type vessels at the actively expanding vascular front at the proximal end of the tibial metaphysis. Vessel orientation was measured using the straight-line tool in Image J, vessel angle deviation was calculated as the absolute value deviation from 90° (arc degrees). Quantification of type H-vessel angle deviation in **B)** neonatal pups (P4) (N=4 for both groups) and **C)** juvenile mice (P28) (N=11 for both groups). Data is represented as Median ± IQR, results were analysed with a Mann-Whitney test. No significant differences were detected (ns).

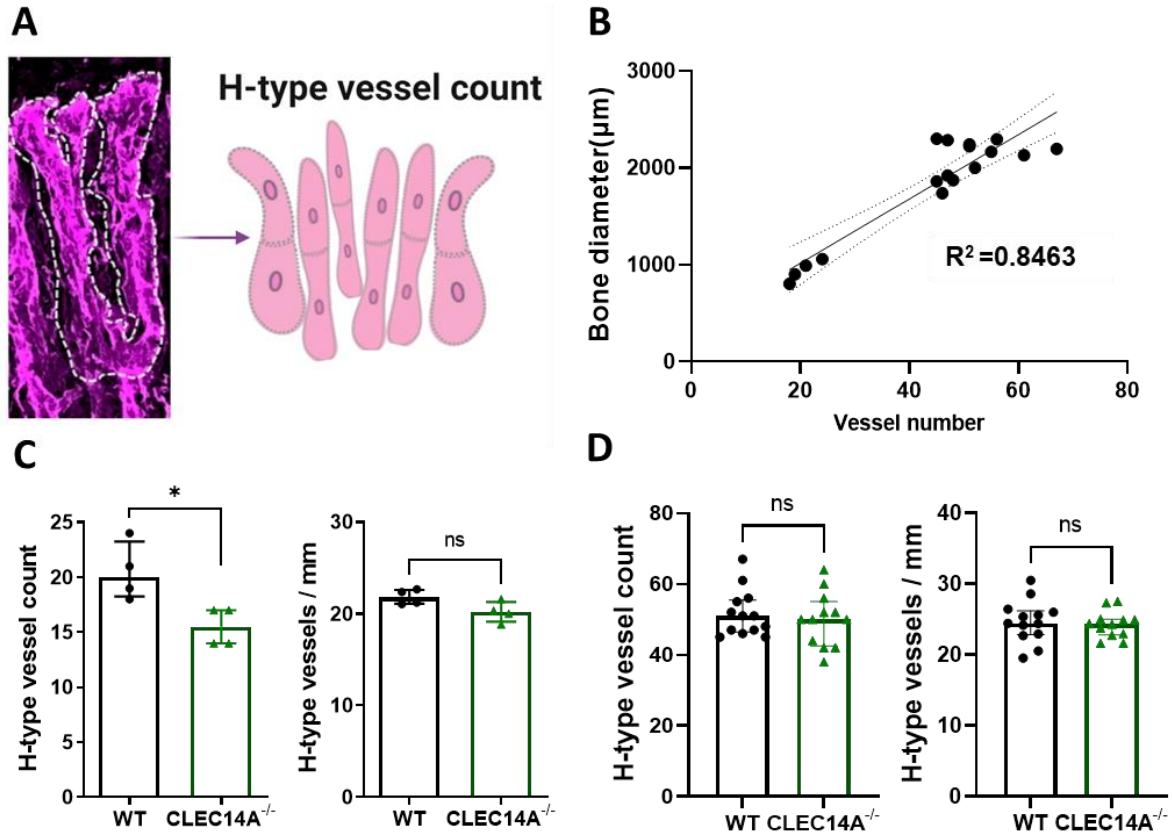


Figure 3.19 Characterisation of H-type vessel density in neonatal and juvenile WT and CLEC14A$^{-/-}$ mice. A) Schematic illustrating the analysis technique utilised to count H-type vessels at the actively expanding vascular front in the proximal end of the tibia metaphysis. Dashed line contours two H-type vessels which are separated at their distal ends at a branching point. **B)** Scatter plot showing the association between H-type vessel number and bone diameter. Data was analysed with a simple linear regression test, $p < 0.0001$. C-D) Quantification of H-type columns and their calculated density at the metaphysis leading edge at **C)** postnatal day 4 (N=4 for all groups) and **D)** 4-weeks of age (P28), (N=14 for all groups). Normalisation of the number of H-type vessel columns to bone diameter (measured as the distance between the most exterior H-vessel columns on each side of the bone section imaged) results in a similar vascular density in neonate and juvenile mice, indicating a bone-size dependant regulation of vessel density. Data is represented as Median ± IQR, results were analysed with a Mann-Whitney test, ns=not significant.

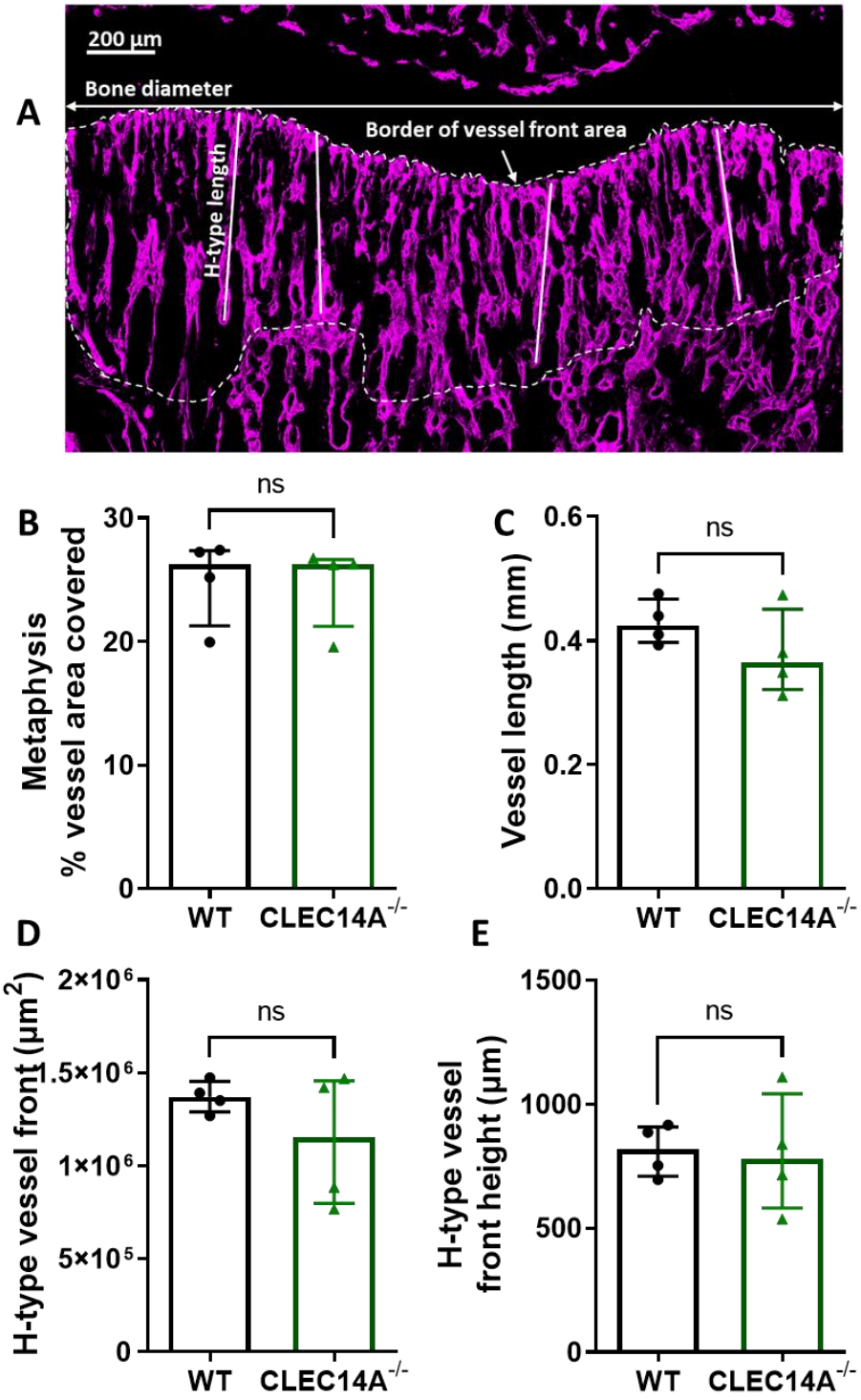


Figure 3.20 Characterisation of H-type vessel coverage in neonatal (P4) WT and CLEC14A$^{-/-}$ mice. **A)** Schematic diagram illustrating the analysis strategy **B)** Quantification of the % area covered by CD31 immunolabeled vessels in the tibia metaphysis; the area analysed encompassed all the vessels in the vasculature from the superior end of the metaphysis to the transition zone. **C)** Quantification of the length of H-type columns in the metaphysis, data represents mean values for each biological replicate obtained from 4-11 vessel measurements in each image **D)** Measurement of the area covered by the H-type vessel front was obtained by drawing around the cranio-latero-caudal borders of parallel H-type columns in the metaphysis. E) Quantitative evaluation of the length of the H-type vessels front. Data is represented as Median ± IQR, results were analysed with a Mann-Whitney test, N=4 for all groups. No significant differences were detected (ns).

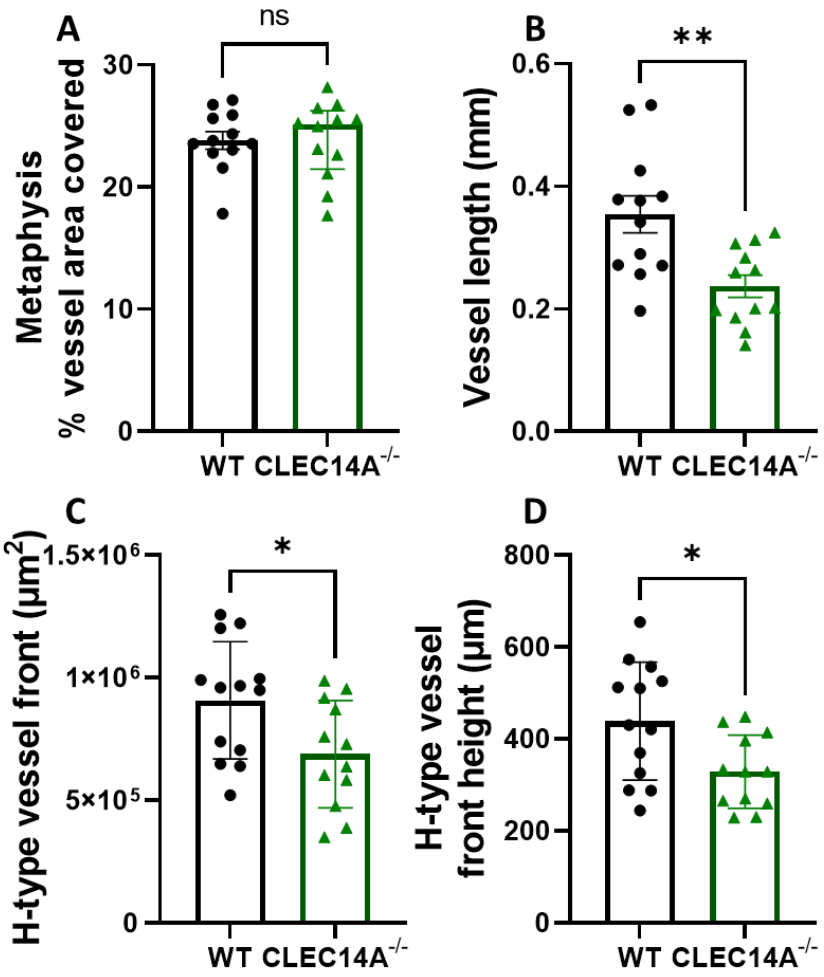


Figure 3.21 Characterisation of H-type vessel coverage in juvenile (4-week old) WT and CLEC14A$^{-/-}$ mice. A) Quantification of the % area covered by CD31 immunolabeled vessels in the tibial metaphysis; the area analysed encompassed all the vessels in the vasculature from the superior end of the metaphysis to the transition zone which was included as well, N=12 for both groups. **B)** Quantification of the length of H-type columns in the metaphysis, data represents mean values for each biological replicate obtained from 9-15 vessel measurements in each image, N=12 for both groups. **C)** Measurement of the area covered by the H-type vessel front was obtained by drawing around the cranio-latero-caudal borders of parallel H-type columns in the metaphysis, N=13 (WT) and N=12 CLEC14A$^{-/-}$. **D)** Quantitative evaluation of the length of the H-type vessels front. Data is represented as Median ± IQR (graph A) and as Mean ± SD (graphs B-D), results were analysed with a Mann-Whitney test for data in graph A and with an unpaired T-test for graphs B-D. ** = $P < 0.01$; * = $P < 0.05$; ns = non-significant.

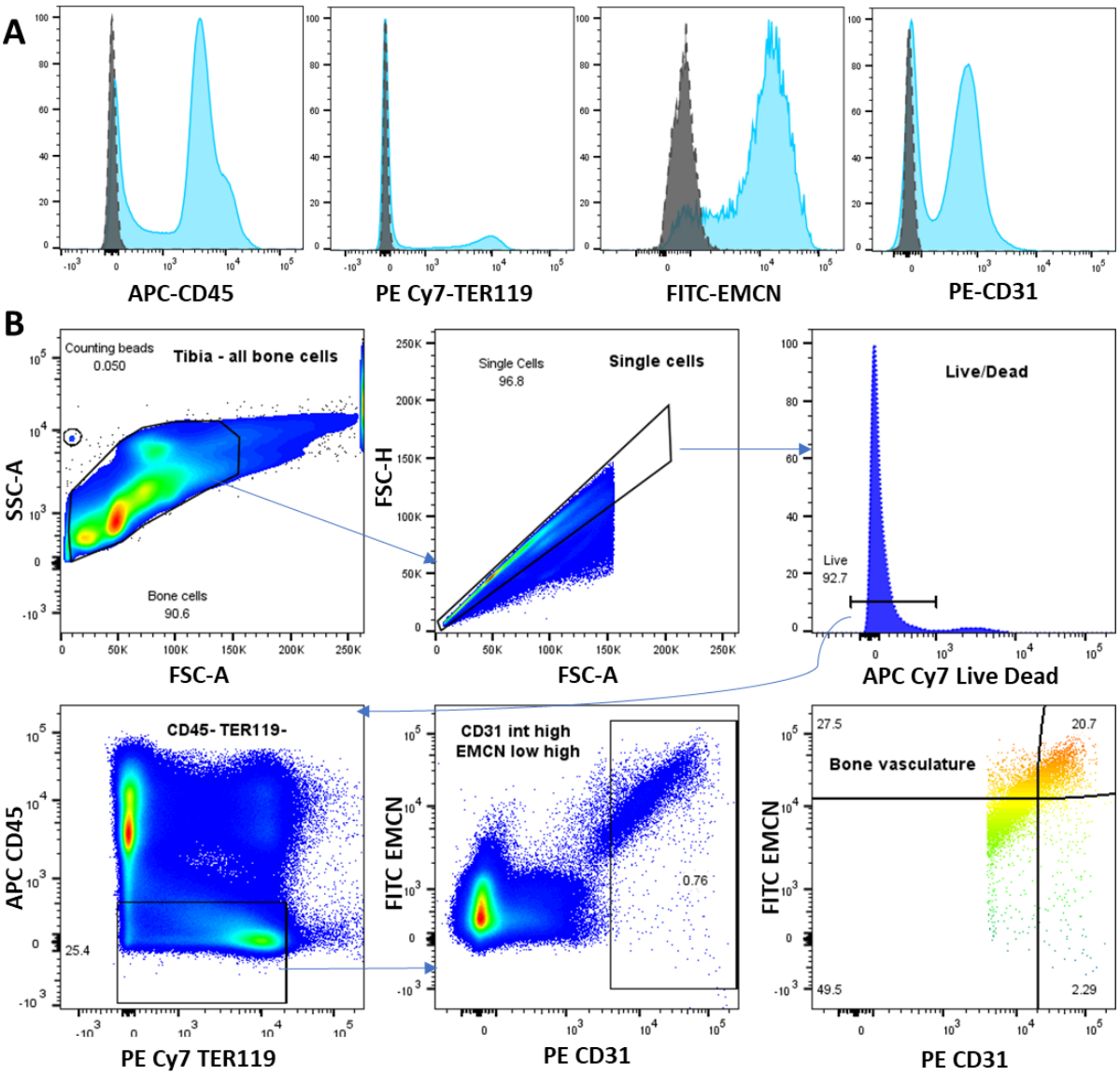


Figure 3.22 Gating strategy for the flow cytometric analysis of CD31^{high} EMCN^{high} EC. **A)** Histograms of antibody panel optimisation, the grey traces represent staining with IgG isotype control and the blue traces represent staining with the indicated antibody**,** CD45, TER119, EMCN, CD31 (left to right). B) Cells were gated based on size using SSC and FCS, before removing doublets based on FSC area vs FSC height. Live cells were gated based on the absence of viability dye staining, then CD45^{+} hemtopoetic cells were gated out. Finally, CD31^{high} EMCN^{high} ECs were defined based on expression of CD31 and EMCN.

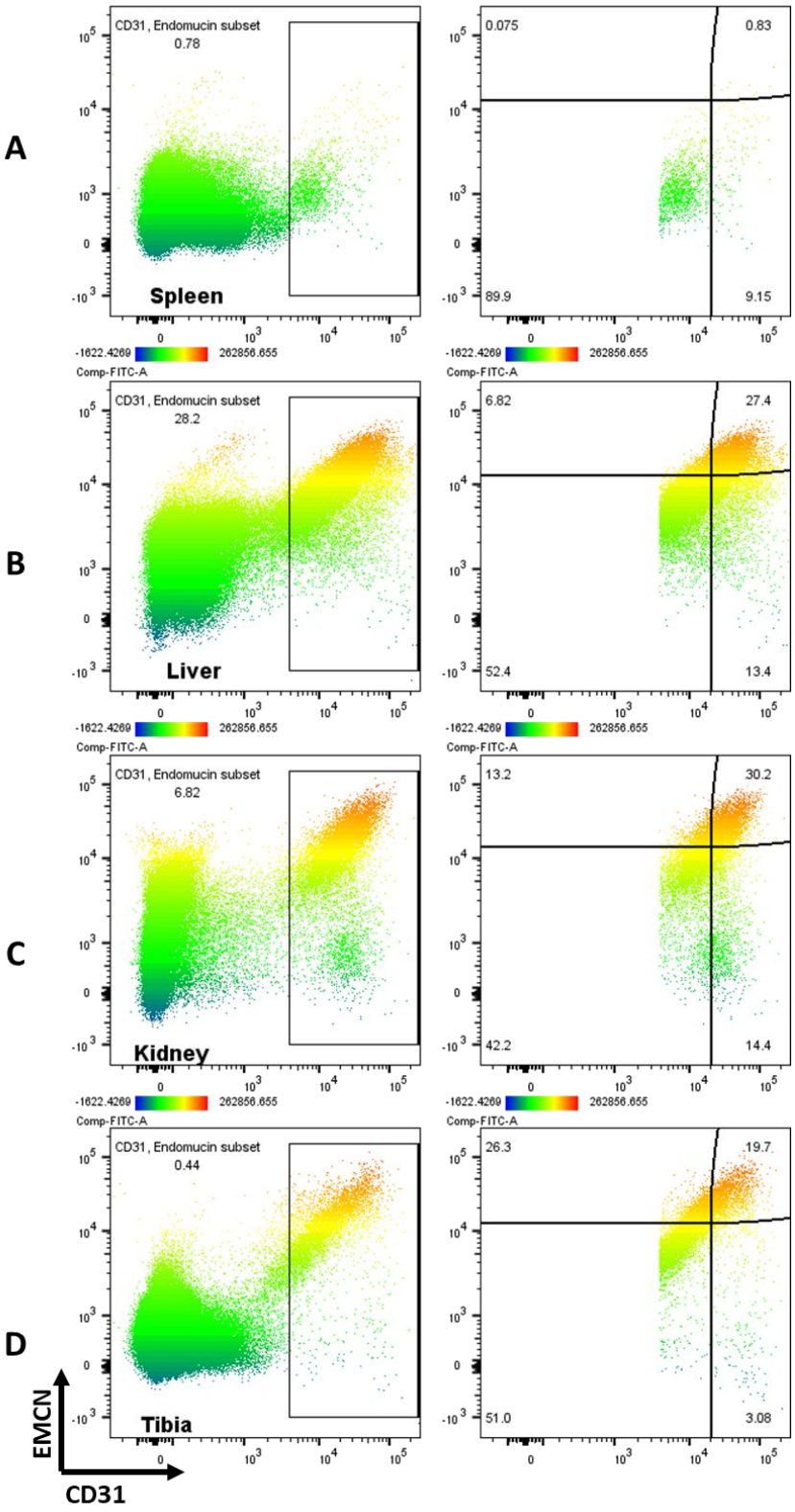


Figure 3.23 CD31^{high} EMCN^{high} EC gating strategy optimised against staining for CD31^{high} EMCN^{high} EC in the spleen, liver and kidney. Heatmap scatter plots of CD31 and EMCN labelling showing the absence of CD31^{high} EMCN^{high} EC in the spleen and positive staining in the liver, kidney, and tibia.

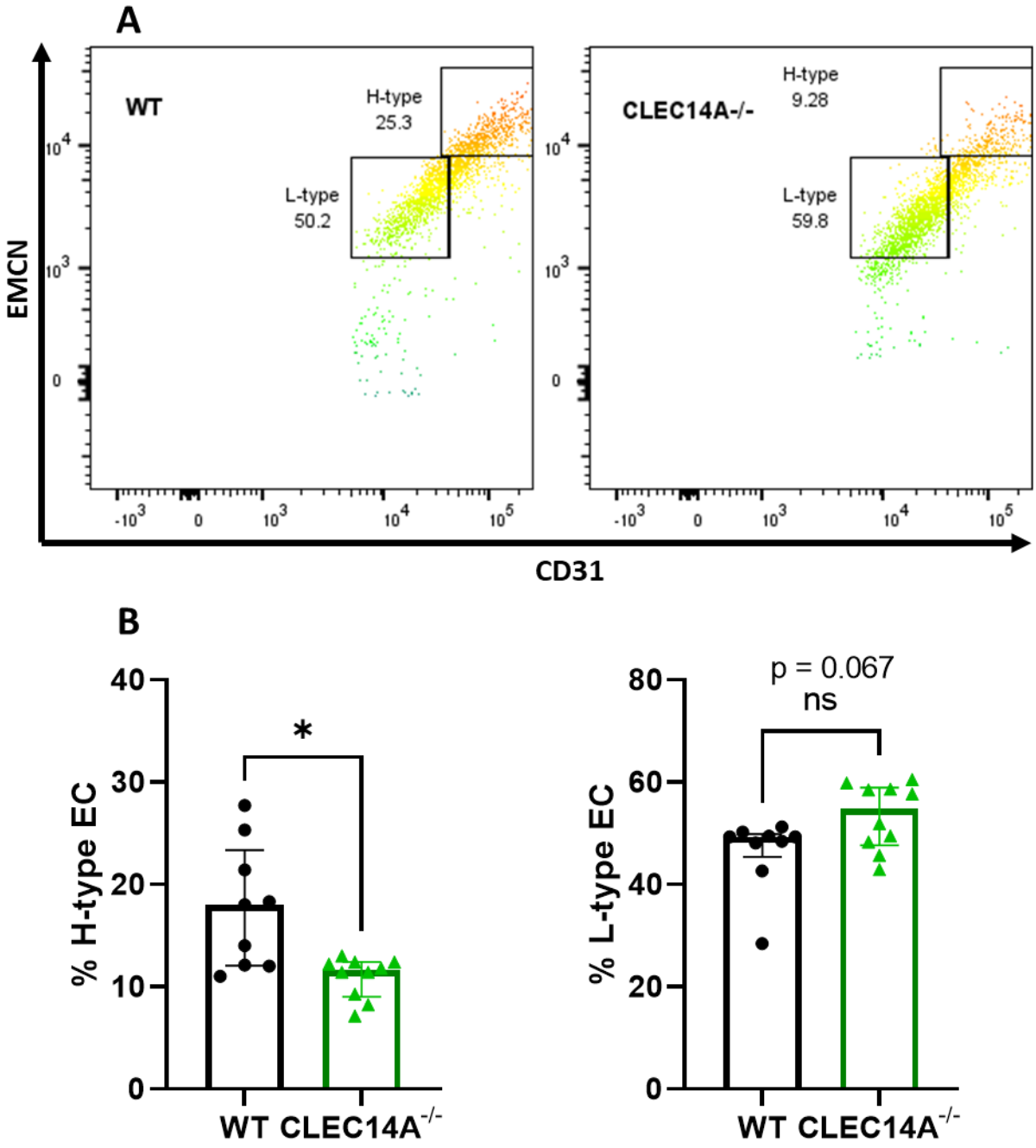


Figure 3.24 CLEC14A$^{-/-}$ mice have lower levels of CD31^{high} EMCN^{high} endothelium. **A)** Representative heatmap scatter plots showing CD31^{high} EMCN^{high} EC in CD45^{-} TER119^{-} bone and bone marrow cells **B)** Relative abundance of CD31^{high} EMCN^{high} (H-type) compared to CD31^{low} EMCN^{low} EC (L-type) in 2-week-old mouse tibiae showing a decrease in the percentage of CD31^{high} EMCN^{high} EC in CLEC14A$^{-/-}$ mice compared to WT, N=9 for both groups. Data was analysed with a Mann-Whitney test, results are presented as Median ± IQR , * = $P < 0.05$, ns = not significant.

3.7. Density of osteoblasts and geographical distribution of immature and mature osteoblasts in CLEC14A$^{-/-}$ tibiae

The spatio-temporal distribution of bone forming osteoblasts and their distribution relative to H-type capillaries was studied in neonatal (P4) and juvenile (4-week-old) WT and CLEC14A$^{-/-}$ mouse tibiae. Bone sections were probed with CD31 or EMCN and Osterix (Osx) or type I collagen (COL1A1) antibodies, counterstaining with Hoechst was employed to identify areas covered by cells in tibia sections and to delineate them from trabecular bone areas which are mostly acellular. Osteoblasts were present in the tibia metaphysis and in the endosteum. In all samples a relatively lower number of osteoblasts was observed downwards towards the diaphysis (Figure 3.25 and Figure 3.26). In the metaphysis, osteoblasts were identified in close proximity to H-type vessels, excepting the bud-like protrusion bulges area, at the top of the vessels, where osteoblasts were completely absent (Figure 3.25, Figure 3.26, and Figure 3.27). Osteoblasts were also observed lining bone pits in the inferior metaphysis and caudally towards the diaphysis, the bone pits were avascular and presented a low cellularity compared to the rest of the bone (Figure 3.27). Endosteal osteoblasts were tightly arranged in columns on either side of the interior part of the bone cortex, with one column lining the medial side of the cortex next to the endosteum and one column lining the lateral side of the cortex towards the periosteum (Figure 3.25 and Figure 3.26). It is unclear if arrangement of osteoblasts in the endosteum is mapped by vessels as the staining strategy employed shows limited vascularisation in this area. A limited number of OSX^{+} cells were also detected in the growth plate.

Osteoblast distance from vessel has previously been reported to be a strong indicator of the osteoblast differentiation status. Osteoblasts in intimate connection to vessels are immature whilst osteoblasts that have detached from vessels are mature secretory osteoblasts (52). To

probe for potential changes in the physical interaction of osteoblasts with H-type vessels in CLEC14A$^{-/-}$ mice, the distance of Osx^{+} cells from the nearest vessel was quantified in the tibia metaphysis and diaphysis of 4-week-old WT and CLEC14A$^{-/-}$ mice. Osteoblasts were localised further away from vessels in the metaphysis compared to the diaphysis, however, no significant differences were observed between WT and CLEC14A$^{-/-}$ images (Figure 3.28).

A trend towards increased osteoblast density in the superior tibial metaphysis was observed in P4 CLEC14A$^{-/-}$ samples but this did not reach statistical significance, however, a statistically significant increase in osteoblast density was identified in the inferior metaphysis towards the diaphysis (Figure 3.29 and Figure 3.31). The increase in inferior metaphysis osteoblast density in CLEC14A$^{-/-}$ samples is attributed to an enrichment in osteoblast chords formed on the lining surface of newly forming trabeculae which were shorter in WT controls (Figure 3.31). To better characterise the extension of the osteoblast covered front in these bones, the length of osteoblast columns from the proximal end of the metaphysis to the lowest point where osteoblasts are observed in the diaphysis was measured - this was termed “osteoblast chord length” (Figure 3.31). Longer osteoblast chord lengths were measured in CLEC14A$^{-/-}$ tibiae compared to controls immediately after birth (P4) but not in 4-week-old juvenile mice. The increase osteoblast density phenotype observed in P4 CLEC14A$^{-/-}$ bone sections was resolved/no longer present at 4-weeks in CLEC14A$^{-/-}$ juvenile mice (Figure 3.30 and Figure 3.31).

The shape of the osteoblast nucleus has been shown to change in response to their migratory status (417). Specifically, elongated nuclei are indicative of an immature migratory osteoblast phenotype, whilst a rounded nucleus is indicative of a mature bone forming osteoblast. To test this concept in CLEC14A$^{-/-}$ and WT control samples, he osteoblast nuclear shape was

measured in both P4 and 4-weeks old mouse tibia samples. A sustained and timepoint-dependent decrease in the elongation of nuclei was observed both in the metaphysis and diaphysis from postnatal day 4 to 4-weeks, however, no striking differences were observed between CLEC14A$^{-/-}$ samples and WT controls (Figure 3.32).

To further probe the maturity status and activity of OSX^{+} osteoblasts, tibia sections were probed with a type I collagen antibody (COL1A1). COL1A1 surrounded osteoblast nuclei but it could also be identified as a component of collagen fibrils deposited throughout the bone, with focal points in the endosteum and on the edges of bone trabeculae in the inferior region of the metaphysis and in the diaphysis (Figure 3.33 and Figure 3.34). At 4-weeks of age WT and CLEC14A$^{-/-}$ mice showed no differences in the amount of COL1A1 identified in the metaphysis whilst a trend for an increased COL1A1 percentage area coverage and COL1A1 quantity (as identified by COL1A1 integrated density) was observed in the lower metaphysis, however, this did not attain statistical significance (Figure 3.34). The mean length of osteoblast COL1A1^{+} chords were longer in CLEC14A$^{-/-}$ tibiae as compared to WT controls (Figure 3.35).

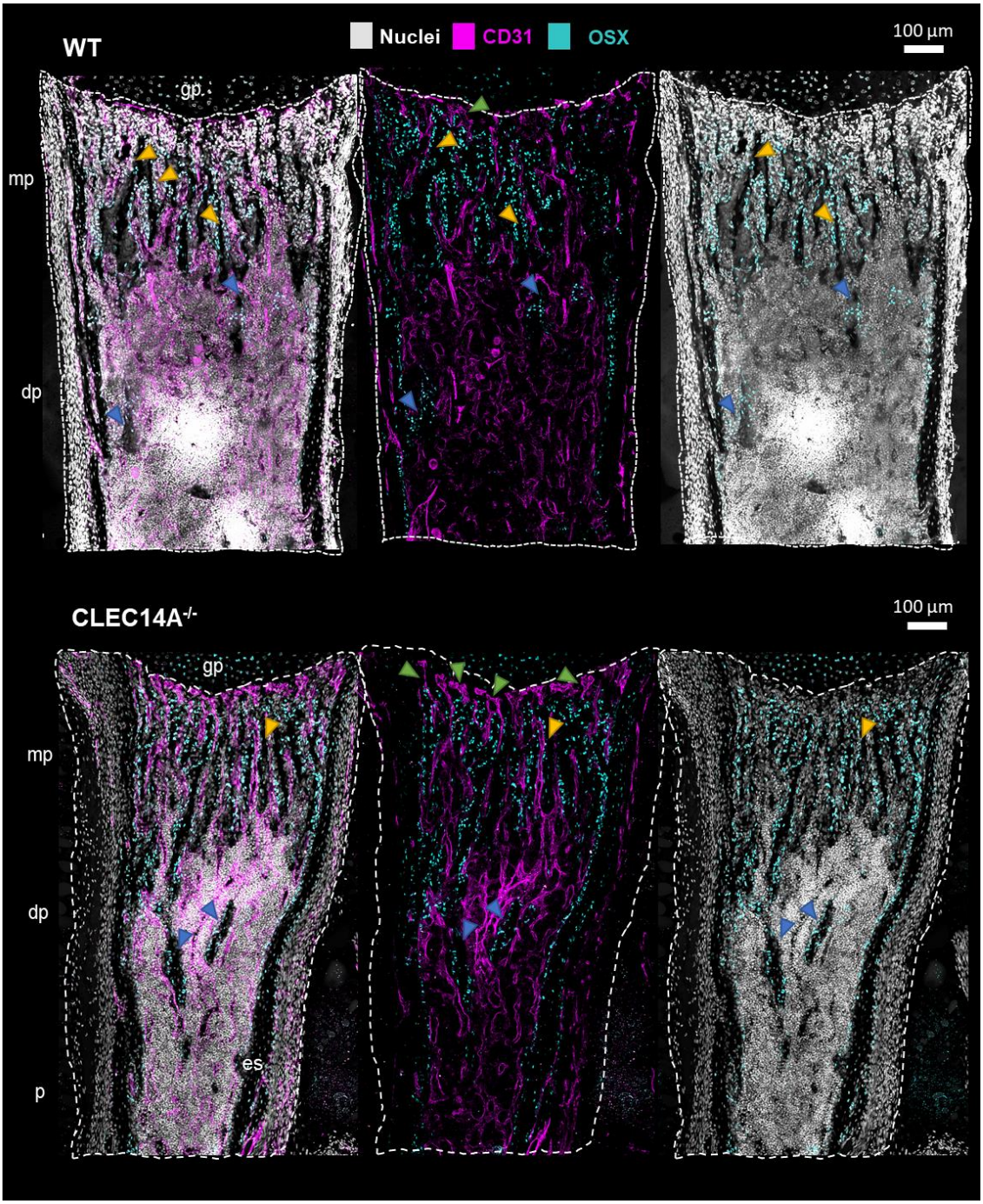


Figure 3.25. Geographical distribution of osteoblasts in neonatal (P4) WT and CLEC14A$^{-/-}$ murine tibia. Representative images show mapping of osteoblast localisation in the murine tibia. Vessels are labelled with CD31 (magenta), whilst osteoblasts are identified by their expression of OSX (cyan), the entire tissue section is counterstained with Hoechst to identify nuclei (grey). Left image = merge; middle image = CD31 (magenta) only; right image = hoescht (grey) only. Note the limited localisation of OSX^{+} cells around H-type vessels in the metaphysis and endosteum. Blue arrow heads indicate bone pits void of vasculature with osteoblasts distributed around the exterior edge of the bone trabecula., yellow arrow heads indicate areas where osteoblasts are in close proximity to columnar H-type vessels, and green arrow heads indicate areas at the leading front of the expanding vasculature which are void of osteoblast coverage. White dashed line demarcates the vascular area encased in the cortical bone envelope interior to the bone endosteum and demarcates the growth plate (avascular) – top metaphysis boundary. Abbreviations: Dp-diaphysis, gp-growth plate, mp-metaphysis, es-endosteum, p-periosteum. Scale bar = 100 µm.

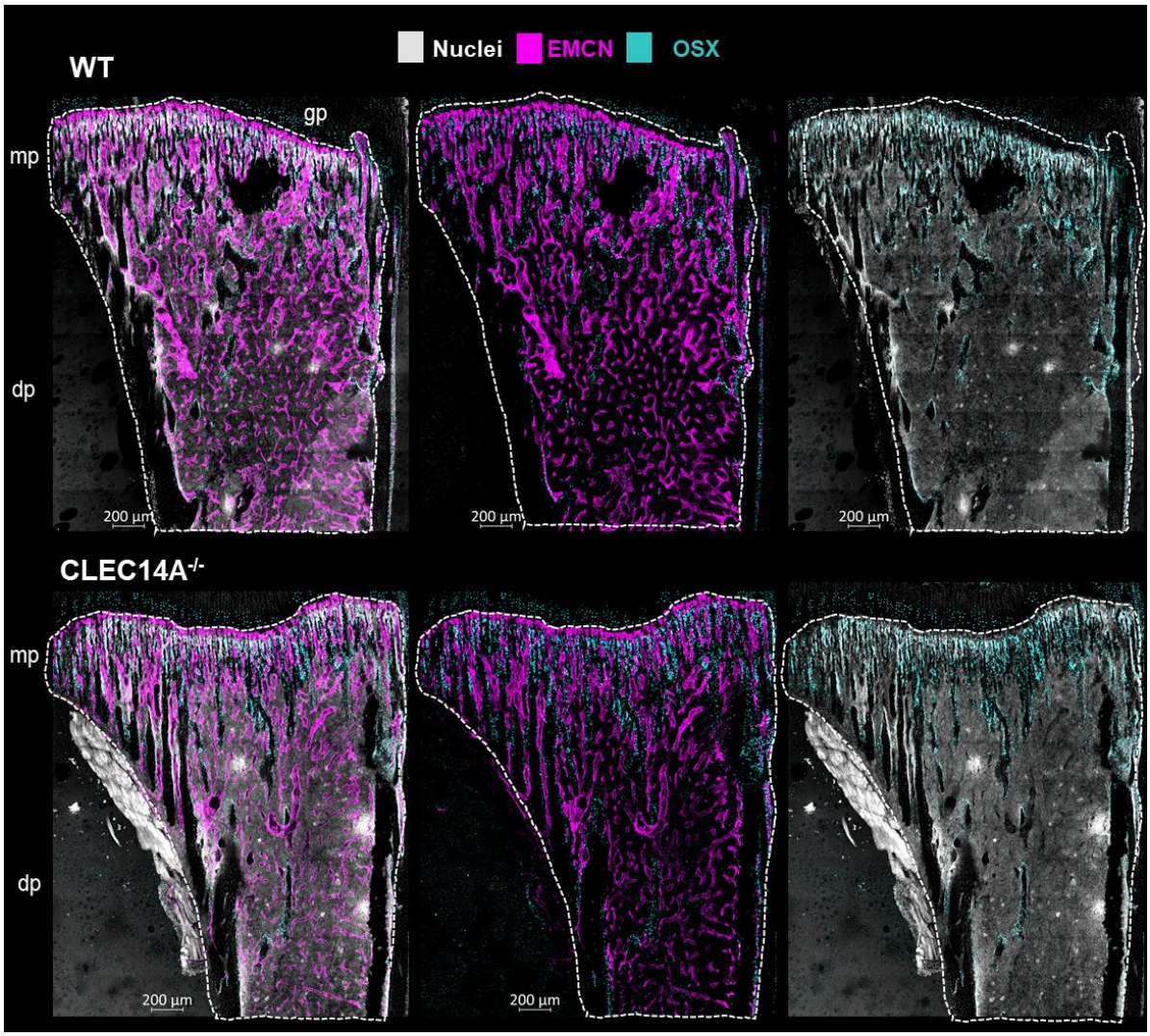


Figure 3.26. Geographical distribution of osteoblasts in juvenile (4-weeks) WT and CLEC14A$^{-/-}$ murine tibia. Representative images show mapping of osteoblast localisation in the murine tibia. Vessels are labelled with EMCN (magenta), whilst osteoblasts are identified by their expression of OSX (cyan), the entire tissue section is counterstained with Hoechst to uncover the presence of nuclei (grey). Left image = merge; middle image = CD31 (magenta) only; right image = hoescht (grey) only. Note the localisation of OSX^{+} cells around H-type vessels in the metaphysis and endosteum. White dashed line demarcates the vascular area encased in the cortical bone envelope interior to the bone endosteum and demarcates the growth plate (avascular) – top metaphysis boundary. Abbreviations: Dp-diaphysis, gp-growth plate, mp-metaphysis, es-endosteum, p-periosteum.

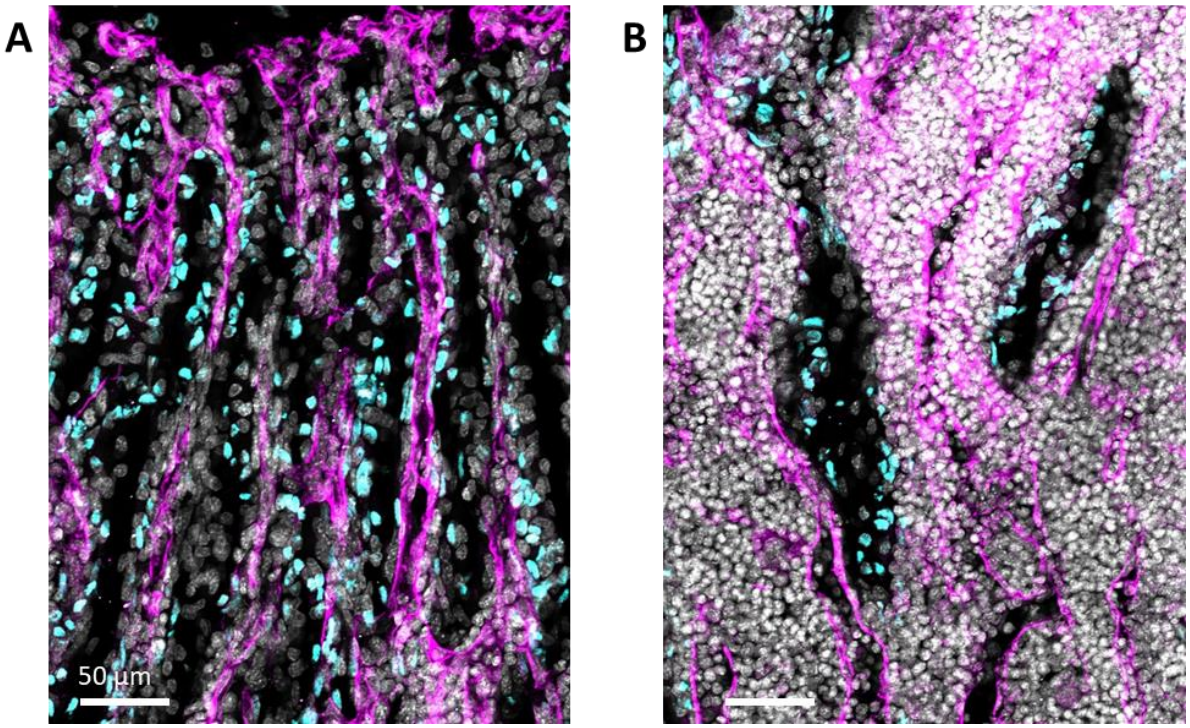


Figure 3.27 High-resolution confocal images showing the distribution of osteoblasts in the murine tibia A) metaphysis B) diaphysis. Bone sections were stained with CD31 (magenta), OSX (cyan) and Hoechst (nuclei, grey), both scale bars are 50 µm. Images show localisation of osteoblasts closer to metaphyseal vessels **(A)** as compared to diaphyseal vessels in **(B)**, OSX^+ cells are sometimes in close contact with the vessel boundary in the metaphysis, whilst loss of cell contact is observed in the diaphysis.

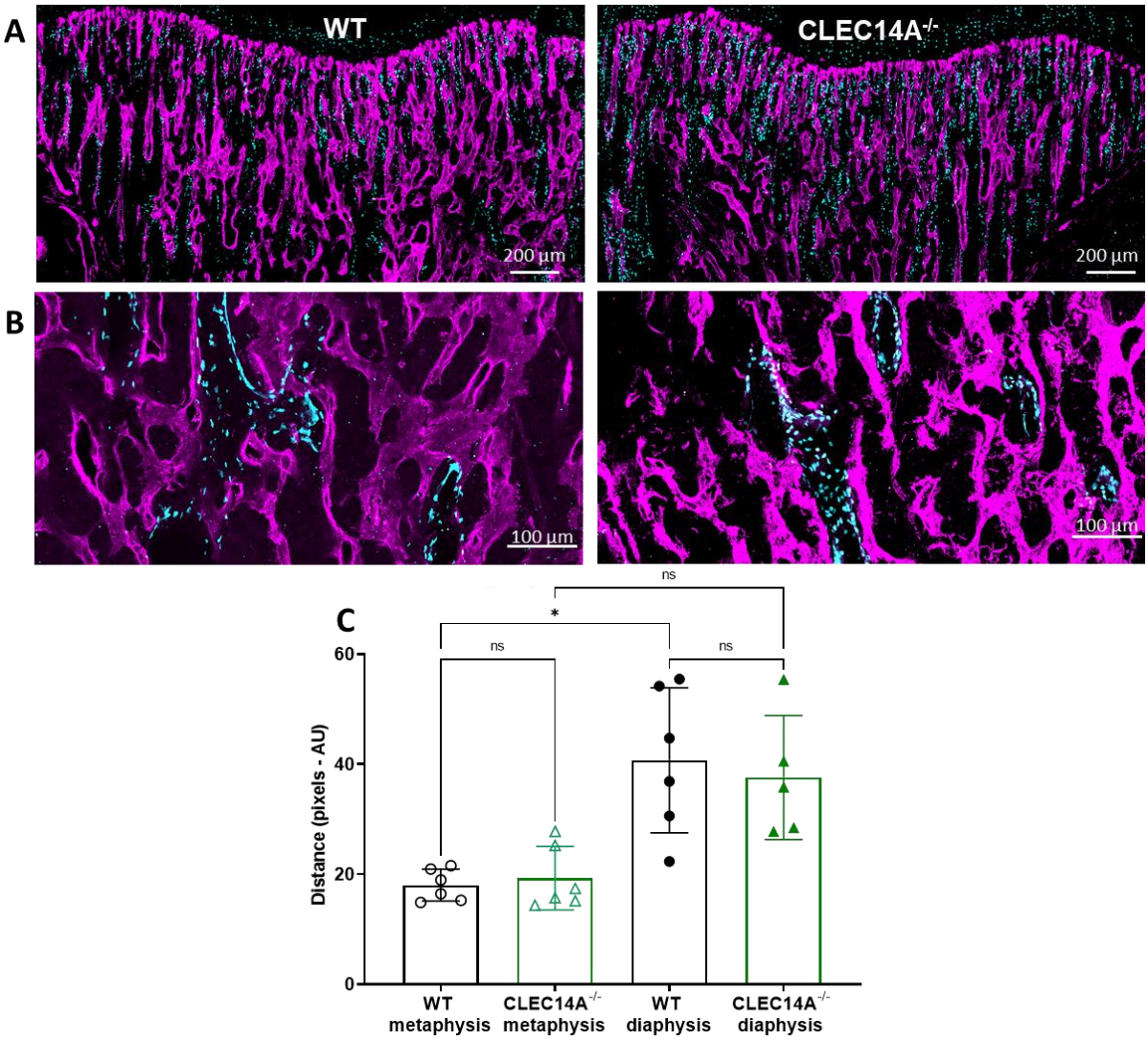


Figure 3.28 Distance of OSX$^+$ cells from vessels in the murine tibia metaphysis and diaphysis in juvenile (4-week-old) WT and CLEC14A$^{-/}$ male mice. Representative images analysed to measure distance of OSX$^+$ cells from the nearest vessel in the **A)** metaphysis and **B)** diaphysis, N=6 for all groups. Bone sections were stained with CD31 (magenta) and OSX (cyan). **C)** Quantitation of distance of OSX$^+$ cells from centre of the nearest neighbouring vessel shows a significant distancing from vessels in the diaphysis region compared to the metaphysis. Scale bars are 200 µm (A) and 100 µm **(B).** Data is represented as Mean ± SD, results were analysed with a Kruskal-Wallis test, * = $P < 0.05$, ns = not significant.

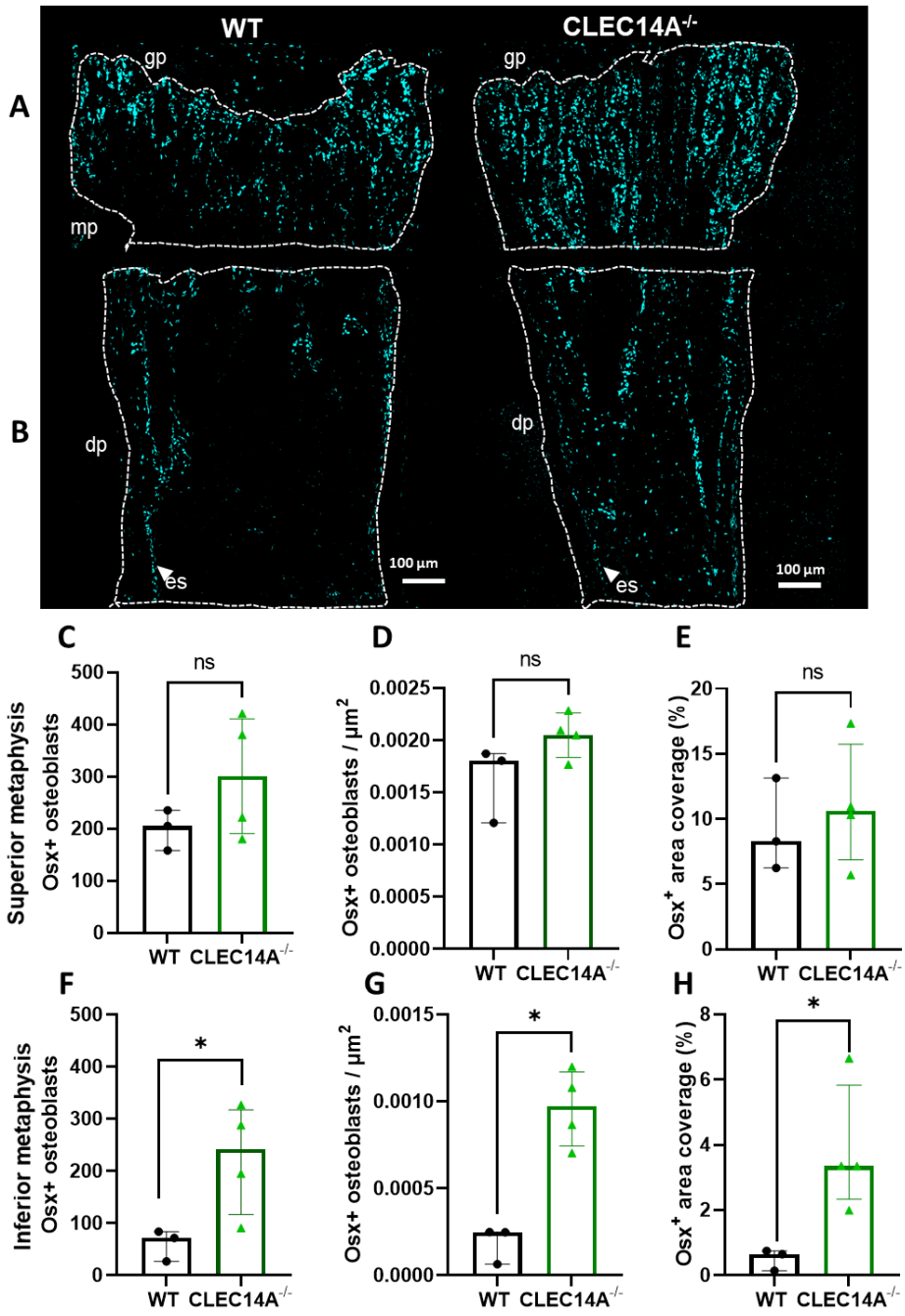


Figure 3.29 Osteoblast density in neonatal (P4) WT and CLEC14A$^{-/-}$ mouse tibiae. A-B) Representative images of OSX immunolabeled bone sections. Dashed line demarcates the superior edge of images in **A)**, the proximal growth plate, at the lateral edged in both A and B the osseous-muscular border, and in panel **B)** at the superior edge it delineates the metaphysis from the diaphysis. **C-H)** Quantitative measurements of osteoblast density in the neonatal mouse tibia metaphysis **(C-E)** and diaphysis **(F-H)**; **C** and **F)** total number of osteoblasts, **D** and **G)** osteoblast density, calculated as total number of osteoblasts normalised to the size of the area measured, **E** and **H)** percentage area covered by osteoblasts, an alternative measurement for osteoblast density. N=3 (WT) and N=4 (CLEC14A$^{-/-}$) Data was analysed with a Mann-Whitney test, results are presented as Median ± IQR, * = $p < 0.05$, ns = not significant. Abbreviations: gp= growth plate, dp = diaphysis, mp= metaphysis.

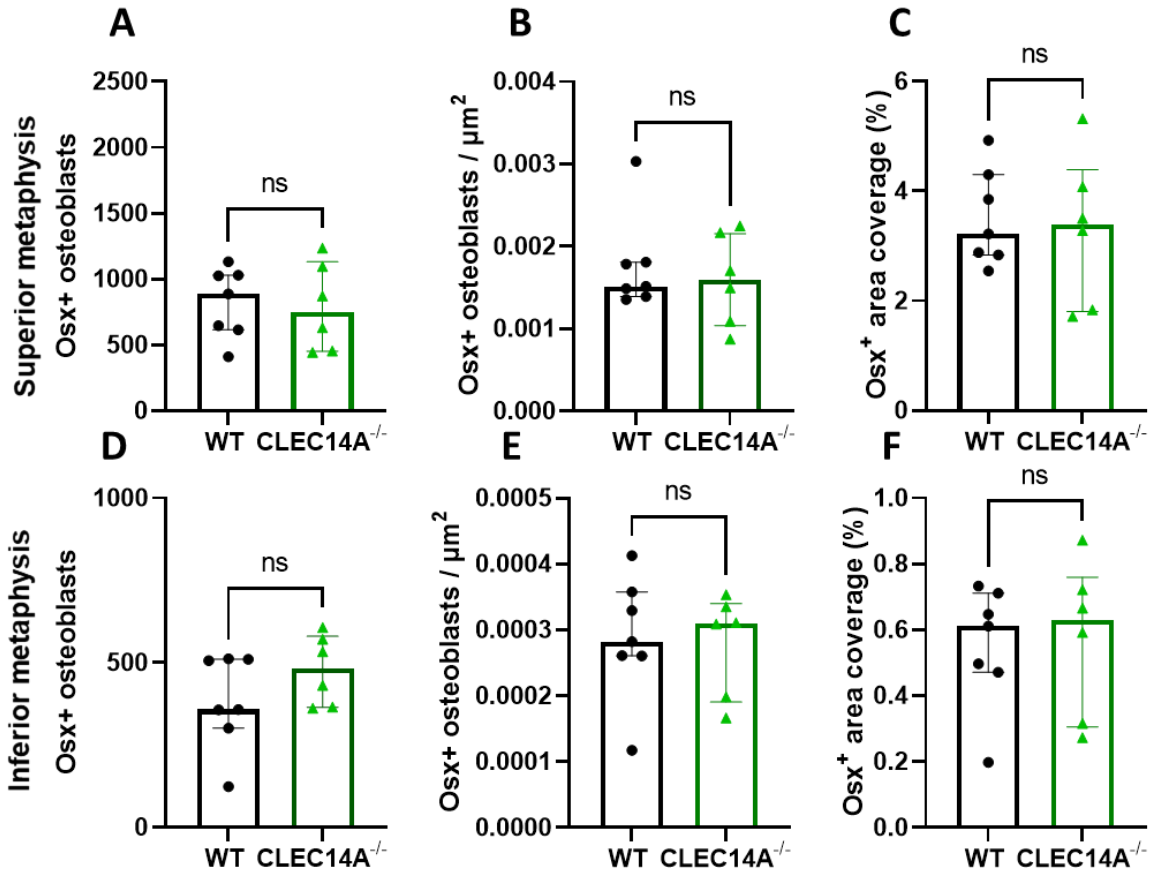


Figure 3.30 Osteoblast density in juvenile (4-week-old) WT and CLEC14A$^{-/-}$ mouse tibiae. Quantitative measurements of osteoblast density in the juvenile mouse tibia metaphysis **(A-C)** and diaphysis **(D-F)**; **A** and **D)** total number of osteoblasts, **B** and **E)** osteoblast density, calculated as total number of osteoblasts normalised to the size of the area measured, **C** and **F)** percentage area covered by osteoblasts, an alternative measurement for osteoblast density. N=6 (WT) and N=7 (CLEC14A$^{-/-}$).Data was analysed with a Mann-Whitney test, results are presented as Median ± IQR, ns=not significant.

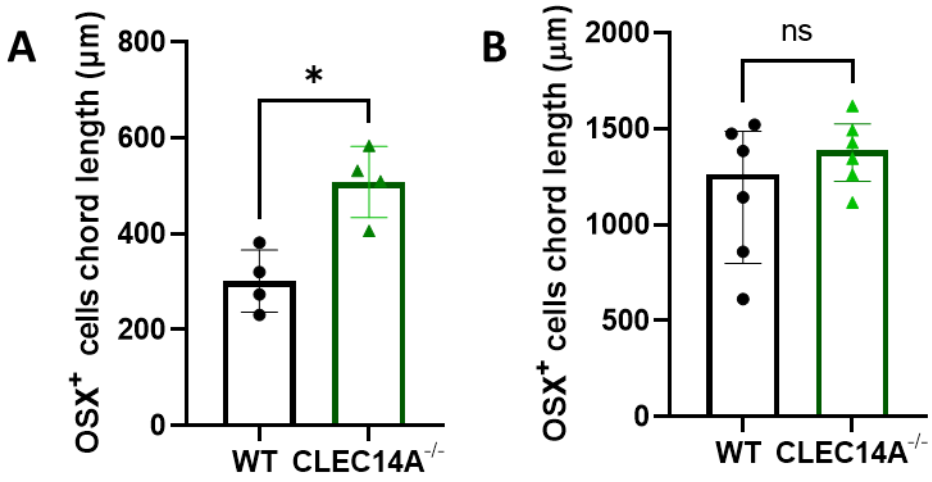


Figure 3.31 Characterisation of the osteoblast-covered front in murine tibia sections. Quantification of the length of osteoblast chords in the neonatal (N=4 for both groups) **(A)** and juvenile (N=6 for both groups) **(B)** murine tibia, each data point represents the mean value of osteoblast chords measured in each individual biological replicate. An osteoblast chord was defined as an aggregation of OSX^+ cells organised in columns in bone sections. The length of osteoblast chords from the proximal end of the metaphysis to the lowest point where osteoblasts are observed in the diaphysis was measured. Individual dots represent the mean length of osteoblast chords in one biological replicate. Data was analysed with a Mann-Whitney test, results are presented as Median ± IQR, * = $P < 0.05$, ns = not significant.

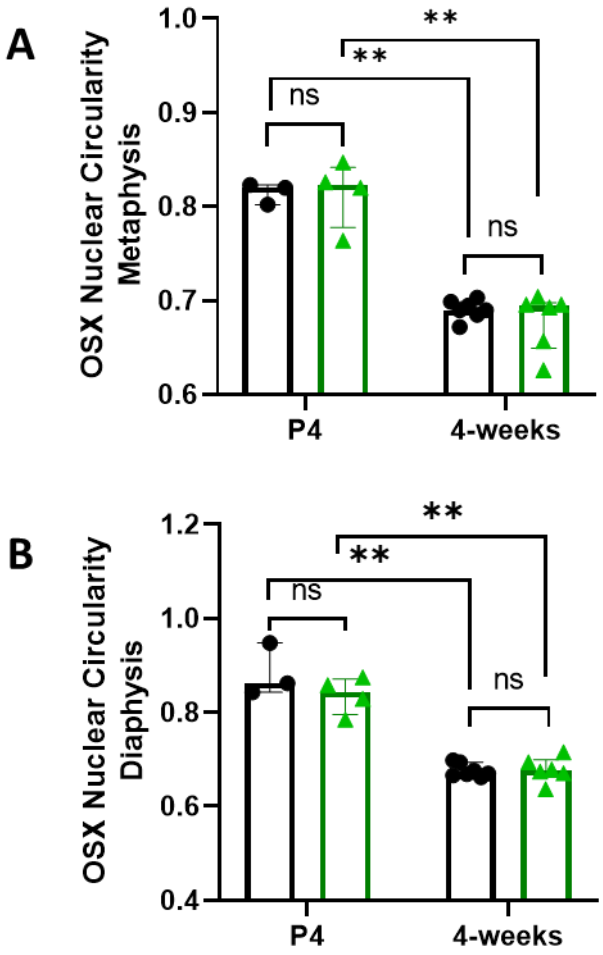


Figure 3.32 Nuclear circularity in neonatal and juvenile WT and CLEC14A$^{-/-}$ mouse tibiae. Quantification of osteoblast nucleus circularity in the tibia **A)** metaphysis and **B)** diaphysis, demonstrates a time-dependent reduction in nucleus elongation in both areas of the bone, P4: N=3 (WT), N=4 (CLEC14A$^{-/-}$), 4-weeks: N=6 for both groups, data was tested with a Kruskal-Wallis test, results are presented as Median ± IQR, ** = $P < 0.01$; ns=not significant.

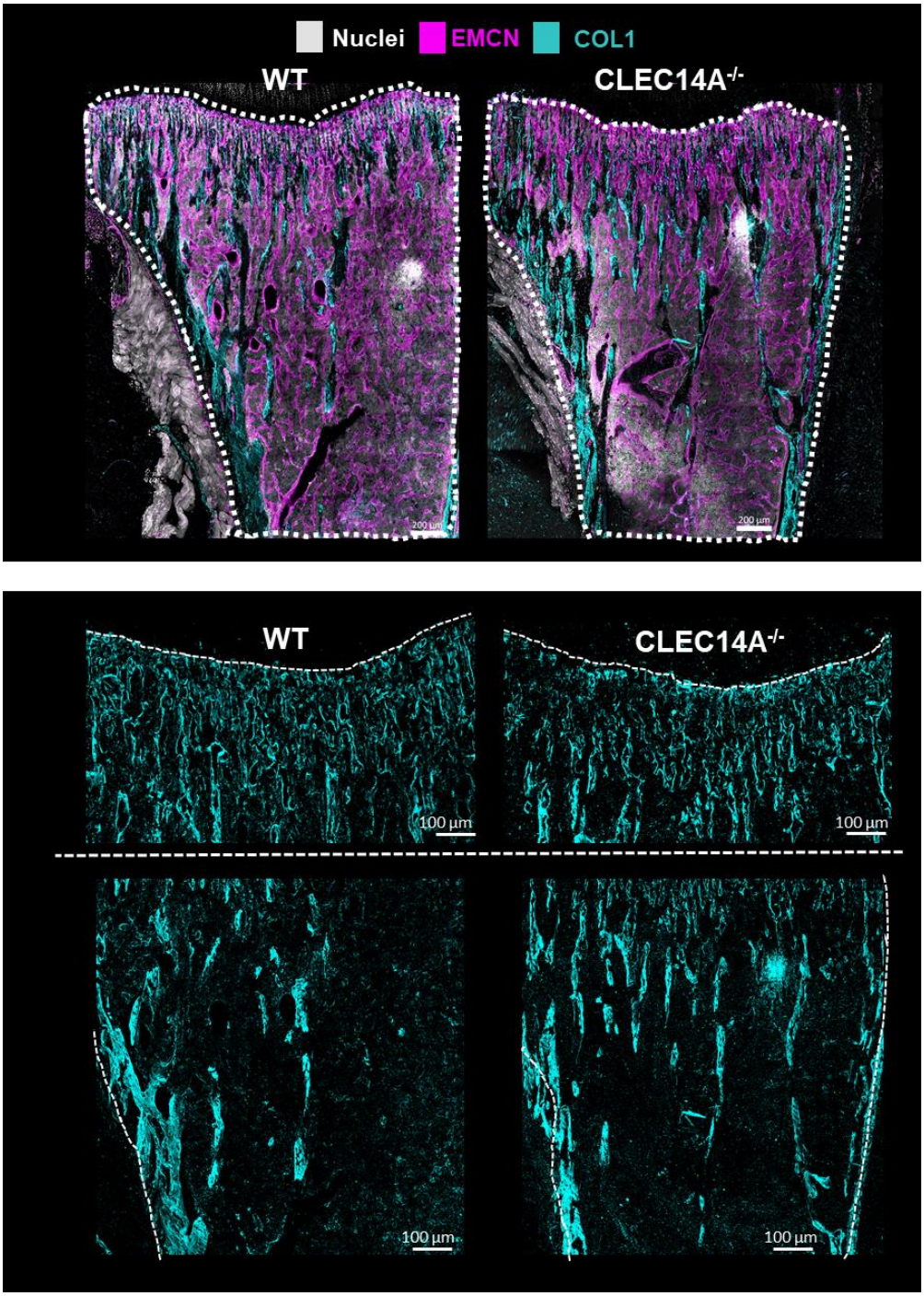


Figure 3.33. CLEC14A$^{-/-}$ (4-week-old) mice COL1A1^{+} cell chords extend further down in the inferior metaphysis and diaphysis compared to WT controls. Top panel: Representative maximum intensity projection images show secretion of COL1A1 around H-type vessels in WT and CLEC14A$^{-/-}$ tibia. Vessels in the tibia section have been immunolabelled with Emcn (magenta), COL1A1 is shown in cyan, nuclei were stained with Hoechst (grey). COL1A1 decorates the outer side of H-type vessels in the bone metaphysis. Bottom panel: representative maximum intensity projections of COL1A1 immunolabeled bone sections. For both panels dashed line demarcates the area in the section covered by bone including the bone endosteum and periosteum and demarcates surrounding muscle tissue from cortical bone, on the top part the white dashed line delineates the boundary between the growth plate (avascular) and the metaphysis. The straight white dashed line in panel B separates the top metaphysis from the inferior part of the metaphysis and the diaphysis.

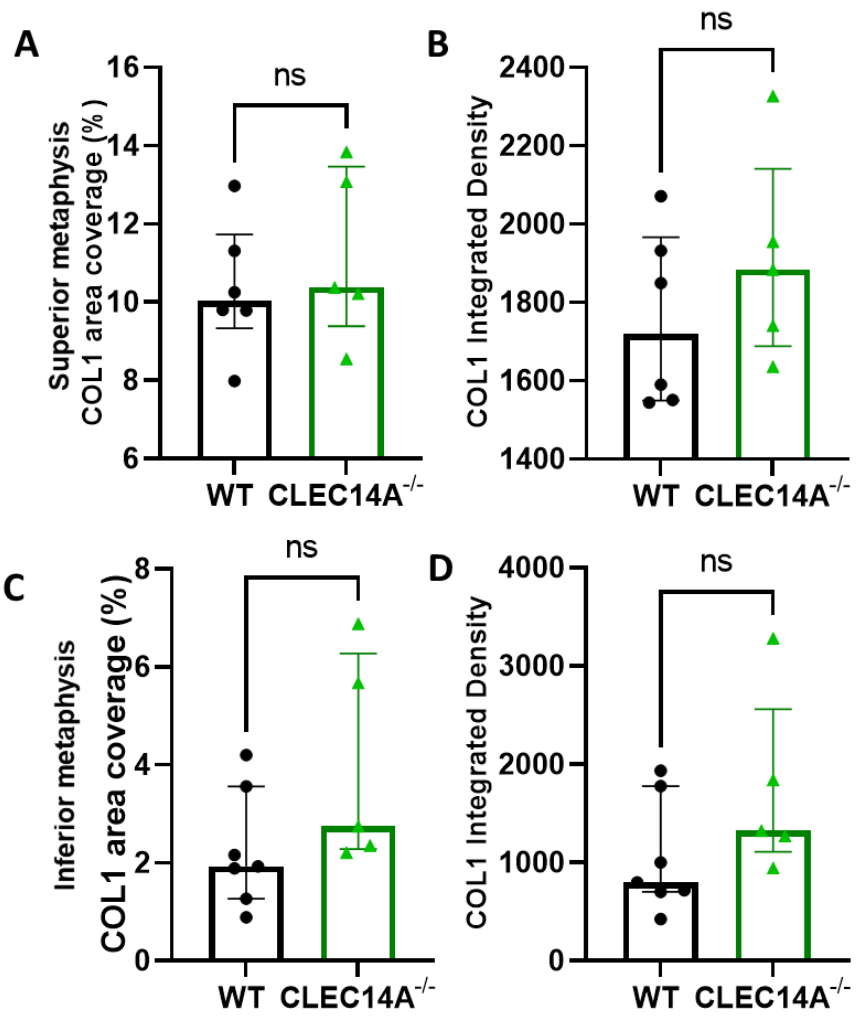


Figure 3.34 Quantification of COL1A1 deposition in the tibia of WT and CLEC14A$^{-/-}$ 4-week-old mice. Quantification of the % area covered by COL1A1 immunolabeling in the tibial **A)** superior, N=6 for all groups and **C)** inferior metaphysis, N=7 (WT), N=5 (CLEC14A$^{-/-}$); COL1A1 staining was also quantified as COL1A1 integrated density in the tibial **B)** superior, N=6 for all groups and **D)** inferior metaphysis, N=7 (WT), N=5 (CLEC14A$^{-/-}$); Integrated density sums all COL1A1 pixels within the analysed area, this was employed to capture information from both dim and bright pixels. The superior metaphysis area analysed extended from the superior end of the metaphysis to the transition zone, which was included as well, the inferior metaphysis area analysed extended 500 µm from the transition zone into diaphysis. Data was analysed with a Mann-Whitney test, results are presented as Median ± IQR, ns = not significant.

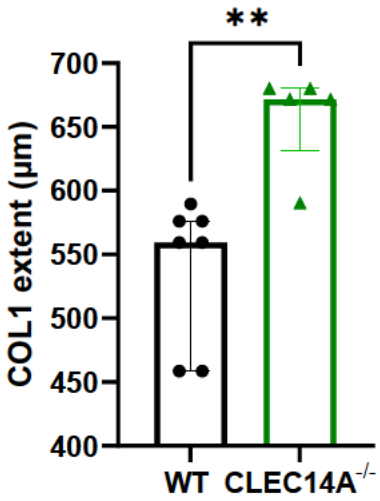


Figure 3.35 Quantification of the length of type I collagen chords in the juvenile (4-week-old) murine tibia. A COL1A chord was defined as the extension of COL1A1 staining from the proximal end of the metaphysis to the lowest point where COL1A1 staining was detected in bone sections. Each data point represents the average length of COL1A1 chords measured in in each individual biological replicate, , N=7 (WT), N=5 (CLEC14A$^{-/-}$). Data was analysed with a Mann-Whitney test, results are presented as Median ± IQR, ** = $P < 0.01$.

3.8. Discussion

3.8.1. Patterns of expression of CLEC14A, MMRN2 and CD248 in the murine tibia

H-type vessels are the only capillary type surrounded by immature osteoblasts, indicating the existence of specific molecular signatures, restricted to type-H EC, which maintain the proximity of osteoprogenitors to these vessels controlling their activity (2, 145). We hypothesised that CLEC14A and MMRN2 are contenders to mediation of osteoblast angiotropism and maturation. Therefore, to yield insight into patterns of expression of CLEC14A and MMRN2 in the murine bone, it was fundamental to start by uncovering their local cellular sources. This was accomplished initially by exploring a recently published and publicly available single cell-RNA sequencing dataset (GSE128423) of bone and bone marrow cells isolated from the long bone (403). Our analysis of this dataset revealed that expression of CLEC14A and MMRN2 was restricted exclusively to EC in the bone stroma (Figure 3.2), reiterating their rightful place in a strong unique signature of genes that drive transcriptional programming of EC angiogenesis (251). Unfortunately, due to the scarcity of H-type EC by 8-weeks of age (130, 145), H-type EC could not be sub-clustered in this dataset, hence a direct comparison could not be made between expression of MMRN2 and CLEC14A by H- and L-type EC. As a work around, the transcriptomic difference between metaphyseal H-type vessel EC and diaphyseal L-type sinusoid EC, was analysed in a bulk RNA sequencing dataset published by Langen and colleagues (136). In this dataset, H-type and L-type EC were FACS sorted from tibiae and femora of P6 mouse pups and sequenced further. Our analysis of this dataset revealed that CLEC14A and MMRN2, as well as some of their known interacting partners, were significantly upregulated at the mRNA level (Figure 3.8, Figure 3.10, and Figure 3.11), MMRN2 and CLEC14A were amongst the most enriched transcripts in H-type EC. Notably, both

CLEC14A and MMRN2 were enriched in H- versus L-type EC even more than the markers initially used to identify the two subtypes (CD31 and EMCN) (2). Immunofluorescent labelling of CLEC14A and MMRN2 in bone sections confirmed the upregulated production and secretion of these proteins in the top section of the tibia metaphysis (Figure 3.13,Figure 3.14), a region known to be populated by the actively expanding H-type capillaries. Upregulation of CLEC14A and MMRN2 at both mRNA and protein levels in H-type EC was reasonably expected considering the high angiogenic activity of H-type vessels in the bone metaphysis and the active roles played by CLEC14A and MMRN2 in angiogenesis (2, 345, 346, 348, 375, 418).

In addition, given the increased blood velocity and shear stress rates previously reported in type-H vessels (138), it is plausible to posit then that the higher transcriptional activity of genes sensitive to shear stress, such as PECAM-1, CDH5. CLEC14A and MMRN2 in type-H EC could also be triggered in response to the blood flow dynamics in these vessels (2, 20, 22, 138). Unpublished data generated in our lab has also identified a link between irregular blood flow and increased expression of CLEC14A. Namely, CLEC14A was reportedly upregulated in arteries at bifurcation sites, a region characterised by irregular blood flow and oscillatory non-laminar shear stress (419). Therefore, upregulation of CLEC14A in H-type capillaries could also be driven by loss of laminar shear stress due to irregular flow patterns, especially in the blunt H-type capillary bud area, which was previously shown to be characterised by unorganised blood flow (138).

In conclusion, increased mRNA and protein levels of CLEC14A and MMRN2 as well as other members of their interactome in H type endothelium provide evidence for a role for these two endothelial cell-derived markers in the regulation of angiogenesis in the bone.

3.8.2. Characterisation of the effect of genetic deletion of CLEC14A on the vascular network morphology in the tibia

Longitudinal bone growth occurs through endochondral ossification, a process characterised by a stepwise expansion of blood vessels and bone cells (osteoblasts, vessel associated osteoclasts and septoclasts) into the growth plate (2, 20, 22). Angiogenic expansion of the blood vessel front is followed by osteoblast co-migration and eventually osteoblast-derived synthesis of extracellular matrix which becomes ossified over time (2, 52, 107, 118). H-type capillaries, a bone specific vessel subtype, map the localisation, cellular activity and metabolism of osteoblasts, providing a framework for bone homeostasis by regulating all aspects of trabecular bone accrual mechanisms (130, 136, 145, 420-422). Given the expression of both CLEC14A and MMRN2 on H-type blood vessel EC, investigating the changes resulting from the genetic deletion of CLEC14A on the bone metaphysis cellular organisation constitutes an important aspect of this project. Major detrimental changes to the bone vasculature morphology and function in CLEC14A$^{-/-}$ mice would be of uttermost importance for therapeutical translatability of this work. Therefore, the morphology and patterning of the vascular bed were investigated in WT and CLEC14A$^{-/-}$ samples, alongside the geographical distribution of osteoblasts.

The status of the endothelium in the tibia was examined in immunofluorescent antibody labelled tibia sections collected from neonatal (P4) and juvenile (4-weeks old) WT and CLEC14A$^{-/-}$ mice. Vessels were labelled using CD31 or EMCN antibodies (as stated). Supporting our currently developing theory that CLEC14A plays an important role in angiogenesis in specific areas of H-type capillaries, a subtle change in the linearity of the advancing vascular front immediately after birth and in juvenile 4-week-old mice at the growth plate-metaphysis interface was observed in CLEC14A$^{-/-}$ sections (Figure 3.17), perhaps indicating a dysregulation

of tip cell formation or modification of EC migration. This would be in line with the role previously attributed to CLEC14A in vascular development, with genetic deletion of CLEC14A resulting in a reduced formation of EC filopodia and reduced EC migration (345, 348).

Imaging analysis also produced various additional parameters including: the number of H-type capillaries in the metaphysis, H-type capillary density, the area covered by the H-type vascular bed front and the angular orientation of H-type capillaries at the growth plate-metaphysis junction. Labelling of the vasculature bed in neonatal and juvenile WT tibia sections indicated an age-dependent increase in the number of H-type columnar vessels in both WT and CLEC14A$^{-/-}$ specimens (Figure 3.19), with a higher number of vessels in 4-week old mice by comparison to P4 pups. Data on the number of vessels as well as their density, was comparable to values previously published by Ramasamy and colleagues at the same timepoints (138). However, when the number of vessels was normalised to the bone diameter the effect was blunted, suggesting that the increase in the total number of H-type capillaries comes as a response to a requirement for a specific type-H vessel density in the bone metaphysis depending on bone size rather than age.

Overall, immunolabelling of the mouse tibia vasculature showed no striking differences in the organisation of either H- and L-type vessels between WT controls and CLEC14A$^{-/-}$ samples (Figure 3.16, Figure 3.17). No differences were identified in relation to H-vessel numbers, their density, or angular orientation in CLEC14A$^{-/-}$ samples when compared to matched controls. Our data contradicts previous *in vivo* work reporting tumoral vascular density changes in response to limitation of CLEC14A expression (348). These opposing phenotypes in healthy bone compared to targeting of CLEC14A in tumours could be explained by differences in the molecular regulation of the tissue microenvironment in healthy tissues compared to tumours (423). For instance, CLEC14A expression might be regulated by different stimuli, furthermore,

the pattern of expression of CLEC14A on the vasculature could vary in tumours compared to the healthy developing bone. In tumours, CLEC14A has been shown to decorate the entire surface of the vessel (345), whilst our imaging of the postnatal tibia shows condensations of CLEC14A expression and a focal expression at the top of the metaphysis where H-type EC vessel buds reside (Figure 3.13 and Figure 3.14). Furthermore, in tumours, CLEC14A is likely exclusively upregulated in response to hypoxia which is a well-recognised hallmark of malignant lesions (424). The unbalanced molecular signalling in tumours most likely contributes to abnormal vascular formation with vessels presenting with reduced shear wall stress (345, 425-430) which would also trigger CLEC14A expression on the entire length of the vessel (431). In addition, downregulation of angiogenesis by means of CLEC14A genetic deletion might have a more sustained and cumulative effect in tumours given the already decreased functional capacity of blood vessels in tumours (432). In contrast, vascular angiogenesis in the bone is a tightly regulated mechanism, hence, in healthy developing tissues such as the bone, CLEC14A expression is likely stimulated by active angiogenesis or by the irregular blood flow, the latter is limited to the H-type blunt ends (H-type buds) of newly developing vessels (as discussed above). All these different physiological characteristics in tumours vessels compared to bone vessels are likely to regulate different patterning of CLEC14A expression which in turn, would result in different regulation of angiogenesis across different tissues.

3.8.3. Potential redundancy for CLEC14A in mediation of the angiogenesis process in the bone

The lack of significant changes in the morphological pattern of H-type vessels in CLEC14A$^{-/-}$ sections is reminiscent of the lack of any striking differences reported in the bone metaphysis following genetic deletion of the shear stress and blood-flow regulated CD31 (138, 433). The lack of morphological or functional alteration of vessels was linked in that case to redundancy for CD31 and compensatory responses by the use of other molecules (434). In the case of CLEC14A$^{-/-}$, CD93 is a strong contender to compensate for CLEC14A due to its similarities in structure (both are members of the C-type lectin group 14 family, which comprise just 4 members) (350). CD93 has been shown to be expressed by EC and its ability to bind MMRN2 at the same region as CLEC14A has already been confirmed (1, 435). CLEC14A CD93 bidirectional redundancy has already been confirmed in the zebrafish (352, 436), however, similar studies have yet to be carried out in a mammalian species. Moreover, CD93 accomplishes similar functions as CLEC14A during angiogenesis, essentially regulating EC adhesion and migration via interaction with MMRN2 (435).

3.8.4. Acceleration of bone vessel maturation in the CLEC14A-/- tibia

Whilst no alterations in the morphological organisation of H-type vessels were identified in CLEC14A$^{-/-}$ tibiae, changes to the H-type vascular front were observed. Namely, blunting of H-type vessel buds was demonstrated in 4-week-old but not P4 CLEC14A$^{-/-}$ mice (Figure 3.17), indicating a fast-tracked maturation of the vascular compartment in the metaphysis, a process previously reported to be characterised by blunting of H-type bulges (2, 130, 145). In further support of the concept that genetic deletion of CLEC14A induces acceleration of H-type vessel maturation, shortening of the H-type vascular front at 4-weeks but not P4 in CLEC14A$^{-/-}$ bone

sections was also demonstrated (Figure 3.21), alongside a decrease in the percentage of $CD31^{high}$ $Emcn^{high}$ EC levels in 2-week old mice (Figure 3.24). The changes we report here, in the H-type vascular front, have been previously reported during maturation of the vascular bed in the metaphysis as bone growth begins to decelerate. For instance, in the later stages of skeletal growth (2-8 weeks post birth) the H-type EC / L-type EC ratio decreases in the favour of L-type sinusoidal capillaries (2, 136, 145). In addition, studies of bone healing by employing intravital microscopy have shown that vessel length is reduced following completion of the callus formation stage and that a fraction of the micro vessels which previously actively supported osteoblast migration change their shape from parallel columnar tubes into large and irregular sinusoidal vessels at a time coinciding with formation of the bone marrow space (153)

In conclusion, the changes we report here indicate an accelerated transition of H-type vessels into L-type vessels in this $CLEC14A^{-/-}$ mice. It remains to be established if this is also mirrored by an acceleration of bone maturation and growth (analysed in chapter 4).

Altogether, the data presented here supports the hypothesis that functional impairment of CLEC14A by means of germline genetic deletion does not directly perturb normal bone angiogenesis, however, it does result in changes to the H-type vascular front which recapitulate the changes reported in maturation of the vascular network in the metaphysis during skeletal growth.

3.8.5. Osteoblast and COL1A1 imaging

To assess the effect of CLEC14A genetic deletion on osteoblast migration to, and maturation at, the metaphysis, we investigated the patterning of immature osteoblasts in the neonatal

and juvenile murine tibia of WT and CLEC14A$^{-/-}$ mice. The pattern of staining for OSX and COL1A1 in the WT long bone metaphysis recapitulated previously published work (53, 437). Data presented here demonstrates changes in the localisation (osteoblast extent) in the metaphysis of CLEC14A deficient mice, providing a cellular indication for changes in bone growth and potentially mineralisation in CLEC14A deficient mice.

In line with previously published observations (2, 145), osteoblasts in the bone metaphysis were aligned alongside H-type ECs (Figure 3.27). Quantification of osteoblasts demonstrated an increase in immature osteoblast density in CLEC14A$^{-/-}$, however this did not reach statistical significance, warranting investigation of additional bone sections. The osteoblast density phenotype was self-resolving and was no longer present at 4 weeks of age. The absence of an increased osteoblast density at 4 weeks of age might be closely correlated with the decrease of the H-type vessel front, which occurs over time as mice age (2, 138). Indeed, a close correlation between vascular volume and osteoblast cell numbers has previously been reported (153). In addition, longitudinal intravital microscopy studies have shown that during bone formation osteoblast density decreases as osteoblasts are being replaced by bone mineral. Essentially, osteoblast density reaches a peak then decreases in a time-dependent fashion over 3-4 weeks, at the same time as the bone osteoid is remodelled in mature fully mineralised bone (153, 417). It is thus plausible that CLEC14A$^{-/-}$ mice reach peak osteoblast density earlier than WT mice and prior to measurement at 4 weeks of age. To confirm this, a time course analysis of osteoblast density is warranted to analyse osteoblast density in WT and CLEC14A$^{-/-}$ pups from P4 to 4-weeks at 1-, 2- and 3- weeks after birth.

The age-specific elongation of OSX^{+} immature osteoblast chords versus COL1A1^{+} mature osteoblast chords, indicate that the immature osteoblasts located in the lower metaphysis in CLEC14A$^{-/-}$ tibiae in neonatal mice actively differentiate over time into matrix deposing cells

and are most likely depicted as COL1A1^{+} cells at 4-weeks of age, rather than undergoing apoptosis and being cleared by phagocytic cells. Changes in osteoblast localisation and COL1A1 secretion are likely to be linked to a perturbed interaction between EC and osteoblasts, given that vascular bone capillaries have been shown to regulate patterning of COL1A1 deposition and mineralisation of the bone matrix by acting as guiding templates (163).

3.8.1. Limitations

Unfortunately, the experimental setup and methods employed to investigate angiogenesis in the CLEC14A$^{-/-}$ bone do not allow for a more detailed analysis of the effect of CLEC14A knock out on H-type EC filopodia formation and migration.

An improvement on the analysis technique would be to measure the H-type vascular front in images immunolabelled with both CD31 and Emcn as this method better differentiates between H- and L-type vessels. Due to the long acquisition time during imaging, adding another channel to staining panel was not possible due to water dehydration between the objective and stained bone slides. Instead, the fraction of H-type EC was compared against that of L-type vessels using flow cytometry, with the hypothesis that if the H-type vascular front was indeed shorter then this decrease would be expected to be reflected by a lower number of H-type ECs.

An alternative model suitable for the study of EC migration during bone formation would be a bone defect healing mouse model. EC migration and invasion of osteoblasts alongside vessels could be study progressively over the course of a few weeks using intravital microscopy. Intravital microscopy methods for the study of bone formation in the tibia and

calvaria have already been published offering excellent replicable results (153, 438). Mouse calvarium defects are more approachable as the equipment required is less complex. Labelling of the vasculature could be easily achieved with the aid of antibodies against CD31 or EMCN, which could be injected intravenously 30 minutes prior to imaging as previously reported (439), however, a transgenic mouse model would be required for the immunofluorescent targeting of osteoblasts.

3.8.2. Conclusion

Taken together, data presented in this chapter shows that as analysed by immunofluorescent staining, the bone vascular bed of CLEC14A$^{-/-}$ mice presents no striking changes in the organisation of the bone vasculature compared to WT controls. For instance, no changes were observed in regard to vascular density or H-type vessel orientation towards the direction of bone growth. However, an increased vascular maturation phenotype was reported. This was characterised by a shortening of H-type column length which was matched by a decrease in the area covered by the H-type column vascular front. Deletion of CLEC14A also increases the geographical dispersion of osteoblasts in the bone; lending support to the theory that CLEC14A plays an important role in the regulation of osteoblast migration to sites of bone formation.

4. CHAPTER IV THE ROLE OF CLEC14A AND CD248 IN BONE FORMATION DURING GROWTH

4.1. Introduction

In high similitude to embryonic bone formation, postnatal long bones are formed through endochondral ossification. This is accomplished by replacing an initial cartilage template in the epiphyseal growth plate with bone. This multistep process is initiated in the growth plate by chondrocyte proliferation and is subsequently followed by chondrocyte maturation and hypertrophy (88, 89, 97). These hypertrophic chondrocytes produce VEGF to attract blood vessels from the highly vascularised metaphysis to the growth plate, initiating at the same time osteoblast migration alongside vessel invasion (440-442). Mineralisation of the growth plate-metaphysis interface by secretion of collagen and hydroxyapatite amongst other organic and inorganic compounds by mature osteoblasts leads to formation of new bone mediating thus its elongation (443). In summary, expansion of blood vessels, osteoclasts and osteoblasts into the growth plate space is followed by an intense period of ossification of the newly occupied space, whereby the newly deposited matrix is being mineralised (also term osteoid or early calcified bone) followed by further ossification. This chapter was dedicated to the study of the dynamic process of bone mineral formation and addressed aim I (To characterise the effect of CLEC14A on bone formation during postnatal bone growth.)
To achieve this, a few parameters were obtained including: bone length, morphometric and biomechanical parameters. External bone measurements were employed to obtain bone length information, micro-computed tomography imaging was utilised to obtain bone morphometric parameters and bone mechanical analysis was performed with the aid of three-point bending testing to obtain information on the quality of cortical bone of CLEC14A$^{-/-}$ mice. Bone morphometric measurements were obtained from male and female bones, all other parameters reported were obtained from male mice only.

4.2. Bone length measurements

Bone length was measured with the assistance of digital callipers, data was collected from the long bones of 2-weeks to 30-weeks-old C57Bl/6J male mice at various time points (Figure 4.1). Briefly, bone length measurements were obtained for the tibia and femur of pups (2-week-old), juvenile (4-week-old), sexually mature (8-week-old), adult (12-weeks-old) and mature adult (30-week-old) C57BL/6J male mice. No changes in body weight were measured between WT and CLEC14A$^{-/-}$ mice (Figure 4.2 A). In both genotypes the most active period of bone elongation was observed between 2 to 4 weeks, where tibiae doubled in size and presented an average increase in length of 42-55% (WT and CLEC14A$^{-/-}$ respectively). Significant changes in tibia, but not femur, length were observed when comparing controls to CLEC14A$^{-/-}$ at each time point examined (Figure 4.2 B-C). The most striking difference was observed at 2 weeks of age where tibiae in WT controls were 1.19 mm shorter than CLEC14A$^{-/-}$ (mean of 10.22 vs 11.41 mm, WT vs CLEC14A$^{-/-}$, $P < 0.05$). A 0.41 mm difference was observed at 4-weeks (mean of 15.86 vs 16.27 mm, WT vs CLEC14A$^{-/-}$, ns), and a 0.65 mm difference in length was also observed at 8 weeks (mean of 16.63 vs 17.28 mm, WT vs CLEC14A$^{-/-}$, $P < 0.01$). Finally, at 30-weeks of age CLEC14A$^{-/-}$ tibiae were 0.98 mm longer than WT (mean of 17.78 vs 18.76 mm, WT vs CLEC14A$^{-/-}$, $P < 0.05$). CLEC14A$^{-/-}$ femora were only significantly longer than WT controls at 30 weeks of age: on average these were 0.49 mm longer than controls (mean of 15.36 vs 15.85, $P < 0.05$, WT vs CLEC14A$^{-/-}$) (Figure 4.2 C).

As an alternative means of measuring bone length, measurements from micro-computed tomography (µCT) tibial scans were used to quantitate the distance from the end of the proximal growth plate to the distal tibiofibular junction. Hereafter this area will be referred to as: the proximal growth plate to tibiofibular junction tibia length or in brevis - PGP TFJ tibia

length. X-ray imaging scans analysis detected significantly longer CLEC14A$^{-/-}$ PGP TFJ tibiae at both 4- (median of 6.52 vs 7.61 mm, $P < 0.05$) and 8-weeks of age (median of 7.82 vs 8.72 mm, $P < 0.05$). No significant difference was detected at the other timepoints (Figure 4.2 D).

The effect of CLEC14A genetic deletion on long bone development was also examined in embryonic life (Figure 4.3) To assess bone elongation, we employed a metatarsal organ explant *in vitro* culture and measured bone elongation of E14.5 embryonic metatarsals at days 3, 5 and 7 in culture. CLEC14A$^{-/-}$ explants were significantly shorter than WT controls at day 1 and 3 in culture (day 1: median length of 1296 vs 1171 µm, $p < 0.0001$, WT vs CLEC14A$^{-/-}$, day 3: median length of 1517 vs 1442 µm, $p < 0.05$, WT vs CLEC14A$^{-/-}$) (Figure 4.3 A), however, at days 5 and 7 no differences in metatarsal length was measured between WT and CLEC14A$^{-/-}$ samples (day 5 : median length of 1713 vs 1682 µm, ns, WT vs CLEC14A$^{-/-}$, day 7: median length of 1820 vs 1800 µm, $p < 0.05$, WT vs CLEC14A$^{-/-}$). In addition, when assessing the percentage increase of embryonic metatarsals compared to day 0, we observed a minor increase in bone length at 3 days post isolation (median of 117 % vs 122 %, WT vs CLEC14A$^{-/-}$, $p < 0.01$), followed by a more sustained and significant increase in the percentage of elongation at days 5 (median of 131 % vs 144 %, $P < 0.0001$, WT vs CLEC14A$^{-/-}$) and 7 (median of 141 % and 150 %, $p < 0.05$, WT vs CLEC14A$^{-/-}$) (Figure 4.3 B).

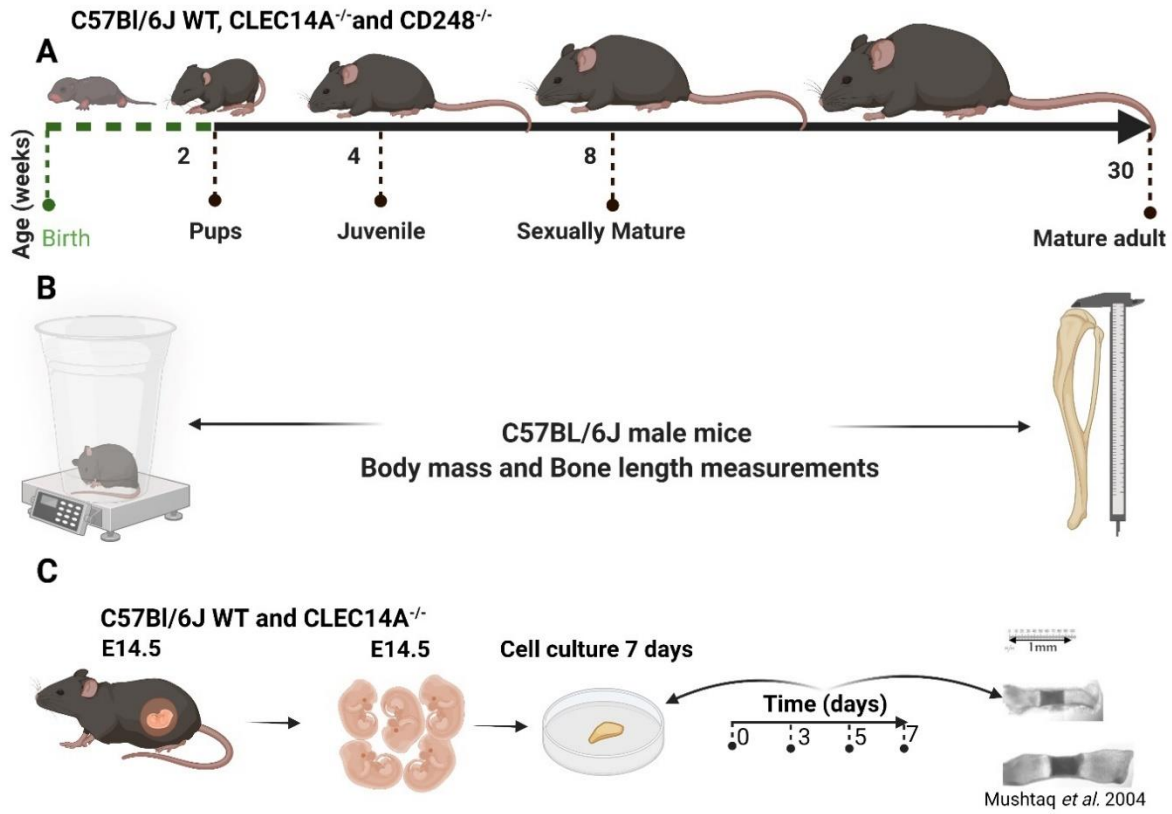


Figure 4.1 Body mass and body length measurement methodology outline. A) Timepoints and **B)** Methods utilised for the investigation of postnatal body and skeletal growth of C57BL/6J WT, CD248$^{-/-}$and CLEC14A$^{-/-}$ males. **C)** Summary for the methodology employed for the in vitro study of embryonic bone elongation of C57BL/6J WT and CLEC14A$^{-/-}$ embryos.

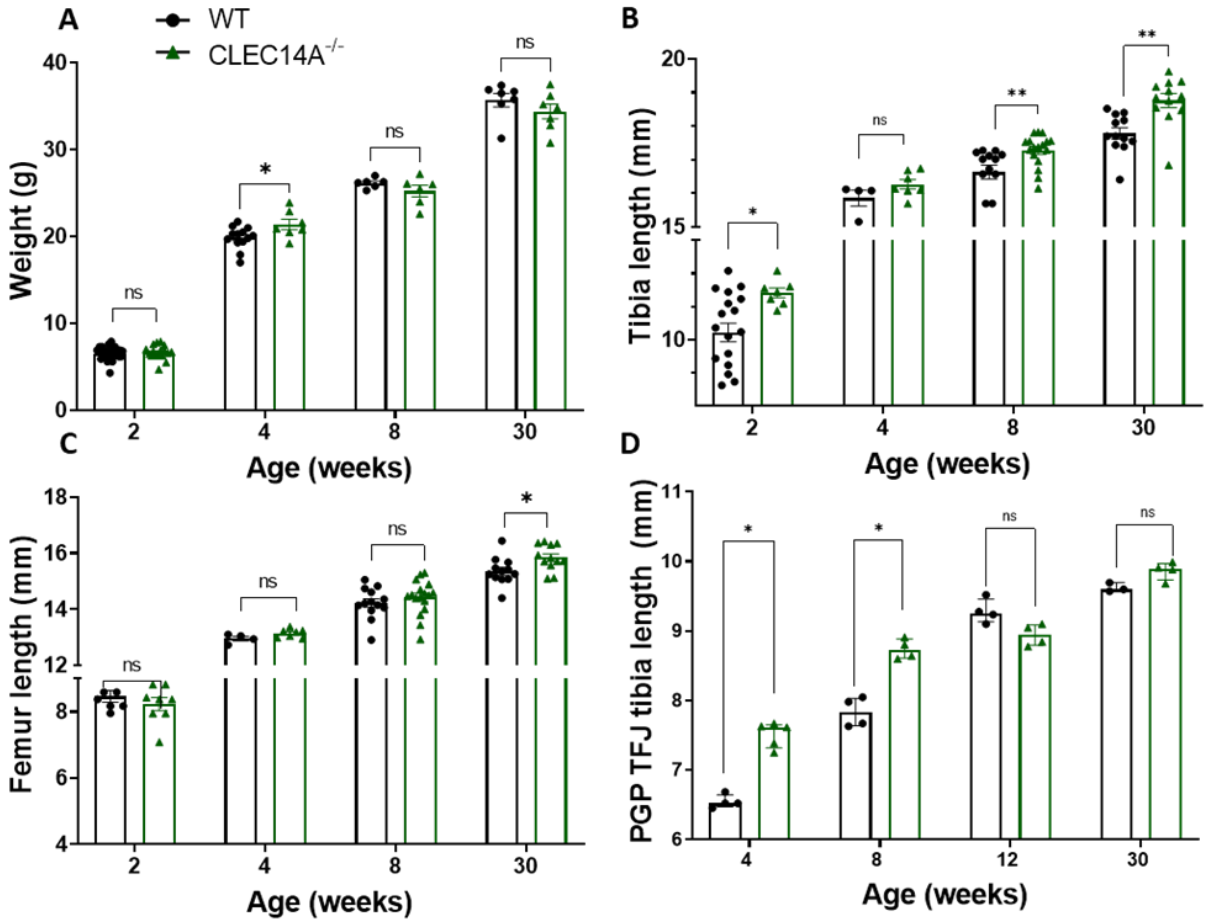


Figure 4.2 Bone mass and long bone measurements in CLEC14A$^{-/-}$ vs WT male mice. **A)** Bone mass **B)** Tibia length **C)** Femur length and **D)** Tibia length (measured from the end of the proximal growth plate to the tibiofibular junction – PGP TFJ tibia length. Sample size varies as represented by each individual dot in the graphs. Results for graphs A-C are presented as Mean ± SEM, data was analysed with Two-way ANOVA, followed by Dunnett's post hoc, results for graph D are presented as Median ± IQR, data was analysed with Multiple Mann-Whitney tests, * = $P < 0.05$ ** = $P < 0.01$; *** = $P < 0.001$; **** = $P < 0.0001$.

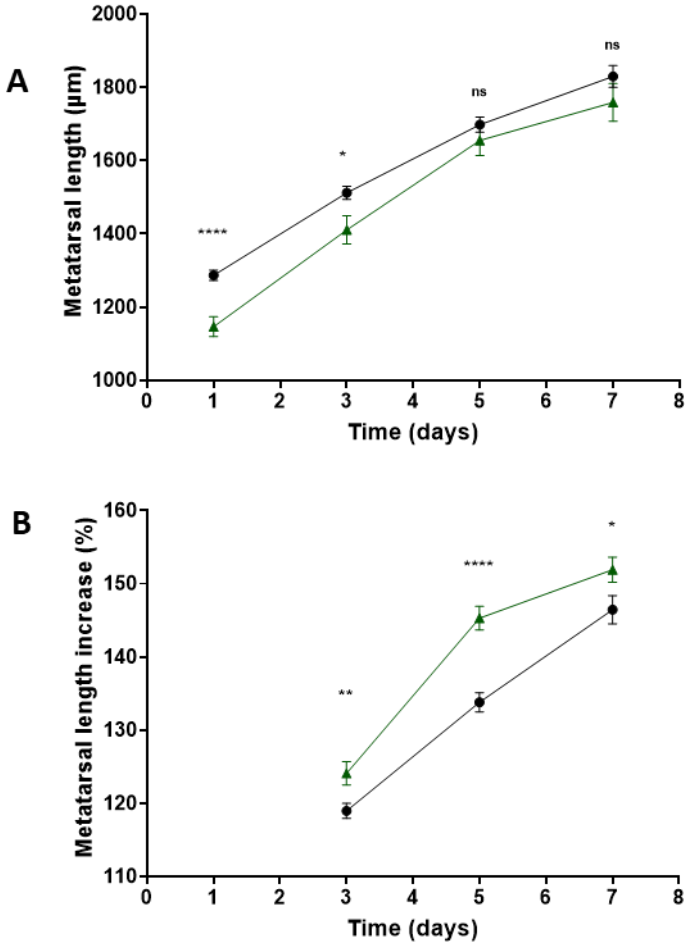


Figure 4.3 Analysis of bone length in embryonic metatarsal explant cultures of CLEC14A$^{-/-}$vs WT male mice. A) Metatarsal length (µm) **B)** Metatarsal bone increase percentage. Results for graph A are presented as Median ± IQR, data was analysed with Multiple Mann-Whitney tests, *=p < 0.05, **=p < 0.01, ****=p < 0.0001. Data was obtained from N=9, n=26 (WT) and N=5, n=6 (CLEC14A$^{-/-}$), where N = individual biological replicates and n = total number of explants analysed.

4.3. Trabecular bone in the metaphysis is increased in CLEC14A and CD248 deficient C57BL/6J male mice

To investigate the quantity and spatial organisation of bone, micro computed tomography (µCT/ micro-CT) was performed. This allowed for the analysis of cortical and trabecular bone parameters separately in C57BL/6J WT, CLEC14A$^{-/-}$ and CD248$^{-/-}$ male and female mice (more information on the timepoints inspected can be found in Figure 4.4). µCT imaging analysis of trabecular and cortical bone in the tibia demonstrated the strikingly different spatial organisation of trabecular bone in the CLEC14A$^{-/-}$ and CD248$^{-/-}$ male groups compared to WT (Figure 4.5-4.9, Table 12). Minimal differences in the microarchitecture of cortical bone were also identified in CLEC14A$^{-/-}$ and CD248$^{-/-}$ male by comparison to WT (Figure 4.10, Table 12). Similar trends were also observed in the trabecular bone of females in our knock-out groups compared to WT controls, however, these changes were not always powered by statistical significance (Figure 4.13-4.18).

Overall, µCT imaging analysis indicated a substantial increase in the tissue volume covered inside the endocortical bone envelope (Figure 4.5 A) in both CLEC14A$^{-/-}$ and CD248$^{-/-}$ mice as compared to WT at 4- and 8-weeks, whilst no major differences were observed post-puberty (12- and 30-weeks). In the first half of the timeline analysed (ages 4-weeks and 8-weeks).

The expansion in tissue volume in both the knock-out groups was also matched by an increase in bone volume compared to controls (4-weeks: mean of 0.05 vs 0.17 mm^3, $P < 0.01$, WT vs CLEC14A$^{-/-}$, mean of 0.05 vs 0.08 mm^3, ns, WT vs CD248$^{-/-}$, 8-weeks: mean of 0.07 vs 0.25 mm^3, $P < 0.0001$, WT vs CLEC14A$^{-/-}$, mean of 0.07 vs 0.39 mm^3, $P < 0.0001$, WT vs CD248$^{-/-}$) (Figure 4.5 C, Figure 4.6, Table 12). In contrast, by the time mice reach full skeletal maturity at 12-weeks of age a significant decrease in bone volume as compared to controls is observed in

CD248$^{-/-}$ and CLEC14A$^{-/-}$ samples (mean of 0.65 vs 0.42 mm^3, P < 0.0001, WT vs CLEC14A$^{-/-}$, mean of 0.65 vs 0.24 mm^3, P < 0.0001,WT vs CD248$^{-/-}$)(Figure 4.5 C). As a normalisation of bone density in the region of bone analysed, data is also presented as a percentage of bone volume (BV) to tissue volume (TV). A higher BV/TV % was identified in CLEC14A$^{-/-}$ than in WT control tibiae during bone growth at 4-weeks (median of 3.83 vs 9.4 %, P < 0.05, WT vs CLEC14A$^{-/-}$) and 8-weeks of age (median of 5.94 vs 9.32 %, p < 0.05,WT vs CLEC14A$^{-/-}$) (Figure 4.5 E,). In the second stage (ages 12-weeks and 30-weeks) of the CLEC14A$^{-/-}$ mouse skeletal life cycle, a decrease in BV/TV % was identified at 12 weeks of age (median of 25.2 vs 17.36 %, P < 0.05,WT vs CLEC14A$^{-/-}$), whilst no significant differences were detected at 30-weeks (Figure 4.5 E). Similar but not identical observations were reported for BV/TV % in CD248$^{-/-}$ mice. A significant increase in the BV/TV % of CD248$^{-/-}$ was observed at 8-weeks (median of 5.94 vs 16.98 %, P < 0.05, WT vs CD248$^{-/-}$) but not at 4-weeks of age (median of 3.83 vs 4.77 %, ns, WT vs CD248$^{-/-}$) (Figure 4.5 E). In line with CLEC14A$^{-/-}$, a remarkable decrease in bone mass was reported in the CD248$^{-/-}$ tibia at 12-weeks and 30-weeks of age (median of 8.09 vs 0.62 %, p = 0.10 ns, WT vs CD248$^{-/-}$) (vs control). This extraordinary decrease in BV/TV % is only matched in the CLEC14A$^{-/-}$ tibiae at 12-weeks, but not 30-weeks of age (Figure 4.5E). Two-dimensional (2D) measurement of bone mass as obtained by the calculation of trabecular bone surface matched the trends reported by the three-dimensional (3D) morphometrical analysis measurements of bone volume (BV/TV%) (Figure 4.5G, Table 12). Figures 4.5 B, 4.5 D, 4.5 F and 4.5 H portray a different presentation method of the same date presented in Figures 4.5 A, 4.5 C, 4.5 E and 4.5 G, respectively. This was completed to allow for the visualisation of changes in bone mass dynamics over time in CLEC14A$^{-/-}$ and CD248$^{-/-}$ vs WT. Our data illustrate that CLEC14A$^{-/-}$ tibiae achieve their maximum metaphyseal tissue volume earlier than WT controls. This can be visualised in Figure 4.5 B which shows that CLEC14A$^{-/-}$ tibiae demonstrate

advanced tissue growth and reach their maximum tissue volume at 8 weeks in contrast to WT and CD248$^{-/-}$ mice which reach their peak tissue volume at 12-weeks of age. Moreover, the expedited trabecular bone formation of CD248$^{-/-}$ mice can be clearly tracked in Figure 4.5 D, 4.5 F and 4.5 H where peak bone volume, top BV/TV% and maximal trabecular bone surface are all achieved at 8 weeks of age in CD248$^{-/-}$ mice, whilst this is only attained at 12-weeks in CLEC14A$^{-/-}$ and WT mice.

The architecture of trabecular bone can also be characterized by the number of trabeculae (Tb.N), their thickness (Tb.Th), and their spatial separation (trabecular separation, Tb.Sp) (Figure 4.7). Each of these microarchitecture trabecular parameters contributes to the overall cancellous bone volume. Data presented here indicates a significant increase in the tibial Tb.Th of CD248$^{-/-}$ vs WT male mice at 8- weeks of age and a minor but significant decrease at 12-weeks in both CD248$^{-/-}$and CLEC14A$^{-/-}$ vs WT. Overall CLEC14A$^{-/-}$ tibiae have similar trabecular thickness to WT mice, expecting for the 12-weeks timepoint (Figure 4.7 A). Maximum values for trabecular thickness and trabecular numbers in CD248$^{-/-}$ samples is reached at 8 weeks of age, in opposition to the CLEC14A$^{-/-}$ and WT which samples attain their upmost values for both parameters at 12-weeks of age (Figure 4.7 B). Tb. N is increased in CLEC14A$^{-/-}$ over WT in the first 2 sets of measurements (4- and 8-weeks) followed by a levelling in the later stage for the period of time studied (12- and 30-weeks), during this stage a trend for the reduction in the number of trabeculae is observed for CLEC14A$^{-/-}$ vs WT, however this did not attain statistical significance (Figure 4.7 C). The number of trabeculae in CD248$^{-/-}$ mice was significantly elevated at 8 weeks of age as compared to WT controls, however, we also report a trend whereby the number of trabeculae is lower than the one in WT tibiae at 12-weeks of age; the average number of trabeculae is again further reduced in 30-week-old mice of both

genotypes, however, at this timepoint the CD248$^{-/-}$ average values are significantly reduced by comparison to WT controls, almost edging complete extinction (Figure 4.7 C, Table 12). The significant increase in trabecular numbers over WT controls commences earlier in life for CLEC14A$^{-/-}$ (4-weeks) as compared to CD248$^{-/-}$ samples and persist at 8 weeks of age, however, this increase is attenuated and no longer different to WT values in 12- and 30- week-old (Figure 4.7, Table 12).

Trabecular separation is a parameter that measures the empty space between trabeculae, this is an important microstructural component affecting bone strength during mechanical stress (444). A significant drop in trabecular separation (Tb.Sp) was observed at 4 weeks in CLEC14A$^{-/-}$ tibiae (mean of 0.47 ± 0.28 mm, $p < 0.0001$, WT vs CLEC14A$^{-/-}$). A further decline in the same parameter was then observed at 8-weeks (mean of 0.37 ± 0.22 mm, $P < 0.0001$, WT vs CLEC14A$^{-/-}$). Similar to the observations reported for Tb.N and Tb.Th, a significant change in Tb.Sp in CD248$^{-/-}$ tibiae was identified at 8-weeks but not in 4-week-old mice (mean values, 4 weeks: 0.47 ± 0.44 mm, ns, WT vs CD248$^{-/-}$, 8 weeks: 0.37 ± 0.27 mm, $P < 0.01$, WT vs CD248$^{-/-}$). At 12- and 30-weeks of age an astonishing increase in Tb.Sp was documented for CD248$^{-/-}$ tibiae (mean values, 12 weeks: 0.22 ± 0.39 mm, $P < 0.0001$, WT vs CD248$^{-/-}$, 30 weeks: 0.38 ± 0.80 mm, $P < 0.0001$, WT vs CD248$^{-/-}$). A more subtle effect was documented for CLEC14A$^{-/-}$ tibiae in 12- and 30-week-old mice, no significant difference was identified at 12 weeks, however, at 30-weeks CLEC14A$^{-/-}$ trabeculae were more distanced from each other than WT controls (0.38 ± 0.31, $P < 0.05$, WT vs CLEC14A$^{-/-}$) (Figure 4.7).

We then quantified the area of the bone metaphysis and diaphysis containing trabecular bone by measuring the extent of the trabecular front from the chondro-osseous interface distally towards the diaphysis in a cranial-caudal direction. Trabecular bone extent was quantified by

measuring the distance from the metaphyseal growth plate to the most distal site of trabecular bone, this identified a pronounced difference between CLEC14A$^{-/-}$ and WT tibias, with an increased trabecular bone extent in CLEC14A$^{-/-}$ tibiae as shown in Figure 4.8 and Figure 4.9. Trabecular bone extent was increased at all stages inspected in CLEC14A$^{-/-}$ but not CD248$^{-/-}$ tibiae, compared to WT controls (Figure 4.8A, Figure 4.9, Table 12). Raw trabecular bone extent is shown in addition to extent normalised to bone length (trabecular extent percent), which was significantly increased in 4- and 8-week old CLEC14A$^{-/-}$ tibiae (Figure 4.8 A, Figure 4.9, Table 12). CD248$^{-/-}$ mice displayed no changes in trabecular bone extent measurements or trabecular bone extent percentages at any of the timepoints investigated with the exception of 30-weeks (Figure 4.8 B and D). At 30-weeks, the CD248$^{-/-}$ raw trabecular extent measurements were significantly lower whilst the trabecular bone extent percentage was considerably but not statistically lower than controls (Figure 4.8 C, Table 12).

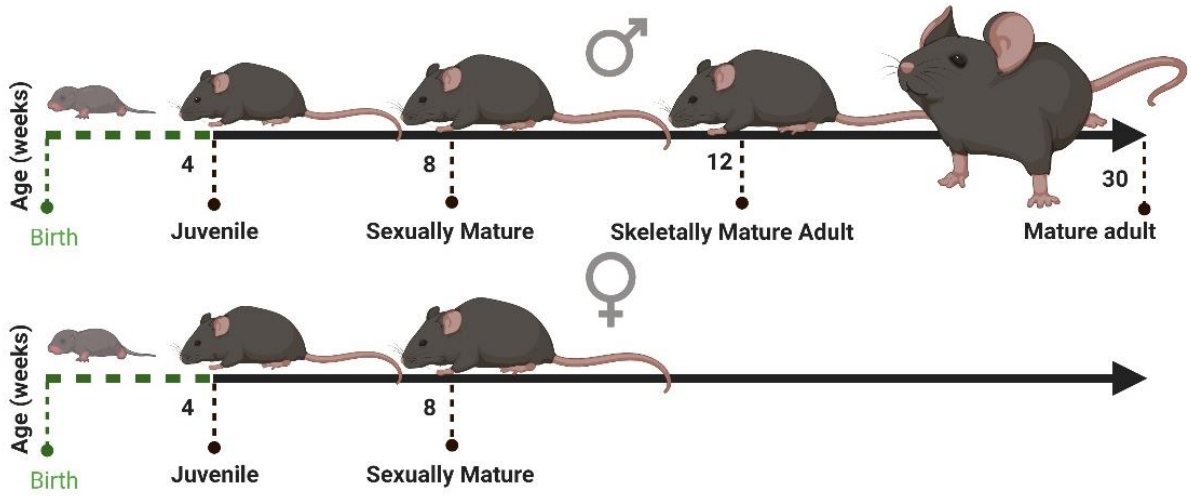


Figure 4.4 Diagram illustrating the timepoints utilised for morphometry analyses for C57Bl/6J males and females. Tibia were collected from C57Bl//6J males and females at different points of skeletal maturation: juvenile (4-weeks old), sexually mature (8-weeks old), sexually mature adult (12-weeks old), and mature adult (30-week-old).

Table 12 Micro-computed tomography 3D trabecular bone parameters – males. Not Applicable (N/A) indicates less than 3 measurements, no statistical analysis was conducted.

Parameter	Age (weeks)	WT	CD248$^{-/-}$	CLEC14A$^{-/-}$
Trabecular bone volume percent (BV/TV %) Median ± IQR	4	3.83 ± 0.66	4.77 ± 2.35	9.4 ± 2.89
	8	5.94 ± 4.32	16.98 ± 9.44	9.32 ± 1.12
	12	25.02 ± 5.05	N/A	17.36 ± 7.75
	30	8.09 ± 2.14	0.62 ± 0.25	6.89 ± 1.01
Trabecular bone surface area (BS mm^2) Mean ± SEM	4	4.23 ± 0.24	7.09 ± 1.08	13.69 ± 1.05
	8	7.00 ± 0.75	23.19 ± 1.72	21.48 ± 0.63
	12	29.91 ± 1.77	N/A	24.23 ± 1.31
	30	13.70 ± 0.65	1.26 ± 0.10	12.31 ± 0.62
Trabecular thickness (Tb.Th mm) Mean ± SEM	4	0.047 ± 0.001	0.046 ± 0.001	0.049 ± 0.001
	8	0.044 ± 0.002	0.065 ± 0.004	0.045 ± 0.0005
	12	0.090 ± 0.003	N/A	0.073 ± 0.004
	30	0.055 ± 0.0010	0.048 ± 0.0030	0.059 ± 0.0009
Trabecular number (Tb.N mm^{-1}) Mean ± SEM	4	0.81 ± 0.03	1.04 ± 0.10	1.71 ± 0.12
	8	1.29 ± 0.19	2.65 ± 0.37	1.98 ± 0.05
	12	2.87 ± 0.07	N/A	2.41 ± 0.19
	30	1.39 ± 0.10	0.361 ± 0.04	1.19 ± 0.03
Trabecular separation (Tb.Sp mm) Mean ± SEM	4	0.47 ± 0.01	0.44 ± 0.03	0.28 ± 0.01
	8	0.37 ± 0.006	0.27 ± 0.02	0.22 ± 0.003
	12	0.22 ± 0.013	N/A	0.23 ± 0.021
	30	0.38 ± 0.015	0.80 ± 0.028	0.31 ± 0.005
Trabecular extent (mm) Mean ± SEM	4	1.81 ± 0.19	2.40 ± 0.28	2.78 ± 0.11
	8	2.48 ± 0.11	2.95 ± 0.22	4.15 ± 0.11
	12	3.42 ± 0.24	N/A	4.38 ± 0.38
	30	3.19 ± 0.53	1.46 ± 0.19	4.69 ± 0.19
***Trabecular extent percentage (%)** Median ± IQR	4	29.65 ± 10.47	33.56 ± 15.24	36.38 ± 4.81
	8	31.0 ± 4.1	37.18 ± 10.99	46.45 ± 6.02
	12	37.22 ± 10.37	N/A	48.98 ± 15.41
	30	28.83 ± 17.97	13.3 ± 5.99	48.23 ± 8.69

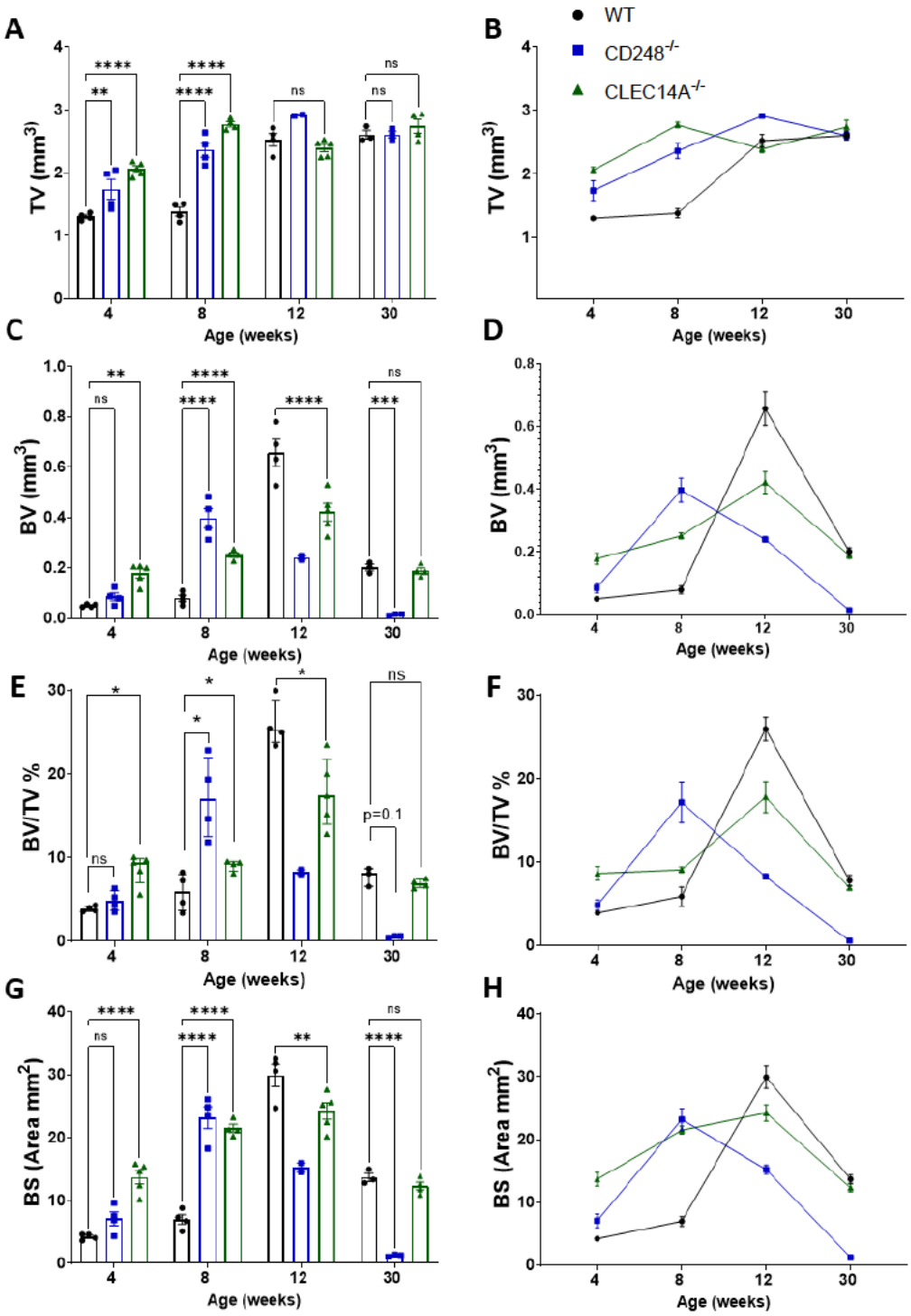


Figure 4.5. Quantitative morphometry of trabecular microarchitectural parameters of CLEC14A$^{-/-}$ and CD248$^{-/-}$ vs WT male mice. (A-H) Micro computed tomography (µCT) analysis of bone trabecular parameters in the proximal tibial metaphysis. **A)** Tissue volume (TV) **B)** Tissue volume presented as a time course **C)** Bone volume (BV) **D)** Bone volume presented as a time course **E)** Trabecular Percent Bone Volume (BV/TV %) **F)** BV/TV % presented as a time course **G)** Trabecular Bone Surface (BS) and **H)** Trabecular Bone Surface presented as a time course. Sample size varies (N=3-6) as represented by each individual dot in the graphs. Results are presented as Mean ± SEM, data was analysed with Two-way ANOVA, followed by Dunnett's post hoc, data in graphs E and F was analysed with Multiple Mann-Whitney tests, * = $P < 0.05$ ** = $P < 0.01$; *** = $P < 0.001$; ****=$P < 0.0001$.

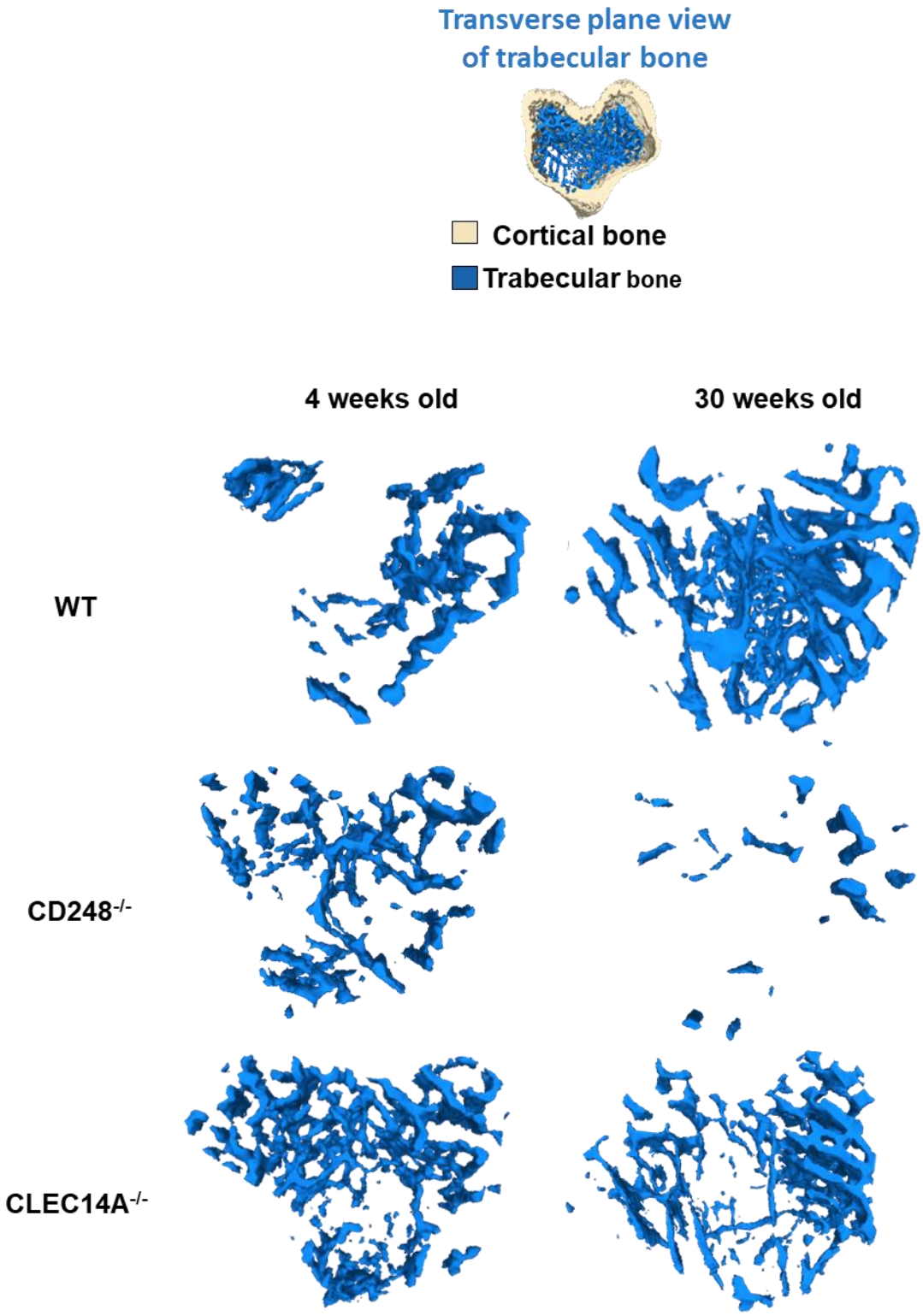


Figure 4.6. Representative µCT analysis transverse plane images starting at the end of the proximal growth plate of 4- and 30- weeks old WT, CD248$^{-/-}$ and CLEC14A$^{-/-}$ male mouse tibias. Images show trabecular bone (blue) density. Note the increased trabecular bone density at 4-weeks of age in CLEC14A$^{-/-}$ and CD248$^{-/-}$ vs WT, and the maintained trabecular bone density in CLEC14A$^{-/-}$ and WT at 30-weeks, compared to the dramatic loss of trabecular bone in the CD248$^{-/-}$ at this age.

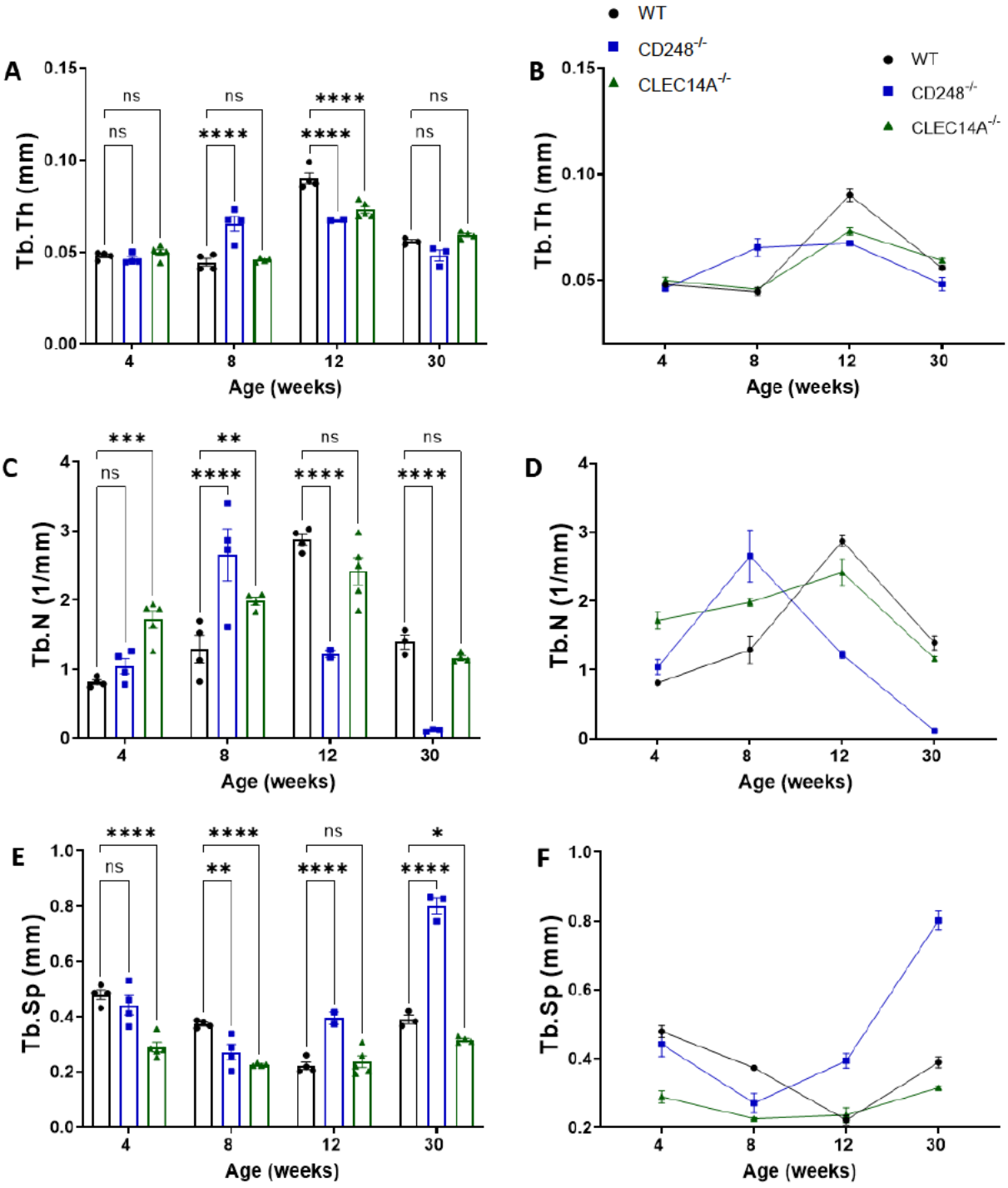


Figure 4.7 Trabecular parameter changes in CLEC14A$^{-/-}$ and CD248$^{-/-}$ vs WT male mice. (A -C) Micro computed tomography (µCT) analysis of **A)** Trabecular thickness (Tb.Th) and **B)** Trabecular thickness presented as a time course **C)** Trabecular number (Tb.N) **D)** Trabecular number presented as a time course **E)** Trabecular Separation (Tb.Sp) **F)** Trabecular Separation presented as a time course. Time course graphs illustrate the dynamics of the measured parameters over time. Sample size varies (N=3-6) as represented by each individual dot in the graphs. Results are presented as Mean ± SEM, data was analysed with Two-way ANOVA, followed by Dunnett's post hoc, * = $p < 0.05$ ** = $p < 0.01$; *** = $p < 0.001$; ****=$p < 0.0001$ compared to WT mice.

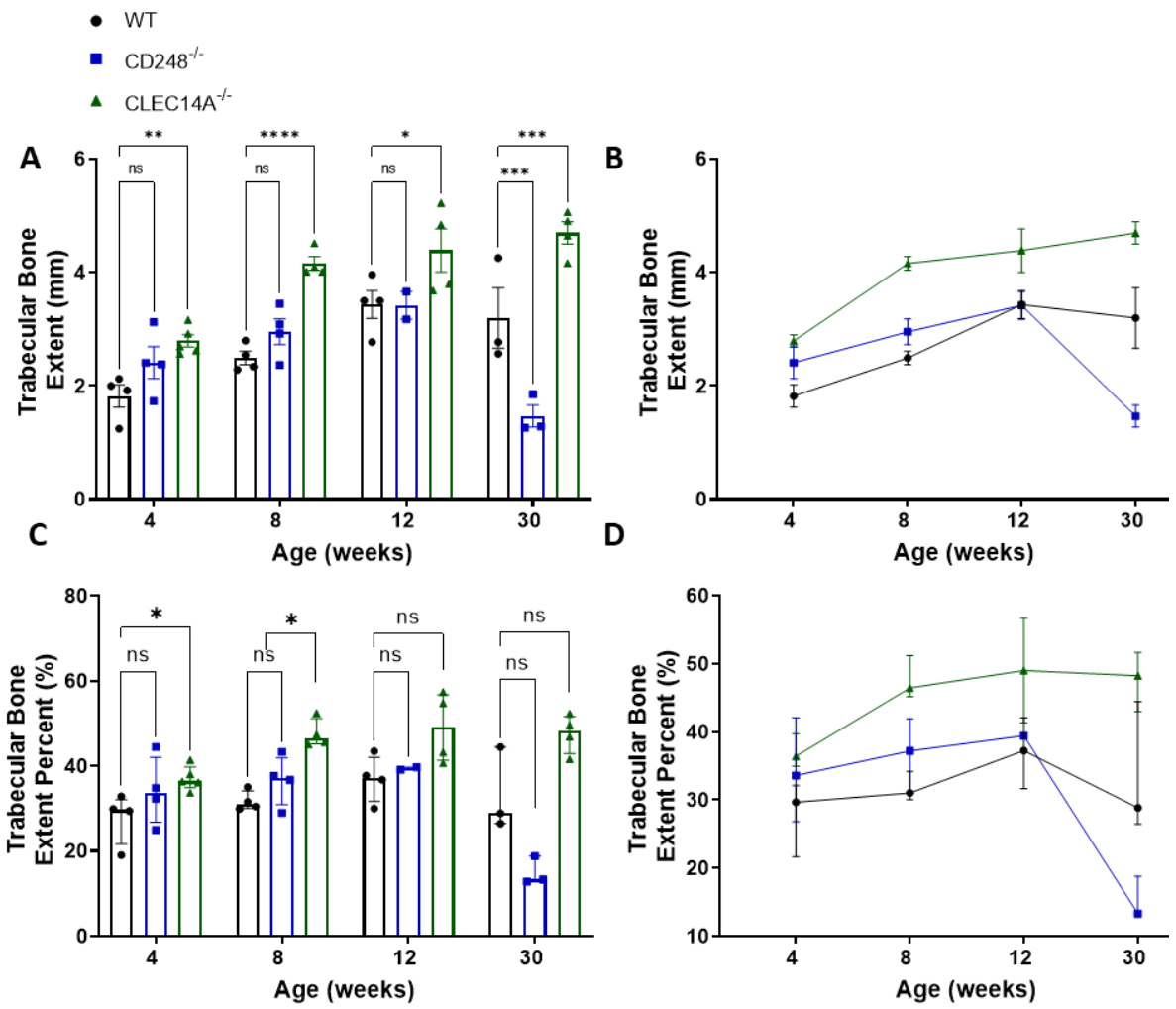


Figure 4.8. Extension of trabecular bone measured from the inferior part of the proximal growth plate to the most distal point in space occupied by trabecular bone towards the diaphysis in CLEC14A$^{-/-}$, CD248$^{-/-}$ and WT male mice. Micro computed tomography (µCT) analysis of **A)** Trabecular Bone Extent **B)** Trabecular Bone Extent presented as a time course **C)** Trabecular Bone Extent Percentage **D)** Trabecular Bone Extent Percentage presented as a time course. Sample size varies (N=3-4) as represented by each individual dot in the graphs. Results are presented as Mean ± SEM, data was analysed with Two-way ANOVA, followed by Dunnett's post hoc for graphs A and B, Results are presented as Median ± IQR, data was analysed with Multiple Mann-Whitney tests, for graphs C and D, * = $P < 0.05$ ** = $P < 0.01$; *** = $P < 0.001$; ****=$P < 0.0001$.

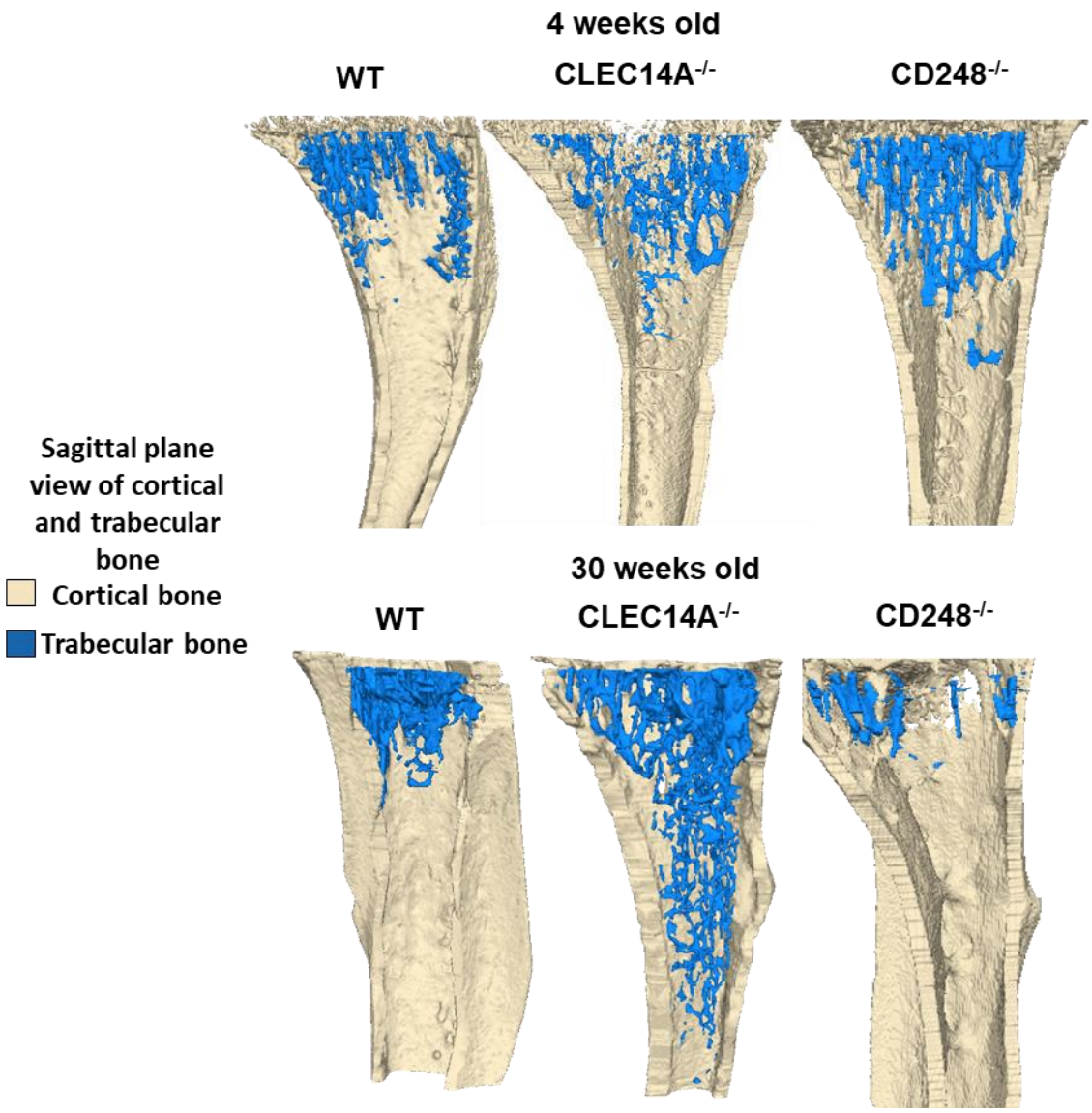


Figure 4.9. Representative µCT sagittal plane images of trabecular bone of 4- and 30- weeks old WT, CD248$^{-/-}$ and CLEC14A$^{-/-}$ male mouse tibias. Images show trabecular bone extent (blue) and the surrounding cortical bone (ivory). Note the increased trabecular bone extent at 4-weeks of age in CLEC14A$^{-/-}$ and CD248$^{-/-}$ vs WT, the loss of this phenotype in CD248$^{-/-}$ mice at 30 weeks of age and the preservation of an increased trabecular bone extent in CLEC14A$^{-/-}$ vs WT mice at 30-weeks of age.

4.4. Minor cortical differences were detected in male CLEC14A$^{-/-}$ and CD248$^{-/-}$ tibiae

Cortical morphology was evaluated in the tibia midshaft by analysing a 1.37 mm long area (the equivalent of 100 scan slices). The following variables were collected: cortical bone area (B.Ar), total bone area (T.Ar), percentage cortical bone area (B.Ar/T.Ar %) and cortical thickness (C.th). A summary definition of cortical parameters is available in Table 10. 2D analysis of cortical bone area of CLEC14A$^{-/-}$ tibia showed an increase in B.Ar and T.Ar as compared to WT tibiae at both 4 and 8 weeks of age (mean values, 4 weeks: B.Ar: 0.40 vs 0.55 mm^2, $P < 0.05$, WT vs CLEC14A$^{-/-}$, T.Ar: 1.33 vs 1.98 mm^2, $P < 0.01$, WT vs CLEC14A$^{-/-}$; 8 weeks: B.Ar: 0.69 vs 1.04 mm^2, $P < 0.05$, WT vs CLEC14A$^{-/-}$, T.Ar: 2.01 vs 3.08 mm^2, $P < 0.05$, WT vs CLEC14A$^{-/-}$). In contrast no significant changes in B.Ar or T.Ar were observed for CD248$^{-/-}$ vs WT specimens (Figure 4.10 A-B). Normalisation of the cortical bone area to the total bone area by calculation of the percentage cortical bone area (B.Ar/T.Ar %) resulted in no significant differences between CLEC14A$^{-/-}$ and WT tibiae (Figure 4.10 C). Moreover, there was also no significant difference between the cortical thickness of CLEC14A$^{-/-}$ and WT tibiae (Figure 4.10 D). Whilst no significant differences were identified between CD248$^{-/-}$ and WT B.Ar or T.Ar, a significantly reduced B.Ar/T.Ar % was identified at 4-weeks in CD248$^{-/-}$ as compared to WT mice (median values of B.Ar/T.Ar %: 30.55 vs 26.87, $P < 0.01$, WT vs CD248$^{-/-}$). In addition, cortical bone thickness was lower in CD248$^{-/-}$ than WT mice at 4- (mean of 0.11 vs 0.09 mm, $P < 0.05$, WT vs CD248$^{-/-}$) but not 8 weeks of age.

4.5. CLEC14A$^{-/-}$ pups are born with more mineralised calvariae

Neonatal pups are born with unmineralised cranial sutures, these are soft-connective tissues localised between the mineralised plates of the cranium which get mineralised in the first month of life (445). To obtain a better understanding of the mineralisation status of CLEC14A$^{-/-}$ pups, freshly isolated calvaria from C57Bl/6J P4 pups, were stained with alizarin red. Calvaria were then imaged and the non-mineralised area at the intersection between the sagittal and lamboid suture was measured. Image analysis showed a lower non-mineralised area in CLEC14A$^{-/-}$ pups compared to WT controls (median unmineralised area size of: 1.70 vs 1.49 mm^2, $p < 0.05$, WT vs CLEC14A$^{-/-}$), indicating that CLEC14A$^{-/-}$ pups were born with more mineralised calvaria (Figure 4.11).

4.6. Mechanical testing of cortical bone strength of mouse tibiae and femora

Three-point bending testing of the murine tibia and femur was employed to calculate biomechanical parameters informing on the architectural strength of 8-week-old murine CLEC14A$^{-/-}$ and CD248$^{-/-}$ long bones compared to WT control. CD248$^{-/-}$ and CLEC14A$^{-/-}$ bones were significantly less stiff than WT control bones (tibia: mean of 69.45 vs 57.58 N/mm, WT vs CD248-/-, $p < 0.05$, and WT vs CLEC14A$^{-/-}$, mean of 57.09 ± 4.76 $p < 0.05$, femur: mean of 69.80 vs 51.62, $p < 0.05$, WT vs CD248$^{-/-}$ and mean of 69.80 vs 44.40, $p < 0.01$ WT vs CLEC14A$^{-/-}$) (Figure 4.12). With the exception of a decrease of the maximal load force sustained by femora before plastic deformation (average maximum force: 15.17 vs 13.14 N, $p < 0.05$, WT vs CLEC14A$^{-/-}$), no other significant differences were identified when comparing CD248$^{-/-}$ and CLEC14A$^{-/-}$ samples to WT. For instance, the failure and fracture forces and the work to failure and work to fracture were all not different to controls (Figure 4.12)

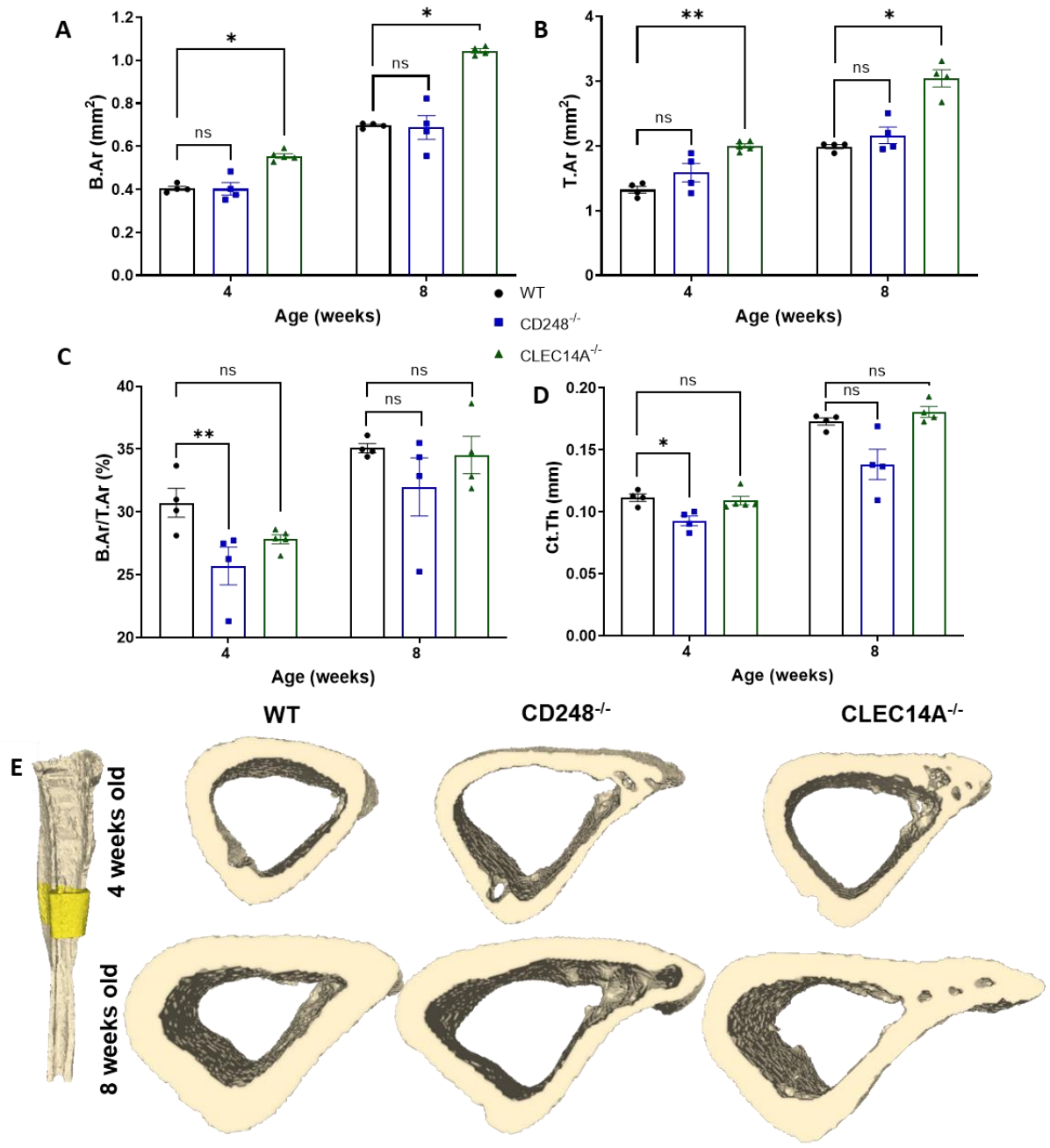


Figure 4.10. Cortical parameter changes in CLEC14A$^{-/-}$ and CD248$^{-/-}$ vs WT male mice tibial midshaft. **(A-D)** Micro computed tomography (µCT) analysis of bone cortical parameters in the male tibia. **A)** Cortical Bone Area **B)** Cortical Tissue Area **C)** Cortical Percent Bone Area (B.Ar/T.Ar %) and D) Cortical Thickness. Sample size (N=4 for all groups) as represented by the number of geometrical shapes in each graph. Results are presented as Mean ± SD (graphs A, B and D), Median ± IQR (graph C), data was analysed with Two-way ANOVA, followed by Dunnett's post hoc for graphs A, B and D, data in graph C is presented as Median ± IQR and was analysed with Multiple Mann-Whitney tests, * = $P < 0.05$ ** = $P < 0.01$; *** = $P < 0.001$; ****=$P < 0.0001$. E) Representative µCT analysis transverse plane images starting at the end of the proximal growth plate of 4- and 30- weeks old WT, CD248$^{-/-}$ and CLEC14A$^{-/-}$ male mouse tibias. Images show cortical bone (ivory).

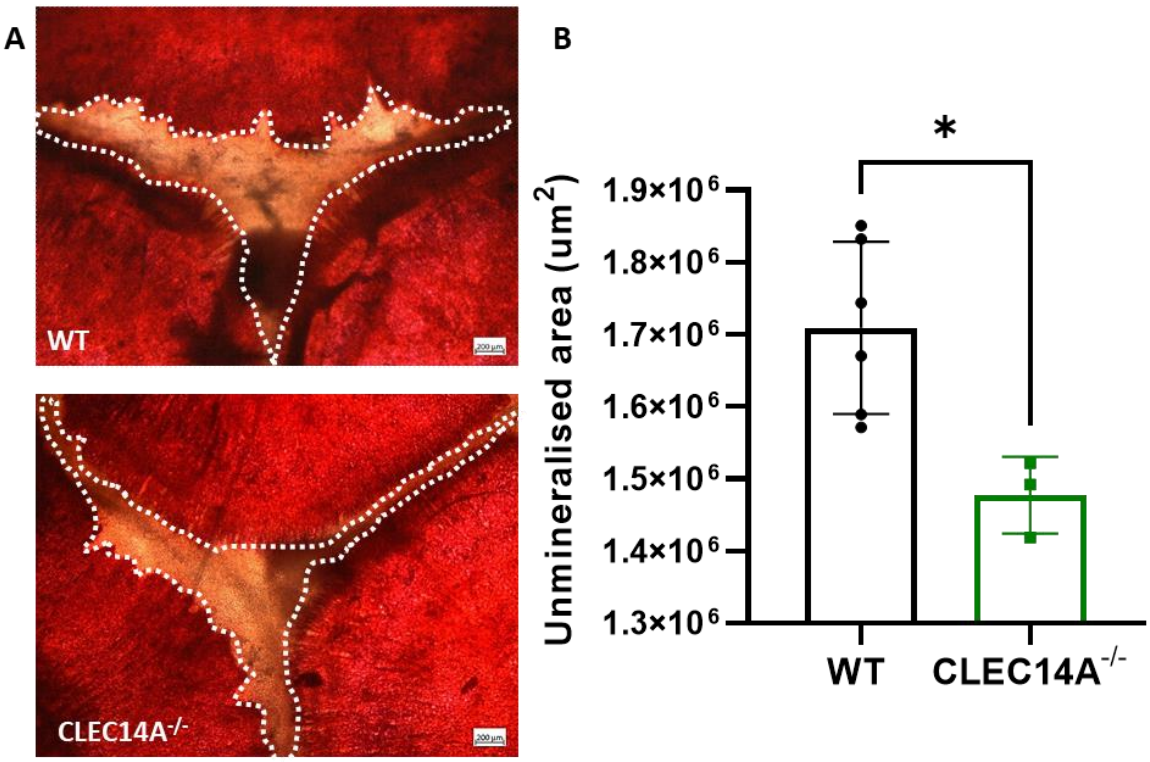


Figure 4.11. Increased mineralisation in the postnatal calvaria of P4 CLEC14A-/- male pups. **A)** Representative images of alizarin red staining of P4 male pups calvarium, areas demarked by white dashed lines represent non-mineralised sutures **B)** Quantification of non-mineralised areas. Sample size (N=3-6) as represented by the number of geometrical shapes in each graph. Results are presented as Median ± IQR, data was analysed with Mann-Whitney, * = $p < 0.05$.

Table 13 CLEC14A$^{-/-}$, CD248 $^{-/-}$ and WT long bones biomechanical parameters of 8-week-old C57BL/6J males. Data is presented as Mean ± SEM

Biomechanical parameter	Bone type	WT	CD248$^{-/-}$	CLEC14A$^{-/-}$
Failure Force (N)	Tibia	14.80 ± 0.65	14.34 ± 0.88	12.69 ± 1.03
Fracture Force (N)		11.03 ± 0.78	4.78 ± 0.67	9.48 ± 1.34
Work to Fracture (AUC)		9.31 ± 1.70	14.34 ± 2.16	6.90 ± 1.96
Work to Failure (AUC)		2.61 ± 0.48	2.25 ± 0.26	2.33 ± 0.60
Stiffness (N/mm)		69.45 ± 1.20	57.58 ± 2.85	57.09 ± 4.76
Failure Force (N)	Femur	15.17 ± 0.23	13.54 ± 0.77	13.14 ± 0.55
Fracture Force (N)		9.73 ± 0.65	8.86 ± 0.86	8.46 ± 1.20
Work to Fracture (N)		11.44 ± 1.04	11.75 ± 1.54	10.05 ± 1.91
Work to Failure (N)		3.54 ± 0.48	4.74 ± 0.74	3.53 ± 0.63
Stiffness (N/mm)		69.80 ± 3.55	51.62 ± 7.06	44.40 ± 3.71

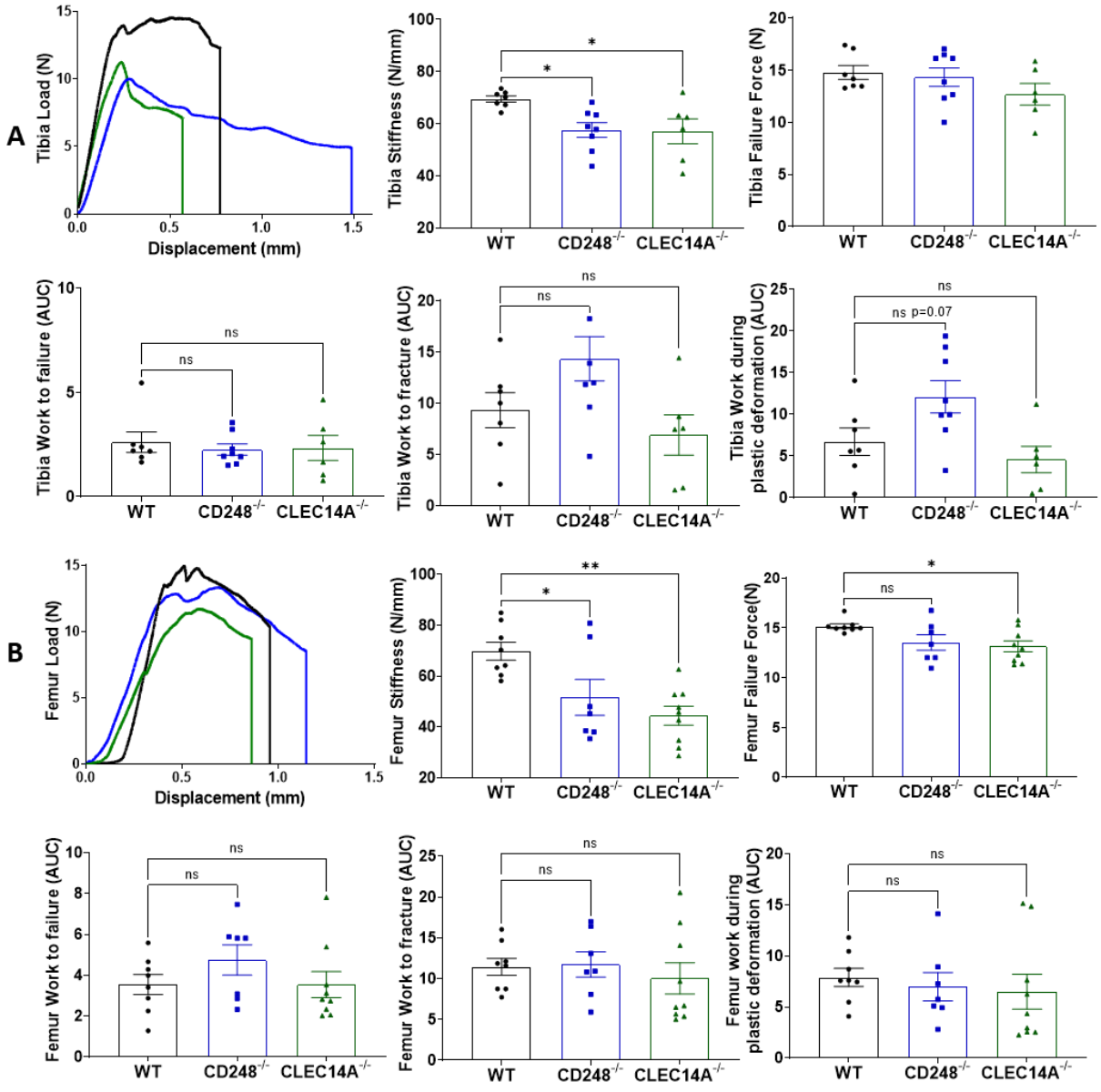


Figure 4.12. Material proprieties of long bones in CLEC14A$^{-/-}$ and CD248$^{-/-}$ vs WT male mice. A) Tibia analysis, top row, left to right: three-point bending load vs displacement graphs of 8-week-old murine tibiae tested to fracture. Data points show one representative trace for each genotype, additional mechanical measurements include: Stiffness, Failure Force; bottom row, left to right: Work to failure, Work to fracture and work during plastic deformation (all three presented as Area Under the Curve (AUC). **B)** Femur analysis, same graph arrangement as for tibia analysis. Sample size (n=6-8 as represented by each individual geometrical shape in each graph bar). Results are presented as Mean ± SEM, data was analysed with One-way ANOVA, followed by Dunnett's post-hoc comparisons test. * = $p < 0.05$, ** = $p < 0.01$, *** = $p < 0.001$.

4.7. Minimal differences were identified in the trabecular and cortical bone of CLEC14A and CD248 deficient C57BL/6J female mice

The tissue volume of CD248 and CLEC14A deficient mice was significantly increased at 4-weeks (1.63 vs 2.08 mm^3, $P < 0.01$, WT vs $CLEC14A^{-/-}$, 1.63 vs 2.02 mm^3, $P < 0.01$, WT vs $CD248^{-/-}$) but not 8-weeks of age in C57BL/6J female mice (Figure 4.13 A, Figure 4.14). An increase in bone volume was only observed in $CD248^{-/-}$ vs WT bones at 8 weeks (0.10 vs 0.25 mm^3, $P < 0.01$) (Figure 4.13 C). This increase in bone volume in the $CD248^{-/-}$ tibiae at 8 weeks is also maintained when normalising bone volume to tissue volume (BV/TV %) in $CD248^{-/-}$ over WT controls (4.20 vs 10.3 %, $P < 0.01$); no changes were reported in any other groups (Figure 4.13 E). Deletion of CD248 or CLEC14A had no significant effect on the area covered by trabecular bone as measured by trabecular bone surface (Figure 4.13 G). Between 4- to 8-weeks all the above parameters increased, in line with the expected growth of the skeletal system in mice at these ages (Figure 4.13 B, D, F, H). The increase in bone volume reported for $CD248^{-/-}$ mice at 8 weeks can be attributed to thicker trabeculae (0.04 vs 0.06 mm, $P < 0.001$, WT vs $CD248^{-/-}$), whilst no significant changes were observed in the number of trabeculae or their separation (Figure 4.15). No changes were observed between CLEC14A and WT trabecular parameters excepting a significant decrease in trabecular separation at 4-weeks (0.45 vs 0.30 mm, $P < 0.01$). At 4-weeks a higher trabecular extent and trabecular extent percentage were observed in $CLEC14A^{-/-}$ tibiae as compared to WT controls (trabecular extent: 1.25 vs 2.02 mm, $P < 0.01$, trabecular extent percentage: 19.02 vs 26.46 %, $P < 0.01$) and no significant changes were noted for $CD248^{-/-}$ samples (Figure 4.16, Figure 4.17). A higher total bone area as well as cortical bone area were observed in $CLEC14A^{-/-}$ female tibiae when compared to WT tibiae at 4-weeks (B.Ar: 0.41 vs 0.61 mm^2, $P < 0.05$ T.Ar: 1.26 vs 1.78 mm^2, p=0.09, T.Ar). No significant difference in B.Ar/T.Ar percentage were identified when comparing $CLEC14A^{-/-}$ and WT tibiae

(Figure 4.18). In high similarity to the observations reported for CD248$^{-/-}$ vs WT male mice at the same age, minimal changes were observed for all cortical parameters, with the exception of a reduction in cortical thickness (0.12 vs 0.11 mm, $P < 0.05$), the same trend was detected at 8-weeks, however this did not attain statistical significance (Figure 4.18).

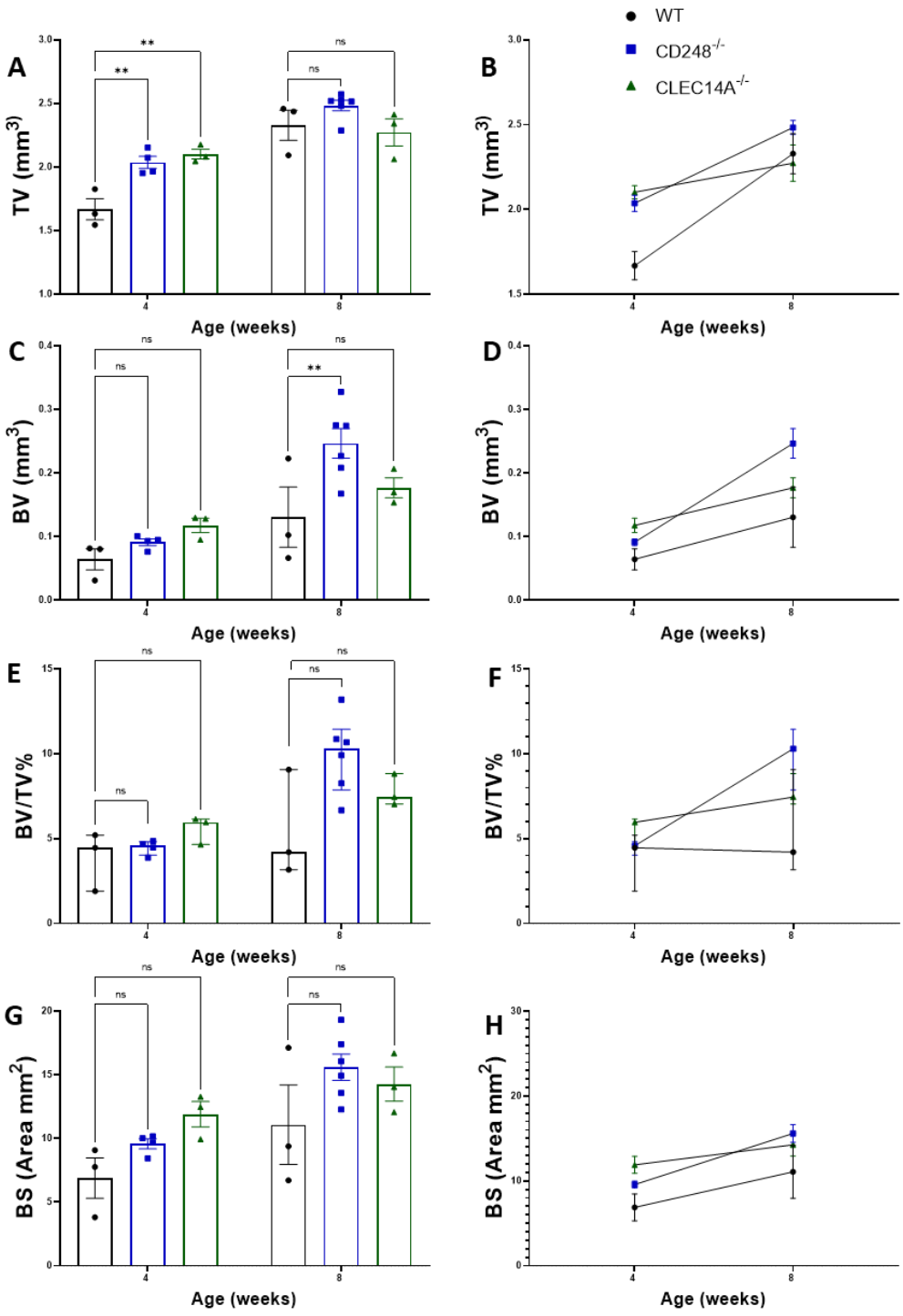


Figure 4.13 Quantitative morphometry of CLEC14A$^{-/-}$, CD248$^{-/-}$ and WT female mouse tibia. (A-H) Micro computed tomography (µCT) analysis of trabecular bone parameters in the proximal metaphysis. A) Tissue volume (TV) **B)** Tissue volume presented as a time course **C)** Bone volume (BV) **D)** Bone volume presented as a time course **E)** Trabecular Percent Bone Volume (BV/TV %) **F)** BV/TV % presented as a time course **G)** Trabecular Bone Surface (BS) and **H)** Trabecular Bone Surface presented as a time course. Sample size varies (N=3-6) as represented by each individual dot in the graphs. Results are presented as Mean ± SEM, data was analysed with Two-way ANOVA, followed by Dunnett's post hoc, data in graphs E and F was analysed with Multiple Mann-Whitney tests, and results are presented as Median ± IQR * = $P < 0.05$ ** = $P < 0.01$; *** = $P < 0.001$; ****=$P < 0.0001$.

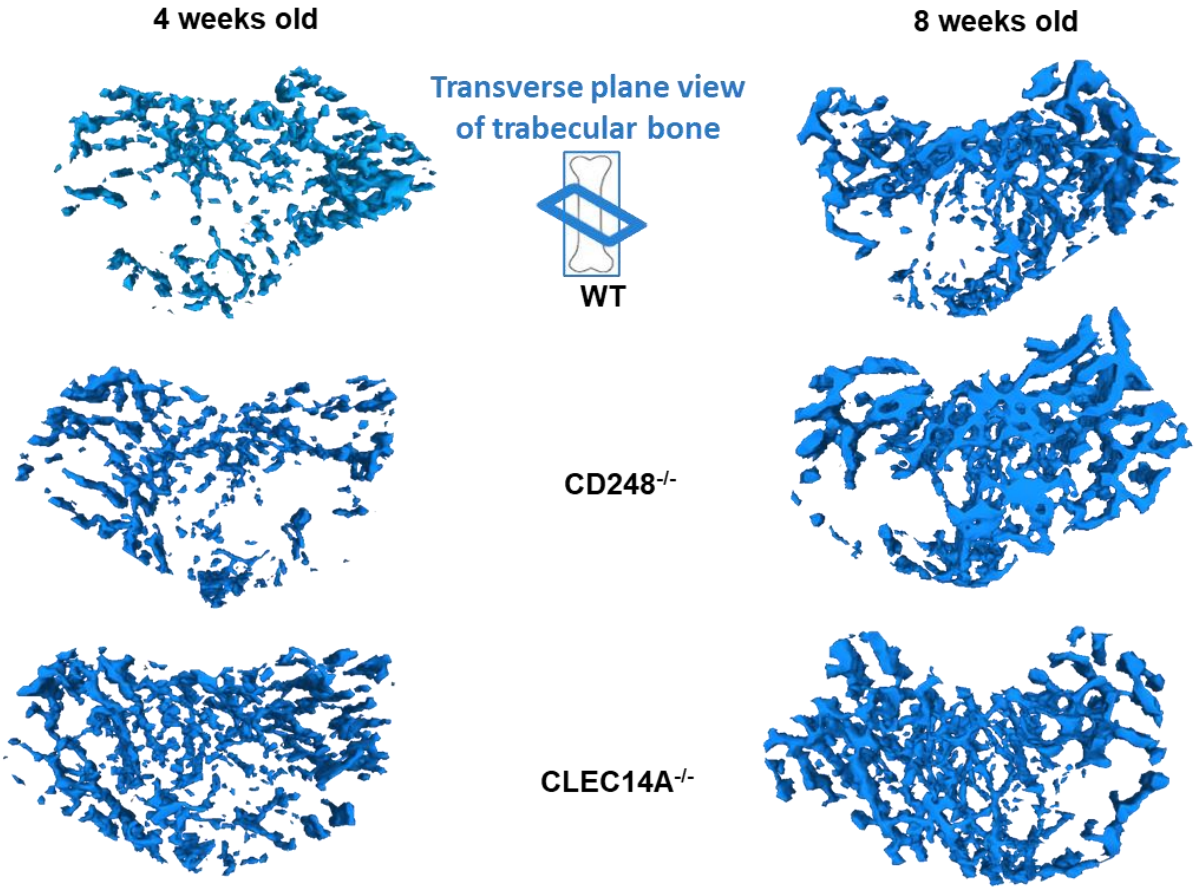


Figure 4.14 Representative µCT analysis transverse plane images starting at the end of the proximal growth plate of 4- and 8- week-old WT, CD248$^{-/-}$ and CLEC14A$^{-/-}$ female mouse tibiae. Images show trabecular bone (blue) density, note the increased trabecular bone density at 8-weeks of age in CD248$^{-/-}$ vs WT.

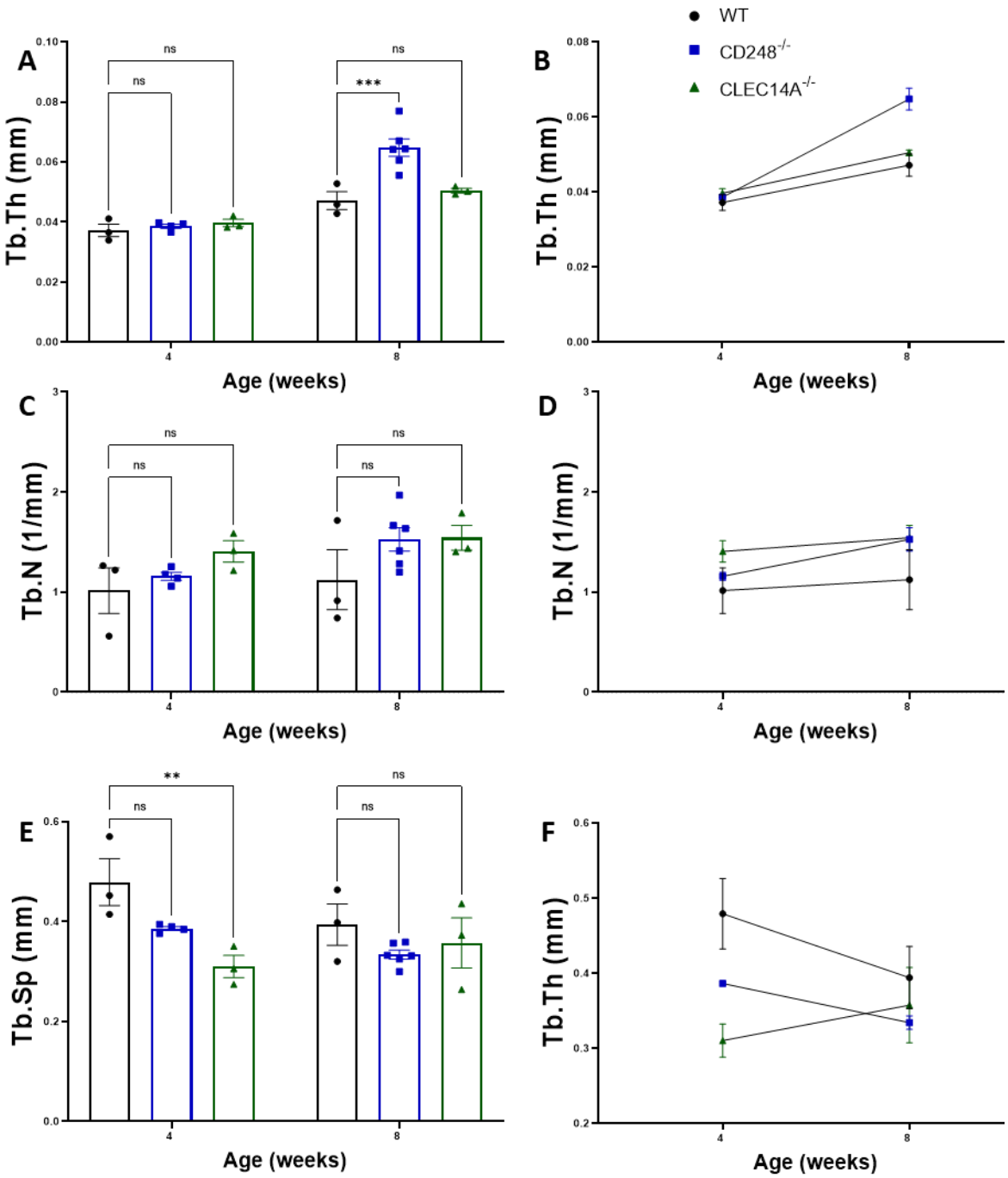


Figure 4.15 Trabecular parameter changes in CLEC14A$^{-/-}$ and CD248$^{-/-}$ compared to WT female mice. **(A-F)** Micro computed tomography (µCT) analysis of **A)** Trabecular thickness (Tb.Th) and **B)** Trabecular thickness presented as a time course **C)** Trabecular number (Tb.N) **D)** Trabecular number presented as a time course **E)** Trabecular Separation (Tb.Sp) **F)** Trabecular Separation presented as a time course. Time course graphs illustrate the dynamics of the measured parameters over time. Sample size varies (N=3-6) as represented by each individual dot in the graphs. Results are presented as Mean ± SEM, data was analysed with Two-way ANOVA, followed by Dunnett's post hoc, * = $p < 0.05$ ** = $p < 0.01$; *** = $p < 0.001$; ****=$p < 0.0001$ compared to WT mice.

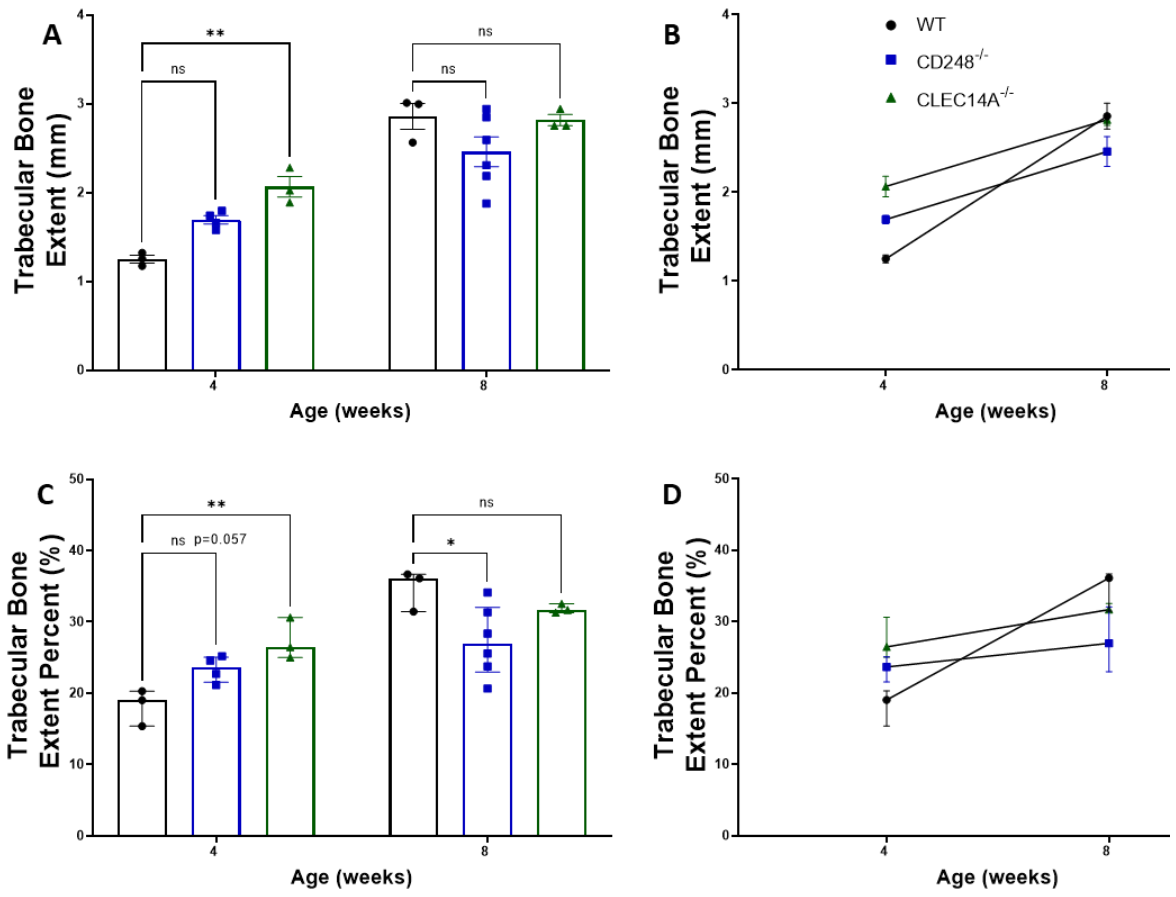


Figure 4.16 Extension of trabecular bone measured from the inferior part of the proximal growth plate to the most distal point in space occupied by trabecular bone towards the diaphysis CLEC14A$^{-/-}$ and CD248$^{-/-}$ vs WT female mice. Micro computed tomography (µCT) analysis of **A)** Trabecular Bone Extent **B)** Trabecular Bone Extent presented as a time course **C)** Trabecular Bone Extent Percentage **D)** Trabecular Bone Extent Percentage presented as a time course. Sample size varies (N=3-4) as represented by each individual dot in the graphs. Results are presented as Mean ± SEM, data was analysed with Two-way ANOVA, followed by Dunnett's post hoc for graphs A and B, Results are presented as Median ± IQR, data was analysed with Multiple Mann-Whitney tests for graphs C and D, * = $P < 0.05$ ** = $P < 0.01$; *** = $P < 0.001$; ****=$P < 0.0001$.

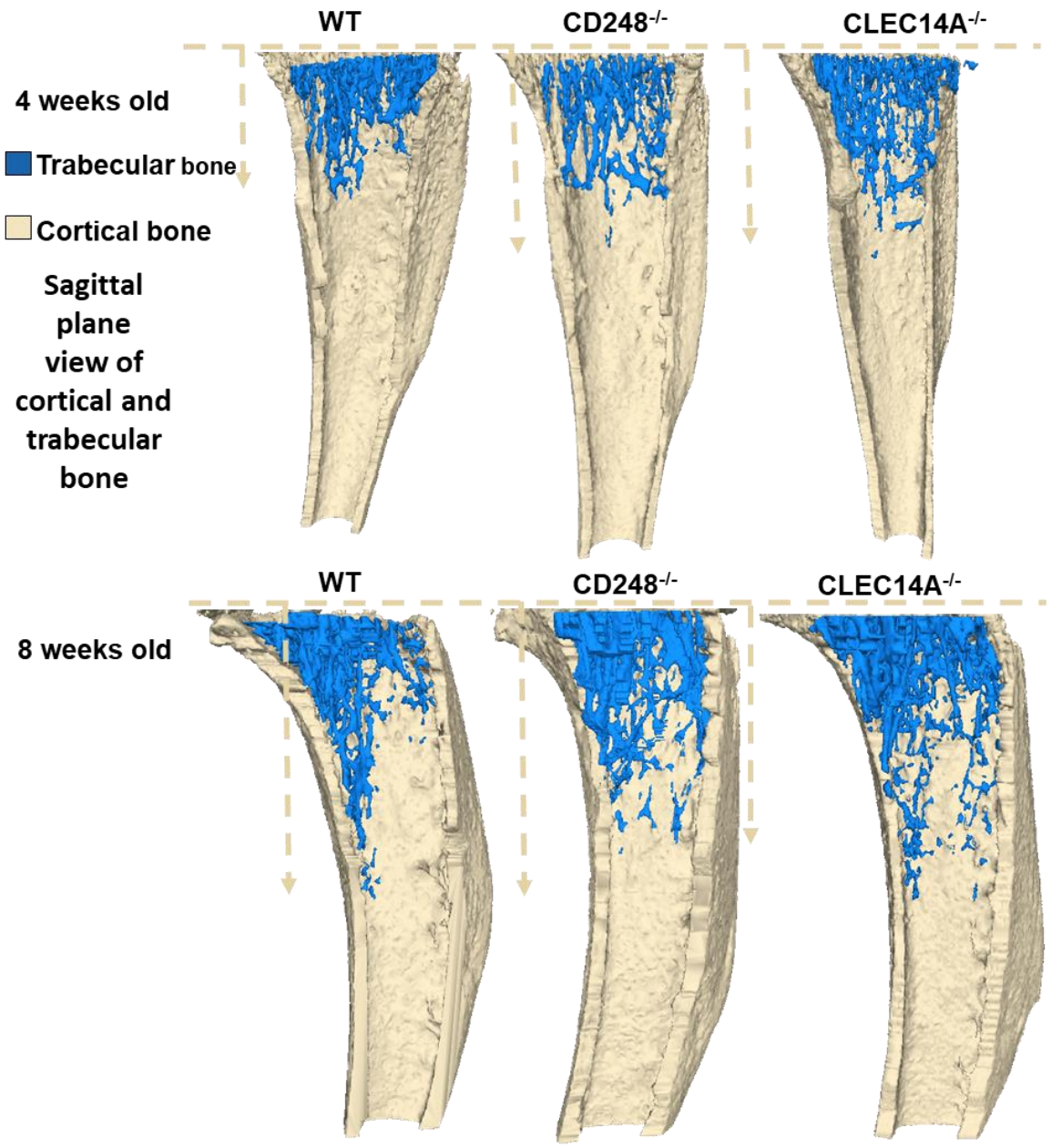


Figure 4.17. Representative µCT sagittal plane images of trabecular bone extent of 4- and 30-weeks old WT, CD248$^{-/-}$ and CLEC14A$^{-/-}$ female mouse tibias. Images show trabecular bone extent (blue) and the surrounding cortical bone (ivory), note the increased trabecular bone extent at 4-weeks of age in CLEC14A$^{-/-}$ vs WT.

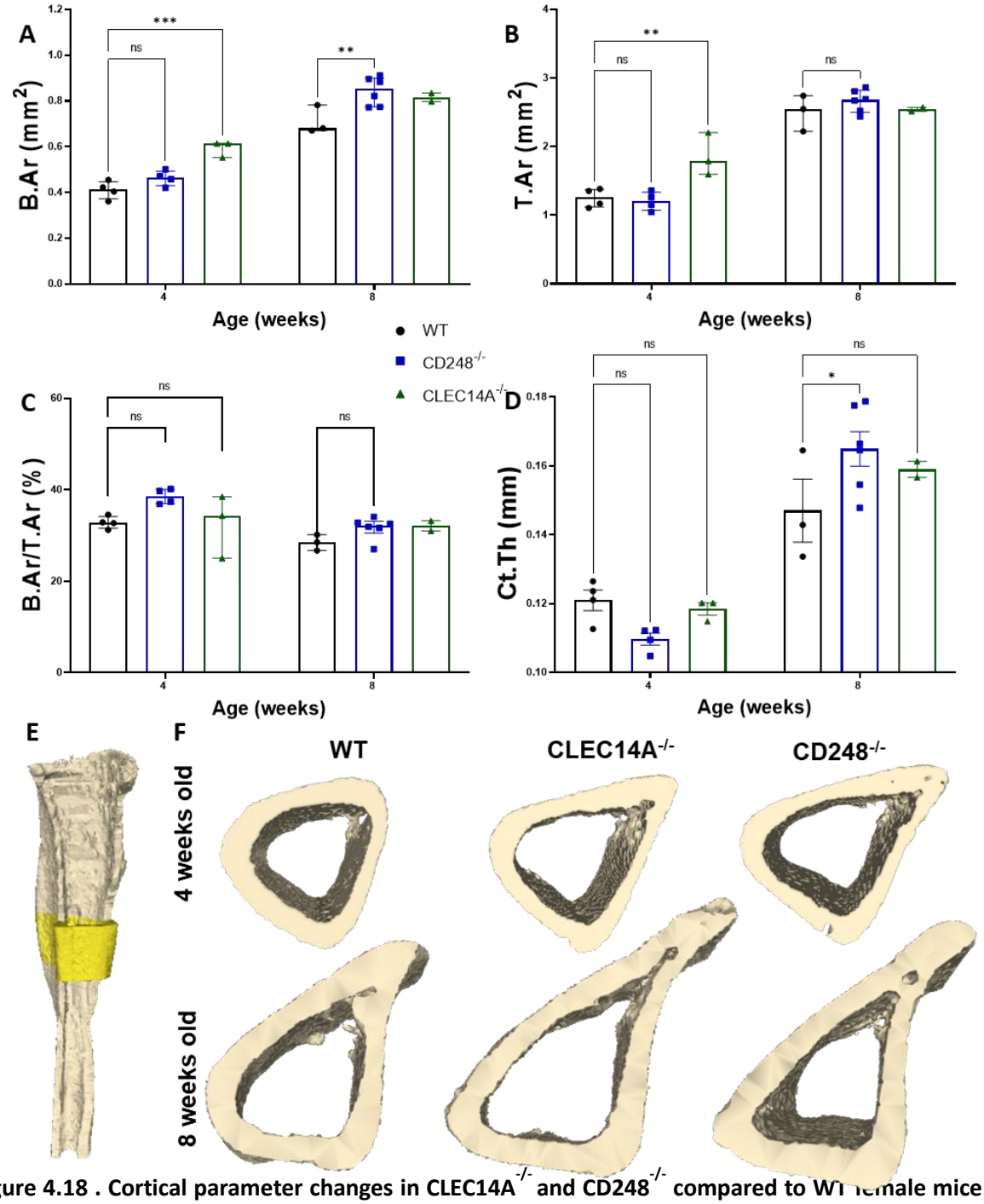


Figure 4.18 . Cortical parameter changes in CLEC14A$^{-/-}$ and CD248$^{-/-}$ compared to WT female mice tibial midshaft. (A-D) Micro computed tomography (µCT) analysis of bone cortical parameters. **A)** Cortical Bone Area (B.Ar) **B)** Cortical Tissue Area (T.Ar) **C)** Cortical Percent Bone Area (B.Ar/T.Ar %) and **D)** Cortical Thickness. Sample size (N=4 for all groups) as represented by the number of geometrical shapes in each graph. Results are presented as Mean ± SD, data was analysed with Two-way ANOVA, followed by Dunnett's post hoc for graphs A, B and D, data in graph C is presented as Median ± IQR and was analysed with Multiple Mann-Whitney tests, * = $p < 0.05$ ** = $p < 0.01$; *** = $p < 0.001$. **E)** Tibia cortical bone µCT imaging mesh, yellow area represents the cortical bone analysed for cortical parameters **F)** Representative µCT analysis cortical bone sagittal images of 4- and 8- weeks old WT, CD248$^{-/-}$ and CLEC14A$^{-/-}$ male mouse tibiae. Images show trabecular bone (blue) density, note the increased trabecular bone density at 4-weeks of age in CLEC14A$^{-/-}$ and CD248$^{-/-}$ vs WT, and the sustained trabecular bone density decrease of CD248$^{-/-}$ but not CLEC14A$^{-/-}$ vs WT.

4.8. Targeting the CLEC14A MMRN2 interaction *In vivo*

Genetic deletion of both CLEC14A and MMRN2 results in a similar angiostatic phenotype (348, 370). MMRN2 has been characterised as a potent angiostatic molecule, previous work has produced evidence that soluble MMRN2 disturbs EC migration and prevents EC tube formation perturbing thus vascularisation driven by angiogenesis processes (370, 374). CLEC14A loss of function mirrors the effect reported for MMRN2 and is accompanied by a decrease in vascularisation related to perturbation of sprouting angiogenesis (1). Further studies have indeed demonstrated that at least partially the interaction between CLEC14A and MMRN2 is responsible for regulation of sprouting angiogenesis. Antibody mediated blockade of this interactions was promptly followed by a reduction in sprouting angiogenesis and a decrease in tumour vascularity (348). To follow up on the germ line deletion of CLEC14A data presented in the section 4.3 in this chapter and to test the hypothesis that CLEC14A MMRN2 interaction is an important regulator of osteogenesis, 4-week old C57Bl6/J male mice were injected intraperitoneally with antibodies binding the CLEC14A C-type lectin domain (CTLD) (Figure 4.19). This was accomplished with the use of in-house mouse monoclonal antibodies binding either the 97-108 amino acid region of CLEC14A CTLD (97ERRRSHCTLENE108), a long loop region in the CTLD where MMRN2 binds, or the sushi domain, an area which is not important for MMRN2 binding (1). The C2 anti-CLEC14A antibody does not restrict MMRN2 binding, whilst C4 binds prevents the interaction between CLEC14A and MMRN2 (355). Previous work has already shown that C4-mediated CLEC14A-MMRN2 interaction blockade alters angiogenic responses both *In vivo* and *in vitro* (348). No difference in the percentage of BV/TV or other trabecular parameters were detected in mice following treatment with C2 or C4 antibodies (Figure 4.20).

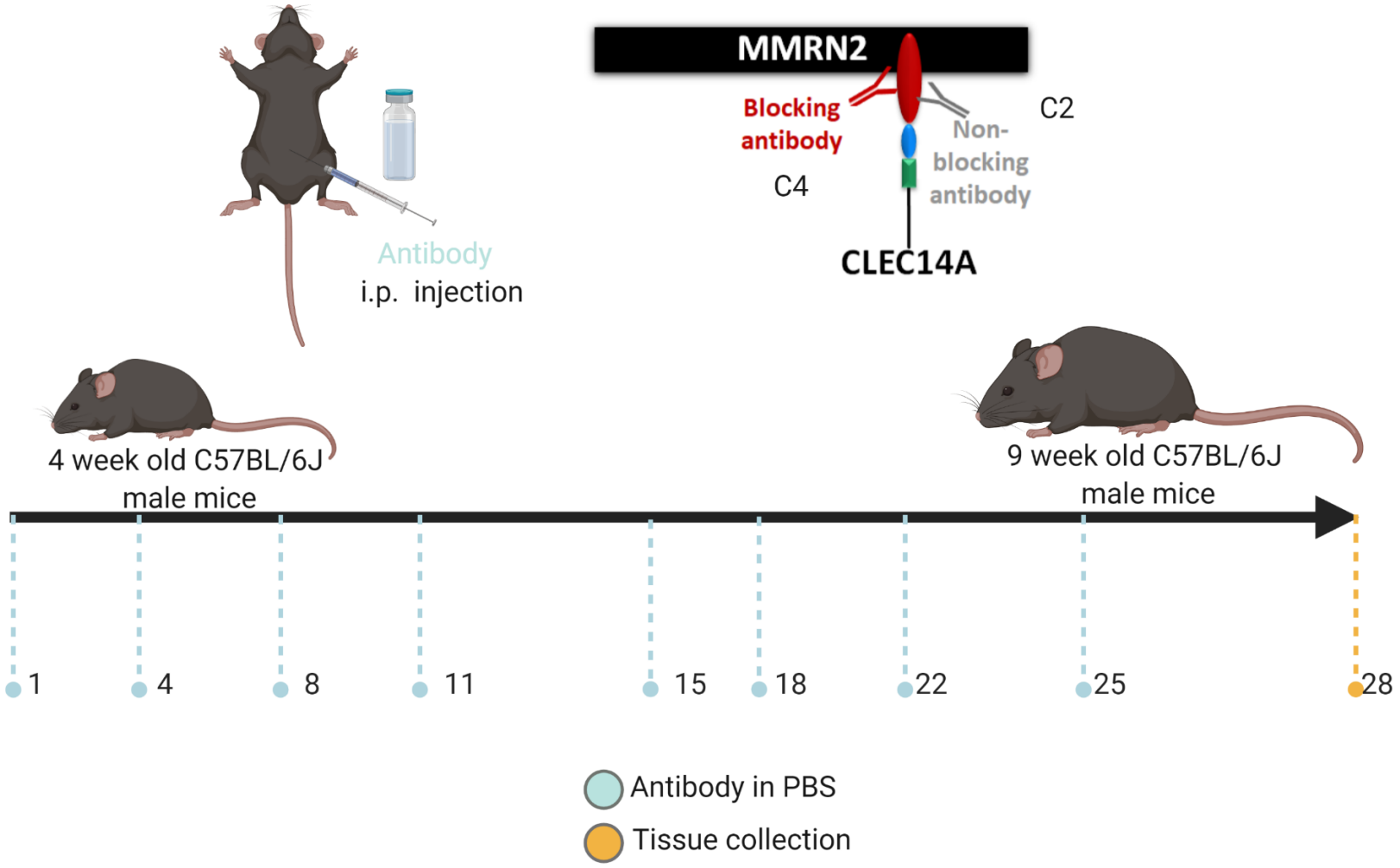


Figure 4.19 Blockade of CLEC14A-MMRN2 interaction in C57Bl/6J 4-week old male mice. Mice were treated with either PBS (vehicle control), or monoclonal antibodies against CLEC14A (C2 or C4) biweekly for 4 weeks; C2 binds CLEC14A but does not prevent MMRN2 binding to the C-type lectin domain (CTLD) of CLEC14A, whilst C4 binds to CLEC14A and blocks its interaction with its ligand MMRN2. Tissue was collected after 4-weeks of treatment and tibiae were prepared for micro-computed tomography.

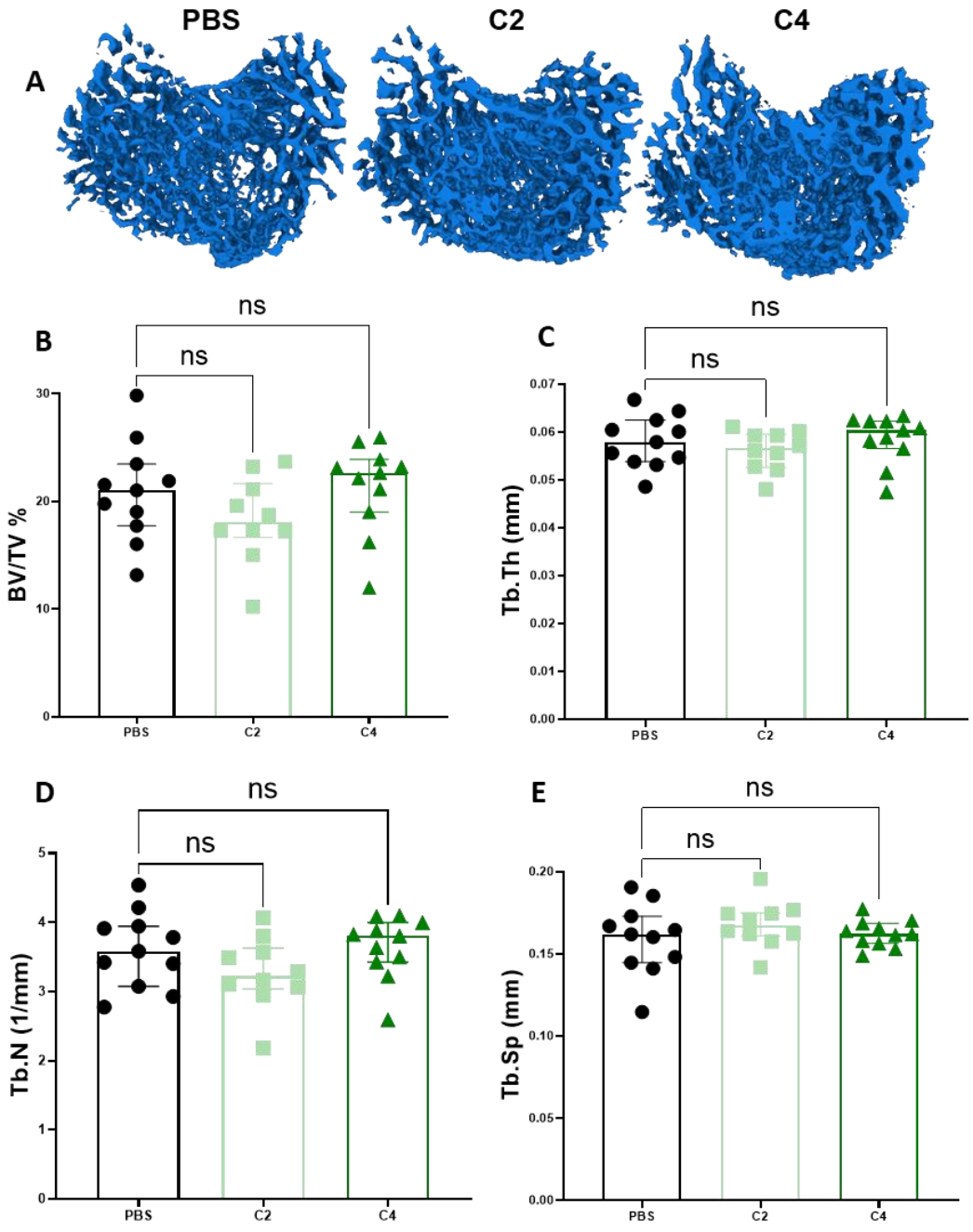


Figure 4.20 *In vivo* blockade of CLEC14A-MMRN2 interaction does not affect trabecular bone mass. 4-week-old C57Bl/6J male mice were injected with PBS, an antibody binding to CLEC14A without blocking MMRN2 interactions (C2) or an antibody binding to CLEC14A and blocking its interaction with MMRN2 (C4). **A)** Representative images of tibial µCT analysis. Images show trabecular bone presented as an axial plane of view. B-E) Quantitative morphometry of trabecular microarchitectural parameters: **B)** Trabecular Percent Bone Volume (BV/TV %), **C)** Trabecular thickness (Tb.Th), **D)** Trabecular number (Tb.N), **E)** Trabecular Separation (Tb.Sp). Sample size varies (n=10-11) as represented by each individual dot in the graphs (PBS control n=11, C2=10, C4=11). Results in graphs C-E are presented as Mean ± SD, data was analysed with One-way ANOVA, followed by Dunnett's post hoc correction for multiple comparisons test; data in graph B was analysed with multiple Kruskal Wallis tests, results in graph B are presented as Median ± IQR., ns = not significant.

4.9. Discussion

Collectively these data show an increase in bone accrual during bone growth in both CLEC14A and CD248 deficient mice. For CLEC14A this was exemplified by anthropometric measurements and micro-computed tomography-derived morphometric measurements, which altogether show that CLEC14A genetic deficiency results in increased longitudinal and radial tibia growth. Impairment of CLEC14A functionality results in longer and larger bones during embryonic and postnatal growth, this is paired with an increase in postnatal bone mass parameters (Figure 4.5, Figure 4.6, Figure 4.7) and a lengthening of the trabecular bone coverage as measured by the extension of trabecular bone towards the diaphysis (Figure 4.8, Figure 4.9). In addition, changes in mechanical competence were observed for CLEC14A$^{-/-}$ bones as judged by three-point bending testing which revealed a deterioration in stiffness and a reduction in the maximum force sustained by these bones (Figure 4.12). In adulthood and at middle age, CLEC14A deficient mouse bones maintained their tibia length advantage and had a comparable bone architecture to the one of WT controls.

An exacerbation in bone mineralisation was also observed for CD248$^{-/-}$ mice, this was noted during the intense skeletal growth phase in juvenile (4-weeks old) and pubertal (8-weeks old) CD248$^{-/-}$ mice which presented increased trabecular bone parameters (Figure 4.5,Figure 4.6). However, a sustained decline in bone mass was ascertained at maturity (12-weeks) and middle age (30-weeks) in the same genotype. In addition to trabecular bone changes, our data also portray CD248 as a regulator of cortical bone homeostasis, with CD248$^{-/-}$ mouse tibiae displaying a decrease in the cortical area percentage and bone cortical thickness, with the most marked differences at 4-weeks of age (Figure 4.12). Similarly, to CLEC14A$^{-/-}$ bones, CD248$^{-/-}$ tibiae and femora present a decrease in bone stiffness.

Whilst the role of CD248 in the regulation of bone formation has been previously described (255), this is the first time CLEC14A, an endothelial cell-specific protein and like CD248, a C-type lectin domain 14 family member, has been ascribed a role in mediation of bone growth and formation.

The work presented in this chapter employs body mass, bone length, bone morphometry and three-point bending methodology to assess the microstructural composition and mechanical characteristics of long bones following genetic deletion of CD248 and CLEC14A during postnatal growth until maturity.

4.9.1. Increased bone elongation in CLEC14A-/- mice

Body mass and bone length measurements were chosen as they are considered a useful tool when investigating bone growth, to this extent previous studies in rodents have reported a strong association between body weight and skeletal development (446). To investigate the effect of CLEC14A genetic disruption on the development of the murine skeletal system during embryonic and postnatal growth, body mass and long bone measurements were obtained from CLEC14A$^{-/-}$ and WT C57BL/6J male mice. Changes in bone parameters (body weight, postnatal tibia/femur, or embryonic metatarsal length) were recorded at pivotal time points for bone growth in the mouse life cycle including: the embryonic stage (E15.5), postnatally: 2- and 4-weeks of age, in adolescence: 8-weeks and at middle age: 30-weeks old. While all body mass measurements reported here were in line with previously published measurements for C57BL/6J male mice for their respective ages (53, 447, 448), no distinction was identified between the body mass of CLEC14A$^{-/-}$ and WT mice for the time points investigated (Figure 4.2 A).

Significant changes in the bone length of postnatal tibia, but not femur, were unearthed indicating that longer than WT control tibiae are a lifelong phenotypic trait for CLEC14A$^{-/-}$ mice (Figure 4.2). The increase in tibia elongation was confirmed using 2 different assessment methods further increasing the strength of this observation. Namely, measurements of bone length using digital callipers or calculations resulting from analysis of μCT scans of the tibia both indicated an increase tibia length in CLEC14A$^{-/-}$ samples. In μCT scans the distance from the growth plate to the tibiofibular junction (proximal growth plate tibiofibular junction tibia length – PGP TFJ tibia length) was higher in CLEC14A$^{-/-}$ mice at 4- and 8-weeks of age, providing further credence to our increased bone length observations and strengthening the hypothesis that CLEC14A regulates bone elongation in postnatal mice. Postnatal long bone growth occurs at the two polarly opposite epiphyseal growth plates, allowing bones to elongate proportionally at each growth plate (449). When analysing bone elongation pertaining exclusively to the proximal growth plate (PGP TFJ tibia length) the observed effect was minimised at the timepoints with a less intensive bone growth phase (12- and 30-weeks) explaining the lack of statistically significant changes and the presence of a trend for an increased PGP TFJ tibia length at these ages. However, an acceleration in total bone elongation is clearly demonstrated when measuring the whole tibia even in the later stages of life of CLEC14A$^{-/-}$ mice. This is matched to an increase in radial bone growth during postnatal and pubertal bone development which was also evidenced when analysing CLEC14A$^{-/-}$ and CD248$^{-/-}$ μCt tibia scans. Bones had a higher metaphyseal tissue volume and an increased total tissue area at the diaphyseal mid shaft.

A trend for a minor increase in the length of CLEC14A$^{-/-}$ femora was noticed, however, this did not attain statistical significance. The reason for this lack of detectable increase is not entirely clear, however, the possibility that the measurement method employed is not sensitive

enough to capture changes in size in femora cannot be excluded. Alternatively, given the significant increase in femur length measured at 30-weeks it is possible that the timepoints utilised in our analysis fail to cover the most intense period of elongation for the femur. In support of this argument, previous work has determined that tibiae commence their elongation and mineralisation earlier than femora during growth as a response to loading during bone growth (450, 451).

Taking into consideration the high expression of CLEC14A during embryogenesis and organ vasculogenesis we set out to also investigate the effect of CLEC14A knock out on the skeletal system in embryogenesis. Our metatarsal data recapitulate the observations identified during postnatal bone growth, demonstrating a boosting in bone lengthening during the embryonic phase of skeletal formation in CLEC14A$^{-/-}$ metatarsal explants (Figure 4.3). Considering that blood flow is absent when culturing the explants *in vitro* these results document that bone elongation in this genotype is not entirely driven by blood supply, lending more support instead to the hypothesis that the bone growth process could be in turn driven by the interaction between EC and osteoblasts.

Furthermore, analysis of mineralisation of cranial sutures has shown increased mineralisation in the calvaria of new-born pups, indicating that CLEC14A genetic deletion also affects mineralisation in the skull of neonatal pups, suggesting that CLEC14A most likely also controls bone morphogenesis and mineralisation during embryogenesis. Previous studies have shown that murine cranial sutures begin to fuse during the first 10 to 20 days after birth, this is closely followed up by an intense mineralisation process leading to complete mineralisation of all cranial sutures by day 45 post birth (452). Staining of cleared calvaria has reported localisation

of H-type EC and osteoprogenitors at suture borders, in a similar morpholigcal organisation to the one reported in the long bone metaphysis (453).

4.9.2. Morphometric and biomechanical changes in the CLEC14A$^{-/-}$ and CD248$^{-/-}$ tibia

The murine long bone densitometric and geometric mineralisation phenotype in C57Bl/6J WT, CD248$^{-/-}$ and CLEC14A$^{-/-}$ mice was assessed using medium-resolution (13.7 µm) micro computed tomography. To assess bone microarchitectural parameters, analyses were conducted during puberty (4- and 8- weeks old), at sexual and skeletal maturity (12-weeks old) and at middle age (30-weeks old). Trabecular parameters obtained in the control (WT) mice were similar to previously reported data (454, 455). The changes in bone parameters indicating exacerbated bone formation in CLEC14A$^{-/-}$ and CD248$^{-/-}$ at 4- and 8-weeks of age are in line with our previously published work (255) introducing CLEC14A as a novel negative regulator of bone formation. It is worth noting that the C57BL/6J strain presents a significantly lower bone mass by comparison to the other genetic background strains used by the bone research field: C3H/HeJ, 129SvEv or BALB/cByJ (255, 456), hence the effect of CLEC14A on osteogenesis during postnatal growth would have been perhaps more evident in another mouse strain.

At 12- and 30-weeks of age a massive decrease in bone mass was reported for CD248$^{-/-}$ mice, an observation which was partly recapitulated in CLEC14A$^{-/-}$ mice, we posit that these trabecular bone parameter changes could be explained by the well-known side-effect of osteoblast maturation boosting interventions which also increase bone resorption via osteoclast maturation and activation (457, 458); this cellular process was confirmed in CD248 deficient mice by our group (not shown here, unpublished). Interestingly, the increase in trabecular bone volume percentage in CD248$^{-/-}$ mice were equally ascribed to changes in

trabecular thickness and numbers, whilst in CLEC14A$^{-/-}$ mice only changes in the number of trabeculae were observed. This evidence argues in favour of different cellular and molecular regulation of bone formation by CLEC14A and CD248. Namely, CD248 is expressed on osteoblasts and previous work has shown its direct effect on osteoblast maturation. Mechanistically, CD248 expression favours PDGFB-PDGFRB signalling to keep osteoprogenitors immature and highly proliferative (52, 53, 255). In this context, it is reasonable to conclude that CD248 genetic deletion increased bone formation on the trabecular surface resulting in increased trabecular thickness. On the other hand, CLEC14A is an EC protein with a role in mediation of sprouting angiogenesis and cell-cell adhesion (1, 348). Taking in consideration the coupling of angiogenesis to osteogenesis (2), it is plausible to hypothesise that CLEC14A genetic deletion regulates bone formation through moderation of bone angiogenesis or through mediation of EC-osteoblast interaction which results in increased trabecular numbers.

The high trabecular bone mass phenotype identified in this chapter for CLEC14A$^{-/-}$ tibiae at 4- and 8-weeks of age were subsequent to the changes in immature osteoblast density reported in CLEC14A$^{-/-}$ neonate pups at postnatal day 4 (P4), suggesting that at least in part, the increased bone mass observed in these mice might be linked to an increase in the number of osteoblasts. Likewise, the increase in the extent of osteoblast chords (both immature and mature) reported in the previous chapter, was matched by an increase in the length of the trabecular front, indicating that not only are osteoblasts extending further towards the diaphysis in CLEC14A$^{-/-}$, but they are also actively inducing mineralisation, a phenotype that is maintained long after peak bone mass is achieved in these males (12-weeks of age), with an increased trabecular bone extent being identified even at 30-weeks of age, a timepoint by

which bone formation is less intense and becomes counterbalanced by bone resorption as exemplified by our micro computed tomography analysis.

µCT analysis of the bone cortex indicated that CLEC14A genetic disruption results in minimal changes in the bone cortex, it is however unclear if cortical bone mass is indeed not affected by the genetic deficiency of CLEC14A, as the possibility that our µCT analysis protocol was not sensitive enough to measure changes cannot be excluded. It is also possible that no biological effect is exerted by CLEC14A in cortical bone accrual. To aid in reaching a better-informed decision, a study of the effect of CLEC14A on cortical bone at a higher scanning resolution and at other skeletal sites is warranted, even more so as changes in cortical bone can be more readily identified in bones such as the ribs (81).

Unlike, CLEC14A$^{-/-}$, CD248$^{-/-}$ mouse tibiae had significantly lower cortical areas which could be explained by the notable decrease in cortical thickness. Taking in consideration the notable trabecular bone loss observed for CD248$^{-/-}$ mice later in life at ages 12-weeks and 30-weeks, the possibility that the same process drives the decrease in cortical bone mass but in this case at 4- and 8-weeks of age cannot be excluded.

4.9.3. Morphometric changes in the CLEC14A$^{-/-}$ and CD248$^{-/-}$ female tibia

Owing to the well-known sexual dimorphism of several proteins in the homeostasis of the skeletal system (459), female trabecular and cortical bone morphometric parameters were also investigated. Overall, the changes in CLEC14A$^{-/-}$ and CD248$^{-/-}$ female mouse tibiae recapitulated the observations reported for males, however, a statistically significant difference was seldomly achieved; this might be attributed to the lower bone mass in females

than males which might require a higher sample population. Given this, all our work was conducted in C57BL/6J male mice unless otherwise indicated.

The three-point bending testing is commonly used for the evaluation of bone strength (460). Differences in bone strength have previously been reported between different bone types (461), hence, to minimise bias the biomechanical proprieties of both the tibia and the femur were evaluated. To understand how CLEC14A and CD248 deficiency affect bone mechanical proprieties we performed three-point bending testing on long bones at 8 weeks of age. The results of our analysis show a significant decrease in bone stiffness in tibiae in spite of the increased trabecular bone mass identified by μCT imaging. Bone contains two phases, collagen, and mineral, both of which contribute to bone stiffness (462). Given the changes observed in the work to fracture area and bone displacement, it is plausible that the quality of the mineral component of the CLEC14A$^{-/-}$ and CD248$^{-/-}$ bones is altered. Previous work has shown that changes in the collagen and/or extracellular matrix phase can affect bone biomechanical proprieties (463), warranting further investigation into the molecular basis of the observed decline in bone stiffness. It is also worth noting that three-point bending, a process where the tibiae and the femora were setup so that the highest point of mechanical stress was directed to the mid diaphysis, is most suitable for testing cortical bone strength. It is less sensitive the mechanical strength proprieties conferred to the whole bone by the trabecular bone in the metaphysis, therefore additional testing by means of nanoindentation in the metaphysis area and torsion testing are highly recommended.

4.9.4. Blockade of CLEC14A MMRN2 interaction in 4-week old C57Bl/6J male mice

Mouse monoclonal antibodies raised against human CLEC14A were utilised to block the interaction between CLEC14A and MMRN2 due to the high amino acid sequence conservation

(72%) in the in the MMRN2 region responsible for CLEC14A binding between human and mice (amino acids 588-620) (355). Antibodies targeting the CLEC14A CTLD have been successfully used *in vitro* and *In vivo* in the past with no effect on cell viability, overall EC morphology or activation (348, 353, 413), hence, no safety issues were expected when targeting the CLEC14A CTLD domain in the murine bone. Indeed, mice showed no changes in body mass or any other alterations in wellbeing behaviour. No changes in trabecular bone parameters as measured by μ-CT were identified following a 2- or a 4-week course of treatment with C2, C4 or PBS control. Antibody tracking experiments have confirmed localisation of the injected antibodies to the bone metaphysis, excluding the possibility that the injection method chosen limits local antibody availability. Whilst localisation of anti-CLEC14A CTLD antibodies to the bone was confirmed, we cannot exclude the possibility of antibody-CLEC14A complex internalisation and high-CLEC14A protein turnover in the *In vivo* experimental setup. Such a side effect would lead to a diminishment of treatment impact. Alternatively, the possibility that not enough antibody was utilised cannot be excluded either. Previous work on antibodies targeting the CLEC14A CTLD has shown that following formation of the antibody-CLEC14A complex, cell-surface CLEC14A expression is downregulated as soon as 10 minutes following CLEC14A-antibody crosslinking (353).

Additionally, CD93 redundancy in binding and retaining MMRN2 close to the EC surface, permitting maintenance of osteoblast immaturity and preventing upregulation of osteogenesis when blocking CLEC14A-MMRN2 interactions cannot be excluded. It is important to note that previous work has shown that indeed C2 and C4 clone anti-CLEC14A CTLD antibodies do not cross react to bind CD93 (355). CD93 has been shown to play a similar role to CLEC14A in angiogenesis, for instance CD93 silencing elicits impaired EC proliferation,

migration and sprouting (464). Moreover, blockade of CD93 MMRN2 interaction also phenocopied the silencing of CD93, resulting in inhibition of EC adhesion and migration (435). It is plausible then to theorise that CD93-MMRN2 interactions are also important in the EC-osteoblast crosstalk during bone growth. To advance understanding of CLEC14A/CD93 redundancy in binding MMRN2 and to dissect the role of each of these interactions in trabecular bone formation, it is imperative to conduct experiments whereby antibodies blocking MMRN2 interactions with either CLEC14A or CD93 are co-administered. Previously published work has shown that utilisation of the clone 4E1 CD93 targeting antibody, leads to changes in EC angiogenesis responses recapitulating the CLEC14-MMRN2 blockade (464).

4.9.5. Conclusion

The results reported here make CLEC14A a negative regulator of bone formation. Germ line deletion of CLEC14A resulted in longer bones with a higher trabecular mass and an elongated trabecular front. Whilst more striking changes were observed in males and not females, it remains unclear if indeed, there is a lack of effect following CLEC14A genetic deletion on females or if the less obvious changes are related to females having lower bone mass than males in general.

5. CHAPTER V MOLECULAR MECHANISMS REGULATED BY CLEC14A MMRN2 CD248 INTERACTION IN THE BONE

5.1. Introduction

This chapter focuses on addressing aim II: Identification and dissection of signalling pathways induced by CD248-MMRN2-CLEC14A interaction. Specifically, the previous two chapters have provided evidence for in *situ* cellular changes produced in response to CLEC14A deficiency in the murine tibia. Furthermore, those changes resulted in modifications in the morphometric composition of CLEC14A$^{-/-}$ murine appendicular skeleton, which were characterised by longer tibiae with increased trabecular bone mass during bone growth. However, the precise signals and molecular signatures governing osteoblast-driven bone accrual in the CLEC14A$^{-/-}$ mice have so far remained unexplored.

In this chapter, molecular alterations at the transcriptomic level in response to CLEC14A genetic deletion were investigated using RNA sequencing of neonatal calvarial cell isolates (section 5.2-5.3.1). To further depict the role of CLEC14A in the molecular control of bone homeostasis, primary calvarial osteoblasts were extracted from CLEC14A$^{-/-}$ and WT C57Bl/6J P4 neonatal pups and their osteogenic capacity in response to mineralisation stimuli was evaluated over time. Evaluation was performed *in vitro* using: 1) PCR to probe changes in mRNA levels of osteoblast maturation markers (section 5.6); 2) ELISA to study patterns of expression of bone formation marker alkaline phosphatase (ALPL) (section 5.7.1); 3) Alizarin red bone nodule staining analysis (section 5.7.1), to detect calcium deposition in maturing osteoblasts as a reflection of their mineralisation capacity; 4) The osteogenic status of CLEC14A$^{-/-}$ mice was also examined by measuring total procollagen type 1 N-terminal propeptide (P1NP) levels in the mouse serum using an ELISA assay (section 5.7.2).

5.2. Bulk RNA sequencing identification of molecular changes in the CLEC14A$^{-/-}$ murine calvaria lysates

Enrichment of osteoblasts in the neonatal pup calvaria was confirmed using 3D imaging of the whole cleared calvaria. Light-sheet fluorescent microscopy imaging of optically cleared calvaria immunolabelled with antibodies against CD31 and OSX confirmed a high density of osteoblasts in the neonatal pup calvaria, moreover, osteoblasts were localised in close proximity to endothelial cells (EC) (Figure 5.1 A). Video renderings of 3D reconstructed images (CD31 red and OSX cyan) can be consulted here: Video1 and Video 2.

In preparation for bulk RNA sequencing, RNA was extracted from WT and CLEC14A$^{-/-}$ postnatal day 4 neonate pup calvarial lysates, following RNA extraction and library generation, reads were sequenced, and data was analysed using R Studio. (Figure 5.1 B bottom panel). No major differences in sample quality were observed across all samples, confirming high quality of the sequencing library (Figure 5.1 C). Unsupervised hierarchical clustering (tree store) (Figure 5.2 A) and principle component (PC) analysis (Figure 5.2 B) showed clustering of cells from the same group (WT or CLEC14A$^{-/-}$) together and separation of samples isolated from different genotypes. The first two principal components (PC1 and PC2) accounted for 28 % and 16 % of morphometric variation in each group. Gene transcripts were sequenced to identify gene set enrichment pathways and differentially expressed genes between the two genotypes (WT and CLEC14A$^{-/-}$). A total of 1223 genes were identified as differentially expressed (DESeq2, padj<0.05, log2FC < 0.5): 522 (0.96%) genes were upregulated, and 701 (1.29%) genes were downregulated in response to genetic deletion of CLEC14A (Figure 5.2 C). Genes identified as differentially expressed were clustered to identify expression trends (up- and downregulation of mRNA transcripts), gene expression was normalised to a Z score to allow comparisons between individual samples for each individual gene. Heatmap clustering identified 2 clusters

wherein upregulation of gene expression was observed in CLEC14A samples, and one cluster that contained genes upregulated in WT samples compared to CLEC14A knock-out (Figure 5.2 D).

5.3. Gene set enrichment analysis

Gene set enrichment analysis (GSEA) was utilised to identify biological pathways enriched in either CLEC14A$^{-/-}$ or WT samples, (an example plot with a legend can be found in section 2.3, Figure 2.2). CLEC14A$^{-/-}$ samples strongly expressed markers enriched in pathways related to responses to angiogenesis and osteogenesis including: hypoxia; endochondral ossification and collagen type I synthesis; osteoblast maturation and osteogenesis (Figure 5.3). In addition, Runx3 expression and activity; regulation of expression of slit guidance ligands (SLITs) and roundabout guidance receptors (ROBOs); and mTORC1 signalling pathways were correlated with the CLEC14A$^{-/-}$ phenotype (Figure 5.3). The most statistically significant pathways correlated with higher enrichment in WT samples were related to cell adhesion molecules pathways listed as follows: adhesion molecules; ECM receptor interaction and tight junction molecules (Figure 5.3). To identify markers whose differential expression drives the enrichment in GSEA gene sets, the leading edge genes were listed in heatmaps for the GSEA plots considered of high relevance for angiogenesis and osteogenesis (Figure 5.4-Figure 5.7). The leading-edge subset of genes represents the cluster of genes that most contribute to the enrichment score for each gene set (393). Leading-edge gene transcription patterns in each sample analysed (N=4 for both WT and CLEC14A$^{-/-}$) were listed for the following gene sets: hypoxia (Figure 5.4), tight junction molecules (Figure 5.5), extracellular matrix (ECM) receptor interactions (Figure 5.6), and endochondral ossification (Figure 5.7, Appendix Figure 9.3, Figure 9.4, and Figure 9.5).

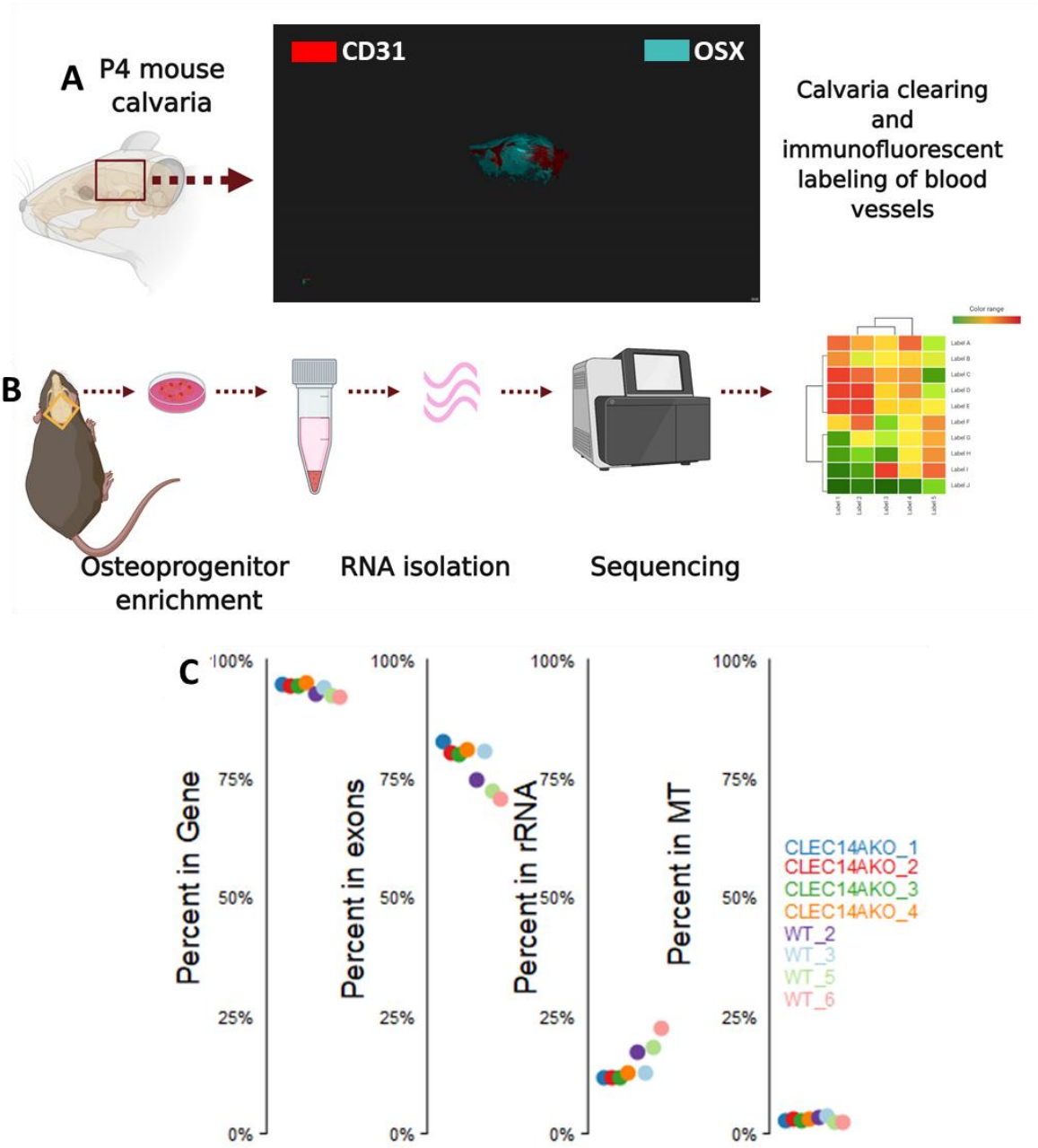


Figure 5.1. RNAseq transcriptomic analysis of neonatal WT and CLEC14A-/- calvarial bone lysates. **A)** Cleared calvaria immunofluorescent image showing vascularisation of neonatal pups - CD31(red), and localisation of OSX^{+} osteoblasts (cyan) in the near vicinity of vessels. Image confirms enrichment of osteoblasts and EC in the neonatal mouse calvaria. **B)** Schematic demonstrating the experimental process performed for extraction of calvarial cell lysates from postnatal day 4 (P4) pups. Osteoblast lineage cells enriched cell suspensions were isolated from C57Bl/6J, four WT and four $CLEC14A^{-/-}$ postnatal day 4 pup calvaria. Single cell suspensions were obtained through serial enzymatic digestion with collagenase D. Total RNA was extracted from calvarial osteoblasts immediately after cell isolation. NGS library prep which was generated with the aid of the Lexogen QuantSeq 3' mRNA-Seq Library Prep Kit and the library was sequenced with the Illumina NextSeq 500. Differential gene expression was obtained through post hoc analysis in R Studio. **C)** Quality control graphs investigating the percentage of reads reported in genes, exons and the percentage of reads originating from ribosomal (rRNA) and mitochondrial (MT) RNA, illustrating no major differences between all the samples analysed.

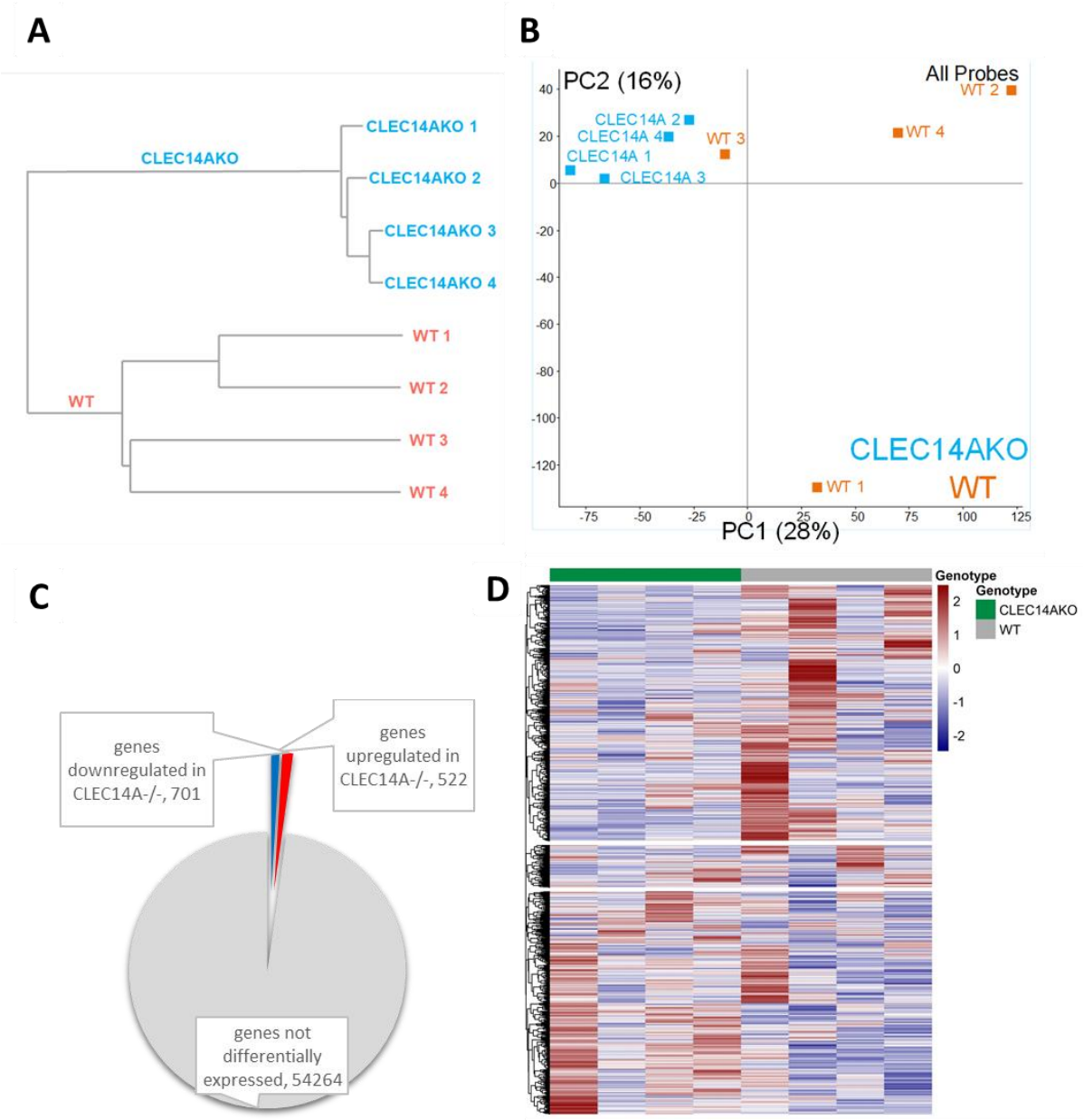


Figure 5.2. Clustering and gene ontology analysis of WT and CLEC14A$^{-/-}$ pup calvaria lysates. A-B) Unsupervised hierarchical clustering, (dendrogram – A and principal component analysis – **B)** of log2 normalised counting reads over exons (RPM-reads per million) for all detected genes, N=3 for both groups. CLEC14A$^{-/-}$ samples (blue), WT samples (orange). Each sample represents a different individual animal. **C)** Differentially expressed gene counts. Raw counts were analysed with DESeq2, significantly expressed genes were cutoff at log2FC values > 0.5, adjusted p (padj) <0.05, p value was corrected for multiple comparisons (Benjamini–Hochberg); Red = genes upregulated in CLEC14A$^{-/-}$ samples; Blue = genes downregulated in CLEC14A$^{-/-}$ samples **D)** Heatmap presenting an overview of the clustering of all genes identified as differentially expressed between WT and CLEC14A$^{-/-}$ samples. Green = CLEC14A$^{-/-}$, Grey = WT. Gene expression is presented as a Z score (scale).

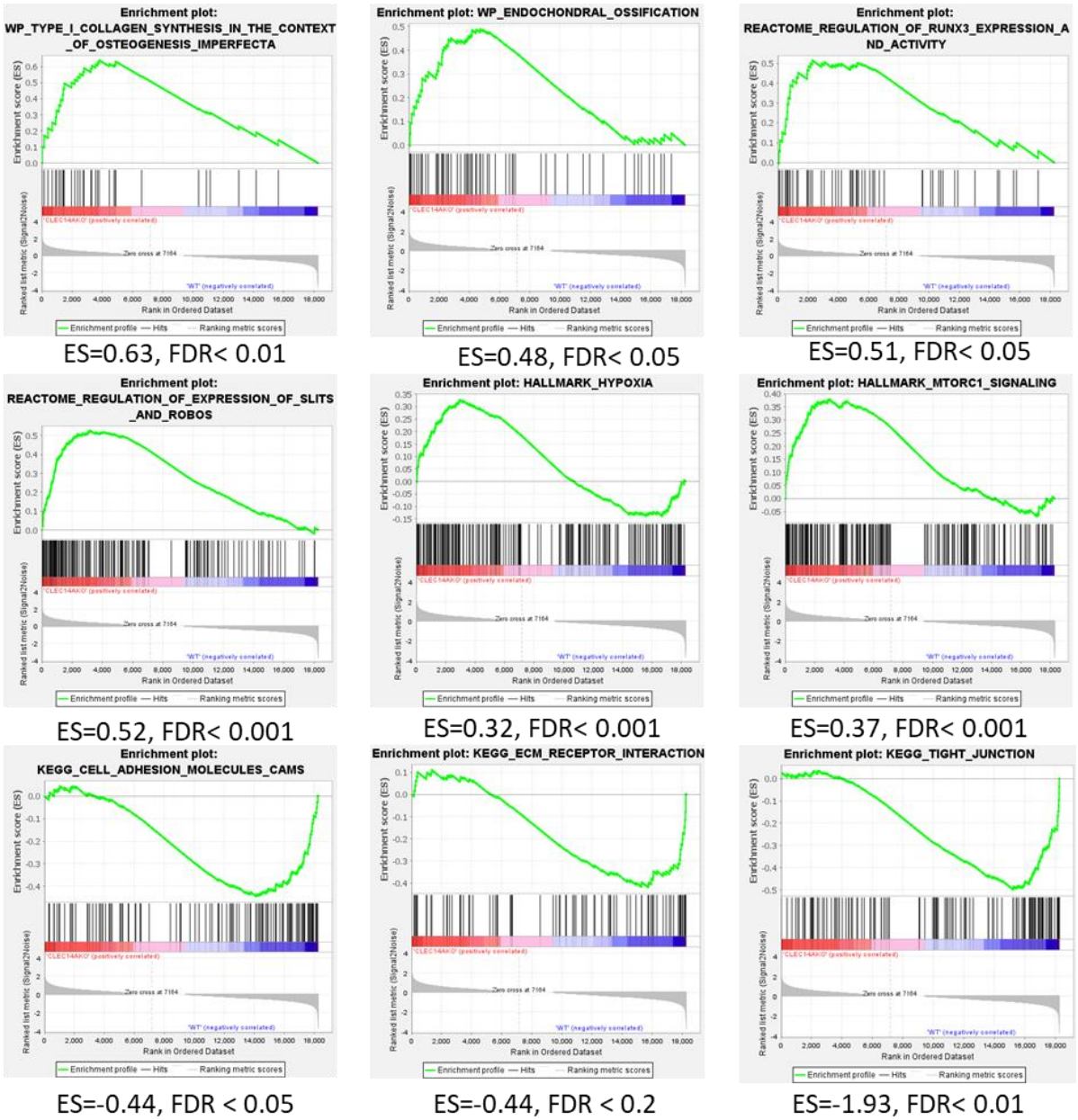


Figure 5.3 List of tested gene sets with top enrichment scores identified by GSEA analysis. The green line shows the trace of the enrichment score (ES) for each gene set across all ranked genes in that set. The peak ES marked by the peak point in each trace also constitutes the ES for a gene set. The black parallel lines underneath the trace represent the number and distribution of ranked genes that are part of the gene set. The ranked genes clustering to the left side, and which are presented with a positive ES value pertain to genes with the highest expression in CLEC14A$^{-/-}$ samples, whilst the ranked genes on the right side, presented with a negative ES value are downregulated in CLEC14A$^{-/-}$ samples. ES-enrichment score, FDR -false discovery rate. Gene expression is presented as a Z score (scale).

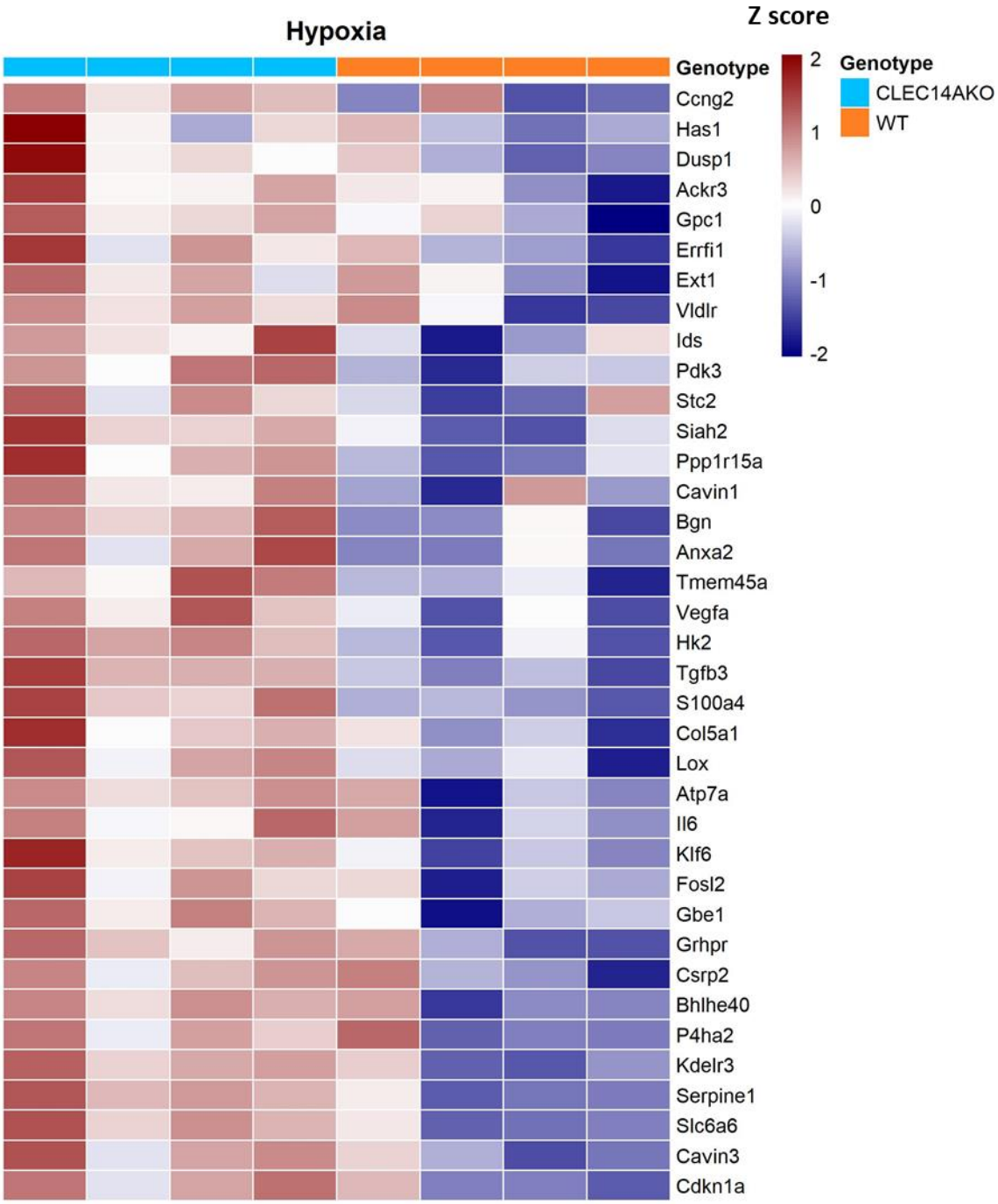


Figure 5.4. GSEA heatmap showing the list of leading edge genes enriched at the top of the Hallmark Hypoxia gene set. Heatmap presents upregulation of hypoxia related transcripts in CLEC14A$^{-/-}$ samples. Gene expression is presented as a Z score (scale). Transcripts presented were identified as statistically significant by GSEA analysis, FDR(Q-value) < 0.05, nominal p <0.01. Blue = CLEC14A$^{-/-}$, Orange = WT.

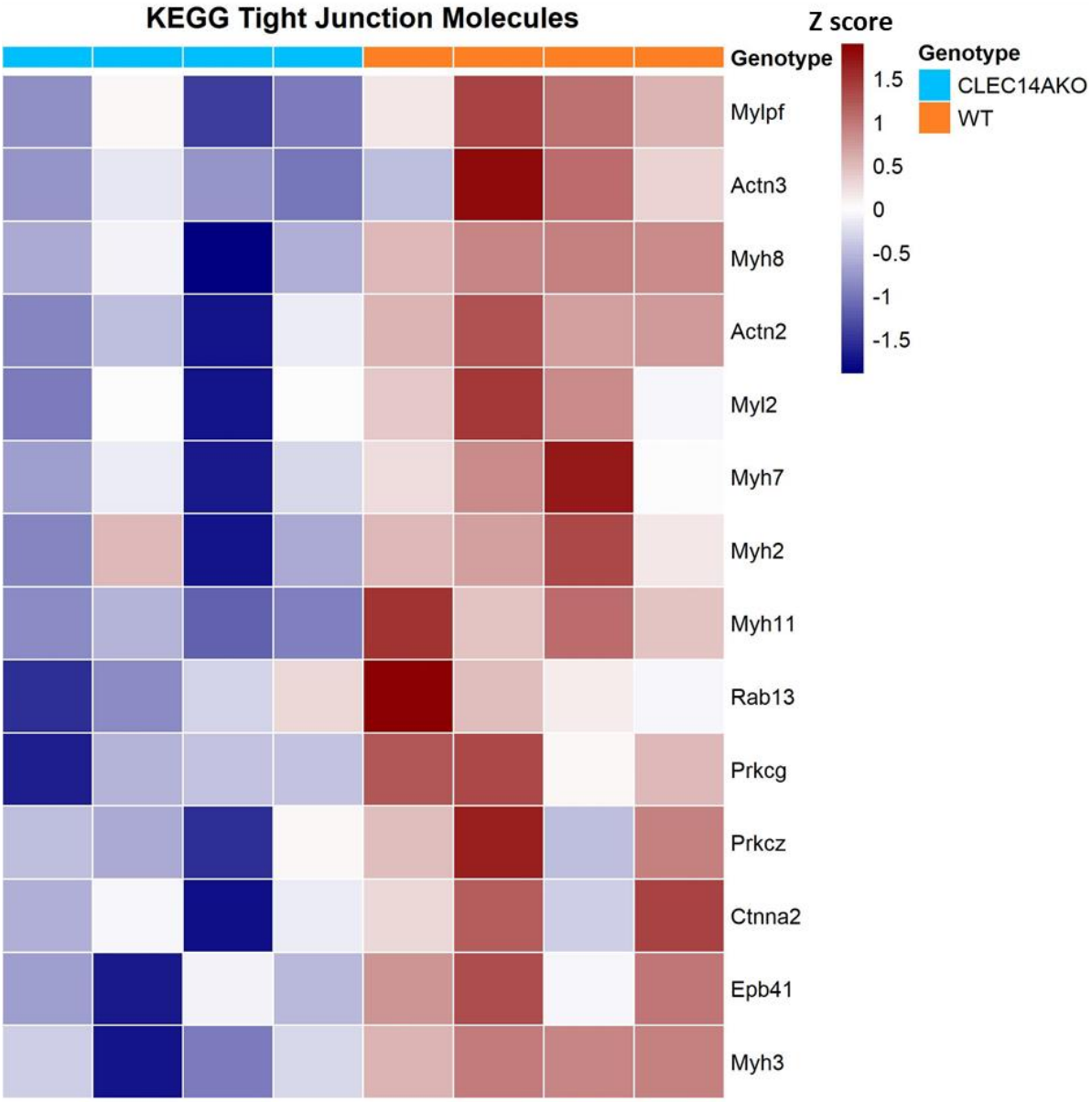


Figure 5.5. GSEA heatmap showing the list of leading edge genes enriched at the top of the KEGG Tight Junction gene set. Heatmap presents downregulation of tight junction complex transcripts in CLEC14A$^{-/-}$ samples. Gene expression is presented as a Z score. Transcripts presented were identified as statistically significant by GSEA analysis, FDR(Q-value) < 0.02, nominal p < 0.001.

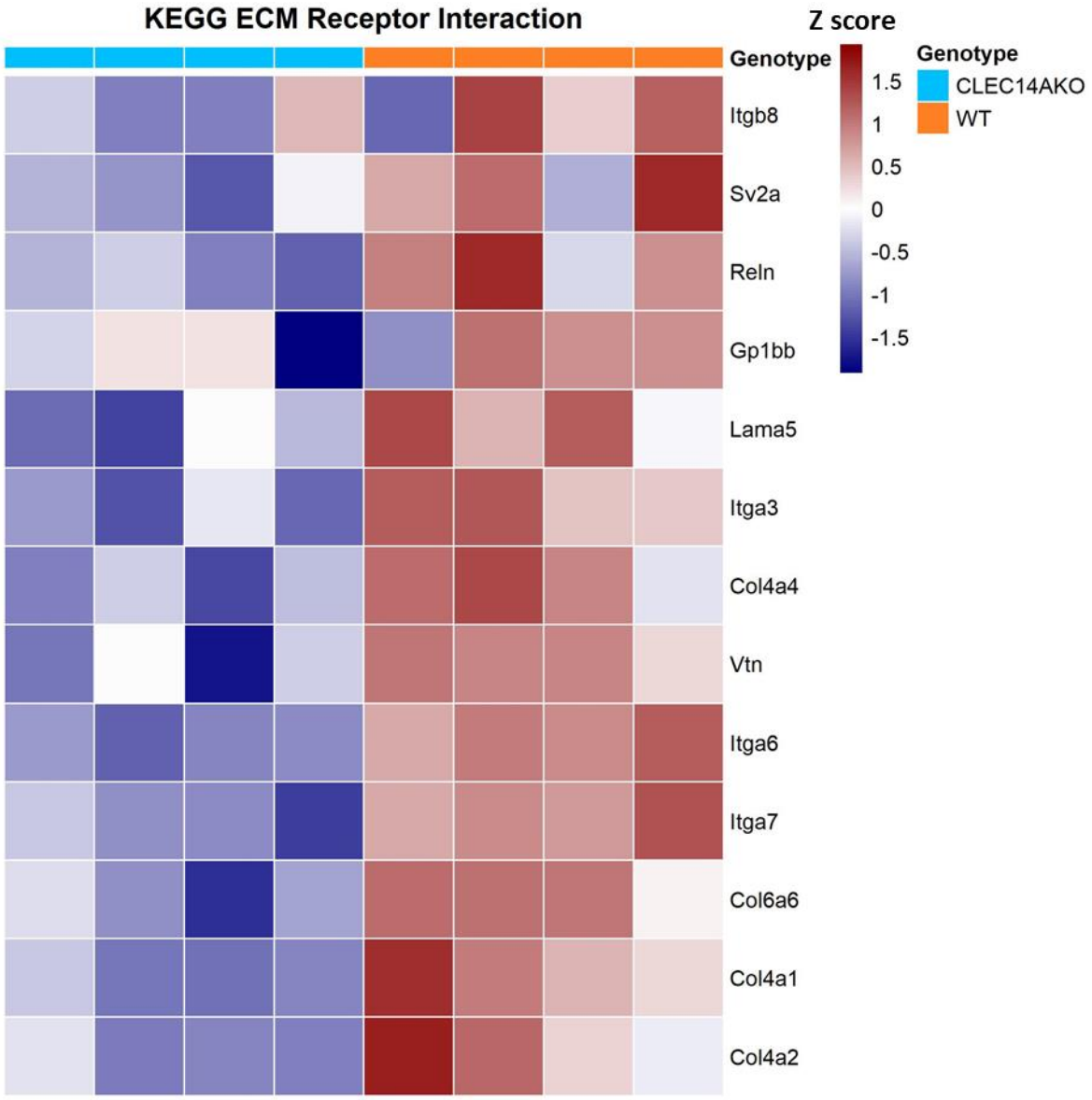


Figure 5.6. GSEA heatmap showing the list of leading edge genes enriched at the top of the KEGG ECM Receptor Interaction gene set. Heatmap presents downregulation of the ECM interactome transcripts in CLEC14A$^{-/-}$ samples. Gene expression is presented as a Z score. Transcripts presented were identified as statistically significant by GSEA analysis, FDR (q-value) < 0.2, nominal p < 0.01.

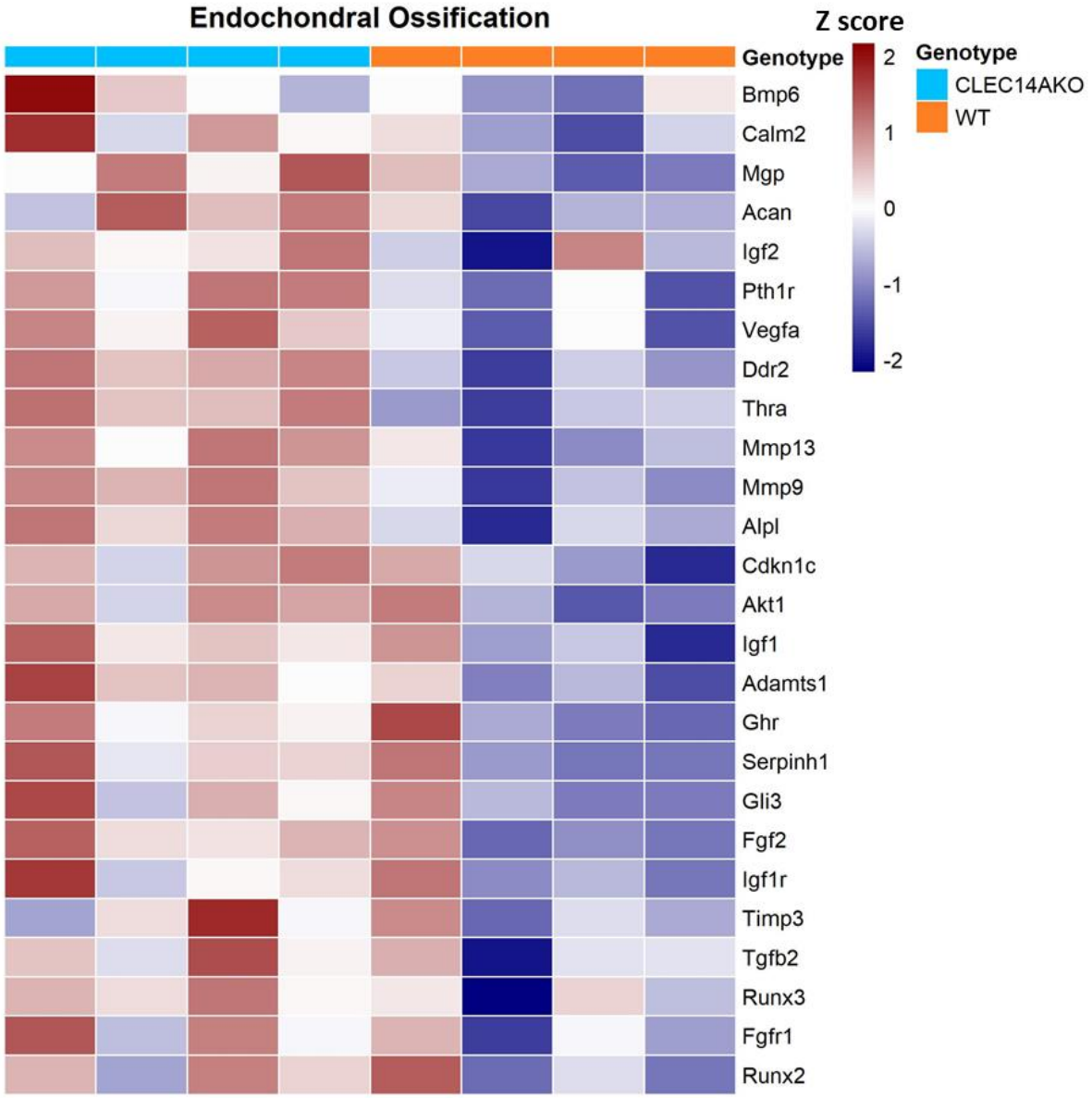


Figure 5.7. GSEA heatmap showing the list of leading edge genes enriched at the top of the Wikipathways Endochondral Ossification gene set. Heatmap presents upregulation of transcripts relevant to endochondral ossification in CLEC14A$^{-/-}$ samples. Gene expression is presented as a Z score. Gene expression is presented as a Z score. Transcripts presented were identified as statistically significant by GSEA analysis, FDR (q-value) < 0.05, nominal p < 0.01.

5.3.1. Differential gene expression analysis

The RNA sequencing of WT and CLEC14A$^{-/-}$ pup calvaria data was explored further to identify differentially expressed genes. Differential gene expression was conducted to identify genes of interest to this project, but which have not been identified as enriched in a particular gene set in the GSEA. Changes in the expression of genes which are known regulators or interacting partners of CLEC14A expression and genes affected by CLEC14A germline deletion were identified following differential gene expression analysis (DESeq2, padj < 0.05). Shear stress regulated transcription factors and upstream regulators of CLEC14A$^{-/-}$ (data not published, from the Roy Bicknell group), kruppel-like factors (KLF) *Klf2* and *Klf4* (465, 466), were upregulated in response to CLEC14A knock-out (Figure 5.8 A). In addition, downregulation of genes with roles in cell-cell adhesion was also reported: *Cldn19*, *Cldn5*, *Cdh5*, as well as that of heat shock protein family A (Hsp70) members (*Hspa1a* and *Hspa1b*) (Figure 5.8 A). *Klf2* upregulation in CLEC14A-deficient calvarial isolates was also confirmed by RT qPCR (Figure 5.8 B). Furthermore, RT qPCR increased expression of CD248 (*Tem1*) was also observed in the CLEC14A$^{-/-}$ samples as compared to WT controls. No change was detected for the mRNA expression of the CLEC14A interacting partner MMRN2 (Mmrn2) or for the other C-type lectin 14 family domain member *Cd93*.

Genes associated with tissue resorption processes, such as matrix metalloproteinases (*Mmp9, Mmp13, Mmp14*) and tissue inhibitor of metalloproteinase inhibitors (*Timp1*, *Timp2*), were also upregulated in CLEC14A$^{-/-}$ mice (Figure 5.9). Some of the metalloprotease family genes are known active contributors to expansion of the H-type vessel vascular front into the growth plate at the chondro-osseous junction e.g. *Mmp9* and *Mmp13* (20), whilst others are part of

the osteoclast specific subset of genes expressed during bone resorption: *Acp5, Nfatc1, Ctsk* (467-469).

The transcriptional architecture of the CLEC14A$^{-/-}$ mouse calvaria was dissected further by depicting the top gene candidates contributing to bone accrual. Markers identified as differentially expressed following DESeq2 analysis were listed in heatmaps (Figure 5.10). Upregulation of known modulators of bone formation was notable, including insulin growth factory family members, transforming growth factor β family members or fibroblast growth factor receptors (Figure 5.10). In addition, enrichment in genes expressed by mature osteoblasts during ossification was also identified, some of the most well-characterised genes included: bone ECM architecture organiser type I collagen (*Col1a1, Col1a2*) (470-472), matrix mineralisation alkaline phosphatase (*Alpl*) (473), and nucleator of hydroxyapatite crystal formation bone sialoprotein (*Ibsp*) (474-476), other genes with reported roles in osteoblast differentiation were also identified: *Rela* and *Cdh11* (477, 478) (Figure 5.10). Finally, decreased expression of the perivascular stromal cell and EC marker nestin (*Nes*) was also observed (20, 22, 459, 479, 480) (not shown in a heatmap).

5.4. Mining of bone and bone marrow sc-RNA seq dataset to deconvolute cellular sources for the differentially expressed cellular markers in bulk RNA sequencing of CLEC14A calvaria lysates

To further map potential cellular sources for the differentially expressed genes identified in our bulk-RNA sequencing of CLEC14A$^{-/-}$calvarial lysates, we probed expression patterns for genes of interest in the bone and bone marrow cell single-cell RNA sequencing dataset (GSE128423).

Firstly, we investigated the pattern of expression of *Col1a1*. Sc-RNA sequencing analysis revealed pericytes, fibroblasts, and MSCs as alternative cellular sources of *Col1a1*, all which

could directly contribute to the expression levels identified in the RT qPCR analysis calvaria lysates (Figure 5.11 A-B). Moreover, *Col1a1* expression exhibited a transcriptional gradient driven by the osteoblast maturation stage with mature osteoblasts showcasing the highest expression and pre-osteoblasts presenting with minimal *Col1a1* expression levels (Figure 5.11 C).

Secondly, CLEC14A$^{-/-}$ calvarial samples were also characterised by an increase in transcription of metalloproteinase genes, hence, the main cells in the bone expressing these transcripts were also mapped (Figure 5.12 A). *Mmp13, Mmp14* and *Timp1,* were all almost exclusively expressed by osteoblasts, *Timp2* was also expressed by osteoblasts, however it was also expressed at a considerably higher level by fibroblasts. *Adamts1* was expressed by a low proportion of EC and at a lower average expression level by MSC.

Our bulk-RNA sequencing analysis identified upregulation of shear stress and CLEC14A regulators *Klf2* and *Klf4.* Mapping *Klf2* and *Klf4* expression in the whole cellular compartment of the bone revealed a promiscuous pattern of expression for these two transcripts, with a low basal expression confirmed in all mesenchymal lineage cells (Figure 5.12 B). In addition, expression of cell adhesion molecules *Cldn5* and *Cdh5* was demonstrated to be exclusive to EC. Limited expression of heat shock proteins and CLEC14A interacting partners *Hsp1a1* and *Hsp1a2* was detected in the single cell RNA sequencing dataset (Figure 5.12 B). *Nes* expression was low in the single cell RNA sequencing dataset (Appendix, Figure 9.2), however expression mostly identified on EC.

Nes, Vegfa, and *Mmp9* transcript expression was tested with the aid of RT qPCR to validate the changes identified by the RNA sequencing analysis. Expression of these transcripts in P4 WT and CLEC14-/- murine calvaria (the same mouse age and methodology as utilised for the bulk RNA seq experiment analysed was employed) was chosen to be further explored were

chosen due to their role in modulation of expansion of the vascular bed in the long bone during bone growth (479, 480). RT qPCR analysis confirmed a trend for the upregulation of *Mmp9* expression in CLEC14A$^{-/-}$ calvaria lysates in line with the RNA sequencing observations, however, this did not reach statistical significance (Figure 5.13). Also reinforcing the changes observed in the RNA sequencing analysis, cytoskeletal intermediate filament protein nestin (*Nes*) expression was strongly downregulated in CLEC14A$^{-/-}$ compared to WT control samples. *Vegfa* mRNA levels were decreased in CLEC14A$^{-/-}$ calvaria lysates in contrast to the increased levels indicated by RNA sequencing analysis of the same tissue (Figure 5.13).

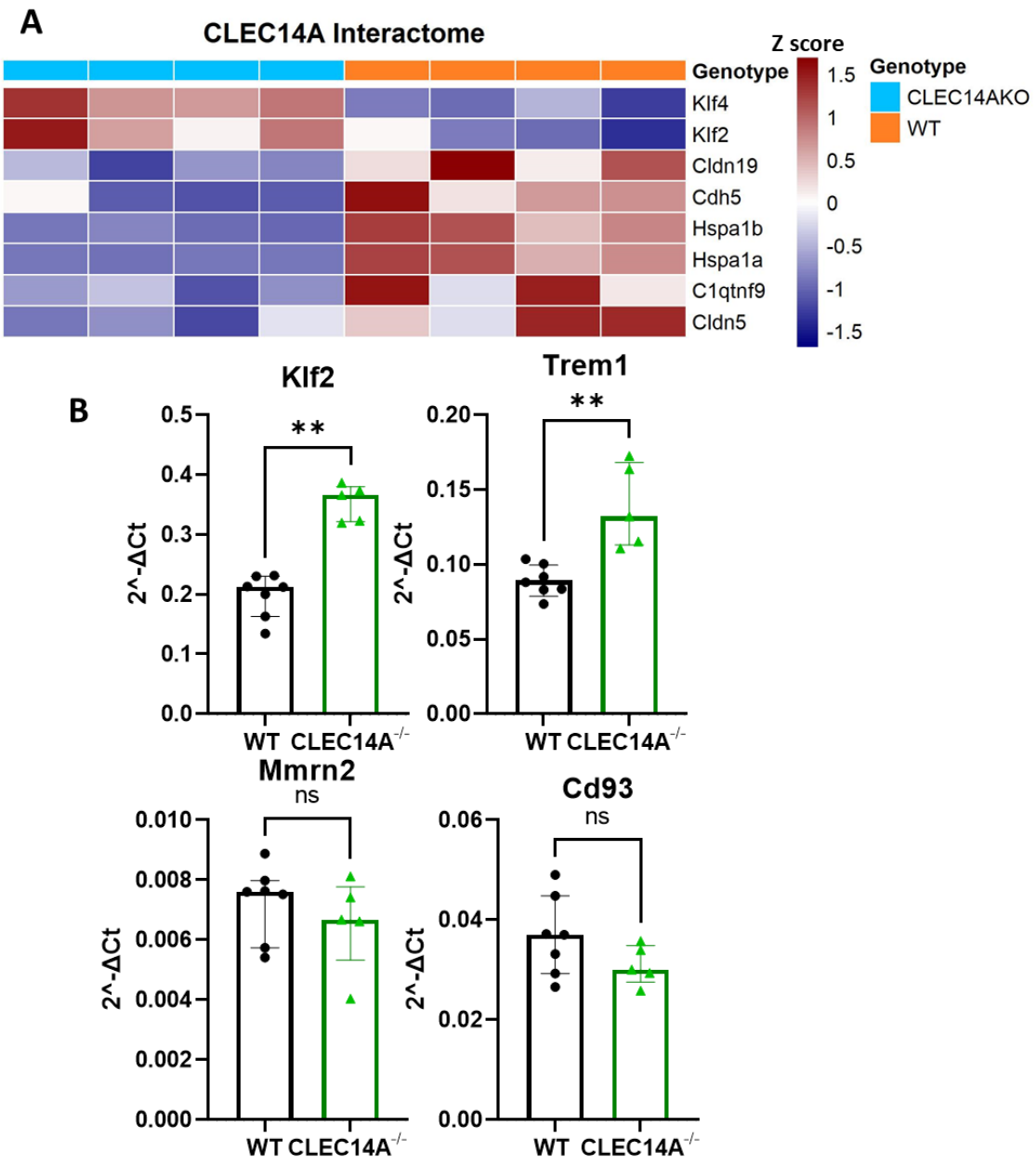


Figure 5.8. Regulation of the CLEC14A interactome in response to CLEC14A loss of function. A) Heatmap presents normalised (Z score) gene expression patterns for transcripts of the CLEC14A interactome. Transcripts presented in the heatmap were identified as statistically significant by DESeq2 analysis, padj < 0.05 **B)** qRT-PCR analysis of P4 pup calvarial lysates, shown here are relative mRNA values of the CLEC14A regulator KLF2 and of the other C-type lectin domain family 14 members – CD248 (Trem1 gene name), MMRN2 and CD93. Expression was normalised to *Gapdh*. Results are representative of one independent experiment, N=7 (WT), N=5 (CLEC14A$^{-/-}$). Data is presented as Median ± IQR, a Mann-Whitney test was used to analyse the results, ** p < 0.01.

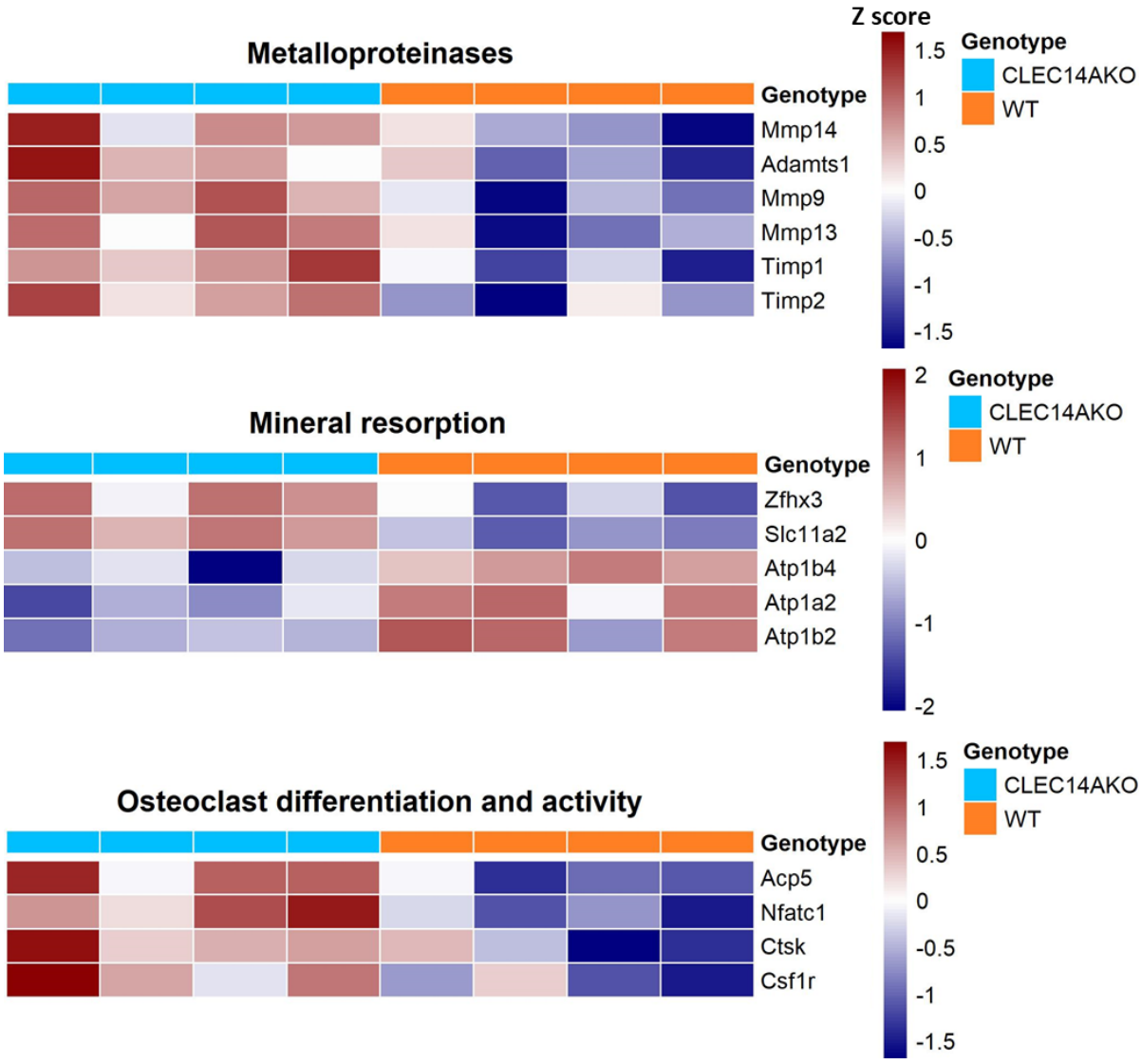


Figure 5.9. Expression levels of genes related to bone resorption. A) Heatmap presents normalised (Z score) gene expression patterns for metalloproteinase transcripts upregulated in CLEC14A$^{-/-}$ samples. **B)** Heatmap presents normalised (Z score) gene expression patterns for transcripts for molecules associated to resorption of bone mineral **C)** Heatmap presents normalised (Z score) transcript levels of genes regulating osteoclast differentiation and activity. Transcripts presented in all heatmaps were identified as statistically significant by DESeq2 analysis, padj < 0.05.

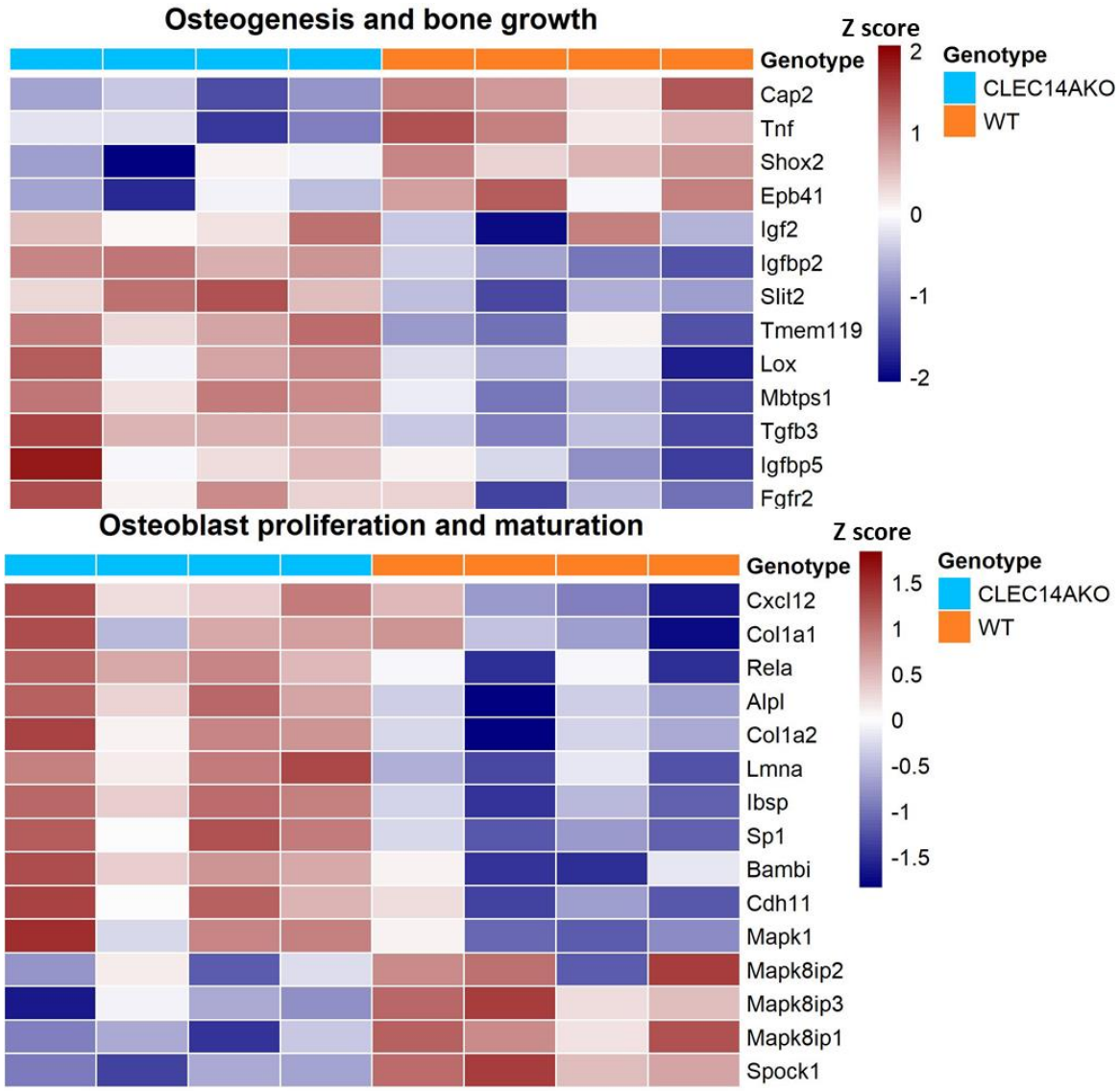


Figure 5.10. Expression of genes regulating bone formation and growth. A) Heatmap presents normalised (Z score) gene expression patterns for osteogenesis and bone growth transcripts differentially expressed in CLEC14A$^{-/-}$ samples. **B)** Heatmap presents normalised (Z score) gene expression patterns for transcripts for molecules moderating osteoblast proliferation and maturation. Transcripts presented in all heatmaps were identified as statistically significant by DESeq2 analysis, padj<0.05

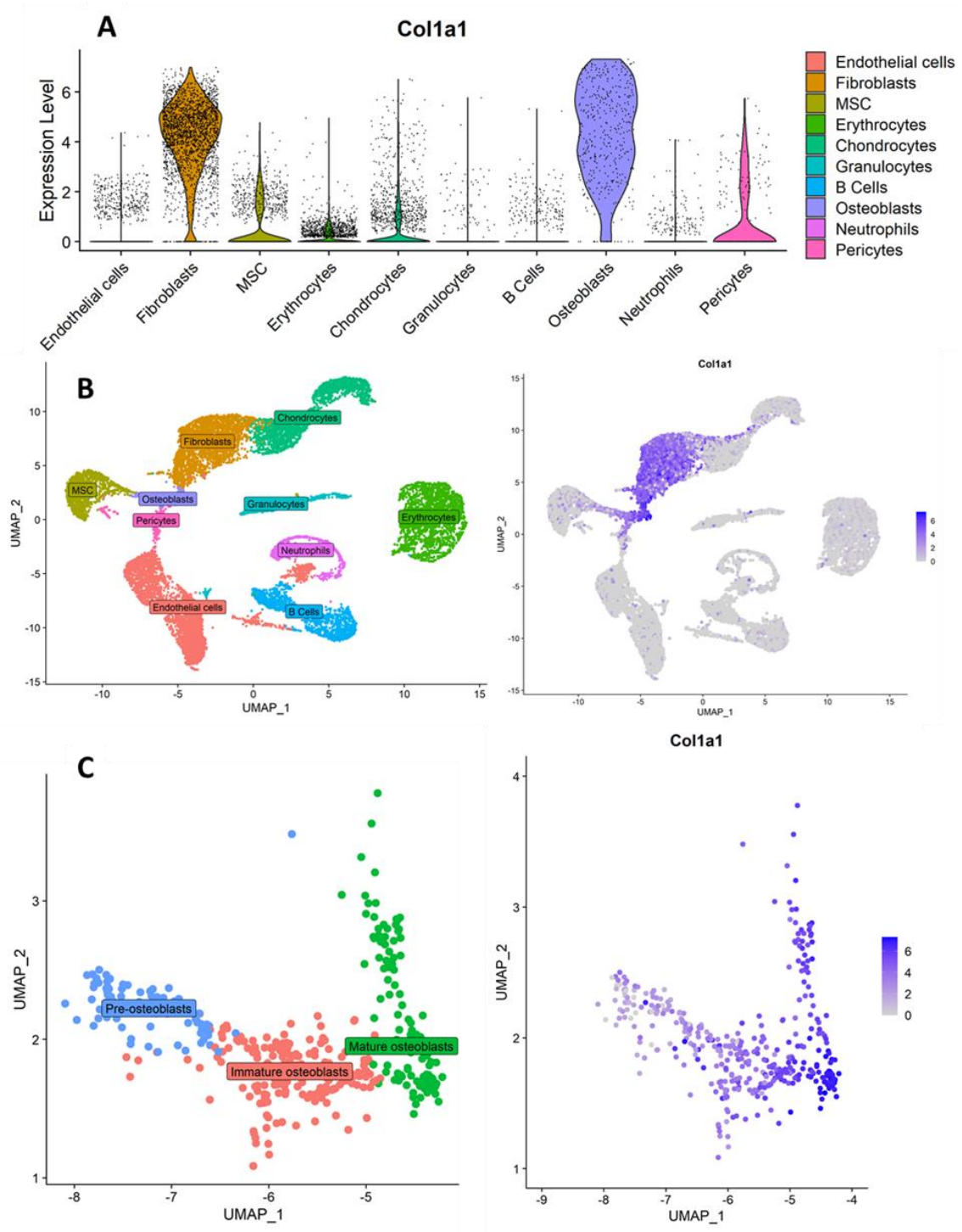


Figure 5.11 Patterns of expression of *Col1a1* in the murine long bone (GSE). A) Violin plot showcasing *Col1a1* expression levels in fibroblasts and osteoblasts. **B)** Left graph: Uniform manifold approximation and projection (UMAP) graph indicating cell cluster identities for the plot on the right. Right graph: Feature plot demonstrating the transcriptional gradient of Col1a1 expression in the bone, the highest expression is noted in osteoblasts with positional dependent gradual decrease in expression in pericytes, MSC and fibroblasts. **C)** Left graph: UMAP plot labelling cluster identities for the plot on the right. Right graph: Feature plot showing transcriptional gradient of expression in osteoblasts with the highest expression in mature osteoblasts, followed by an intermediate level of expression in immature osteoblasts and minimal levels of expression in pre-osteoblasts.

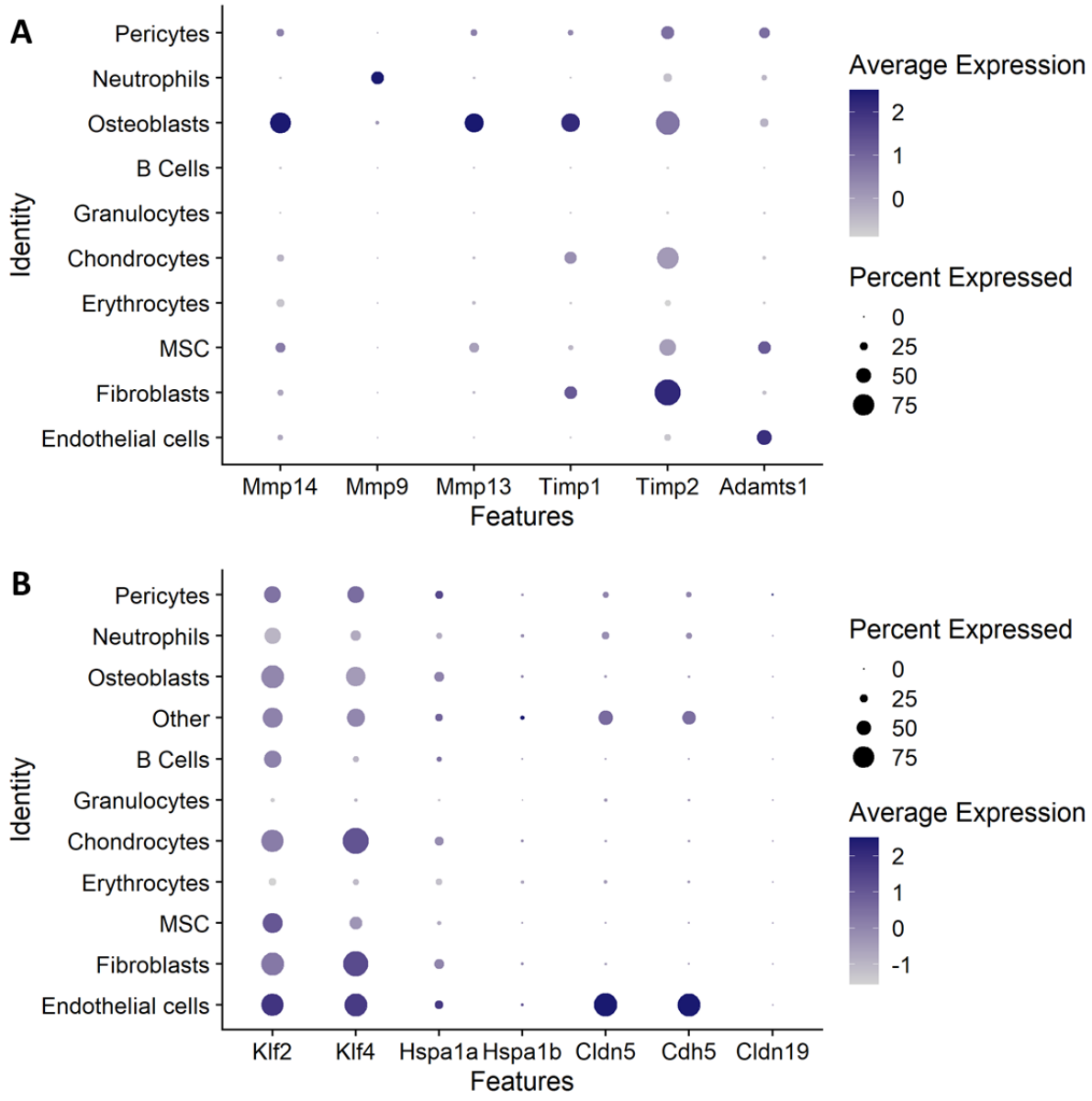


Figure 5.12 Identification of bone cellular sources for proteins of interest for this project using single-cell sequencing (dataset GSE128423). The bone mesenchymal and haematopoietic compartments were separated in cell clusters according to cell type. Dotplot graphs show expression of: **A)** metalloproteases **B)** CLEC14A known regulators or interacting partners expression in the 8-week-old C57Bl/6J mouse tibia.

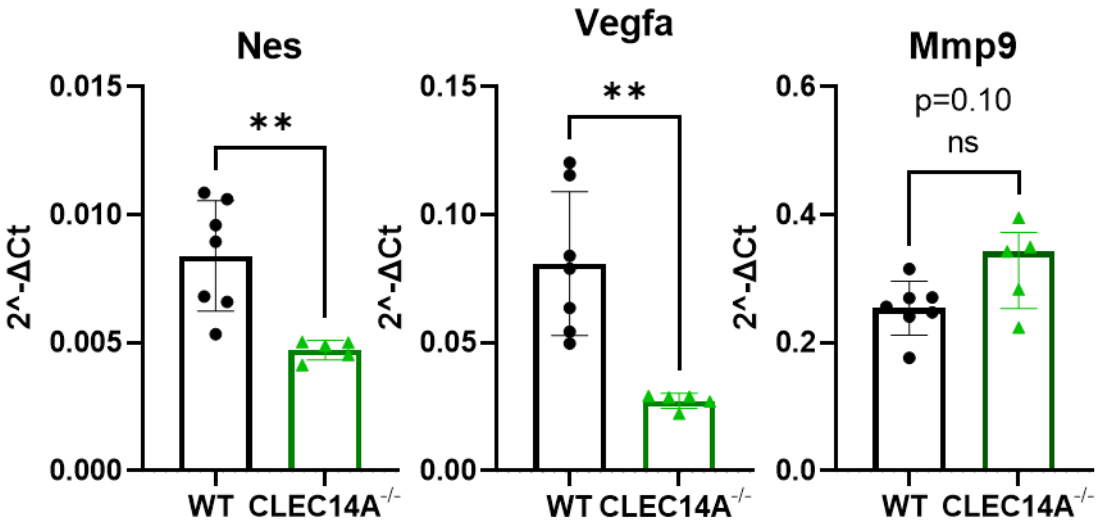


Figure 5.13. Expression of genes regulating expansion of the vascular bed during bone growth. Male P4 pup calvarial lysates were subjected to RT qPCR analysis to dissect expression patterns of genes known to regulate invasion of vessels into the growth plate during bone growth, gene expression was normalised to expression of the housekeeping gene *Gapdh*, shown as arbitrary units (2^-ΔCT). Data is presented as Median ± IQR, a Mann-Whitney test was used to analyse the results. Plots represent results from two independent experiments (N=7 WT, N=5 CLEC14A$^{-/-}$), data points in each graph are representative of biological replicates.

5.5. Assembly of an osteoblast maturation gene signature from single cell RNA sequencing data

To identify the molecular signature of osteoblasts during differentiation, an osteoblast maturation gene signature was produced to identify top markers expressed in pre-osteoblasts, immature osteoblasts, and mature osteoblasts. To achieve this, single cell RNA sequencing of bone and bone marrow cells was explored (403) (GSE128423).

Osteoblasts were identified according to expression of the osteoblast specialisation master regulators *Sp7* (*Sp7*) and *Runx2* (481-483). *Runx2* and *Sp7* were both expressed by mesenchymal stem cells (MSC), chondrocytes and osteoblasts. In line with the function accomplished by *Runx2* in directing MSC down the pre-osteoblastic lineage (484), a high proportion of MSC express *Runx2*. On the other hand, only a small proportion of MSC express *Sp7*, reflecting the role played by *Sp7* in further differentiation of pre-osteoblasts into immature and mature osteoblasts (485) (Figure 5.14 A). Following sub clustering of the osteoblast main cluster, three distinct osteoblast subsets were identified, each with a relatively similar expression of *Runx2* and *Sp7* (Figure 5.14 B).

Analysis of top markers for each osteoblast sub-cluster allowed for the identification of markers that are most upregulated in pre-osteoblasts (Lepr, Pdgfrb and Cxcl12), immature osteoblasts (Serpine2, Spp1 and *Alpl*) and mature osteoblasts (*Col1a1*, Col1a2, Sparc and *Bglap*) (Figure 5.15). Lepr is expressed at low levels in pre-osteoblasts, minimal expression is observed in immature but not mature osteoblasts. Pdgfrb is expressed at similar levels by both pre-osteoblasts and immature osteoblasts, its expression is completely abolished in mature osteoblasts. Cxcl12 presents a transcriptomic gradient with the highest expression on pre-osteoblasts, followed by an intermediate level of expression on immature osteoblasts and a low level of expression in mature osteoblasts. Immature osteoblasts are characterised by

markers that are the least specifically enriched compared to the other 2 osteoblast clusters, indicating their transitory transcriptomic state. Both Serpine2 and Spp1 are expressed at high levels in pre-osteoblasts and immature osteoblasts and are heavily downregulated in mature osteoblasts. *Alpl* is expressed at similar transcriptomic levels across all three osteoblast sub-types, with a minor relative downregulation in mature osteoblasts. Transcriptomic gradients were also observed for mature osteoblast markers: *Col1a1*, Col1a2 and Sparc, with expression increasing stepwise in tandem with the maturation status of osteoblasts from a low expression in pre-osteoblasts, to an intermediate expression in immature osteoblasts and a sustained expression in mature osteoblasts. *Bglap* is expressed at intermediate levels in pre-osteoblasts and immature osteoblasts and its expression is further increased in mature osteoblasts (Figure 5.16).

Using the markers that best characterised each osteoblast maturation stage, an osteoblast maturation gene signature was assembled and used to test WT and CLEC14A$^{-/-}$ calvarial osteoblast responses to osteoinductive stimulation by means of enrichment of media with β-glycerophosphate and L-ascorbic acid (Figure 5.16).

5.6. Validation of RNA sequencing differentially expressed genes by RT qPCR

To validate target genes identified via bulk RNA sequencing analysis (GSEA or DESeq2 analysis), the expression of a list of key factors deemed important for angio- and osteogenesis was probed using RT qPCR analysis of P4 mouse calvaria lysate cells (the same age as utilised for the bulk RNA seq experiment analysed in sections 5.3 and 5.4). The following genes were chosen for validation –*Cxcl12, Sp7, Alpl, Ibsp, Col1a1, Col1a2, Bglap, Spock3*. *Cxcl12, Sp7, Alpl, Ibsp, Col1a1, Col1a2, Bglap and Sparc/Spock3*, were investigated due to their role in osteoblast

maturation and activity (Table 1). Expression of mesenchymal stem cell stemness transcript, C-X-C motif chemokine ligand 12 (*Cxcl12*), and that of osteoblast commitment and maturation markers: *Sp7, Alpl, Col1a1, Ibsp, Bglap* and *Spock3/Sparc*, all of which were increased in the RNA sequencing results, were also investigated using RT qPCR. Expression of *Col1a1, Col1a2, Ibsp and Bglap* was significantly increased in CLEC14A$^{-/-}$ calvaria lysates whilst no changes were identified for *Cxcl12, Osx, Alpl and Spock 3* (Figure 5.17).

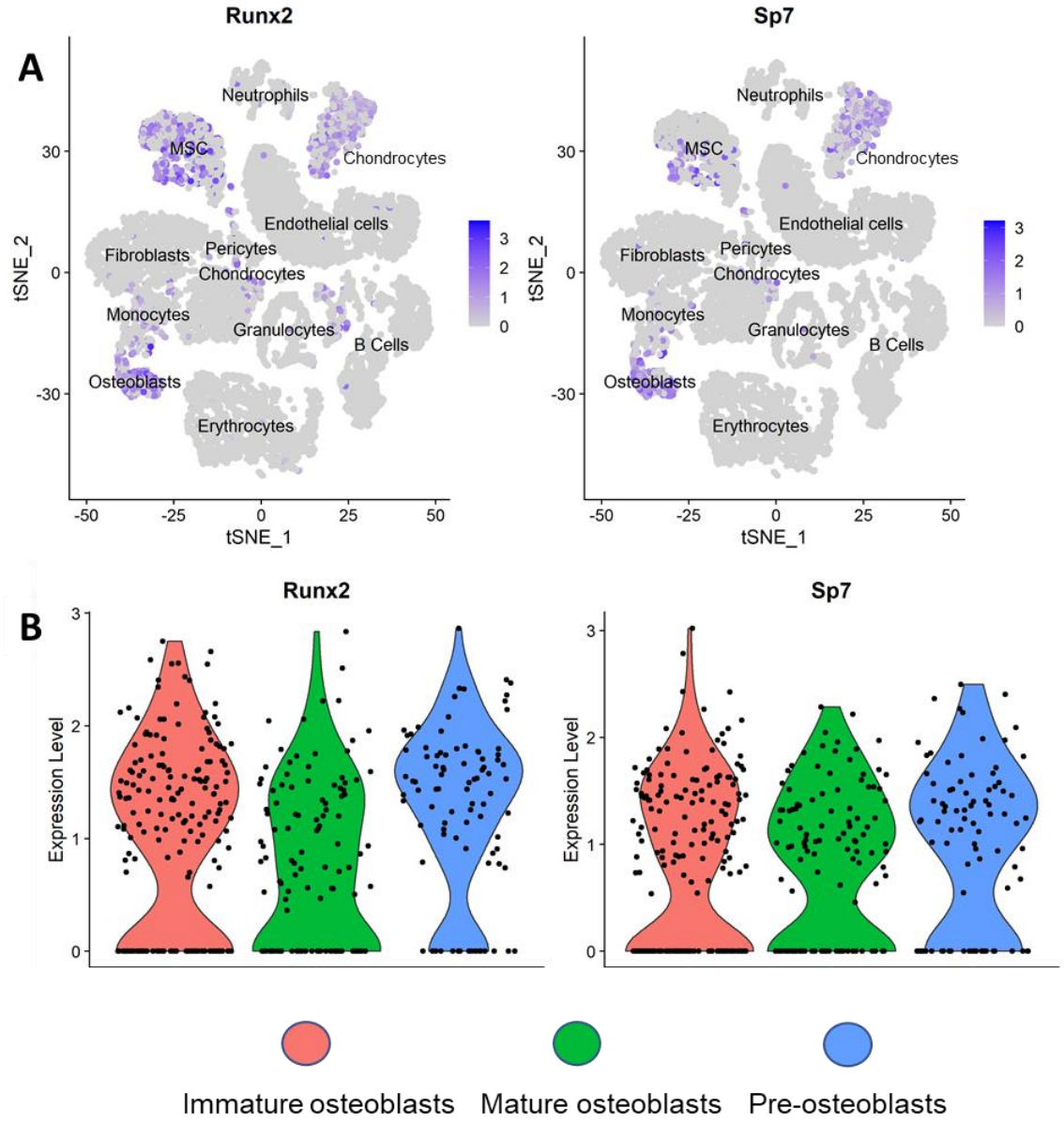


Figure 5.14. Expression of master regulators of commitment to osteoblast differentiation in stromal cells isolated from the murine bone and bone marrow. A) Feature plot showing expression of *Runx2* and *Sp7* in mesenchymal lineage cells: chondrocytes, mesenchymal cells, and osteoblasts. A relatively lower expression of *Runx2* and *Sp7* expression was noticed in chondrocyte and mesenchymal stem cell (MSC) clusters compared to osteoblasts. **B)** Violin plots showing expression of *Runx2* and *Sp7* gene name across all stages of osteoblast differentiation: pre-osteoblasts, immature- and mature osteoblasts.

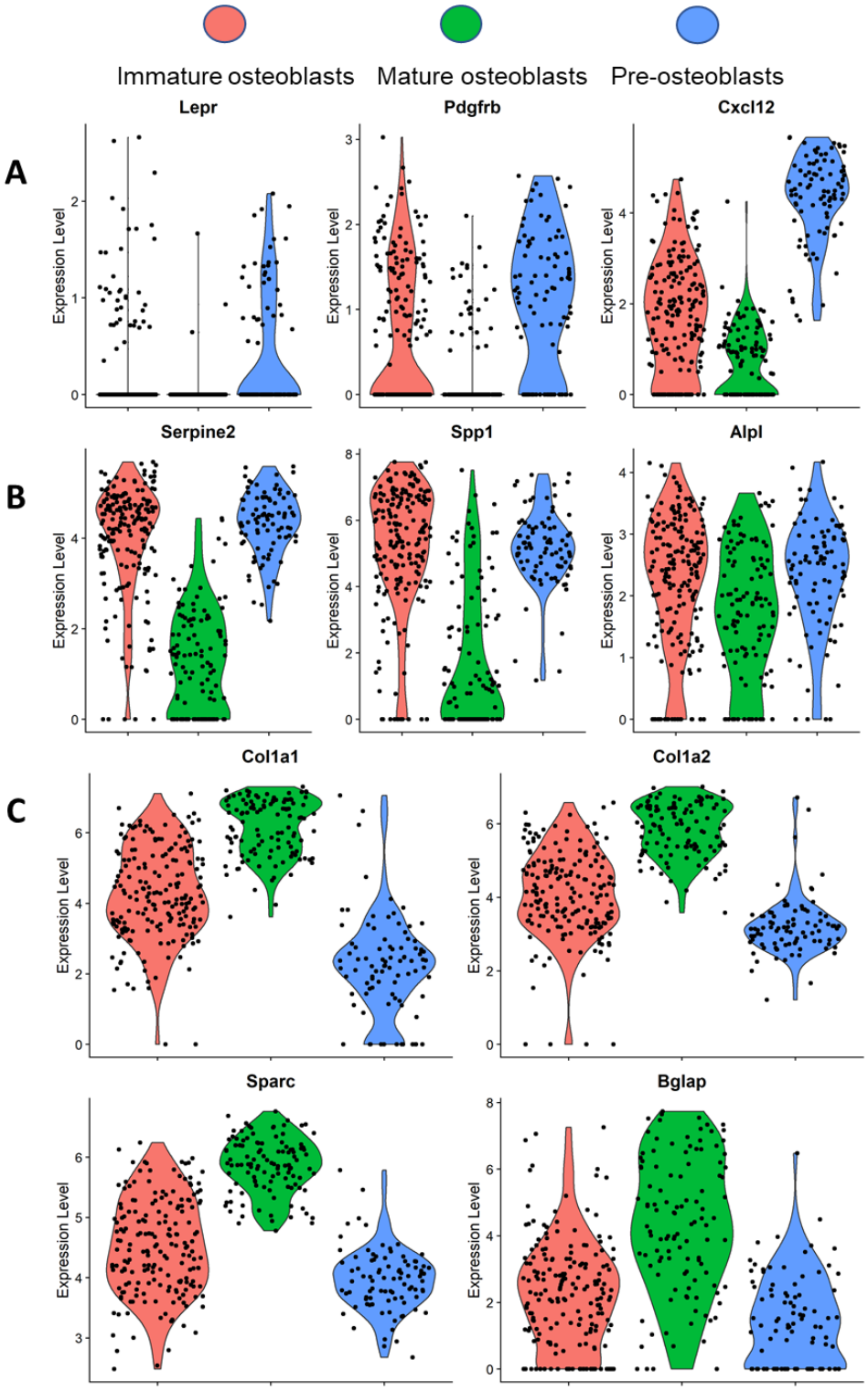


Figure 5.15 Identification of top markers defining osteoblast subsets. Sub-clustering of the osteoblast subset resulted in identification of 3 clusters of cells, all expressing osteoblast lineage markers OSX and RUNX2. Analysis of the top differentially expressed markers in the osteoblast cluster resulted in classification of the three clusters according to their maturation stage: pre-osteoblasts expressing stem and progenitor cell markers: *Lepr*, *Pdgfrb* and Cxcl12 **(A)**, immature osteoblasts expressing Serpine2 and Spp1 **(B)** and mature osteoblasts expressing transcripts that contribute to the bone ECM during ossification: *Col1a1*, *Col1a2*, *Bglap* and *Sparc*.

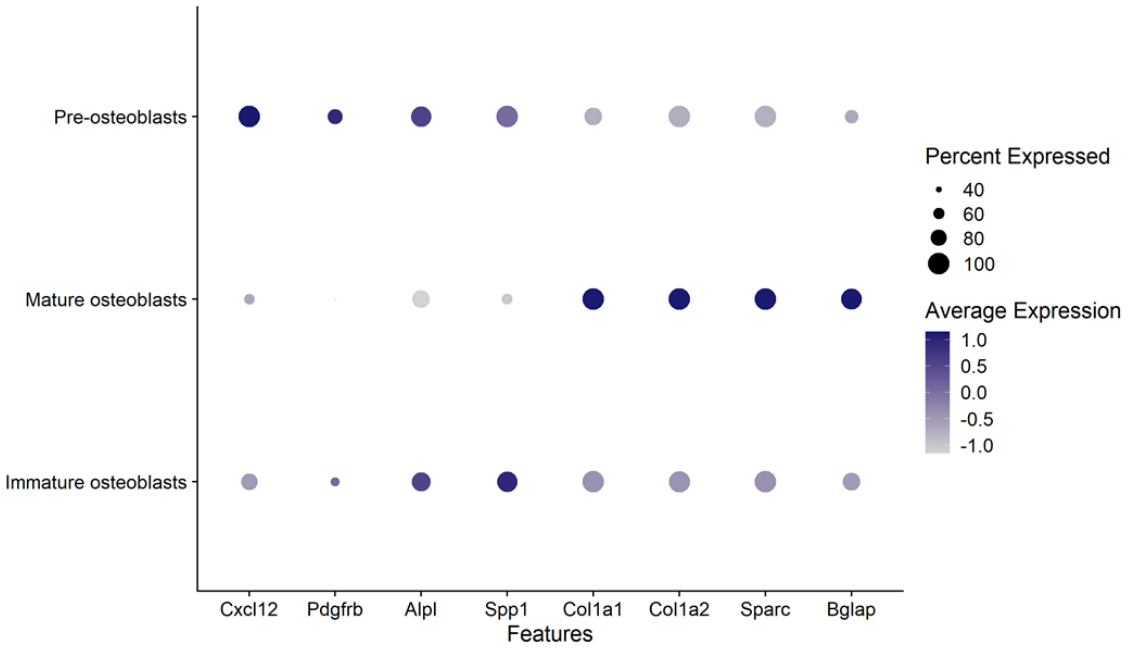


Figure 5.16. Osteoblast maturation gene signature. Dotplot showing gene expression levels across the three different stages of osteoblast maturation. The size of the dot encodes the percentage of cells within that cluster that express the gene studied, the colour encodes the average expression level across all cells within the cluster. Pre-osteoblasts express Cxcl12 and *Pdgfrb* at higher levels than immature and mature osteoblasts, Alpl is equally expressed by pre-osteoblasts as well as immature osteoblasts. Spp1 is expressed at the highest level in immature osteoblasts, however pre-osteoblasts also express it but at a lower level. Mature osteoblasts are characterised by expression of *Col1a1*, *Col1a2*, *Bglap* and *Sparc*. These markers are also expressed by immature osteoblast but at a considerably lower level.

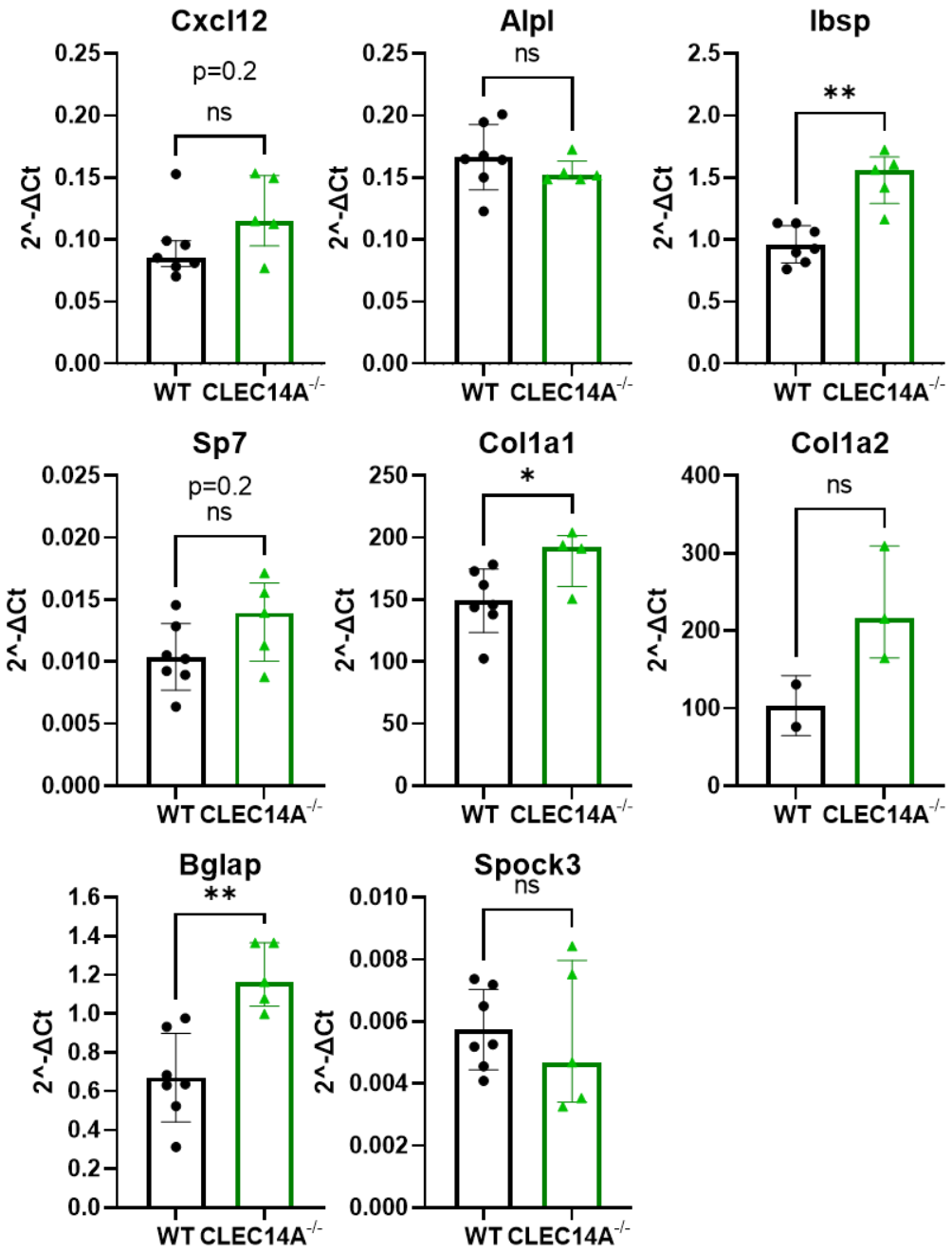


Figure 5.17. Analysis of expression of genes linked to osteoblast maturation and osteogenic activity. P4 pup calvarial lysates were subjected to RT qPCR analysis to dissect expression patterns of genes known to regulate commitment to osteoblast lineage and osteoblast maturation, gene expression was normalised to *Gapdh*, shown as arbitrary units (2^-ΔCT). Data is presented as Median ± IQR, a Mann-Whitney test was used to analyse the results. Plots represent results from two independent experiments (n=7 WT, n=5 CLEC14A$^{-/-}$), data points in each graph are representative of biological replicates .

5.7. Increased mineralisation activity of CLEC14A$^{-/-}$ osteoblasts in vitro

5.7.1. Expression pattern of osteoblast maturation genes - RT qPRC

Analysis of bulk RNA-sequencing of the mouse calvaria indicated changes in osteoblast maturation markers, suggesting a quicker maturation of osteoblasts or augmented mature osteoblast activity, both of which could lead to enhancement of bone mineralisation in CLEC14A$^{-/-}$ mice as presented in Chapter IV section 4.3. To test the maturity status of CLEC14A$^{-/-}$ calvarial osteoblasts, expression of osteoblast maturation genes was examined in osteoblasts isolated from the calvaria of WT and CLEC14A$^{-/-}$ neonatal P4 pups. PCR analysis of transcript levels were assessed for the most common markers of osteoblast maturation over 21 days *in vitro* in samples incubated with osteoinductive media enriched with β-glycerophosphate and L-ascorbic acid α or in expansion media (Figure 5.18). This experiment aimed to test the hypothesis that CLEC14A$^{-/-}$ isolated osteoblasts are more mature and in response to osteoinduction stimulation they can produce markers of matrix mineralisation earlier than WT osteoblasts.

Gene expression was determined relative to that of *Gapdh* by quantitative PCR (RT qPCR), *B2m* was also incorporated in the experimental design and similar trends were reported when gene expression was calculated relative to *B2m* (not shown). Baseline expression levels of all genes examined were compared at day 0 (before osteoinduction) in WT and CLEC14A$^{-/-}$ osteoblasts and no differences in transcript levels were identified (Figure 5.19). No significant changes were identified in gene expression for pre-osteoblast markers *Cxcl12* or Pdgfrb (Figure 5.20 A-B). A trend for downregulation in expression was observed in response to the

differentiation treatment, this was most evident at days 8 and 12, however, this did not reach statistical significance. RT qPCR analysis also showed minimal changes in the expression of the osteolineage marker *Sp7* across all the timepoints studied, a transient significant increase in *Sp7* expression was noted after 4 days in culture in the osteoblasts treated with differentiation media in both WT and CLEC14A$^{-/-}$ samples (Figure 5.20 C). The mature osteoblast marker *Col1a1* was expressed at higher levels than the housekeeping gene *Gapdh* throughout all the time points investigated, however, culturing over 21 days with osteoinduction media failed to increase *Col1a1* expression (Figure 5.22 A). *Bglap* mRNA levels increased in both WT and CLEC14A$^{-/-}$ osteoblasts in response to maturation stimuli, this reached statistical significance at days 8 and 12; limited *Bglap* expression was noted in all osteoblast groups at day 16 and 21.

Increased *Alpl* expression in calvarial osteoblasts, was observed in response to differentiation treatment in both WT control and CLEC14A$^{-/-}$ samples, CLEC14A$^{-/-}$ osteoblasts reach their peak *Alpl* expression at day 4, at this timepoint *Alpl* expression was significantly increased in CLEC14A$^{-/-}$ but not in WT control osteoblasts. In contrast, peak *Alpl* expression in WT osteoblasts was only observed 8 days later, at day 12. Following achievement of peak expression, mRNA transcript levels decreased in a time-dependent fashion in both groups. Given the increase in *Alpl* mRNA transcripts in CLEC14A$^{-/-}$ isolated osteoblasts at day 4, ALPL activity was investigated at days 6, 8 and 10 in calvarial osteoblasts in culture. Osteoblasts were cultured with the same experimental parameters as explained in sections 5.6. and 2.13 (Figure 5.21). I*n vitro* osteoblast proliferation was explored from the start of the experiment every two days, up until day 10 to ensure that any changes identified in ALPL activity did not originate from a change in osteoblast proliferation as the experimental setup is sensitive to cell number. Osteoblast proliferation was interrogated by counting cells at the same

timepoints as the ones investigated for examination of ALPL activity. Cell numbers increased steadily over time in all treatment groups, at days 8 and 10 higher numbers of cells were observed in samples treated with the osteoinductive media. A minor delay in proliferation was observed at day 8 in the treatment group in CLEC14A deficient osteoblasts as compared to the number of cells in WT control samples (Figure 5.23).

No changes were observed in WT and CLEC14A$^{-/-}$ samples in the basal media (undifferentiated group) across all the time points investigated. Additionally, no upregulation of ALPL activity was observed in these two groups over time. CLEC14A$^{-/-}$ osteoblasts presented increased ALPL activity compared to WT controls in response to osteoblast maturation treatment at days 6 and 8. Whilst a trend for increased ALPL activity was also observed in WT samples statistical significance was not achieved in this group. Considering the lack of expression of CLECA14A on osteoblasts, we theorised that calvarial osteoblasts isolated from CLEC14A$^{-/-}$ pups maintained a residual phenotype when exposed to osteoblast maturation stimulation at passage 1 (P1). To test this hypothesis, ALPL activity was examined in P2 WT and CLEC14A$^{-/-}$ osteoblasts, and indeed pre-culturing the osteoblasts for 2 passages before setting up the experiment has resulted in abrogation of the increase of ALPL activity in CLEC14A$^{-/-}$ osteoblasts treated with β-glycerophosphate and L-ascorbic acid over the ALPL activity measured in WT control osteoblasts (Figure 5.24).

5.7.1. Alizarin Red nodule staining

To follow up on the increased ALPL expression at both transcriptomic and protein levels, it was next important to establish if CLEC14A$^{-/-}$ osteoblasts were able to functionally produce more mineralised matrix by comparison to WT control osteoblasts.

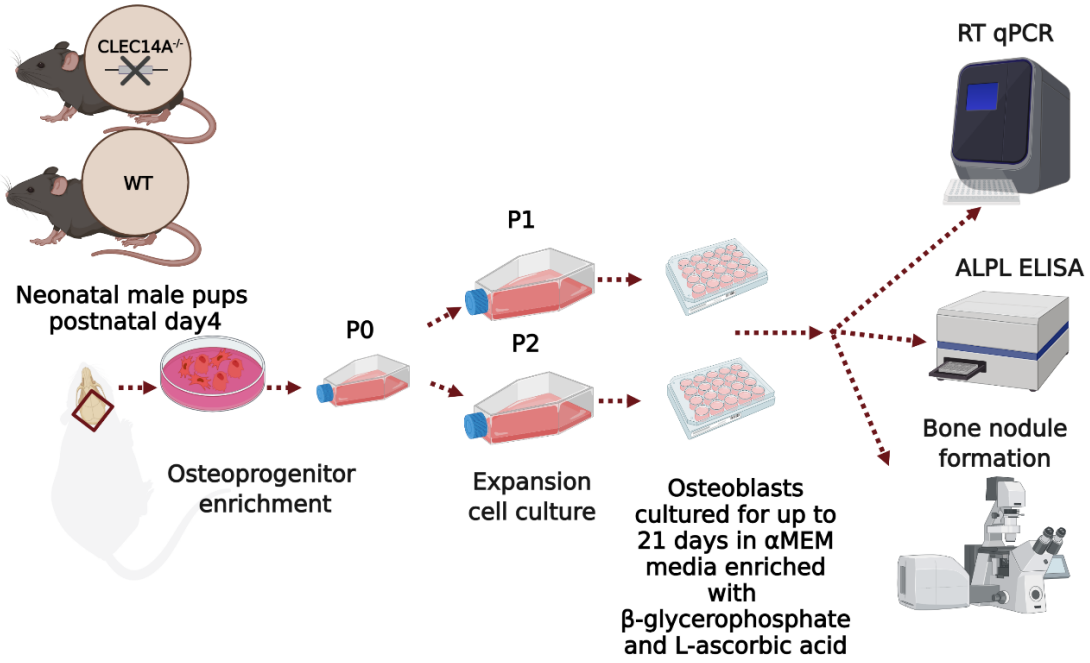


Figure 5.18. Analysis of in vitro osteoblast maturation. Calvarial osteoblasts were isolated from the calvaria of WT and CLEC14A$^{-/-}$ postnatal day 4 pups. Osteoblast lineage enriched cells were cultured in expansion media for up to 2 passages. Experiments were set up in 48-well plates and cells were seeded at a density of 8 x 10^3 cells/well, cells were cultured either in expansion media (undifferentiated control group) or in differentiation media (expansion media enriched with β-glycerophosphate and L-ascorbic acid) for up to 21 days. Cells were analysed at different time points using RT qPCR to investigate the changes in expression of osteoblast maturation genes, ELISA to examine the expression levels of alkaline phosphatase and alizarin red staining to inspect bone nodule formation.

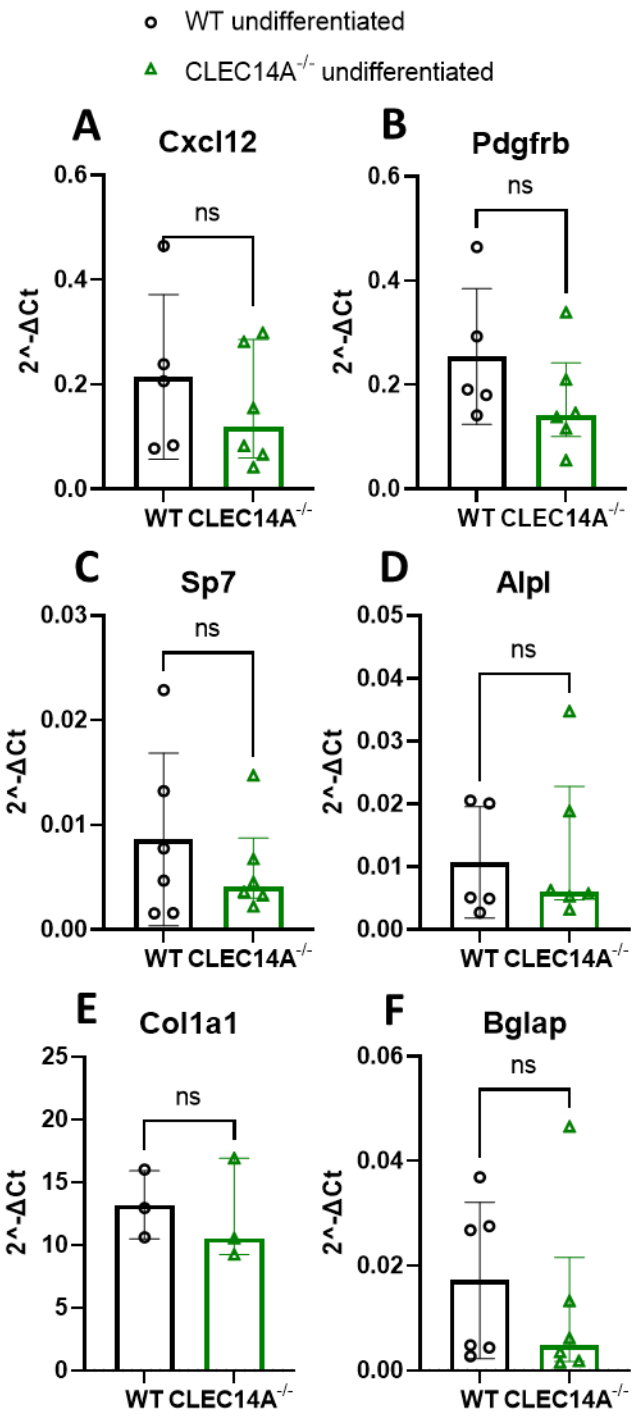


Figure 5.19. No baseline changes in skeletogenic markers gene expression identified between WT and CLEC14A$^{-/-}$ isolated osteoblasts. Calvarial osteoblasts isolated from WT and CLEC14A$^{-/-}$ neonatal pups were cultured in expansion media for one passage, cells were setup in 48 well plates, and allowed to reach confluence over the next 2-3 days, at the beginning of the experiment, before stimulation with β-glycerophosphate and L-ascorbic acid, gene expression was analysed at day 0 in osteoblasts cultured in expansion media only. Data is presented as relative expression to *Gapdh*. No significant differences were identified between WT and CLEC14A$^{-/-}$ samples for **A)** *Cxcl12* **B)** *Pdgfrb* **C)** *Sp7* **D)** *Alpl* **E)** *Col1a1* **F)** *Bglap*. Data is collated from two independent experiments, N=6 for WT, N=5 for CLEC14A$^{-/-}$. Results were analysed with a Mann-Whitney test, data is presented as Median ± IQR, ns – not significant.

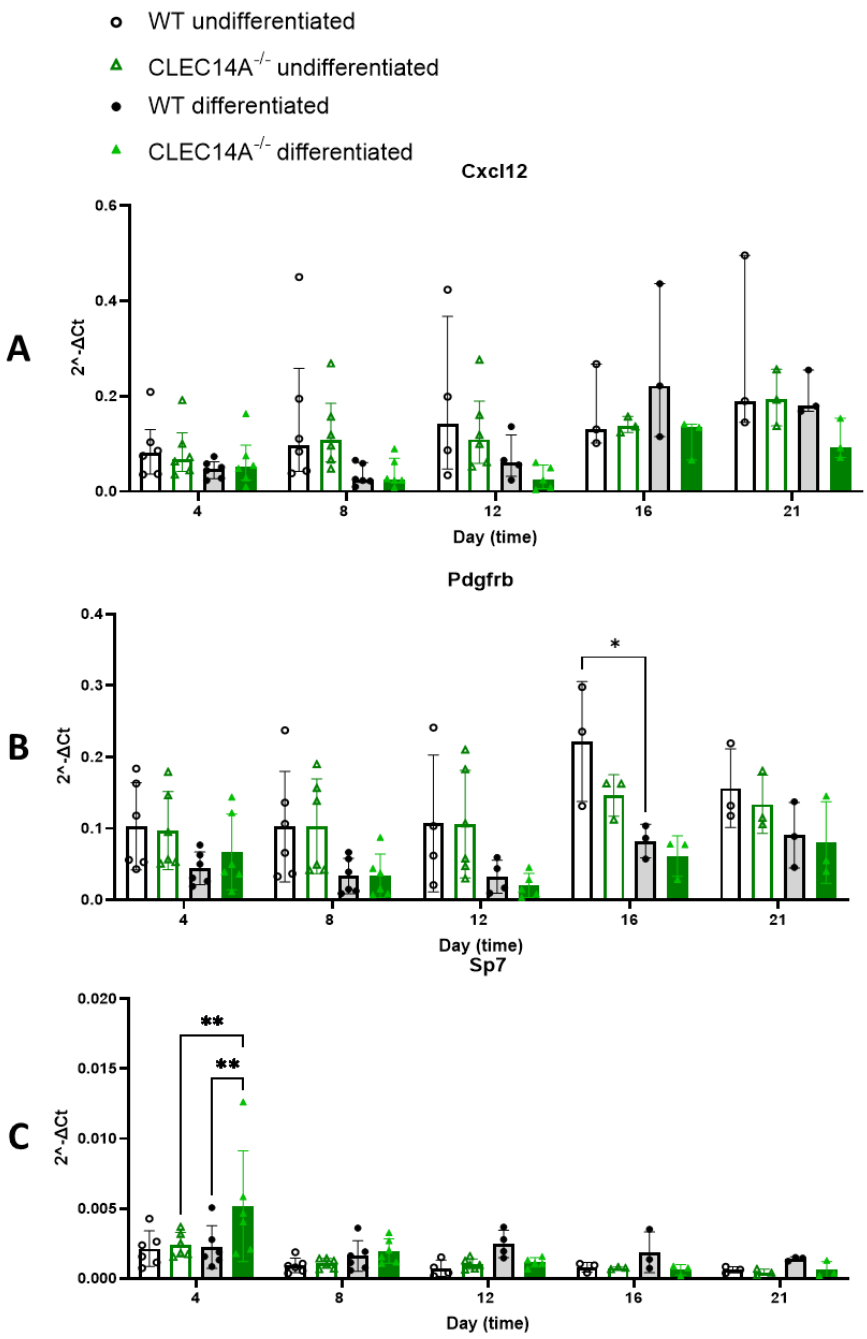


Figure 5.20. No significant changes in expression of markers of osteoblast immaturity and lineage commitment over 21 days in culture. Expression of **A)** *Cxcl12* and **B)** *Pdgfrb* at mRNA level was analysed by RT qPCR in osteoblasts cultured for up to 21 days with or without β-glycerophosphate and L-ascorbic acid. No significant changes were identified in gene expression for either Cxcl12 or *Pdgfrb*. **C)** RT qPCR analysis shows minimal changes in the expression of the osteolineage marker *Sp7* across all the timepoints studied. β-glycerophosphate and L-ascorbic acid treated groups are labelled WT differentiated and CLEC14A$^{-/-}$ differentiated, osteoblasts cultured in expansion media in the absence of β-glycerophosphate and L-ascorbic acid were labelled undifferentiated WT and undifferentiated CLEC14A$^{-/-}$. Data is presented as relative expression to *Gapdh*. Sample size is variable and is represented by each individual dot in the graphs (N=3-5), data was obtained from 2 independent experiments. Results were analysed with a two-way ANOVA followed by Dunnett's post hoc; data is presented as Mean ± SD.

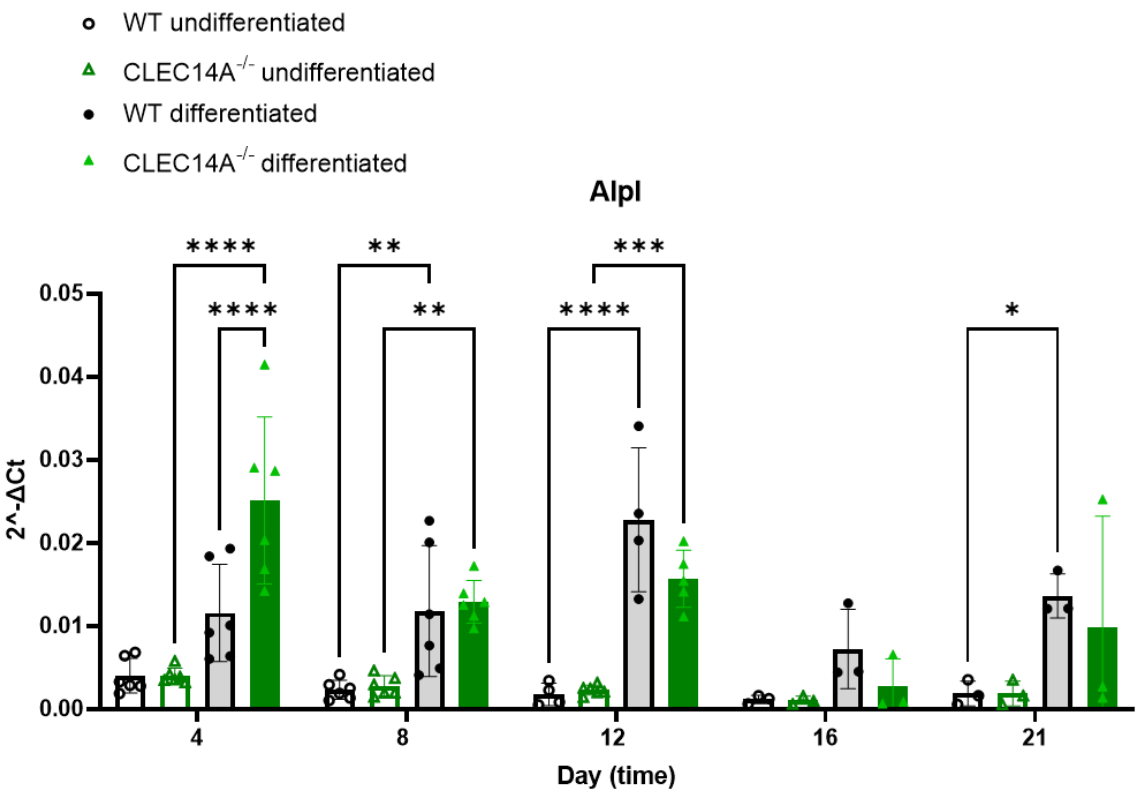


Figure 5.21 Tissue non-specific alkaline phosphatase gene expression peaks earlier in CLEC14A$^{-/-}$ isolated osteoblasts. Alpl mRNA expression was analysed by RT qPCR in calvarial osteoblasts. β-glycerophosphate and L-ascorbic acid treated group are labelled WT differentiated and CLEC14A$^{-/-}$ differentiated, osteoblasts cultured in the absence of β-glycerophosphate, and L-ascorbic acid are labelled undifferentiated WT and undifferentiated CLEC14A$^{-/-}$. Data is presented as relative expression to *Gapdh*. Sample size is variable and is represented by each individual dot in the graphs (N=3-5), data was obtained from 2 independent experiments and presented together. Results were analysed with a two-way ANOVA followed by Dunnett's correction for multiple testing, data is presented as Mean ± SD.

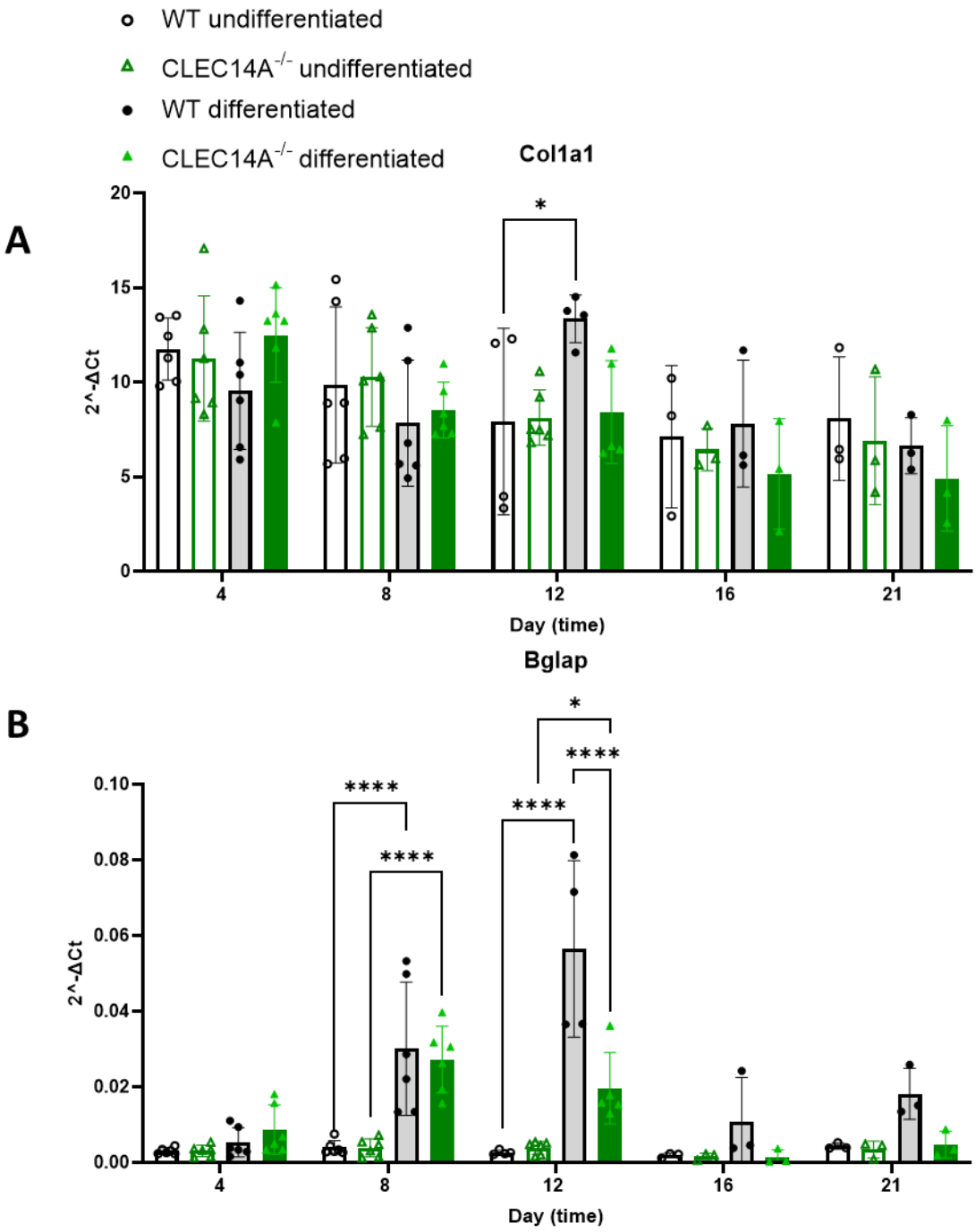
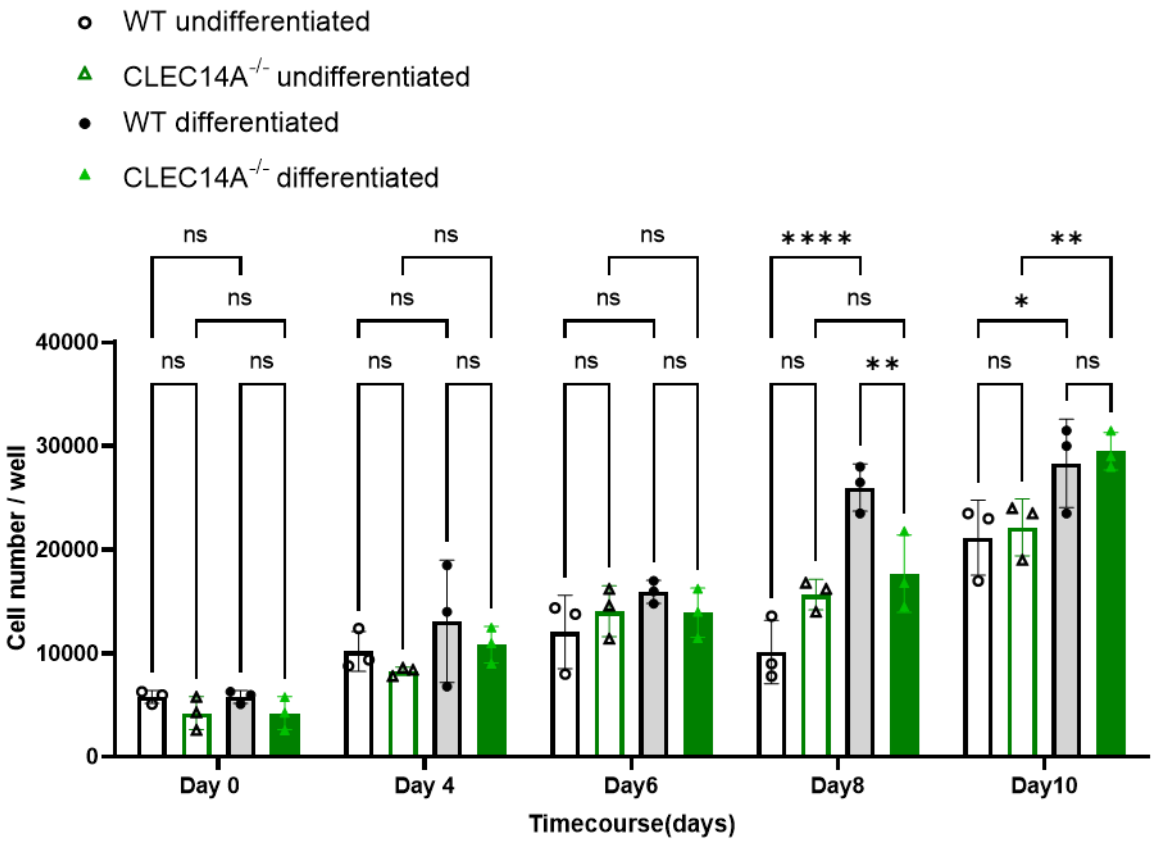


Figure 5.22. Changes in mRNA levels in mature osteoblast markers *Col1a1* and *Bglap* in WT and CLEC14A$^{-/-}$ calvarial osteoblasts over 21 days in culture. *Col1a1* **(A)** and *Bglap* **(B)** mRNA expression was analysed by RT qPCR in calvarial osteoblasts. β-glycerophosphate and L-ascorbic acid treated group are labelled WT differentiated and CLEC14A$^{-/-}$ differentiated, osteoblasts cultured in the absence of β-glycerophosphate and L-ascorbic acid were labelled undifferentiated WT and undifferentiated CLEC14A$^{-/-}$. Data is presented as relative expression to *Gapdh*. Sample size is variable and is represented by each individual dot in the graphs (N=3-5), data was obtained from 2 independent experiments. Results were analysed with a Two-Way ANOVA followed by Dunnett's post hoc; data is presented as Mean ± SD.


WT undifferentiated
CLEC14A-/- undifferentiated
WT differentiated
CLEC14A-/- differentiated
ns
ns
ns

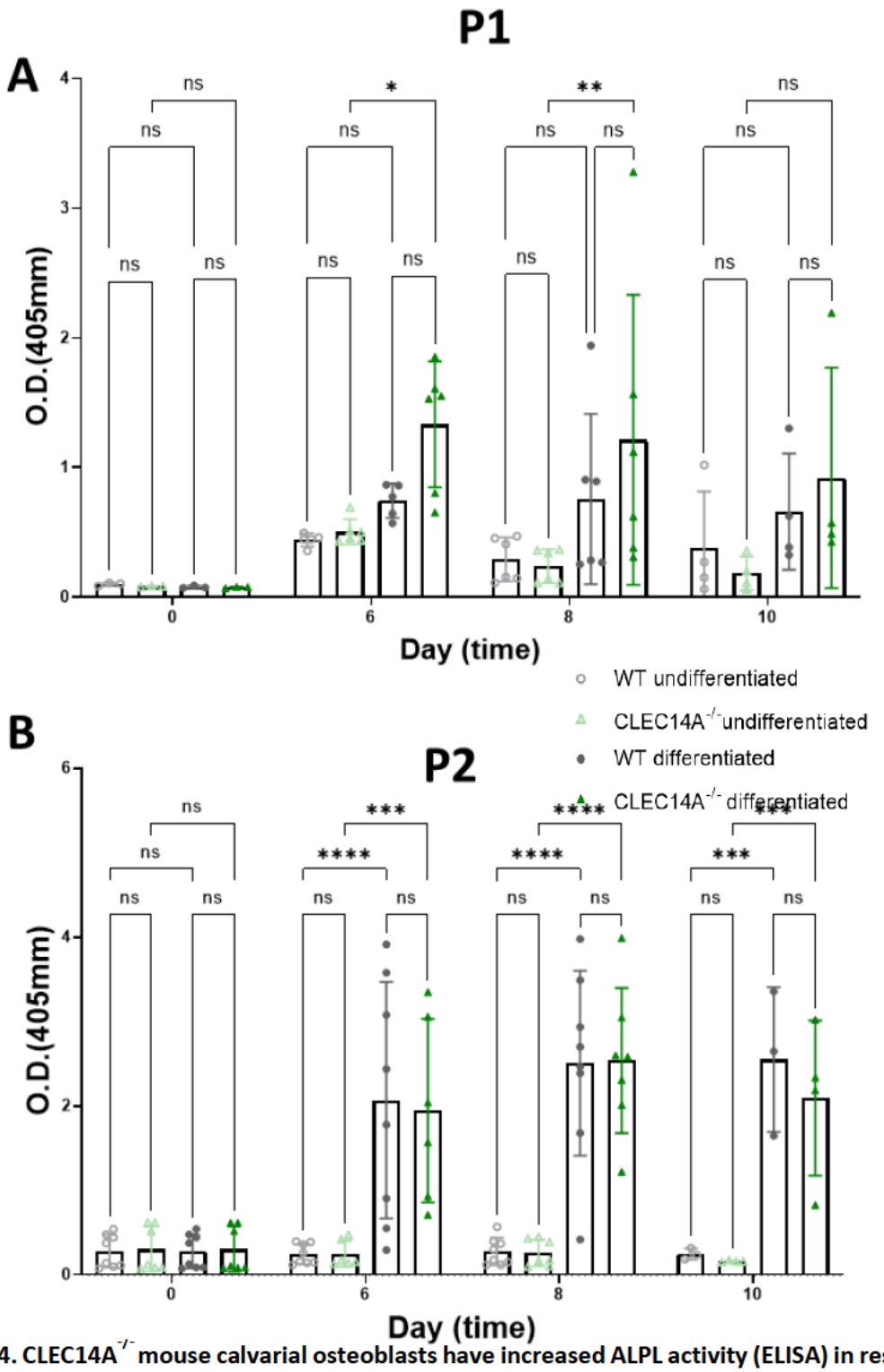


Figure 5.24. CLEC14A$^{-/-}$ mouse calvarial osteoblasts have increased ALPL activity (ELISA) in response to differentiation stimulation. Murine calvarial osteoblasts were isolated from WT and CLEC14A$^{-/-}$ neonatal pups at postnatal day 4 and osteogenesis was induced with osteoinduction media at passage 1 (P1) (**A**) or passage 2 (P2) **(B)**. ALPL activity was measured (ELISA) after 0,6, 8 and 10 days in culture, in WT and CLEC14A$^{-/-}$ osteoblasts that were incubated with either expansion media or osteoinduction media. Data is presented as optical density (O.D.), results are representative of two independent experiments, (graph A: N=3 for all measurements at day 0, N=5-6 for measurements at day 6, N=6 for all data at day 8, N=4 for all measurements at day 10; graph B: n=7-8 for all measurements for days 0-8, n=3-4 for all measurements for day 10). Results were analysed with a two-way ANOVA followed by Dunnett's post hoc, data is presented as Mean ± SD. * $p<0.05$, ** $p<0.01$, *** $p<0.001$.

Maturation of calvarial osteoblasts isolated from WT and CLEC14A$^{-/-}$ pup calvaria was investigated over 18 days to assess the mineralisation capacity of osteoblasts in response to genetic deficiency of CLEC14A. Bone nodules were counterstained with alizarin red, an anthraquinone family red dye commonly utilised to visualise calcified elements of the skeleton due to its capacity to bind calcium and form alizarin red – calcium complexes that are readily visible under an optical microscope (486). Percentage area covered by bone nodules was quantitated and showed increased mineralisation in CLEC14A$^{-/-}$ samples at day 18 but not at day 16 (Figure 5.25).

5.7.2. P1NP

The tertiary structure of mature type I collagen is organised as a triple helix composed of two α1 and one α2 type I collagen chains (COL1A1 and Col1a2 respectively). COL1A1 and Col1a2 chains are initially synthetised as immature type I collagen molecules (procollagen) with pro-peptides flanking the mature region of the molecule at both the N- and C-termini (487). The blood circulating N-terminus peptide resulting from the posttranslational cleavage of type I procollagen, procollagen Type I N-terminal pro-peptide (P1NP), has been proposed as a biomarker which can be used for assessment of bone formation. Serum circulating P1NP was measured in 4- and 30-week old WT and CLEC14A$^{-/-}$ mice with the aid of a P1NP competitive ELISA which detects the trimeric form of P1NP (488). A striking decrease in the concentration of P1NP was observed in 30-week-old mice compared to the younger 4-week-old juvenile mice, however no changes were identified when comparing P1NP expression in WT and CLEC14A$^{-/-}$ mice (Figure 5.26).

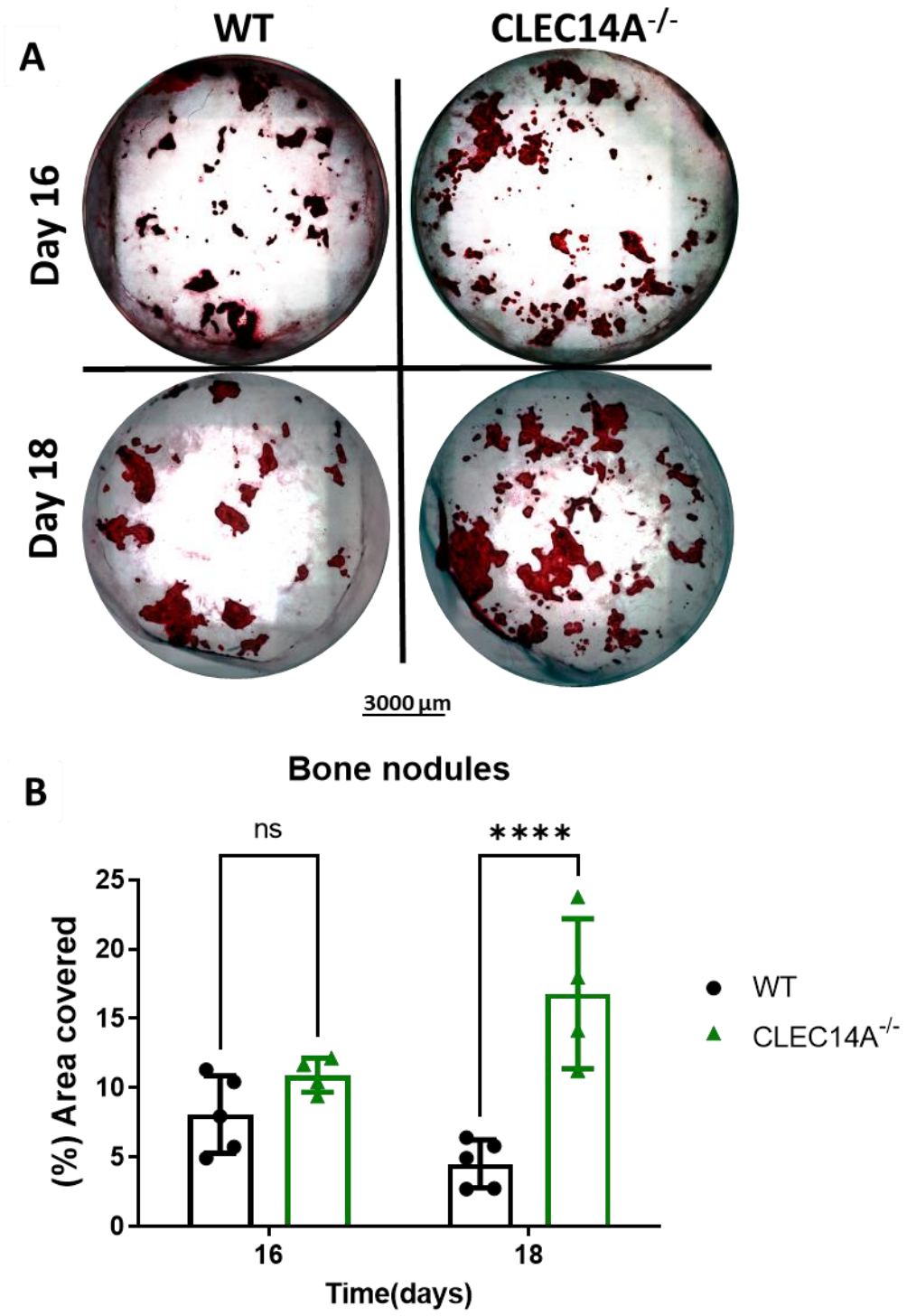


Figure 5.25. CLEC14A$^{-/-}$ calvarial osteoblasts have an increased bone mineral coverage over 18 days in culture. *Col1a1* and *Bglap* mRNA expression was analysed by RT qPCR in calvarial osteoblasts. β-glycerophosphate and L-ascorbic acid treated group are labelled WT differentiated and CLEC14A$^{-/-}$ differentiated, osteoblasts cultured in the absence of β-glycerophosphate and L-ascorbic acid were labelled undifferentiated WT and undifferentiated CLEC14A$^{-/-}$. Data is presented as relative expression to *Gapdh*. Sample size is variable and is represented by each individual dot in the graphs (N=3-5), data was obtained from 2 independent experiments. Results were analysed with a two-way ANOVA followed by Dunnett's post hoc, data is presented as Mean ± SD, ns- not significant, **** p<0.0001.

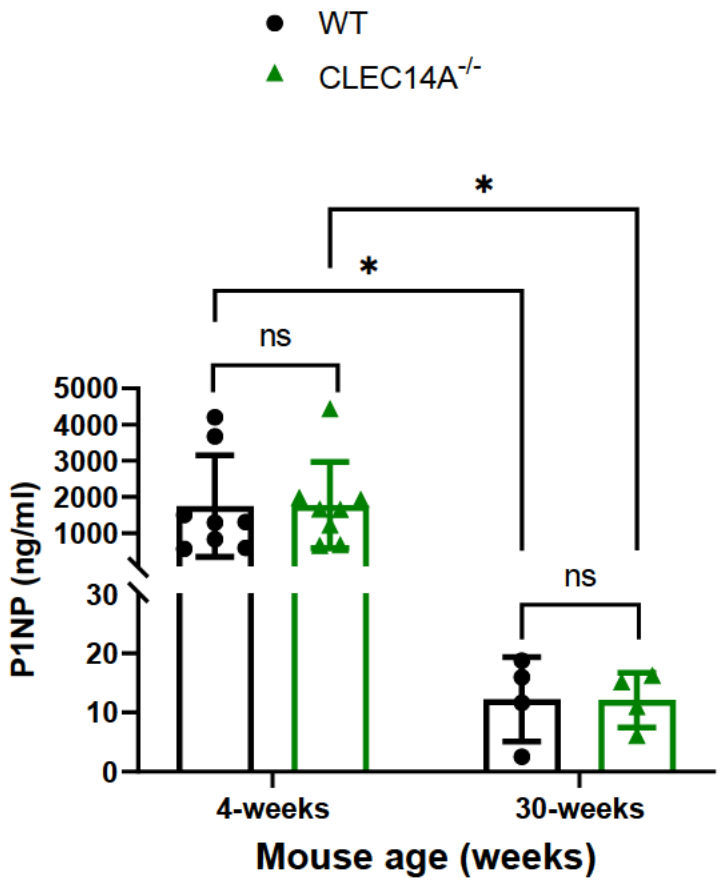


Figure 5.26. CLEC14A$^{-/-}$ does not affect serum circulating pro-collagen levels (P1NP). Serum was collected from 4-week and 30-week-old WT and CLEC14A$^{-/-}$ male mice via cardiac bleeding to measure the circulating levels of P1NP. Sample size is represented by each individual dot in the graphs (N=8 for 4-week-old mouse samples, N=4 for 30-weeks old samples), data was obtained from 2 independent experiments. Results were analysed with two-way ANOVA followed by Dunnett's post hoc; data is presented as Mean ± SD. * $p<0.05$.

5.8. Discussion

5.8.1. Summary and interpretation of molecular and functional changes pertaining to osteoblast maturation in response to CLEC14A deficiency

The molecular changes identified by bulk RNA sequencing of CLEC14A$^{-/-}$ calvarial lysates support our hypothesis that CLEC14A is a negative regulator of bone formation. In support of this theory, cells isolated from the murine calvaria presented enrichment of genes with known functions in bone formation (Figure 5.7, Figure 5.10). Gene sets identified for this genotype included: endochondral ossification; type I collagen synthesis; regulation of SLITs and ROBO receptors; and mTORC1 signalling (Figure 5.3, Appendix Figure 9.3) - all pathways previously shown to regulate osteoblast lineage commitment and maturation (172, 489-494). RNA sequencing and RT qPCR analysis of CLEC14A$^{-/-}$ calvaria lysates identified *Sp7*, *Col1a1*, *Col1a2*, *Alpl* and Ibsp as contributors whose likely concerted activity regulates osteoblast differentiation and maturation in CLEC14A$^{-/-}$ mice (Figure 5.3, Figure 5.7, Appendix Figure 9.4, Figure 9.5). The increase in both early (*Sp7*) and late (*Alpl*, Ibsp, *Col1a1*, *Col1a2*) osteolineage markers identified in the RNA sequencing dataset, suggest a balanced osteogenic differentiation in CLEC14A knock out mice, indicating a controlled and balanced differentiation and maturation of osteoblasts. This is also observed at the cellular level in bone sections, in neonatal (P4) and juvenile mice (4-weeks old), as demonstrated in chapter III, section 3.7.

Further arguing for a role played by CLEC14A in bone mineralisation CLEC14A$^{-/-}$ primary calvarial osteoblasts presented with an increase in ALPL expression (Figure 5.24) and an evident increase in connectivity and in the number of nodules was observed in CLEC14A$^{-/-}$ samples (Figure 5.25).

5.8.2. Variation in patterns of expression of genes upregulated in response to osteoblast maturation

To further dissect the changes driven by CLEC14A in osteoblast maturation, primary calvarial mouse osteoblasts were used in *in vitro* osteoblast monoculture and expression of osteoblast maturation genes and proteins was examined. Osteoblasts were isolated from WT and CLEC14A$^{-/-}$ calvaria and cultured *in vitro* to test the effect imprinted by CLEC14A deficiency in EC. Calvarial-isolated osteoblasts have been shown to produce and release type I collagen and alkaline phosphatase. In addition, they can also generate mineralized bone nodules containing hydroxyapatite crystals when cultured with β-glycerophosphate and L-ascorbic acid (495). Hence, primary calvarial mouse osteoblasts represented an appropriate osteoblast cell type to investigate the role of CLEC14A in osteoblast maturation.

The osteoblast maturation molecular signature we constructed was identical to the differentiation transcriptomic trajectory recently published in another sc-RNA sequencing analysis of *Col1a1*$^{+}$ bone cells (54). Mirroring the same observations as the ones published by Yoshioka and colleagues, analysis of osteoblast clusters from the bone and bone marrow cell sc-RNA sequencing dataset (GSE128423), has identified constant expression of osteolineage markers *Sp7* and *Runx2* across all osteoblasts irrespective of their maturation stage. In addition, the high level of expression of Cxcl12 was also confined to MSC and pre-osteoblasts and the increase in mRNA levels for *Bglap* and *Col1a1* and Col1a2 were also confirmed to be characteristic of mature matrix depositing osteoblasts, reinforcing the relevance of *Col1a1*, Col1a2 and *Bglap* as markers of osteoblast maturation and activity, and that of Cxcl12 as a suitable indicator of cell stemness (Figure 5.16). RT q-PCR analysis of osteoblasts isolated from CLEC14A$^{-/-}$ and WT P4 pups and treated with osteoinductive media over 21 days revealed changes in the expression of transcripts relevant for osteoblast maturation. Sp7 and Col1a1

expression in both CLEC14A$^{-/-}$ and WT osteoblasts was unchanged throughout the entire course of the experiment (Figure 5.20, Figure 5.22). The lack of variation in *Sp7* gene expression across all maturation levels in sc-RNA seq analysis (GSE128423 dataset) and in the *in vitro* culturing of calvarial osteoblasts matches previously published sc-RNA seq in the bone, which also indicated no difference in *Sp7* expression between chondrocytes and osteoblasts in both the tibia and the humerus (53). Previous *in vitro* experiments using calvarial osteoblasts or other osteoblast cell lines also reported minimal changes in *Sp7* expression in response to osteoinductive stimulation (496). The lack of changes in *Sp7* expression in osteoblasts in culture indicates that the increased *Sp7* expression identified in whole calvaria lysates originates from an increase in the number of *Sp7* expression osteoblasts rather than from an increase in *Sp7* expression in each individual cell. The lack of changes in *Col1a1* expression from neonatal primary calvarial mouse cells in response to β- glycerophosphate and L-ascorbic acid treatment was previously reported (283). We also noted that the relative measured expression of *Col1a1* in *in vitro* culturing of osteoblasts stimulated with osteinductive media was substantially lower in cultured osteoblasts than in calvaria lysates, when measured by RT qPCR. This might indicate alternative cellular sources of *Col1a1* that contribute to the expression levels detected in lysates, we mined the sc-RNA seq dataset (dataset GSE128423) to identify *Col1a1* patterns of expression in the murine long bone (Figure 5.11 A-B) and identified fibroblasts and chondrocytes as alternative sources of *Col1a1*.

Increases in *Alpl* and *Bglap* expression have previously been reported in calvarial osteoblasts in response to maturation signals (283, 497-499). Our WT control data recapitulates the same timeline of variation in *Alpl* expression in cultured calvarial osteoblasts, as previously

reported. Specifically, significantly increased *Alpl* mRNA transcripts were reported at day 4, *Alpl* expression constantly increased over time and plateaued by day 9 (283).

The lack of striking changes in genes of the osteoblast maturation signature in CLEC14A$^{-/-}$ samples cultured in vitro (*Cxcl12*, *Bglap*) (Figure 5.20, Figure 5.22), as opposed to those isolated and analysed directly after isolation (Figure 5.17), and in contrast to the RNA sequencing analysis, suggest a dependency on the crosstalk, and potentially direct contact, of osteoblasts with blood vessel EC for the CLEC14A$^{-/-}$ phenotype.

A plateau in gene expression in all four treatment groups of calvarial osteoblasts was observed at days 16 and 21 in culture, indicating a downregulation of osteoblast activity at these two timepoints. This phenomenon could be triggered by cells reaching high densities in 2D culture, this has previously been shown to inhibit osteoblast activity. Attainment of high cell densities is highly probable, as folding/contraction of the cellular and matrix layers towards the centre of the plate was observed equally in all wells. The possibility that matrix encasing induces cell apoptosis in these cultures cannot be excluded either. For these reasons, caution has been taken when interpreting the relevance of the gene expression levels measured for days 16 and 21. It is also important to note that a major limitation of primary calvarial osteoblast cell culture is their heterogeneous nature. Osteoblasts at varying stages of maturity are likely isolated within the culture which, in addition, contain different levels of contaminating fibroblasts and periosteal cells (495).

5.8.3. Changes in ALPL activity in CLEC14A$^{-/-}$ osteoblasts

Detectable expression of ALPL has been previously reported from culture day 6 in primary calvaria osteoblasts (283, 500). The increase in ALPL activity in passage 1 (P1) CLEC14A$^{-/-}$ isolated osteoblasts after 6 days in culture with osteoblast maturation media (**Figure 5.24** A) was subsequent to a significant upregulation of *Alpl* transcription at day 4 (Figure 5.21). The failure of WT osteoblasts to reach a statistically significant increase in ALPL in response to osteoinduction treatment does not represent a failure to mineralise and produce ALPL per se, but rather a lower expression, given the high variation of data in this experiment. Prior to drawing firm conclusions, a third experimental repeat is warranted to further explore this matter. Moreover, the lack of difference in ALPL expression in P2 cultured osteoblasts between WT and CLEC14A$^{-/-}$ (Figure 5.24 B), might indicate imprinting of osteoblasts isolated from CLEC14A$^{-/-}$ with an osteogenic phenotype which is lost following 2 passages in *in vitro* culture.

5.8.4. Type I collagen expression in CLEC14A$^{-/-}$ isolated osteoblasts

Serum circulating P1NP analysis has demonstrated a reduction in this marker of bone formation in both WT and CLEC14A$^{-/-}$ mice in response to ageing. This is in alignment with the decrease in bone formation capacity associated with ageing (189), explaining the remarkable drop observed in mature adult 30-week-old male mice by comparison to juvenile 4-week-old mice. However, no changes in P1NP were observed between CLEC14A$^{-/-}$ and WT samples.

In spite of the increased expression of *Col1a1* and Col1a2 in CLEC14A$^{-/-}$ mice as indicated by our RNA sequencing data, no changes were measured in any of the experiments conducted in this project: no changes in *Col1a1* expression were noticed in osteoblasts cultured with

osteoblast maturation media (Figure 5.22); no differences in P1NP were measured in the serum (Figure 5.26); and finally, no alterations in the area covered by COL1A1 was observed in bone sections of 4-week old mice (section 3.7,Figure 3.33). In this context, the possibility that the mouse age targeted in our studies is not suitable for P1NP changes in CLEC14A deficient mice cannot be excluded. The bulk RNA sequencing data, which analysed *Col1a1* and *Col1a2* expression in P4 calvaria lysates has indeed identified upregulation of type I collagen genes in CLEC14A$^{-/-}$. The increase in type I collagen could be transient in CLEC14A deficient mice, and if any changes in type I collagen are present in mice of this genotype, it is possible that these occur much earlier in life, prior to the time points investigated. To develop this hypothesis further, it would be valuable to explore P1NP levels and type I collagen patterning in the bone in mice younger than 4 weeks of age.

5.8.5. Additional potential biological and functional implications for the enriched or differentially expressed genes identified by bulk RNA sequencing of the CLEC14A$^{-/-}$ pup calvaria

5.8.5.1. Predicted changes in vessel permeability in CLEC14A$^{-/-}$ pups

Transcript analysis of the CLEC14A$^{-/-}$ and WT control calvaria cells revealed the molecular pathways altered in response to genetic deletion of CLEC14A. For instance, genes in the KEGG "Tight Junction Molecules" gene-set were downregulated in CLEC14A$^{-/-}$ samples compared to WT controls. This implies potential changes in the vascular function of CLEC14A$^{-/-}$ mice. Tight junction transmembrane proteins regulate cell adhesion by forming large protein complexes which act as diffusion barriers to restrict paracellular permeability (501). In the bone, tight junction proteins have been shown to be equally expressed by bone cells such as osteoblasts and osteocytes (502, 503) as well as endothelial cells (504). Furthermore, tight junction molecules have the ability to mediate skeletal development (503, 505-507), providing a good

reason to speculate that the downregulation of tight junction molecules in CLEC14A$^{-/-}$ samples might have an effect on the bone phenotype we observed in these mice.

The sustained downregulation of tight junction molecules (Figure 5.5) as well as cell adhesion molecules (*Cldn5* and Cdh5, Figure 5.12) in CLEC14A$^{-/-}$ mice could alter blood vessel functionality, resulting in increased bone vessel permeability and elevated extracellular lipid availability. Blood vessel-derived lipids have been previously shown to be essential for osteogenic differentiation of skeletal progenitor cells into osteoblasts (151). Previously published work on CLEC14A knock-out mice, reported an increase in blood vessel permeability in the neonatal mouse pup brain (414) and increased haemorrhage in murine tumours implanted in CLEC14A deficient mice (347). Vessel permeability in the absence of CLEC14A is further augmented in response to ischemia reperfusion injury in the brain of adult mice (414). Blood flow during reperfusion is greatly increased compared to baseline (439), in high similitude to the high blood flow velocity reported in H-type vessels in the bone (138). Hence, it is possible that the bone metaphysis of CLEC14A$^{-/-}$ mice have increased blood vessel permeability which allows diffusion of extracellular lipids prompting increased osteoblast differentiation. To further test this hypothesis, bone blood vessel permeability could be tested *In vivo* using administration of fluorescently tagged BSA and intravital microscopy imaging of the bone.

It is also plausible to hypothesise that the concerted and independent molecular changes reported for the ECM receptor interaction (Figure 5.6), tight junction (Figure 5.5) and cell adhesion molecules (Figure 5.8) could negatively influence cell contacts between H-type EC and osteoblasts, coercing maturation of immature osteoblasts that have a perivascular localisation in the bone metaphysis. Previous work has indeed confirmed that downregulation of *Lama5* and integrin expression on EC induces changes in the organisation and morphology

of the type-H vascular bed, which is also accompanied by changes in osteolineage commitment (53, 136).

Our working hypothesis is that the interaction between CLEC14A, MMRN2 and CD248, retains osteoblasts close to the bone vasculature during postnatal bone growth. Ablation of CLEC14A could result in abnormal osteoblast-EC interaction resulting in maturation of osteoblasts quicker in CLEC14A deficient mice than in WT control. However, we cannot exclude the possibility that an indirect effect contributes to the phenotype observed in CLEC14A$^{-/-}$ mice. The downregulation of expression of the molecules discussed above, in response to CLEC14A genetic deletion, might be one mean of achieving this effect.

Improper osteoblast EC interactions leading to maturation of osteoblasts could also be triggered by downregulation of integrins on the surface of EC. Downregulation of the transcriptome linked to cell junction molecules in CLEC14A null samples might be responsible for the matched downregulation of integrin receptors, as the former have been previously shown to be main regulators for the production, expression, and function of the later (508). Reduction of integrin expression on EC could affect the interaction of osteoblasts with blood vessels resulting in alterations of osteoblast angiotropism or osteoblast maturation.

5.8.5.2. Alteration of tissue remodelling and bone resorption in the skeletal system of CLEC14A$^{-/-}$ mice

The increase in CLEC14A$^{-/-}$ calvaria lysates in mRNA levels for metalloproteases such as *Mmp9, Mmp13, Timp1 and Timp2* - all recognised molecules which dissolve the ECM during

angiogenesis to allow for EC migration (501), might be favourable for the expansion of the H-type vascular front into the growth plate contributing to the increased bone length we reported in chapter IV for these mice (Figure 4.3)(2, 98).

In the bone metaphysis, MMP9 is expressed by EC, osteoblasts and septoclasts (2, 98). Recently published data has characterised MMP9 as a potent moderator of osteoblast migration, showing that this protein is expressed in the near vicinity of osteoblasts and blood vessels in the metaphysis (53). Previous research has shown that MMP9 is secreted to aid with tissue degradation and remodelling for expansion of blood vessels and migration of osteoblasts in the growth plate to induce longitudinal bone growth (20, 22).

Mining of Sc-RNA sequencing indicates that in the bone *Mmp13*, *Mmp14, Timp1 and Timp2* are almost exclusively expressed by osteoblasts, whilst *Adamts1* is mostly expressed by EC but also MSC. Considering the shared localisation of the expanding H-type vasculature and that of osteoblasts in the bone metaphysis it is plausible to speculate that CLEC14A$^{-/-}$ mice are characterised by differential tissue remodelling activity at the chondro-osseous junction which directly and indirectly contributes to the longer bones in this genotype. A clear understanding of the patterns and levels of expression of these metalloproteases will provide insights into the mechanistic role of these molecular changes, warranting further research.

5.8.5.3. Changes in the expression of CLEC14A regulators and interacting partners

Upregulation of *Klf2* and *Klf4* was identified in our calvaria sequencing data, increased expression was also validated with follow-up PCR experiments. Considering that both *Klf2* (509) and *Klf4* (unpublished data Roy Bicknell laboratory) have been shown to be upstream regulators of CLEC14A expression, the *Klf2* and *Klf4* upregulation can be explained as a

negative regulation loop response in an attempt to induce CLEC14A expression in the knock-out mice.

5.8.6. Limitations

Caution should be employed when interpreting molecular changes identified by bulk RNA sequencing. Whilst tissue preparation for cell isolation was conducted with matched WT and CLEC14A$^{-/-}$ samples, proportional representation of all cell types across experiments conducted in different days cannot be guaranteed. It is thus necessary to consider that some of the alterations in gene expression might reflect a change in the proportion of certain cell types in the whole sample warranting further validation of these observations in FACS sorted EC and osteoblasts.

It is useful to note that culturing of osteoblast isolated from CLEC14A$^{-/-}$ mice reflect changes imprinted into these cells before isolation from their local niche. To further and expand our understanding of the interaction between CLEC14A expressing EC and osteoblasts in bone formation EC-osteoblast co-cultures would constitute a necessary next step. This has been discussed in more detail in section 7.6.

5.8.7. Conclusion

In conclusion, the work presented in this chapter provides evidence to the argument that CLEC14A is a negative regulator of bone formation and that its germline deletion influences molecular regulation of osteoblast maturation to enhance bone formation. Altogether, data presented in this chapter has helped shed light into changes in the molecular repertoire of mice with a genetic deficiency of CLEC14A, furthering understanding of the biological

processes that may contribute to the cellular and morphometric changes identified in the skeletal system of CLEC14A$^{-/-}$ mice in chapters III and IV.

The enrichment in genes related to endochondral ossification and bone resorption provide a molecular explanation for the increased trabecular bone mass and increased calvaria mineralisation in CLEC14A$^{-/-}$ mice as demonstrated in sections 4.3 and 4.6, respectively. The subsequent osteoblast monoculture work helped validate ALPL as one of the key genes promoting increased osteoblast mineralisation; most likely contributing towards the increased osteoblast ECM mineralisation in the bone nodule assays, and to the osteoanabolic effect identified in CLEC14A$^{-/-}$ mice in Chapter IV. Furthermore, the osteoblast *in vitro* culture experiments demonstrate that CLEC14A$^{-/-}$ osteoblasts lose their propensity to mature earlier than WT osteoblasts following passage. This suggests that changes in CLEC14A$^{-/-}$ osteoblast activity are reliant on the local niche microenvironment. Once removed from this environment, they no longer retain their increased mineralisation activity. This is expected, given that CLEC14A expression is limited to endothelial cells and is not expressed on osteoblasts themselves, and provides additional evidence for the hypothesis that CLEC14A exerts its osteogenic modulation function via a mechanism which depends on the crosstalk between osteoblasts and EC.

6. THE ROLE OF CLEC14A AND ITS INTERACTION WITH MMRN2 IN BONE LOSS DURING OVARIECTOMY-INDUCED OSTEOPOROSIS

6.1. Introduction

Results presented in chapters III and IV have helped uncover the osteoregulatory role played by CLEC14A during bone formation in juvenile mice. Morphometric measurements of trabecular bone in the tibia of CLEC14A$^{-/-}$ mice show that once mice achieved peak bone mass, CLEC14A germline deletion no longer conferred them a trabecular bone mass advantage later in life (Figure 4.5). It is plausible to theorise that this is driven by retraction of the H-type vascular front in adult mice due to a cessation of the need for active angiogenesis as bone growth massively slows down as previously reported (145). To further our understanding of the context within which CLEC14A is important for bone formation and to determine if CLEC14A continuously participates in the regulation of bone formation or if this is limited to postnatal bone growth only, we examined the effect of CLEC14A deletion in ovariectomy-induced bone loss. Mice respond to ovary removal-induced oestrogen withdrawal with bone loss, which in this disease model simulates post-menopausal osteoporosis in humans (221, 510). Ovariectomy was induced in adult mice (12-weeks of age) once peak bone mass is achieved, an age at which H-type vessel number has dropped dramatically compared to the juvenile growth phase (145), data generated from these experiments will enable inference of the importance of CLEC14A in bone maintenance as opposed to bone development, a processes already studied in previous chapters. Here we tested the hypothesis that CLEC14A genetic deletion is protective against ovariectomy-induced bone loss. In addition, the role of the CLEC14A-MMRN2 interaction during ovariectomy-induced osteoporosis was studied, using antibodies that block the interaction as described previously described (1, 348).

6.2. Induction of osteoporosis by bilateral ovariectomy

Osteoporosis was induced in 12-week-old C57Bl/6J females by bilateral surgical removal of ovaries, a process herein referred to as ovariectomy (OVX). Tibiae were collected at 1-, 2- and 4- weeks post-OVX to establish a timeline for trabecular and cortical bone loss in this model (Figure 6.1). Successful induction of osteoporosis was confirmed utilising µCT analysis of the tibia (Figure 6.2 A-B). A significant reduction in BV/TV % was observed in response to OVX at 2- and 4-weeks after surgery as compared to tissue collected at the beginning of the experiment (week 0) (2-weeks: median BV/TV% of 13.36 vs 10.05, $p < 0.05$, week 0 vs week2; 4-weeks: median BV/TV% of 13.36 vs 7.51, $p < 0.05$ week o vs week 4) (Figure 6.2 B). A transient increase in trabecular thickness (Tb.Th) was noted in tibiae, 1-week post-surgery (mean Tb.Th (mm) of 0.055 vs 0.067, $p < 0.05$, week 0 vs week 1) (Figure 6.2 C). A constant and timepoint-dependant decrease in trabecular number was demonstrated in response to OVX, and significant reductions were reached 2- and 4-weeks post-surgery. Matching the same trend, a constant increase in trabecular separation was noted from week 0 to week 4 post-OVX, with a significant increase being observed at the final collection timepoint (Figure 6.2D and E). No significant changes were noted in the cortical compartment of tibiae of OVX mice (Figure 6.3) at any of the measured timepoints.

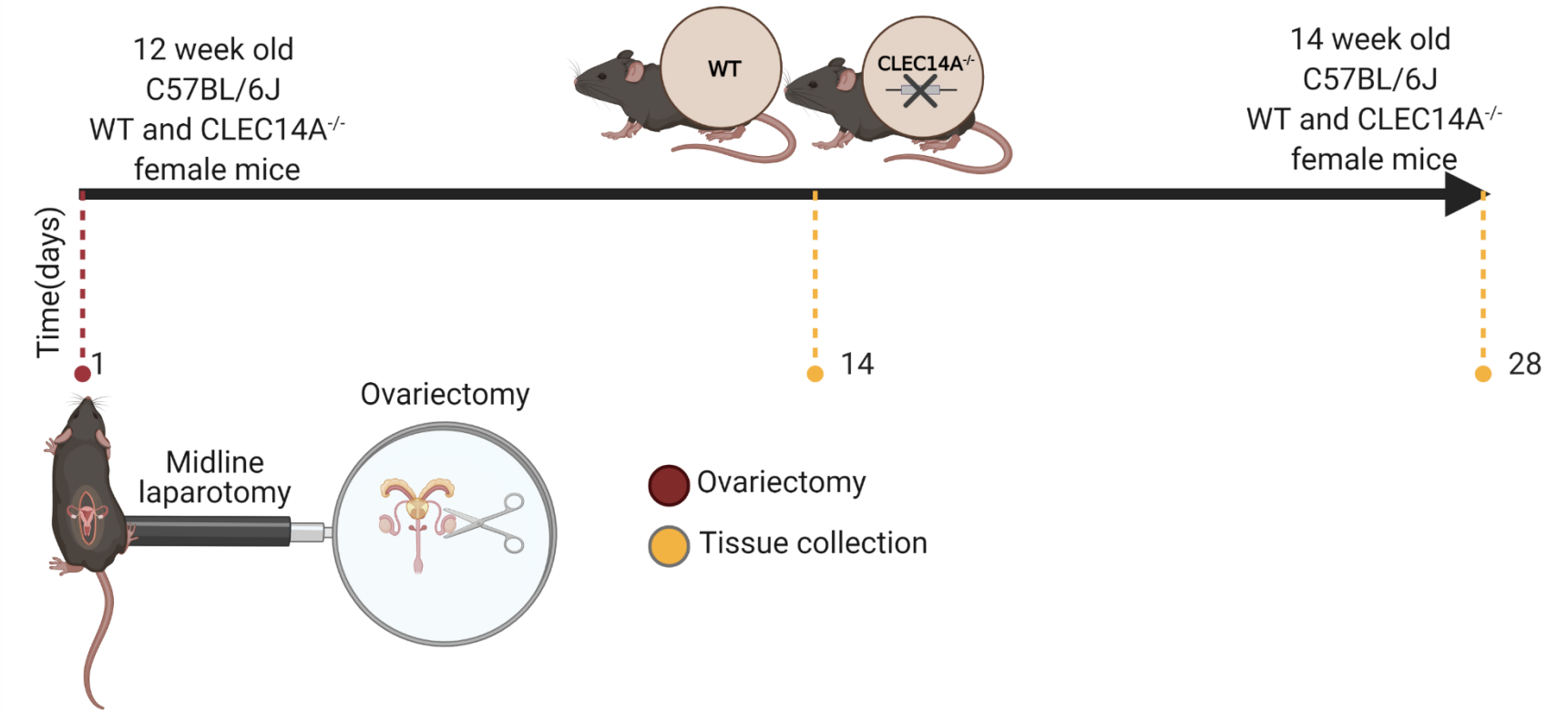


Figure 6.1. Induction of osteoporosis by bilateral ovariectomy (OVX). 12-week-old C57Bl/6J female mice were anesthetised, ovaries were removed through a midline laparotomy incision. Briefly, the ovarian fat pad was retracted outside of the peritoneal cavity through a small incision (< 1 cm), ovaries were separated from the oviduct, taking care not to rupture the uterus to limit the amount of inflammation and other surgical complications. Mice were allowed to recover, and tissue was collected at 1-, 2- and 4 weeks following surgery. Method development for this disease model was conducted in collaboration with Jonathan Lewis, another PhD student in the Naylor group.

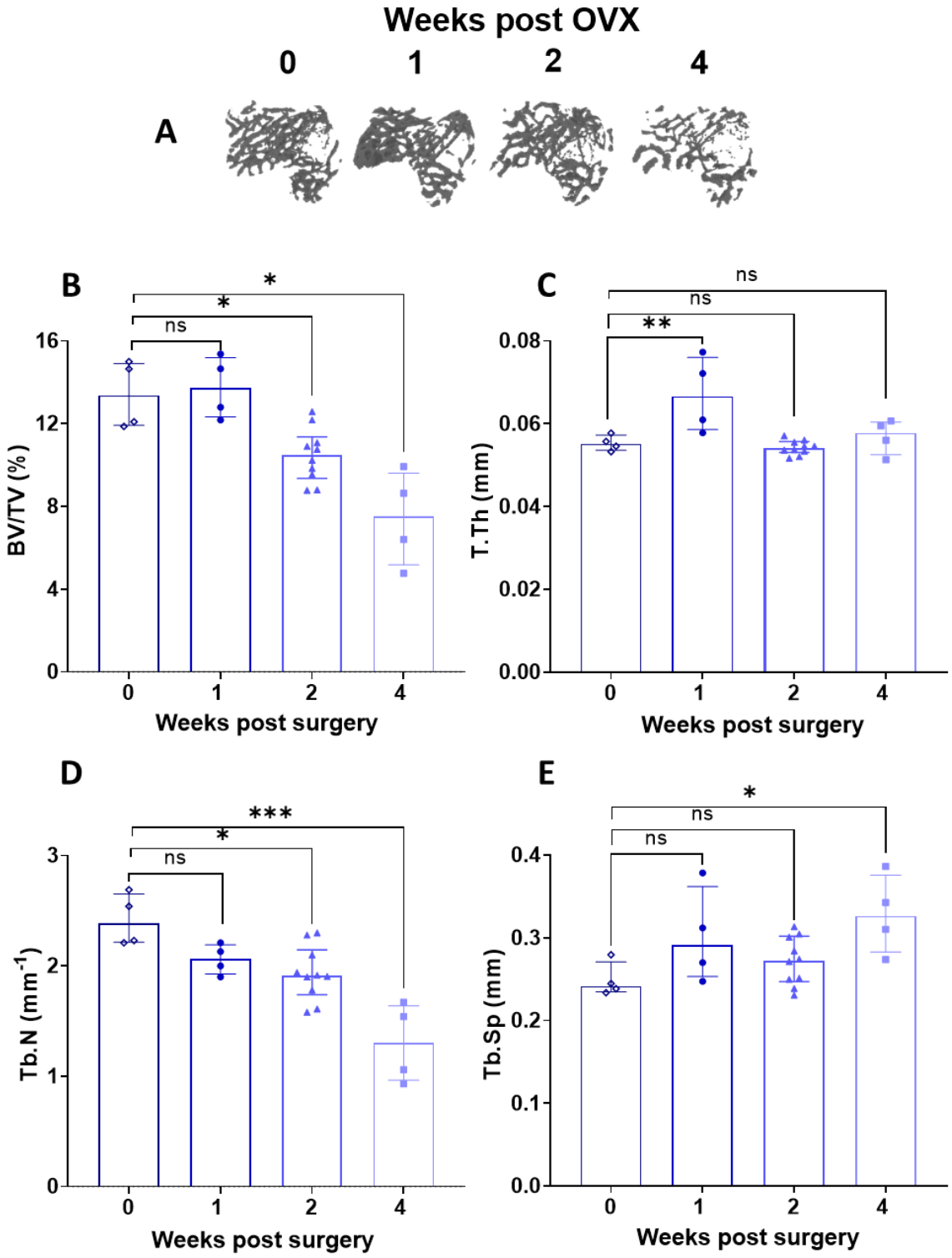


Figure 6.2. Timeline of trabecular bone loss in 12-week-old ovariectomised C57Bl/6J female mice. A) Representative images of tibia µCT analysis, images show trabecular bone from an axial plane of view. **B-E)** Quantitative morphometry of trabecular microarchitectural parameters: **B)** Trabecular Percent Bone Volume (BV/TV %), **C)** Trabecular thickness (Tb.*Th*), **D)** Trabecular number (Tb.*N*)**, E)** Trabecular Separation (Tb.Sp). Sample size varies (n=4-10) as represented by each individual dot in the graphs. Results in graphs C-E are presented as Mean ± SD, data was analysed with One-way ANOVA, followed by Dunnett's post hoc correction for multiple comparisons test; data in graph B was analysed with multiple Kruskal Wallis tests, results in graph B are presented as Median ± IQR, * = $P < 0.05$ ** = $P < 0.01$; *** = $P < 0.001$.

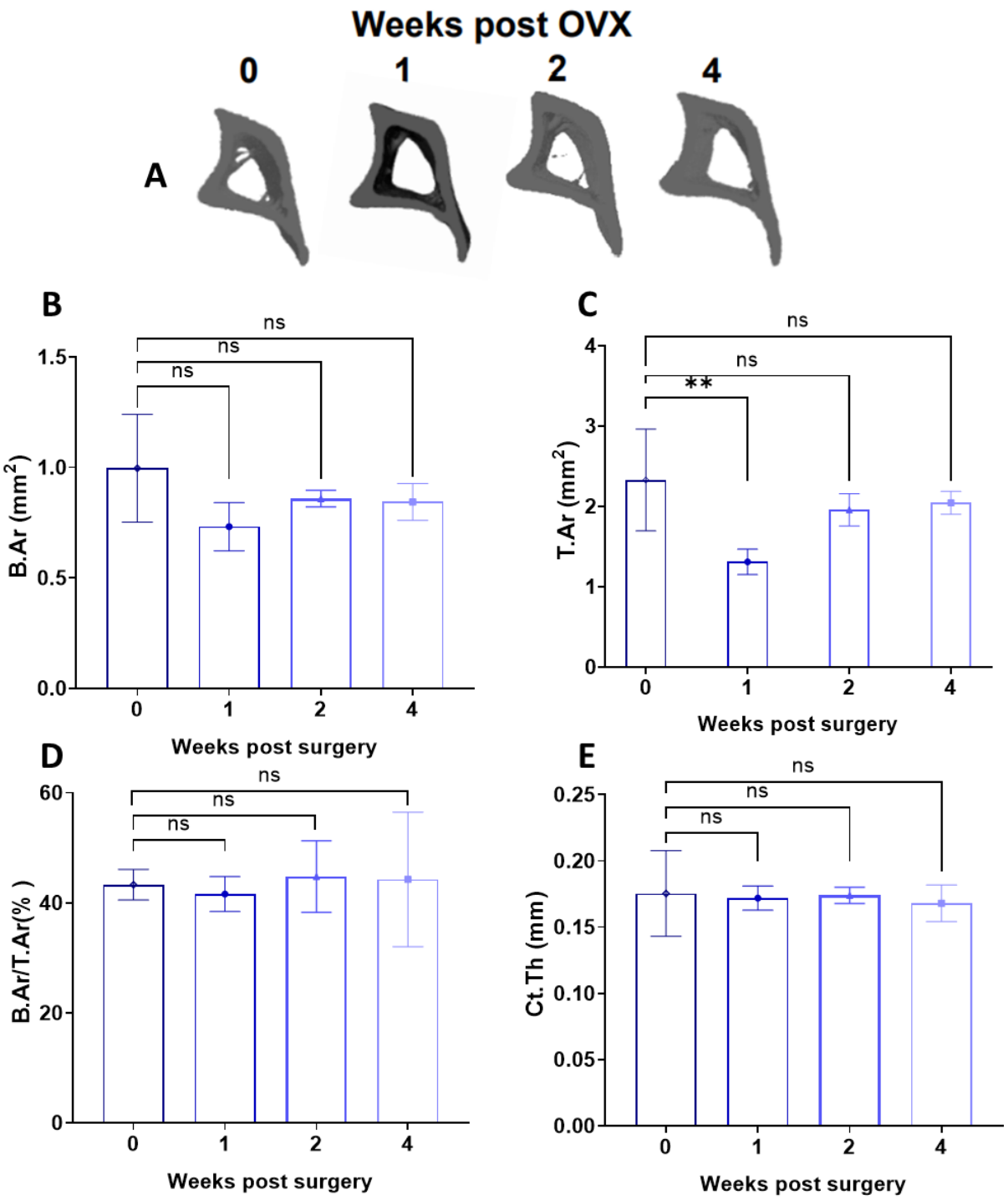


Figure 6.3. Timeline of cortical changes in 12-week-old ovariectomised C57Bl/6J female mice tibial midshaft. A) Representative µCT images of cortical bone (axial orientation) at each of the tissue collection timepoints. B-E) Micro computed tomography (µCT) analysis of bone cortical parameters. **B)** Cortical Bone Area (B.Ar) **C)** Total Bone Tissue Area (T.Ar) **D)** Cortical Percent Bone Area (B.Ar/T.Ar %) and **E)** Cortical Thickness (Ct.Th). Sample size N=4 for all groups). For graphs B, C and E, results are presented as Mean ± SD, data was analysed with One-way ANOVA, followed by Dunnett's post hoc; data in graph D was analysed with multiple Kruskal Wallis tests, results in graph B are presented as Median ± IQR ** = $p < 0.01$.

6.3. Trabecular bone analysis of CLEC14A deficient and WT control adult (12-week-old) C57BL/6J ovariectomised mice

Osteoporosis was induced in WT and CLEC14A$^{-/-}$ 12-week old female mice by ovariectomy. Genotype and age-matched non-ovariectomised female mice served as controls. Tissue was collected from ovariectomised mice 4-weeks post-surgery and from non-ovariectomised control mice at the same time. µ-CT analysis of tibiae confirmed changes in response to OVX surgery, with similar values as the ones reported during the OVX optimisation reported in the section above (6.2). Overall, significant trabecular bone loss was detected in both CLEC14A$^{-/-}$ and WT ovariectomised females by comparison to non-ovariectomised controls, thus, CLEC14A$^{-/-}$ OVX mice were not protected from ovariectomy-induced osteoporotic bone loss (Figure 6.4A). In more detail, a significant decrease in BV/TV % was noted in both WT and CLEC14A$^{-/-}$ mice in response to ovariectomy, however, no significant differences were observed between ovariectomised WT and CLEC14A$^{-/-}$ groups (Figure 6.4 B). In addition, a small but significant decrease in trabecular thickness was detected in ovariectomised CLEC14A$^{-/-}$ tibiae compared to non-ovariectomised control CLEC14A$^{-/-}$ tibiae, a similar trend was observed for WT samples (control WT vs OVX WT), however, this did not reach statistical significance (Figure 6.4 C). A decline in the number of trabeculae was also shown to contribute towards the reduction in bone volume (BV/TV %) observed in ovariectomised mice. Specifically, a significant drop in Tb.N was observed in both OVX WT and OVX CLEC14A$^{-/-}$ groups by comparison to their matched non-ovariectomised controls (Figure 6.4 D). Interestingly, non-ovariectomised CLEC14A$^{-/-}$ mice also had fewer trabeculae than non-ovariectomised. Tb.Sp was increased in WT OVX mice compared to their matched WT controls and compared to OVX CLEC14A$^{-/-}$ mice (Figure 6.4 E).

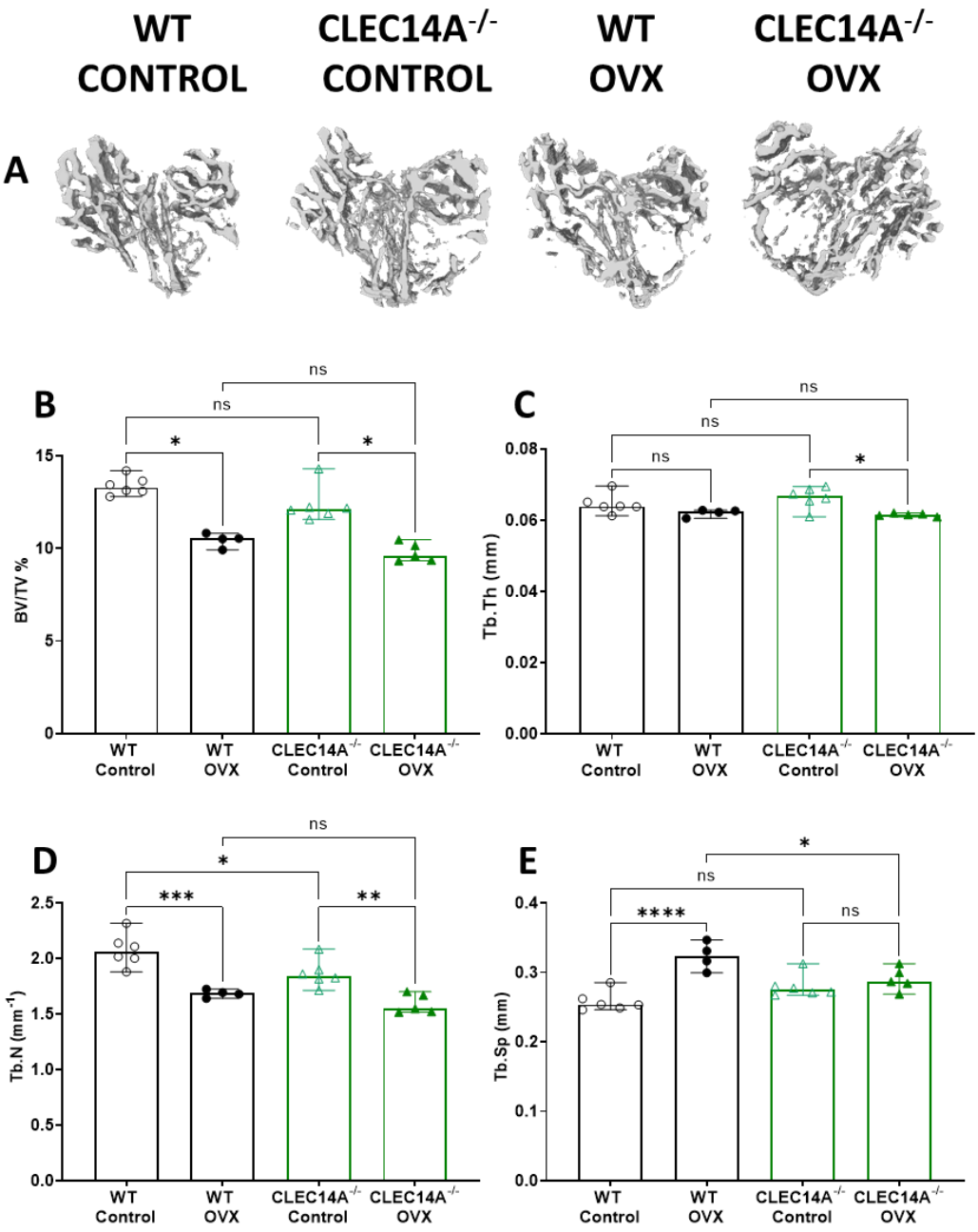


Figure 6.4. CLEC14A$^{-/-}$ mice are not protected from ovariectomy-induced bone loss. A) Representative images of tibial µCT analysis. Images show trabecular bone presented as an axial plane of view. **B-E)** Quantitative morphometry of trabecular microarchitectural parameters: **B)** Trabecular Percent Bone Volume (BV/TV %), **C)** Trabecular thickness (Tb.Th), **D)** Trabecular number (Tb.N), **E)** Trabecular Separation (Tb.Sp). Sample size varies (n=4-6) as represented by each individual dot in the graphs (WT non-OVX control N=6, WT OVX N=4, CLEC14A$^{-/-}$ non-OVX control N=5, CLEC14A$^{-/-}$ OVX N=5). Results in graphs C-E are presented as Mean ± SD, data was analysed with One-way ANOVA, followed by Dunnett's post hoc correction for multiple comparisons test; data in graph B was analysed with multiple Kruskal Wallis tests, results in graph B are presented as Median ± IQR., * = P < 0.05 ** = P < 0.01; *** = P < 0.001; ****=P < 0.0001.

6.4. Trabecular bone in 12-week-old C57BL/6J ovariectomised mice following treatment with a CLEC14A-MMRN2 blocking antibody

Wildtype mice were injected with an antibody that blocks the interaction between CLEC14A and MMRN2. This experiment was also conducted to determine whether the interaction between MMRN2 and CLEC14A is important for bone formation in ovariectomy-induced osteoporosis. To this end, 12-week old C57Bl/6J mice were ovariectomised and allowed to rest for a week, then mice were injected bi-weekly intraperitoneally (i.p.) with 100 μg mouse monoclonal antibodies against CLEC14A: C2- an antibody that binds CLEC14A but does not block the interaction with MMRN2; or C4 - an antibody that binds to the CTLD of CLECA14A and blocks its interaction with MMRN2 (Figure 6.5).

No protection against ovariectomy-induced osteoporosis bone loss was observed in WT mice treated with the CLEC14A-MMRN2 blocking antibody. No differences in BV/TV %, trabecular thickness, number or separation were noted in response to blockade of CLEC14A-MMRN2 interaction in the female mouse tibia (Figure 6.6).

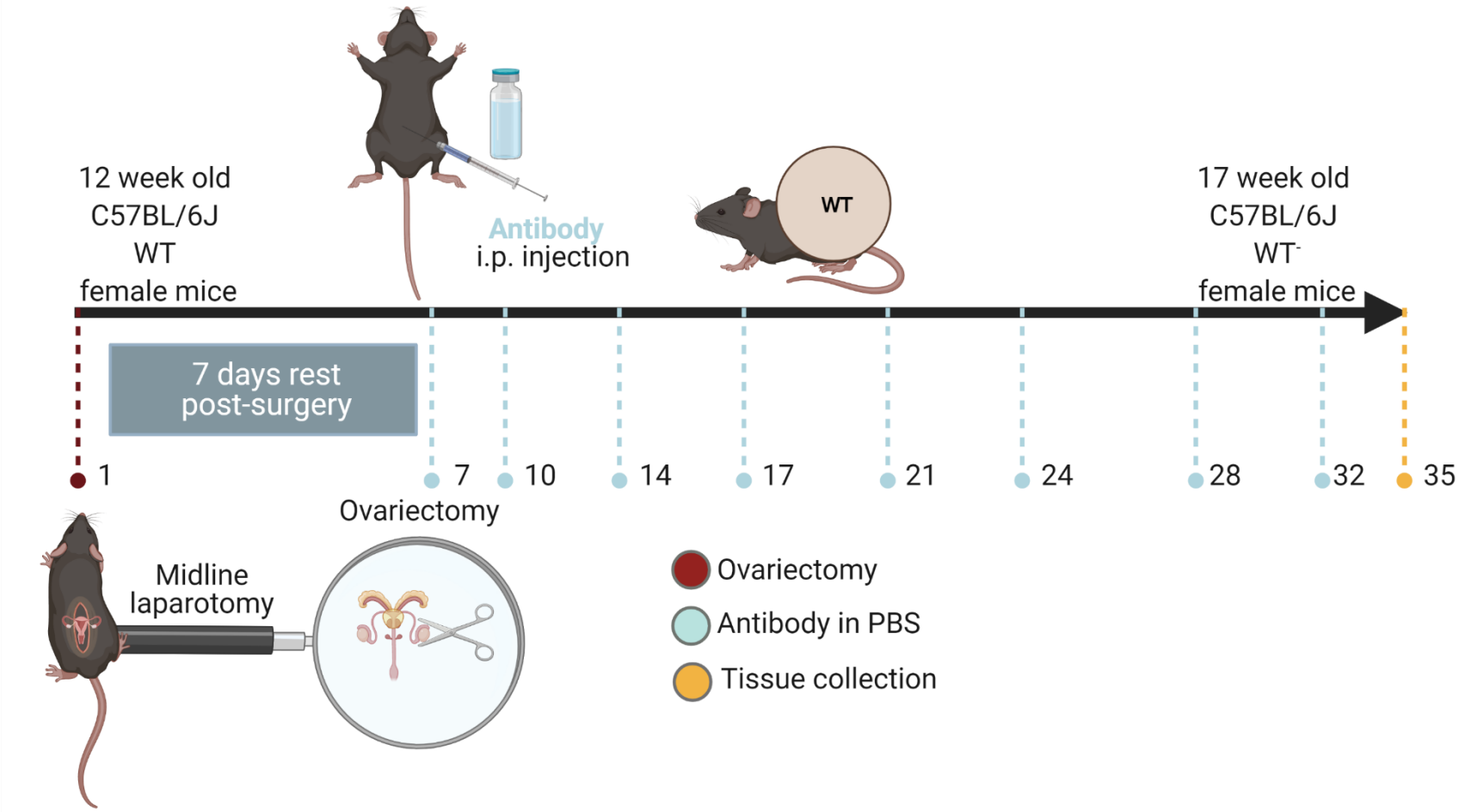


Figure 6.5. Blockade of CLEC14A-MMRN2 interaction in ovariectomy induced osteoporosis bone loss. Osteoporosis was initiated in 12-week-old C57Bl/6J females by surgical bilateral removal of ovaries. After a week of rest, mice were treated with either PBS (vehicle control), or monoclonal antibodies against CLEC14A (C2 or C4) biweekly for 4 weeks; C2 binds CLEC14A but does not prevent MMRN2 binding to the C-type lectin domain (CTLD) of CLEC14A, whilst C4 binds to CLEC14A and blocks its interaction with its ligand MMRN2. Tissue was collected after 4-weeks of treatment and 5 weeks post-surgery.

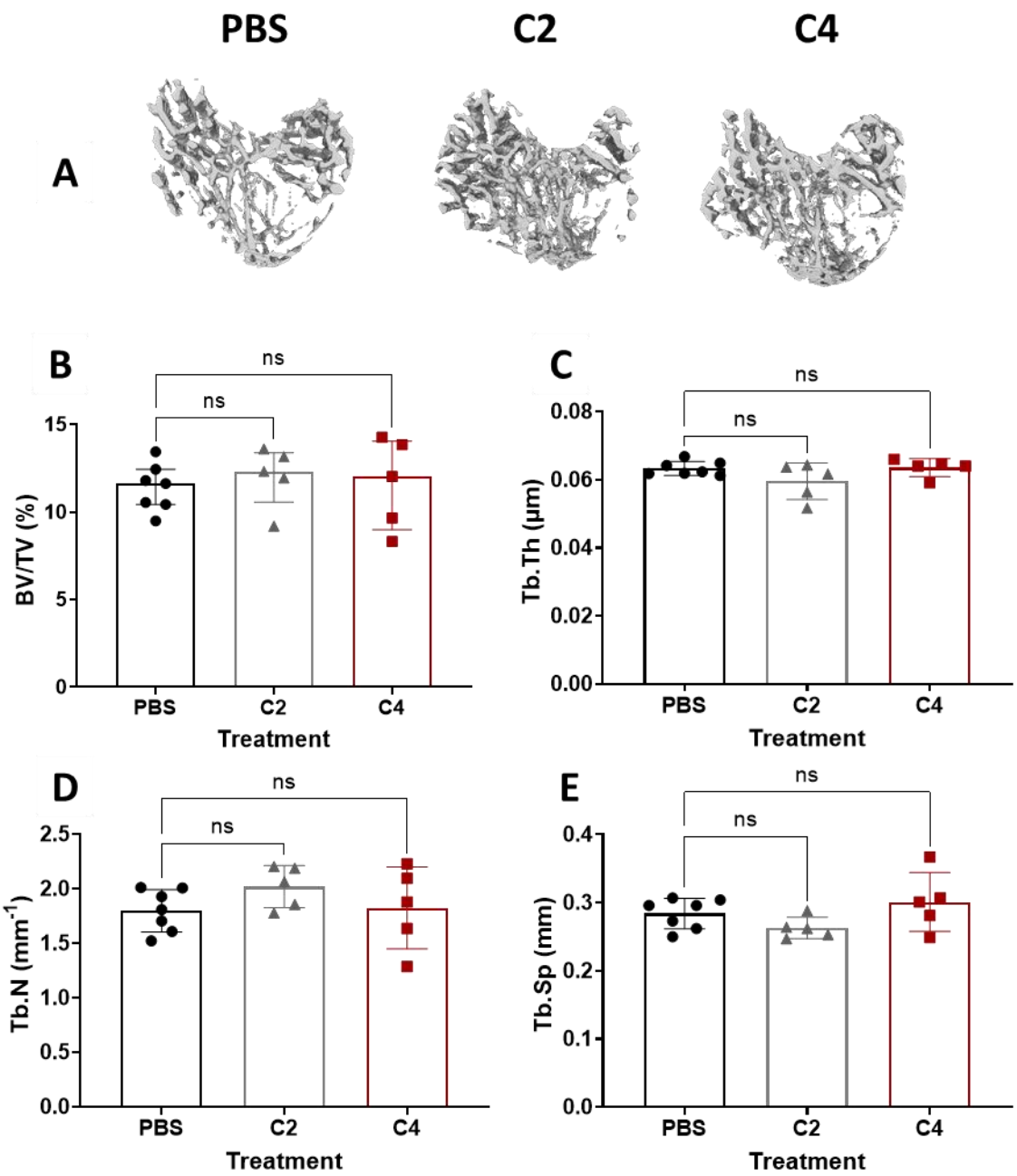


Figure 6.6. Blockade of CLEC14A-MMRN2 interaction does not protect against ovariectomy induced osteoporosis bone loss. A) Representative images of tibial µCT analysis. Images show trabecular bone density presented as an axial plane of view. **B-E)** Quantitative morphometry of trabecular microarchitectural parameters: **B)** Trabecular Percent Bone Volume (BV/TV %), **C)** Trabecular thickness (Tb.Th), **D)** Trabecular number (Tb.N), **E)** Trabecular Separation (Tb.Sp). Sample size varies (N=5-6) as represented by each individual dot in the graphs (PBS N=6, C2 N=5, C4 N=5). Results in graphs C-E are presented as Mean ± SD, data was analysed with One-way ANOVA, followed by Dunnett's post hoc correction for multiple comparisons test; data in graph B was analysed with multiple Kruskal Wallis tests, results in graph B are presented as Median ± IQR., ns- not significant.

6.5. Discussion

Data presented in this chapter focused on pathological changes in the bone and the role played by CLEC14A and MMRN2 during such pathological bone loss. Ovariectomy-induced osteoporosis was chosen as the most suitable model of bone loss as this is the osteoporosis model that induces the most striking changes in trabecular bone mass in the tibial metaphysis (511). Bilateral ovariectomy (OVX) in female mice has been proven to be a consistent pre-clinical model employed to induce postmenopausal osteoporosis, unlike glucocorticoid-induced osteoporosis, which, does not provide a repeatable induction of osteoporosis in rodents (510). Furthermore, glucocorticoid treatment massively impairs osteoblast proliferation and differentiation (512-514), potentially limiting detection of any effects triggered by CLEC14A deficiency in this osteoporosis model. On the other hand, oestrogen deficiency, such as the one induced by removal of ovaries is followed by a sustained decrease in oestrogen levels which leads to major changes in the bone microenvironment, triggering a rapid decrease in bone mass. Bone loss in oestrogen deficiency is characterised by increased bone turnover, instigating both increased osteoblast and osteoclast activation, however overall, this is characterised by an imbalance towards bone resorption, a processes mediated by enhancement of osteoclast survival and activity (515, 516) and impairment in osteoblast mineralisation function (517).

Our results do not demonstrate a therapeutic effect of genetic deletion of CLEC14A, or of CLEC14A-MMRN2 interaction blockade. The reasons for this cannot be fully understood with the data available, however we can postulate that the microenvironment of the bone at this stage does not support CLEC14A activity. A continuously increasing body of work now indicates that type-H vessels are substantially reduced in ovariectomy- and ageing-induced osteoporosis

models (145, 172), and that prevention of their decline can be achieved by using mechanical loading (518), pulse electromagnetic field stimulation (519) or pharmaceutical intervention (518); these in turn lead to prevention of bone loss in osteoporotic mouse models of disease. Given the strong connection between the presence of H-type vessels and osteogenesis and the strong effect of genetic deletion of CLEC14A on trabecular bone parameters during postnatal bone growth in juvenile mice (reported in chapter 4), it is plausible to posit that the lack of a therapeutic effect observed in OVX CLEC14A$^{-/-}$ female mice reflects the cellular environment in the metaphysis, which is characterised by a regression of angiogenesis activity matched by a reduction in the H-type vascular front by 12 weeks of age. This indicates that the role played by CLEC14A in bone formation is context and timepoint dependent and is restricted to periods of high angiogenic activity. This recommends a role for CLEC14A in coupling of angiogenesis to osteogenesis in trabecular bone formation but not in later stages of development or in the control of pathological bone loss.

To further develop this hypothesis additional research is required. Deferoxamine mesylate, a pharmaceutical agent that leads to stabilisation of Hif1α, has been shown to induce H vessel angiogenesis in the aged mouse bone, leading to a matched increase in trabecular volume (145). It is thus strongly recommended to test the effect of induced angiogenesis in pairing with CLEC14A deficiency in aged and osteoporotic mice to investigate the CLEC14A mechanism of action and to probe its therapeutic potential *in vitro*. However, it is worth noting that blockade of the CLEC14A -MMRN2 interaction in juvenile mice, from the age of 4 weeks to the age of 7- and 9- weeks also resulted in minimal changes in trabecular bone parameters (section 4.8).

6.6. Conclusion

CLEC14A deficiency confers no protection against OVX-induced osteoporosis bone loss. This indicates that CLEC14A moderates angiogenic processes in the bone in association and high dependence of expansion of the H-type vasculature. Data presented here and in chapter 4 demonstrate that CLEC14A-MMRN2 blockade does not affect bone turnover during postnatal bone growth or osteoporosis (discussed in detail in chapter VII, section 7.4). From this we conclude that the changes in trabecular bone morphometry measured in young mice during bone growth could be independent of the interaction of CLEC14A with MMRN2. To obtain a better understanding of the role of this interaction in bone formation, further *in vitro* experiments testing the blockade of EC expressing CLEC14A and MMRN2 on osteoblasts are necessary. It is also important to note the limitations in sensitivity of the analyses employed for these experiments. The possibility that bone quality-related changes at the cellular and molecular level were present cannot be excluded warranting further investigation.

7. DISCUSSION

7.1. Bone formation EC-osteoblast communication - gaps in research

Current therapeutic interventions targeting bone formation rather than the standard therapy of blocking bone resorption using bisphosphonates (185-188, 210, 520) in treatment of osteoporosis and non-union fractures are limited and rely on administration of a handful of osteo anabolic treatments: parathyroid hormone-related protein (227, 521, 522) or anti-sclerostin antibodies (222, 523, 524). However, these treatments are accompanied by a variety of unwanted effects, including cardiovascular complications, osteosarcoma, osteonecrosis of the jaw or atypical fractures (186, 525). Furthermore, loss of therapeutic efficacy over time has been reported for the novel anti-sclerostin treatments (523, 526). Specifically, weekly injection treatment of ovariectomised Sprague–Dawley rats or *Macaca fascicularis* monkeys with sclerostin (SOST) neutralising antibodies for 5/6-weeks and 6 months, resulted in increased bone formation parameters following 5/6-weeks of treatment (523, 527, 528) but the osteoinductive phenotype was no longer observed after 26-weeks of treatment (523, 526). This reinforces the need for identification of new therapeutic targets which can be used indecently or alongside existing therapies to increase bone formation following bone damage or in osteoporotic elderly patients, with continuous pro-bone anabolic effects and limited side-effects.

The current model of mechanisms driving skeletal mineralisation implicates numerous bone cells (osteoblasts, osteocytes, chondrocytes and osteoclasts) as key sources of proteins that contribute to regulation of osteoblast differentiation and activity. More recently, blood vessel endothelial cells (EC) have also garnered attention for their vital role in regulation of osteogenesis (2, 130, 136, 138, 145, 151, 422). Specifically, H-type capillaries have been shown to be the mainstay architectural guides for osteoblast angiotropism to sites of bone formation

and the main regulators of osteoblast progenitor cell expansion and maturation (2, 53, 172). In spite of their fundamental importance, EC are yet to be directly targeted for therapeutic interventions, partly due to lack of cell specific markers and a relatively poor characterisation of the exact molecular pathways involved in regulation of EC-osteoblast crosstalk. Understanding the molecular mechanisms behind regulation of osteoblast activity by EC and perturbation thereof is essential in accelerating identification and validation of therapeutic targets for prevention and treatment of bone disorders to the like of osteoporosis and non-fracture union.

7.2. Summary of findings

The work presented here has uncovered a novel role for CLEC14A, identifying for the first time a new function for this EC specific protein in coordination of osteoblast activity during postnatal bone growth. A key point summary of our main findings categorised according to their relevance to this project's aims is presented as follows:

Aim I. Characterise the effect of CLEC14A on bone formation during postnatal bone growth.

- CLEC14A and MMRN2 were detected in the bone metaphysis, the region where H-type vessels localise and regulate bone growth and bone mineralisation during postnatal skeletal development. Immunofluorescent labelling of bone sections and RNA sequencing analysis of EC confirmed local availability of CLEC14A, MMRN2 and CD248 of in the bone, demonstrating the expression of CLEC14A and MMRN2 by EC, and that of CD248, by osteoblasts.
- Germline deletion of CLEC14A prompted the creation of an osteogenic milieu evoking accelerated bone growth and boosting of extracellular matrix (ECM) mineralisation, as

demonstrated by bone length measurements and µCT analysis of murine tibiae, and alizarin red imaging of neonatal pup calvariae.

- At the cellular level, high-resolution imaging of CLEC14A$^{-/-}$ tibia sections uncovered changes in osteoblast angiotropism, marked by variation in the anatomical distribution of osteoblasts. OSX^{+} cells covered a larger area in the metaphysis extending towards the diaphysis in juvenile pups. Furthermore, the CLEC14A$^{-/-}$ tibial metaphysis was also characterised by collagen deposition further down towards the diaphysis, as compared to WT controls. Whilst osteoblast were distributed further down towards the diaphysis in CLEC14A$^{-/-}$ samples, they were not localised further away from vessels neither in the metaphysis nor further down towards the diaphysis in the inferior part of the metaphysis.
- Cellular changes in geographical distribution of osteoblasts were matched by an extension of the trabecular bone front further down into the distal diaphysis (µCT analysis), indicating that osteoblasts were not only located further down in the metaphysis, but they also actively matured and mineralised their surrounding ECM.
- Retraction of the H-type vascular front in the metaphysis was detected in response to CLEC14A deficiency in juvenile 4-week-old mice, a change which indicates skeletal maturation-dependent plateauing of H-type vasculature development.

Aim II. Identify and dissect any signalling pathways induced by CLEC14A-MMRN2-CD248 interaction.

- Inactivation of the CLEC14A gene in mice is accompanied by an enrichment in pathways related to endochondral ossification and osteoblast maturation, mineral resorption, and osteoclast activity as well as hypoxia responses, as demonstrated by bulk RNA sequencing analysis of neonatal pup calvariae. In addition, downregulation

of mRNA expression of cell-to-cell interaction molecules was identified in response to CLEC14A deficiency

- CLEC14A deficiency triggers changes in osteoblast maturation status which results in increased mineralisation activity of osteoblasts *in vitro* in response to osteoinductive stimulation.

Aim III. Assess the therapeutic potential of in-house CLEC14A-MMRN2 interaction blocking antibodies to protect against age-induced bone loss using murine models of osteoporosis.

- CLEC14A deficiency does not protect C57BL6/J female mice against ovariectomy-induced bone loss, as compared to controls.
- Blocking CLEC14A-MMRN2 interaction *In vivo* does not change trabecular bone parameters in mice from 4- to 9-weeks of age. Neither 2-week, nor 4-week long biweekly treatment with CRT4, a monoclonal antibody which blocks CLEC14A-MMRN2 interactions, induced any measurable changes in trabecular bone mass in C57Bl6/J male mice.
- Blocking CLEC14A-MMRN2 interaction *in vivo* does not change trabecular bone parameters in C57Bl6/J female mice. Biweekly injection with CRT4, over 4 weeks post-surgical removal of ovaries, did not protect mice from osteoporosis-induced bone loss.

7.3. Phenotype comparison to other EC molecules

Altogether our findings indicate that CLEC14A is important for bone formation in the early stages of postnatal development of the skeleton. CLEC14A, alongside integrin β1 (ITGB1), and Laminin Subunit Alpha 5 (LAMA5), are part of a group of EC cell-surface bound proteins which have been shown to localise to the long bone metaphysis and mediate osteoblast activity (136, 529). Previous research has indeed confirmed the importance of the EC cell secreted proteome

in guiding osteoblast activity in the bone metaphysis (DLL4 and RBPJ and their receptor NOTCH1 (130, 530), bone morphogenetic proteins (2), fibroblast growth factors (2, 94, 531) and platelet derived growth factors (2, 53). However, in spite of the importance of H-type EC in coupling angiogenesis to osteogenesis, the role played by EC cell surface and ECM deposited proteins in bone formation remains ill-defined. For instance, EC-osteoblast interactions mediated by EC-expressed integrins (integrin β1) and osteoblast-expressed cell adhesion molecules (Vascular Cell Adhesion Molecule 1-VCAM1) have been previously shown to couple angiogenesis and osteogenesis mechanisms (53, 136). Lack of expression of any of these molecules has been linked to changes in bone shape, alterations of the vascular front by way of shortening of H-type columns in the metaphysis and alterations of osteolineage commitment resulting in a decreased metaphyseal osteoblast density, a phenotype that was also partially recapitulated by the genetically induced loss of function of ECM molecule laminin subunit alpha 5 (LAMA5) in EC (136).

In addition to cell-adhesion molecules, angiocrine secreted factors have also been shown to moderate osteogenesis. One such secreted factor is PDGFB, which in the bone is released by EC and pre-osteoclasts (131, 170). Similar to the phenotype presented here for CLEC14A, PDGFB has been shown to be an important negative regulator of osteoblast maturation, in addition, PDGFB also acts as a positive regulator of osteoblast proliferation and angiotropism (53, 145, 170, 532). PDGFB-PDGFRβ signalling ensures maintenance of osteoblast progenitor proximity to H-type EC during postnatal bone growth (53). The geographical location of osteoblasts in rapport to H-type vessels has been shown to be an important indicator of osteoblast maturity. Namely, osteoprogenitors expressing only the osteolineage commitment transcription factor OSX have been shown to be tightly bound to metaphyseal vessels, whilst

mature type I collagen secreting osteoblasts have been reported to localise relatively further away from capillaries in the bone (52).

Loss of PDGF signalling results in disproportionate trabecular and cortical bone formation, characterised by lower bone mass (131). Furthermore, PDGFB-PDGFRβ signalling blockade also results in aberrant fracture repair processes (53). Essentially, PDGFRβ signalling blockade inhibits proper bone vascularisation, diminishes expansion of skeletal stems and progenitor cells, and induces hastened osteoblast maturation, leading to the formation of repair calluses that are smaller and more minerally dense and are characterised by reduced ECM composition and increased fibrosis (53, 131).

Work presented in this thesis portrays CLEC14A as a negative regulator of bone formation. Unlike the results reported for genetic deletion of other EC derived proteins such as integrins or growth factors, our observations in CLEC14A deficient mice show minimal changes in the morphology of the vascular bed in the bone, no changes in bone shape and no alterations in osteoblast density in the bone metaphysis. Furthermore, whilst targeting of newly identified molecular regulators of bone formation ITGB1, LAMA5 and PDGFB result in diminished bone formation, prevention of CLEC14A production by germline deletion leads to increased bone formation during postnatal bone growth. This provides support for the potential of this molecule as a therapeutic target to support bone formation. In addition, given the limited postnatal expression of CLEC14A in other organs of the body than the bone, CLEC14A could be easily targeted with minimal side effects.

A caveat for the translatability of this work into clinic is that while loss of CLEC14A function in EC resulted in increased osteoblast maturation in neonatal, and juvenile mice, this osteogenic advantage was lost in adulthood and in ovariectomy-induced osteoporotic mice. This indicates

that CLEC14A only plays a role in regulation of osteoblast activity during periods of high angiogenic activity, in line with previously published work showing that CLEC14A is expressed on tip EC and mediates EC migration and tube formation (345, 348). To better understand the therapeutic potential of CLEC14A it will be essential to test its effects alongside a pro-angiogenic pharmacological intervention in osteoporosis and fracture pre-clinal models of disease.

7.4. Mechanism of action

We have yet to understand the intimate biochemical details of how CLEC14A is implicated in regulation of bone formation mechanisms in the metaphysis. Here, we have shown that CLEC14A deletion results in increased elongation of long bones alongside an augmentation in their mineralisation. The latter occurs by means of increased osteoblast maturation, suggesting that CLEC14A, directly or indirectly, moderates the crosstalk between EC and osteoblasts. Considering the existing literature, it is possible to hypothesise that one or several of the following processes are involved in the increased bone mineralisation phenotype observed following genetic deletion of CLEC14A: (i) Interaction between CLEC14A-MMRN2-CD248 favours maintenance of osteoblast immaturity; this interaction is important for osteoblast migration during blood vessel bed expansion and is key to allowing osteoblasts to be exposed to negative regulatory signals secreted by EC to keep osteoblasts immature, proliferative and migratory; (ii) interactions between CLEC14A and other known ligands i.e. HSPG2 or LAMA4, are involved in regulation of osteoblast maturation, in addition to / instead of MMRN2; (iii) genetic deletion of CLEC14A indirectly affects osteolineage commitment and osteoblast maturation by increasing vascular leakage and increasing local fatty acid availability in the metaphysis during bone growth (Figure 7.1).

Our data suggests that CLEC14A does not directly affect physical EC-osteoblast interactions. Results presented in chapter III (Figure 3.29, Figure 3.31, Figure 3.33, Figure 3.35) demonstrated localisation of osteoblasts further down in the metaphysis compared to WT controls, indicating downregulation of osteoblast migration capacity alongside capillaries during postnatal bone growth. It remains unclear how exactly CLEC14A deficiency results in defective osteoblast angiotropism alongside H type vessels. Angiotropism could be affected by an impairment in the adhesion of osteoblasts to EC which would physically limit binding of osteoblasts to EC or by an aberrant EC-osteoblast crosstalk which would result in premature maturation of osteoblasts. Imaging analysis of osteoblasts and vessels in tibia sections has shown the lack of changes in the distance of OSX^+ osteoblasts from H-type vessels (Figure 3.28), providing more credence to the theory that CLEC14A germline deletion affects EC-osteoblast crosstalk. The precise signalling cascade regulating EC-osteoblast crosstalk in bone development, maintenance, remodelling and disease remains yet to be identified. However, it is plausible to posit that the lack of CLEC14A prevents retention of MMRN2 to the EC cell surface which in turn hampers retention of immature osteoblasts close enough to EC to ensure exposure of immature osteoblasts to important paracrine signals to the like of PDGFBB-PDGFRβ which regulate maintenance of osteoblast immaturity states.

The work presented here, has focused exclusively on the hypothesis that CLEC14A-MMRN2-CD248 interaction is important for negative regulation of osteoblast maturation. *In vivo* targeting of the interaction of CLEC14A with MMRN2, resulted in limited changes in trabecular bone mass in 4-week old mice (Figure 4.20 and Figure 6.2). Whilst we have demonstrated localisation of antibodies targeting the interaction between CLEC14A and MMRN2 to the bone metaphysis (Figure 3.14), and previous work utilising the antibodies at same doses and administration route has resulted in changes in tumour growth (1, 348), blockade of the

CLEC14A-MMRN2 interaction in juvenile 4-week old male mice for 4-weeks has not been able to show therapeutic value for this intervention either in resting mice. In addition, blockade of CLEC14A-MMRN2 interactions conferred no protection against ovariectomy-induced osteoporosis in 12-week old female mice. In light of these findings, it is essential to further test this interaction *in vitro* to be able to draw absolute conclusions. It is also recommended that the other two hypotheses are investigated further.

In order to obtain a better understanding of the timeline of activity of CLEC14A and MMRN2 in the bone, it is important to fully understand the pattern of expression of these proteins across different ages and pathological contexts. Previous work has indeed confirmed that postnatal expression of CLEC14A is limited to a few organs including the murine retina and brain (346, 347, 414) as well as in growing tumours (345). However, spatio-temporal data of CLEC14A and MMRN2 expression in both healthy and pathological conditions within the bone are yet to be elucidated, thus requiring further investigation, especially in adult and aged mice. Our data shows that CLEC14A is expressed in the metaphysis of 4-week-old mice and that CLEC14A genetic deficiency results in an increased trabecular bone phenotype that is present from 4- until 8-weeks of age but not at 12- and 30-weeks of age. This suggests that CLEC14A might only be expressed (and thus assert its osteogenic regulatory function) in the bone during periods of high angiogenetic activity. In the postnatal bone, the H-type vascular front expands to support the bone growth needs of the appendicular skeleton until peak bone mass is achieved at approximately 12-weeks of age (20, 130, 136, 138, 145, 422). However, a time dependent decrease in the H-type vascular front in the metaphysis has been previously reported to commence as early as at 4 weeks of age (138), providing a biological reasoning for the limitation of the effect of CLEC14A deletion to juvenile mice and reasserting the role played by CLEC14A in coupling angiogenesis to osteogenesis in the bone.

7.5. Similarity in mechanism to CD248

Previously published work from our groups has demonstrated that CD248, another group 14 C-type lectin family member, regulates bone formation by maintaining osteoblasts in an immature state (255). The mechanism identified for the increased maturation and matrix mineralisation activity in CD248$^{-/-}$ osteoblasts was linked to deficient PDGFBB-PDGFRβ signalling (255). Data presented in this project furthers our understanding of the changes exerted by CD248 in bone formation and brings forward evidence that CD248 triggers increased bone formation in 4- and 8-week-old mice, however, in 12-week old adult and 30-week old mature adult mice, CD248 germline deletion is characterised by a striking reduction in trabecular bone volume (Figure 4.5, Figure 4.6). This could be explained by its regulation of PDGFBB-PDGFRβ signalling, which in the long term might result in complete depletion of stem and skeletal progenitor pool of cells. Of note, whilst a decrease in trabecular bone volume in comparison to WT controls is observed in CLEC14A$^{-/-}$ mice tibiae at 12-weeks of age, by 30-weeks of age CLEC14A$^{-/-}$ mice have a comparable trabecular bone mass to WT controls. In addition, CLEC14A$^{-/-}$ mice exhibit an increased length of their trabecular bone front in the tibia, with trabeculae being present further down towards the diaphysis, an observation that was not mirrored in CD248-/- samples (Figure 4.8). The conflicting observations for CLEC14A$^{-/-}$ and CD248$^{-/-}$ mice suggests that whilst both CLEC14A and CD248 negatively regulate osteoblast activity, this might be regulated by different mechanisms of action. On the other hand, we cannot exclude the possibility that CLEC14A genetic deletion also indirectly downregulates PDGFBB-PDGFRβ signalling by perturbing the adhesion of osteoblasts to EC. CLEC14A$^{-/-}$ calvaria RNA sequencing analysis identified no changes in PDGFB or PDGFRβ expression at transcriptomic level or that of any related pathway members compared to controls. No

definitive conclusion can be drawn regarding alteration of PDGFB signalling in CLEC14A$^{-/-}$ mice, calling for additional EC-osteoblast co-culture experiments *in vitro.*

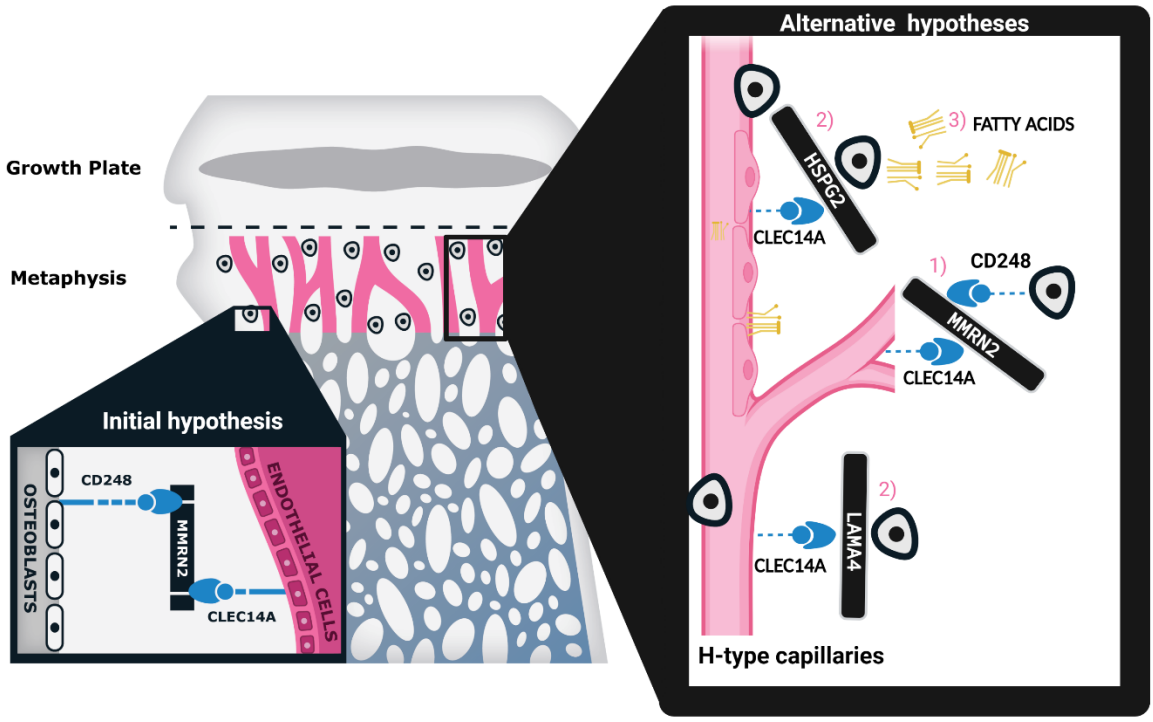


Figure 7.1 Overview of mechanisms of action important for CLEC14A-driven mediation of bone formation. The increased bone formation we identified in response to CLEC14A genetic deficiency could have been regulated by: 1) interactions between CLEC14A and MMRN2, 2) interactions between CLEC14A and other interacting partners: LAMA4 and HSPG2. Alternatively, bone formation could also be partially upregulated by an increased local availability of fatty acids released from bone vessels due to increased vessel permeability in CLEC14A$^{-/-}$ mice.

7.6. Wider impact of this project and further research

By demonstrating the role of CLEC14A in the molecular tuning of osteoblast maturation, this project presents evidence of the important role of the EC cell-surface proteomic signature in bone formation and remodeling during postnatal bone growth, providing insight into the importance of EC-osteoblast cross talk for maintenance of bone homeostasis. The newly identified stimulation of bone growth and ossification in CLEC14A$^{-/-}$ mice, makes CLEC14A a target of interest for further experiments to better characterise the role and mechanisms governed by this protein in relation to bone formation and also to test its translatability into clinic. Understanding the role of CLEC14A in modulation of osteoblast activity will open the avenue for new strategies of prevention of age-related bone loss and maybe of stimulation of bone healing following fractures. There are nevertheless gaps in our knowledge that must be addressed in order to achieve this. These are listed below alongside suggested experiments that would help obtain a better understanding of the operating timelines and of the specific environment within which CLEC14A moderates bone formation.

- The spatio-temporal expression of CLEC14A and MMRN2 remains unclear. We have yet to study when CLEC14A and MMRN2 achieve their peak expression in the long bone and when their expression is discontinued whilst the angiogenic processed is dimmed during postnatal bone formation. In addition, the pattern of expression of CLEC14A and MMRN2 in bone pathological conditions such as osteoporosis or bone fracture healing has not been investigated. Investigating these aspects would provide clearer timeline for targeted interventions for blockade of CLEC14A expression or of its interaction with MMRN2. It is therefore recommended that CLEC14A and MMRN2 expression in the long bone is mapped as a timeline starting with neonatal mice and

extending until CLEC14A and MMRN2 expression has peaked and begins to decrease. This could be achieved via immunolabelling of bone sections and high-resolution confocal microscopy.

- Here, we reported a lack of protection against bone loss in CLEC14A$^{-/-}$ ovariectomised female mice. It is currently unclear however, if this was mediated by CLEC14A sexual dimorphism or by the lack of angiogenic activity previously reported in this model of osteoporosis (172). To clear this and to test the hypothesis that the pro-osteogenic effect observed in response to CLEC14A deficiency is linked and limited to periods of high angiogenic activity, a study of the effect of CLEC14A deficiency in osteoporotic mice that have been treated with a pharmaceutical intervention to induce angiogenesis is recommended. This could be accomplished, by a 4-week treatment of ovariectomised WT and CLEC14A$^{-/-}$ female mice with deferoxamine mesylate (DFM). DFM is a Hif-1α stabiliser, which has been previously used to induce angiogenesis in the bone in aged mice, resulting in increased vascularisation of the metaphysis (145). If treatment of CLEC41A$^{-/-}$ ovariectomised mice with DFM results in increased trabecular bone accrual as compared to the WT control this would refute the hypothesis that CLEC14A is a sexually dysmorphic protein and reinforce the theory that the effect of CLEC14A is strongly associated to high angiogenic activity. In contrast, if DFM treatment does not boost osteogenic activity in CLEC14A$^{-/-}$ mice, then, to further pursue the hypothesis that the effect of CLEC14A on bone formation is sexual dysmorphic, DFM treatment in an ageing-induced osteoporosis model could be investigated. In this context, trabecular bone mass would be compared between DFM treated WT and CLEC14A$^{-/-}$ male mice.

- An alternative disease model system to investigate the role of CLEC14A in bone formation would be fracture healing in a tibia fracture model as previously published (52). Unlike osteoporosis models, bone healing models rely on angiogenesis for bone formation, moreover, previous work has shown that, bone healing is dependent on migration of osteoblasts into the bone defect (533).

    - The quality of bones formed by CLEC14A$^{-/-}$ mice remains poorly characterised by our current work. Three point bending analysis identified no changes in the mechanical proprieties of cortical bone, however, the mechanical proprieties of trabecular bone have remained poorly characterised. It would therefore be important to examine trabecular bone strength in CLEC14A bone sections with the aid of micro nano indentation, this method would specifically probe trabecular bone quality, which is the bone phase our work has demonstrated to be most affected by genetic deletion of CLEC14A. In addition, from a therapeutical perspective, it would be important to shed light on the potential changes triggered by CLEC14A deficiency in respect to the composition and organisation of the bone extracellular matrix and minerals, as these two are the main molecular contributors to bone quality. To this extent, investigation of bone matrix and mineral composition parameters to the like of: carbonate to phosphate ratio, mineral to matrix ratio and collagen crosslink maturity are warranted to aid in further understanding of the phenotypical changes that result from the loss of function of CLEC14A.
    - To address crucial questions regarding the precise effect of CLEC14A expression on EC on osteoblast activity and to shed light into the cellular and molecular changes governed by this molecule in the bone, it is important to closely examine the crosstalk

between EC and osteoblasts *in vitro.* Co-culturing of EC and osteoblasts whereby CLEC14A if knocked down, overexpressed or the interaction of CLEC14A with MMRN2 is blocked will provide precious information on the mechanism of action of this protein. Considering the minor changes identified in CLEC14A$^{-/-}$ osteoblasts in monoculture, and to completely address our aim to identify the effect of CLEC14A genetic deficiency on osteoblast differentiation and maturation, further investigation of osteoblast molecular changes in response to co-culture of EC and osteoblasts is warranted. Moreover, given the site-specific differences in osteoblast phenotype (534, 535) and the different ossification processes in the calvaria and long bones, it is also important to test the EC-osteoblast crosstalk utilising osteoblasts isolated from the mouse tibia or femur as previously reported (53).

- No investigations on potential redundancy for CLEC14A in murine models have been yet published or conducted by our group. Redundancy for the role played by CLEC14A and CD93 have been previously reported in zebrafish (352, 436). Moreover, CD93 has also been recently shown to interact with MMRN2 (1, 371, 372, 435). Additional work has also confirmed that CD93 genetic deletion and blockade of the CD93-MMRN2 interaction mirrors the same observations published for CLEC14A genetic deletion in EC and blockade of CLEC14A-MMRN2 interaction, resulting in reduced sprouting angiogenesis-dependent vascularisation of the retina i*n vitro and in vivo (371).* It would therefore be vital to understand if CD93 also plays a role in bone formation, and more over if operates as a redundant or compensatory mechanism for CLEC14A deficiency. This could be addressed by studying the bone phenotype of a CD93 deficient mouse or that of a double CLEC14A CD93 knock out in a mouse. Alternatively, this could also be investigated by co-culture of CLEC14A and/or CD93 deficient EC with osteoblasts. The

latter experiment would provide a direct read out of the effect of these two proteins on osteoblast activity, whilst the formed would provide an overview of the role of CLEC14A and CD93 *in vivo* on bone formation.

7.7. Conclusion

This work provides insight into the CLEC14A activity in the skeletal system. Based on the sum of the findings presented here, we propose that CLEC14A has a proven functional role in orchestration of signalling in the bone to support osteoblast maturation and mineralisation activity. Our data provides evidence that CLEC14A is a targetable EC-specific molecule whose loss of expression creates a microenvironment conducive to accelerated bone formation and growth during postnatal bone development. Whilst the therapeutic value of targeting CLEC14A requires further investigation, the role played by CLEC14A in bone formation reiterates the importance of agents targeting bone vasculature receptors that mediate osteoblast activity, as a potential new type of bone anabolic agents. This raises the possibility that vascular-osteoblast interaction targeted interventions could have a bone formation potentiating effect when used in combination with a bone angiogenesis enhancing pharmacological agent.

8. REFERENCE LIST

1. Khan KA, Naylor AJ, Khan A, Noy PJ, Mambretti M, Lodhia P, et al. Multimerin-2 is a ligand for group 14 family C-type lectins CLEC14A, CD93 and CD248 spanning the endothelial pericyte interface. Oncogene. 2017;36(44):6097-108.
2. Kusumbe AP, Ramasamy SK, Adams RH. Coupling of angiogenesis and osteogenesis by a specific vessel subtype in bone. Nature. 2014;507(7492):323-8.
3. Neag G, Finlay M, Naylor AJ. The Cellular Choreography of Osteoblast Angiotropism in Bone Development and Homeostasis. Int J Mol Sci. 2021;22(14).
4. Clarke B. Normal bone anatomy and physiology. Clin J Am Soc Nephrol. 2008;3 Suppl 3:S131-9.
5. Buckwalter JA, Cooper RR. Bone structure and function. Instr Course Lect. 1987;36:27-48.
6. Müller R. Hierarchical microimaging of bone structure and function. Nat Rev Rheumatol. 2009;5(7):373-81.
7. Moreno-Jiménez I, Cipitria A, Sánchez-Herrero A, van Tol AF, Roschger A, Lahr CA, et al. Human and mouse bones physiologically integrate in a humanized mouse model while maintaining species-specific ultrastructure. Sci Adv. 2020;6(44).
8. Oftadeh R, Perez-Viloria M, Villa-Camacho JC, Vaziri A, Nazarian A. Biomechanics and mechanobiology of trabecular bone: a review. J Biomech Eng. 2015;137(1):0108021-01080215.
9. Morgan EF, Unnikrisnan GU, Hussein AI. Bone Mechanical Properties in Healthy and Diseased States. Annu Rev Biomed Eng. 2018;20:119-43.
10. Seeman E, Delmas PD. Bone quality--the material and structural basis of bone strength and fragility. N Engl J Med. 2006;354(21):2250-61.
11. Kelly NH, Schimenti JC, Ross FP, van der Meulen MC. Transcriptional profiling of cortical versus cancellous bone from mechanically-loaded murine tibiae reveals differential gene expression. Bone. 2016;86:22-9.
12. Mao SS, Li D, Luo Y, Syed YS, Budoff MJ. Application of quantitative computed tomography for assessment of trabecular bone mineral density, microarchitecture and mechanical property. Clin Imaging. 2016;40(2):330-8.
13. Dunning D. Basic mammalian bone anatomy and healing. Vet Clin North Am Exot Anim Pract. 2002;5(1):115-28.
14. Florencio-Silva R, Sasso GR, Sasso-Cerri E, Simões MJ, Cerri PS. Biology of Bone Tissue: Structure, Function, and Factors That Influence Bone Cells. Biomed Res Int. 2015;2015:421746.
15. Spencer GJ, Hitchcock IS, Genever PG. Emerging neuroskeletal signalling pathways: a review. FEBS Lett. 2004;559(1-3):6-12.
16. Sivaraj KK, Adams RH. Blood vessel formation and function in bone. Development. 2016;143(15):2706-15.
17. Tikhonova AN, Dolgalev I, Hu H, Sivaraj KK, Hoxha E, Cuesta-Dominguez A, et al. The bone marrow microenvironment at single-cell resolution. Nature. 2019;569(7755):222-8.
18. Sims NA, Walsh NC. Intercellular cross-talk among bone cells: new factors and pathways. Curr Osteoporos Rep. 2012;10(2):109-17.
19. Esser M. Osteoblasts and osteoclasts in bone marrow smears. Schweiz Med Wochenschr. 1945;75:271.

20. Romeo SG, Alawi KM, Rodrigues J, Singh A, Kusumbe AP, Ramasamy SK. Endothelial proteolytic activity and interaction with non-resorbing osteoclasts mediate bone elongation. Nat Cell Biol. 2019;21(4):430-41.
21. Jensen VK, Karsdal MA, Henriksen K. The ability of human osteoclasts to acidify the resorption lacuna is augmented by rankl and in vitro acidosis. Bone. 2009;44:S337-S8.
22. Sivaraj KK, Majev PG, Jeong HW, Dharmalingam B, Zeuschner D, Schröder S, et al. Mesenchymal stromal cell-derived septoclasts resorb cartilage during developmental ossification and fracture healing. Nat Commun. 2022;13(1):571.
23. Udagawa N, Takahashi N, Jimi E, Matsuzaki K, Tsurukai T, Itoh K, et al. Osteoblasts/stromal cells stimulate osteoclast activation through expression of osteoclast differentiation factor/RANKL but not macrophage colony-stimulating factor: receptor activator of NF-kappa B ligand. Bone. 1999;25(5):517-23.
24. D'Amelio P, Grimaldi A, Cristofaro MA, Ravazzoli M, Molinatti PA, Pescarmona GP, et al. Alendronate reduces osteoclast precursors in osteoporosis. Osteoporos Int. 2010;21(10):1741-50.
25. Yang S, Zhang Y, Rodriguiz RM, Ries WL, Key LL. Functions of the M-CSF receptor on osteoclasts. Bone. 1996;18(4):355-60.
26. Mbalaviele G, Orcel P, Morieux C, Nijweide PJ, De Vernejoul MC. Osteoclast formation from human cord blood mononuclear cells co-cultured with mice embryonic metatarsals in the presence of M-CSF. Bone. 1995;16(1):171-7.
27. Hodge JM, Collier FM, Pavlos NJ, Kirkland MA, Nicholson GC. M-CSF potently augments RANKL-induced resorption activation in mature human osteoclasts. PLoS One. 2011;6(6):e21462.
28. Boyle WJ, Simonet WS, Lacey DL. Osteoclast differentiation and activation. Nature. 2003;423(6937):337-42.
29. Blair HC, Kahn AJ, Crouch EC, Jeffrey JJ, Teitelbaum SL. Isolated osteoclasts resorb the organic and inorganic components of bone. J Cell Biol. 1986;102(4):1164-72.
30. Williams JP, Blair HC, McDonald JM, McKenna MA, Jordan SE, Williford J, et al. Regulation of osteoclastic bone resorption by glucose. Biochem Biophys Res Commun. 1997;235(3):646-51.
31. Mulari MT, Zhao H, Lakkakorpi PT, Väänänen HK. Osteoclast ruffled border has distinct subdomains for secretion and degraded matrix uptake. Traffic. 2003;4(2):113-25.
32. Dodds RA, James IE, Rieman D, Ahern R, Hwang SM, Connor JR, et al. Human osteoclast cathepsin K is processed intracellularly prior to attachment and bone resorption. J Bone Miner Res. 2001;16(3):478-86.
33. Li YP, Chen W. Characterization of mouse cathepsin K gene, the gene promoter, and the gene expression. J Bone Miner Res. 1999;14(4):487-99.
34. Teitelbaum SL. Bone resorption by osteoclasts. Science. 2000;289(5484):1504-8.
35. Rauch A, Mandrup S. Transcriptional networks controlling stromal cell differentiation. Nat Rev Mol Cell Biol. 2021;22(7):465-82.
36. Wolock SL, Krishnan I, Tenen DE, Matkins V, Camacho V, Patel S, et al. Mapping Distinct Bone Marrow Niche Populations and Their Differentiation Paths. Cell Rep. 2019;28(2):302-11.e5.
37. Datta HK, Ng WF, Walker JA, Tuck SP, Varanasi SS. The cell biology of bone metabolism. J Clin Pathol. 2008;61(5):577-87.
38. Claes L, Recknagel S, Ignatius A. Fracture healing under healthy and inflammatory conditions. Nat Rev Rheumatol. 2012;8(3):133-43.

39. Clines GA. Prospects for osteoprogenitor stem cells in fracture repair and osteoporosis. Curr Opin Organ Transplant. 2010;15(1):73-8.
40. Ji C, Eickelberg O, McCarthy TL, Centrella M. Control and counter-control of TGF-beta activity through FAST and Runx (CBFa) transcriptional elements in osteoblasts. Endocrinology. 2001;142(9):3873-9.
41. Lee KS, Kim HJ, Li QL, Chi XZ, Ueta C, Komori T, et al. Runx2 is a common target of transforming growth factor beta1 and bone morphogenetic protein 2, and cooperation between Runx2 and Smad5 induces osteoblast-specific gene expression in the pluripotent mesenchymal precursor cell line C2C12. Mol Cell Biol. 2000;20(23):8783-92.
42. Park MH, Shin HI, Choi JY, Nam SH, Kim YJ, Kim HJ, et al. Differential expression patterns of Runx2 isoforms in cranial suture morphogenesis. J Bone Miner Res. 2001;16(5):885-92.
43. Prince M, Banerjee C, Javed A, Green J, Lian JB, Stein GS, et al. Expression and regulation of Runx2/Cbfa1 and osteoblast phenotypic markers during the growth and differentiation of human osteoblasts. J Cell Biochem. 2001;80(3):424-40.
44. Xiao ZS, Liu SG, Hinson TK, Quarles LD. Characterization of the upstream mouse Cbfa1/Runx2 promoter. J Cell Biochem. 2001;82(4):647-59.
45. Banerjee C, Javed A, Choi JY, Green J, Rosen V, van Wijnen AJ, et al. Differential regulation of the two principal Runx2/Cbfa1 n-terminal isoforms in response to bone morphogenetic protein-2 during development of the osteoblast phenotype. Endocrinology. 2001;142(9):4026-39.
46. Gutierrez S, Javed A, Tennant DK, van Rees M, Montecino M, Stein GS, et al. CCAAT/enhancer-binding proteins (C/EBP) beta and delta activate osteocalcin gene transcription and synergize with Runx2 at the C/EBP element to regulate bone-specific expression. J Biol Chem. 2002;277(2):1316-23.
47. Kim YJ, Kim HN, Park EK, Lee BH, Ryoo HM, Kim SY, et al. The bone-related Zn finger transcription factor Osterix promotes proliferation of mesenchymal cells. Gene. 2006;366(1):145-51.
48. Meury T, Verrier S, Alini M. Human endothelial cells inhibit BMSC differentiation into mature osteoblasts in vitro by interfering with osterix expression. J Cell Biochem. 2006;98(4):992-1006.
49. Milona MA, Gough JE, Edgar AJ. Expression of alternatively spliced isoforms of human Sp7 in osteoblast-like cells. BMC Genomics. 2003;4:43.
50. Nishio Y, Dong Y, Paris M, O'Keefe RJ, Schwarz EM, Drissi H. Runx2-mediated regulation of the zinc finger Osterix/Sp7 gene. Gene. 2006;372:62-70.
51. Tai G, Polak JM, Bishop AE, Christodoulou I, Buttery LD. Differentiation of osteoblasts from murine embryonic stem cells by overexpression of the transcriptional factor osterix. Tissue Eng. 2004;10(9-10):1456-66.
52. Maes C, Kobayashi T, Selig MK, Torrekens S, Roth SI, Mackem S, et al. Osteoblast precursors, but not mature osteoblasts, move into developing and fractured bones along with invading blood vessels. Dev Cell. 2010;19(2):329-44.
53. Bohm AM, Dirckx N, Tower RJ, Peredo N, Vanuytven S, Theunis K, et al. Activation of Skeletal Stem and Progenitor Cells for Bone Regeneration Is Driven by PDGFRbeta Signaling. Dev Cell. 2019;51(2):236-54 e12.
54. Yoshioka H, Okita S, Nakano M, Minamizaki T, Nubukiyo A, Sotomaru Y, et al. Single-Cell RNA-Sequencing Reveals the Breadth of Osteoblast Heterogeneity. JBMR plus. 2021;5(6):e10496-e.

55. Rodrigues AM, Caetano-Lopes J, Vale AC, Vidal B, Lopes A, Aleixo I, et al. Low osteocalcin/collagen type I bone gene expression ratio is associated with hip fragility fractures. Bone. 2012;51(6):981-9.
56. Schlesinger PH, Blair HC, Beer Stolz D, Riazanski V, Ray EC, Tourkova IL, et al. Cellular and extracellular matrix of bone, with principles of synthesis and dependency of mineral deposition on cell membrane transport. Am J Physiol Cell Physiol. 2020;318(1):C111-c24.
57. Dacic S, Kalajzic I, Visnjic D, Lichtler AC, Rowe DW. Col1a1-driven transgenic markers of osteoblast lineage progression. J Bone Miner Res. 2001;16(7):1228-36.
58. Franceschi RT, Iyer BS, Cui Y. Effects of ascorbic acid on collagen matrix formation and osteoblast differentiation in murine MC3T3-E1 cells. J Bone Miner Res. 1994;9(6):843-54.
59. Millán JL. The role of phosphatases in the initiation of skeletal mineralization. Calcif Tissue Int. 2013;93(4):299-306.
60. Wennberg C, Hessle L, Lundberg P, Mauro S, Narisawa S, Lerner UH, et al. Functional characterization of osteoblasts and osteoclasts from alkaline phosphatase knockout mice. J Bone Miner Res. 2000;15(10):1879-88.
61. Fauran-Clavel MJ, Oustrin J. Alkaline phosphatase and bone calcium parameters. Bone. 1986;7(2):95-9.
62. Komori T. Functions of Osteocalcin in Bone, Pancreas, Testis, and Muscle. Int J Mol Sci. 2020;21(20).
63. Bailey S, Karsenty G, Gundberg C, Vashishth D. Osteocalcin and osteopontin influence bone morphology and mechanical properties. Ann N Y Acad Sci. 2017;1409(1):79-84.
64. Hara K, Kobayashi M, Akiyama Y. Influence of bone osteocalcin levels on bone loss induced by ovariectomy in rats. J Bone Miner Metab. 2007;25(6):345-53.
65. Moriishi T, Ozasa R, Ishimoto T, Nakano T, Hasegawa T, Miyazaki T, et al. Osteocalcin is necessary for the alignment of apatite crystallites, but not glucose metabolism, testosterone synthesis, or muscle mass. PLoS Genet. 2020;16(5):e1008586.
66. Nikel O, Poundarik AA, Bailey S, Vashishth D. Structural role of osteocalcin and osteopontin in energy dissipation in bone. J Biomech. 2018;80:45-52.
67. Manolagas SC. Birth and death of bone cells: basic regulatory mechanisms and implications for the pathogenesis and treatment of osteoporosis. Endocr Rev. 2000;21(2):115-37.
68. Ayoubi M, van Tol AF, Weinkamer R, Roschger P, Brugger PC, Berzlanovich A, et al. 3D Interrelationship between Osteocyte Network and Forming Mineral during Human Bone Remodeling. Adv Healthc Mater. 2021;10(12):e2100113.
69. Bozal CB, Sánchez LM, Ubios AM. The lacuno-canalicular system (LCS) and osteocyte network of alveolar bone by confocal laser scanning microscopy (CLSM). Acta Odontol Latinoam. 2012;25(1):123-31.
70. Buenzli PR, Sims NA. Quantifying the osteocyte network in the human skeleton. Bone. 2015;75:144-50.
71. Weinkamer R, Kollmannsberger P, Fratzl P. Towards a Connectomic Description of the Osteocyte Lacunocanalicular Network in Bone. Curr Osteoporos Rep. 2019;17(4):186-94.
72. Dallas SL, Moore DS. Using confocal imaging approaches to understand the structure and function of osteocytes and the lacunocanalicular network. Bone. 2020;138:115463.
73. Weinkamer R, Kollmannsberger P, Fratzl P. Towards a Connectomic Description of the Osteocyte Lacunocanalicular Network in Bone. Current osteoporosis reports. 2019;17(4):186-94.

74. Schneider P, Meier M, Wepf R, Müller R. Towards quantitative 3D imaging of the osteocyte lacuno-canalicular network. Bone. 2010;47(5):848-58.
75. Robling AG, Bonewald LF. The Osteocyte: New Insights. Annu Rev Physiol. 2020;82:485-506.
76. Bonewald LF, Johnson ML. Osteocytes, mechanosensing and Wnt signaling. Bone. 2008;42(4):606-15.
77. Burger EH, Klein-Nulend J. Mechanotransduction in bone--role of the lacuno-canalicular network. Faseb j. 1999;13 Suppl:S101-12.
78. Li J, Sarosi I, Cattley RC, Pretorius J, Asuncion F, Grisanti M, et al. Dkk1-mediated inhibition of Wnt signaling in bone results in osteopenia. Bone. 2006;39(4):754-66.
79. Liu M, Kurimoto P, Zhang J, Niu QT, Stolina M, Dechow PC, et al. Sclerostin and DKK1 Inhibition Preserves and Augments Alveolar Bone Volume and Architecture in Rats with Alveolar Bone Loss. J Dent Res. 2018;97(9):1031-8.
80. Ray S, Khassawna TE, Sommer U, Thormann U, Wijekoon ND, Lips K, et al. Differences in expression of Wnt antagonist Dkk1 in healthy versus pathological bone samples. J Microsc. 2017;265(1):111-20.
81. Zhang W, Drake MT. Potential role for therapies targeting DKK1, LRP5, and serotonin in the treatment of osteoporosis. Curr Osteoporos Rep. 2012;10(1):93-100.
82. Nakashima T, Hayashi M, Fukunaga T, Kurata K, Oh-Hora M, Feng JQ, et al. Evidence for osteocyte regulation of bone homeostasis through RANKL expression. Nat Med. 2011;17(10):1231-4.
83. Ajubi NE, Klein-Nulend J, Nijweide PJ, Vrijheid-Lammers T, Alblas MJ, Burger EH. Pulsating fluid flow increases prostaglandin production by cultured chicken osteocytes--a cytoskeleton-dependent process. Biochem Biophys Res Commun. 1996;225(1):62-8.
84. Klein-Nulend J, Bacabac RG, Mullender MG. Mechanobiology of bone tissue. Pathol Biol (Paris). 2005;53(10):576-80.
85. Kringelbach TM, Aslan D, Novak I, Ellegaard M, Syberg S, Andersen CK, et al. Fine-tuned ATP signals are acute mediators in osteocyte mechanotransduction. Cell Signal. 2015;27(12):2401-9.
86. Tian F, Wang Y, Bikle DD. IGF-1 signaling mediated cell-specific skeletal mechano-transduction. J Orthop Res. 2018;36(2):576-83.
87. Hardie DL, Baldwin MJ, Naylor A, Haworth OJ, Hou TZ, Lax S, et al. The stromal cell antigen CD248 (endosialin) is expressed on naive CD8+ human T cells and regulates proliferation. Immunology. 2011;133(3):288-95.
88. Mackie EJ, Ahmed YA, Tatarczuch L, Chen KS, Mirams M. Endochondral ossification: how cartilage is converted into bone in the developing skeleton. Int J Biochem Cell Biol. 2008;40(1):46-62.
89. Mackie EJ, Tatarczuch L, Mirams M. The skeleton: a multi-functional complex organ: the growth plate chondrocyte and endochondral ossification. J Endocrinol. 2011;211(2):109-21.
90. Lefebvre V, Smits P. Transcriptional control of chondrocyte fate and differentiation. Birth Defects Res C Embryo Today. 2005;75(3):200-12.
91. Lefebvre V, Bhattaram P. Vertebrate skeletogenesis. Curr Top Dev Biol. 2010;90:291-317.
92. Long F, Ornitz DM. Development of the endochondral skeleton. Cold Spring Harb Perspect Biol. 2013;5(1):a008334.

93. Kronenberg HM. Developmental regulation of the growth plate. Nature. 2003;423(6937):332-6.
94. Itkin T, Gur-Cohen S, Spencer JA, Schajnovitz A, Ramasamy SK, Kusumbe AP, et al. Distinct bone marrow blood vessels differentially regulate haematopoiesis. Nature. 2016;532(7599):323-8.
95. Berendsen AD, Olsen BR. Bone development. Bone. 2015;80:14-8.
96. Aubin JE, Liu F, Malaval L, Gupta AK. Osteoblast and chondroblast differentiation. Bone. 1995;17(2 Suppl):77S-83S.
97. Ortega N, Behonick DJ, Werb Z. Matrix remodeling during endochondral ossification. Trends Cell Biol. 2004;14(2):86-93.
98. Kusumbe AP, Adams RH. Osteoclast progenitors promote bone vascularization and osteogenesis. Nat Med. 2014;20(11):1238-40.
99. Silberstein L, Goncalves KA, Kharchenko PV, Turcotte R, Kfoury Y, Mercier F, et al. Proximity-Based Differential Single-Cell Analysis of the Niche to Identify Stem/Progenitor Cell Regulators. Cell Stem Cell. 2016;19(4):530-43.
100. Su P, Tian Y, Yang C, Ma X, Wang X, Pei J, et al. Mesenchymal Stem Cell Migration during Bone Formation and Bone Diseases Therapy. Int J Mol Sci. 2018;19(8).
101. Joshi V, Yamaguchi T, Matsuda Y, Kaneko N, Maki K, Okano T. Skeletal maturity assessment with the use of cone-beam computerized tomography. Oral Surg Oral Med Oral Pathol Oral Radiol. 2012;113(6):841-9.
102. Jourieh A, Khan H, Mheissen S, Assali M, Alam MK. The Correlation between Dental Stages and Skeletal Maturity Stages. Biomed Res Int. 2021;2021:9986498.
103. Utczas K, Muzsnai A, Cameron N, Zsakai A, Bodzsar EB. A comparison of skeletal maturity assessed by radiological and ultrasonic methods. Am J Hum Biol. 2017;29(4).
104. Mangiavini L, Merceron C, Schipani E. Analysis of Mouse Growth Plate Development. Curr Protoc Mouse Biol. 2016;6(1):67-130.
105. Varsano N, Kahil K, Haimov H, Rechav K, Addadi L, Weiner S. Characterization of the growth plate-bone interphase region using cryo-FIB SEM 3D volume imaging. J Struct Biol. 2021;213(4):107781.
106. Xie M, Gol'din P, Herdina AN, Estefa J, Medvedeva EV, Li L, et al. Secondary ossification center induces and protects growth plate structure. Elife. 2020;9.
107. Katsimbri P. The biology of normal bone remodelling. Eur J Cancer Care (Engl). 2017;26(6).
108. Kenkre JS, Bassett J. The bone remodelling cycle. Ann Clin Biochem. 2018;55(3):308-27.
109. Seeman E. Age- and menopause-related bone loss compromise cortical and trabecular microstructure. J Gerontol A Biol Sci Med Sci. 2013;68(10):1218-25.
110. Agerbaek MO, Eriksen EF, Kragstrup J, Mosekilde L, Melsen F. A reconstruction of the remodelling cycle in normal human cortical iliac bone. Bone Miner. 1991;12(2):101-12.
111. Orwoll ES. Toward an expanded understanding of the role of the periosteum in skeletal health. J Bone Miner Res. 2003;18(6):949-54.
112. Dempster DW, Cosman F, Kurland ES, Zhou H, Nieves J, Woelfert L, et al. Effects of daily treatment with parathyroid hormone on bone microarchitecture and turnover in patients with osteoporosis: a paired biopsy study. J Bone Miner Res. 2001;16(10):1846-53.
113. Bliziotes M, Sibonga JD, Turner RT, Orwoll E. Periosteal remodeling at the femoral neck in nonhuman primates. J Bone Miner Res. 2006;21(7):1060-7.

114. Burggren WW, Christoffels VM, Crossley DA, 2nd, Enok S, Farrell AP, Hedrick MS, et al. Comparative cardiovascular physiology: future trends, opportunities and challenges. Acta Physiol (Oxf). 2014;210(2):257-76.
115. Watson EC, Adams RH. Biology of Bone: The Vasculature of the Skeletal System. Cold Spring Harb Perspect Med. 2018;8(7).
116. Stegen S, Carmeliet G. The skeletal vascular system - Breathing life into bone tissue. Bone. 2018;115:50-8.
117. Carmeliet P. Angiogenesis in health and disease. Nat Med. 2003;9(6):653-60.
118. van Gastel N, Stegen S, Eelen G, Schoors S, Carlier A, Daniels VW, et al. Lipid availability determines fate of skeletal progenitor cells via SOX9. Nature. 2020;579(7797):111-7.
119. Maes C, Carmeliet P, Moermans K, Stockmans I, Smets N, Collen D, et al. Impaired angiogenesis and endochondral bone formation in mice lacking the vascular endothelial growth factor isoforms VEGF164 and VEGF188. Mech Dev. 2002;111(1-2):61-73.
120. Maes C, Goossens S, Bartunkova S, Drogat B, Coenegrachts L, Stockmans I, et al. Increased skeletal VEGF enhances beta-catenin activity and results in excessively ossified bones. Embo j. 2010;29(2):424-41.
121. Schipani E, Maes C, Carmeliet G, Semenza GL. Regulation of osteogenesis-angiogenesis coupling by HIFs and VEGF. J Bone Miner Res. 2009;24(8):1347-53.
122. Gerber HP, Ferrara N. Angiogenesis and bone growth. Trends Cardiovasc Med. 2000;10(5):223-8.
123. Gerhardt H, Golding M, Fruttiger M, Ruhrberg C, Lundkvist A, Abramsson A, et al. VEGF guides angiogenic sprouting utilizing endothelial tip cell filopodia. J Cell Biol. 2003;161(6):1163-77.
124. Duran CL, Howell DW, Dave JM, Smith RL, Torrie ME, Essner JJ, et al. Molecular Regulation of Sprouting Angiogenesis. Compr Physiol. 2017;8(1):153-235.
125. Eilken HM, Adams RH. Dynamics of endothelial cell behavior in sprouting angiogenesis. Curr Opin Cell Biol. 2010;22(5):617-25.
126. Risau W. Mechanisms of angiogenesis. Nature. 1997;386(6626):671-4.
127. Matsumoto K, Ema M. Roles of VEGF-A signalling in development, regeneration, and tumours. J Biochem. 2014;156(1):1-10.
128. Carmeliet P, Ferreira V, Breier G, Pollefeyt S, Kieckens L, Gertsenstein M, et al. Abnormal blood vessel development and lethality in embryos lacking a single VEGF allele. Nature. 1996;380(6573):435-9.
129. Carmeliet P, Collen D. Molecular basis of angiogenesis. Role of VEGF and VE-cadherin. Ann N Y Acad Sci. 2000;902:249-62; discussion 62-4.
130. Ramasamy SK, Kusumbe AP, Wang L, Adams RH. Endothelial Notch activity promotes angiogenesis and osteogenesis in bone. Nature. 2014;507(7492):376-80.
131. Xie H, Cui Z, Wang L, Xia Z, Hu Y, Xian L, et al. PDGF-BB secreted by preosteoclasts induces angiogenesis during coupling with osteogenesis. Nat Med. 2014;20(11):1270-8.
132. Wang Y, Singh AR, Zhao Y, Du T, Huang Y, Wan X, et al. TRIM28 regulates sprouting angiogenesis through VEGFR-DLL4-Notch signaling circuit. FASEB J. 2020;34(11):14710-24.
133. Ripamonti U. Soluble and insoluble signals sculpt osteogenesis in angiogenesis. World J Biol Chem. 2010;1(5):109-32.
134. Gurel Pekozer G, Torun Kose G, Hasirci V. Influence of co-culture on osteogenesis and angiogenesis of bone marrow mesenchymal stem cells and aortic endothelial cells. Microvascular Research. 2016;108:1-9.

135. Inglis S, Christensen D, Wilson DI, Kanczler JM, Oreffo RO. Human endothelial and foetal femur-derived stem cell co-cultures modulate osteogenesis and angiogenesis. Stem Cell Res Ther. 2016;7:13.
136. Langen UH, Pitulescu ME, Kim JM, Enriquez-Gasca R, Sivaraj KK, Kusumbe AP, et al. Cell-matrix signals specify bone endothelial cells during developmental osteogenesis. Nat Cell Biol. 2017;19(3):189-201.
137. Grüneboom A, Hawwari I, Weidner D, Culemann S, Müller S, Henneberg S, et al. A network of trans-cortical capillaries as mainstay for blood circulation in long bones. Nat Metab. 2019;1(2):236-50.
138. Ramasamy SK, Kusumbe AP, Schiller M, Zeuschner D, Bixel MG, Milia C, et al. Blood flow controls bone vascular function and osteogenesis. Nat Commun. 2016;7:13601.
139. Wang L, Zhou F, Zhang P, Wang H, Qu Z, Jia P, et al. Human type H vessels are a sensitive biomarker of bone mass. Cell Death Dis. 2017;8(5):e2760.
140. Xu X, Wang F, Yang Y, Zhou X, Cheng Y, Wei X, et al. LIPUS promotes spinal fusion coupling proliferation of type H microvessels in bone. Sci Rep. 2016;6:20116.
141. Yang M, Li CJ, Xiao Y, Guo Q, Huang Y, Su T, et al. Ophiopogonin D promotes bone regeneration by stimulating CD31(hi) EMCN(hi) vessel formation. Cell Prolif. 2020;53(3):e12784.
142. Kuhn A, Brachtendorf G, Kurth F, Sonntag M, Samulowitz U, Metze D, et al. Expression of endomucin, a novel endothelial sialomucin, in normal and diseased human skin. J Invest Dermatol. 2002;119(6):1388-93.
143. Newman PJ, Albelda SM. Cellular and molecular aspects of PECAM-1. Nouv Rev Fr Hematol. 1992;34 Suppl:S9-13.
144. Yan ZQ, Wang XK, Zhou Y, Wang ZG, Wang ZX, Jin L, et al. H-type blood vessels participate in alveolar bone remodeling during murine tooth extraction healing. Oral Dis. 2020;26(5):998-1009.
145. Kusumbe AP, Ramasamy SK, Itkin T, Mae MA, Langen UH, Betsholtz C, et al. Age-dependent modulation of vascular niches for haematopoietic stem cells. Nature. 2016;532(7599):380-4.
146. Liu Y, Chen Q, Jeong HW, Koh BI, Watson EC, Xu C, et al. A specialized bone marrow microenvironment for fetal haematopoiesis. Nat Commun. 2022;13(1):1327.
147. Zhu Y, Ruan Z, Lin Z, Long H, Zhao R, Sun B, et al. The association between CD31(hi)Emcn(hi) endothelial cells and bone mineral density in Chinese women. J Bone Miner Metab. 2019;37(6):987-95.
148. Caire R, Roche B, Picot T, Aanei CM, He Z, Campos L, et al. Parathyroid Hormone Remodels Bone Transitional Vessels and the Leptin Receptor-Positive Pericyte Network in Mice. J Bone Miner Res. 2019;34(8):1487-501.
149. Li XM, Hu Z, Jorgenson ML, Slayton WB. High levels of acetylated low-density lipoprotein uptake and low tyrosine kinase with immunoglobulin and epidermal growth factor homology domains-2 (Tie2) promoter activity distinguish sinusoids from other vessel types in murine bone marrow. Circulation. 2009;120(19):1910-8.
150. Acar M, Kocherlakota KS, Murphy MM, Peyer JG, Oguro H, Inra CN, et al. Deep imaging of bone marrow shows non-dividing stem cells are mainly perisinusoidal. Nature. 2015;526(7571):126-30.
151. van Gastel N, Stegen S, Eelen G, Schoors S, Carlier A, Daniëls VW, et al. Lipid availability determines fate of skeletal progenitor cells via SOX9. Nature. 2020;579(7797):111-7.

152. Wrotnowski U, Mills SE, Cooper PH. Malignant angioendotheliomatosis. An angiotropic lymphoma? Am J Clin Pathol. 1985;83(2):244-8.
153. Huang C, Ness VP, Yang X, Chen H, Luo J, Brown EB, et al. Spatiotemporal Analyses of Osteogenesis and Angiogenesis via Intravital Imaging in Cranial Bone Defect Repair. J Bone Miner Res. 2015;30(7):1217-30.
154. Gerber HP, Vu TH, Ryan AM, Kowalski J, Werb Z, Ferrara N. VEGF couples hypertrophic cartilage remodeling, ossification and angiogenesis during endochondral bone formation. Nat Med. 1999;5(6):623-8.
155. Street J, Bao M, deGuzman L, Bunting S, Peale FV, Jr., Ferrara N, et al. Vascular endothelial growth factor stimulates bone repair by promoting angiogenesis and bone turnover. Proc Natl Acad Sci U S A. 2002;99(15):9656-61.
156. Henriksen K, Karsdal M, Delaisse JM, Engsig MT. RANKL and vascular endothelial growth factor (VEGF) induce osteoclast chemotaxis through an ERK1/2-dependent mechanism. J Biol Chem. 2003;278(49):48745-53.
157. Peng H, Wright V, Usas A, Gearhart B, Shen HC, Cummins J, et al. Synergistic enhancement of bone formation and healing by stem cell-expressed VEGF and bone morphogenetic protein-4. J Clin Invest. 2002;110(6):751-9.
158. Riehl BD, Lee JS, Ha L, Kwon IK, Lim JY. Flowtaxis of osteoblast migration under fluid shear and the effect of RhoA kinase silencing. PLoS One. 2017;12(2):e0171857.
159. Chen Z, Xu XH, Hu J. Role of pericytes in angiogenesis: focus on cancer angiogenesis and anti-angiogenic therapy. Neoplasma. 2016;63(2):173-82.
160. Huang H. Pericyte-Endothelial Interactions in the Retinal Microvasculature. Int J Mol Sci. 2020;21(19).
161. Ribatti D, Nico B, Crivellato E. The role of pericytes in angiogenesis. Int J Dev Biol. 2011;55(3):261-8.
162. Liang Y, Diehn M, Bollen AW, Israel MA, Gupta N. Type I collagen is overexpressed in medulloblastoma as a component of tumor microenvironment. J Neurooncol. 2008;86(2):133-41.
163. Ben Shoham A, Rot C, Stern T, Krief S, Akiva A, Dadosh T, et al. Deposition of collagen type I onto skeletal endothelium reveals a new role for blood vessels in regulating bone morphology. Development. 2016;143(21):3933-43.
164. Huang J, Yin H, Rao SS, Xie PL, Cao X, Rao T, et al. Harmine enhances type H vessel formation and prevents bone loss in ovariectomized mice. Theranostics. 2018;8(9):2435-46.
165. Clarkin CE, Emery RJ, Pitsillides AA, Wheeler-Jones CP. Evaluation of VEGF-mediated signaling in primary human cells reveals a paracrine action for VEGF in osteoblast-mediated crosstalk to endothelial cells. J Cell Physiol. 2008;214(2):537-44.
166. Jeon SA, Lee JH, Kim DW, Cho JY. E3-ubiquitin ligase NEDD4 enhances bone formation by removing TGFβ1-induced pSMAD1 in immature osteoblast. Bone. 2018;116:248-58.
167. Nam B, Park H, Lee YL, Oh Y, Park J, Kim SY, et al. TGFβ1 Suppressed Matrix Mineralization of Osteoblasts Differentiation by Regulating SMURF1-C/EBPβ-DKK1 Axis. Int J Mol Sci. 2020;21(24).
168. Nesti LJ, Caterson EJ, Wang M, Chang R, Chapovsky F, Hoek JB, et al. TGF-beta1 calcium signaling increases alpha5 integrin expression in osteoblasts. J Orthop Res. 2002;20(5):1042-9.
169. Spinella-Jaegle S, Roman-Roman S, Faucheu C, Dunn FW, Kawai S, Galléa S, et al. Opposite effects of bone morphogenetic protein-2 and transforming growth factor-beta1 on osteoblast differentiation. Bone. 2001;29(4):323-30.

170. Zaidi M, Lizneva D, Yuen T. The role of PDGF-BB in the bone-vascular relationship during aging. J Clin Invest. 2021;131(20).
171. Hu K, Olsen BR. Osteoblast-derived VEGF regulates osteoblast differentiation and bone formation during bone repair. J Clin Invest. 2016;126(2):509-26.
172. Xu R, Yallowitz A, Qin A, Wu Z, Shin DY, Kim JM, et al. Targeting skeletal endothelium to ameliorate bone loss. Nat Med. 2018;24(6):823-33.
173. Goldstein SA, Goulet R, McCubbrey D. Measurement and significance of three-dimensional architecture to the mechanical integrity of trabecular bone. Calcif Tissue Int. 1993;53 Suppl 1:S127-32; discussion S32-3.
174. Farr JN, Khosla S. Cellular senescence in bone. Bone. 2019;121:121-33.
175. Farr JN, Xu M, Weivoda MM, Monroe DG, Fraser DG, Onken JL, et al. Targeting cellular senescence prevents age-related bone loss in mice. Nat Med. 2017;23(9):1072-9.
176. Singh L, Brennan TA, Russell E, Kim JH, Chen Q, Brad Johnson F, et al. Aging alters bone-fat reciprocity by shifting in vivo mesenchymal precursor cell fate towards an adipogenic lineage. Bone. 2016;85:29-36.
177. Wang H, Chen Q, Lee SH, Choi Y, Johnson FB, Pignolo RJ. Impairment of osteoblast differentiation due to proliferation-independent telomere dysfunction in mouse models of accelerated aging. Aging Cell. 2012;11(4):704-13.
178. Garnero P, Sornay-Rendu E, Chapuy MC, Delmas PD. Increased bone turnover in late postmenopausal women is a major determinant of osteoporosis. J Bone Miner Res. 1996;11(3):337-49.
179. Yeh PS, Lee YW, Chang WH, Wang W, Wang JL, Liu SH, et al. Biomechanical and tomographic differences in the microarchitecture and strength of trabecular and cortical bone in the early stage of male osteoporosis. PLoS One. 2019;14(8):e0219718.
180. Burr DB. Muscle strength, bone mass, and age-related bone loss. J Bone Miner Res. 1997;12(10):1547-51.
181. Meunier PJ, Boivin G. Bone mineral density reflects bone mass but also the degree of mineralization of bone: therapeutic implications. Bone. 1997;21(5):373-7.
182. Mundy GR. Osteoporosis: pathophysiology and non-pharmacological management. Best Pract Res Clin Rheumatol. 2001;15(5):727-45.
183. Ström O, Borgström F, Kanis JA, Compston J, Cooper C, McCloskey EV, et al. Osteoporosis: burden, health care provision and opportunities in the EU: a report prepared in collaboration with the International Osteoporosis Foundation (IOF) and the European Federation of Pharmaceutical Industry Associations (EFPIA). Arch Osteoporos. 2011;6:59-155.
184. Herrero-Beaumont G, Roman-Blas JA, Castañeda S, Jimenez SA. Primary osteoarthritis no longer primary: three subsets with distinct etiological, clinical, and therapeutic characteristics. Semin Arthritis Rheum. 2009;39(2):71-80.
185. Arceo-Mendoza RM, Camacho PM. Postmenopausal Osteoporosis: Latest Guidelines. Endocrinol Metab Clin North Am. 2021;50(2):167-78.
186. Camacho PM, Petak SM, Binkley N, Diab DL, Eldeiry LS, Farooki A, et al. AMERICAN ASSOCIATION OF CLINICAL ENDOCRINOLOGISTS/AMERICAN COLLEGE OF ENDOCRINOLOGY CLINICAL PRACTICE GUIDELINES FOR THE DIAGNOSIS AND TREATMENT OF POSTMENOPAUSAL OSTEOPOROSIS-2020 UPDATE. Endocr Pract. 2020;26(Suppl 1):1-46.
187. Chandran M. AACE/ACE Clinical Practice Guidelines for the Diagnosis and Treatment of Postmenopausal Osteoporosis-2020 Update: Risk Stratification and Intervention Thresholds. Endocr Pract. 2021;27(4):378.

188. Kanis JA, Cooper C, Rizzoli R, Reginster JY. European guidance for the diagnosis and management of osteoporosis in postmenopausal women. Osteoporos Int. 2019;30(1):3-44.
189. Alonso-Bouzon C, Duque G. [Senile osteoporosis: an update]. Rev Esp Geriatr Gerontol. 2011;46(4):223-9.
190. Atik OS, Uslu MM, Eksioglu F, Satana T. Etiology of senile osteoporosis: a hypothesis. Clin Orthop Relat Res. 2006;443:25-7.
191. Duque G, Troen BR. Understanding the mechanisms of senile osteoporosis: new facts for a major geriatric syndrome. J Am Geriatr Soc. 2008;56(5):935-41.
192. Kaufman JM, Goemaere S. Osteoporosis in men. Best Pract Res Clin Endocrinol Metab. 2008;22(5):787-812.
193. Adler RA, Hochberg MC. Glucocorticoid-induced osteoporosis in men. J Endocrinol Invest. 2011;34(6):481-4.
194. Civitelli R, Ziambaras K. Epidemiology of glucocorticoid-induced osteoporosis. J Endocrinol Invest. 2008;31(7 Suppl):2-6.
195. Clowes JA, Peel N, Eastell R. Glucocorticoid-induced osteoporosis. Curr Opin Rheumatol. 2001;13(4):326-32.
196. Compston J. Management of glucocorticoid-induced osteoporosis. Nat Rev Rheumatol. 2010;6(2):82-8.
197. Compston J. Glucocorticoid-induced osteoporosis: an update. Endocrine. 2018;61(1):7-16.
198. Jackson RD. Topical Corticosteroids and Glucocorticoid-Induced Osteoporosis-Cumulative Dose and Duration Matter. JAMA Dermatol. 2021;157(3):269-70.
199. Lane NE. Glucocorticoid-Induced Osteoporosis: New Insights into the Pathophysiology and Treatments. Curr Osteoporos Rep. 2019;17(1):1-7.
200. Ahmed SF, Elmantaser M. Secondary osteoporosis. Endocr Dev. 2009;16:170-90.
201. Rolvien T, Amling M. Disuse Osteoporosis: Clinical and Mechanistic Insights. Calcif Tissue Int. 2022;110(5):592-604.
202. Takata S, Yasui N. Disuse osteoporosis. J Med Invest. 2001;48(3-4):147-56.
203. Chuang MH, Chuang TL, Koo M, Wang YF. Trabecular Bone Score Reflects Trabecular Microarchitecture Deterioration and Fragility Fracture in Female Adult Patients Receiving Glucocorticoid Therapy: A Pre-Post Controlled Study. Biomed Res Int. 2017;2017:4210217.
204. Wright NC, Saag KG, Dawson-Hughes B, Khosla S, Siris ES. The impact of the new National Bone Health Alliance (NBHA) diagnostic criteria on the prevalence of osteoporosis in the United States: supplementary presentation. Osteoporos Int. 2017;28(11):3283-4.
205. Cooper C, Campion G, Melton LJ, 3rd. Hip fractures in the elderly: a world-wide projection. Osteoporos Int. 1992;2(6):285-9.
206. Gullberg B, Johnell O, Kanis JA. World-wide projections for hip fracture. Osteoporos Int. 1997;7(5):407-13.
207. Lane NE. Epidemiology, etiology, and diagnosis of osteoporosis. Am J Obstet Gynecol. 2006;194(2 Suppl):S3-11.
208. Szeliga A, Maciejewska-Jeske M, Męczekalski B. Bone health and evaluation of bone mineral density in patients with premature ovarian insufficiency. Prz Menopauzalny. 2018;17(3):112-6.
209. Kameda T, Mano H, Yuasa T, Mori Y, Miyazawa K, Shiokawa M, et al. Estrogen inhibits bone resorption by directly inducing apoptosis of the bone-resorbing osteoclasts. J Exp Med. 1997;186(4):489-95.

210. Compston J, Cooper A, Cooper C, Gittoes N, Gregson C, Harvey N, et al. UK clinical guideline for the prevention and treatment of osteoporosis. Arch Osteoporos. 2017;12(1):43.
211. Ahern T, Wu FC. New horizons in testosterone and the ageing male. Age Ageing. 2015;44(2):188-95.
212. The Lancet Diabetes E. Osteoporosis: a roadmap to close the treatment gap. Lancet Diabetes Endocrinol. 2018;6(11):833.
213. Khosla S, Hofbauer LC. Osteoporosis treatment: recent developments and ongoing challenges. Lancet Diabetes Endocrinol. 2017;5(11):898-907.
214. Adler RA, El-Hajj Fuleihan G, Bauer DC, Camacho PM, Clarke BL, Clines GA, et al. Managing Osteoporosis in Patients on Long-Term Bisphosphonate Treatment: Report of a Task Force of the American Society for Bone and Mineral Research. J Bone Miner Res. 2016;31(1):16-35.
215. Fink HA, MacDonald R, Forte ML, Rosebush CE, Ensrud KE, Schousboe JT, et al. Long-Term Drug Therapy and Drug Discontinuations and Holidays for Osteoporosis Fracture Prevention: A Systematic Review. Ann Intern Med. 2019;171(1):37-50.
216. Sheibani-Rad S. Femoral Fractures Following Long-term Bisphosphonate Use. Orthopedics. 2016;39(6):e1036-e40.
217. Ferreira Jr LH, Jr., Mendonça Jr KD, Jr., Chaves de Souza J, Soares Dos Reis DC, do Carmo Faleiros Veloso Guedes C, de Souza Castro Filice L, et al. Bisphosphonate-associated osteonecrosis of the jaw. Minerva Dent Oral Sci. 2021;70(1):49-57.
218. Patel RN, Ashraf A, Sundaram M. Atypical Fractures Following Bisphosphonate Therapy. Semin Musculoskelet Radiol. 2016;20(4):376-81.
219. Bindon B, Adams W, Balasubramanian N, Sandhu J, Camacho P. OSTEOPOROTIC FRACTURES DURING BISPHOSPHONATE DRUG HOLIDAY. Endocr Pract. 2018;24(2):163-9.
220. Mignot MA, Taisne N, Legroux I, Cortet B, Paccou J. Bisphosphonate drug holidays in postmenopausal osteoporosis: effect on clinical fracture risk. Osteoporos Int. 2017;28(12):3431-8.
221. Rauner M, Taipaleenmäki H, Tsourdi E, Winter EM. Osteoporosis Treatment with Anti-Sclerostin Antibodies-Mechanisms of Action and Clinical Application. J Clin Med. 2021;10(4).
222. McClung MR, Grauer A, Boonen S, Bolognese MA, Brown JP, Diez-Perez A, et al. Romosozumab in postmenopausal women with low bone mineral density. N Engl J Med. 2014;370(5):412-20.
223. Cosman F, Crittenden DB, Adachi JD, Binkley N, Czerwinski E, Ferrari S, et al. Romosozumab Treatment in Postmenopausal Women with Osteoporosis. N Engl J Med. 2016;375(16):1532-43.
224. Prather C, Adams E, Zentgraf W. Romosozumab: A first-in-class sclerostin inhibitor for osteoporosis. Am J Health Syst Pharm. 2020;77(23):1949-56.
225. Lindsay R, Krege JH, Marin F, Jin L, Stepan JJ. Teriparatide for osteoporosis: importance of the full course. Osteoporos Int. 2016;27(8):2395-410.
226. Stroup J, Kane MP, Abu-Baker AM. Teriparatide in the treatment of osteoporosis. Am J Health Syst Pharm. 2008;65(6):532-9.
227. Saag KG, Shane E, Boonen S, Marín F, Donley DW, Taylor KA, et al. Teriparatide or alendronate in glucocorticoid-induced osteoporosis. N Engl J Med. 2007;357(20):2028-39.
228. Alford AI, Kozloff KM, Hankenson KD. Extracellular matrix networks in bone remodeling. Int J Biochem Cell Biol. 2015;65:20-31.
229. Lin X, Patil S, Gao YG, Qian A. The Bone Extracellular Matrix in Bone Formation and Regeneration. Front Pharmacol. 2020;11:757.

230. Chen J, Lippo L, Labella R, Tan SL, Marsden BD, Dustin ML, et al. Decreased blood vessel density and endothelial cell subset dynamics during ageing of the endocrine system. Embo j. 2021;40(1):e105242.
231. Reznikov N, Shahar R, Weiner S. Bone hierarchical structure in three dimensions. Acta Biomater. 2014;10(9):3815-26.
232. Mansour A, Mezour MA, Badran Z, Tamimi F. (*) Extracellular Matrices for Bone Regeneration: A Literature Review. Tissue Eng Part A. 2017;23(23-24):1436-51.
233. Salbach-Hirsch J, Rauner M, Hofbauer C, Hofbauer LC. New insights into the role of glycosaminoglycans in the endosteal bone microenvironment. Biol Chem. 2021;402(11):1415-25.
234. Komori T. Regulation of bone development and extracellular matrix protein genes by RUNX2. Cell Tissue Res. 2010;339(1):189-95.
235. Velleman SG. The role of the extracellular matrix in skeletal development. Poult Sci. 2000;79(7):985-9.
236. Nikitovic D, Aggelidakis J, Young MF, Iozzo RV, Karamanos NK, Tzanakakis GN. The biology of small leucine-rich proteoglycans in bone pathophysiology. J Biol Chem. 2012;287(41):33926-33.
237. Matsubara H, Hogan DE, Morgan EF, Mortlock DP, Einhorn TA, Gerstenfeld LC. Vascular tissues are a primary source of BMP2 expression during bone formation induced by distraction osteogenesis. Bone. 2012;51(1):168-80.
238. Chen Y, Yang S, Lovisa S, Ambrose CG, McAndrews KM, Sugimoto H, et al. Type-I collagen produced by distinct fibroblast lineages reveals specific function during embryogenesis and Osteogenesis Imperfecta. Nat Commun. 2021;12(1):7199.
239. Johnson KA, Hessle L, Vaingankar S, Wennberg C, Mauro S, Narisawa S, et al. Osteoblast tissue-nonspecific alkaline phosphatase antagonizes and regulates PC-1. Am J Physiol Regul Integr Comp Physiol. 2000;279(4):R1365-77.
240. Halling Linder C, Ek-Rylander B, Krumpel M, Norgård M, Narisawa S, Millán JL, et al. Bone Alkaline Phosphatase and Tartrate-Resistant Acid Phosphatase: Potential Co-regulators of Bone Mineralization. Calcif Tissue Int. 2017;101(1):92-101.
241. Anderson HC. Matrix vesicles and calcification. Curr Rheumatol Rep. 2003;5(3):222-6.
242. Hartman CD, Isenberg BC, Chua SG, Wong JY. Extracellular matrix type modulates cell migration on mechanical gradients. Exp Cell Res. 2017;359(2):361-6.
243. Jeon J, Lee MS, Yang HS. Differentiated osteoblasts derived decellularized extracellular matrix to promote osteogenic differentiation. Biomater Res. 2018;22:4.
244. Movilla N, Borau C, Valero C, Garcia-Aznar JM. Degradation of extracellular matrix regulates osteoblast migration: A microfluidic-based study. Bone. 2018;107:10-7.
245. Rauch U, Schafer KH. The extracellular matrix and its role in cell migration and development of the enteric nervous system. Eur J Pediatr Surg. 2003;13(3):158-62.
246. Bagley RG, Honma N, Weber W, Boutin P, Rouleau C, Shankara S, et al. Endosialin/TEM 1/CD248 is a pericyte marker of embryonic and tumor neovascularization. Microvasc Res. 2008;76(3):180-8.
247. Naylor AJ, McGettrick HM, Maynard WD, May P, Barone F, Croft AP, et al. A differential role for CD248 (Endosialin) in PDGF-mediated skeletal muscle angiogenesis. PLoS One. 2014;9(9):e107146.
248. Lax S, Hardie DL, Wilson A, Douglas MR, Anderson G, Huso D, et al. The pericyte and stromal cell marker CD248 (endosialin) is required for efficient lymph node expansion. Eur J Immunol. 2010;40(7):1884-9.

249. Becker R, Lenter MC, Vollkommer T, Boos AM, Pfaff D, Augustin HG, et al. Tumor stroma marker endosialin (Tem1) is a binding partner of metastasis-related protein Mac-2 BP/90K. FASEB J. 2008;22(8):3059-67.
250. Andreuzzi E, Colladel R, Pellicani R, Tarticchio G, Cannizzaro R, Spessotto P, et al. The angiostatic molecule Multimerin 2 is processed by MMP-9 to allow sprouting angiogenesis. Matrix Biol. 2017;64:40-53.
251. Masiero M, Simoes FC, Han HD, Snell C, Peterkin T, Bridges E, et al. A core human primary tumor angiogenesis signature identifies the endothelial orphan receptor ELTD1 as a key regulator of angiogenesis. Cancer Cell. 2013;24(2):229-41.
252. Zanivan S, Maione F, Hein MY, Hernandez-Fernaud JR, Ostasiewicz P, Giraudo E, et al. SILAC-based proteomics of human primary endothelial cell morphogenesis unveils tumor angiogenic markers. Mol Cell Proteomics. 2013;12(12):3599-611.
253. Delile J, Rayon T, Melchionda M, Edwards A, Briscoe J, Sagner A. Single cell transcriptomics reveals spatial and temporal dynamics of gene expression in the developing mouse spinal cord. Development. 2019;146(12).
254. Huang HP, Hong CL, Kao CY, Lin SW, Lin SR, Wu HL, et al. Gene targeting and expression analysis of mouse Tem1/endosialin using a lacZ reporter. Gene Expr Patterns. 2011;11(5-6):316-26.
255. Naylor AJ, Azzam E, Smith S, Croft A, Poyser C, Duffield JS, et al. The mesenchymal stem cell marker CD248 (endosialin) is a negative regulator of bone formation in mice. Arthritis Rheum. 2012;64(10):3334-43.
256. Maia M, DeVriese A, Janssens T, Moons M, Lories RJ, Tavernier J, et al. CD248 facilitates tumor growth via its cytoplasmic domain. BMC Cancer. 2011;11:162.
257. Croft AP, Naylor AJ, Marshall JL, Hardie DL, Zimmermann B, Turner J, et al. Rheumatoid synovial fibroblasts differentiate into distinct subsets in the presence of cytokines and cartilage. Arthritis Res Ther. 2016;18(1):270.
258. Tikhonova AN, Dolgalev I, Hu H, Sivaraj KK, Hoxha E, Cuesta-Domínguez Á, et al. The bone marrow microenvironment at single-cell resolution. Nature. 2019;569(7755):222-8.
259. Ohradanova A, Gradin K, Barathova M, Zatovicova M, Holotnakova T, Kopacek J, et al. Hypoxia upregulates expression of human endosialin gene via hypoxia-inducible factor 2. Br J Cancer. 2008;99(8):1348-56.
260. Tomkowicz B, Rybinski K, Foley B, Ebel W, Kline B, Routhier E, et al. Interaction of endosialin/TEM1 with extracellular matrix proteins mediates cell adhesion and migration. Proc Natl Acad Sci U S A. 2007;104(46):17965-70.
261. Tomkowicz B, Rybinski K, Sebeck D, Sass P, Nicolaides NC, Grasso L, et al. Endosialin/TEM-1/CD248 regulates pericyte proliferation through PDGF receptor signaling. Cancer Biol Ther. 2010;9(11):908-15.
262. Christian S, Winkler R, Helfrich I, Boos AM, Besemfelder E, Schadendorf D, et al. Endosialin (Tem1) is a marker of tumor-associated myofibroblasts and tumor vessel-associated mural cells. Am J Pathol. 2008;172(2):486-94.
263. Nanda A, Karim B, Peng Z, Liu G, Qiu W, Gan C, et al. Tumor endothelial marker 1 (Tem1) functions in the growth and progression of abdominal tumors. Proc Natl Acad Sci U S A. 2006;103(9):3351-6.
264. Wilhelm A, Aldridge V, Haldar D, Naylor AJ, Weston CJ, Hedegaard D, et al. CD248/endosialin critically regulates hepatic stellate cell proliferation during chronic liver injury via a PDGF-regulated mechanism. Gut. 2016;65(7):1175-85.

265. Smith SW, Croft AP, Morris HL, Naylor AJ, Huso DL, Isacke CM, et al. Genetic Deletion of the Stromal Cell Marker CD248 (Endosialin) Protects against the Development of Renal Fibrosis. Nephron. 2015;131(4):265-77.
266. MacFadyen JR, Haworth O, Roberston D, Hardie D, Webster MT, Morris HR, et al. Endosialin (TEM1, CD248) is a marker of stromal fibroblasts and is not selectively expressed on tumour endothelium. FEBS Lett. 2005;579(12):2569-75.
267. Rybinski K, Imtiyaz HZ, Mittica B, Drozdowski B, Fulmer J, Furuuchi K, et al. Targeting endosialin/CD248 through antibody-mediated internalization results in impaired pericyte maturation and dysfunctional tumor microvasculature. Oncotarget. 2015;6(28):25429-40.
268. Di Benedetto P, Liakouli V, Ruscitti P, Berardicurti O, Carubbi F, Panzera N, et al. Blocking CD248 molecules in perivascular stromal cells of patients with systemic sclerosis strongly inhibits their differentiation toward myofibroblasts and proliferation: a new potential target for antifibrotic therapy. Arthritis Res Ther. 2018;20(1):223.
269. Itagaki T, Honma T, Takahashi I, Echigo S, Sasano Y. Quantitative analysis and localization of mRNA transcripts of type I collagen, osteocalcin, MMP 2, MMP 8, and MMP 13 during bone healing in a rat calvarial experimental defect model. Anat Rec (Hoboken). 2008;291(8):1038-46.
270. Nakano K, Iwamatsu T, Wang CM, Tarasima M, Nakayama T, Sasaki K, et al. High bone turnover of type I collagen depends on fetal growth. Bone. 2006;38(2):249-56.
271. Kream BE, Harrison JR, Krebsbach PH, Bogdanovic Z, Bedalov A, Pavlin D, et al. Regulation of type I collagen gene expression in bone. Connect Tissue Res. 1995;31(4):261-4.
272. Kram V, Kilts TM, Bhattacharyya N, Li L, Young MF. Small leucine rich proteoglycans, a novel link to osteoclastogenesis. Sci Rep. 2017;7(1):12627.
273. Douglas T, Heinemann S, Bierbaum S, Scharnweber D, Worch H. Fibrillogenesis of collagen types I, II, and III with small leucine-rich proteoglycans decorin and biglycan. Biomacromolecules. 2006;7(8):2388-93.
274. Berendsen AD, Pinnow EL, Maeda A, Brown AC, McCartney-Francis N, Kram V, et al. Biglycan modulates angiogenesis and bone formation during fracture healing. Matrix Biol. 2014;35:223-31.
275. Parisuthiman D, Mochida Y, Duarte WR, Yamauchi M. Biglycan modulates osteoblast differentiation and matrix mineralization. J Bone Miner Res. 2005;20(10):1878-86.
276. Jongwattanapisan P, Terajima M, Miguez PA, Querido W, Nagaoka H, Sumida N, et al. Identification of the effector domain of biglycan that facilitates BMP-2 osteogenic function. Sci Rep. 2018;8(1):7022.
277. Wang H, Sun W, Ma J, Pan Y, Wang L, Zhang WB. Biglycan mediates suture expansion osteogenesis via potentiation of Wnt/beta-catenin signaling. J Biomech. 2015;48(3):432-40.
278. Jin SL, Bai YM, Zhao BY, Wang QH, Zhang HS. Silencing of miR-330-5p stimulates osteogenesis in bone marrow mesenchymal stem cells and inhibits bone loss in osteoporosis by activating Bgn-mediated BMP/Smad pathway. Eur Rev Med Pharmacol Sci. 2020;24(8):4095-102.
279. Hamaya E, Fujisawa T, Tamura M. Osteoadherin serves roles in the regulation of apoptosis and growth in MC3T3E1 osteoblast cells. Int J Mol Med. 2019;44(6):2336-44.
280. Tashima T, Nagatoishi S, Sagara H, Ohnuma S, Tsumoto K. Osteomodulin regulates diameter and alters shape of collagen fibrils. Biochem Biophys Res Commun. 2015;463(3):292-6.

281. Myren M, Kirby DJ, Noonan ML, Maeda A, Owens RT, Ricard-Blum S, et al. Biglycan potentially regulates angiogenesis during fracture repair by altering expression and function of endostatin. Matrix Biol. 2016;52-54:141-50.
282. Hauschka PV, Lian JB, Cole DE, Gundberg CM. Osteocalcin and matrix Gla protein: vitamin K-dependent proteins in bone. Physiol Rev. 1989;69(3):990-1047.
283. Doolittle ML, Ackert-Bicknell CL, Jonason JH. Isolation and Culture of Neonatal Mouse Calvarial Osteoblasts. Methods Mol Biol. 2021;2230:425-36.
284. Guedes JAC, Esteves JV, Morais MR, Zorn TM, Furuya DT. Osteocalcin improves insulin resistance and inflammation in obese mice: Participation of white adipose tissue and bone. Bone. 2018;115:68-82.
285. Zhou H, Seibel MJ. Bone: Osteoblasts and global energy metabolism - beyond osteocalcin. Nat Rev Rheumatol. 2017;13(5):261-2.
286. Diegel CR, Hann S, Ayturk UM, Hu JCW, Lim KE, Droscha CJ, et al. An osteocalcin-deficient mouse strain without endocrine abnormalities. PLoS Genet. 2020;16(5):e1008361.
287. Zhang J, Ma Z, Yan K, Wang Y, Yang Y, Wu X. Matrix Gla Protein Promotes the Bone Formation by Up-Regulating Wnt/beta-Catenin Signaling Pathway. Front Endocrinol (Lausanne). 2019;10:891.
288. Zhang Y, Zhao L, Wang N, Li J, He F, Li X, et al. Unexpected Role of Matrix Gla Protein in Osteoclasts: Inhibiting Osteoclast Differentiation and Bone Resorption. Mol Cell Biol. 2019;39(12).
289. Li R, Li X, Zhou M, Han N, Zhang Q. Quantitative determination of matrix Gla protein (MGP) and BMP-2 during the osteogenic differentiation of human periodontal ligament cells. Arch Oral Biol. 2012;57(10):1408-17.
290. Yao J, Guihard PJ, Blazquez-Medela AM, Guo Y, Liu T, Bostrom KI, et al. Matrix Gla protein regulates differentiation of endothelial cells derived from mouse embryonic stem cells. Angiogenesis. 2016;19(1):1-7.
291. Zhu S, Barbe MF, Amin N, Rani S, Popoff SN, Safadi FF, et al. Immunolocalization of Periostin-like factor and Periostin during embryogenesis. J Histochem Cytochem. 2008;56(4):329-45.
292. Merle B, Garnero P. The multiple facets of periostin in bone metabolism. Osteoporos Int. 2012;23(4):1199-212.
293. Wen L, Chen J, Duan L, Li S. Vitamin K-dependent proteins involved in bone and cardiovascular health (Review). Mol Med Rep. 2018;18(1):3-15.
294. Bonnet N, Conway SJ, Ferrari SL. Regulation of beta catenin signaling and parathyroid hormone anabolic effects in bone by the matricellular protein periostin. Proc Natl Acad Sci U S A. 2012;109(37):15048-53.
295. Bonnet N, Standley KN, Bianchi EN, Stadelmann V, Foti M, Conway SJ, et al. The matricellular protein periostin is required for sost inhibition and the anabolic response to mechanical loading and physical activity. J Biol Chem. 2009;284(51):35939-50.
296. Duchamp de Lageneste O, Julien A, Abou-Khalil R, Frangi G, Carvalho C, Cagnard N, et al. Periosteum contains skeletal stem cells with high bone regenerative potential controlled by Periostin. Nat Commun. 2018;9(1):773.
297. Cobo T, Viloria CG, Solares L, Fontanil T, Gonzalez-Chamorro E, De Carlos F, et al. Role of Periostin in Adhesion and Migration of Bone Remodeling Cells. PLoS One. 2016;11(1):e0147837.

298. Solmaz D, Uslu S, Kozaci D, Karaca N, Bulbul H, Tarhan EF, et al. Evaluation of periostin and factors associated with new bone formation in ankylosing spondylitis: Periostin may be associated with the Wnt pathway. Int J Rheum Dis. 2018;21(2):502-9.
299. Boskey AL, Spevak L, Paschalis E, Doty SB, McKee MD. Osteopontin deficiency increases mineral content and mineral crystallinity in mouse bone. Calcif Tissue Int. 2002;71(2):145-54.
300. Si J, Wang C, Zhang D, Wang B, Zhou Y. Osteopontin in Bone Metabolism and Bone Diseases. Med Sci Monit. 2020;26:e919159.
301. Foster BL, Ao M, Salmon CR, Chavez MB, Kolli TN, Tran AB, et al. Osteopontin regulates dentin and alveolar bone development and mineralization. Bone. 2018;107:196-207.
302. Hunter GK, Hauschka PV, Poole AR, Rosenberg LC, Goldberg HA. Nucleation and inhibition of hydroxyapatite formation by mineralized tissue proteins. Biochem J. 1996;317 (Pt 1):59-64.
303. Luukkonen J, Hilli M, Nakamura M, Ritamo I, Valmu L, Kauppinen K, et al. Osteoclasts secrete osteopontin into resorption lacunae during bone resorption. Histochem Cell Biol. 2019;151(6):475-87.
304. Senger DR, Perruzzi CA. Cell migration promoted by a potent GRGDS-containing thrombin-cleavage fragment of osteopontin. Biochim Biophys Acta. 1996;1314(1-2):13-24.
305. de Bruyn JR, Goiko M, Mozaffari M, Bator D, Dauphinee RL, Liao Y, et al. Dynamic light scattering study of inhibition of nucleation and growth of hydroxyapatite crystals by osteopontin. PLoS One. 2013;8(2):e56764.
306. Dong M, Yu X, Chen W, Guo Z, Sui L, Xu Y, et al. Osteopontin Promotes Bone Destruction in Periapical Periodontitis by Activating the NF-kappaB Pathway. Cell Physiol Biochem. 2018;49(3):884-98.
307. Kruger TE, Miller AH, Godwin AK, Wang J. Bone sialoprotein and osteopontin in bone metastasis of osteotropic cancers. Crit Rev Oncol Hematol. 2014;89(2):330-41.
308. Cao H, Cao B, Heazlewood CK, Domingues M, Sun X, Debele E, et al. Osteopontin is An Important Regulative Component of the Fetal Bone Marrow Hematopoietic Stem Cell Niche. Cells. 2019;8(9).
309. Qian J, Xu L, Sun X, Wang Y, Xuan W, Zhang Q, et al. Adiponectin aggravates bone erosion by promoting osteopontin production in synovial tissue of rheumatoid arthritis. Arthritis Res Ther. 2018;20(1):26.
310. Tarquini C, Mattera R, Mastrangeli F, Agostinelli S, Ferlosio A, Bei R, et al. Comparison of tissue transglutaminase 2 and bone biological markers osteocalcin, osteopontin and sclerostin expression in human osteoporosis and osteoarthritis. Amino Acids. 2017;49(3):683-93.
311. Wei QS, Huang L, Tan X, Chen ZQ, Chen SM, Deng WM. Serum osteopontin levels in relation to bone mineral density and bone turnover markers in postmenopausal women. Scand J Clin Lab Invest. 2016;76(1):33-9.
312. Wein M, Huelter-Hassler D, Nelson K, Fretwurst T, Nahles S, Finkenzeller G, et al. Differential osteopontin expression in human osteoblasts derived from iliac crest and alveolar bone and its role in early stages of angiogenesis. J Bone Miner Metab. 2019;37(1):105-17.
313. Poundarik AA, Boskey A, Gundberg C, Vashishth D. Biomolecular regulation, composition and nanoarchitecture of bone mineral. Sci Rep. 2018;8(1):1191.
314. Klement JD, Paschall AV, Redd PS, Ibrahim ML, Lu C, Yang D, et al. An osteopontin/CD44 immune checkpoint controls CD8+ T cell activation and tumor immune evasion. J Clin Invest. 2018;128(12):5549-60.

315. Feng JQ, Ward LM, Liu S, Lu Y, Xie Y, Yuan B, et al. Loss of DMP1 causes rickets and osteomalacia and identifies a role for osteocytes in mineral metabolism. Nat Genet. 2006;38(11):1310-5.
316. Bhatia A, Albazzaz M, Espinoza Orias AA, Inoue N, Miller LM, Acerbo A, et al. Overexpression of DMP1 accelerates mineralization and alters cortical bone biomechanical properties in vivo. J Mech Behav Biomed Mater. 2012;5(1):1-8.
317. Kulkarni GV, Chen B, Malone JP, Narayanan AS, George A. Promotion of selective cell attachment by the RGD sequence in dentine matrix protein 1. Arch Oral Biol. 2000;45(6):475-84.
318. Liu Z, Kennedy OD, Cardoso L, Basta-Pljakic J, Partridge NC, Schaffler MB, et al. DMP-1-mediated Ghr gene recombination compromises skeletal development and impairs skeletal response to intermittent PTH. FASEB J. 2016;30(2):635-52.
319. Lu Y, Yuan B, Qin C, Cao Z, Xie Y, Dallas SL, et al. The biological function of DMP-1 in osteocyte maturation is mediated by its 57-kDa C-terminal fragment. J Bone Miner Res. 2011;26(2):331-40.
320. Neve A, Corrado A, Cantatore FP. Osteocytes: central conductors of bone biology in normal and pathological conditions. Acta Physiol (Oxf). 2012;204(3):317-30.
321. Maginot M, Lin S, Liu Y, Yuan B, Feng JQ, Aswath PB. The in vivo role of DMP-1 and serum phosphate on bone mineral composition. Bone. 2015;81:602-13.
322. Turan S, Aydin C, Bereket A, Akcay T, Guran T, Yaralioglu BA, et al. Identification of a novel dentin matrix protein-1 (DMP-1) mutation and dental anomalies in a kindred with autosomal recessive hypophosphatemia. Bone. 2010;46(2):402-9.
323. Unterbrink A, O'Sullivan M, Chen S, MacDougall M. TGF beta-1 downregulates DMP-1 and DSPP in odontoblasts. Connect Tissue Res. 2002;43(2-3):354-8.
324. Rosset EM, Trombetta-eSilva J, Hepfer G, Yao H, Bradshaw AD. SPARC and the N-propeptide of collagen I influence fibroblast proliferation and collagen assembly in the periodontal ligament. PLoS One. 2017;12(2):e0173209.
325. Trombetta-eSilva J, Rosset EA, Hepfer RG, Wright GJ, Baicu C, Yao H, et al. Decreased Mechanical Strength and Collagen Content in SPARC-Null Periodontal Ligament Is Reversed by Inhibition of Transglutaminase Activity. J Bone Miner Res. 2015;30(10):1914-24.
326. Rosset EM, Bradshaw AD. SPARC/osteonectin in mineralized tissue. Matrix Biol. 2016;52-54:78-87.
327. Bradshaw AD. The role of SPARC in extracellular matrix assembly. J Cell Commun Signal. 2009;3(3-4):239-46.
328. Boskey AL, Moore DJ, Amling M, Canalis E, Delany AM. Infrared analysis of the mineral and matrix in bones of osteonectin-null mice and their wildtype controls. J Bone Miner Res. 2003;18(6):1005-11.
329. Delany AM, Amling M, Priemel M, Howe C, Baron R, Canalis E. Osteopenia and decreased bone formation in osteonectin-deficient mice. J Clin Invest. 2000;105(7):915-23.
330. Zhu YS, Gu Y, Jiang C, Chen L. Osteonectin regulates the extracellular matrix mineralization of osteoblasts through P38 signaling pathway. J Cell Physiol. 2020;235(3):2220-31.
331. Ribeiro N, Sousa SR, Brekken RA, Monteiro FJ. Role of SPARC in bone remodeling and cancer-related bone metastasis. J Cell Biochem. 2014;115(1):17-26.
332. Hunter GK, Goldberg HA. Nucleation of hydroxyapatite by bone sialoprotein. Proc Natl Acad Sci U S A. 1993;90(18):8562-5.

333. Xu L, Zhang Z, Sun X, Wang J, Xu W, Shi L, et al. Glycosylation status of bone sialoprotein and its role in mineralization. Exp Cell Res. 2017;360(2):413-20.
334. Luedde M, Roy S, Hippe HJ, Cardenas DV, Spehlmann M, Vucur M, et al. Elevated serum levels of bone sialoprotein during ICU treatment predict long-term mortality in critically ill patients. Sci Rep. 2018;8(1):9750.
335. Im BJ, Lee SC, Lee MH, Leesungbok R, Ahn SJ, Kang YG, et al. Promotion of osteoblastic differentiation and osteogenic transcription factor expression on a microgroove titanium surface with immobilized fibronectin or bone sialoprotein II. Biomed Mater. 2016;11(3):035020.
336. Bouleftour W, Juignet L, Bouet G, Granito RN, Vanden-Bossche A, Laroche N, et al. The role of the SIBLING, Bone Sialoprotein in skeletal biology - Contribution of mouse experimental genetics. Matrix Biol. 2016;52-54:60-77.
337. Gordon JA, Tye CE, Sampaio AV, Underhill TM, Hunter GK, Goldberg HA. Bone sialoprotein expression enhances osteoblast differentiation and matrix mineralization in vitro. Bone. 2007;41(3):462-73.
338. Simonavicius N, Robertson D, Bax DA, Jones C, Huijbers IJ, Isacke CM. Endosialin (CD248) is a marker of tumor-associated pericytes in high-grade glioma. Mod Pathol. 2008;21(3):308-15.
339. Simonavicius N, Ashenden M, van Weverwijk A, Lax S, Huso DL, Buckley CD, et al. Pericytes promote selective vessel regression to regulate vascular patterning. Blood. 2012;120(7):1516-27.
340. Viski C, Konig C, Kijewska M, Mogler C, Isacke CM, Augustin HG. Endosialin-Expressing Pericytes Promote Metastatic Dissemination. Cancer Res. 2016;76(18):5313-25.
341. Huang R, Li Z, Zhang J, Zeng Z, Zhang J, Li M, et al. Construction of Bone Metastasis-Specific Regulation Network Based on Prognostic Stemness-Related Signatures in Breast Invasive Carcinoma. Front Oncol. 2020;10:613333.
342. Kondo Y, Honoki K, Kishi S, Mori S, Fujiwara-Tani R, Tsukamoto S, et al. Endosialin/CD248 may be a potential therapeutic target to prevent the invasion and metastasis in osteosarcoma. Oncol Lett. 2022;23(2):42.
343. Maia M, de Vriese A, Janssens T, Moons M, van Landuyt K, Tavernier J, et al. CD248 and its cytoplasmic domain: a therapeutic target for arthritis. Arthritis Rheum. 2010;62(12):3595-606.
344. Sumanas S, Jorniak T, Lin S. Identification of novel vascular endothelial-specific genes by the microarray analysis of the zebrafish cloche mutants. Blood. 2005;106(2):534-41.
345. Mura M, Swain RK, Zhuang X, Vorschmitt H, Reynolds G, Durant S, et al. Identification and angiogenic role of the novel tumor endothelial marker CLEC14A. Oncogene. 2012;31(3):293-305.
346. Rho SS, Choi HJ, Min JK, Lee HW, Park H, Park H, et al. Clec14a is specifically expressed in endothelial cells and mediates cell to cell adhesion. Biochem Biophys Res Commun. 2011;404(1):103-8.
347. Lee S, Rho SS, Park H, Park JA, Kim J, Lee IK, et al. Carbohydrate-binding protein CLEC14A regulates VEGFR-2- and VEGFR-3-dependent signals during angiogenesis and lymphangiogenesis. J Clin Invest. 2017;127(2):457-71.
348. Noy PJ, Lodhia P, Khan K, Zhuang X, Ward DG, Verissimo AR, et al. Blocking CLEC14A-MMRN2 binding inhibits sprouting angiogenesis and tumour growth. Oncogene. 2015;34(47):5821-31.

349. Ruhrberg C, Gerhardt H, Golding M, Watson R, Ioannidou S, Fujisawa H, et al. Spatially restricted patterning cues provided by heparin-binding VEGF-A control blood vessel branching morphogenesis. Genes Dev. 2002;16(20):2684-98.
350. Khan KA, McMurray JL, Mohammed F, Bicknell R. C-type lectin domain group 14 proteins in vascular biology, cancer and inflammation. Febs j. 2019;286(17):3299-332.
351. Sandoval DR, Gomez Toledo A, Painter CD, Tota EM, Sheikh MO, West AMV, et al. Proteomics-based screening of the endothelial heparan sulfate interactome reveals that C-type lectin 14a (CLEC14A) is a heparin-binding protein. J Biol Chem. 2020;295(9):2804-21.
352. Pociute K, Schumacher JA, Sumanas S. Clec14a genetically interacts with Etv2 and Vegf signaling during vasculogenesis and angiogenesis in zebrafish. BMC Dev Biol. 2019;19(1):6.
353. Ki MK, Jeoung MH, Choi JR, Rho SS, Kwon YG, Shim H, et al. Human antibodies targeting the C-type lectin-like domain of the tumor endothelial cell marker clec14a regulate angiogenic properties in vitro. Oncogene. 2013;32(48):5449-57.
354. Noy PJ, Swain RK, Khan K, Lodhia P, Bicknell R. Sprouting angiogenesis is regulated by shedding of the C-type lectin family 14, member A (CLEC14A) ectodomain, catalyzed by rhomboid-like 2 protein (RHBDL2). FASEB J. 2016;30(6):2311-23.
355. Khan KA. Investigating the extracellular interactions of the tumour endothelial marker CLEC14A. Birmingham: University of Birmingham; 2016.
356. Jang J, Kim MR, Kim TK, Lee WR, Kim JH, Heo K, et al. CLEC14a-HSP70-1A interaction regulates HSP70-1A-induced angiogenesis. Sci Rep. 2017;7(1):10666.
357. Pircher A, Fiegl M, Untergasser G, Heidegger I, Medinger M, Kern J, et al. Favorable prognosis of operable non-small cell lung cancer (NSCLC) patients harboring an increased expression of tumor endothelial markers (TEMs). Lung Cancer. 2013;81(2):252-8.
358. Bocci M, Sjolund J, Kurzejamska E, Lindgren D, Marzouka NA, Bartoschek M, et al. Activin receptor-like kinase 1 is associated with immune cell infiltration and regulates CLEC14A transcription in cancer. Angiogenesis. 2018.
359. Krishna Priya S, Kumar K, Hiran KR, Bindhu MR, Nagare RP, Vijaykumar DK, et al. Expression of a novel endothelial marker, C-type lectin 14A, in epithelial ovarian cancer and its prognostic significance. Int J Clin Oncol. 2017;22(1):107-17.
360. Krishnapriya S, Malipatil B, Surekha S, Sundersingh S, Sridevi V, Ananthi B, et al. Microvessel Density (MVD) in Locally Advanced Breast Cancer. Asian Pac J Cancer Prev. 2019;20(5):1537-45.
361. Zheng W, Zhang S, Guo H, Chen X, Huang Z, Jiang S, et al. Multi-omics analysis of tumor angiogenesis characteristics and potential epigenetic regulation mechanisms in renal clear cell carcinoma. Cell Commun Signal. 2021;19(1):39.
362. Zhuang X, Maione F, Robinson J, Bentley M, Kaul B, Whitworth K, et al. CAR T cells targeting tumor endothelial marker CLEC14A inhibit tumor growth. JCI Insight. 2020;5(19).
363. Grainger AT, Jones MB, Chen MH, Shi W. Polygenic Control of Carotid Atherosclerosis in a BALB/cJ × SM/J Intercross and a Combined Cross Involving Multiple Mouse Strains. G3 (Bethesda). 2017;7(2):731-9.
364. Hagg S, Skogsberg J, Lundstrom J, Noori P, Nilsson R, Zhong H, et al. Multi-organ expression profiling uncovers a gene module in coronary artery disease involving transendothelial migration of leukocytes and LIM domain binding 2: the Stockholm Atherosclerosis Gene Expression (STAGE) study. PLoS Genet. 2009;5(12):e1000754.
365. Liang X, Lai Y, Wu W, Chen D, Zhong F, Huang J, et al. LncRNA-miRNA-mRNA expression variation profile in the urine of calcium oxalate stone patients. BMC Med Genomics. 2019;12(1):57.

366. Gene Lab OSfLiS. GeneLab Visualization Study Search. In: Lab NG, editor. 2022.
367. Mancuso P, Calleri A, Gregato G, Labanca V, Quarna J, Antoniotti P, et al. A subpopulation of circulating endothelial cells express CD109 and is enriched in the blood of cancer patients. PLoS One. 2014;9(12):e114713.
368. Li J, Xing X, Li D, Zhang B, Mutch DG, Hagemann IS, et al. Whole-Genome DNA Methylation Profiling Identifies Epigenetic Signatures of Uterine Carcinosarcoma. Neoplasia. 2017;19(2):100-11.
369. Lee J, Kotliarova S, Kotliarov Y, Li A, Su Q, Donin NM, et al. Tumor stem cells derived from glioblastomas cultured in bFGF and EGF more closely mirror the phenotype and genotype of primary tumors than do serum-cultured cell lines. Cancer Cell. 2006;9(5):391-403.
370. Lorenzon E, Colladel R, Andreuzzi E, Marastoni S, Todaro F, Schiappacassi M, et al. MULTIMERIN2 impairs tumor angiogenesis and growth by interfering with VEGF-A/VEGFR2 pathway. Oncogene. 2012;31(26):3136-47.
371. Tosi GM, Neri G, Barbera S, Mundo L, Parolini B, Lazzi S, et al. The Binding of CD93 to Multimerin-2 Promotes Choroidal Neovascularization. Invest Ophthalmol Vis Sci. 2020;61(8):30.
372. Liang Q, Su L, Zhang D, Jiao J. CD93 negatively regulates astrogenesis in response to MMRN2 through the transcriptional repressor ZFP503 in the developing brain. Proceedings of the National Academy of Sciences of the United States of America. 2020;117(17):9413-22.
373. Galvagni F, Nardi F, Spiga O, Trezza A, Tarticchio G, Pellicani R, et al. Dissecting the CD93-Multimerin 2 interaction involved in cell adhesion and migration of the activated endothelium. Matrix Biology. 2017;64:112-27.
374. Colladel R, Pellicani R, Andreuzzi E, Paulitti A, Tarticchio G, Todaro F, et al. MULTIMERIN2 binds VEGF-A primarily via the carbohydrate chains exerting an angiostatic function and impairing tumor growth. Oncotarget. 2016;7(2):2022-37.
375. Pellicani R, Poletto E, Andreuzzi E, Paulitti A, Doliana R, Bizzotto D, et al. Multimerin-2 maintains vascular stability and permeability. Matrix Biol. 2020;87:11-25.
376. Vento-Tormo R, Efremova M, Botting RA, Turco MY, Vento-Tormo M, Meyer KB, et al. Single-cell reconstruction of the early maternal-fetal interface in humans. Nature. 2018;563(7731):347-53.
377. Li C, Wang J, Hu J, Feng Y, Hasegawa K, Peng X, et al. Development, optimization, and validation of novel anti-TEM1/CD248 affinity agent for optical imaging in cancer. Oncotarget. 2014;5(16):6994-7012.
378. St Croix B, Rago C, Velculescu V, Traverso G, Romans KE, Montgomery E, et al. Genes expressed in human tumor endothelium. Science. 2000;289(5482):1197-202.
379. Dominguez CX, Muller S, Keerthivasan S, Koeppen H, Hung J, Gierke S, et al. Single-Cell RNA Sequencing Reveals Stromal Evolution into LRRC15(+) Myofibroblasts as a Determinant of Patient Response to Cancer Immunotherapy. Cancer Discov. 2020;10(2):232-53.
380. Tran T, Lindstrom NO, Ransick A, De Sena Brandine G, Guo Q, Kim AD, et al. In Vivo Developmental Trajectories of Human Podocyte Inform In Vitro Differentiation of Pluripotent Stem Cell-Derived Podocytes. Dev Cell. 2019;50(1):102-16 e6.
381. Schwalie PC, Dong H, Zachara M, Russeil J, Alpern D, Akchiche N, et al. A stromal cell population that inhibits adipogenesis in mammalian fat depots. Nature. 2018;559(7712):103-8.
382. Vanlandewijck M, He L, Mae MA, Andrae J, Ando K, Del Gaudio F, et al. A molecular atlas of cell types and zonation in the brain vasculature. Nature. 2018;554(7693):475-80.

383. MacFadyen J, Savage K, Wienke D, Isacke CM. Endosialin is expressed on stromal fibroblasts and CNS pericytes in mouse embryos and is downregulated during development. Gene Expr Patterns. 2007;7(3):363-9.
384. Rouleau C, Curiel M, Weber W, Smale R, Kurtzberg L, Mascarello J, et al. Endosialin protein expression and therapeutic target potential in human solid tumors: sarcoma versus carcinoma. Clin Cancer Res. 2008;14(22):7223-36.
385. Sun DX, Liao GJ, Liu KG, Jian H. Endosialinexpressing bone sarcoma stemlike cells are highly tumorinitiating and invasive. Mol Med Rep. 2015;12(4):5665-70.
386. Brady J, Neal J, Sadakar N, Gasque P. Human endosialin (tumor endothelial marker 1) is abundantly expressed in highly malignant and invasive brain tumors. J Neuropathol Exp Neurol. 2004;63(12):1274-83.
387. Consortium TTM. Single-cell transcriptomics of 20 mouse organs creates a Tabula Muris. Nature. 2018;562(7727):367-72.
388. Davidson S, Efremova M, Riedel A, Mahata B, Pramanik J, Huuhtanen J, et al. Single-Cell RNA Sequencing Reveals a Dynamic Stromal Niche That Supports Tumor Growth. Cell Rep. 2020;31(7):107628.
389. Cheng HW, Onder L, Novkovic M, Soneson C, Lutge M, Pikor N, et al. Origin and differentiation trajectories of fibroblastic reticular cells in the splenic white pulp. Nat Commun. 2019;10(1):1739.
390. Schyns J, Bai Q, Ruscitti C, Radermecker C, De Schepper S, Chakarov S, et al. Non-classical tissue monocytes and two functionally distinct populations of interstitial macrophages populate the mouse lung. Nat Commun. 2019;10(1):3964.
391. He L, Vanlandewijck M, Mae MA, Andrae J, Ando K, Del Gaudio F, et al. Single-cell RNA sequencing of mouse brain and lung vascular and vessel-associated cell types. Sci Data. 2018;5:180160.
392. Peyser R, MacDonnell S, Gao Y, Cheng L, Kim Y, Kaplan T, et al. Defining the Activated Fibroblast Population in Lung Fibrosis Using Single-Cell Sequencing. Am J Respir Cell Mol Biol. 2019;61(1):74-85.
393. Subramanian A, Tamayo P, Mootha VK, Mukherjee S, Ebert BL, Gillette MA, et al. Gene set enrichment analysis: a knowledge-based approach for interpreting genome-wide expression profiles. Proc Natl Acad Sci U S A. 2005;102(43):15545-50.
394. Andrews S. FastQC. [Online]2015.
395. Ewels P, Magnusson M, Lundin S, Käller M. MultiQC: summarize analysis results for multiple tools and samples in a single report. Bioinformatics. 2016;32(19):3047-8.
396. Martin M. Cutadapt removes adapter sequences from high-throughput sequencing reads. 2011. 2011;17(1):3.
397. Dobin A, Davis CA, Schlesinger F, Drenkow J, Zaleski C, Jha S, et al. STAR: ultrafast universal RNA-seq aligner. Bioinformatics. 2013;29(1):15-21.
398. Liao Y, Smyth GK, Shi W. The R package Rsubread is easier, faster, cheaper and better for alignment and quantification of RNA sequencing reads. Nucleic Acids Res. 2019;47(8):e47.
399. Love MI, Huber W, Anders S. Moderated estimation of fold change and dispersion for RNA-seq data with DESeq2. Genome Biology. 2014;15(12):550.
400. Mootha VK, Lindgren CM, Eriksson KF, Subramanian A, Sihag S, Lehar J, et al. PGC-1alpha-responsive genes involved in oxidative phosphorylation are coordinately downregulated in human diabetes. Nat Genet. 2003;34(3):267-73.
401. Institute B. Using RNA-seq Datasets with GSEA 2019 [

402. Kuhn M, von Mering C, Campillos M, Jensen LJ, Bork P. STITCH: interaction networks of chemicals and proteins. Nucleic Acids Res. 2008;36(Database issue):D684-8.
403. Baryawno N, Przybylski D, Kowalczyk MS, Kfoury Y, Severe N, Gustafsson K, et al. A Cellular Taxonomy of the Bone Marrow Stroma in Homeostasis and Leukemia. Cell. 2019;177(7):1915-32.e16.
404. Stuart T, Butler A, Hoffman P, Hafemeister C, Papalexi E, Mauck WM, 3rd, et al. Comprehensive Integration of Single-Cell Data. Cell. 2019;177(7):1888-902.e21.
405. Satija R, Farrell JA, Gennert D, Schier AF, Regev A. Spatial reconstruction of single-cell gene expression data. Nature Biotechnology. 2015;33(5):495-502.
406. Kusumbe AP, Ramasamy SK, Starsichova A, Adams RH. Sample preparation for high-resolution 3D confocal imaging of mouse skeletal tissue. Nat Protoc. 2015;10(12):1904-14.
407. Renier N, Wu Z, Simon DJ, Yang J, Ariel P, Tessier-Lavigne M. iDISCO: a simple, rapid method to immunolabel large tissue samples for volume imaging. Cell. 2014;159(4):896-910.
408. Houston DA, Staines KA, MacRae VE, Farquharson C. Culture of Murine Embryonic Metatarsals: A Physiological Model of Endochondral Ossification. J Vis Exp. 2016(118):54978.
409. Bouxsein ML, Boyd SK, Christiansen BA, Guldberg RE, Jepsen KJ, Müller R. Guidelines for assessment of bone microstructure in rodents using micro-computed tomography. J Bone Miner Res. 2010;25(7):1468-86.
410. Bakker AD, Klein-Nulend J. Osteoblast isolation from murine calvaria and long bones. Methods Mol Biol. 2012;816:19-29.
411. Hoemann CD, El-Gabalawy H, McKee MD. In vitro osteogenesis assays: influence of the primary cell source on alkaline phosphatase activity and mineralization. Pathol Biol (Paris). 2009;57(4):318-23.
412. Idris AI. Ovariectomy/orchidectomy in rodents. Methods Mol Biol. 2012;816:545-51.
413. Kim TK, Park CS, Jang J, Kim MR, Na HJ, Lee K, et al. Inhibition of VEGF-dependent angiogenesis and tumor angiogenesis by an optimized antibody targeting CLEC14a. Mol Oncol. 2018;12(3):356-72.
414. Kim Y, Lee S, Zhang H, Lee S, Kim H, Kim Y, et al. CLEC14A deficiency exacerbates neuronal loss by increasing blood-brain barrier permeability and inflammation. J Neuroinflammation. 2020;17(1):48.
415. Sweeney M, Foldes G. It Takes Two: Endothelial-Perivascular Cell Cross-Talk in Vascular Development and Disease. Front Cardiovasc Med. 2018;5:154.
416. Tuckermann J, Adams RH. The endothelium-bone axis in development, homeostasis and bone and joint disease. Nat Rev Rheumatol. 2021;17(10):608-20.
417. Hashimoto K, Kaito T, Furuya M, Seno S, Okuzaki D, Kikuta J, et al. In vivo dynamic analysis of BMP-2-induced ectopic bone formation. Sci Rep. 2020;10(1):4751.
418. Wragg JW, Durant S, McGettrick HM, Sample KM, Egginton S, Bicknell R. Shear stress regulated gene expression and angiogenesis in vascular endothelium. Microcirculation. 2014;21(4):290-300.
419. Soulis J, Fytanidis D, Seralidou K, Giannoglou G. Wall shear stress oscillation and its gradient in the normal left coronary artery tree bifurcations. Hippokratia. 2014;18(1):12-6.
420. Ramasamy SK, Kusumbe AP, Adams RH. Regulation of tissue morphogenesis by endothelial cell-derived signals. Trends Cell Biol. 2015;25(3):148-57.
421. Ramasamy SK, Kusumbe AP, Itkin T, Gur-Cohen S, Lapidot T, Adams RH. Regulation of Hematopoiesis and Osteogenesis by Blood Vessel-Derived Signals. Annu Rev Cell Dev Biol. 2016;32:649-75.

422. Sivan U, De Angelis J, Kusumbe AP. Role of angiocrine signals in bone development, homeostasis and disease. Open Biol. 2019;9(10):190144.
423. Anastasiou D. Tumour microenvironment factors shaping the cancer metabolism landscape. Br J Cancer. 2017;116(3):277-86.
424. Delcourt N, Quevedo C, Nonne C, Fons P, O'Brien D, Loyaux D, et al. Targeted identification of sialoglycoproteins in hypoxic endothelial cells and validation in zebrafish reveal roles for proteins in angiogenesis. J Biol Chem. 2015;290(6):3405-17.
425. Fisher DT, Muhitch JB, Kim M, Doyen KC, Bogner PN, Evans SS, et al. Intraoperative intravital microscopy permits the study of human tumour vessels. Nat Commun. 2016;7:10684.
426. Zhuang X, Cross D, Heath VL, Bicknell R. Shear stress, tip cells and regulators of endothelial migration. Biochem Soc Trans. 2011;39(6):1571-5.
427. Krishna Priya S, Nagare RP, Sneha VS, Sidhanth C, Bindhya S, Manasa P, et al. Tumour angiogenesis-Origin of blood vessels. Int J Cancer. 2016;139(4):729-35.
428. Lopes-Bastos BM, Jiang WG, Cai J. Tumour-Endothelial Cell Communications: Important and Indispensable Mediators of Tumour Angiogenesis. Anticancer Res. 2016;36(3):1119-26.
429. Jiang X, Wang J, Deng X, Xiong F, Zhang S, Gong Z, et al. The role of microenvironment in tumor angiogenesis. J Exp Clin Cancer Res. 2020;39(1):204.
430. Liao D, Johnson RS. Hypoxia: a key regulator of angiogenesis in cancer. Cancer Metastasis Rev. 2007;26(2):281-90.
431. Hanahan D, Weinberg RA. The hallmarks of cancer. Cell. 2000;100(1):57-70.
432. Chung AS, Lee J, Ferrara N. Targeting the tumour vasculature: insights from physiological angiogenesis. Nat Rev Cancer. 2010;10(7):505-14.
433. Conway DE, Breckenridge MT, Hinde E, Gratton E, Chen CS, Schwartz MA. Fluid shear stress on endothelial cells modulates mechanical tension across VE-cadherin and PECAM-1. Curr Biol. 2013;23(11):1024-30.
434. Duncan GS, Andrew DP, Takimoto H, Kaufman SA, Yoshida H, Spellberg J, et al. Genetic evidence for functional redundancy of Platelet/Endothelial cell adhesion molecule-1 (PECAM-1): CD31-deficient mice reveal PECAM-1-dependent and PECAM-1-independent functions. J Immunol. 1999;162(5):3022-30.
435. Galvagni F, Nardi F, Spiga O, Trezza A, Tarticchio G, Pellicani R, et al. Dissecting the CD93-Multimerin 2 interaction involved in cell adhesion and migration of the activated endothelium. Matrix Biol. 2017;64:112-27.
436. Du J, Yang Q, Luo L, Yang D. C1qr and C1qrl redundantly regulate angiogenesis in zebrafish through controlling endothelial Cdh5. Biochem Biophys Res Commun. 2017;483(1):482-7.
437. Coutu DL, Kokkaliaris KD, Kunz L, Schroeder T. Multicolor quantitative confocal imaging cytometry. Nat Methods. 2018;15(1):39-46.
438. Reismann D, Stefanowski J, Gunther R, Rakhymzhan A, Matthys R, Nutzi R, et al. Longitudinal intravital imaging of the femoral bone marrow reveals plasticity within marrow vasculature. Nat Commun. 2017;8(1):2153.
439. Kavanagh DPJ, Lokman AB, Neag G, Colley A, Kalia N. Imaging the injured beating heart intravitally and the vasculoprotection afforded by haematopoietic stem cells. Cardiovasc Res. 2019;115(13):1918-32.
440. Maes C, Stockmans I, Moermans K, Van Looveren R, Smets N, Carmeliet P, et al. Soluble VEGF isoforms are essential for establishing epiphyseal vascularization and regulating chondrocyte development and survival. J Clin Invest. 2004;113(2):188-99.

441. Beckmann R, Houben A, Tohidnezhad M, Kweider N, Fragoulis A, Wruck CJ, et al. Mechanical forces induce changes in VEGF and VEGFR-1/sFlt-1 expression in human chondrocytes. Int J Mol Sci. 2014;15(9):15456-74.
442. Clarkin C, Olsen BR. On bone-forming cells and blood vessels in bone development. Cell Metab. 2010;12(4):314-6.
443. Sadeghian SM, Shapiro FD, Shefelbine SJ. Computational model of endochondral ossification: Simulating growth of a long bone. Bone. 2021;153:116132.
444. Hemmatian H, Conrad S, Furesi G, Mletzko K, Krug J, Faila AV, et al. Reorganization of the osteocyte lacuno-canalicular network characteristics in tumor sites of an immunocompetent murine model of osteotropic cancers. Bone. 2021;152:116074.
445. Mao JJ. Mechanobiology of craniofacial sutures. J Dent Res. 2002;81(12):810-6.
446. Fritz H. Prenatal ossification in rabbits as indicative of fetal maturity. Teratology. 1975;11(3):313-9.
447. Smith BJ, Graef JL, Wronski TJ, Rendina E, Williams AA, Clark KA, et al. Effects of dried plum supplementation on bone metabolism in adult C57BL/6 male mice. Calcif Tissue Int. 2014;94(4):442-53.
448. Wagner BM, Robinson JW, Lin YW, Lee YC, Kaci N, Legeai-Mallet L, et al. Prevention of guanylyl cyclase-B dephosphorylation rescues achondroplastic dwarfism. JCI Insight. 2021;6(9).
449. Hunziker EB. Mechanism of longitudinal bone growth and its regulation by growth plate chondrocytes. Microsc Res Tech. 1994;28(6):505-19.
450. Zhang P, Tanaka SM, Sun Q, Turner CH, Yokota H. Frequency-dependent enhancement of bone formation in murine tibiae and femora with knee loading. J Bone Miner Metab. 2007;25(6):383-91.
451. Zhang P, Hamamura K, Turner CH, Yokota H. Lengthening of mouse hindlimbs with joint loading. J Bone Miner Metab. 2010;28(3):268-75.
452. Hermann CD, Richards MA, Chang R, Olivares-Navarrete R, Williams JK, Guldberg RE, et al. Biphasic fusion of the murine posterior frontal suture. Plast Reconstr Surg. 2013;131(4):727-40.
453. Rindone AN, Liu X, Farhat S, Perdomo-Pantoja A, Witham TF, Coutu DL, et al. Quantitative 3D imaging of the cranial microvascular environment at single-cell resolution. Nature Communications. 2021;12(1):6219.
454. Michel PA, Kronenberg D, Neu G, Stolberg-Stolberg J, Frank A, Pap T, et al. Microsurgical reconstruction affects the outcome in a translational mouse model for Achilles tendon healing. J Orthop Translat. 2020;24:1-11.
455. Lee S, Prisby RD. Short-term intermittent PTH 1-34 administration and bone marrow blood vessel ossification in Mature and Middle-Aged C57BL/6 mice. Bone Rep. 2019;10:100193.
456. Klinck RJ, Campbell GM, Boyd SK. Radiation effects on bone architecture in mice and rats resulting from in vivo micro-computed tomography scanning. Med Eng Phys. 2008;30(7):888-95.
457. Kim JM, Lin C, Stavre Z, Greenblatt MB, Shim JH. Osteoblast-Osteoclast Communication and Bone Homeostasis. Cells. 2020;9(9).
458. O'Brien CA, Plotkin LI, Galli C, Goellner JJ, Gortazar AR, Allen MR, et al. Control of bone mass and remodeling by PTH receptor signaling in osteocytes. PLoS One. 2008;3(8):e2942.
459. Goring A, Sharma A, Javaheri B, Smith RC, Kanczler JM, Boyde A, et al. Regulation of the Bone Vascular Network is Sexually Dimorphic. J Bone Miner Res. 2019;34(11):2117-32.

460. Jämsä T, Jalovaara P, Peng Z, Väänänen HK, Tuukkanen J. Comparison of three-point bending test and peripheral quantitative computed tomography analysis in the evaluation of the strength of mouse femur and tibia. Bone. 1998;23(2):155-61.
461. Schriefer JL, Robling AG, Warden SJ, Fournier AJ, Mason JJ, Turner CH. A comparison of mechanical properties derived from multiple skeletal sites in mice. J Biomech. 2005;38(3):467-75.
462. Zhang H, Zhang Y, Terajima M, Romanowicz G, Liu Y, Omi M, et al. Loss of BMP signaling mediated by BMPR1A in osteoblasts leads to differential bone phenotypes in mice depending on anatomical location of the bones. Bone. 2020;137:115402.
463. Creecy A, Uppuganti S, Girard MR, Schlunk SG, Amah C, Granke M, et al. The age-related decrease in material properties of BALB/c mouse long bones involves alterations to the extracellular matrix. Bone. 2020;130:115126.
464. Orlandini M, Galvagni F, Bardelli M, Rocchigiani M, Lentucci C, Anselmi F, et al. The characterization of a novel monoclonal antibody against CD93 unveils a new antiangiogenic target. Oncotarget. 2014;5(9):2750-60.
465. Dekker RJ, van Soest S, Fontijn RD, Salamanca S, de Groot PG, VanBavel E, et al. Prolonged fluid shear stress induces a distinct set of endothelial cell genes, most specifically lung Krüppel-like factor (KLF2). Blood. 2002;100(5):1689-98.
466. Fledderus JO, van Thienen JV, Boon RA, Dekker RJ, Rohlena J, Volger OL, et al. Prolonged shear stress and KLF2 suppress constitutive proinflammatory transcription through inhibition of ATF2. Blood. 2007;109(10):4249-57.
467. Bernhardt A, Skottke J, von Witzleben M, Gelinsky M. Triple Culture of Primary Human Osteoblasts, Osteoclasts and Osteocytes as an In Vitro Bone Model. Int J Mol Sci. 2021;22(14).
468. Yang Y, Chung MR, Zhou S, Gong X, Xu H, Hong Y, et al. STAT3 controls osteoclast differentiation and bone homeostasis by regulating NFATc1 transcription. J Biol Chem. 2019;294(42):15395-407.
469. Littlewood-Evans A, Kokubo T, Ishibashi O, Inaoka T, Wlodarski B, Gallagher JA, et al. Localization of cathepsin K in human osteoclasts by in situ hybridization and immunohistochemistry. Bone. 1997;20(2):81-6.
470. Lynch MP, Stein JL, Stein GS, Lian JB. The influence of type I collagen on the development and maintenance of the osteoblast phenotype in primary and passaged rat calvarial osteoblasts: modification of expression of genes supporting cell growth, adhesion, and extracellular matrix mineralization. Exp Cell Res. 1995;216(1):35-45.
471. Karsenty G, Park RW. Regulation of type I collagen genes expression. Int Rev Immunol. 1995;12(2-4):177-85.
472. Shi S, Kirk M, Kahn AJ. The role of type I collagen in the regulation of the osteoblast phenotype. J Bone Miner Res. 1996;11(8):1139-45.
473. Henrichsen E. Alkaline phosphatase in osteoblasts and fibroblasts cultivated in vitro. Exp Cell Res. 1956;11(1):115-27.
474. Bianco P, Fisher LW, Young MF, Termine JD, Robey PG. Expression of bone sialoprotein (BSP) in developing human tissues. Calcif Tissue Int. 1991;49(6):421-6.
475. Rodan GA, Noda M. Gene expression in osteoblastic cells. Crit Rev Eukaryot Gene Expr. 1991;1(2):85-98.
476. Chen J, Zhang Q, McCulloch CA, Sodek J. Immunohistochemical localization of bone sialoprotein in foetal porcine bone tissues: comparisons with secreted phosphoprotein 1 (SPP-1, osteopontin) and SPARC (osteonectin). Histochem J. 1991;23(6):281-9.

477. Wang J, Cui X, Zhou Y, Xiang Q. Core-shell PLGA/collagen nanofibers loaded with recombinant FN/CDHs as bone tissue engineering scaffolds. Connect Tissue Res. 2014;55(4):292-8.
478. Zhang Y, Zhou Y, Zhu J, Dong S, Li C, Xiang Q. Effect of a novel recombinant protein of fibronectinIII7-10/cadherin 11 EC1-2 on osteoblastic adhesion and differentiation. Biosci Biotechnol Biochem. 2009;73(9):1999-2006.
479. Matsuda Y, Hagio M, Ishiwata T. Nestin: a novel angiogenesis marker and possible target for tumor angiogenesis. World J Gastroenterol. 2013;19(1):42-8.
480. Méndez-Ferrer S, Michurina TV, Ferraro F, Mazloom AR, Macarthur BD, Lira SA, et al. Mesenchymal and haematopoietic stem cells form a unique bone marrow niche. Nature. 2010;466(7308):829-34.
481. Rashid H, Ma C, Chen H, Wang H, Hassan MQ, Sinha K, et al. Sp7 and Runx2 molecular complex synergistically regulate expression of target genes. Connect Tissue Res. 2014;55 Suppl 1(0 1):83-7.
482. Kawane T, Qin X, Jiang Q, Miyazaki T, Komori H, Yoshida CA, et al. Runx2 is required for the proliferation of osteoblast progenitors and induces proliferation by regulating Fgfr2 and Fgfr3. Sci Rep. 2018;8(1):13551.
483. Hojo H, Ohba S, He X, Lai LP, McMahon AP. Sp7/Osterix Is Restricted to Bone-Forming Vertebrates where It Acts as a Dlx Co-factor in Osteoblast Specification. Dev Cell. 2016;37(3):238-53.
484. Komori T. Molecular Mechanism of Runx2-Dependent Bone Development. Mol Cells. 2020;43(2):168-75.
485. Komori T. Regulation of osteoblast differentiation by transcription factors. J Cell Biochem. 2006;99(5):1233-9.
486. Churukian CJ. 14 - Pigments and Minerals. In: Bancroft JD, Gamble M, editors. Theory and Practice of Histological Techniques (Sixth Edition). Edinburgh: Churchill Livingstone; 2008. p. 233-59.
487. Licini C, Vitale-Brovarone C, Mattioli-Belmonte M. Collagen and non-collagenous proteins molecular crosstalk in the pathophysiology of osteoporosis. Cytokine Growth Factor Rev. 2019;49:59-69.
488. Brandt J, Krogh TN, Jensen CH, Frederiksen JK, Teisner B. Thermal instability of the trimeric structure of the N-terminal propeptide of human procollagen type I in relation to assay technology. Clin Chem. 1999;45(1):47-53.
489. Chen J, Tu X, Esen E, Joeng KS, Lin C, Arbeit JM, et al. WNT7B promotes bone formation in part through mTORC1. PLoS Genet. 2014;10(1):e1004145.
490. Iezaki T, Horie T, Fukasawa K, Kitabatake M, Nakamura Y, Park G, et al. Translational Control of Sox9 RNA by mTORC1 Contributes to Skeletogenesis. Stem Cell Reports. 2018;11(1):228-41.
491. Qi S, Sun X, Choi HK, Yao J, Wang L, Wu G, et al. FAK Promotes Early Osteoprogenitor Cell Proliferation by Enhancing mTORC1 Signaling. J Bone Miner Res. 2020;35(9):1798-811.
492. Iqbal J, Yuen T, Kim SM, Zaidi M. Opening windows for bone remodeling through a SLIT. J Clin Invest. 2018;128(4):1255-7.
493. Niimi T. Roles of Slit Ligands and Their Roundabout (Robo) Family of Receptors in Bone Remodeling. Adv Exp Med Biol. 2021;21:143-54.
494. Wang S, Huang S, Johnson S, Rosin V, Lee J, Colomb E, et al. Tissue-specific angiogenic and invasive properties of human neonatal thymus and bone MSCs: Role of SLIT3-ROBO1. Stem Cells Transl Med. 2020;9(9):1102-13.

495. Bellows CG, Aubin JE, Heersche JN, Antosz ME. Mineralized bone nodules formed in vitro from enzymatically released rat calvaria cell populations. Calcif Tissue Int. 1986;38(3):143-54.
496. Izumiya M, Haniu M, Ueda K, Ishida H, Ma C, Ideta H, et al. Evaluation of MC3T3-E1 Cell Osteogenesis in Different Cell Culture Media. Int J Mol Sci. 2021;22(14).
497. Cray JJ, Jr., Khaksarfard K, Weinberg SM, Elsalanty M, Yu JC. Effects of thyroxine exposure on osteogenesis in mouse calvarial pre-osteoblasts. PLoS One. 2013;8(7):e69067.
498. Jongen JW, Bos MP, van der Meer JM, Herrmann-Erlee MP. Parathyroid hormone-induced changes in alkaline phosphatase expression in fetal calvarial osteoblasts: differences between rat and mouse. J Cell Physiol. 1993;155(1):36-43.
499. Yee JA. Stimulation of alkaline phosphatase activity in cultured neonatal mouse calvarial bone cells by parathyroid hormone. Calcif Tissue Int. 1985;37(5):530-8.
500. Orriss IR, Key ML, Brandao-Burch A, Patel JJ, Burnstock G, Arnett TR. The regulation of osteoblast function and bone mineralisation by extracellular nucleotides: The role of p2x receptors. Bone. 2012;51(3):389-400.
501. Jain RK. Molecular regulation of vessel maturation. Nat Med. 2003;9(6):685-93.
502. Weinger JM, Holtrop ME. An ultrastructural study of bone cells: the occurrence of microtubules, microfilaments and tight junctions. Calcif Tissue Res. 1974;14(1):15-29.
503. Baek JM, Cheon YH, Kwak SC, Jun HY, Yoon KH, Lee MS, et al. Claudin 11 regulates bone homeostasis via bidirectional EphB4-EphrinB2 signaling. Exp Mol Med. 2018;50(4):1-18.
504. Zhen-Zhou C, Xiao-Dan J, Gui-Tao L, Jiang-Hua S, Ling-Hui L, Mou-Xuan D, et al. Functional and ultrastructural analysis of endothelial-like cells derived from bone marrow stromal cells. Cytotherapy. 2008;10(6):611-24.
505. Alshbool FZ, Mohan S. Emerging multifunctional roles of Claudin tight junction proteins in bone. Endocrinology. 2014;155(7):2363-76.
506. Lindsey RC, Xing W, Pourteymoor S, Godwin C, Gow A, Mohan S. Novel Role for Claudin-11 in the Regulation of Osteoblasts via Modulation of ADAM10-Mediated Notch Signaling. J Bone Miner Res. 2019;34(10):1910-22.
507. Linares GR, Brommage R, Powell DR, Xing W, Chen ST, Alshbool FZ, et al. Claudin 18 is a novel negative regulator of bone resorption and osteoclast differentiation. J Bone Miner Res. 2012;27(7):1553-65.
508. Tzima E, Irani-Tehrani M, Kiosses WB, Dejana E, Schultz DA, Engelhardt B, et al. A mechanosensory complex that mediates the endothelial cell response to fluid shear stress. Nature. 2005;437(7057):426-31.
509. Boon RA. The transcription factor KLF2 in vascular biology: University of Amsterdam; 2008.
510. Komori T. Animal models for osteoporosis. Eur J Pharmacol. 2015;759:287-94.
511. Roberts BC, Giorgi M, Oliviero S, Wang N, Boudiffa M, Dall'Ara E. The longitudinal effects of ovariectomy on the morphometric, densitometric and mechanical properties in the murine tibia: A comparison between two mouse strains. Bone. 2019;127:260-70.
512. Shi C, Wu J, Yan Q, Wang R, Miao D. Bone marrow ablation demonstrates that estrogen plays an important role in osteogenesis and bone turnover via an antioxidative mechanism. Bone. 2015;79:94-104.
513. Wang FS, Lin CL, Chen YJ, Wang CJ, Yang KD, Huang YT, et al. Secreted frizzled-related protein 1 modulates glucocorticoid attenuation of osteogenic activities and bone mass. Endocrinology. 2005;146(5):2415-23.

514. Luppen CA, Smith E, Spevak L, Boskey AL, Frenkel B. Bone morphogenetic protein-2 restores mineralization in glucocorticoid-inhibited MC3T3-E1 osteoblast cultures. J Bone Miner Res. 2003;18(7):1186-97.
515. Binder NB, Niederreiter B, Hoffmann O, Stange R, Pap T, Stulnig TM, et al. Estrogen-dependent and C-C chemokine receptor-2–dependent pathways determine osteoclast behavior in osteoporosis. Nature Medicine. 2009;15(4):417-24.
516. Hughes DE, Dai A, Tiffee JC, Li HH, Mundy GR, Boyce BF. Estrogen promotes apoptosis of murine osteoclasts mediated by TGF–β. Nature Medicine. 1996;2(10):1132-6.
517. Zhang H, Shi X, Wang L, Li X, Zheng C, Gao B, et al. Intramembranous ossification and endochondral ossification are impaired differently between glucocorticoid-induced osteoporosis and estrogen deficiency-induced osteoporosis. Scientific Reports. 2018;8(1):3867.
518. Abdurahman A, Li X, Li J, Liu D, Zhai L, Wang X, et al. Loading-driven PI3K/Akt signaling and erythropoiesis enhanced angiogenesis and osteogenesis in a postmenopausal osteoporosis mouse model. Bone. 2022;157:116346.
519. Wang Q, Zhou J, Wang X, Xu Y, Liang Z, Gu X, et al. Coupling induction of osteogenesis and type H vessels by pulsed electromagnetic fields in ovariectomy-induced osteoporosis in mice. Bone. 2022;154:116211.
520. Qaseem A, Forciea MA, McLean RM, Denberg TD, Barry MJ, Cooke M, et al. Treatment of Low Bone Density or Osteoporosis to Prevent Fractures in Men and Women: A Clinical Practice Guideline Update From the American College of Physicians. Ann Intern Med. 2017;166(11):818-39.
521. Dempster DW, Zhou H, Ruff VA, Melby TE, Alam J, Taylor KA. Longitudinal Effects of Teriparatide or Zoledronic Acid on Bone Modeling- and Remodeling-Based Formation in the SHOTZ Study. J Bone Miner Res. 2018;33(4):627-33.
522. Leder BZ, Tsai JN, Uihlein AV, Wallace PM, Lee H, Neer RM, et al. Denosumab and teriparatide transitions in postmenopausal osteoporosis (the DATA-Switch study): extension of a randomised controlled trial. Lancet. 2015;386(9999):1147-55.
523. Stolina M, Dwyer D, Niu QT, Villasenor KS, Kurimoto P, Grisanti M, et al. Temporal changes in systemic and local expression of bone turnover markers during six months of sclerostin antibody administration to ovariectomized rats. Bone. 2014;67:305-13.
524. Ominsky MS, Vlasseros F, Jolette J, Smith SY, Stouch B, Doellgast G, et al. Two doses of sclerostin antibody in cynomolgus monkeys increases bone formation, bone mineral density, and bone strength. J Bone Miner Res. 2010;25(5):948-59.
525. Langdahl BL, Hofbauer LC, Forfar JC. Cardiovascular Safety and Sclerostin Inhibition. J Clin Endocrinol Metab. 2021;106(7):1845-53.
526. Ominsky MS, Boyd SK, Varela A, Jolette J, Felx M, Doyle N, et al. Romosozumab Improves Bone Mass and Strength While Maintaining Bone Quality in Ovariectomized Cynomolgus Monkeys. J Bone Miner Res. 2017;32(4):788-801.
527. Li X, Ominsky MS, Warmington KS, Morony S, Gong J, Cao J, et al. Sclerostin antibody treatment increases bone formation, bone mass, and bone strength in a rat model of postmenopausal osteoporosis. J Bone Miner Res. 2009;24(4):578-88.
528. Li X, Warmington KS, Niu QT, Asuncion FJ, Barrero M, Grisanti M, et al. Inhibition of sclerostin by monoclonal antibody increases bone formation, bone mass, and bone strength in aged male rats. J Bone Miner Res. 2010;25(12):2647-56.
529. Marie PJ. Targeting integrins to promote bone formation and repair. Nature Reviews Endocrinology. 2013;9(5):288-95.

530. Benedito R, Roca C, Sörensen I, Adams S, Gossler A, Fruttiger M, et al. The notch ligands Dll4 and Jagged1 have opposing effects on angiogenesis. Cell. 2009;137(6):1124-35.
531. Montero A, Okada Y, Tomita M, Ito M, Tsurukami H, Nakamura T, et al. Disruption of the fibroblast growth factor-2 gene results in decreased bone mass and bone formation. J Clin Invest. 2000;105(8):1085-93.
532. Zhen G, Dan Y, Wang R, Dou C, Guo Q, Zarr M, et al. An antibody against Siglec-15 promotes bone formation and fracture healing by increasing TRAP(+) mononuclear cells and PDGF-BB secretion. Bone Res. 2021;9(1):47.
533. van Gastel N, Carmeliet G. Metabolic regulation of skeletal cell fate and function in physiology and disease. Nat Metab. 2021;3(1):11-20.
534. Gharibi B, Ghuman MS, Cama G, Rawlinson SCF, Grigoriadis AE, Hughes FJ. Site-specific differences in osteoblast phenotype, mechanical loading response and estrogen receptor-related gene expression. Mol Cell Endocrinol. 2018;477:140-7.
535. Xu Y, Malladi P, Zhou D, Longaker MT. Molecular and cellular characterization of mouse calvarial osteoblasts derived from neural crest and paraxial mesoderm. Plast Reconstr Surg. 2007;120(7):1783-95.

9. APPENDIX

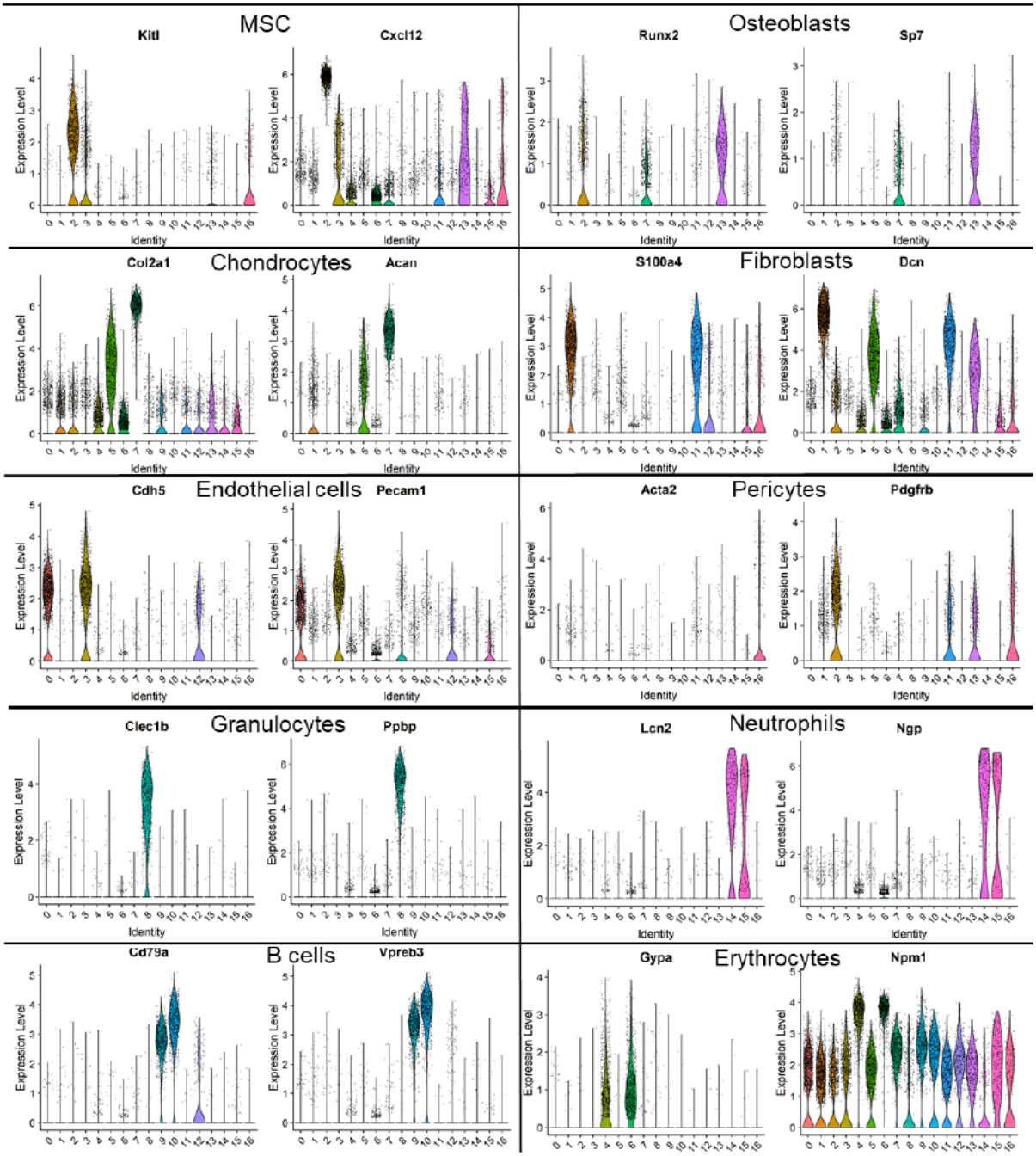


Figure 9.1 Top markers in single cell RNA sequencing clusters (GSE128423). Single-cell RNA sequencing of bone and bone marrow cells extracted and isolated from 8-10weeks C57BL/6J mice. Cells were distributed to cell clusters according to gene expression patterning, cell type identities were established by analysis of top differentially expressed markers in each cluster. Violin plots of cell clusters show top markers utilised to name each cell cluster.

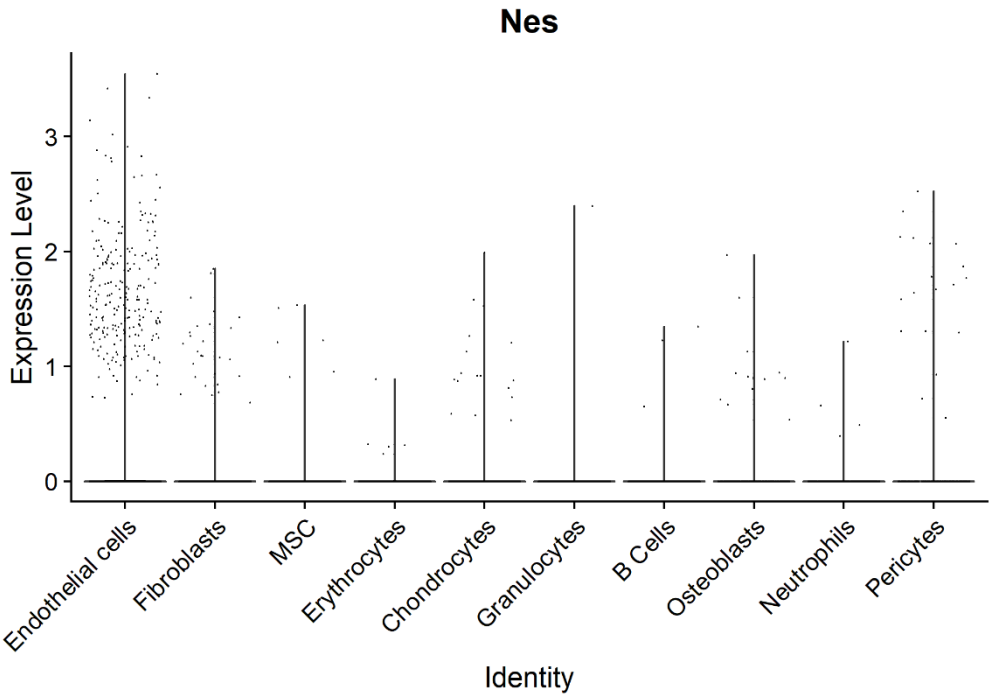


Figure 9.2 Expression of Nes in single cell RNA sequencing clusters (dataset GSE128423). Violin plots of cell clusters identified from all cells isolated from the bone and bone marrow of 8-10weeks C57BL/6J mice shows a relative increased expression of Nes in EC.

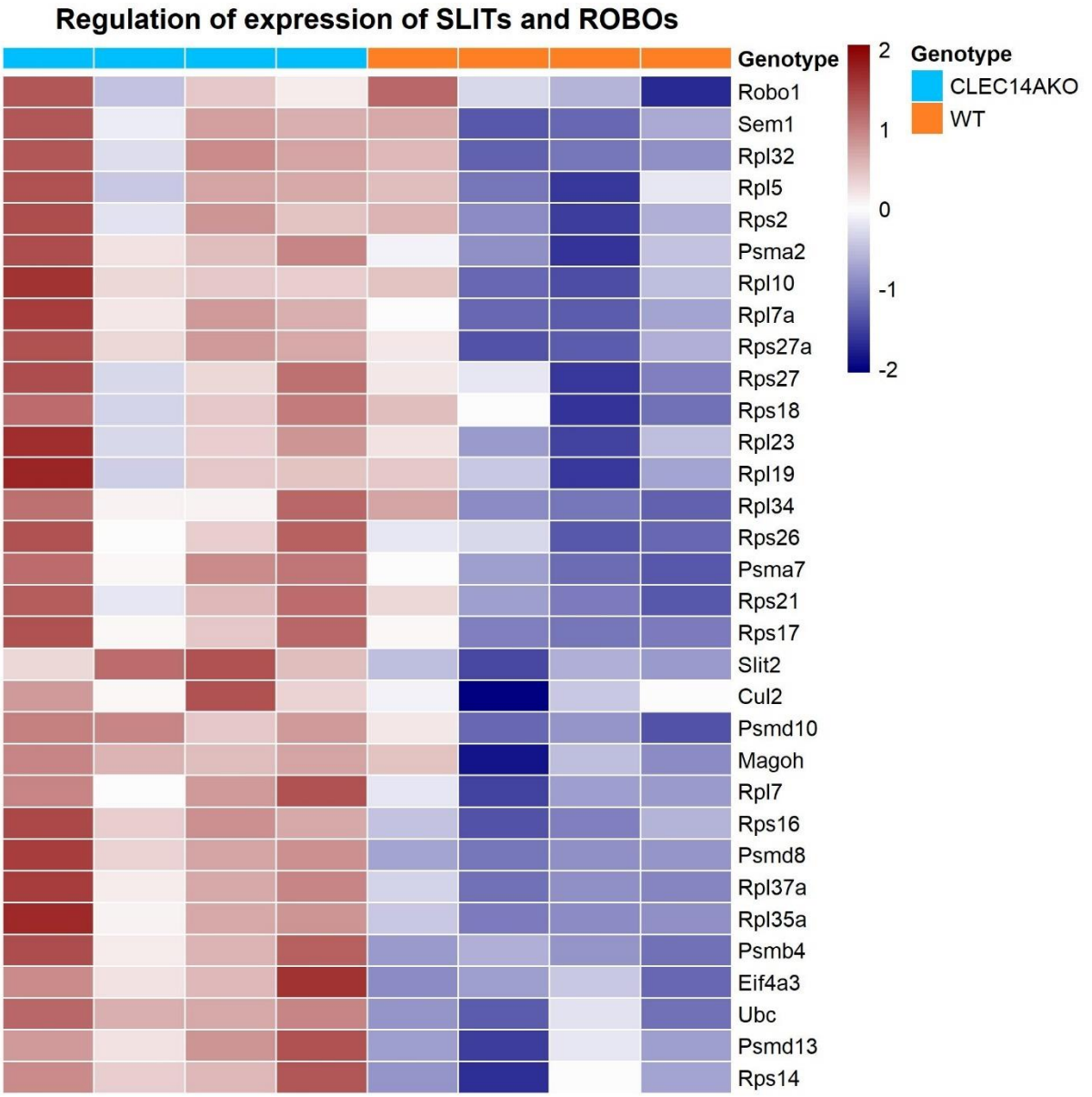


Figure 9.3 GSEA heatmap showing the list of leading edge genes enriched at the top of the Regulation of expression of SLITs and ROBOs gene set. Heatmap presents upregulation of genes related to regulation of expression of SLIT and ROBO receptors in CLEC14A$^{-/-}$ samples. Gene expression is presented as a Z score. Transcripts presented were identified as statistically significant by GSEA analysis, FDR (q-value) < 0.01, nominal p < 0.01.

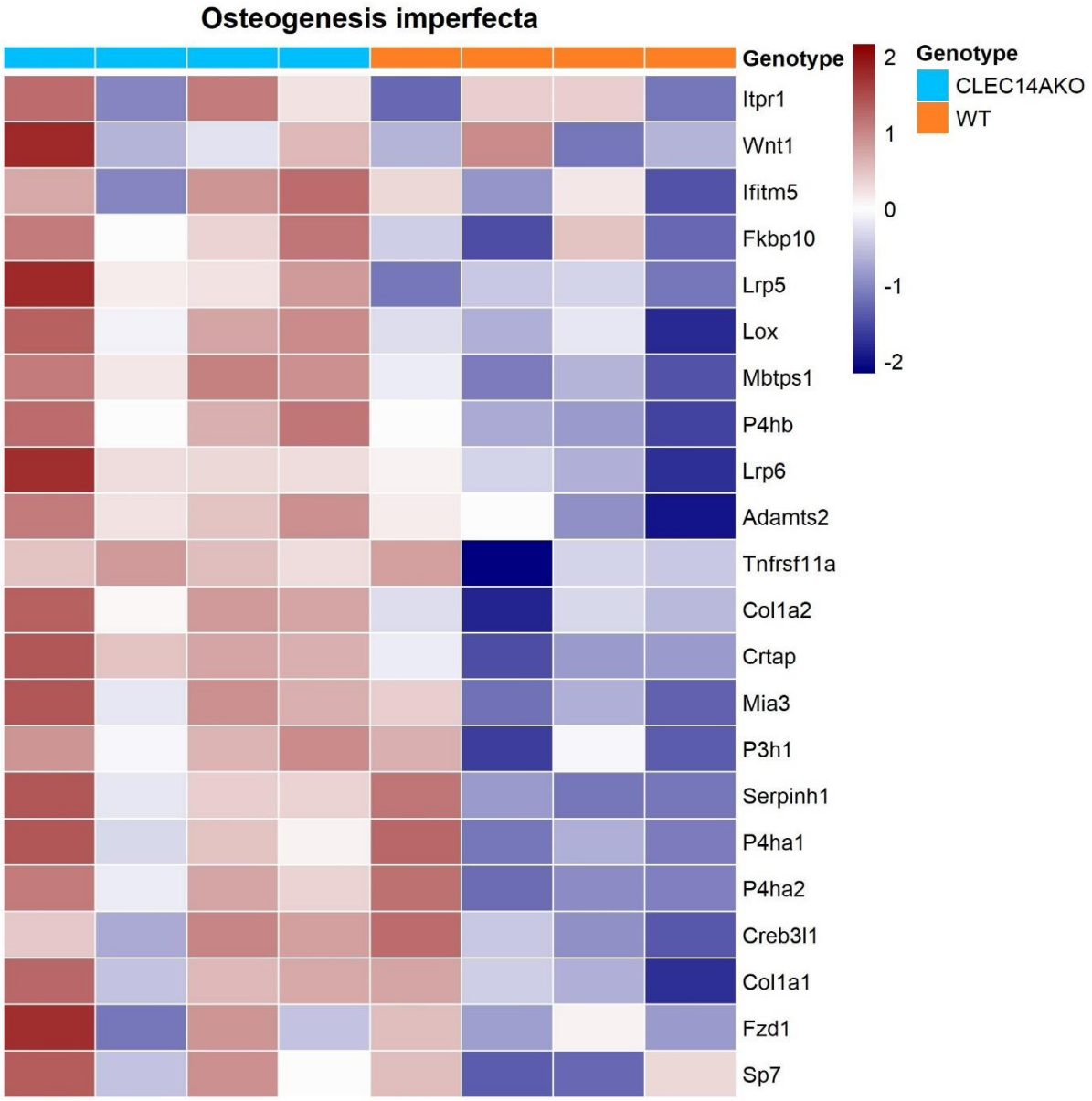


Figure 9.4 GSEA heatmap showing the list of leading edge genes enriched at the top of the Osteogenesis Imperfecta gene set. Heatmap presents upregulation of genes related to Osteogenesis Imperfecta in CLEC14A$^{-/-}$ samples. Gene expression is presented as a Z score. Transcripts presented were identified as statistically significant by GSEA analysis, FDR (q-value) < 0.01, nominal $p < 0.01$.

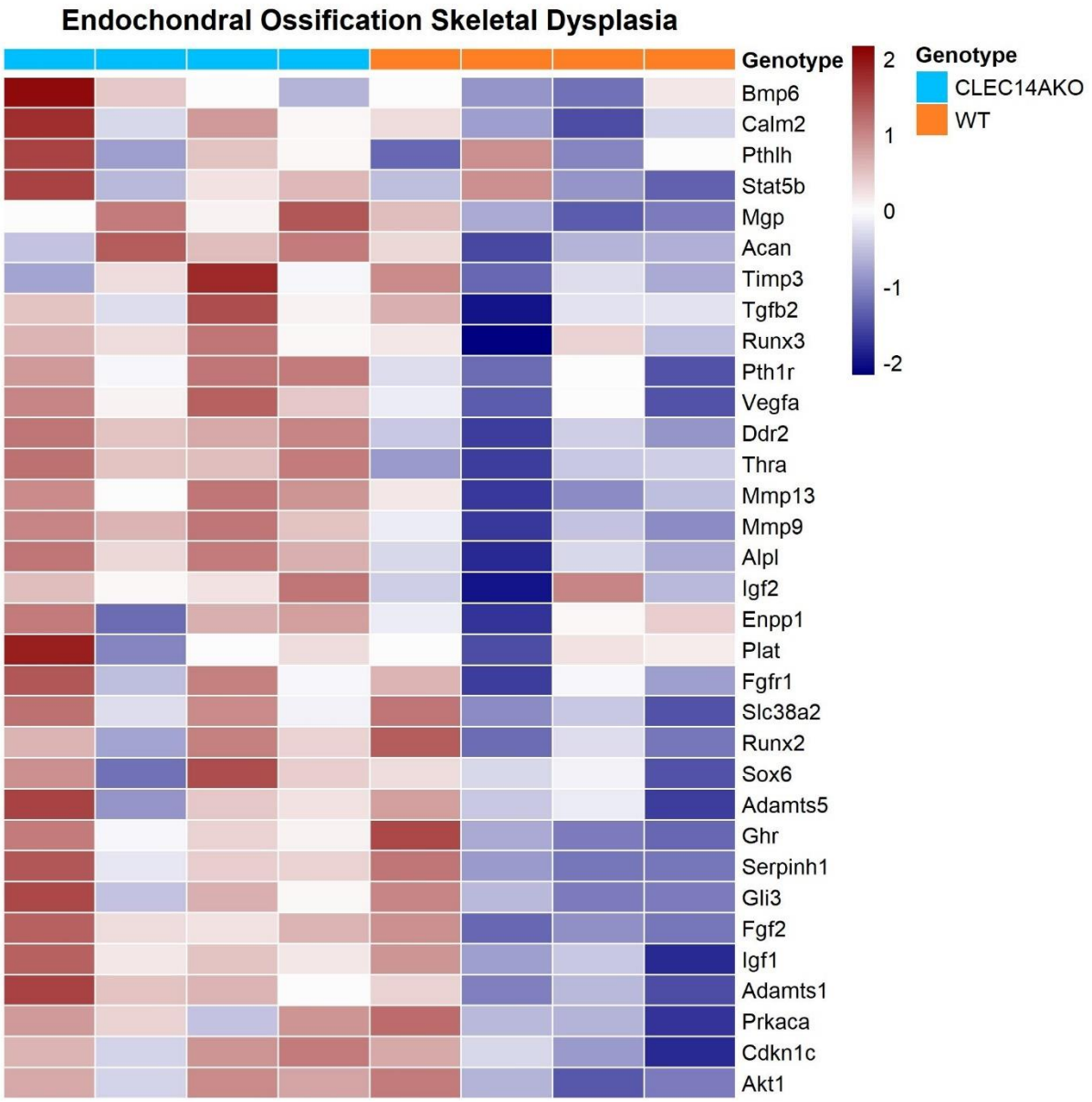


Figure 9.5 GSEA heatmap showing the list of leading edge genes enriched at the top of the Endochondral Ossification in Skeletal Dysplasia gene set. Heatmap presents upregulation of genes related to endochondral ossification in CLEC14A$^{-/-}$ samples. Gene expression is presented as a Z score. Transcripts presented were identified as statistically significant by GSEA analysis, FDR (q-value) < 0.05, nominal p < 0.01.

9.1. Script for RNA seq QC

9.1.1. Quality Control

Code used to Merge fastq.gz files generated by Genomics Birmingham

```
folders <- list.dirs()
for (index in 1:90) {to_merge <- list.files(path=grep(paste("GN_", index, "_",sep=""), folders,
value=T ), full.names=T)
  if(length(to_merge)>0){
        print(paste("Merging:", to_merge, sep=""))
        newdir <- paste("merge_GN", index, sep="_")
        dir.create(newdir)
              for (file in to_merge) {
        file.copy(file, newdir)
        }}}
```

Code submitted to BEAR to merge fastq.gz files

```
set -e
module purge; module load bluebear # this line is required
module load bear-apps/2020a
module load R/4.0.0-foss-2020a
Rscript mergeFileFolders.R
```

FASTQC analysis

```
set -e
module purge; module load bluebear
```

```
module load FastQC/0.11.5-Java-1.8.0_74

mkdir FASTQC

fastqc `find . -name '*.fastq*' -print` --outdir=FASTQC
```

Code used to remove adapter contamination, polyA tails, and low-quality reads

```
set -e

module purge; module load bluebear # this line is required


module load BBMap/38.87-GCC-8.3.0

#module load R/4.0.0-foss-2020a
```

Code used to remove adapter contamination, polyA read throughgh, and low quality reads

```
bbduk.sh in=CD248KO_1_merge_sorted.fastq \

out=CD248ko_1_merge_sorted_trimmed_clean.fastq \

ref=truseq_rna.fa.gz literal=AAAAAAAAAAAAAAAAAA \

k=13 \

ktrim=r \

useshortkmers=t \

mink=5 \

qtrim=r \

trimq=10 \

minlength=20
```

Second FASTQC analysis to compare samples before and after sample cleaning

```
set -e

module purge; module load bluebear

module load FastQC/0.11.5-Java-1.8.0_74

mkdir FASTQC

fastqc `find . -name '*.fastq*' -print` --outdir=FASTQC
```

Code used for multiQC

```
set -e

module purge; module load bluebear # this line is required

module load MultiQC/1.9-foss-2019b-Python-3.7.4

multiqc /rds/projects/w/wilsonay-naylor-rnaseq/GB110920-GN/GB110920-GN-203602406/FASTQ_Generation_2020-10-20_21_59_49Z-331426095/Merged/Merge
```

Code used to align reads back to the mouse genome (STAR aligner)

```
set -e

module purge; module load bluebear

module load STAR/2.7.2b-GCC-8.3.0

module load SAMtools/1.9-foss-2018b

#STAR aligner

#STAR --runThreadN $SLURM_NTASKS\

        --genomeDir /rds/projects/w/wilsonay-naylor-rnaseq/GenomeBuild/Mouse \

        --readFilesIn CD248KO_4_merge_sorted_trimmed_clean.fastq \

        --outFilterType BySJout \

        --outFilterMultimapNmax 20 \
```

```
--alignSJoverhangMin 8 \
--alignSJDBoverhangMin 1 \
--outFilterMismatchNmax 999 \
--outFilterMismatchNoverLmax 0.1 \
--alignIntronMin 20 \
--alignIntronMax 1000000 \
--alignMatesGapMax 1000000 \
--limitBAMsortRAM 16000000000 \
--outSAMattributes NH HI NM MD \
--outSAMtype BAM SortedByCoordinate \
--outFileNamePrefix CLEC14AKO_4_merge_sorted_trimmed_clean_ \
```

Sam tools statistics and index

```
samtools index GN_merge_sorted_trimmed_clean_Aligned.sortedByCoord.out.bam
samtools flagstat GN_merge_sorted_trimmed_clean_Aligned.sortedByCoord.out.bam
```

Code used to generate transcript counts (Subread)

```
set -e
module purge; module load bluebear
module load bear-apps/2020a
module load Subread/2.0.1-GCC-8.3.0
mkdir Counts
featureCounts -p \
                -t exon \
```

```
                -s 0 \
                -g gene_id \
 -a /rds/projects/w/wilsonay-naylor-rnaseq/GenomeBuild/Mouse/Mus_musculus.GRCm38.101.gtf \
 -o /rds/projects/w/wilsonay-naylor-rnaseq/GB110920-GN/GB110920-GN-203602406/FASTQ_Generation_2020-10-20_21_59_49Z-331426095/Merged/BAMfiles/Counts/counts.txt \
 /rds/projects/w/wilsonay-naylor-rnaseq/GB110920-GN/GB110920-GN-203602406/FASTQ_Generation_2020-10-20_21_59_49Z-331426095/Merged/BAMfiles/*.out.bam
```

DESeq2 analysis for differential gene expression analysis

```
library(tidyverse)
library(dplyr)
library(matrixStats)
library(DESeq2)
library(ggfortify)
library(ggplot2)
library(ggrepel)
library(gggenes)
library(tidyverse)
library(DESeq2)
sampleinfo <- read_tsv("SampleInfo-8samples.txt")
```

```
sampleinfo

seqdata <- read_tsv("countsfinal-8samples.txt")

countdata <- seqdata %>%

 column_to_rownames("Geneid") %>% # turn the geneid column into rownames

 rename_all(str_remove, ".bam") %>% # remove the ".bam" from the column names

 rename_all(str_remove, "/rds/projects/w/wilsonay-naylor-rnaseq/GB110920-
GN/GB110920-GN-203602406/FASTQ_Generation_2020-10-20_21_59_49Z-
331426095/Merged/BAMfiles/")


 countdata <- countdata %>%

  rename_all(str_remove, "_merge_sorted_trimmed_clean_Aligned.sortedByCoord.out")


 countdata <- countdata %>%

 select(sampleinfo$FileName) %>% # keep sample columns using sampleinfo$Sample

  as.matrix()


keep <- rowSums(countdata) >5

table(keep, useNA = "always")

matrix <- countdata[keep,]

dim(matrix)

range(matrix)

boxplot(matrix, main='Raw counts distribution',

      xlab="",

      ylab="Raw Counts",
```

```
      las=1.5, cex.axis=0.65, ylim=c(0,100000))
plot(rowMeans(matrix), rowSds(matrix),
    main='Raw Counts : Mean Vs SD',
    xlab="Mean Counts",
    ylab="Standard Deviation (S.D.)",
    xlim=c(0,10000),
    ylim=c(0,5000))
```

Count data normalisation

```
#log2 transformation
logcounts <- log2(matrix + 1)
# summary(logcounts[,1]) # summary for first column
# summary(logcounts) # summary for each column

boxplot(logcounts,
      main='Log2 transformation',
      xlab="",
      ylab="Log2 Counts",
      cex.axis=0.65,
      las=1.5)
abline(h=median(logcounts), col="blue")
# Log2 counts mean expression Vs standard Deviation (SD)
plot(rowMeans(logcounts), rowSds(logcounts),
    main='Log2 Counts : Mean Vs SD',
    xlab="Mean Counts",
```

```
    ylab="Standard Deviation (S.D.)")


#VST transformation
vst_counts <- vst(matrix)
boxplot(vst_counts,
        main='VST transformation',
        xlab="",
        ylab="VST counts",
        las=1.5)
# VST counts mean expression Vs standard Deviation (SD)
plot(rowMeans(vst_counts), rowSds(vst_counts),
    main='VST Counts : Mean Vs SD',
    xlab="VST Transformed Counts",
    ylab="Standard Deviation (S.D.)")


#Rlog
Rlog_counts <- rlog(matrix)
boxplot(Rlog_counts,
        main='R log transformation',
        xlab="",
        ylab="R log counts",
        las=1.5)


plot(rowMeans(Rlog_counts), rowSds(Rlog_counts),
```

```
    main='R log counts : Mean Vs SD',
    xlab="R log Transformed Counts",
    ylab="Standard Deviation (S.D.)")

#PCA - Rlog
pcDat <- prcomp(t(Rlog_counts))
prcompRlog <- autoplot(pcDat,
        data = sampleinfo,
        colour="Genotype",
        Shape="FileName",
        size=5)
prcompRlog <- prcompRlog + theme_bw() + theme(panel.background =
element_blank(),panel.grid.major = element_blank(), panel.grid.minor = element_blank())
prcompRlog
# use this if you want to create an R.Data #####
#save(countdata, sampleinfo, file="Rlog-preprocessing.RData")

#PCA - vst
pcDat <- prcomp(t(vst_counts))
prcompVst <- autoplot(pcDat,
        data = sampleinfo,
        colour="Genotype",
        Shape="FileName",
        size=5)
```

```
prcompVst <- prcompVst + theme_bw() + theme(panel.background = element_blank(),panel.grid.major = element_blank(), panel.grid.minor = element_blank())
prcompVst

#PCA - Log2
pcDat <- prcomp(t(logcounts))
prcomplog2 <- autoplot(pcDat,
                data = sampleinfo,
                colour="Genotype",
                Shape="FileName",
                size=5)
prcomplog2
prcomplog2 <- prcomplog2 + theme_bw() + theme(panel.background = element_blank(),panel.grid.major = element_blank(), panel.grid.minor = element_blank())
prcomplog2
```

9.1.2. Quantitation of differential gene expression with DEseq2

```
design <- as.formula(~ Genotype)#formula to model gene expression against genotype
design
modelMatrix <- model.matrix(design, data = sampleinfo)
modelMatrix
sampleinfo$Genotype <- factor(sampleinfo$Genotype)
modelMatrix <- model.matrix(design, data = sampleinfo)
modelMatrix
```

```
ddsObj.raw <- DESeqDataSetFromMatrix(countData = countdata,
                                     colData = sampleinfo,
                                     design = design)
#estimateSizeFactors
ddsObj <- estimateSizeFactors(ddsObj.raw)
colData(ddsObj.raw)
colData(ddsObj)

logcounts <- log2(countdata + 1)
limma::plotMA(logcounts)
abline(h=0, col="red")

#estimate dispersion
ddsObj <- estimateDispersions(ddsObj)
#apply Negative Binomial GLM fitting and calculate Wald statistics
ddsObj <- nbinomWaldTest(ddsObj)

#DEseq performs the three steps above in one command
ddsObj <- DESeq(ddsObj.raw)

#generate results table, 55487 raw reads compared-all genes identified in the data set, cutoff
p<0.05

res <- results(ddsObj, alpha=0.05)
```

```
write.csv(res, file ="All-genes-withallvalues-DEseq225012022-CambridgeQCcode-Jason.txt")


res_genotype <- results(ddsObj,
                        name= "Genotype_KO_vs_CTRL",
                        alpha = 0.05)
#looks at the number of diff sig genes and removes NA values for p - with this data set it should
be 1366
sum(res_genotype$padj < 0.05, na.rm = TRUE)
#prints info of no of genes diff expressed with up and down regulation numbers and
percentages
summary(res_genotype)


topGenes <- as.data.frame(res_genotype) %>%
  rownames_to_column("GeneID") %>%
  arrange(padj) %>%
  head(1366)


topGenes
write.csv( topGenes, file ="Top-DEG-Jason-DEseq225012022-CambridgeQCcode.txt")
save(countdata, sampleinfo, ddsObj, ddsObj.raw,modelMatrix,res,res_genotype,topGenes,
file="DEseq2.RData")


#gene set log2 normalised counts for Gene Set Enrichment Analysis
```

```
ddsObj <- estimateSizeFactors(ddsObj)

sizeFactors(ddsObj)

normalized_counts <- counts(ddsObj, normalized=TRUE)

#rownames(normalized_counts) <- colData(dds)$Genename

write.table(normalized_counts, file="4-samples-GSEA-normalized_counts.txt", sep="\t",

quote=F, col.names=NA)


ddsObj <- estimateSizeFactors(ddsObj)

sizeFactors(ddsObj)

normalized_counts <- counts(ddsObj, normalized=TRUE)
```

9.1.3. Heatmap generation code

```
library(ggplot2)

library(tibble)

library(tidyverse)

library(pheatmap)

library(matrixStats)

library(dplyr)

library(ggfortify)

library(ggrepel)

library(gggenes)

#Gene Sets – curated from GSEA and DESeq2 analysis
```

OsteogenesisImperfecta = c("Crtap", "Col1a2", "Lrp5", "P4hb", "Lox", "Mbtps1", "Lrp6", "Tnfrsf11a", "Adamts2", "Mia3","Fkbp10", "P4ha2", "Serpinh1", "*Sp7*", "*Col1a1*", "P4ha1", "Ifitm5", "P3h1", "Creb3l1", "Itpr1", "Fzd1", "Wnt1")

EndochondralOssification_Skeletal_Dysplasia = c("*Alpl*", "*Mmp9*", "Ddr2", "*Mmp13*", "Vegfa", "Thra", "Adamts1", "Ctsv", "Fgf2", "Pth1r","Acan", "Calm2", "Gli3", "Runx3", "Akt1", "Serpinh1", "Fgfr1", "Bmp6", "Mgp", "Igf1", "Gh1", "Sox9", "Slc38a2", "Ptch1", "Igf2", "Cdkn1c", "Stat5b", "Timp3", "Ghr", "Plat", "Tgfb2", "Pthlh", "Sox6", "Igf1R", "Adamts5", "*Runx2*", "Enpp1", "Prkaca")

Endochondral_Ossification = c("*Alpl*", "*Mmp9*", "Ddr2", "*Mmp13*", "Adamts1", "Vegfa", "Thra","Ctsv", "Fgf2","Pth1r","Acan","Calm2", "Gli3", "Runx3","*Runx2*", "Akt1", "Serpinh1", "Fgfr1", "Bmp6", "Mgp", "Igf1", "Igf1r", "Gh1", "Sox9","Ptch1","Igf2", "Cdkn1c", "Timp3","Ghr", "Tgfb2")

Regulation_of_expression_of_Slits_and_Robos = c("Rps16",Rps27a","Rps3a","Rpl35a","Rpl7a","Slit2","Rps14","Ubc","Rpl32","Rpl37a","Rpa12","PSma3","Sem1","Rpl10","Magoh","Rps2","Psma2","Psmd8","Psmb4","Cul2","Rps27","Rps17","Psmd10","Psmd13","Rps21","Rpl7","Rps23","Rpl19","Rpl36A","Rpl39L","Psma7","Eif4a3","Rps26","Rpl5","Rps18","Rpl34","Rpl23","Robo1")

Reactome_signaling_by_ROBO_receptors=c("Rps16","Rps27a","Rpa3a", “Rpl35A","Rpl7A","Psme2","Abl2","Slit2","Rps14","Ubc","Rpl32","RPpl37a","Pfn2","Cxcl12"," Rps12","Psma3","Sem1","Rpl10","Magoh","Rps2", "Psma2","Psmd8","Psmb4","Slit3")

Hallmark_Hypoxia = c("Slc6a6", "Ccn2", "Serpine1", "S100a4", "Tgfb3","Kdelr3","Hk2","Ppp1r15a","Klf6","Vegfa","Ccn5","Bhlhe40","Gpc1","Grhpr","Cavin3","Pdk3","Lox","Gapdh","Ackr3","Siah2","Galk1","Anxa2","Dusp1","Col5a1",“Bgn","Ccng2","T

mem45a","Atp7a","Il6","Fbp1","Cdkn1a","Gbe1","Errfi1","P4ha2","Csrp2","Vldlr","Stc2","Ext1","Fosl2","Has1","Ids","Cavin1")

KEGG_CELL_ADHESION_MOLECULES = c("Itga6","Cldn3","Mag","Mpz","Ncam2","Cdh5","Cdh1","Icam2","Ocln","Negr1","Cldn6","Cldn15","Cldn19","L1cam","Cntn1","Cd40","Cldn7","Cadm3","Cldn23","Sell","Cdh15","Itgam","Itgb8","Cldn10","Sele","Itga4")

KEGG_ECM_RECEPTOR_INTERACTION = c ("Itga3", "Itga6", "Itga7", "Col6a6", "Col4a6", "Col4a4", "Col4a2", "Lama5", "Thbs4","Col4a1","Reln","Vtn","Sv2a","Itga2b","Gp1bb","itgb4","Itgb8")

KEGG_TIGHT_JUNCTION = c("Myh3", "Myh11", "Myh8","Actn2","Prkcg","Mylpf","Ocln","Cgn" ,"Epb41","Actn3","Myl2", "Prkcz", "Ctnna2", "Rab13", "Myh7", "Myh2")

CLEC14A_interactome = c("Hspa1a","Hspa1b","Cldn19", "Ocln", "*Klf2*", "*Klf4*","C1qtnf9", "Cdh5", "Cldn5")

Osteogenesis_and_Bone_Growth = c("Slit2","Lox","Mbtps1","Igfbp5", "Igfbp2","Fgfr2","Tgfb3", "Fgf10","Cap2", "Shox2", "Tnf", "Epb41", "Igf2","Lox","Tmem119")

Osteoblast_proliferation_and_maturation = c("*Alpl*","*Col1a1*", "Col1a2","Ibsp", "Spock1", "Mapk8ip2","Mapk8ip3", "Mapk8ip1","Map3k1", "Lmna", "Sp1","Mapk1","Cdh11","Rela", "Bambi")

EC_function = c("Pcdha12", "Vegfa", "Serpine1")

Adhesion_Gap_Junction = c("Gjc3","Gjc2")

Metalloproteases = c("Adamts1", "Timp2", "*Mmp14*", "Timp1","*Mmp13*", "*Mmp9*")

Mineral_resorption = c("Atp1b4", "Atp1a2", "Atp1b2","Slc11a2", "Zfhx3")

```
Osteoclasts = c("Csf1r", "Acp5", "Ctsk", "Nfatc1")

TGFB_SMAD_Singalling = c("Dact2","Tgfb3","Dact1")

Regulation_OF_GROWTH_PLATE_processes = c("Col10a1", "Brd2")


#read in transcript count data (all 49609 transcripts mapped back to the genome)

sampleinfo <- read_tsv("SampleInfo-8samples.txt")

seqdata <- read_tsv("countsfinal-8samples-modified-for-heatmaps-addedgenename.txt")


#rename column names and subset seqdata with the gene names heatmap

countdata <- seqdata %>%

 column_to_rownames("GeneID") %>% # turn the geneid column into rownames

 rename_all(str_remove, ".bam") %>% # remove the ".bam" from the column names

 rename_all(str_remove, "/rds/projects/w/wilsonay-naylor-rnaseq/GB110920-
GN/GB110920-GN-203602406/FASTQ_Generation_2020-10-20_21_59_49Z-
331426095/Merged/BAMfiles/")

countdata <- countdata %>%

 rename_all(str_remove, "_merge_sorted_trimmed_clean_Aligned.sortedByCoord.out")

#subset data for GSEA heatmaps from a list of Subread-generated counts

countdata <- subset(countdata, rownames(countdata) %in%
Regulation_OF_GROWTH_PLATE_processes)

#subset data to remove values lower than 40 -across all 8 samples, so at least 5 reads in each
group

countdata_subset = countdata

keep <- rowSums(countdata_subset) >40
```

```
table(keep, useNA = "always")

countdata_subset2 <- countdata[keep,]
```

#generate a new variable to be used for heatmap called heatmap_alldata

```
countdata_subset2-> heatmap_alldata

#log2normalise data

heatmap_alldata %>%

  log2() -> heatmap_data_log2
```

#column annotations

```
data.frame(row.names = colnames(heatmap_data_log2),

        Genotype                                                                    =

c("CLEC14AKO","CLEC14AKO","CLEC14AKO","CLEC14AKO","WT","WT","WT","WT"))          ->

col_annotations_alldata
```

#generate heatmaps with log2 normalised data, Z score normalisation was generated by using the scale = "row" argument in pheatmap as bellow

```
heatmap_data_log2 %>%

  pheatmap(show_rownames = TRUE,

        show_colnames = FALSE,

        cluster_cols = F,

        scale = "row",

        border_color = "white",

        angle_col = 45,

        fontsize = 10,
```

```
        treeheight_row = 0,
        cutree_rows = 1,
        cutree_cols = 1,
        cellheight = 15,
        main = "Regulation of growth plate processes",
        color = colorRampPalette(c("navyblue", "white", "red4"))(100),
        annotation_col = col_annotations_alldata,
        annotation_colors = list( Genotype = c("CLEC14AKO" = "deepskyblue", "WT" =
"chocolate1")),
        filename = "Regulation_OF_GROWTH_PLATE_processes.jpeg")
```

9.2. Code for single-cell sequencing analysis of GSE 128423

```
BiocManager::install(c("RDCOMClient "), update = TRUE, ask = FALSE)

install.packages("installr")

install.packages("tibble")

install.packages("dplyr")

install.packages("Seurat")

install.packages("tsne")

library(tsne)

library(dplyr)

library(Seurat)

library(patchwork)

library(ggplot2)

#load barcodes matrix and metadata

data_dir <- "D:/ScRNA-seq/Raw files/std1/std1/std1/"

list.files(data_dir) # Should show barcodes.tsv, genes.tsv, and matrix.mtx

expression_matrix <- Read10X(data.dir = data_dir)

std1 = CreateSeuratObject(counts = expression_matrix)

data_dir <- "D:/ScRNA-seq/Raw files//std2/std2/std2"

list.files(data_dir) # Should show barcodes.tsv, genes.tsv, and matrix.mtx

expression_matrix <- Read10X(data.dir = data_dir)

std2 = CreateSeuratObject(counts = expression_matrix)

data_dir <-  "D:/ScRNA-seq/Raw files//std3"

list.files(data_dir) # Should show barcodes.tsv, genes.tsv, and matrix.mtx
```

```
expression_matrix <- Read10X(data.dir = data_dir)

std3 = CreateSeuratObject(counts = expression_matrix)


data_dir <- "D:/ScRNA-seq/Raw files//std4"

list.files(data_dir) # Should show barcodes.tsv, genes.tsv, and matrix.mtx

expression_matrix <- Read10X(data.dir = data_dir)

std4 = CreateSeuratObject(counts = expression_matrix)

data_dir <- "D:/ScRNA-seq/Raw files//std5"

list.files(data_dir) # Should show barcodes.tsv, genes.tsv, and matrix.mtx

expression_matrix <- Read10X(data.dir = data_dir)

std5 = CreateSeuratObject(counts = expression_matrix)

data_dir <- "D:/ScRNA-seq/Raw files//std6"

list.files(data_dir) # Should show barcodes.tsv, genes.tsv, and matrix.mtx

expression_matrix <- Read10X(data.dir = data_dir)

std6 = CreateSeuratObject(counts = expression_matrix)

#merge files to one project

Scadden <- merge(std1, y = c(std2, std3, std4, std5, std6), add.cell.ids = c("1", "2", "3", “4”, “5”,

“6”), project = "Scadden")

Scadden

#check mitochondrial genes expression

Scadden[["percent.mt"]] <- PercentageFeatureSet(Scadden, pattern = "^mt-")

#n.Feature = number  read of RNA , nCount number of different RNAs, percent of all RNA

how much is mitochondrial RNA per cell

VlnPlot(Scadden, features = c("nFeature_RNA", "nCount_RNA", "percent.mt"), ncol = 3)
```

```
plot1 <- FeatureScatter(Scadden, feature1 = "nCount_RNA", feature2 = "percent.mt")
plot2 <- FeatureScatter(Scadden, feature1 = "nCount_RNA", feature2 = "nFeature_RNA")
plot1 + plot2
```

#remove cells with a higher percentage of mitochondria genes than 5% you do not wamt (mt<5 - is <5% mRNA content)

```
Scadden <- subset(Scadden, subset = nFeature_RNA > 200 & nFeature_RNA < 6000 & percent.mt < 5)
Scadden <- NormalizeData(Scadden, normalization.method = "LogNormalize", scale.factor = 10000)
Scadden <- FindVariableFeatures(Scadden, selection.method = "vst", nfeatures = 2000)
top10 <- head(VariableFeatures(Scadden), 10)
top20 <- head(VariableFeatures(Scadden), 20)
```

#plot all genes differentially expressed

```
plot1 <- VariableFeaturePlot(Scadden)
plot2 <- LabelPoints(plot = plot1, points = top10, repel = TRUE)
plot1 + plot2
```

```
#Scale data and run PCA
all.genes <- rownames(Scadden)
Scadden <- ScaleData(Scadden, features = all.genes)
```

```
Scadden <- RunPCA(Scadden, features = VariableFeatures(object = Scadden))
```

```
print(Scadden[["pca"]], dims = 1:16, nfeatures = 16)

DimHeatmap(Scadden, dims = 1:15, cells = 500, balanced = TRUE)

#Resolution should be chosen based on the dataset (can use resolution ranging from 2 down to 0.25)

Scadden <- FindNeighbors(Scadden, dims = 1:10)

Scadden <- FindClusters(Scadden, resolution = 0.5)


Scadden <- RunUMAP(Scadden, dims = 1:10)

DimPlot(Scadden, reduction = "umap", pt.size=1, label = TRUE, label.box = TRUE)

Scadden <- RunTSNE(Scadden, dims = 1:10, check_duplicates = FALSE)

DimPlot(Scadden, reduction = "tsne")

TSNEPlot(Scadden, pt.size=1, label = TRUE, label.box = TRUE)


#Find differentially expressed markers for each cell cluster

#Note: Limit testing to genes which show, on average, at least X-fold difference (log-scale) between the two groups of cells. Default is 0.25 Increasing logfc.threshold speeds up the function, but can miss weaker signals.

Scadden.markers <- FindAllMarkers(Scadden, only.pos = TRUE, features = NULL, min.pct = 0.25, logfc.threshold = 0.25, verbose = TRUE)

Scadden.markers %>% group_by(cluster) %>% top_n(n = 10, wt = avg_log2FC)

write.csv(Scadden.markers, file = "AllDEG.csv")

top10 <- Scadden.markers %>% group_by(cluster) %>% top_n(n = 10, wt = avg_log2FC)

#Rename cell clusters according to expression of top 10 differentially expressed markers
```

```
new.cluster.ids <- c("Endothelial cells", "Fibroblasts", "MSC", "Endothelial cells",
"Erythrocytes","Chondrocytes", "Erythrocytes","Chondrocytes","Granulocytes",
                     "B Cells", "B Cells", "Monocytes", "Endothelial cells", "Osteoblasts",
"Neutrophils", "Neutrophils", "Pericytes")
names(new.cluster.ids) <- levels(Scadden)
Scadden <- RenameIdents(Scadden, new.cluster.ids)
```

#Subclustering of osteoblast cluster

```
Osteoblast <- subset(Scadden, idents = "Osteoblasts")
DimPlot(Osteoblast, label = TRUE, pt.size = 1.8) + NoLegend()
FeaturePlot(Osteoblast, features = c("Bglap"), label = TRUE, reduction = "tsne")
Osteoblast <- FindNeighbors(Osteoblast, dims = 1:10)
Osteoblast <- FindClusters(Osteoblast, resolution = 0.2)
head(Idents(Osteoblast), 5)

Osteoblast <- RunTSNE(Osteoblast, dims = 1:10)
DimPlot(Osteoblast, reduction = "tsne", pt.size = 1)

Obs.markers <- FindAllMarkers(Osteoblast, only.pos = TRUE, min.pct = 0.25, logfc.threshold =
0.25)
Obs.markers %>% group_by(cluster) %>% top_n(n = 10, wt = avg_log2FC)

top10obs <- Obs.markers %>% group_by(cluster) %>% top_n(n = 10, wt = avg_log2FC)
print(top10obs)
```

```
write.csv(top10obs,file = "Obstop10DEGv2.csv")
DoHeatmap(Osteoblast, features = top10obs$gene)
ggsave("Obs-heatmap.tiff")

new.cluster.ids <- c("Immature osteoblasts", "Mature osteoblasts", "Pre-osteoblasts")
names(new.cluster.ids) <- levels(Osteoblast)
Osteoblast <- RenameIdents(Osteoblast, new.cluster.ids)
DimPlot(Scadden, reduction = "tsne", label = TRUE, pt.size=1.8, label.box = TRUE, label.size =
4)+ NoLegend()
ggsave("DimPlot_Obsnamed.tiff")

FeaturePlot(Osteoblast, features = c("Runx2","Sp7", "Spp1", "Alpl"),
        label = FALSE,
        reduction = "tsne",
        pt.size=2)
ggsave("FeaturePlot-Sp7.tiff")

FeaturePlot(Scadden, features = c("Ibsp"),pt.size=1.8, ncol = 2,
        reduction = "tsne",label = TRUE, label.size = 4.5)
ggsave("FeaturePlot-Ibsp.tiff")

VlnPlot(Osteoblast, features = c("Runx2","Sp7"),pt.size = 1.5, ncol = 2)
ggsave("ViolinPlot-Sp7-Runx2.tiff")
VlnPlot(Osteoblast, features = c("Lrp4","Spp1", "Serpine2"),pt.size = 1.5, ncol = 3)
```

```
ggsave("ViolinPlot-Lrp4-Spp1-Serpine2.tiff")
FeaturePlot(Osteoblast, features = c("Lepr","Kitl", "Cxcl12", "Grem1"), label = TRUE, reduction
= "tsne")
ggsave("FeaturePlot-Cxcl12.tiff")
RidgePlot(Osteoblast, features = c("Lepr","Kitl", "Cxcl12", "Grem1"), ncol = 2)
ggsave("RidgePlot-Cxcl12.tiff")
VlnPlot(Osteoblast, features = c("Lepr","Kitl", "Cxcl12", "Grem1"),pt.size = 1, ncol = 2)
ggsave("ViolinPlot-Cxcl12.tiff")
FeaturePlot(Osteoblast, features = c("Il7","Adipoq"), label = TRUE, reduction = "tsne")
ggsave("FeaturePlot-Adipoq.tiff")
RidgePlot(Osteoblast, features = c("Il7","Adipoq"), ncol = 2)
ggsave("RidgePlot-Adipoq.tiff")
VlnPlot(Osteoblast, features = c("Il7","Adipoq"),pt.size = 1, ncol = 2)
ggsave("ViolinPlot-Adipoq.tiff")

FeaturePlot(Osteoblast, features = c("Col1a1","Col1a2", "Sparc", "Bglap"), label = TRUE,
reduction = "tsne")
ggsave("FeaturePlot-Col1a.tiff")
RidgePlot(Osteoblast, features = c("Col1a1","Col1a2", "Sparc", "Bglap"), ncol = 2)
ggsave("RidgePlot-Col1a.tiff")
VlnPlot(Osteoblast, features = c("Col1a1","Col1a2", "Sparc", "Bglap"),pt.size = 1, ncol = 2)
ggsave("ViolinPlot-Col1a.tiff")

genes<-c("Cxcl12", "Pdgfrb", "Alpl", "Spp1", "Col1a1", "Col1a2", "Sparc", "Bglap")
```

```
DotPlot(Osteoblast, features = genes,
        cols = c("lightgrey", "midnightblue",
                 cluster.idents = genes ))
ggsave("Dotplot-osteoblastmaturation.tiff")
```

9.3. Published review

International Journal of *Molecular Sciences*

MDPI

Review

The Cellular Choreography of Osteoblast Angiotropism in Bone Development and Homeostasis

Georgiana Neag, Melissa Finlay and Amy J. Naylor *

Rheumatology Research Group, Institute of Inflammation and Ageing, University of Birmingham, Birmingham B15 2TT, UK; [redacted] (G.N.); [redacted] (M.F.)
* Correspondence: [redacted]

Abstract: Interaction between endothelial cells and osteoblasts is essential for bone development and homeostasis. This process is mediated in large part by osteoblast angiotropism, the migration of osteoblasts alongside blood vessels, which is crucial for the homing of osteoblasts to sites of bone formation during embryogenesis and in mature bones during remodeling and repair. Specialized bone endothelial cells that form "type H" capillaries have emerged as key interaction partners of osteoblasts, regulating osteoblast differentiation and maturation and ensuring their migration towards newly forming trabecular bone areas. Recent revolutions in high-resolution imaging methodologies for bone as well as single cell and RNA sequencing technologies have enabled the identification of some of the signaling pathways and molecular interactions that underpin this regulatory relationship. Similarly, the intercellular cross talk between endothelial cells and entombed osteocytes that is essential for bone formation, repair, and maintenance are beginning to be uncovered. This is a relatively new area of research that has, until recently, been hampered by a lack of appropriate analysis tools. Now that these tools are available, greater understanding of the molecular relationships between these key cell types is expected to facilitate identification of new drug targets for diseases of bone formation and remodeling.

Keywords: bone; remodeling; endothelial cell; blood vessel; osteoblast; osteocyte

check for updates

Citation: Neag, G.; Finlay, M.; Naylor, A.J. The Cellular Choreography of Osteoblast Angiotropism in Bone Development and Homeostasis. *Int. J. Mol. Sci.* **2021**, *22*, 7253. https://doi.org/10.3390/ijms22147253

Academic Editor: Giacomina Brunetti

Received: 7 May 2021
Accepted: 29 June 2021
Published: 6 July 2021

Publisher's Note: MDPI stays neutral with regard to jurisdictional claims in published maps and institutional affiliations.

Copyright: © 2021 by the authors. Licensee MDPI, Basel, Switzerland. This article is an open access article distributed under the terms and conditions of the Creative Commons Attribution (CC BY) license (https://creativecommons.org/licenses/by/4.0/).

1. The Function, Anatomy, and Cellular Overview of the Skeletal System

The mammalian skeletal system is highly dynamic with multiple crucial roles, most notably providing architectural and mechanical support to the whole body, protection of the vital organs, metabolic and endocrine modulation, and, in the case of long bones, a site for hematopoiesis [1]. Bones are morphologically compartmentalized into two distinct and contrasting structural arrangements: a cancellous type called trabecular bone and a compact solid type termed cortical bone. Trabecular bone is present within the metaphysis of the long bones, vertebral bodies, ribs, and the iliac crest, while cortical bone forms the outer layer of all bones. Cortical bone bears most of the mechanical load in the body. However, the importance of trabecular bone is more apparent for overall bone strength and resilience during periods of high mechanical force [2,3].

Although the predominant appearance of bone matrix is of a compact mineralised tissue, this unique biomaterial is highly cellular and contains a wide variety of specialised cell types that contribute to its formation, maintenance, and continual remodelling.

Highly regulated processes establish intercellular communication between bone-resident cells, each with its own distinctive role, to ensure a finely tuned balance between bone resorption and bone formation. The major bone-resorbing cell type is the osteoclast. Osteoclasts are multinucleated cells formed by the fusion of mononuclear, monocyte-derived, macrophage precursors, and their main function is resorption of cartilage and bone matrices. Vessel-associated osteoclasts drive cartilage resorption during bone growth [4], whereas bona fide osteoclasts regulate resorption of mineralised bone

matrix during bone maintenance and repair. Furthermore, with bone being the largest reservoir for calcium storage in the body, resorption also facilitates calcium release to maintain optimal circulating levels [5]. Osteoblasts play the opposite role to osteoclasts, constituting the major bone-forming cell type. Mesenchymal stem cells (MSCs) are situated at the apex of the osteoblast lineage cell hierarchy, differentiating stepwise into osteoprogenitors, bone lining cells, osteoblasts, and, ultimately, osteocytes [6,7]. Osteoblast lineage cells have numerous roles depending on their differentiation stage. Osteoprogenitors and bone lining cells constitute a pool of immature osteoblasts, maintained in a quiescent state that can be utilized for bone remodelling and repair. Mature osteoblasts ensure production and secretion of a new protein-rich bone matrix and its subsequent mineralization. Osteocytes are terminally differentiated osteoblasts, entombed within mineralised bone, acting as the main regulatory unit of skeletal homeostasis. Additional cells supporting bone homeostasis include endothelial cells (ECs), adipocytes, and chondrocytes.

ECs, in particular, have recently been at the forefront of scientific investigation, due to major technological advances allowing for a detailed exploration of the bone vascular bed; it is now widely accepted that ECs form blood vessels that act as supporting conduits to bone cells. In addition, ECs perform multiple pivotal roles in the vascular system including vasculogenesis, angiogenesis, vascular maturation, and remodelling, as well as control of vascular tone and blood flow [8,9]. In addition to these traditional roles, the bone vascular endothelium mediates the compartmentalization of osteogenesis and hematopoiesis by creating niche local environments favorable to each of these two processes [9–13].

Skeletal development, growth, remodelling, and repair rely on a complex cellular ecosystem, wherein cells are engaged in continuous cross talk via the release of a panoply of autocrine and paracrine signals. This review focuses specifically on the bidirectional molecular interactions that occur between ECs and osteoblast lineage cells and details our current understanding of how these interactions facilitate and control bone homeostasis throughout life.

2. Recent Advances in Bone Endothelial Cell Diversity

The vascular system ensures delivery of nutrients and metabolites, oxygen availability, removal of waste products, and trafficking of a wide variety of cells throughout the body using a series of vessels of different sizes and structures, the lining of which is composed of ECs, differentiated from the mesoderm during embryogenesis [14]. The bone vascular network is composed of arteries, the central draining vein, and a myriad of capillaries. The latter form a compact, interconnected vascular bed throughout the length of long bones. In the last decade, three distinct subtypes of blood capillaries have been identified and characterised in the murine bone: types L, H, and E capillaries [10,15,16]. Type H vessels have been subsequently confirmed in the human tibia and femur [17].

A clear distinction between capillary types can be made based on their relative expression of Endomucin (EMCN), a marker for non-arterial vessels, and CD31 (encoded by the PECAM-1 gene), a canonical marker for ECs [18,19]. Types H and E capillaries have higher expression of both EMCN and CD31, whereas type L capillaries express these markers at comparatively lower levels. This highly double-positive expression of EMCN and CD31 is driven by Notch signalling, which prompts the increased transcription of PECAM-1, EMCN, as well as Kinase Insert Domain Receptor (KDR), a Vascular Endothelial Growth Factor (VEGF) receptor [20]. In mice, type L vessels are present during both bone embryogenesis (from embryonic day (E)16.5) and in the postnatal long bone in juveniles and adults (assessed from birth until 70 weeks of age) [10,15,21]. The proportion of ECs with the type L phenotype increases steadily from embryogenesis to maturity (32% to 88.9%, at E16.5 and postnatal day (P)28, respectively) [15]. On the other hand, types E and H vessels present a contrasting trend. The proportion of type E capillaries decreases from E16.5, until nearly undetectable at P28 (58% and 2%, respectively), while that of type H capillaries increases from E16.5 to P6, then decreases until P28 (9%, 26%, and 9%, respectively) [15]. During embryogenesis, the majority of vessels in the murine long bone

are types H and E capillaries, whereas postnatally, type L vessels comprise the majority of capillary ECs [15].

Invasion of the vascular plexus into the long bone occurs between E15.5 and E16.5, succeeding initiation of MSC osteoblast differentiation at E14.5 and preceding initiation of bone formation at the primary ossification center [15,22]. At birth, type H vessels are expressed throughout the long-bone vascular bed; however, postnatally their geographical distribution becomes more distinct and they are located almost exclusively within the metaphysis region. Types H and L vessels in the postnatal long bone can be readily distinguished according to their localization and morphological organization (illustrated in Figure 1) [15]. Type H vessels are columnar capillaries that end in anastomosis bulges at the caudal point of the avascular growth plate [10]. Recently published work by Romeo and colleagues identified an important role for the anastomosis bulges in angiogenesis during bone growth, particularly during resorption of the chondrocyte-deposited matrix in the growth plate region [4]. Conversely, type L vessels are confined to the diaphysis, where they form a sinusoidal, highly branched, and relatively hypoxic vessel bed, through which immune cells can readily pass from the bone marrow into the bloodstream [16].

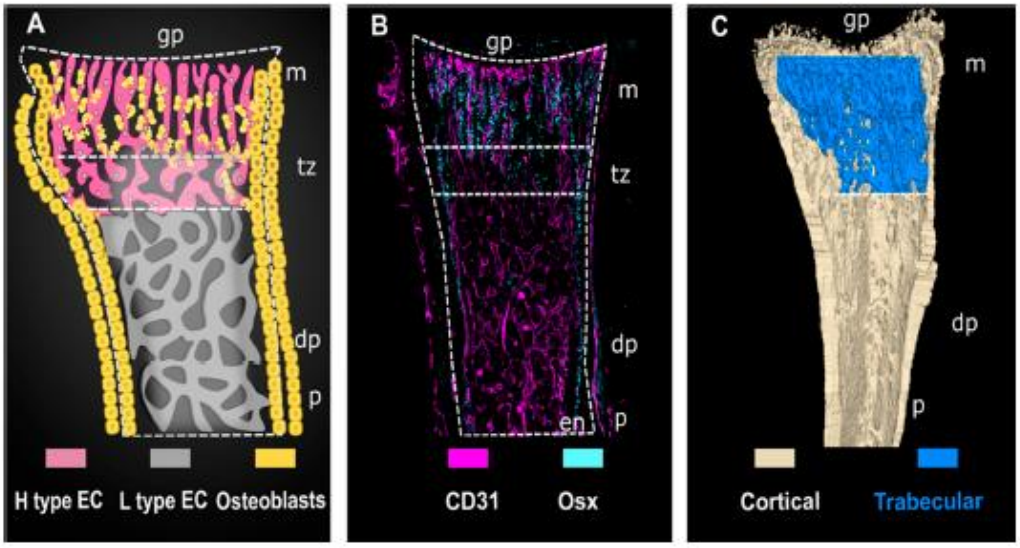


Figure 1. Compartmentalization of the murine long bone and its capillary network. H-type vessels are presented with their main interacting partners, Osx$^+$ cells, in the postnatal murine long bone. Left to right: (**A**) Schematic diagram illustrates H- (magenta) and L-type (grey) vessels with their distinct morphology and emphasizes the strict geographical distribution of Osx$^+$ osteoprogenitors in the metaphysis as compared to the diaphysis. Osteoprogenitors in the metaphysis (indicated by yellow, irregular-shaped cells) are presented closely associated to H-type capillaries during their migration to sites of trabecular bone formation. Located in the endosteum and periosteum is a pool of osteoprogenitors (indicated by yellow, cuboid-shaped cells) not associated with H-type vessels. H-type vessels are columnar formations perpendicularly oriented against the lowermost point of the avascular growth plate in long bones. L-type vessels are localised to the diaphysis where they form a sinusoidal hypoxic vessel bed surrounded by bone marrow cells (not represented). H- and L-type vessels form a continuous vascular network; the area where these H-type capillaries begin to converge into L-type capillaries has been branded the transition zone, an area with a vascular web of an intermediate phenotype between these two capillaries. (**B**) High-resolution confocal imaging of CD31 and Osx, labelling endothelial cells (magenta) and osteoprogenitors (cyan), respectively. Postnatal day 4 (P4) tibia sectioned on the axial plane illustrates the specific localization of bone-forming cells around H vessels in the metaphysis, endosteum, and periosteum. Note the formation of arches and bulges at the caudal point of the growth plate, as previously described. (**C**) Illustration of the compartmentalization of the long bone. Pseudocolored, micro-computed tomography, 2D plane snapshot from a 3D bone mesh model. Trabecular bone (blue) is

superimposed on cortical bone (ivory). The uppermost and lowermost regions of the long bone start and end at the epiphysis at each end of the bone (not shown). The growth plate is localised at the interface between the epiphysis, and the metaphysis, the region where trabecular bone is localised in the long bone (blue). The middle part of the bone, the diaphysis, is void of trabecular bone and houses the bone marrow. Abbreviations: diaphysis-dp, endosteum-en, growth plate-gp, metaphysis-m, periosteum-p, H-type vessel to L-type vessel transition zone-tz.

Lineage-tracing experiments have confirmed that type E ECs are developmentally the most upstream capillary EC in the bone, constituting the origin of types L and H ECs [15]. Type H vessels have been identified in the long bones (murine and human) and alveolar bones (murine), as well as the spine, sternum, and calvarium (murine) [10,23,24]. In the murine long bone, peak vessel density is reached at P6. However, this progressively declines during adulthood and aging [15,21]. A similar decline in type H vessel number and density has also been reported in humans with increasing age, a loss that has been associated with osteoporosis and osteopenia, although a causal link in humans has yet to be established [17,25].

While type L capillaries are surrounded by hematopoietic stem cells, type H vessels interact with osteoblasts [15,26]. A strong indicator that type H vessels are essential for the coupling of osteogenesis and angiogenesis is demonstrated by the fact that both type H and E capillaries are the only ones surrounded by osteoprogenitor cells in the whole bone, with the exception of transcortical vessels in the endosteum and periosteum [10,15,21], although it remains unclear whether the newly identified transcortical blood vessels [27,28] are in essence type H capillaries.

3. Bidirectional Cross Talk between Endothelial Cell and Osteoblast Regulates Bone Formation during Embryogenesis and Development

Embryonic osteogenesis occurs through developmental processes of either endochondral or intramembranous ossification. Long bones are formed via endochondral ossification, a process during which the pre-existing matrix of an avascular, cartilaginous, and relatively homogenous tissue template (anlage) is resorbed and remodelled into a highly vascularised, architecturally complex, multicellular, and multifunctional bone tissue. Remodelling of the initial anlage is accomplished via osteoclast degradation and co-invasion of vessels and osteoblast progenitor cells differentiated from MSCs. Osteoblast lineage commitment unfolds in the perichondrium of the anlage where MSCs undergo stepwise differentiation into osteoprogenitors and other cell types. Consequently, osteoprogenitors undergo proliferation and proceed to build the cortical bone collar (perichondrium) that surrounds the anlage [22,29]. On the other hand, flat bones, such as the calvarial bones of the skull, form through intramembranous ossification with no initial cartilaginous template required. This process relies on local MSCs to undergo a stepwise differentiation into osteoprogenitors and then into osteoid-secreting mature osteoblasts. Both of these developmental processes have been reviewed in depth previously [30–32].

The first stage of endochondral bone formation during embryogenesis is initiated by MSC differentiation. Stem cells destined to differentiate into osteoblasts will progress through three precisely timed and regulated stages of differentiation, each of which can be identified by changes in the expression of a well-defined set of proteins and transcription factors. This has been reviewed in more detail previously [6,33,34], and can be summarised as follows.

Commitment to the lineage: Under the influence of the local niche MSCs begin to selectively express osteoblast master transcriptional regulators: Runt related 2 (RUNX2), β-catenin, and Osterix (OSX). The concerted actions of these regulators and of locally expressed stem cell factors induce osteo-lineage commitment programming, giving rise to cells interchangeably termed progenitor cells, osteoprogenitors, immature osteoblasts, and pre-osteoblasts, herein called osteoprogenitors.

Mitosis: Following commitment, osteoprogenitors, marked by OSX but lacking Collagen type I expression, undergo a period of high proliferation.

Osteoid production and mineralization: Cuboidal-shaped mature osteoblasts, characterised by production of collagen I and alkaline phosphatase, produce the extracellular matrix of the bone that later undergoes mineralization.

Given the plethora of functions accomplished by osteoblast lineage cells throughout their differentiation journey, it comes as no surprise that cellular metabolic functions differ between cell differentiation status, in line with geographical oxygen and nutrient availability, both of which are locally delivered by vessels. Osteoblast differentiation requires increased oxygen consumption, as previously reported in vitro [35], in silico, and in vivo [36]. Low oxygen availability hampers osteogenesis commitment by limiting the MSC metabolic shift towards mitochondrial oxidative phosphorylation, a change driven by the increased expression levels of the oxygen-sensing transcription factor, Hypoxia-Inducible Factor 1 Alpha (HIF-1α) [37,38]. Hypoxia and HIF-1α also impede osteoblast proliferation via the coupled HIF-1α-Osterix signalling pathway, which inhibits WNT signalling [39,40]. While MSCs are highly dependent on oxygen availability during their differentiation and proliferation, they exhibit multivalency in relation to nutrient availability, being able to either undertake glycolysis, fatty acid oxidation, or ketolysis (ketone body oxidation) to meet their metabolic needs (reviewed in detail previously) [41,42]. On the other hand, substrate excess, such as high-glucose environments associated with diabetes, can decrease osteoblast migration, due to a decline in phosphorylation of cell motility regulators protein kinase B (AKT) and mitogen activated protein kinase ERK [43]. This body of work demonstrates the importance of bone vascularization for osteoblast regulation through oxygen and nutrient availability; however, there is still a lack of clarity regarding the involvement of EC-derived signalling in this process.

The second stage of endochondral bone formation, whereby the remaining cartilaginous template is replaced with bone tissue, is initiated in embryogenesis and continues postnatally. In embryonic life, this starts with the invasion of types E and H ECs into the primary ossification center [15], followed by a subsequent longitudinal and radial expansion of vessels, and then terminates at the secondary ossification centers. Vascularization of the bone template spans from E15.5 until peak bone mass is attained, which, in mice, is at 11–12 weeks of age [10,15,44]. Expansion of the bone vascular supply relies heavily on sprouting angiogenesis [45,46], a sequential process involving: (1) initial selection of EC tip cells, which subsequently initiate and lead the vessel sprout; (2) EC migration for extension of the sprout and vessel tube formation; (3) connection of vessel sprouts via anastomosis and sprout pruning [47–51]. During the angiogenesis-driven expansion of the capillary network, type H vessels and osteoblasts engage in a feed forward loop and trigger the secretion of a plethora of angiocrine prototypical signals [15,52] (Table 1). Type H capillaries also act as guides, supporting OSX^+ osteoprogenitors bound to them and driving their migration to sites of bone formation, a process known as angiotropism [22,42]. This is better defined as the propensity of cells to have an affinity for and move towards and along blood vessels, a process that was first described in the 1980s in lymphoma migration [53]. EC-mediated osteoblast angiotropism on the outside of the vessel lumen has been identified more recently [22]. However, the fundamentals of this process and its molecular mechanisms have yet to be fully characterised. During osteoblast angiotropism, OSX^+ cells behave like pericytes, extending their cellular processes and wrapping themselves around the invading blood vessels to facilitate migration towards the bone metaphysis, where they proceed to form trabecular bone [12,22] (Figure 2).

Table 1. Pro-angiogenic factors expressed by type H EC within the developing and growing bone [15]. A brief overview of their known function is given.

Protein	Role
NOTCH4 SEMA6	Angiogenesis-regulators of stalk/tip cell phenotype balance
FLT1 FLT4	Angiogenesis-VEGF receptors
Roundabout family receptor 1 (ROBO1)	Angiogenesis-VEGF signaling mediator
Claudin5 (CLD5)	Vascular permeability-cell-motility and vascular permeability mediator EC tight junction protein

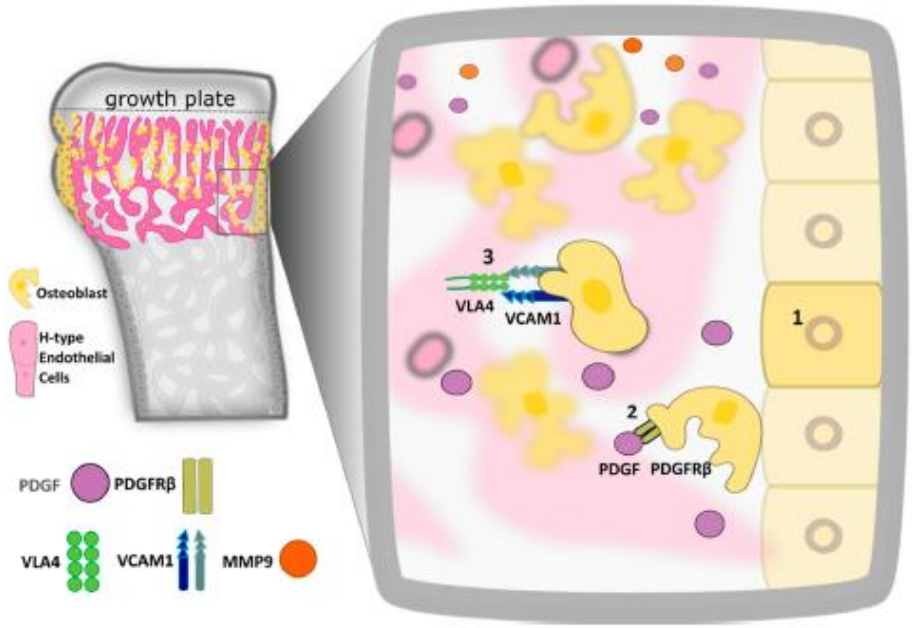


Figure 2. Cellular and molecular factors regulating osteoblast-EC angiotropism during bone growth and repair. Diagram illustrates the three main stages of osteoblast angiotropism. (1) MSC to osteoprogenitor differentiation occurs in response to local cues from the bone niche. Factors include oxygen and nutrient availability as well as HIF-1α and WNT/β Catenin signaling. Note the different morphology of osteoprogenitors not associated to vessels and their localization in the endosteum and periosteum. (2) Expansion of the Osx+ osteoprogenitor pool via proliferation under the influence of PDGF-PDGFRβ signaling, which favors maintenance of a pro-migratory immature osteoblast phenotype. (3) Osteoblast migration to sites of bone formation and repair alongside expanding H-type capillaries. PDGF acts as a chemoattractant to PDGFRβ$^+$ osteoprogenitors in the near vicinity. Subsequent to PDGF-PDGFRβ signaling, MMP-9 is also secreted by osteoblasts to aid in degradation of the surrounding matrix. MMP-9 expression is particularly increased at the vascular front during active angiogenesis. Cell-to-cell contact is required to facilitate osteoblast adhesion to EC. For example, VLA4-VCAM-1 interaction facilitates osteoblast angiotropism by enabling anchorage of the osteoblast cell membrane to H-type vessels.

Osteoblast angiotropism is regulated by interactions with ECs, which are restricted to types H and E vessels in the metaphysis, the H- and E- type EC specific interaction with OSX$^+$ cells was demonstrated with the aid of EC-Osteoblast co-cultures [10,15]. In vitro co-culture of H or E type ECs with MSCs demonstrated that either EC type induced morphological changes in 3D spheroids. Specifically, MSCs underwent osteo-lineage commitment in the presence of ECs, as confirmed by increased expression of RUNX2, Osteocalcin, and Alkaline Phosphatase (ALPL). Over time, osteoblasts also migrated to the edges of the spheroid, whereas EC condensations formed in the center [15]. While this demonstrates the importance of cell-to-cell contact for osteoblast angiotropism, previous work by Clarkin and colleagues indicated that it is not required for osteoblast differentiation by EC, thus beautifully showcasing the importance of EC-secreted factors in driving osteoblast differentiation [54]. In these experiments, non-contact co-culture of human umbilical vein endothelial cells (HUVEC) and human osteoblasts also resulted in increased osteoblast differentiation and a sustained rise in secretion of ALPL from osteoblasts [54].

The blood flow in types H and E capillaries, characterised by high shear rates, is probably another key factor promoting osteoblast angiotropism. Migratory osteoblasts exhibit a preference for higher shear stress, which positively correlates with regulation of flow directionality [55]. Modelling of low blood pressure through pharmaceutical interventions or artery ligation, which is de facto accompanied by low shear rates and stress, results in decreased density of OSX^+ cells in the metaphysis and a loss of bone formation capacity as measured by micro-computed trabecular bone parameters [11]. From an anatomical perspective, the reported higher shear rates linked to high blood velocity in types H and E vessels (compared to sinusoidal type L capillaries in the diaphysis) can be explained by their direct connection to arteries and arterioles, which also grants them a highly oxygenated status [11]. Elevated oxygen concentrations (compared to type L capillaries) allow them to meet the greater energy demands of bone formation in the metaphyseal region, which is the site of trabecular bone formation. This is in accordance with the high turnover rate of trabecular bone, making this area more metabolically active than the bone cortex [56].

A seminal study by Langen and colleagues identified that changes in the expression of EC adhesion molecules, such as the ones described by the EC-specific genetic deletion of Integrin β-1 (ITGB1), can also affect osteoblast differentiation and, potentially, angiotropism [15]. ITGB1 is a multifaceted integrin that is the component of various integrin complexes including Very Late Antigen 4 (VLA4), a protein with an ascribed role in cell adhesion [57]. EC-specific genetic deletion of ITGB1 leads to transformation of type H vasculature morphology, function, and metabolism. Namely, type H vessel columns are shorter, more branched, and lose their specific parallel organization. This is accompanied by a sustained reduction in proliferation and a decrease in the non-hypoxic area characteristic of the metaphysis where type H vessels reside. Changes in the metabolic function of these ITGB1-deficient ECs are also driven by a decrease in the activity of the phosphorylated mitogen activated protein kinase ERK (phospho-ERK1/2) [15]. These type H vessel changes coincide with defective bone formation, as exemplified by shorter bones with reduced trabecular bone parameters. Perturbed bone formation in this instance is characterised by improper osteoblast differentiation and maturation, with mutant mice displaying increased density of RUNX2-positive cells and decreased OSX^+ cell abundance as well as a diminished deposition of proteins secreted by mature osteoblasts or osteocytes (Collagen type I and Osteocalcin). Additionally, considering the reported bone shortening alongside contraction of the type H capillary columnar front in ITGB1 knockout mice, abnormal osteoblast angiotropism is strongly suspected [15]. The same study reported similar but milder observations following genetic deletion of genes coding for the extracellular matrix (ECM) proteins, LAMA5 and Osteopontin, suggesting that ECM proteins are key drivers of osteoblast maturation and vascular angiogenesis, an area that warrants further investigation.

In a reversal of roles, osteoblasts, osteoclasts, and hypertrophic chondrocytes also secrete proangiogenic factors to support angiogenic processes [10,45,46]. For instance, VEGF is not only secreted by ECs as an autocrine signal, it is also released from osteoblasts [58]. This process is triggered by Fibroblast Growth Factors, hormones, HIF-1α, and other signals secreted in the bone niche that induce secretion of lipid-signalling mediators such as Prostaglandins (e.g., PGE2 and PGI2) from ECs, which prompt VEGF secretion from osteoblasts [54,59,60].

The bidirectional nature of the EC–osteoblast relationship is further evidenced by research by Xu and colleagues, who showed that in addition to VEGF, osteoblasts secrete other proangiogenic factors that regulate and increase type H vessel density [61]. In particular, they identified osteoblast-derived SLIT3, which interacts with VEGF signalling mediator, ROBO1, expressed on ECs, to positively regulate both endothelium expansion and bone formation. The potent role of SLIT3 was evidenced during bone growth, where genetic deletion of SLIT3 in osteoblasts results in a decrease in cortical thickness and a reduction in trabecular bone volume.

4. Osteoblast Differentiation and Angiotropism Control Bone Healing in Mature Tissues

Mature bone is continually undergoing renewal and micro-damage repair [62,63]. This dynamic property of bone is attained through remodelling, whereby bone is resorbed then new bone matrix is deposited accordingly, to maintain and meet ever-changing physiological demands throughout an individual's lifetime. This process requires coordination and appropriate balance between the rates of resorption and formation, which have been reviewed extensively [64,65]. Activation is the first distinct phase of bone remodelling, where a Bone-Modelling Unit (BMU) forms at the site to be remodelled and consists of precursor and differentiated bone cells, connective tissue, and blood vessels [62,63].

In the case of injury or trauma adequate local vascularization of the assembled BMU, is vital for successful repair and regeneration of damaged bone. ECs aid in the recruitment and differentiation of osteoblast progenitors through similar, if not identical, mechanisms as during embryogenesis [22]. Fracture healing is characterised initially by formation of a fibrin clot, which is highly vascularised and rich in VEGF. It is believed that this consistently high concentration of VEGF, initially produced by fibrin clot platelets and thrombocytes, and later secreted by osteoblast lineage cells via HIF-1α activity, aids in differentiation of osteoblasts and initial angiogenesis and osteogenesis [66–68]. Successful remodelling of the initial fibrin clot into bone tissue recapitulates many of the processes seen during endochondral ossification [69]. Therefore, fracture and osteotomy studies are used to study both healing and regenerative processes [70–72].

Long bone remodelling and repair relies on activity of OSX^+ osteoprogenitors originating from a pool of skeletal stem progenitor cells spread across different locations in the long bone including the periosteum [22,73] and the bone marrow [74,75]. Osteoprogenitors, which are additionally marked by expression of Cathepsin K (CTSK) [73], are located to the periosteum, whereas Leptin receptor (LEPR) and C-X-C motif chemokine ligand 12 (CXCL12) double positive cells reside in the bone marrow [74,76]. Following bone injury, these skeletal stem progenitor cells give rise to OSX^+ osteoprogenitors, which undergo a period of intense proliferation [77], followed by migration to newly forming bone areas by association with vessels [22]. Recent studies provide evidence that geographical location within the bone can modulate lineage commitment potential, most likely due to the direct influence of signalling of cells in the near vicinity [22,74,76]. $CXCL12^+$ $LEPR^+$ progenitors are localised in close proximity to L capillaries or arterioles in the bone marrow and contribute to osteoblast and osteocyte generation following bone injury, dependent on WNT-β Catenin signalling [76]. All these osteoprogenitors have been only shown to regenerate cortical bone [73,76]. However, the fracture models employed failed to address their potential to regenerate trabecular bone, a phenomenon that remains to be elucidated. It also remains unclear how differentiation and maturation of osteoprogenitors is regulated by EC-derived signals. While the transcriptomic signature of osteo-lineage cells is becoming more clearly delineated, there is still little insight into the metabolic activity of MSCs whilst undergoing differentiation into osteoprogenitors during fracture healing and regulation of these processes by ECs.

One of the other mainstay processes for fracture healing is vessel invasion into the fracture callus. Newly formed capillaries enable a sufficient supply of adequate nutrition, oxygen, and systemic factors and facilitate the recruitment of osteoclast and osteoblast progenitor cells to sites of bone repair [42,78]. The importance of vascularization of the fracture callus for successful bone healing has been known for over 3 decades [79] and has been well described previously [58,80] and recently [26,42]. Failure of clot formation, or its inadequate vascularization, is a hallmark of fracture non-union, where fractures fail to heal adequately [81]. Inhibition of angiogenesis via physical barriers, or by blocking VEGF signalling, are widely used experimental techniques to probe the importance of vascularization for bone formation during fracture healing. Angiogenesis blockade results in a sustained decrease of osteoblast and osteoclast migration towards sites of bone formation [82–85] and, in line with this, Van Gastel and colleagues utilised an in vivo periosteal

bone healing model, employing polycarbonate filters, to inhibit revascularization of a periosteal callus implanted in a femur fracture [42]. This resulted in a reduction in the overall cell numbers populating the bone callus area, alongside a decrease in cell proliferation, and an increase in cell death, similarly to results presented in previously published work [82–85].

To further expand our understanding of the role of vascularization in osteo-lineage commitment of skeletal progenitors, Van Gastel et al. reported that reduced vascularization of the callus was characterised by an expansion of cells expressing the chondrocyte commitment master regulator, SOX9, indicating a preferential chondrocyte lineage commitment at the expense of osteo-lineage differentiation [42]. The observed changes could be explained by the importance of lipid availability for MSC to osteoblast differentiation considering that lipid scarcity results in chondrocyte commitment [42]. Delving into this further, the role of angiogenesis progression for the composition of the periosteal callus proximal to the fracture site was predicted using computational modelling and then tested in vivo and demonstrated the importance of vascularization for reduction of the hypoxic environment [36]. An increase in callus vascularization led to changes in MSC fate, promoting osteoblast lineage commitment to the detriment of differentiation into chondrocytes, resulting in a faster rate of healing [36].

Osteoblasts regulate expansion of the endothelial vessel front as well as their own invasiveness via release of the extracellular matrix degradation protease, Matrix Metallo-Proteinase 9 (MMP-9) [4,26]. Increased MMP-9 production by skeletal stem and progenitor cells is a downstream response to (Platelet Derived Growth Factor and Platelet Derived Growth Factor Receptor β) PDGF-PDGFRβ signalling [26]. Using distinct profiles as a guide to osteoblast differentiation stages has allowed dissection of the paracrine signalling of OSX^+ immature versus Collagen I-secreting mature osteoblasts at the molecular level. OSX^+ osteoprogenitors produce a plethora of angiogenic and proliferative factors when compared against whole long bone or calvaria digestion without enrichment for OSX expression. Specifically, qPCR analysis of the OSX^+ cell transcriptome showed increased expression of VEGF, Angiopoietin-1, and PDGF receptor β mRNA [22,86]. The well-characterised cellular migration and invasiveness regulator, SLIT3 is a newly identified factor which has been shown to also expand the endothelial footprint in the bone [87,88]. SLIT3 is another osteoblast-derived protein that mediates bone healing by directly acting on ECs to drive callus vascularization. This was confirmed following local administration of recombinant SLIT3 in a model of open femoral midshaft fracture healing. Treatment with SLIT3 resulted in thicker cortical bones, a rise in trabecular bone volume and stiffer bones with a higher load-bearing capacity [61].

The expression of the aforementioned angiogenic factors is a clear indication of cross talk occurring between ECs and osteoblasts and provides evidence of their bidirectional communication and of a mechanism by which vessel and osteoprogenitor invasion is coupled [22,86]. Angiogenesis and osteogenesis coupling plays a key role in bone healing. However, identification of the precise vessel type invading the callus and its spatio-temporal and molecular regulation remains elusive, even if H-type vessels are strongly suspected to be the blood vessel type regulating bone healing, this is yet to be tested experimentally. Van Gastel et al. have nonetheless shown that bone repair is reliant on blood vessel expansion into the fractured zone [42]. Evidence has mounted of the importance of the vasculature in regulating mature bone remodelling whereby newly forming capillaries influence osteoprogenitor cell fate by supporting their angiotropism to sites of bone remodelling and repair [22,26] (Figure 2). EC-secreted PDGFB binds PDGFR-β expressed on migrating osteoblasts, maintaining them in an immature state and upregulating their intensely proliferative status. PDGF downstream signalling also leads to expression of cell adhesion molecule VCAM1 by osteoblasts to presumably facilitate their migration on EC via interaction with Integrin β1 Integrin α 4 dimer VLA4 [26].

During the maturation process osteoblasts lose their attachment to ECs, as shown by Maes et al. [22], further indicating that cell-to-cell contact between ECs and osteoprogen-

XL

itors regulates maintenance of osteoblasts in an immature and highly proliferative state, favorable to angiotropism [46]. Mature osteoblasts adhere to the cartilage and work as functional units, via a series of tight, gap, and adherens' junctions, to produce and lay down the new osteoid, a protein-rich bone matrix [22,26]. The newly deposited osteoid is then mineralised through nucleation of hydroxyapatite to collagen fibrils, which are initially regulated by the non-collagenous proteins, such as Osteocalcin and Bone Sialoprotein, found within this immature bone matrix [89]

5. The Extent of Osteocyte-Endothelial Cell Cross Talk Remains an Important, and Outstanding, Area for Research

The importance of the cross talk between osteoblast lineage cells and ECs implies that such a relationship will continue as osteoblasts further differentiate into the most numerous bone cell type at skeletal maturity, osteocytes. Given the vital roles osteocytes play in preserving optimal bone health, investigating whether such an association exists, and how it may or may not contribute to the repair and maintenance of mature bone, is entirely justified.

Following osteoid deposition, around 10–30% of the osteoblast population differentiates into osteocytes [90,91]. Osteocytes are long-lived, terminally differentiated osteoblasts and estimates calculate that the average osteocyte lifespan is in excess of 10 years. Osteocytes use their highly dendritic morphology to create a vast, interconnected cytoplasmic network throughout the bone, via gap junctions at dendritic contact points. This enables communication between osteocytes within the network, as well as with other bone cells, blood vessels, and the inner and outer surfaces of bone, through chemical and mechanical signalling transduction [92]. It has been shown that physical connections are present between osteocyte dendritic processes and blood vessels, where the dendrites are oriented in the direction of the blood supply [93,94]. The highly extensive cytoplasmic lacunocanalicular network enables inter- and extra-cellular communication through chemical and mechanotransduction signalling. Thus, this physical connection suggests that the relationship between osteocytes and ECs has a communicative function.

Investigations have found that the cross talk between osteocytes and ECs has roles in regulating angiogenesis. Culturing of HUVECs in osteocyte-conditioned media results in an increase in expression of genes with a proliferative phenotype, including PDGFR and MMP-9, which is closely followed by an increase in HUVEC proliferation, migration, and formation of capillary-like vessels [94]. In addition, the same study indicates that osteocyte-expressed VEGF induces MAPK–ERK phosphorylation in HUVECs, a signalling pathway required to promote EC proliferation in the earlier stages of angiogenesis [94].

Additional work also identifies an important role in regulation of angiogenesis and bone repair for apoptotic osteocytes. When bone experiences trauma, osteoclast progenitor cells are activated by the apoptotic bodies of newly exposed apoptotic osteocytes through stimulation with Tumor Necrosis Factor- α (TNF-α), a known driver of osteoclastogenesis, independent of Receptor Activator of Nuclear factor Kappa-β (RANK)-Receptor Activator of Nuclear factor Kappa-β Ligand (RANKL) activity [95] In addition, apoptotic osteocytes also aid in the delivery and recruitment of osteoclast progenitors by regulating angiogenesis at the damaged site and adhesion of circulating osteoclast progenitors to the vascular endothelium [96]. There is an upregulation of VEGF production by apoptotic osteocytes, which encourages EC proliferation and tubule formation, as well as branching at the site of damage [97,98]. Furthermore, there is an increased expression of Interleukin-6 (IL-6) and soluble Interleukin-6 Receptor (sIL-6R) by apoptotic osteocytes and TNF-α by osteoclast progenitors. This precedes endothelial ICAM-1 expression [95,99]. As a result, IL-6, sIL-6R, and TNF-α increase the adhesion of circulating osteoclast progenitors to the vascular endothelium via ICAM-1 [100], which promotes localised recruitment and activation of these progenitor cells to osteoclasts [101]. However, excessive osteocyte apoptosis can result in abnormal angiogenesis, which is implicated in imbalanced bone remodelling, resulting in deleterious bone conditions such as osteoporosis. Recently, it has been discovered that osteocyte apoptosis also occurs in response to the accumulation of

Advanced Glycation End products (AGEs) [102]. AGEs result from proteins and lipids that have been non-enzymatically modified and their accumulation is a common occurrence in metabolic conditions, such as type II diabetes, which also comes hand in hand with higher bone fracture risks [103,104]. Chen et al. described a mechanism whereby incubation of the osteocytic cell line, MLO-Y4, with AGEs induced osteocyte apoptosis and, at the same time, upregulated the expression of proangiogenic factors, IL-6 and VEGF-A [102]. It can be assumed that, in vivo, a subsequent angiogenic effect would occur and result in significant inflammation and increased osteoclast activation. Increased osteoclast activation then further implies increased bone resorption and bone destruction, thus accounting for the higher incidence of fractures, osteopenia, and osteoporosis that occur in type II diabetic patients which readily accumulate AGEs [105]. Growing evidence is enabling the recognition that there is a strong correlation between AGE accumulation and increased bone fragility [106–108]. However, the exact mechanism for this has not been conclusively established and requires further investigation.

Sclerostin (SOST), a glycoprotein primarily expressed by osteocytes, is an inhibitor of bone formation and was more recently discovered to also regulate angiogenesis. It was previously found that its expression increases EC migration [109], leading to the discovery that sclerostin can promote angiogenesis by increasing production of proangiogenic factors, VEGF and Placental Growth Factor (PLGF) [96]. Furthermore, the same publication also found SOST can also directly induce angiogenic effects by binding to its receptor, low-density lipoprotein receptor-related protein 6, expressed on HUVECs in response to SOST exposure and subsequently antagonising WNT signalling [96].

A common theme among the studies investigating osteocyte-EC cross talk identifies the need for an appropriate model in which to study primary osteocytes, rather than a cell line, to validate initial findings. The location of osteocytes within bone has posed the main barrier to enabling further investigation of their physiological roles. Furthermore, removal of osteocytes from the bone and into culture causes them to rapidly dedifferentiate back into an osteoblast- or fibroblast-like phenotype, making them extremely challenging to study in vitro [110]. Several cell lines have been produced to study the osteocyte at different differentiation stages, with MLO-Y4 being the most commonly used as it represents a mature stage osteocyte. However, their low expression of SOST, in comparison to physiological levels, and the requirement of exogenous chemicals, such as Thiazolidinediones, makes them an imperfect cell line for in vitro modelling [111,112]. Indeed, the study of any cells cultured as a 2D monolayer is unlikely to ever adequately reflect the environment found in vivo, and this is particularly true of osteocytes whose extracellular environment is so intrinsically linked to their cell activity and behavior. The comparison of 2D and 3D cell culture has been recently reviewed [113], concluding that the advantages intrinsic to 3D models will inevitably change the way in which research and discovery is conducted. Over the last 5 years, a number of long-term osteocyte culture methods have been developed [114,115], which could begin to enable the dissection of some of these unanswered research questions and hypotheses, including elucidating the details of the signalling relationship between osteocytes and ECs. This further investigation may yet reveal further vital roles played by osteocytes and bridge the gaps in our knowledge of the link between angiogenesis and osteogenesis during bone development, growth, repair, and maintenance, with implications for treatment or prevention of detrimental bone conditions.

6. Conclusions

Endothelial cells and osteoblasts engage in a continuous and complex courtship ritual from embryogenesis, throughout postnatal life and in aging. Blood vessels are integral and crucial to the differentiation of osteoblasts by influencing MSC differentiation into various osteoprogenitor subtypes, reflecting the different bone tissues and their local niche environments. During bone growth and bone maintenance throughout maturity, endothelial cells act as companions to osteoblasts, guiding them to sites where osteogenesis is necessary, providing them with proliferation signals and supporting their angiotropism

by expressing molecules that directly interact with the osteoblasts to keep them bound to EC and supplying glucose and fatty acids for their metabolic needs. In aging, the remarkable decline in vessel density characteristic of age-associated alterations [116] is also marked by a sustained change in type H capillary morphology and, presumably, function, this is swiftly accompanied by a significant decrease in the number of osteoblasts in the bone metaphysis [21]. This impairment in osteogenic potential can leave bones porous, brittle, and prone to fracture. However, the ever-increasing understanding of the cellular interactions that control these processes, combined with rapid improvements in in vivo/ex vivo and intravital imaging and in vitro 3D culture methods, will undoubtedly lead to the identification of novel signalling pathways controlling endothelial cell–osteolineage cell cross talk and ultimately new treatment methods for bone diseases.

Author Contributions: Conceptualization, G.N.; writing—original draft preparation, G.N., M.F. and A.J.N.; writing—review and editing G.N., M.F. and A.J.N. All authors have read and agreed to the published version of the manuscript.

Funding: A.J.N. is funded by a Career Development Fellowship from Versus Arthritis #21743. G.N. is supported by a PhD stipend from the Centre for Musculoskeletal and Ageing Research (CMAR), funded by the Medical Research Charity and Versus Arthritis. M.F. is supported by a PhD stipend from the National Centre for the Replacement, Refinement and Reduction of Animals in Research.

Institutional Review Board Statement: Not applicable.

Informed Consent Statement: Not applicable.

Conflicts of Interest: The authors declare no conflict of interest.

References

1. Clarke, B. Normal bone anatomy and physiology. *Clin. J. Am. Soc. Nephrol.* **2008**, *3* (Suppl. S3), S131–S139. [CrossRef]
2. Kelly, N.H.; Schimenti, J.C.; Ross, F.P.; van der Meulen, M.C. Transcriptional profiling of cortical versus cancellous bone from mechanically-loaded murine tibiae reveals differential gene expression. *Bone* **2016**, *86*, 22–29. [CrossRef]
3. Seeman, E.; Delmas, P.D. Bone quality–the material and structural basis of bone strength and fragility. *N. Engl. J. Med.* **2006**, *354*, 2250–2261. [CrossRef]
4. Romeo, S.G.; Alawi, K.M.; Rodrigues, J.; Singh, A.; Kusumbe, A.P.; Ramasamy, S.K. Endothelial proteolytic activity and interaction with non-resorbing osteoclasts mediate bone elongation. *Nat. Cell Biol.* **2019**, *21*, 430–441. [CrossRef] [PubMed]
5. Li, Z.; Kong, K.; Qi, W. Osteoclast and its roles in calcium metabolism and bone development and remodeling. *Biochem. Biophys. Res. Commun.* **2006**, *343*, 345–350. [CrossRef]
6. Rauch, A.; Mandrup, S. Transcriptional networks controlling stromal cell differentiation. *Nat. Rev. Mol. Cell Biol.* **2021**, *22*, 465–482. [CrossRef]
7. Wolock, S.L.; Krishnan, I.; Tenen, D.E.; Matkins, V.; Camacho, V.; Patel, S.; Agarwal, P.; Bhatia, R.; Tenen, D.G.; Klein, A.M.; et al. Mapping Distinct Bone Marrow Niche Populations and Their Differentiation Paths. *Cell Rep.* **2019**, *28*, 302–311.e305. [CrossRef] [PubMed]
8. dela Paz, N.G.; D'Amore, P.A. Arterial versus venous endothelial cells. *Cell Tissue Res.* **2009**, *335*, 5–16. [CrossRef] [PubMed]
9. Ramasamy, S.K.; Kusumbe, A.P.; Itkin, T.; Gur-Cohen, S.; Lapidot, T.; Adams, R.H. Regulation of Hematopoiesis and Osteogenesis by Blood Vessel-Derived Signals. *Annu. Rev. Cell Dev. Biol.* **2016**, *32*, 649–675. [CrossRef] [PubMed]
10. Kusumbe, A.P.; Ramasamy, S.K.; Adams, R.H. Coupling of angiogenesis and osteogenesis by a specific vessel subtype in bone. *Nature* **2014**, *507*, 323–328. [CrossRef] [PubMed]
11. Ramasamy, S.K.; Kusumbe, A.P.; Schiller, M.; Zeuschner, D.; Bixel, M.G.; Milia, C.; Gamrekelashvili, J.; Limbourg, A.; Medvinsky, A.; Santoro, M.M.; et al. Blood flow controls bone vascular function and osteogenesis. *Nat. Commun.* **2016**, *7*, 13601. [CrossRef] [PubMed]
12. Ramasamy, S.K.; Kusumbe, A.P.; Wang, L.; Adams, R.H. Endothelial Notch activity promotes angiogenesis and osteogenesis in bone. *Nature* **2014**, *507*, 376–380. [CrossRef] [PubMed]
13. Xu, C.; Liu, H.; He, Y.; Li, Y.; He, X. Endothelial progenitor cells promote osteogenic differentiation in co-cultured with mesenchymal stem cells via the MAPK-dependent pathway. *Stem Cell Res. Ther.* **2020**, *11*, 537. [CrossRef]
14. Stegen, S.; Carmeliet, G. The skeletal vascular system—Breathing life into bone tissue. *Bone* **2018**, *115*, 50–58. [CrossRef] [PubMed]
15. Langen, U.H.; Pitulescu, M.E.; Kim, J.M.; Enriquez-Gasca, R.; Sivaraj, K.K.; Kusumbe, A.P.; Singh, A.; Di Russo, J.; Bixel, M.G.; Zhou, B.; et al. Cell-matrix signals specify bone endothelial cells during developmental osteogenesis. *Nat. Cell Biol.* **2017**, *19*, 189–201. [CrossRef]
16. Itkin, T.; Gur-Cohen, S.; Spencer, J.A.; Schajnovitz, A.; Ramasamy, S.K.; Kusumbe, A.P.; Ledergor, G.; Jung, Y.; Milo, I.; Poulos, M.G.; et al. Distinct bone marrow blood vessels differentially regulate haematopoiesis. *Nature* **2016**, *532*, 323–328. [CrossRef]

17. Wang, L.; Zhou, F.; Zhang, P.; Wang, H.; Qu, Z.; Jia, P.; Yao, Z.; Shen, G.; Li, G.; Zhao, G.; et al. Human type H vessels are a sensitive biomarker of bone mass. *Cell Death Dis.* **2017**, *8*, e2760. [CrossRef]
18. Kuhn, A.; Brachtendorf, G.; Kurth, F.; Sonntag, M.; Samulowitz, U.; Metze, D.; Vestweber, D. Expression of endomucin, a novel endothelial sialomucin, in normal and diseased human skin. *J. Investig. Dermatol.* **2002**, *119*, 1388–1393. [CrossRef] [PubMed]
19. Newman, P.J.; Albelda, S.M. Cellular and molecular aspects of PECAM-1. *Nouv. Rev. Fr. Hematol.* **1992**, *34*, S9–S13.
20. Yan, Z.Q.; Wang, X.K.; Zhou, Y.; Wang, Z.G.; Wang, Z.X.; Jin, L.; Yin, H.; Xia, K.; Tan, Y.J.; Feng, S.K.; et al. H-type blood vessels participate in alveolar bone remodeling during murine tooth extraction healing. *Oral Dis.* **2020**, *26*, 998–1009. [CrossRef]
21. Kusumbe, A.P.; Ramasamy, S.K.; Itkin, T.; Mäe, M.A.; Langen, U.H.; Betsholtz, C.; Lapidot, T.; Adams, R.H. Age-dependent modulation of vascular niches for haematopoietic stem cells. *Nature* **2016**, *532*, 380–384. [CrossRef] [PubMed]
22. Maes, C.; Kobayashi, T.; Selig, M.K.; Torrekens, S.; Roth, S.I.; Mackem, S.; Carmeliet, G.; Kronenberg, H.M. Osteoblast precursors, but not mature osteoblasts, move into developing and fractured bones along with invading blood vessels. *Dev. Cell* **2010**, *19*, 329–344. [CrossRef] [PubMed]
23. Xu, X.; Wang, F.; Yang, Y.; Zhou, X.; Cheng, Y.; Wei, X.; Li, M. LIPUS promotes spinal fusion coupling proliferation of type H microvessels in bone. *Sci. Rep.* **2016**, *6*, 20116. [CrossRef]
24. Yang, M.; Li, C.J.; Xiao, Y.; Guo, Q.; Huang, Y.; Su, T.; Luo, X.H.; Jiang, T.J. Ophiopogonin D promotes bone regeneration by stimulating CD31(hi) EMCN(hi) vessel formation. *Cell Prolif.* **2020**, *53*, e12784. [CrossRef]
25. Zhu, Y.; Ruan, Z.; Lin, Z.; Long, H.; Zhao, R.; Sun, B.; Cheng, L.; Tang, L.; Xia, Z.; Li, C.; et al. The association between CD31(hi)Emcn(hi) endothelial cells and bone mineral density in Chinese women. *J. Bone Miner. Metab.* **2019**, *37*, 987–995. [CrossRef]
26. Böhm, A.M.; Dirckx, N.; Tower, R.J.; Peredo, N.; Vanuytven, S.; Theunis, K.; Nefyodova, E.; Cardoen, R.; Lindner, V.; Voet, T.; et al. Activation of Skeletal Stem and Progenitor Cells for Bone Regeneration Is Driven by PDGFRβ Signaling. *Dev. Cell* **2019**, *51*, 236–254.e212. [CrossRef]
27. Grüneboom, A.; Hawwari, I.; Weidner, D.; Culemann, S.; Müller, S.; Henneberg, S.; Brenzel, A.; Merz, S.; Bornemann, L.; Zec, K.; et al. A network of trans-cortical capillaries as mainstay for blood circulation in long bones. *Nat. Metab.* **2019**, *1*, 236–250. [CrossRef] [PubMed]
28. Grüneboom, A.; Kling, L.; Christiansen, S.; Mill, L.; Maier, A.; Engelke, K.; Quick, H.H.; Schett, G.; Gunzer, M. Next-generation imaging of the skeletal system and its blood supply. *Nat. Rev. Rheumatol.* **2019**, *15*, 533–549. [CrossRef] [PubMed]
29. Berendsen, A.D.; Olsen, B.R. Bone development. *Bone* **2015**, *80*, 14–18. [CrossRef]
30. Mackie, E.J.; Ahmed, Y.A.; Tatarczuch, L.; Chen, K.S.; Mirams, M. Endochondral ossification: How cartilage is converted into bone in the developing skeleton. *Int. J. Biochem. Cell Biol.* **2008**, *40*, 46–62. [CrossRef]
31. Mackie, E.J.; Tatarczuch, L.; Mirams, M. The skeleton: A multi-functional complex organ: The growth plate chondrocyte and endochondral ossification. *J. Endocrinol.* **2011**, *211*, 109–121. [CrossRef]
32. Long, F.; Ornitz, D.M. Development of the endochondral skeleton. *Cold Spring Harb. Perspect. Biol.* **2013**, *5*, a008334. [CrossRef]
33. Jensen, E.D.; Gopalakrishnan, R.; Westendorf, J.J. Regulation of gene expression in osteoblasts. *Biofactors* **2010**, *36*, 25–32. [CrossRef]
34. Rutkovskiy, A.; Stensløkken, K.O.; Vaage, I.J. Osteoblast Differentiation at a Glance. *Med. Sci. Monit. Basic Res.* **2016**, *22*, 95–106. [CrossRef] [PubMed]
35. Jonitz, A.; Lochner, K.; Lindner, T.; Hansmann, D.; Marrot, A.; Bader, R. Oxygen consumption, acidification and migration capacity of human primary osteoblasts within a three-dimensional tantalum scaffold. *J. Mater. Sci. Mater. Med.* **2011**, *22*, 2089–2095. [CrossRef]
36. Burke, D.; Dishowitz, M.; Sweetwyne, M.; Miedel, E.; Hankenson, K.D.; Kelly, D.J. The role of oxygen as a regulator of stem cell fate during fracture repair in TSP2-null mice. *J. Orthop. Res.* **2013**, *31*, 1585–1596. [CrossRef]
37. Hsu, S.H.; Chen, C.T.; Wei, Y.H. Inhibitory effects of hypoxia on metabolic switch and osteogenic differentiation of human mesenchymal stem cells. *Stem Cells* **2013**, *31*, 2779–2788. [CrossRef] [PubMed]
38. Feigenson, M.; Eliseev, R.A.; Jonason, J.H.; Mills, B.N.; O'Keefe, R.J. PGE2 Receptor Subtype 1 (EP1) Regulates Mesenchymal Stromal Cell Osteogenic Differentiation by Modulating Cellular Energy Metabolism. *J. Cell Biochem.* **2017**, *118*, 4383–4393. [CrossRef] [PubMed]
39. Chen, D.; Li, Y.; Zhou, Z.; Xing, Y.; Zhong, Y.; Zou, X.; Tian, W.; Zhang, C. Synergistic inhibition of Wnt pathway by HIF-1α and osteoblast-specific transcription factor osterix (Osx) in osteoblasts. *PLoS ONE* **2012**, *7*, e52948. [CrossRef]
40. Chen, D.; Li, Y.; Zhou, Z.; Wu, C.; Xing, Y.; Zou, X.; Tian, W.; Zhang, C. HIF-1α inhibits Wnt signaling pathway by activating Sost expression in osteoblasts. *PLoS ONE* **2013**, *8*, e65940. [CrossRef] [PubMed]
41. van Gastel, N.; Carmeliet, G. Metabolic regulation of skeletal cell fate and function in physiology and disease. *Nat. Metab.* **2021**, *3*, 11–20. [CrossRef]
42. van Gastel, N.; Stegen, S.; Eelen, G.; Schoors, S.; Carlier, A.; Daniëls, V.W.; Baryawno, N.; Przybylski, D.; Depypere, M.; Stiers, P.J.; et al. Lipid availability determines fate of skeletal progenitor cells via SOX9. *Nature* **2020**, *579*, 111–117. [CrossRef] [PubMed]
43. Pahwa, H.; Khan, M.T.; Sharan, K. Hyperglycemia impairs osteoblast cell migration and chemotaxis due to a decrease in mitochondrial biogenesis. *Mol. Cell Biochem.* **2020**, *469*, 109–118. [CrossRef] [PubMed]
44. Sivaraj, K.K.; Adams, R.H. Blood vessel formation and function in bone. *Development* **2016**, *143*, 2706–2715. [CrossRef]

45. Maes, C.; Carmeliet, P.; Moermans, K.; Stockmans, I.; Smets, N.; Collen, D.; Bouillon, R.; Carmeliet, G. Impaired angiogenesis and endochondral bone formation in mice lacking the vascular endothelial growth factor isoforms VEGF164 and VEGF188. *Mech. Dev.* **2002**, *111*, 61–73. [CrossRef]
46. Maes, C.; Goossens, S.; Bartunkova, S.; Drogat, B.; Coenegrachts, L.; Stockmans, I.; Moermans, K.; Nyabi, O.; Haigh, K.; Naessens, M.; et al. Increased skeletal VEGF enhances beta-catenin activity and results in excessively ossified bones. *EMBO J.* **2010**, *29*, 424–441. [CrossRef]
47. Gerber, H.P.; Ferrara, N. Angiogenesis and bone growth. *Trends Cardiovasc. Med.* **2000**, *10*, 223–228. [CrossRef]
48. Fruttiger, M. Development of the mouse retinal vasculature: Angiogenesis versus vasculogenesis. *Investig. Ophthalmol. Vis. Sci.* **2002**, *43*, 522–527.
49. Carmeliet, P. Angiogenesis in health and disease. *Nat. Med.* **2003**, *9*, 653–660. [CrossRef] [PubMed]
50. Ahmed, Z.; Bicknell, R. Angiogenic signalling pathways. *Methods Mol. Biol.* **2009**, *467*, 3–24. [CrossRef] [PubMed]
51. Herbert, S.P.; Stainier, D.Y. Molecular control of endothelial cell behaviour during blood vessel morphogenesis. *Nat. Rev. Mol. Cell Biol* **2011**, *12*, 551–564. [CrossRef]
52. Sivan, U.; De Angelis, J.; Kusumbe, A.P. Role of angiocrine signals in bone development, homeostasis and disease. *Open Biol.* **2019**, *9*, 190144. [CrossRef]
53. Wrotnowski, U.; Mills, S.E.; Cooper, P.H. Malignant angioendotheliomatosis. An angiotropic lymphoma? *Am. J. Clin. Pathol.* **1985**, *83*, 244–248. [CrossRef] [PubMed]
54. Clarkin, C.E.; Emery, R.J.; Pitsillides, A.A.; Wheeler-Jones, C.P. Evaluation of VEGF-mediated signaling in primary human cells reveals a paracrine action for VEGF in osteoblast-mediated crosstalk to endothelial cells. *J. Cell Physiol.* **2008**, *214*, 537–544. [CrossRef]
55. Riehl, B.D.; Lee, J.S.; Ha, L.; Kwon, I.K.; Lim, J.Y. Flowtaxis of osteoblast migration under fluid shear and the effect of RhoA kinase silencing. *PLoS ONE* **2017**, *12*, e0171857. [CrossRef] [PubMed]
56. Parfitt, A.M. Targeted and nontargeted bone remodeling: Relationship to basic multicellular unit origination and progression. *Bone* **2002**, *30*, 5–7. [CrossRef]
57. Liang, Y.; Diehn, M.; Bollen, A.W.; Israel, M.A.; Gupta, N. Type I collagen is overexpressed in medulloblastoma as a component of tumor microenvironment. *J. Neurooncol.* **2008**, *86*, 133–141. [CrossRef]
58. Wang, Y.; Wan, C.; Deng, L.; Liu, X.; Cao, X.; Gilbert, S.R.; Bouxsein, M.L.; Faugere, M.C.; Guldberg, R.E.; Gerstenfeld, L.C.; et al. The hypoxia-inducible factor alpha pathway couples angiogenesis to osteogenesis during skeletal development. *J. Clin. Investig.* **2007**, *117*, 1616–1626. [CrossRef] [PubMed]
59. Clarkin, C.E.; Garonna, E.; Pitsillides, A.A.; Wheeler-Jones, C.P. Heterotypic contact reveals a COX-2-mediated suppression of osteoblast differentiation by endothelial cells: A negative modulatory role for prostanoids in VEGF-mediated cell: Cell communication? *Exp. Cell Res.* **2008**, *314*, 3152–3161. [CrossRef] [PubMed]
60. Chen, D.; Tian, W.; Li, Y.; Tang, W.; Zhang, C. Osteoblast-specific transcription factor Osterix (Osx) and HIF-1α cooperatively regulate gene expression of vascular endothelial growth factor (VEGF). *Biochem. Biophys. Res. Commun.* **2012**, *424*, 176–181. [CrossRef] [PubMed]
61. Xu, R.; Yallowitz, A.; Qin, A.; Wu, Z.; Shin, D.Y.; Kim, J.M.; Debnath, S.; Ji, G.; Bostrom, M.P.; Yang, X.; et al. Targeting skeletal endothelium to ameliorate bone loss. *Nat. Med.* **2018**, *24*, 823–833. [CrossRef]
62. Bergmann, P.; Body, J.J.; Boonen, S.; Boutsen, Y.; Devogelaer, J.P.; Goemaere, S.; Kaufman, J.; Reginster, J.Y.; Rozenberg, S. Loading and skeletal development and maintenance. *J. Osteoporos.* **2010**, *2011*, 786752. [CrossRef]
63. Claes, L.; Recknagel, S.; Ignatius, A. Fracture healing under healthy and inflammatory conditions. *Nat. Rev. Rheumatol.* **2012**, *8*, 133–143. [CrossRef]
64. Kenkre, J.S.; Bassett, J. The bone remodelling cycle. *Ann. Clin. Biochem.* **2018**, *55*, 308–327. [CrossRef]
65. Siddiqui, J.A.; Partridge, N.C. Physiological Bone Remodeling: Systemic Regulation and Growth Factor Involvement. *Physiology* **2016**, *31*, 233–245. [CrossRef] [PubMed]
66. Hu, K.; Olsen, B.R. Osteoblast-derived VEGF regulates osteoblast differentiation and bone formation during bone repair. *J. Clin. Investig.* **2016**, *126*, 509–526. [CrossRef]
67. Popsuishapka, O.K.; Ashukina, N.O.; Litvishko, V.O.; Grigorjev, V.V.; Pidgaiska, O.O.; Popsuishapka, K.O. Fibrin-blood clot as an initial stage of formation of bone regeneration after a bone fracture. *Regul. Mech. Biosyst.* **2018**, *9*. [CrossRef]
68. Wan, C.; Gilbert, S.R.; Wang, Y.; Cao, X.; Shen, X.; Ramaswamy, G.; Jacobsen, K.A.; Alaql, Z.S.; Eberhardt, A.W.; Gerstenfeld, L.C.; et al. Activation of the hypoxia-inducible factor-1alpha pathway accelerates bone regeneration. *Proc. Natl. Acad. Sci. USA* **2008**, *105*, 686–691. [CrossRef]
69. Bujoli, B.; Scimeca, J.C.; Verron, E. Fibrin as a Multipurpose Physiological Platform for Bone Tissue Engineering and Targeted Delivery of Bioactive Compounds. *Pharmaceutics* **2019**, *11*, 556. [CrossRef]
70. Yuasa, M.; Mignemi, N.A.; Nyman, J.S.; Duvall, C.L.; Schwartz, H.S.; Okawa, A.; Yoshii, T.; Bhattacharjee, G.; Zhao, C.; Bible, J.E.; et al. Fibrinolysis is essential for fracture repair and prevention of heterotopic ossification. *J. Clin. Investig.* **2015**, *125*, 3117–3131. [CrossRef] [PubMed]
71. Damsaz, M.; Castagnoli, C.Z.; Eshghpour, M.; Alamdari, D.H.; Alamdari, A.H.; Noujeim, Z.E.F.; Haidar, Z.S. Evidence-Based Clinical Efficacy of Leukocyte and Platelet-Rich Fibrin in Maxillary Sinus Floor Lift, Graft and Surgical Augmentation Procedures. *Front. Surg.* **2020**, *7*, 537138. [CrossRef]

72. Franklin, S.P.; Burke, E.E.; Holmes, S.P. The effect of platelet-rich plasma on osseous healing in dogs undergoing high tibial osteotomy. *PLoS ONE* **2017**, *12*, e0177597. [CrossRef]
73. Debnath, S.; Yallowitz, A.R.; McCormick, J.; Lalani, S.; Zhang, T.; Xu, R.; Li, N.; Liu, Y.; Yang, Y.S.; Eiseman, M.; et al. Discovery of a periosteal stem cell mediating intramembranous bone formation. *Nature* **2018**, *562*, 133–139. [CrossRef] [PubMed]
74. Zhou, B.O.; Yue, R.; Murphy, M.M.; Peyer, J.G.; Morrison, S.J. Leptin-receptor-expressing mesenchymal stromal cells represent the main source of bone formed by adult bone marrow. *Cell Stem Cell* **2014**, *15*, 154–168. [CrossRef] [PubMed]
75. Sacchetti, B.; Funari, A.; Michienzi, S.; Di Cesare, S.; Piersanti, S.; Saggio, I.; Tagliafico, E.; Ferrari, S.; Robey, P.G.; Riminucci, M.; et al. Self-renewing osteoprogenitors in bone marrow sinusoids can organize a hematopoietic microenvironment. *Cell* **2007**, *131*, 324–336. [CrossRef] [PubMed]
76. Matsushita, Y.; Nagata, M.; Kozloff, K.M.; Welch, J.D.; Mizuhashi, K.; Tokavanich, N.; Hallett, S.A.; Link, D.C.; Nagasawa, T.; Ono, W.; et al. A Wnt-mediated transformation of the bone marrow stromal cell identity orchestrates skeletal regeneration. *Nat. Commun.* **2020**, *11*, 332. [CrossRef] [PubMed]
77. Maes, C.; Coenegrachts, L.; Stockmans, I.; Daci, E.; Luttun, A.; Petryk, A.; Gopalakrishnan, R.; Moermans, K.; Smets, N.; Verfaillie, C.M.; et al. Placental growth factor mediates mesenchymal cell development, cartilage turnover, and bone remodeling during fracture repair. *J. Clin. Investig.* **2006**, *116*, 1230–1242. [CrossRef]
78. Kristensen, H.B.; Andersen, T.L.; Marcussen, N.; Rolighed, L.; Delaisse, J.M. Increased presence of capillaries next to remodeling sites in adult human cancellous bone. *J. Bone Miner. Res.* **2013**, *28*, 574–585. [CrossRef]
79. Mann, F.A.; Payne, J.T. Bone healing. *Semin Vet. Med. Surg Small Anim* **1989**, *4*, 312–321.
80. Hausman, M.R.; Schaffler, M.B.; Majeska, R.J. Prevention of fracture healing in rats by an inhibitor of angiogenesis. *Bone* **2001**, *29*, 560–564. [CrossRef]
81. Tomlinson, R.E.; Silva, M.J. Skeletal Blood Flow in Bone Repair and Maintenance. *Bone Res.* **2013**, *1*, 311–322. [CrossRef]
82. Gerber, H.P.; Vu, T.H.; Ryan, A.M.; Kowalski, J.; Werb, Z.; Ferrara, N. VEGF couples hypertrophic cartilage remodeling, ossification and angiogenesis during endochondral bone formation. *Nat. Med.* **1999**, *5*, 623–628. [CrossRef]
83. Street, J.; Bao, M.; de Guzman, L.; Bunting, S.; Peale, F.V., Jr.; Ferrara, N.; Steinmetz, H.; Hoeffel, J.; Cleland, J.L.; Daugherty, A.; et al. Vascular endothelial growth factor stimulates bone repair by promoting angiogenesis and bone turnover. *Proc. Natl. Acad. Sci. USA* **2002**, *99*, 9656–9661. [CrossRef] [PubMed]
84. Henriksen, K.; Karsdal, M.; Delaisse, J.M.; Engsig, M.T. RANKL and vascular endothelial growth factor (VEGF) induce osteoclast chemotaxis through an ERK1/2-dependent mechanism. *J. Biol. Chem.* **2003**, *278*, 48745–48753. [CrossRef]
85. Peng, H.; Wright, V.; Usas, A.; Gearhart, B.; Shen, H.C.; Cummins, J.; Huard, J. Synergistic enhancement of bone formation and healing by stem cell-expressed VEGF and bone morphogenetic protein-4. *J. Clin. Investig.* **2002**, *110*, 751–759. [CrossRef] [PubMed]
86. Schipani, E.; Maes, C.; Carmeliet, G.; Semenza, G.L. Regulation of osteogenesis-angiogenesis coupling by HIFs and VEGF. *J. Bone Miner. Res.* **2009**, *24*, 1347–1353. [CrossRef] [PubMed]
87. Dun, X.P.; Carr, L.; Woodley, P.K.; Barry, R.W.; Drake, L.K.; Mindos, T.; Roberts, S.L.; Lloyd, A.C.; Parkinson, D.B. Macrophage-Derived Slit3 Controls Cell Migration and Axon Pathfinding in the Peripheral Nerve Bridge. *Cell Rep.* **2019**, *26*, 1458–1472.e1454. [CrossRef] [PubMed]
88. Geutskens, S.B.; Hordijk, P.L.; van Hennik, P.B. The chemorepellent Slit3 promotes monocyte migration. *J. Immunol.* **2010**, *185*, 7691–7698. [CrossRef]
89. Gorski, J.P.; Hankenson, K.D. *Secreted Noncollagenous Proteins of Bone*, 4th ed.; Academic Press: Cambridge, MA, USA, 2019.
90. Franz-Odendaal, T.A.; Hall, B.K.; Witten, P.E. Buried alive: How osteoblasts become osteocytes. *Dev. Dyn.* **2006**, *235*, 176–190. [CrossRef]
91. Prideaux, M.; Findlay, D.M.; Atkins, G.J. Osteocytes: The master cells in bone remodelling. *Curr. Opin. Pharmacol.* **2016**, *28*, 24–30. [CrossRef]
92. Qin, L.; Liu, W.; Cao, H.; Xiao, G. Molecular mechanosensors in osteocytes. *Bone Res.* **2020**, *8*, 23. [CrossRef]
93. Bonewald, L.F. Generation and function of osteocyte dendritic processes. *J. Musculoskelet. Neuronal Interact.* **2005**, *5*, 321–324.
94. Prasadam, I.; Zhou, Y.; Du, Z.; Chen, J.; Crawford, R.; Xiao, Y. Osteocyte-induced angiogenesis via VEGF-MAPK-dependent pathways in endothelial cells. *Mol. Cell Biochem.* **2014**, *386*, 15–25. [CrossRef] [PubMed]
95. Kogianni, G.; Mann, V.; Noble, B.S. Apoptotic bodies convey activity capable of initiating osteoclastogenesis and localized bone destruction. *J. Bone Miner. Res.* **2008**, *23*, 915–927. [CrossRef]
96. Oranger, A.; Brunetti, G.; Colaianni, G.; Tamma, R.; Carbone, C.; Lippo, L.; Mori, G.; Pignataro, P.; Cirulli, N.; Zerlotin, R.; et al. Sclerostin stimulates angiogenesis in human endothelial cells. *Bone* **2017**, *101*, 26–36. [CrossRef]
97. Cheung, W.Y.; Liu, C.; Tonelli-Zasarsky, R.M.; Simmons, C.A.; You, L. Osteocyte apoptosis is mechanically regulated and induces angiogenesis in vitro. *J. Orthop. Res.* **2011**, *29*, 523–530. [CrossRef] [PubMed]
98. Schaffler, M.B.; Cheung, W.Y.; Majeska, R.; Kennedy, O. Osteocytes: Master orchestrators of bone. *Calcif. Tissue Int.* **2014**, *94*, 5–24. [CrossRef] [PubMed]
99. Kindle, L.; Rothe, L.; Kriss, M.; Osdoby, P.; Collin-Osdoby, P. Human microvascular endothelial cell activation by IL-1 and TNF-alpha stimulates the adhesion and transendothelial migration of circulating human CD14+ monocytes that develop with RANKL into functional osteoclasts. *J. Bone Miner. Res.* **2006**, *21*, 193–206. [CrossRef]

100. Cheung, W.Y.; Simmons, C.A.; You, L. Osteocyte apoptosis regulates osteoclast precursor adhesion via osteocytic IL-6 secretion and endothelial ICAM-1 expression. *Bone* **2012**, *50*, 104–110. [CrossRef] [PubMed]
101. Ma, Y.V.; Xu, L.; Mei, X.; Middleton, K.; You, L. Mechanically stimulated osteocytes reduce the bone-metastatic potential of breast cancer cells in vitro by signaling through endothelial cells. *J. Cell Biochem.* **2018**. [CrossRef]
102. Chen, H.; Liu, W.; Wu, X.; Gou, M.; Shen, J.; Wang, H. Advanced glycation end products induced IL-6 and VEGF-A production and apoptosis in osteocyte-like MLO-Y4 cells by activating RAGE and ERK1/2, P38 and STAT3 signalling pathways. *Int. Immunopharmacol.* **2017**, *52*, 143–149. [CrossRef]
103. Asadipooya, K.; Uy, E.M. Advanced Glycation End Products (AGEs), Receptor for AGEs, Diabetes, and Bone: Review of the Literature. *J. Endocr. Soc.* **2019**, *3*, 1799–1818. [CrossRef]
104. Shanbhogue, V.V.; Mitchell, D.M.; Rosen, C.J.; Bouxsein, M.L. Type 2 diabetes and the skeleton: New insights into sweet bones. *Lancet Diabetes Endocrinol.* **2016**, *4*, 159–173. [CrossRef]
105. Heidari, F.; Rabizadeh, S.; Rajab, A.; Heidari, F.; Mouodi, M.; Mirmiranpour, H.; Esteghamati, A.; Nakhjavani, M. Advanced glycation end-products and advanced oxidation protein products levels are correlates of duration of type 2 diabetes. *Life Sci.* **2020**, *260*, 118422. [CrossRef] [PubMed]
106. Piccoli, A.; Cannata, F.; Strollo, R.; Pedone, C.; Leanza, G.; Russo, F.; Greto, V.; Isgrò, C.; Quattrocchi, C.C.; Massaroni, C.; et al. Sclerostin Regulation, Microarchitecture, and Advanced Glycation End-Products in the Bone of Elderly Women With Type 2 Diabetes. *J. Bone Miner. Res.* **2020**, *35*, 2415–2422. [CrossRef] [PubMed]
107. Lamb, L.S.; Alfonso, H.; Norman, P.E.; Davis, T.M.E.; Forbes, J.; Müench, G.; Irrgang, F.; Almeida, O.P.; Golledge, J.; Hankey, G.J.; et al. Advanced Glycation End Products and esRAGE Are Associated With Bone Turnover and Incidence of Hip Fracture in Older Men. *J. Clin. Endocrinol. Metab.* **2018**, *103*, 4224–4231. [CrossRef] [PubMed]
108. Moon, J.S.; Lee, S.Y.; Kim, J.H.; Choi, Y.H.; Yang, D.W.; Kang, J.H.; Ko, H.M.; Cho, J.H.; Koh, J.T.; Kim, W.J.; et al. Synergistic alveolar bone resorption by diabetic advanced glycation end products and mechanical forces. *J. Periodontol.* **2019**, *90*, 1457–1469. [CrossRef] [PubMed]
109. Craig, T.A.; Bhattacharya, R.; Mukhopadhyay, D.; Kumar, R. Sclerostin binds and regulates the activity of cysteine-rich protein 61. *Biochem. Biophys. Res. Commun.* **2010**, *392*, 36–40. [CrossRef] [PubMed]
110. Zhang, C.; Bakker, A.D.; Klein-Nulend, J.; Bravenboer, N. Studies on Osteocytes in Their 3D Native Matrix Versus 2D In Vitro Models. *Curr. Osteoporos. Rep.* **2019**, *17*, 207–216. [CrossRef] [PubMed]
111. Mabilleau, G.; Mieczkowska, A.; Edmonds, M.E. Thiazolidinediones induce osteocyte apoptosis and increase sclerostin expression. *Diabet. Med.* **2010**, *27*, 925–932. [CrossRef]
112. Papanicolaou, S.E.; Phipps, R.J.; Fyhrie, D.P.; Genetos, D.C. Modulation of sclerostin expression by mechanical loading and bone morphogenetic proteins in osteogenic cells. *Biorheology* **2009**, *46*, 389–399. [CrossRef]
113. Jensen, C.; Teng, Y. Is It Time to Start Transitioning From 2D to 3D Cell Culture? *Front. Mol. Biosci.* **2020**, *7*, 33. [CrossRef]
114. Iordachescu, A.; Amin, H.D.; Rankin, S.M.; Williams, R.L.; Yapp, C.; Bannerman, A.; Pacureanu, A.; Addison, O.; Hulley, P.A.; Grover, L.M. An In Vitro Model for the Development of Mature Bone Containing an Osteocyte Network. *Adv. Biosyst.* **2018**, *2*, 1700156. [CrossRef]
115. Akiva, A.; Melke, J.; Ansari, S.; Liv, N.; van der Meijden, R.; van Erp, M.; Zhao, F.; Stout, M.; Nijhuis, W.H.; de Heus, C.; et al. An Organoid for Woven Bone. *Adv. Funct. Mater.* **2021**, *31*, 2010524. [CrossRef]
116. Chen, J.; Lippo, L.; Labella, R.; Tan, S.L.; Marsden, B.D.; Dustin, M.L.; Ramasamy, S.K.; Kusumbe, A.P. Decreased blood vessel density and endothelial cell subset dynamics during ageing of the endocrine system. *Embo J.* **2021**, *40*, e105242. [CrossRef] [PubMed]